

ORGANISATION EUROPÉENNE POUR LA RECHERCHE NUCLÉAIRE  
**CERN** EUROPEAN ORGANIZATION FOR NUCLEAR RESEARCH

**High-Luminosity Large Hadron Collider (HL-LHC)**  
**Preliminary Design Report**

Editors: Apollinari G.  
Béjar Alonso I. (Executive Editor)  
Brüning O.  
Lamont M.  
Rossi L.

ISBN 978-92-9083-422-9 (paperback)  
ISBN 978-92-9083-423-6 (PDF)  
ISSN 0007-8328  
DOI <http://dx.doi.org/10.5170/CERN-2015-005>

Available online at <https://cds.cern.ch/>

Copyright © CERN, 2015

© Creative Commons Attribution 4.0

Knowledge transfer is an integral part of CERN's mission.

CERN publishes this report Open Access under the Creative Commons Attribution 4.0 license (<http://creativecommons.org/licenses/by/4.0/>) in order to permit its wide dissemination and use.

The submission of a contribution to a CERN Yellow Report shall be deemed to constitute the contributor's agreement to this copyright and license statement. Contributors are requested to obtain any clearances that may be necessary for this purpose.

This report is indexed in: CERN Document Server (CDS), INSPIRE.

This report should be cited as:

High-Luminosity Large Hadron Collider (HL-LHC). Preliminary Design Report, edited by G. Apollinari, I. Béjar Alonso, O. Brüning, M. Lamont, L. Rossi, CERN-2015-005 (CERN, Geneva, 2015), DOI: <http://dx.doi.org/10.5170/CERN-2015-005>

A contribution in this report should be cited as:

[Author name(s)], in High-Luminosity Large Hadron Collider (HL-LHC). Preliminary Design Report, edited by G. Apollinari, I. Béjar Alonso, O. Brüning, M. Lamont, L. Rossi, CERN-2015-005 (CERN, Geneva, 2015), pp. [first page] – [lastpage], DOI: <http://dx.doi.org/10.5170/CERN-2015-005>. [first page]

## Preface

The High Luminosity LHC (HL-LHC) Project was setup in 2010 by the CERN Director for Accelerators and Technology, Dr. Steve Myers, following a change of strategy and subsequent merging of the LHC upgrade Phase I and Phase II into one unique project. To this end CERN in consortium with 15 European Institutions applied in November 2010 to the call for European funding under the 7th Framework Programme Design Study category: the application was approved with full budget in 2011 with the name FP7 High Luminosity Large Hadron Collider Design Study (also known as HiLumi LHC, Grant n. 284404).

The new European Strategy for Particle Physics, adopted by the special CERN Council of Brussels on 30 May 2013, placed HL-LHC as a first priority project for the next decade. Consequently, CERN management inserted the project in the Medium Term Plan (5-year plan) and a kick off meeting of HL-LHC as a construction project was swiftly organized with the strong support of the newly designated CERN Director of Accelerators and Technology, Dr. Frédérick Bordry, in Daresbury on 11 November 2013.

This Preliminary Design Report is the main deliverable of the Design Study phase period 2011-2014 and served as a reference for the international Cost and Schedule Review called by the CERN Director of Accelerators and Technology in March 2015. Following the very positive results of the reviews, the CERN management endorsed the cost and plan (with some changes mainly related to civil engineering and the financial profile) and the CERN Council approved the project in September 2015 (formal approval for the MTP period 2016-2020, and endorsement of the full Cost-to-Completion until 2026).

The project leadership is particularly grateful to the CERN management for its continuous support and encouragement and in particular to the Director-General Rolf Heuer for his personal engagement in having the project initiated and approved during his mandate.

Lucio Rossi, HL-LHC Project Leader  
Oliver Brüning, HL-LHC Deputy Project Leader



## **Abstract**

The Large Hadron Collider (LHC) is one of the largest scientific instruments ever built. Since opening up a new energy frontier for exploration in 2010, it has gathered a global user community of about 7,000 scientists working in fundamental particle physics and the physics of hadronic matter at extreme temperature and density. To sustain and extend its discovery potential, the LHC will need a major upgrade in the 2020s. This will increase its luminosity (rate of collisions) by a factor of five beyond the original design value and the integrated luminosity (total collisions created) by a factor ten. The LHC is already a highly complex and exquisitely optimised machine so this upgrade must be carefully conceived and will require about ten years to implement. The new configuration, known as High Luminosity LHC (HL-LHC), will rely on a number of key innovations that push accelerator technology beyond its present limits. Among these are cutting-edge 11-12 tesla superconducting magnets, compact superconducting cavities for beam rotation with ultra-precise phase control, new technology and physical processes for beam collimation and 300 metre-long high-power superconducting links with negligible energy dissipation. The present document describes the technologies and components that will be used to realise the project and is intended to serve as the basis for the detailed engineering design of HL-LHC.



# Table of contents

TABLE OF CONTENTS .....	VII
TABLE OF FIGURES .....	XIII
TABLE OF TABLES .....	XXI
CONTRIBUTOR LIST .....	XXIII
<b>1 HIGH LUMINOSITY LARGE HADRON COLLIDER HL-LHC .....</b>	<b>1</b>
1.1 INTRODUCTION .....	1
1.2 HL-LHC IN A NUTSHELL .....	2
1.2.1 Luminosity .....	4
1.2.2 Present luminosity limitations and hardware constraints.....	4
1.2.3 Luminosity levelling, availability.....	6
1.2.4 HL-LHC parameters and main systems for the upgrade.....	7
1.2.5 Planning and costings .....	10
1.3 THE COLLABORATION.....	12
1.3.1 FP7-Hilumi LHC.....	12
1.3.2 LHC Accelerator R&D Program (LARP) .....	14
1.3.3 KEK.....	16
1.3.4 Other collaborations.....	16
1.4 GOVERNANCE AND PROJECT STRUCTURE .....	17
1.5 REFERENCES .....	19
<b>2 MACHINE LAYOUT AND PERFORMANCE .....</b>	<b>21</b>
2.1 PERFORMANCE GOALS (NOMINAL SCHEME) .....	21
2.1.1 Parameter space and basic parameter choices.....	22
2.2 PROPOSED SYSTEMS UPGRADES AND IMPROVEMENTS .....	26
2.2.1 Insertion region magnets .....	26
2.2.2 TAXS/TAXN absorbers .....	27
2.2.3 Crab cavities .....	27
2.2.4 Collimation .....	28
2.2.5 New cold powering.....	28
2.2.6 Enhanced machine protection and remote handling .....	29
2.2.7 New cryogenics plants and distribution .....	29
2.2.8 Enhanced beam instrumentation .....	29
2.2.9 Beam transfer and kickers.....	30
2.3 BASELINE OPTICS AND LAYOUT.....	30
2.3.1 Basic optics and layout choices for the High Luminosity insertions .....	30
2.3.2 Target field quality and dynamic aperture.....	35
2.4 PERFORMANCE .....	39
2.4.1 Beam stability.....	39
2.4.2 Beam–beam effects.....	41
2.4.3 Beam-induced heat load on the cryogenic system.....	44
2.4.4 Luminosity performance.....	46
2.5 VARIANTS AND OPTIONS .....	50
2.5.1 Pile-up density management.....	51
2.5.2 Alternative scenarios.....	51
2.6 THE HL-LHC AS A NUCLEUS–NUCLEUS COLLIDER .....	51
2.7 ACKNOWLEDGEMENTS.....	53
2.8 REFERENCES .....	53

<b>3</b>	<b>INSERTION MAGNETS .....</b>	<b>61</b>
3.1	OVERVIEW .....	61
3.2	TRIPLET .....	64
3.3	ORBIT CORRECTORS .....	67
3.4	HIGH-ORDER CORRECTORS .....	68
3.5	SEPARATION DIPOLE D1.....	70
3.6	RECOMBINATION DIPOLE D2.....	72
3.7	D2 AND Q4 CORRECTORS .....	73
3.8	LARGE APERTURE TWO-IN-ONE QUADRUPOLE Q4 .....	73
3.9	Q5 .....	74
3.10	POWERING.....	75
3.11	COOLING .....	75
3.12	INSTRUMENTATION .....	76
3.13	TEST .....	77
3.14	REFERENCES .....	77
<b>4</b>	<b>RF SYSTEMS .....</b>	<b>81</b>
4.1	INTRODUCTION .....	81
4.2	CRAB CAVITIES .....	81
4.2.1	<i>Beam and RF system parameters.....</i>	<i>82</i>
4.2.2	<i>RF cavity design.....</i>	<i>83</i>
4.2.3	<i>Beam loading and RF power .....</i>	<i>84</i>
4.2.4	<i>RF power coupler.....</i>	<i>85</i>
4.2.5	<i>Coupled bunch instabilities.....</i>	<i>85</i>
4.2.6	<i>Impedance budget.....</i>	<i>86</i>
4.2.7	<i>Higher order mode couplers.....</i>	<i>87</i>
4.2.8	<i>RF multipoles.....</i>	<i>88</i>
4.2.9	<i>Lorentz force detuning and multipacting .....</i>	<i>88</i>
4.2.10	<i>Cryomodule and integration .....</i>	<i>88</i>
4.2.11	<i>RF powering and control architecture .....</i>	<i>95</i>
4.2.12	<i>Low level RF architecture and operational scenarios.....</i>	<i>97</i>
4.2.13	<i>Cavity failure scenarios .....</i>	<i>98</i>
4.2.14	<i>Failure scenario mitigation .....</i>	<i>98</i>
4.2.15	<i>Heat loads and cryogenics .....</i>	<i>99</i>
4.2.16	<i>Vacuum system.....</i>	<i>100</i>
4.2.17	<i>Interlocks for machine protection .....</i>	<i>100</i>
4.2.18	<i>SM18 and SPS beam tests.....</i>	<i>100</i>
4.3	HARMONIC SYSTEMS .....	103
4.4	TRANSVERSE DAMPER (ADT) UPGRADE .....	105
4.5	REFERENCES .....	105
<b>5</b>	<b>COLLIMATION SYSTEM.....</b>	<b>109</b>
5.1	LHC MULTI-STAGE COLLIMATION SYSTEM.....	109
5.1.1	<i>Motivation.....</i>	<i>109</i>
5.1.2	<i>Collimation system inherited from the LHC.....</i>	<i>110</i>
5.2	BASELINE UPGRADES TO THE LHC COLLIMATION SYSTEM .....	113
5.2.1	<i>Upgrades for cleaning improvement.....</i>	<i>113</i>
5.2.2	<i>Upgrades for impedance improvement.....</i>	<i>118</i>
5.2.3	<i>Upgrades to the collimation of the incoming beam in the experimental IRs .....</i>	<i>120</i>
5.3	ADVANCED COLLIMATION CONCEPTS .....	121
5.3.1	<i>Halo diffusion control techniques.....</i>	<i>121</i>



5.3.2	<i>Crystal collimation</i> .....	124
5.3.3	<i>Improved optics scenarios for collimation insertions</i> .....	125
5.3.4	<i>Rotatory collimator design</i> .....	125
5.4	OTHER COLLIMATORS FROM THE PRESENT SYSTEM REQUIRED IN THE HL-LHC .....	125
5.4.1	<i>IR3 and IR7 primary collimators (target collimator primary and TCP with pick-up)</i> .....	126
5.4.2	<i>IR3 and IR7 secondary collimators (target collimator secondary graphite)</i> .....	126
5.4.3	<i>IR3 and IR7 active shower absorbers collimators (target collimator long absorber)</i> .....	127
5.4.4	<i>IR6 secondary collimators with pick-up (target collimator secondary with pick-up)</i> .....	127
5.4.5	<i>Passive absorbers in IR3 and IR7 (TCAPA, TCAPB, TCAPC, TCAPD)</i> .....	127
5.4.6	<i>Tertiary collimators with pick-up in the experimental regions (target collimator tertiary with pick-up)</i> ..	128
5.4.7	<i>Physics debris collimators in the experimental regions (Target Collimators Long - TCL)</i> .....	128
5.5	REFERENCES .....	128
<b>6</b>	<b>COLD POWERING .....</b>	<b>131</b>
6.1	OVERVIEW .....	131
6.1.1	<i>Cold Powering Systems at LHC P1, P5, and P7</i> .....	132
6.1.2	<i>Superconducting link</i> .....	133
6.2	COLD POWERING SYSTEM DESIGN.....	135
6.2.1	<i>Cryostat for the superconducting link</i> .....	135
6.3	INTERFACES TO THE SUPERCONDUCTING LINK .....	136
6.3.1	<i>Electrical interface between the superconducting link and the current leads</i> .....	136
6.3.2	<i>Cryogenic interface between the superconducting link and the current leads</i> .....	136
6.3.3	<i>Control</i> .....	137
6.4	INTERFACE TO THE LHC MACHINE .....	137
6.4.1	<i>General</i> .....	137
6.4.2	<i>Interface cryostat for the HL-LHC insertions</i> .....	137
6.4.3	<i>Interface cryostat for the matching sections</i> .....	137
6.4.4	<i>Interface cryostat for the arcs</i> .....	138
6.5	INTEGRATION OF THE COLD POWERING SYSTEMS IN THE LHC MACHINE .....	138
6.5.1	<i>Integration of the Cold Powering Systems at LHC P7</i> .....	138
6.5.2	<i>Integration of the Cold Powering Systems at LHC P1</i> .....	140
6.5.3	<i>Integration of the Cold Powering Systems at LHC P5</i> .....	141
6.6	POWERING LAYOUT.....	142
6.7	POWER CONVERTERS.....	143
6.7.1	<i>Performance of the power converters</i> .....	143
6.7.2	<i>Location of the power converters</i> .....	144
6.7.3	<i>Power converters for the HL-LHC</i> .....	144
6.8	RADIATION-TOLERANT POWER CONVERTERS .....	145
6.9	REFERENCE.....	146
<b>7</b>	<b>MACHINE PROTECTION, INTERLOCKS AND AVAILABILITY .....</b>	<b>147</b>
7.1	MACHINE PROTECTION WITH A 700 MJ BEAM .....	147
7.2	PROTECTION AGAINST UNCONTROLLED BEAM LOSSES.....	148
7.2.1	<i>Beam interlock system</i> .....	150
7.2.2	<i>Fast magnet current change monitor</i> .....	151
7.3	MAGNET POWERING PROTECTION.....	152
7.3.1	<i>Quench protection system</i> .....	152
7.3.2	<i>Energy extraction system</i> .....	153
7.3.3	<i>Powering interlock system</i> .....	153
7.3.4	<i>Warm magnet interlock system (WIC)</i> .....	154
7.4	AVAILABILITY REQUIREMENTS TO ACHIEVE HL-LHC GOALS FOR INTEGRATED LUMINOSITY .....	154

7.5	REFERENCES .....	156
<b>8</b>	<b>INTERFACE WITH EXPERIMENTS .....</b>	<b>157</b>
8.1	INTRODUCTION .....	157
8.2	INTERACTION REGIONS.....	157
8.3	EXPERIMENTAL BEAM PIPES .....	158
8.4	THE PASSIVE FORWARD ABSORBERS.....	159
8.4.1	<i>The charged particle passive absorber – TAXS</i> .....	159
8.4.2	<i>The neutral particle passive absorber – TAXN</i> .....	159
8.5	REFERENCES .....	160
<b>9</b>	<b>CRYOGENICS FOR THE HL-LHC.....</b>	<b>161</b>
9.1	INTRODUCTION .....	161
9.2	LHC MACHINE UPGRADES .....	162
9.2.1	<i>Upgraded beam parameters and constraints</i> .....	162
9.3	TEMPERATURE LEVEL AND HEAT LOADS .....	164
9.4	IMPACT ON EXISTING SECTOR CRYOGENIC PLANTS.....	165
9.5	NEW CRYOGENICS FOR POINT 4 INSERTION.....	167
9.6	NEW CRYOGENICS FOR HIGH LUMINOSITY INSERTIONS AT POINT 1 AND POINT 5 .....	168
9.7	BUILDING AND GENERAL SERVICE REQUIREMENT .....	169
9.8	CONCLUSIONS.....	169
<b>10</b>	<b>ENERGY DEPOSITION AND RADIATION TO ELECTRONICS.....</b>	<b>171</b>
10.1	CHARACTERIZATION OF THE RADIATION SOURCE.....	171
10.2	POWER AND DOSE EVALUATIONS CONCERNING THE TRIPLET-D1 REGION.....	172
10.2.1	<i>FLUKA–MARS modeling</i> .....	172
10.2.2	<i>Operational radiation loads</i> .....	174
10.2.3	<i>Lifetime radiation loads</i> .....	174
10.3	CRITICAL DEPENDENCIES.....	175
10.4	IMPACT ON THE MATCHING SECTION AND PROTECTION STRATEGY.....	177
10.5	EXPOSURE OF THE SUPERCONDUCTING LINKS.....	179
10.6	RADIATION TO ELECTRONICS .....	181
10.7	REFERENCES .....	185
<b>11</b>	<b>11 T DIPOLE FOR THE DISPERSION SUPPRESSOR COLLIMATORS .....</b>	<b>187</b>
11.1	INTRODUCTION .....	187
11.2	THE CRYO-ASSEMBLY .....	187
11.2.1	<i>Description</i> .....	187
11.2.2	<i>Equipment parameters</i> .....	188
11.3	THE 11 T DIPOLE .....	189
11.3.1	<i>Description</i> .....	189
11.3.2	<i>Equipment parameters</i> .....	191
11.3.3	<i>Protection</i> .....	193
11.3.4	<i>Radiation</i> .....	194
11.3.5	<i>Installation and dismantling</i> .....	194
11.4	INVENTORY OF UNITS TO BE INSTALLED AND SPARE POLICY .....	194
11.5	REFERENCES .....	194
<b>12</b>	<b>VACUUM SYSTEM .....</b>	<b>195</b>
12.1	OVERVIEW .....	195
12.2	BEAM VACUUM REQUIREMENTS .....	195
12.3	VACUUM LAYOUT REQUIREMENTS.....	196

12.3.1	Room temperature vacuum system requirements.....	197
12.3.2	Cryogenic temperature beam vacuum system requirements .....	198
12.4	INSULATION VACUUM REQUIREMENTS .....	198
12.5	EXPERIMENTAL VACUUM SYSTEM REQUIREMENTS .....	199
12.5.1	High luminosity experiments: ATLAS and CMS .....	200
12.5.2	ALICE and LHCb experiments .....	201
12.6	BEAM SCREEN REQUIREMENTS .....	202
12.6.1	Shielded beam screen .....	203
12.6.2	Non-shielded beam screen.....	204
12.6.3	Vacuum beam line interconnection .....	204
12.7	REFERENCES .....	204
<b>13</b>	<b>BEAM INSTRUMENTATION AND LONG-RANGE BEAM–BEAM COMPENSATION .....</b>	<b>207</b>
13.1	INTRODUCTION .....	207
13.2	BEAM LOSS MEASUREMENT .....	207
13.2.1	Beam loss monitors for the HL-LHC triplet magnets.....	208
13.2.2	A rad-tolerant application-specific integrated circuit for the HL-LHC beam loss monitoring system ...	209
13.3	BEAM POSITION MONITORING.....	210
13.3.1	Current performance and limitations .....	210
13.3.2	A high resolution orbit measurement system for the HL-LHC.....	211
13.3.3	High directivity strip-line pick-ups for the HL-LHC insertion regions.....	212
13.3.4	Collimator beam position monitors .....	213
13.4	BEAM PROFILE MEASUREMENTS .....	213
13.4.1	Fast wire scanners .....	213
13.4.2	A Beam gas vertex profile monitor (BGV).....	214
13.5	DIAGNOSTICS FOR CRAB CAVITIES.....	215
13.5.1	Bunch shape monitoring using electromagnetic pick-ups .....	215
13.5.2	Bunch shape monitoring using streak cameras .....	215
13.6	HALO DIAGNOSTICS.....	216
13.7	LUMINOSITY MEASUREMENT.....	217
13.8	LONG-RANGE BEAM–BEAM COMPENSATION .....	217
13.8.1	Long-range beam–beam demonstrator.....	218
13.9	REFERENCES .....	219
<b>14</b>	<b>INJECTION AND DUMPING SYSTEMS.....</b>	<b>221</b>
14.1	INJECTION AND DUMPING SYSTEMS OVERVIEW .....	221
14.2	INJECTION SYSTEMS.....	221
14.2.1	Injection absorber (TDIS).....	222
14.2.2	Auxiliary injection protection collimator (TCLIA).....	223
14.2.3	Auxiliary injection protection collimator [TCLIB].....	224
14.2.4	Injection protection masks TCDD and TCDDM.....	224
14.2.5	Injection protection mask (TCLIM) .....	225
14.2.6	Injection kicker magnet (MKI).....	225
14.3	BEAM DUMPING SYSTEM.....	226
14.3.1	Beam dumping system limitations.....	226
14.3.2	Beam dumping system absorber (TCDS).....	227
14.4	REFERENCES .....	227
<b>15</b>	<b>INTEGRATION AND (DE-)INSTALLATION.....</b>	<b>229</b>
15.1	GEOGRAPHICAL DISTRIBUTION OF HL-LHC UPGRADE INTERVENTIONS.....	229
15.2	POINT 4.....	229

15.3	POINT 7.....	230
15.3.1	<i>The horizontal superconducting links .....</i>	230
15.3.2	<i>New collimators in the dispersion suppressor.....</i>	231
15.4	POINT 2.....	231
15.5	POINT 6.....	231
15.6	POINT 1 AND POINT 5 .....	231
15.6.1	<i>LHC machine tunnel .....</i>	231
15.6.2	<i>Existing LHC tunnel service areas.....</i>	232
15.6.3	<i>New HL-LHC tunnel service areas.....</i>	232
15.6.4	<i>New connection from the LHC tunnel and HL-LHC service areas to the surface .....</i>	234
15.6.5	<i>New surface installation .....</i>	234
15.6.6	<i>Activity sequence considerations .....</i>	236
<b>16</b>	<b>COMMISSIONING AND OPERATION .....</b>	<b>237</b>
16.1	COMMISSIONING AND OPERATION .....	237
16.1.1	<i>The nominal cycle.....</i>	237
16.1.2	<i>Availability and operational efficiency.....</i>	238
16.1.3	<i>Discussion.....</i>	241
16.2	HARDWARE COMMISSIONING.....	241
16.2.1	<i>Commissioning of the superconducting circuits.....</i>	241
16.2.2	<i>Electrical Quality Assurance tests .....</i>	242
16.2.3	<i>Powering tests .....</i>	242
16.3	HARDWARE COMMISSIONING OF THE HL COLLIMATION SYSTEM.....	244
16.4	COMMISSIONING OF THE CRYOGENIC SYSTEMS .....	244
16.5	COMMISSIONING OF THE CRAB CAVITIES.....	244
16.6	COMMISSIONING WITH BEAM .....	245
16.6.1	<i>Operation with heavy ions .....</i>	246
16.7	REFERENCES .....	248
<b>17</b>	<b>SAFETY .....</b>	<b>249</b>
17.1	RADIATION TO PERSONNEL .....	249
17.1.1	<i>Design constraints.....</i>	249
17.1.2	<i>The As Low As Reasonably Achievable (ALARA) principle in the design of the Long Straight Sections.....</i>	249
17.1.3	<i>The FLUKA Monte Carlo code for radiation protection studies.....</i>	250
17.1.4	<i>FLUKA simulations .....</i>	250
17.1.5	<i>Results.....</i>	251
17.1.6	<i>Conclusions .....</i>	254
17.2	GENERAL SAFETY .....	254
17.2.1	<i>Implementation of safety in the HL-LHC.....</i>	254
17.2.2	<i>Launch Safety Agreement (LSA).....</i>	254
17.2.3	<i>Safety folder, safety files and safety documentation.....</i>	254
17.3	REFERENCES .....	256
<b>A.</b>	<b>LIST OF MACHINE AND BEAM PARAMETERS.....</b>	<b>259</b>
A.1.	NOMINAL BEAM PARAMETERS.....	259
A.2.	MAIN MACHINE PARAMETERS .....	260
A.3.	MAIN INSERTION REGION MAGNET PARAMETERS .....	261
A.4.	FIELD ERROR SPECIFICATION FOR THE NEW INSERTION REGION MAGNETS .....	262
A.5.	REFERENCES .....	267
<b>B.</b>	<b>HL-LHC ACRONYMS.....</b>	<b>271</b>

## Table of figures

FIGURE 1-1: LHC BASELINE PLAN FOR THE NEXT DECADE AND BEYOND SHOWING THE ENERGY OF THE COLLISIONS (UPPER RED LINE) AND LUMINOSITY (LOWER GREEN LINES). THE FIRST LONG SHUTDOWN (LS1) IN 2013–2014 WILL ALLOW THE DESIGN PARAMETERS OF BEAM ENERGY AND LUMINOSITY TO BE REACHED. THE SECOND LONG SHUTDOWN (LS2) IN 2018–2019, WILL CONSOLIDATE LUMINOSITY AND RELIABILITY AS WELL AS THE UPGRADING OF THE LHC INJECTORS. AFTER LS3, 2023–2025, THE MACHINE WILL BE IN THE HIGH LUMINOSITY CONFIGURATION (HL-LHC).2

FIGURE 1-2: LHC LUMINOSITY PLAN FOR THE NEXT DECADE, BOTH PEAK (RED DOTS) AND INTEGRATED (BLUE LINE). MAIN SHUTDOWN PERIODS ARE INDICATED. .... 3

FIGURE 1-3: (A) LUMINOSITY PROFILE FOR A SINGLE LONG FILL: STARTING AT NOMINAL PEAK LUMINOSITY (BLACK LINE), WITH UPGRADE NO LEVELLING (RED LINE), WITH LEVELLING (BLUE LINE). (B) LUMINOSITY PROFILE WITH OPTIMIZED RUN TIME, WITHOUT AND WITH LEVELLING (BLUE AND RED DASHED LINES), AND AVERAGE LUMINOSITY IN BOTH CASES (SOLID LINES). .... 6

FIGURE 1-4: LUMINOSITY CYCLE FOR HL-LHC WITH LEVELLING AND A SHORT DECAY (OPTIMIZED FOR INTEGRATED LUMINOSITY). .... 7

FIGURE 1-5: BEHAVIOUR OF GEOMETRICAL LUMINOSITY REDUCTION FACTOR VS.  $B^*$  FOR A CONSTANT NORMALIZED BEAM SEPARATION WITH THE INDICATION OF TWO OPERATIONAL POINTS: NOMINAL LHC AND HL-LHC. THE BUNCH CROSSING SKETCH SHOWS THE REDUCTION MECHANISM. .... 9

FIGURE 1-6: EFFECT OF THE CRAB CAVITY ON THE BEAM (SMALL ARROWS INDICATE THE TORQUE ON THE BUNCH GENERATED BY THE TRANSVERSE RF FIELD). .... 9

FIGURE 1-7: FORECAST FOR PEAK LUMINOSITY (RED DOTS) AND INTEGRATED LUMINOSITY (BLUE LINE) IN THE HL-LHC ERA, FOR THE CASE OF ULTIMATE HL-LHC PARAMETERS. NOTE THAT FOR THE SAKE OF SIMPLICITY THERE IS NO LEARNING CURVE FOR LUMINOSITY AFTER LS3. .... 10

FIGURE 1-8: SCHEMATIC REPRESENTATION OF THE MAIN HL-LHC MILESTONES ..... 11

FIGURE 1-9: BUDGET ALLOCATION 2015 TO 2025 ..... 11

FIGURE 1-10: TIMELINE OF THE VARIOUS COLLABORATION BRANCHES, CONVERGING TOWARD THE LHC LUMINOSITY UPGRADE ..... 12

FIGURE 1-11: (A) TOTAL ESTIMATION OF THE COST OF THE DESIGN STUDY, SUBDIVIDED BY THE US AND JAPAN, EU INSTITUTES AND CERN. (B) TOTAL COST WITH THE US AND JAPAN REMOVED (I.E. ONLY COSTS THAT ARE ELIGIBLE FOR FUNDING BY THE EC). (C) EFFECT OF CERN WAIVING THE COST FOR TECHNICAL WORKS (RECOGNIZING THAT THE HL-LHC IS PART OF THE CORE CERN PROGRAMME FINANCED VIA THE NORMAL BUDGET), WHILE KEEPING THE EXTRA COST GENERATED BY THE MANAGEMENT AND COORDINATION OF THE PROJECT. THIS IS THE TOTAL COST DECLARED TO THE EC. (D) COST CLAIMED FROM THE EC: 50% OF THE DECLARED COST (ELIGIBLE COST REDUCED BY CERN WAIVING ACTION). .... 13

FIGURE 1-12: (A) TABLE SHOWING THE 15 MEMBERS (‘BENEFICIARIES’) OF THE FP7 HiLUMI LHC DESIGN STUDY AND (B) THE FIVE LARP LABORATORIES THAT ARE ASSOCIATED WITH THE PROJECT. .... 14

FIGURE 1-13: LEFT: IMPROVEMENT IN  $J_c$  (CURRENT DENSITY) IN Nb<sub>3</sub>Sn SUPERCONDUCTOR DURING THE LAST THREE DECADES COMPARED WITH Nb-Ti  $J_c$  PERFORMANCE. .... 15

FIGURE 1-14: (A) QUENCH PERFORMANCE OF THE LONG QUADRUPOLE (LQ), THE FIRST QUADRUPOLE DEMONSTRATING THE SCALE-UP OF Nb<sub>3</sub>Sn TECHNOLOGY TO LENGTHS OF INTEREST FOR LHC APPLICATIONS (~3 M), (B) QUENCH PERFORMANCE OF HQ02 (120 MM APERTURE) AFTER SEVERAL RE-ASSEMBLIES, SHOWING THAT IN ALL CASES THE MAGNET ACHIEVED AND PASSED THE TARGET (80% OF THE SHORT SAMPLE LIMIT (SSL)). .... 15

FIGURE 1-15: THE GENERAL GOVERNANCE SCHEME OF FP-7 HiLUMI LHC, USED FOR THE WHOLE HL-LHC PROJECT (SEE TEXT FOR DETAILS) ..... 18

FIGURE 1-16: HL-LHC PROJECT STRUCTURE, WITH FP7 PART INDICATED IN DARK GREEN. THE ORANGE BOX REFERS TO THE HIGH-FIELD MAGNETS WORK PACKAGE, WHICH WAS STARTED BEFORE THE HL-LHC IN THE FRAMEWORK OF GENERIC R&D FOR THE LHC UPGRADE. .... 18

FIGURE 2-1: (A) EXPECTED ANNUAL INTEGRATED LUMINOSITY; (B) OPTIMUM FILL LENGTH AS A FUNCTION OF THE ‘VIRTUAL’ PEAK LUMINOSITY FOR THREE DIFFERENT VALUES OF THE LUMINOSITY AT WHICH LEVELLING IS

PERFORMED. A CIRCULATING CURRENT OF 1.1 A (CORRESPONDING TO $N_{\text{BEAM}} = 6.1 \times 10^{14}$ p), A MINIMUM TURNAROUND TIME OF 3 HOURS AND A PERFORMANCE EFFICIENCY $\square$ OF 50% HAVE BEEN ASSUMED. ONLY BURN-OFF FOR A TOTAL HADRON CROSS-SECTION OF 100 MB HAS BEEN CONSIDERED FOR THE ESTIMATE OF THE BEAM POPULATION AND VIRTUAL LUMINOSITY EVOLUTION. TWO HIGH-LUMINOSITY INTERACTION POINTS HAVE BEEN ASSUMED.....	22
FIGURE 2-2: PARAMETER $R\Sigma_z/B^*$ VS. $B^*$ FOR DIFFERENT BUNCH LENGTHS FOR A ROUND OPTICS AND CONSTANT NORMALIZED LONG-RANGE BEAM-BEAM SEPARATION $D_{\text{BB}}$ (A) WITHOUT CRAB CAVITIES AND (B) WITH CRAB CAVITIES. THE SMALL EFFECT OF RF CURVATURE IN THE CRAB CAVITIES IS NOT INCLUDED. ....	24
FIGURE 2-3: OVERALL LAYOUT OF THE INSERTION REGION BETWEEN THE IP AND Q4. THE DARK BLUE AND RED AREAS REPRESENT THE $2\sigma$ BEAM ENVELOPE. THE LIGHT REGIONS CORRESPOND TO A $12\sigma$ VALUE OF THE BEAM ENVELOPE FOR AN EMITTANCE OF 3.5 MM WITH A TOLERANCE OF 20% FOR BETA-BEATING AND 2 MM OF CLOSED ORBIT DISTORTION. THE SHADED GREY AREAS IN THE TRIPLET REGION REPRESENT THE LOCATIONS OF THE PARASITIC BEAM-BEAM ENCOUNTERS.....	32
FIGURE 2-4: OPTICAL FUNCTIONS AT (A) INJECTION AND (B) COLLISION. NOTE THE DIFFERENT VERTICAL SCALES: AT COLLISION, THE BETA FUNCTIONS IN THE TRIPLETS ARE LARGE, TO PROVIDE THE LOW $B^*$ AT THE IP.....	35
FIGURE 2-5: DA OF HLHC V1.0. (A) DA AT 7 TeV WITH ADJUSTED ESTIMATED FIELD QUALITY OF NEW MAGNETS. (B) DA AT 450 GeV WITH ESTIMATED FIELD QUALITY OF NEW MAGNETS. THE R.M.S. BEAM SIZE IS THAT CORRESPONDING TO A NORMALIZED EMITTANCE OF 3.75 MM. ....	38
FIGURE 2-6: (A) FIRST ESTIMATE OF THE HORIZONTAL DIPOLAR IMPEDANCE OF HL-LHC, INCLUDING BOTH CRAB CAVITIES AND BEAM-BEAM WIRE COMPENSATORS. THE VERTICAL DIPOLAR IMPEDANCE IS SIMILAR TO THE HORIZONTAL. (B) LONGITUDINAL IMPEDANCE. ....	39
FIGURE 2-7: SINGLE-BEAM (25 NS) INTENSITY LIMIT VS. TRANSVERSE EMITTANCE WITH TRANSVERSE DAMPER (50-TURN DAMPING TIME) AT TOP ENERGY, FOR A CHROMATICITY $Q' \sim 15$ FOR THE TWO EXTREME CASES (CFC COLLIMATORS WITH ODU/SLAC CRAB CAVITIES AND MO-COATED COLLIMATORS WITHOUT CRAB CAVITIES) AND FOR POSITIVE POLARITY OF THE LANDAU OCTUPOLES. ....	41
FIGURE 2-8: MINIMUM DA FOR (A) $B^* = 40$ CM OPTICS AND (B) $B^* = 15$ CM OPTICS AS A FUNCTION OF CROSSING ANGLE FOR DIFFERENT BUNCH INTENSITIES. THE R.M.S. BEAM SIZE CORRESPONDS TO A NORMALIZED EMITTANCE OF 2.5 MM. ....	43
FIGURE 2-9: HEAT LOAD FROM E-CLOUD IN THE ARC MAIN MAGNETS AS A FUNCTION OF BUNCH INTENSITY AND SEY. ....	45
FIGURE 2-10: HEAT LOAD FROM THE E-CLOUD ALONG THE FUTURE HL-LHC TRIPLETS.....	46
FIGURE 2-11: EVOLUTION OF LUMINOSITY, PILE-UP AND PILE-UP DENSITY ASSUMING LEVELLING AT 140 EVENTS/CROSSING (A, C, E) AND 210 EVENTS/CROSSING (B, D, F) IN IP1 AND IP5. THE SMALL EFFECTS OF RF CURVATURE IN THE CRAB CAVITIES IS NOT INCLUDED. ....	48
FIGURE 2-12: EVOLUTION OF $B^*$ , EMITTANCE AND LONG-RANGE BEAM-BEAM NORMALIZED SEPARATION ( $D_{\text{BB}}$ ) FOR LEVELLING AT 140 (A, C, E) AND AT 210 EVENTS/CROSSING (B, D, F) IN IP1 AND IP5. ....	49
FIGURE 2-13: EVOLUTION OF $B^*$ IN IP8, HEAD-ON BEAM-BEAM TUNE SPREAD ASSUMING LEVELLING AT 140 EVENTS/CROSSING (A, C) AND AT 210 EVENTS/CROSSING (B, D) IN IP1 AND IP5.....	50
FIGURE 2-14: PERFORMANCE EXPECTATION OF DIFFERENT ALTERNATIVES. THE RED MARKERS REPRESENT THE BASELINE SCENARIOS (FLAT OR ROUND) FOR DIFFERENT TARGET OF TOTAL PILE-UP (140 AND 200 EVENTS PER CROSSING). IN THE CASE OF THE CRAB CAVITIES ARE ABSENT (BLACK MARKER) ANNUAL INTEGRATED LUMINOSITY COULD BE RECOVERED BY USING FLAT OPTICS FOR AN INCREASE OF THE PEAK PILE-UP DENSITY THAT CAN BE LIMITED WITH LONG-RANGE COMPENSATORS. THE CRAB-KISSING SCHEME (MAGENTA MARKERS) ON THE OTHER HAND OFFERS THE TARGET ANNUAL LUMINOSITY WITH THE MEANS TO CONTROL THE PILE-UP DENSITY AND TO REDUCE IT CONSIDERABLY WITH RESPECT TO THE NOMINAL SCHEME. PEAK PILE-UP DENSITY CAN ALSO BE LEVELLED WITH $B^*$ (MAGENTA MARKERS). IF E-CLOUD EFFECTS NEEDS TO BE MITIGATED, A 200 MHz RF SYSTEM OR THE 8B+4E FILLING SCHEMES (GREEN AND BLUE MARKERS) COULD BE DEPLOYED. ....	50
FIGURE 2-15: INITIAL LUMINOSITY FOR EACH COLLIDING BUNCH PAIR ALONG THE FULL TRAIN IN THE LHC.....	52
FIGURE 2-16: (A) TOTAL LUMINOSITY (RED) AND INTEGRATED LUMINOSITY (BLUE) DURING A FILL STARTING WITH THE BUNCH-PAIR LUMINOSITIES SHOWN IN FIGURE 2-15. (B) AVERAGE LUMINOSITY PER DAY AS A FUNCTION OF TURNAROUND TIME (DUMP TO NEXT STABLE BEAMS) WHEN FILL LENGTHS ARE OPTIMIZED, WITH LENGTHS VARYING BETWEEN 3 H AND 6 H, WITH THE LUMINOSITY DEPENDENCE SHOWN IN THE LEFT PLOT. ....	53

FIGURE 3-1: CONCEPTUAL LAYOUT OF THE IR REGION OF HL-LHC. THICK BOXES ARE MAGNETS, THIN BOXES ARE CRYOSTATS. ....	62
FIGURE 3-2: SCHEMATIC LAYOUT OF THE CURRENT IR REGION OF THE LHC. THICK BOXES ARE MAGNETS, THIN BOXES ARE CRYOSTATS. ....	62
FIGURE 3-3: BEAM SCREEN (GREY) WITH TUNGSTEN SHIELDING (DARK BROWN) AND COOLING TUBES IN Q1 (LEFTHAND SIDE) AND IN Q2-D1 (RIGHTHAND SIDE). ....	63
FIGURE 3-4: SKETCH OF TRIPLET QUADRUPOLE MAGNET CROSS-SECTION .....	65
FIGURE 3-5: (A) QUENCH HEATERS FOR THE OUTER LAYER; (B) A DESIGN FOR THE INNER LAYER. STAINLESS STEEL (SS) IN GREY AND COPPER CLADDING IN RED. ....	66
FIGURE 3-6: POSSIBLE CROSS-SECTIONS OF THE CRYOSTAT: (A) LARGER DIAMETER AND (B) ELLIPTICAL SOLUTION .....	67
FIGURE 3-7: SKETCH OF ORBIT CORRECTOR CROSS-SECTION (SHORT VERSION MCBXB, IN THE COLD MASS OF THE TRIPLET MAGNETS Q2A AND Q2B). ....	68
FIGURE 3-8: LAYOUT OF THE CORRECTOR REGION .....	68
FIGURE 3-9: (A) CROSS-SECTION OF THE SKEW QUADRUPOLE; (B) 3D VIEW OF A SEXTUPOLE .....	69
FIGURE 3-10: SKETCH OF NONLINEAR CORRECTOR CROSS-SECTIONS OF (A) NORMAL SEXTUPOLE; (B) OCTUPOLE; (C) DECAPOLE; (D) DODECAPOLE CORRECTORS .....	69
FIGURE 3-11: SKETCH OF SEPARATION DIPOLE CROSS-SECTION .....	71
FIGURE 3-12: SKETCH OF RECOMBINATION DIPOLE CROSS-SECTION. (A) ASYMMETRIC COIL; (B) MAGNET CROSS-SECTION. ....	72
FIGURE 3-13: SKETCH OF Q4 CROSS-SECTION .....	74
FIGURE 3-14: SKETCH OF BASELINE FOR TRIPLET POWERING (TRIMS NOT SHOWN) .....	75
FIGURE 3-15: SKETCH OF THE COOLING SYSTEM .....	76
FIGURE 4-1: BUNCHES COLLIDING WITH (A) A CROSSING ANGLE WITHOUT CRAB CROSSING; (B) WITH THE CRAB CROSSING. ....	82
FIGURE 4-2: COMPACT CAVITIES. (A): DOUBLE QUARTER WAVE CAVITY (DQW), COURTESY OF BROOKHAVEN NATIONAL LAB. (B) RF DIPOLE CAVITY (RFD), COURTESY OF OLD DOMINION UNIVERSITY. (C) FOUR-ROD CAVITY, COURTESY OF LANCASTER UNIVERSITY. ....	83
FIGURE 4-3: FORWARD POWER VS. CAVITY QL FOR CENTRED (RED), 1 MM OFFSET (GREEN), AND 2 MM OFFSET (BLUE) BEAMS. ASSUMED $RQ = 400 \Omega$ , 3.4 MV RF, 1.1 A DC. ....	84
FIGURE 4-4: (A) INPUT COUPLER ASSEMBLY; (B) TEST BOX FOR RF CONDITIONING .....	85
FIGURE 4-5: (A) REAL PART OF THE DEFLECTING MODE IMPEDANCE WITH A DETUNING OF 1.5 KHZ FROM FROM 400 MHZ. THE VERTICAL LINES REPRESENT THE DIFFERENCE IN $\Re\{Z\}$ EVALUATED AT $\pm 0.3 F_{REV}$ FOR THE COMPUTATION OF DAMPING RATE (MODE L = -64). (B) MODULUS OF THE CAVITY IMPEDANCE SEEN BY THE BEAM WITH THE RF FEEDBACK ON (RED) AND OFF (BLUE) NORMALIZED TO THE CAVITY IMPEDANCE AT THE FUNDAMENTAL MODE. ....	86
FIGURE 4-6: HOM FILTER FOR (A) DQW; (B) RFD .....	87
FIGURE 4-7: SCHEMATIC VIEW OF THE CAVITY WITH INTERFACES (A) DQW; (B) RFD .....	89
FIGURE 4-8: DIMENSIONAL PLOT WITH TOLERANCES OF THE DQW CAVITY .....	89
FIGURE 4-9: DIMENSIONAL PLOT WITH TOLERANCES OF THE RFD CAVITY .....	90
FIGURE 4-10: MECHANICAL STRESS INDUCED BY MAXIMUM PRESSURE ON THE DQW CAVITY INSIDE ITS HELIUM TANK. RED INDICATES REGIONS WITH HIGHEST STRESS, WHICH CAN BE TOLERATED IF CONFINED TO SMALL AREAS. ....	91
FIGURE 4-11: (A) THE DQW CAVITY INSIDE ITS HELIUM TANK WITH THE FIELD PROBE PORT (FRONT), BEAM PORT (RIGHT) AND TUNER FRAME AROUND. (B) SECTIONAL VIEW OF THE DQW CAVITY INSIDE ITS HELIUM TANK WITH THE POWER COUPLER (TOP RIGHT, ORANGE), HOM COUPLER (LEFT, TOP AND BOTTOM), AND TUNER (CENTRE, TOP, AND BOTTOM). ....	91
FIGURE 4-12: (A) THE RFD CAVITY INSIDE ITS HELIUM TANK WITH THE FIELD PROBE PORT (CENTRE LEFT), BEAM PORT (CENTRE RIGHT), TUNER FRAME AROUND HELIUM VESSEL AND TUNER ACTUATION (TOP CENTRE). (B) SCHEMATIC SECTIONAL VIEW OF THE RFD CAVITY INSIDE ITS HELIUM TANK WITH THE POWER COUPLER (ORANGE) AND HOM COUPLER (VIOLET). ....	91
FIGURE 4-13: (A) ACTUATION SYSTEM OF THE PROTOTYPE TUNING SYSTEM FOR DQW AND RFD CAVITIES. (B) CROSS-SECTION. ....	92

FIGURE 4-14: FORWARD POWER REQUIRES A FUNCTION OF $Q_{\text{EXT}}$ FOR DIFFERENT DETUNING OF THE CAVITY. THE CROSS-HATCHED AREA INDICATES THE NOMINAL RANGE OF $Q_{\text{EXT}}$ .....	93
FIGURE 4-15: CRYOMODULE LAYOUT FOR ONE SIDE OF THE INTERACTION REGION IN THE LHC .....	93
FIGURE 4-16: CRYOMODULES FOR (A) DQW CAVITY; (B) RFD CAVITY .....	94
FIGURE 4-17: (A) COLD MAGNETIC SHIELDING INSIDE THE HELIUM VESSEL; (B), MAGNETIC FIELD AMPLITUDE INSIDE THE TWO-CAVITY CM WITHOUT THE SECOND INTERNAL COLD MAGNETIC SHIELD, SCALE 0 TO 1 mT. AN EXTERNAL FIELD OF 60 mT IN THE DIRECTION PARALLEL TO X (LONGITUDINAL) IS USED. ....	95
FIGURE 4-18: SCHEMATIC OF THE RF SYSTEM LAYOUT IN (A) THE LHC TUNNEL; (B) THE ELECTRONICS RACKS IN A SHIELDED CAVERN CLOSE TO THE CAVITIES; (C) THE SURFACE BUILDING. NOTE THAT THESE ARE ONLY ESTIMATED VALUES OF SPACE REQUIREMENTS. ....	96
FIGURE 4-19: PRELIMINARY SKETCH OF A HIGH-POWER RF, CONTROLS AND LLRF LAYOUT IN A SURFACE BUILDING, DISTRIBUTED OVER TWO LEVELS. (A) LOWER LEVEL CONTAINING PUMPS AND GENERAL SERVICES; (B) UPPER LEVEL CONTAINING RF AMPLIFIERS AND EQUIPMENT RACKS. COURTESY OF C. MAGNIER AND P. FESSIA. ....	97
FIGURE 4-20: PROPOSED LLRF ARCHITECTURE FOR ONE RING AT ONE IP.....	97
FIGURE 4-21: VOLTAGE RESPONSE WITH STRONGLY COUPLED CAVITIES ACROSS THE IP AS A FUNCTION OF TIME [MS]. AT 50 MS, ONE CAVITY TRIPS (RED TRACE) AND THE OTHER ONE IS FORCED BY THE RF CONTROLLER TO FOLLOW (BLUE TRACE).....	99
FIGURE 4-22: 3D INTEGRATION OF THE CRYOMODULE, RF ASSEMBLY, AND THE CRYOGENICS IN THE SPS.....	101
FIGURE 4-23: (A) CRYOMODULE AND RF SYSTEM LAYOUT IN THE LSS44 CAVERN; (B) A 400 MHz TETRODE AMPLIFIER UNDER TEST. ....	102
FIGURE 5-1: SCHEMATIC ILLUSTRATION OF MULTI-STAGE COLLIMATION CLEANING AT THE LHC. PRIMARY AND SECONDARY COLLIMATORS (DARKEST GREY) ARE THE DEVICES CLOSEST TO THE CIRCULATING BEAM AND ARE MADE OF ROBUST CARBON-FIBRE COMPOSITES. SHOWER ABSORBERS AND TERTIARY COLLIMATORS (LIGHTER GREY) SIT AT LARGER APERTURES AND ARE MADE OF A TUNGSTEN ALLOY TO IMPROVE ABSORPTION. COLLIMATORS OF DIFFERENT FAMILIES ARE ORDERED IN A PRE-DEFINED COLLIMATION HIERARCHY THAT MUST BE RESPECTED IN ORDER TO ENSURE THE REQUIRED SYSTEM FUNCTIONALITIES. THE COLLIMATOR HIERARCHY IS ENSURED BY DEFINING COLLIMATOR SETTINGS IN UNITS OF LOCAL BEAM SIZE AT THE COLLIMATOR LOCATION .....	110
FIGURE 5-2: (A) HORIZONTAL LHC COLLIMATOR; (B) SKEW LHC COLLIMATOR. THE LATTER HAS THE VACUUM TANK OPEN TO SHOW THE TWO MOVABLE CFC JAWS. ....	111
FIGURE 5-3: PHOTOGRAPH OF THE ACTIVE ABSORBER TCLA.B6R7.B1 AS INSTALLED IN THE BETATRON CLEANING INSERTION.....	111
FIGURE 5-4: NEW CARBON/CARBON COLLIMATOR JAW WITH INTEGRATED BPMs AT EACH EXTREMITY ('BUTTONS') TO BE INSTALLED AS THE SECONDARY COLLIMATOR IN THE DUMP INSERTION IR6. A DETAIL OF THE BPM IS GIVEN ON THE LEFT HAND SIDE. A VARIANT OF THIS DESIGN, MADE WITH A GLIDCOP SUPPORT AND TUNGSTEN INSERTS ON THE ACTIVE JAW PART, WILL BE USED FOR THE TERTIARY COLLIMATORS IN ALL IRS.....	112
FIGURE 5-5: (A–C) SCHEMATIC VIEW OF THE ASSEMBLY OF TWO SHORTER 11 T DIPOLES WITH A COLLIMATOR IN BETWEEN, WHICH CAN REPLACE ONE STANDARD MAIN DIPOLE. (COURTESY OF V. PARMA.) (D) PRELIMINARY 3D MODEL OF A TCLD ASSEMBLY SHOWING THE COLLIMATOR (IN GREEN), THE TWO SHORT DIPOLE CRYOSTATS AND THE CONNECTION CRYOSTAT. NOTE THE VERY TIGHT SPACE CONSTRAINTS FOR THE COLLIMATOR UNIT.....	114
FIGURE 5-6: SIMULATED POWER DENSITY MAP IN THE HORIZONTAL PLANE OF DS DIPOLES FOR NOMINAL 7 TeV OPERATION AND A BEAM LIFETIME OF 0.2 h ( $4.5 \times 10^{11}$ PROTONS LOST PER SECOND). THE MAP MAKES A COMPARISON BETWEEN THE PRESENT LAYOUT AND A LAYOUT WITH TWO TCLDS. RESULTS CORRESPOND TO RELAXED COLLIMATOR SETTINGS. BEAM DIRECTION IS FROM THE RIGHT TO THE LEFT. FROM REF. [19]. ....	115
FIGURE 5-7: DETAIL OF ONE CORNER OF THE TCLD COLLIMATOR TO BE INSTALLED IN THE DS BETWEEN TWO NEW 11 T DIPOLES. THE PRESENT DESIGN FORESEES AN 80 CM LONG JAW MADE OF TUNGSTEN (THE FIRST OF FOUR 20 CM TUNGSTEN TILES IS SHOWN) AND WILL HAVE TWO JAWS. DESIGNS WITH TRANSVERSE RF FINGERS OR FERRITE TILES ARE BEING COMPARATIVELY ASSESSED TO REDUCE THE DETRIMENTAL EFFECTS OF TRAPPED RF MODES. ....	116
FIGURE 5-8: $1\sigma$ ENVELOPE OF THE MAIN Pb <sup>82+</sup> BEAM (VIOLET) TOGETHER WITH THE DISPERSIVE TRAJECTORIES OF IONS UNDERGOING BFPP1 (RED), BFPP2 (ORANGE), EMD1 (LIGHT GREEN), AND EMD2 (DARK GREEN), COMING OUT OF THE ALICE EXPERIMENT IN NOMINAL OPTICS. THE DS COLLIMATOR APPEARS AS A BLACK LINE. VARYING ITS	



OPENING ALLOWS DIFFERENT SECONDARY BEAMS TO BE INTERCEPTED (NOTE THAT THE ORANGE BFPP2 BEAM CARRIES ENERGIES WELL BELOW THE QUENCH LIMIT).....	117
FIGURE 5-9: (A) MO-GR PLATE RECENTLY PRODUCED BY BREVETTI BIZZ, ITALY. DIMENSIONS OF THE PLATE: 90 MM DIAMETER AND 24.3 MM THICKNESS. IT IS A MASSIVE PIECE PREPARED IN VIEW OF THE PRODUCTION OF THE LHC COLLIMATOR JAW INSERTS. (B) A DETAIL OF THE MICROSTRUCTURE, WHERE THE GRAPHITE FLAKES MATRIX WELL SINTERED WITH THE CARBON FIBERS IS VISIBLE TOGETHER WITH A FEW MOLYBDENUM CARBIDE ‘ISLANDS’ OF ABOUT 5 MM LENGTH. ....	119
FIGURE 5-10: COLLIMATION IMPEDANCE VERSUS FREQUENCY: IMPEDANCE RATIO BETWEEN MO COATING ON MO-GR (50 MM LAYER) AND PRESENT CFC JAW FOR THE REAL (SOLID) AND IMAGINARY (DOTTED) PARTS. A SECONDARY COLLIMATOR IS CONSIDERED. COURTESY OF N. MOUNET.....	119
FIGURE 5-11: PRELIMINARY DESIGN OF THE TCSMP JAW (A) AND OF ITS CROSS-SECTION (B). THE JAW ASSEMBLY FEATURES 10 MOGR BLOCKS. ALSO NOTE THAT THE JAW TAPERING IS LENGTHENED, FURTHER REDUCING ITS CONTRIBUTION TO HOM RF INSTABILITIES IN THE GEOMETRICAL TRANSITION ZONES.....	120
FIGURE 5-12: ILLUSTRATIVE VIEW (A) OF THE COLLIMATION SYSTEM WITH INTEGRATED HOLLOW E-LENS OR EQUIVALENT HALO DIFFUSION MECHANISM; (B) AN IDEAL CRYSTAL-BASED COLLIMATION. A SIMPLIFIED COLLIMATOR LAYOUT TO THAT IN FIGURE 5-1 IS ADOPTED TO SHOW THE BETATRON CLEANING FUNCTIONALITY ONLY (ONE SIDE ONLY). HALO CONTROL TECHNIQUES ARE USED TO GLOBALLY CHANGE THE DIFFUSION SPEED OF HALO PARTICLES, AND RELY ON THE FULL COLLIMATION SYSTEM REMAINING IN PLACE. CRYSTALS ENTAIL A CHANGE OF CONCEPT WHERE THE WHOLE BEAM LOSSES ARE CONCENTRATED, IDEALLY, IN ONE SINGLE BEAM ABSORBER PER PLANE. ....	122
FIGURE 5-13: PHOTOGRAPH OF THE SLAC ROTATORY COLLIMATOR PROTOTYPE JAWS BEFORE ASSEMBLY IN THE VACUUM TANK. COURTESY OF T. MARKIEWICZ (SLAC, LARP).....	125
FIGURE 6-1: SUPERCONDUCTING LINKS AT LHC P1 AND P5.....	134
FIGURE 6-2: CABLE ASSEMBLIES FOR SUPERCONDUCTING LINKS AT LHC P1 AND P5. (A) SUB-UNIT OF 20 kA CABLE, $\Phi \sim 6.5$ MM; (B) 20 kA CABLE, $\Phi \sim 19.5$ MM; (C) CONCENTRIC $2 \times 3$ kA CABLE, $\Phi \sim 8.5$ MM; (D) 0.4 kA CABLE (TOP) AND 0.12 kA CABLE (BOTTOM), $\Phi < 3$ MM; (E) 165 kA CABLE ASSEMBLY FOR LHC P1 AND P5 ( $6 \times 20$ kA, $7 \times 2 \times 3$ kA, $4 \times 0.4$ kA, $18 \times 0.12$ kA), $\Phi \sim 65$ MM. THE CABLES ARE MADE OF COPPER STABILIZER (RED) AND MGB <sub>2</sub> WIRE (GREEN). ....	134
FIGURE 6-3: TWO VIEWS OF THE TEST STATION DESIGNED AND OPERATED AT CERN FOR THE TEST OF SUPERCONDUCTING LINKS UP TO 20 M LONG. THE CABLES ARE COOLED BY FORCED FLOW OF HELIUM GAS OPERATING AT ANY TEMPERATURE FROM ABOUT 5 K TO 35 K. TEMPERATURES OF UP TO 70 K CAN BE ACHIEVED, ENABLING APPRAISAL OF CABLES MADE FROM DIFFERENT TYPES OF CONDUCTOR.....	135
FIGURE 6-4: UNDERGROUND LAYOUT AT LHC P7.....	139
FIGURE 6-5: PASSAGE THROUGH UJ76 WITH ROUTING OF THE LINKS IN THE UJ76 AREA.....	139
FIGURE 6-6: PASSAGE OF LINKS THROUGH UJ76 WITH ADDITIONAL DUCTS.....	140
FIGURE 6-7: (A) ROUTING OF THE TWO LINKS AND THE TWO HE RETURN LINES IN THE SERVICE GALLERY. (B) INSTALLATION OF THE DFH AND OF THE POWER CONVERTERS IN TZ76.....	140
FIGURE 6-8: ROUTING OF THE LINKS TO SURFACE FOR THE LOW- <i>B</i> TRIPLET RIGHT OF LHC P1.....	141
FIGURE 6-9: LAYOUT OF UNDERGROUND PREMISES AND OF SURFACE BUILDINGS AT P5.....	142
FIGURE 6-10: POWERING LAYOUT OF THE PRESENT LHC INNER TRIPLETS.....	142
FIGURE 6-11: POWERING LAYOUT OF THE HL-LHC INNER TRIPLETS.....	143
FIGURE 7-1: STORED BEAM ENERGY AS A FUNCTION OF HL-LHC BEAM MOMENTUM IN COMPARISON WITH OTHER PARTICLE ACCELERATORS.....	147
FIGURE 7-2: SOME FAILURE DETECTION TIMES AT THE LHC. THE SHORTEST FAILURE DETECTION TIME IS CURRENTLY ASSURED BY THE BLM SYSTEM, WITH A FASTEST INTEGRATION TIME OF 40 MS, WHICH IS EQUIVALENT TO HALF A LHC TURN. ....	148
FIGURE 7-3: CURRENT MPS RESPONSE TIME FROM FAILURE DETECTION TO COMPLETION OF BEAM DUMP.....	149
FIGURE 7-4: SCHEMATIC OVERVIEW OF CRAB CAVITY FAILURE CATEGORIES [5].....	150
FIGURE 7-5: SENSITIVITY ANALYSIS OF INTEGRATED LUMINOSITY TO THE MACHINE FAILURE RATE AND AVERAGE FAULT TIME.....	155
FIGURE 8-1: SCHEMATIC LAYOUT OF THE LHC WITH THE FOUR INTERACTION REGIONS THAT HOUSE THE ALICE, ATLAS, CMS, AND LHCb EXPERIMENTS. ....	157

FIGURE 9-1: OVERALL LHC CRYOGENIC LAYOUT, INCLUDING THE UPGRADED INFRASTRUCTURE .....	161
FIGURE 9-2: UPGRADED LAYOUT OF THE CONTINUOUS CRYOSTAT AT P2 (AS WELL AT P1, P5, AND P7) .....	163
FIGURE 9-3: POSSIBLE UPGRADED LAYOUT OF THE P4 INSERTION REGION .....	163
FIGURE 9-4: UPGRADED LAYOUT OF THE P7 INSERTION REGION.....	163
FIGURE 9-5: UPGRADED LAYOUT OF THE P1/P5 INSERTION REGION (HALF INSERTION) .....	164
FIGURE 9-6: COOLING CAPACITY REQUIREMENT OF SECTOR CRYOGENIC PLANTS. (A) COLD MASS; (B) CURRENT LEADS; (C) THERMAL SHIELDS; (D) BEAM SCREEN (DIPOLE OFF); (E) BEAM SCREEN (DIPOLE ON).....	166
FIGURE 9-7: UPGRADED CRYOGENIC ARCHITECTURE AT P4 .....	167
FIGURE 9-8: UPGRADED CRYOGENIC ARCHITECTURE AT P1 AND P5.....	168
FIGURE 10-1: NUMBER OF DEBRIS PARTICLES PER SINGLE PROTON–PROTON INELASTIC INTERACTION AT 5 MM FROM THE INTERACTION POINT (BLACK) AND AT THE EXIT OF EACH 60 MM TAS APERTURE (RED).....	172
FIGURE 10-2: HL-LHC INNER TRIPLET WITH MCBX/CP CORRECTORS AND D1 DIPOLE. ....	173
FIGURE 10-3: DETAILS OF THE FLUKA–MARS MODEL IN THE INNERMOST REGIONS OF (A) THE Q2–Q3 QUADRUPOLES; (B) MCBX ORBIT CORRECTORS. ....	173
FIGURE 10-4: (A) POWER DENSITY ISOCONTOURS AT THE IP END OF Q2A; (B) LONGITUDINAL PEAK POWER DENSITY PROFILE ON THE INNER COILS OF THE IT MAGNETS. ....	174
FIGURE 10-5: LONGITUDINAL DISTRIBUTIONS OF (A) PEAK DOSE ON INNER COILS AND NEARBY INSULATORS; (B) PEAK DPA ON INNER COILS .....	175
FIGURE 10-6: (A) BEAM SCREEN MODEL AS PER THE FIRST CONCEPTUAL DESIGN DEVELOPED BY WP12 (BS#2); (B) BEAM SCREEN MODEL WITH THE MODIFICATION OF THE ABSORBERS DRIVEN BY ENERGY DEPOSITION CONSIDERATIONS (BS#3). ....	176
FIGURE 10-7: LONGITUDINAL DISTRIBUTIONS OF PEAK DOSE ON THE INNER COILS OF THE IR MAGNETS REFERRING TO (A) DIFFERENT BEAM SCREEN DESIGNS; (B) DIFFERENT LENGTHS OF THE BEAM SCREEN GAP IN THE INTERCONNECTS..	177
FIGURE 10-8: DEBRIS PARTICLE DISTRIBUTION AT THE EXIT OF THE OUTGOING BEAM PIPE OF THE TAN, (A) FOR THE LHC; (B) FOR THE HL-LHC. RED POINTS INDICATE PROTONS WITH MAGNETIC RIGIDITY WITHIN 5% WITH RESPECT TO BEAM PROTONS AND GREEN POINTS INDICATE PROTONS WITH LOWER MAGNETIC RIGIDITY. BLUE POINTS INDICATE NEUTRAL PARTICLES (PHOTONS AND NEUTRONS). IN BOTH CASES THE SAME NUMBER OF COLLISION IS SIMULATED. THE BLACK ELLIPSE SHOWS THE $10\sigma$ OUTGOING BEAM SPOT. ....	178
FIGURE 10-9: LONGITUDINAL PROFILE OF PEAK POWER DENSITY ALONG (A) D2; (B)Q4; (C) Q5, LOG SCALE; (D) Q6, LOG SCALE, AT THE HL-LHC TARGET LUMINOSITY OF $5 \times 10^{34} \text{ cm}^{-2} \text{ s}^{-1}$ . DIFFERENT LAYOUTS AND SETTINGS ARE COMPARED. ERROR BARS INDICATE STATISTICAL UNCERTAINTIES.....	179
FIGURE 10-10: COOLING SCHEME OF THE COLD POWERING SYSTEM. LEFTHAND SIDE: LOW TEMPERATURE (LT) SIDE, WHERE THERE ARE THE CONNECTIONS WITH THE SC MAGNET CABLE. RIGHTHAND SIDE: CONNECTION WITH THE CURRENT LEADS (CL). ....	180
FIGURE 10-11: (A) 20 kA MGB <sub>2</sub> CABLE, $\varnothing = 19.5$ MM, TWO MGB <sub>2</sub> CONCENTRIC CABLES FOR 3 kA TOTAL CURRENT, $\varnothing = 8.2$ MM. (B) 150 kA CABLE ASSEMBLY FOR LHC P1 AND P5 ( $6 \times 20$ kA, $7 \times 3$ kA, $4 \times 0.4$ kA, $20 \times 0.12$ kA), $\varnothing = 65$ MM. (C)THE FLUKA MODEL OF THE CABLE. ....	180
FIGURE 10-12: MAPS OF DOSE RELEASED IN THE SC LINK IN THE P1 SHUFFLING MODULE. (A) SUPERCONDUCTING HORIZONTAL CABLE SHUFFLE MODULE DOSE; (B) SUPERCONDUCTING VERTICAL CABLE SHUFFLE MODULE DOSE. VALUES (IN MGY) ARE NORMALIZED TO $3000 \text{ FB}^{-1}$ . ....	181
FIGURE 10-13: LHC BEAM DUMPS DUE TO SINGLE-EVENT EFFECTS AGAINST BEAM LUMINOSITY. DOTS (2011 AND 2012) REFER TO MEASUREMENTS, WHEREAS LINES SHOW ANNUAL AVERAGES FOR BOTH PAST AND FUTURE OPERATIONS. ....	182
FIGURE 10-14: ANNUAL HEH FLUENCE EXPECTED IN THE IT REGION AND IN THE ADJACENT UJ/UL/UP AREAS AT P1 DURING THE HL-LHC ERA (NORMALIZED TO $300 \text{ FB}^{-1}$ ). ....	184
FIGURE 10-15: CUMULATED HEH FLUENCE EXPECTED IN THE MATCHING SECTION REGION AND IN THE ADJACENT RR AREA AT P5 FOR THE OPERATION OF THE PRESENT LHC AT 7 TeV BEAM ENERGY. (A) CONTRIBUTION FROM THE COLLISION DEBRIS NORMALIZED TO $300 \text{ FB}^{-1}$ . (B) CONTRIBUTION FROM INTERACTIONS OF THE OUTGOING BEAM (BEAM 1) WITH THE RESIDUAL GAS, NORMALIZED TO NOMINAL CURRENT OVER $3 \times 10^7$ S (I.E. THE TIME NEEDED TO ACCUMULATE $300 \text{ FB}^{-1}$ AT NOMINAL LUMINOSITY) AND TO A GAS DENSITY OF $10^{15} \text{ H}_2$ -EQUIVALENT MOLECULES/M <sup>3</sup> . TCL COLLIMATOR SETTINGS: $15\sigma$ (TCL4), $35\sigma$ (TCL5), $10\sigma$ (TCL6).....	184

FIGURE 11-1: LONGITUDINAL SECTION OF THE 11 T CRYO-ASSEMBLY SHOWING THE COLLIMATOR AND THE COLD-TO-WARMWARM TRANSITIONS.....	188
FIGURE 11-2: LONGITUDINAL SECTION OF THE COLD MASS ASSEMBLY OF THE MBH.....	189
FIGURE 11-3: LONGITUDINAL SECTION OF THE COIL.....	189
FIGURE 11-4: CROSS-SECTION THROUGH (A) THE 11 T DIPOLE COLLARED COIL; (B) COLD MASS ASSEMBLY.....	190
FIGURE 11-5: THE BLUE LINE SHOWS THE DIFFERENCE IN INTEGRATED FIELD BETWEEN A PAIR OF MBHS AND AN MB, BOTH DELIVERING 119 T M AT 11.85 KA. THE RED LINE SHOWS THE TRIM CURRENT NEEDED TO CORRECT THE DIFFERENCE AT CURRENTS BELOW 11.85 KA .....	190
FIGURE 13-1: CHARGE COLLECTION EFFICIENCY FOR SILICON AND DIAMOND DETECTORS WITH INCREASING RADIATION FLUENCE IN A CRYOGENIC ENVIRONMENT.....	209
FIGURE 13-2: SCHEMATIC REPRESENTATION OF THE ASIC IMPLEMENTATION CURRENTLY UNDER DEVELOPMENT.....	209
FIGURE 13-3: COMPARISON OF THE NEW LHC ORBIT SYSTEM ELECTRONICS WITH THE EXISTING SYSTEM DURING A VAN DER MEER SCAN.....	211
FIGURE 13-4: A SKETCH DEMONSTRATING THE BEAM GAS VERTEX MEASUREMENT CONCEPT.....	214
FIGURE 13-5: THE DEMONSTRATOR BEAM GAS VERTEX DETECTOR INSTALLED IN THE LHC DURING LS1.....	215
FIGURE 13-6: ILLUSTRATION OF THE COMPENSATION PRINCIPLE [12].....	218
FIGURE 13-7: SKETCH OF AN ELECTRON COOLER TYPE LAYOUT FOR LONG-RANGE BEAM-BEAM COMPENSATION .....	218
FIGURE 13-8: TECHNICAL DRAWING OF THE WIRE-IN-JAW COLLIMATOR DESIGN.....	219
FIGURE 14-1: OVERVIEW OF THE PRESENT INJECTION SYSTEM INTO THE LHC AND THE ASSOCIATED PROTECTION DEVICES (BEAM 1, IR2). THE BEAM IS INJECTED FROM THE LEFT HAND SIDE. ....	222
FIGURE 14-2: ENERGY DEPOSITION IN A TDIS CONSISTING OF THREE MODULES (GRAPHITE, GRAPHITE AND ALUMINIUM, AND COPPER) FOR GRAZING BEAM IMPACT AND SHOWING THE EFFECT OF A 1 $\Sigma$ ALIGNMENT DIFFERENCE BETWEEN THE FIRST AND SECOND MODULE (COURTESY OF N. SHETTY). ....	223
FIGURE 14-3: FRACTION OF 5 $\Sigma$ SINGLE PARTICLE EMITTANCE ABSORBED BY THE DIFFERENT INJECTION PROTECTION ABSORBERS TDIS, TCLIA, OR TCLIB FOR DIFFERENT INJECTION KICKER AMPLITUDES (COURTESY OF F.M. VELOTTI).....	224
FIGURE 14-4: VIEW OF THE CAPACITIVELY COUPLED EXTREMITY OF THE MKI BEAM SCREEN SUPPORTING THE 24 SCREEN CONDUCTORS AND THE CONDUCTOR OVERLAP (COURTESY OF M.J. BARNES).....	226
FIGURE 14-5: SWEEP FORM OF 25 NS SPACING LHC BEAM ON TDE DUMP BLOCK WITH A BUNCH INTENSITY OF $1.7 \times 10^{11}$ PROTONS PER BUNCH AND THE RESULTING TEMPERATURE RISE .....	226
FIGURE 14-6: SCHEMATIC LAYOUT OF THE BEAM DUMP AREA RIGHT OF P6 AS USED DURING LHC RUN 1, SHOWING THE EXTRACTION ABSORBER ELEMENT TCDS ON BEAM 2 AND THE TCDQ ON BEAM 1.....	227
FIGURE 15-1: VOLUME RESERVED FOR THE INSTALLATION OF THE NEW COLD BOX UNIT DEDICATED TO RF SYSTEM COOLING (LIGHT BLUE). ....	229
FIGURE 15-2: VIEW OF THE LHC CIVIL WORKS AT P4 .....	230
FIGURE 15-3: VIEW OF THE FORESEEN INSTALLATION OF THE SUPERCONDUCTING LINK SYSTEM AT P7. POWER CONVERTERS IN TZ76, ROUTING OF THE LINK FROM TZ76, VIA UJ76 TO RR77.....	230
FIGURE 15-4: POSSIBLE OPTION FOR UNDERGROUND WORK AT P5 INCLUDING LINKS TO THE LHC TUNNEL. THIS SOLUTION IS WITHOUT AN INDEPENDENT SHAFT TO ACCESS TO THE SURFACE. NEW STRUCTURES ARE IN LIGHT RED, AND ZONES OF THE LHC TUNNEL TO BE IMPACTED BY CONSTRUCTION THE NEW STRUCTURES ARE IN GREEN. ....	233
FIGURE 15-5: POSSIBLE OPTION FOR UNDERGROUND WORK AT P5 INCLUDING LINKS TO THE LHC TUNNEL. THIS SOLUTION HAS AN INDEPENDENT SHAFT FOR ACCESS TO THE SURFACE. NEW STRUCTURES ARE IN LIGHT RED AND YELLOW, AND ZONES OF THE LHC TUNNEL TO BE IMPACTED BY CONSTRUCTION OF THE NEW STRUCTURES ARE IN GREEN. ....	233
FIGURE 15-6: POSSIBLE OPTION FOR UNDERGROUND WORK AT P5 INCLUDING LINKS TO THE LHC TUNNEL. THIS SOLUTION HAS AN INDEPENDENT SHAFT FOR ACCESS TO THE SURFACE, AND A LARGER CONNECTION TUNNEL FOR POSSIBLE POWER CONVERTER UNDERGROUND INSTALLATION. NEW STRUCTURES ARE IN LIGHT RED AND YELLOW, AND ZONES OF THE LHC TUNNEL TO BE IMPACTED BY CONSTRUCTION OF THE NEW STRUCTURES ARE IN GREEN. ....	233
FIGURE 15-7: POSSIBLE OPTION FOR UNDERGROUND WORK AT P5 INCLUDING LINKS TO THE LHC TUNNEL. THIS SOLUTION HAS AN INDEPENDENT SHAFT FOR ACCESS TO THE SURFACE. A CROSS-SECTION THROUGH THE CRYOGENIC EQUIPMENT IS SHOWN. NEW STRUCTURES ARE IN LIGHT RED AND YELLOW. ....	234
FIGURE 15-8: SURFACE POSITION OF THE TWO NEW CRAB CAVITY SERVICE BUILDINGS (IN YELLOW) AT P5. ....	235

FIGURE 15-9: PRELIMINARY STUDY OF THE LHC P5 BUILDING FOOTPRINT. BUILDING 1 : POWER CONVERTERS AND SC LINK TERMINALS; BUILDING 2: CRYOGENIC SURFACE EQUIPMENT; BUILDING 3: ACCESS TO SHAFT. POSSIBLE TECHNICAL GALLERIES ARE IN LIGHT BLUE. ....	236
FIGURE 17-1: RESIDUAL DOSE EQUIVALENT RATES IN UNITS OF $\mu\text{SV}/\text{H}$ AROUND THE INNER TRIPLET AND D1 MAGNETS WHEN $3060 \text{ FB}^{-1}$ HAS BEEN REACHED AFTER ONE MONTH OF COOLING TIME. DOSES ARE SHOWN FOR A HORIZONTAL SECTION AT THE LEVEL OF THE BEAM LINES. THE ORIGIN OF THE COORDINATE FRAME IS AT THE INTERACTION POINT. ....	252
FIGURE 17-2: AMBIENT DOSE EQUIVALENT RATE PROFILES FOR THE NOMINAL SCENARIO IN THE AISLE AT 40 CM FROM THE CRYOSTAT AT FOUR DIFFERENT COOLING TIMES: 1 WEEK IN BLUE, 1 MONTH IN RED, 4 MONTHS IN GREEN AND 1 YEAR IN VIOLET. ....	252
FIGURE 17-3: RESIDUAL DOSE EQUIVALENT RATES IN UNITS OF $\mu\text{SV}/\text{H}$ AROUND THE INNER TRIPLET AND D1 MAGNETS WHEN $3910 \text{ FB}^{-1}$ HAS BEEN REACHED AFTER ONE MONTH OF COOLING TIME. DOSES ARE SHOWN FOR A HORIZONTAL SECTION AT THE LEVEL OF THE BEAM LINES. THE ORIGIN OF THE COORDINATE FRAME IS AT THE INTERACTION POINT. ....	253
FIGURE 17-4: AMBIENT DOSE EQUIVALENT RATE PROFILES FOR THE ULTIMATE SCENARIO IN THE AISLE AT 40 CM FROM THE CRYOSTAT AT FOUR DIFFERENT COOLING TIMES: 1 WEEK IN BLUE, 1 MONTH IN RED, 4 MONTHS IN GREEN AND 1 YEAR IN VIOLET. ....	253
FIGURE 17-5: AMBIENT DOSE EQUIVALENT RATE PROFILES ALONG THE AISLE AT 40 CM DISTANCE TO THE CRYOSTAT AT ONE MONTH COOLING TIME. THE PROFILE IN LIGHT BLUE IS FOR THE NOMINAL SCENARIO (ABOUT $3000 \text{ FB}^{-1}$ TOTAL INTEGRATED LUMINOSITY), THE PROFILE IN PINK IS FOR THE ULTIMATE SCENARIO (ABOUT $4000 \text{ FB}^{-1}$ TOTAL INTEGRATED LUMINOSITY). ....	253
FIGURE 17-6: ORGANIZATION OF THE SAFETY DOCUMENTATION. ....	255

# Table of tables

TABLE 1-1: HIGH LUMINOSITY LHC PARAMETERS.....	7
TABLE 2-1: HL-LHC NOMINAL PARAMETERS FOR 25 NS OPERATION [14] FOR TWO PRODUCTION MODES OF THE LHC BEAM IN THE INJECTORS DESCRIBED IN REF. [3].....	25
TABLE 2-2: MAIN HL-LHC OPTICS VARIANTS CURRENTLY UNDER STUDY. THE BASELINE COLLISION OPTICS CORRESPONDS TO $b^* = 15$ CM IN BOTH TRANSVERSE PLANES (ROUND OPTICS) WITH A FULL CROSSING ANGLE OF 590 MRAD. OTHER COLLISION OPTICS ARE AVAILABLE, ROUND OR FLAT, FOR DEDICATED STUDIES. ....	31
TABLE 2-3: NEW OR REFURBISHED QUADRUPOLES FOR HL-LHC, ALL OPERATING AT 1.9 K. THE ORIENTATION OF THE RECTELLIPSE APERTURE ( $R$ ) [40] CAN BE CHANGED TO OPTIMIZE THE MECHANICAL APERTURE. ....	33
TABLE 2-4: NEW DIPOLE MAGNETS FOR HL-LHC, ALL OPERATING AT 1.9 K. THE ORIENTATION OF THE RECTELLIPSE ( $R$ ) APERTURE CAN BE CHANGED TO OPTIMIZE THE MECHANICAL APERTURE. THE ORBIT CORRECTORS CAN BE NESTED OR CONSECUTIVE AS INDICATED.....	33
TABLE 2-5: NEW MULTIPOLAR SUPERFERRIC CORRECTORS FOR HL-LHC, ALL OPERATING AT 1.9 K.....	34
TABLE 2-6: NEW ABSORBERS FOR HL-LHC, ALL OPERATING AT 1.9 K. THE ORIENTATION OF THE RECTELLIPSE APERTURE CAN BE CHANGED TO OPTIMIZE THE MECHANICAL APERTURE. ....	34
TABLE 2-7: AVAILABLE OPTICAL CONFIGURATIONS FOR THE BASELINE LAYOUT. IR3 AND IR7 ARE NOT REPORTED HERE AS THEY HAVE STATIC OPTICS FROM INJECTION TO COLLISION AND DO NOT TAKE PART IN THE ATS SCHEME. SOME ALTERNATIVE CONFIGURATIONS (OTHER THAN THE NOMINAL) ARE ALSO SHOWN. ....	35
TABLE 2-8: EVOLUTION OF LOW ORDER TERMS OF THE ESTIMATED D2 FIELD QUALITY AT 7 TeV ( $R_0 = 35$ MM). ....	37
TABLE 2-9: SUMMARY OF THE IMPEDANCE-INDUCED HEAT LOAD COMPUTATIONS FOR SEVERAL KEY SYSTEMS .....	44
TABLE 2-10: IMPEDANCE-INDUCED HEAT LOADS FOR THE DIFFERENT TYPES OF BEAM SCREENS (INCLUDING THE EFFECTS OF THE LONGITUDINAL WELD, TWO COUNTER-ROTATING BEAMS, AND THE MAGNETO-RESISTANCE) VS. TEMPERATURE: VALUES ARE GIVEN FOR THE 25 NS BEAM AND FOR THE 50 NS BEAM (IN PARENTHESES).....	45
TABLE 2-11: INTEGRATED PERFORMANCE ESTIMATE FOR LEVELLING SCENARIOS AT PILE-UP LEVELS OF 140 (PU 140) AND 210 (PU 210) EVENTS/CROSSING, RESPECTIVELY.....	47
TABLE 2-12: PARAMETERS ASSUMED FOR HL-LHC PERFORMANCE ESTIMATE. ....	47
TABLE 2-13: AVERAGE VALUES OF PRINCIPAL BEAM PARAMETERS AT START OF PHYSICS .....	53
TABLE 3-1: OVERVIEW OF THE MAIN PARAMETERS OF THE INSERTION MAGNETS – SEE THE TEXT FOR DEFINITIONS OF FOOTNOTES .....	63
TABLE 3-2: EXPECTED SYSTEMATIC HARMONICS AND RANDOM COMPONENTS IN THE TRIPLET.....	66
TABLE 3-3: OVERVIEW OF THE MAIN PARAMETERS OF THE TRIPLET CORRECTOR MAGNETS.....	70
TABLE 3-4: EXPECTED SYSTEMATIC HARMONICS AND RANDOM COMPONENTS OF D1 .....	71
TABLE 3-5: EXPECTED SYSTEMATIC HARMONICS AND RANDOM COMPONENTS .....	74
TABLE 4-1: RELEVANT RF PARAMETERS FOR HL-LHC CRAB CAVITIES .....	83
TABLE 4-2: OVERVIEW OF CRAB CAVITY PLANNING FROM R&D TO INSTALLATION IN THE LHC .....	84
TABLE 4-3: CRYMODULE ENVELOPE DIMENSIONS .....	101
TABLE 4-4: DETUNING RANGES FOR THE LHC AND SPS .....	102
TABLE 4-5: RELEVANT RF PARAMETERS FOR 800MHZ RF CAVITIES .....	104
TABLE 4-6: RELEVANT RF PARAMETERS FOR 200 MHzc RF CAVITIES .....	104
TABLE 5-1: COLLIMATORS FOR THE LHC RUN 2, STARTING IN 2015. FOR EACH TYPE, ACRONYMS, ROTATION PLANE (HORIZONTAL, VERTICAL OR SKEW), MATERIAL AND NUMBER OF DEVICES, SUMMED OVER THE TWO BEAMS, ARE GIVEN. FOR COMPLETENESS, MOVABLE INJECTION AND DUMP PROTECTION DEVICES ARE ALSO LISTED. IN ADDITION, THE COLLIMATION SYSTEM COMPRISES 10 FIXED-APERTURE ABSORBERS IN IR3 AND IR7 TO REDUCE TOTAL DOSES TO WORM MAGNETS OF THE CLEANING INSERTIONS. ....	113
TABLE 5-2: KEY PARAMETERS OF TCLD COLLIMATORS .....	116
TABLE 5-3: PARAMETERS OF TCSMP COLLIMATORS .....	120
TABLE 5-4: EQUIPMENT PARAMETERS OF THE TCTPM .....	121
TABLE 5-5: HOLLOW ELECTRON BEAM EQUIPMENT PARAMETERS .....	123
TABLE 6-1: LIST OF NEW POWER CONVERTERS FOR INNER TRIPLET AND MATCHING SECTION MAGNETS .....	144
TABLE 6-2: MAGNETS AT EACH SIDE OF LHC P1 AND P5 .....	145

TABLE 8-1: TARGET LUMINOSITIES FOR P-P OPERATION FOR THE HL-LHC. THE LUMINOSITIES FOR LHC RUN 2 ARE ALSO INCLUDED FOR COMPARISON. TOTAL TARGET INTEGRATED LUMINOSITY IN CMS AND ATLAS IS 3000 FB <sup>-1</sup> AFTER 12 YEARS OF OPERATION.....	158
TABLE 8-2: ORIGINAL AND REDUCED INNER BEAM PIPE RADII AT THE IPS.....	158
TABLE 9-1: LHC UPGRADED BEAM PARAMETERS FOR 25NS BUNCH SPACING.....	162
TABLE 9-2: STATIC HEAT IN-LEAKS OF HL-LHC MACHINE (WITHOUT CONTINGENCY).....	164
TABLE 9-3: DYNAMIC HEAT LOADS ON HL-LHC MACHINE (WITHOUT CONTINGENCY).....	165
TABLE 9-4: INSTALLED CAPACITY REQUIREMENTS OF THE NEW CRYOGENIC PLANT AT P4.....	167
TABLE 9-5: INSTALLED CAPACITY REQUIREMENTS OF THE NEW CRYOGENIC PLANTS AT P1 AND P5.....	168
TABLE 9-6: BUILDING AND GENERAL SERVICE REQUIREMENT.....	169
TABLE 10-1: PREDICTED AND MEASURED ANNUAL HEH FLUENCE IN CRITICAL SHIELDED AREAS FOR A CUMULATED ATLAS/CMS LUMINOSITY OF 15 FB <sup>-1</sup> DURING 2012 OPERATIONS, THEN EXTRAPOLATED BASED ON THE MEASUREMENT TO THE EXPECTED NOMINAL AND HL-LHC PERFORMANCE (50 FB <sup>-1</sup> /Y FOR NOMINAL AND 300 FB <sup>-1</sup> /Y FOR HL-LHC PERFORMANCE, EXCEPT FOR P8 WHERE 2012 CAN ALREADY BE CONSIDERED AS ALMOST NOMINAL AND HL-LHC REFERS TO A FIVE-FOLD INCREASE). FOR THE HL-LHC AN ESTIMATE FOR CORRESPONDING ANNUAL TID LEVELS IS ALSO GIVEN.....	183
TABLE 11-1: MAIN PARAMETERS OF THE 11 T CRYO-ASSEMBLY.....	188
TABLE 11-2: FIELD ERRORS – $R_{REF} = 17$ MM.....	192
TABLE 11-3: MAIN PARAMETERS OF THE MBH.....	193
TABLE 12-1: SINGLE GAS SPECIES MOLECULAR GAS DENSITY (M <sup>-3</sup> ) TO SATISFY 100 H VACUUM LIFETIME IN THE LHC AND THE HL-LHC [2].....	196
TABLE 13-1: CHARACTERISTICS OF THE PROTOTYPE HL-LHC BLM SYSTEM ASIC.....	210
TABLE 14-1: TDIS POSITION RELATIVE TO THE ORBIT.....	222
TABLE 16-1: POTENTIAL BREAKDOWN OF A STANDARD HL-LHC YEAR.....	239
TABLE 16-2: BREAKDOWN OF TURNAROUND AND ESTIMATED MINIMUM TIME FOR EACH PHASE.....	240
TABLE 16-3: OUTLINE OF INITIAL COMMISSIONING FOLLOWING LS3.....	245
TABLE 17-1: LHC OPERATIONAL PARAMETERS. THE SECOND AND THIRD COLUMNS REFER TO THE SO-CALLED ‘NOMINAL SCENARIO’, WHICH WILL LEAD TO A TOTAL INTEGRATED LUMINOSITY OF 3060 FB <sup>-1</sup> . THE FOURTH AND FIFTH COLUMNS REFER TO THE SO-CALLED ‘ULTIMATE SCENARIO’. THIS SCENARIO WILL LEAD TO A TOTAL INTEGRATED LUMINOSITY OF 3910 FB <sup>-1</sup> . FOR THE TOTAL INTEGRATED LUMINOSITY 310 FB <sup>-1</sup> ARE TAKEN INTO ACCOUNT AS INTEGRATED IN THE OPERATIONAL PERIOD BEFORE LS3.....	251

# Contributor list

C. Adorisio	CERN, Accelerator & Technology Sector, CH-1211, Geneva, Switzerland
A. Adraktas	CERN, Accelerator & Technology Sector, CH-1211, Geneva, Switzerland
L. Alberty	CERN, Accelerator & Technology Sector, CH-1211, Geneva, Switzerland
D. Alesini	INFN-LNF, Via E. Fermi 40, 00044 Frascati, Rome, Italy
G. Ambrosio	Fermi National Accelerator Laboratory, Batavia, P.O. Box 500, IL, USA
M. Anerella	BNL, Brookhaven National Laboratory, Upton, NY 11973, USA
D. Angal-Kalinin	ASTeC, STFC, Daresbury Laboratory, Warrington WA4 4AD, UK
G. Apollinari	Fermi National Accelerator Laboratory, Batavia, P.O. Box 500, IL, USA
A. Apollonio	CERN, Accelerator & Technology Sector, CH-1211, Geneva, Switzerland
R.B. Appleby	UMAN, The University of Manchester, and the Cockcroft Institute, UK
G. Arduini	CERN, Accelerator & Technology Sector, CH-1211, Geneva, Switzerland
K. Artoos	CERN, Accelerator & Technology Sector, CH-1211, Geneva, Switzerland
S. Atieh	CERN, Accelerator & Technology Sector, CH-1211, Geneva, Switzerland
B. Auchmann	CERN, Accelerator & Technology Sector, CH-1211, Geneva, Switzerland
T. Baer	CERN, Accelerator & Technology Sector, CH-1211, Geneva, Switzerland
V. Baglin	CERN, Accelerator & Technology Sector, CH-1211, Geneva, Switzerland
M. Bajko	CERN, Accelerator & Technology Sector, CH-1211, Geneva, Switzerland
A. Ballarino	CERN, Accelerator & Technology Sector, CH-1211, Geneva, Switzerland
D. Banfi	EPFL, Lausanne, Switzerland
R. Barlow	UHUD, University of Huddersfield, Huddersfield, UK
M. Barnes	CERN, Accelerator & Technology Sector, CH-1211, Geneva, Switzerland
J. Barranco	EPFL, Lausanne, Switzerland
W. Bartmann	CERN, Accelerator & Technology Sector, CH-1211, Geneva, Switzerland
E. Barzi	Fermi National Accelerator Laboratory, Batavia, P.O. Box 500, IL, USA
P. Baudrenghien	CERN, Accelerator & Technology Sector, CH-1211, Geneva, Switzerland
I. Bejar Alonso	CERN, Accelerator & Technology Sector, CH-1211, Geneva, Switzerland
S. Belomestnykh	BNL, Brookhaven National Laboratory, Upton, NY 11973, USA
A. Benoit	CERN, Accelerator & Technology Sector, CH-1211, Geneva, Switzerland
I. Ben-Zvi	BNL, Brookhaven National Laboratory, Upton, NY 11973, USA
A. Bertarelli	CERN, Accelerator & Technology Sector, CH-1211, Geneva, Switzerland
N. Biancacci	CERN, Accelerator & Technology Sector, CH-1211, Geneva, Switzerland
A. Bignami	INFN-LASA, Milan, Italy
N. Bliss	STFC, Daresbury Laboratory, Warrington WA4 4AD, UK
J. Borburgh	CERN, Accelerator & Technology Sector, CH-1211, Geneva, Switzerland
B. Bordini	CERN, Accelerator & Technology Sector, CH-1211, Geneva, Switzerland
R. Bossert	Fermi National Accelerator Laboratory, Batavia, P.O. Box 500, IL, USA
L. Bottura	CERN, Accelerator & Technology Sector, CH-1211, Geneva, Switzerland
A. Boucherie	CERN, Accelerator & Technology Sector, CH-1211, Geneva, Switzerland
C. Bracco	CERN, Accelerator & Technology Sector, CH-1211, Geneva, Switzerland
E. Bravin	CERN, Accelerator & Technology Sector, CH-1211, Geneva, Switzerland
G. Bregliozzi	CERN, Accelerator & Technology Sector, CH-1211, Geneva, Switzerland
D. Brett	The University of Manchester and the Cockcroft Institute, UK

K. Brodzinski	CERN, Accelerator & Technology Sector, CH-1211, Geneva, Switzerland
F. Broggi	INFN-LASA, Milan, Italy
R. Bruce	CERN, Accelerator & Technology Sector, CH-1211, Geneva, Switzerland
M. Brugger	CERN, Accelerator & Technology Sector, CH-1211, Geneva, Switzerland
O. Brüning	CERN, Accelerator & Technology Sector, CH-1211, Geneva, Switzerland
X. Buffat	CERN, Accelerator & Technology Sector, CH-1211, Geneva, Switzerland
H. Burkhardt	CERN, Accelerator & Technology Sector, CH-1211, Geneva, Switzerland
J.P. Burnet	CERN, Accelerator & Technology Sector, CH-1211, Geneva, Switzerland
A. Burov	Fermi National Accelerator Laboratory, Batavia, P.O. Box 500, IL, USA
G. Burt	University of Lancaster, Lancaster, UK and Cockcroft Institute Sci-Tech Daresbury, Warrington UK
Y. Cai	SLAC National Accelerator Laboratory, 2575 Sand Hill Road, Menlo Park California 94025 USA
R. Calaga	CERN, Accelerator & Technology Sector, CH-1211, Geneva, Switzerland
S. Calatroni	CERN, Accelerator & Technology Sector, CH-1211, Geneva, Switzerland
O. Capatina	CERN, Accelerator & Technology Sector, CH-1211, Geneva, Switzerland
T. Capelli	CERN, Accelerator & Technology Sector, CH-1211, Geneva, Switzerland
E. Carlier	CERN, Accelerator & Technology Sector, CH-1211, Geneva, Switzerland
F. Carra	CERN, Accelerator & Technology Sector, CH-1211, Geneva, Switzerland
F. Caspers	CERN, Accelerator & Technology Sector, CH-1211, Geneva, Switzerland
F. Cerutti	CERN, Accelerator & Technology Sector, CH-1211, Geneva, Switzerland
A. Chancé	CEA/SACLAY, DSM/Irfu/SACM – 91191 Gif-sur-Yvette – France
S. Chemli	CERN, Accelerator & Technology Sector, CH-1211, Geneva, Switzerland
D. Cheng	LBNL, Lawrence Berkeley National Laboratory, Berkeley, CA 94720, USA
P. Chiggiato	CERN, Accelerator & Technology Sector, CH-1211, Geneva, Switzerland
G. Chlachidze	Fermi National Accelerator Laboratory, Batavia, P.O. Box 500, IL, USA
S. Claudet	CERN, Accelerator & Technology Sector, CH-1211, Geneva, Switzerland
P. Costa Pinto	CERN, Accelerator & Technology Sector, CH-1211, Geneva, Switzerland
M. Crouch	The University of Manchester and the Cockcroft Institute, UK
P. Cruikshank	CERN, Accelerator & Technology Sector, CH-1211, Geneva, Switzerland
K. Dahlerup-Petersen	CERN, Accelerator & Technology Sector, CH-1211, Geneva, Switzerland
B. Dalena	CEA/SACLAY, DSM/Irfu/SACM – 91191 Gif-sur-Yvette – France
H. Day	CERN, Accelerator & Technology Sector, CH-1211, Geneva, Switzerland
J.P. De Carvalho Saraiva	CERN, Accelerator & Technology Sector, CH-1211, Geneva, Switzerland
B. Dehning	CERN, Accelerator & Technology Sector, CH-1211, Geneva, Switzerland
J. Delayen	Old Dominion University, 5115 Hampton Boulevard, Norfolk, VA 23529, USA
B. Delille	CERN, Accelerator & Technology Sector, CH-1211, Geneva, Switzerland
R. De Maria	CERN, Accelerator & Technology Sector, CH-1211, Geneva, Switzerland
R. Denz	CERN, Accelerator & Technology Sector, CH-1211, Geneva, Switzerland
G. De Rijk	CERN, Accelerator & Technology Sector, CH-1211, Geneva, Switzerland
S. De Silva	Old Dominion University, 5115 Hampton Boulevard, Norfolk, VA 23529, USA
A. Dexter	University of Lancaster, Lancaster, UK and Cockcroft Institute Sci-Tech Daresbury, Warrington UK
D. Dietderich	LBNL, Lawrence Berkeley National Laboratory, Berkeley, CA 94720, USA
A. Doherty	University of Lancaster, Lancaster, UK and Cockcroft Institute Sci-Tech Daresbury, Warrington UK



A. Drago	INFN-LNF, Via E. Fermi 40, 00044 Frascati, Rome, Italy
D. Duarte Ramos	CERN, Accelerator & Technology Sector, CH-1211, Geneva, Switzerland
L. Ducimetière	CERN, Accelerator & Technology Sector, CH-1211, Geneva, Switzerland
I. Efthymiopoulos	CERN, Accelerator & Technology Sector, CH-1211, Geneva, Switzerland
L. Esposito	CERN, Accelerator & Technology Sector, CH-1211, Geneva, Switzerland
J. Esteban Muller	CERN, Accelerator & Technology Sector, CH-1211, Geneva, Switzerland
P. Fabbricatore	INFN, Sezione di Genova, I-16146 Genova, Italy
S. Farinon	INFN, Sezione di Genova, I-16146 Genova, Italy
S. Fartoukh	CERN, Accelerator & Technology Sector, CH-1211, Geneva, Switzerland
A. Faus-Golfe	IFIC, Instituto de Física Corpuscular, CSIC,E-46071 Valencia, Spain
G. Favre	CERN, Accelerator & Technology Sector, CH-1211, Geneva, Switzerland
H. Felice	LBNL, Lawrence Berkeley National Laboratory, Berkeley, CA 94720, USA
G. Ferlin	CERN, Accelerator & Technology Sector, CH-1211, Geneva, Switzerland
P. Ferracin	CERN, Accelerator & Technology Sector, CH-1211, Geneva, Switzerland
A. Ferrari	CERN, Accelerator & Technology Sector, CH-1211, Geneva, Switzerland
L. Ferreira	CERN, Accelerator & Technology Sector, CH-1211, Geneva, Switzerland
P. Fessia	CERN, Accelerator & Technology Sector, CH-1211, Geneva, Switzerland
L. Ficcadenti	CERN, Accelerator & Technology Sector, CH-1211, Geneva, Switzerland
L. Fiscarelli	CERN, Accelerator & Technology Sector, CH-1211, Geneva, Switzerland
M. Fitterer	CERN, Accelerator & Technology Sector, CH-1211, Geneva, Switzerland
R. Folch	CERN, Accelerator & Technology Sector, CH-1211, Geneva, Switzerland
G. Foffano	CERN, Accelerator & Technology Sector, CH-1211, Geneva, Switzerland
O. Frasciello	INFN-LNF, Via E. Fermi 40, 00044 Frascati, Rome, Italy
M. Fraser	CERN, Accelerator & Technology Sector, CH-1211, Geneva, Switzerland
P. Freijedo Menendez	CERN, Accelerator & Technology Sector, CH-1211, Geneva, Switzerland
M. Gallilee	CERN, Accelerator & Technology Sector, CH-1211, Geneva, Switzerland
A. Gallo	INFN-LNF, Via E. Fermi 40, 00044 Frascati, Rome, Italy
J. Garcia Matos	CIEMAT, Madrid, Spain
H. Garcia Morales	URHL, Royal Holloway, London, UK
C. Garion	CERN, Accelerator & Technology Sector, CH-1211, Geneva, Switzerland
J.C. Gascon	CERN, Accelerator & Technology Sector, CH-1211, Geneva, Switzerland
L. Gentini	CERN, Accelerator & Technology Sector, CH-1211, Geneva, Switzerland
A. Ghosh	BNL, Brookhaven National Laboratory, Upton, NY 11973, USA
K. Gibran Hernandez	CERN, Accelerator & Technology Sector, CH-1211, Geneva, Switzerland
S.M. Gibson	URHL, Royal Holloway, London, UK
C. Ginburg	Fermi National Accelerator Laboratory, Batavia, P.O. Box 500, IL, USA
M. Giovannozzi	CERN, Accelerator & Technology Sector, CH-1211, Geneva, Switzerland
B. Goddard	CERN, Accelerator & Technology Sector, CH-1211, Geneva, Switzerland
P. Gomes	CERN, Accelerator & Technology Sector, CH-1211, Geneva, Switzerland
P. Goudket	ASTeC, STFC, Daresbury Laboratory, Warrington WA4 4AD, UK
P. Gradassi	CERN, Accelerator & Technology Sector, CH-1211, Geneva, Switzerland
L. Grand-Clément	CERN, Accelerator & Technology Sector, CH-1211, Geneva, Switzerland
M. Guinchard	CERN, Accelerator & Technology Sector, CH-1211, Geneva, Switzerland
P. Hagen	CERN, Accelerator & Technology Sector, CH-1211, Geneva, Switzerland

B. Hall University of Lancaster, Lancaster, UK and Cockcroft Institute Sci-Tech Daresbury, Warrington UK

W. Herr CERN, Accelerator & Technology Sector, CH-1211, Geneva, Switzerland

C. Hill STFC, Daresbury Laboratory, Warrington WA4 4AD, UK

W. Höfle CERN, Accelerator & Technology Sector, CH-1211, Geneva, Switzerland

B. Holzer CERN, Accelerator & Technology Sector, CH-1211, Geneva, Switzerland

J. Hrivnak CERN, Accelerator & Technology Sector, CH-1211, Geneva, Switzerland

G. Iadarola CERN, Accelerator & Technology Sector, CH-1211, Geneva, Switzerland

S. Izquierdo Bermudez CERN, Accelerator & Technology Sector, CH-1211, Geneva, Switzerland

E. Jensen CERN, Accelerator & Technology Sector, CH-1211, Geneva, Switzerland

R. Jones CERN, Accelerator & Technology Sector, CH-1211, Geneva, Switzerland

T. Jones STFC, Daresbury Laboratory, Warrington WA4 4AD, UK

J.M. Jowett CERN, Accelerator & Technology Sector, CH-1211, Geneva, Switzerland

M. Juchno CERN, Accelerator & Technology Sector, CH-1211, Geneva, Switzerland

C. Julie CERN, Accelerator & Technology Sector, CH-1211, Geneva, Switzerland

T. Junginger CERN, Accelerator & Technology Sector, CH-1211, Geneva, Switzerland

V. Kain CERN, Accelerator & Technology Sector, CH-1211, Geneva, Switzerland

P. Kardasopoulos CERN, Accelerator & Technology Sector, CH-1211, Geneva, Switzerland

M. Karppinen CERN, Accelerator & Technology Sector, CH-1211, Geneva, Switzerland

R. Kersevan CERN, Accelerator & Technology Sector, CH-1211, Geneva, Switzerland

F. Kiling CERN, Accelerator & Technology Sector, CH-1211, Geneva, Switzerland

M. Korostelev University of Liverpool, Liverpool L69 7ZE, UK

N. Kos CERN, Accelerator & Technology Sector, CH-1211, Geneva, Switzerland

S. Krave Fermi National Accelerator Laboratory, Batavia, P.O. Box 500, IL, USA

N. Kuder CERN, Accelerator & Technology Sector, CH-1211, Geneva, Switzerland

R. Kwee-Hinzmann URHL, Royal Holloway, London, UK

F. Lackner CERN, Accelerator & Technology Sector, CH-1211, Geneva, Switzerland

M. Lamont CERN, Accelerator & Technology Sector, CH-1211, Geneva, Switzerland

L. Lari IFIC, Instituto de Fisica Corpuscular, CSIC,E-46071 Valencia, Spain (now at European Spallation Source)

A. Lechner CERN, Accelerator & Technology Sector, CH-1211, Geneva, Switzerland

T. Lefevre CERN, Accelerator & Technology Sector, CH-1211, Geneva, Switzerland

R. Leuxe CERN, Accelerator & Technology Sector, CH-1211, Geneva, Switzerland

K. Li CERN, Accelerator & Technology Sector, CH-1211, Geneva, Switzerland

Z. Li SLAC National Accelerator Laboratory, 2575 Sand Hill Road, Menlo Park California 94025 USA

C. Lingwood University of Lancaster, Lancaster, UK and Cockcroft Institute Sci-Tech Daresbury, Warrington UK

C. Löffler CERN, Accelerator & Technology Sector, CH-1211, Geneva, Switzerland

F.L. Maciariello CERN, Accelerator & Technology Sector, CH-1211, Geneva, Switzerland

R. Losito CERN, Accelerator & Technology Sector, CH-1211, Geneva, Switzerland

P. Macintosh ASTeC, STFC, Daresbury Laboratory, Warrington WA4 4AD, UK

A. Macpherson CERN, Accelerator & Technology Sector, CH-1211, Geneva, Switzerland

P. Maesen CERN, Accelerator & Technology Sector, CH-1211, Geneva, Switzerland

F. Marcellini INFN-LNF, Via E. Fermi 40, 00044 Frascati, Rome, Italy

M. Marchevsky LBNL, Lawrence Berkeley National Laboratory, Berkeley, CA 94720, USA

K. Marinov	ASTeC, STFC, Daresbury Laboratory, Warrington WA4 4AD, UK
T. Markiewicz	SLAC National Accelerator Laboratory, 2575 Sand Hill Road, Menlo Park California 94025 USA
A. Marsili	CERN, Accelerator & Technology Sector, CH-1211, Geneva, Switzerland
A. Masi	CERN, Accelerator & Technology Sector, CH-1211, Geneva, Switzerland
T. Mastoridis	California Polytechnic State University, San Luis Obispo, USA
A. May	ASTeC, STFC, Daresbury Laboratory, Warrington WA4 4AD, UK
J. Mazet	CERN, Accelerator & Technology Sector, CH-1211, Geneva, Switzerland
E. McIntosh	CERN, Accelerator & Technology Sector, CH-1211, Geneva, Switzerland
P. Menendez	CERN, Accelerator & Technology Sector, CH-1211, Geneva, Switzerland
M. Mensi	CERN, Accelerator & Technology Sector, CH-1211, Geneva, Switzerland
A. Mereghetti	CERN, Accelerator & Technology Sector, CH-1211, Geneva, Switzerland
T. Mertens	CERN, Accelerator & Technology Sector, CH-1211, Geneva, Switzerland
E. Métral	CERN, Accelerator & Technology Sector, CH-1211, Geneva, Switzerland
M. Migliorati	University of Rome “La Sapienza”, Rome, Italy
P. Minginette	CERN, Accelerator & Technology Sector, CH-1211, Geneva, Switzerland
N.V. Mokhov	Fermi National Accelerator Laboratory, Batavia, P.O. Box 500, IL, USA
J. Molson	UMAN, The University of Manchester and the Cockcroft Institute, UK
E. Montesinos	CERN, Accelerator & Technology Sector, CH-1211, Geneva, Switzerland
R. Moron-Ballester	CERN, Accelerator & Technology Sector, CH-1211, Geneva, Switzerland
A. Mostacci	University of Rome “La Sapienza”, Rome, Italy
N. Mounet	CERN, Accelerator & Technology Sector, CH-1211, Geneva, Switzerland
B. Muratori	ASTeC, STFC, Daresbury Laboratory, Warrington WA4 4AD, UK
M. Navarro-Tapia	CERN, Accelerator & Technology Sector, CH-1211, Geneva, Switzerland
T. Nakamoto	KEK, Oho, Tsukuba, 305-0801, Japan
H. Neupert	CERN, Accelerator & Technology Sector, CH-1211, Geneva, Switzerland
L.J. Nevay	URHL, Royal Holloway, London, UK
T. Nicol	Fermi National Accelerator Laboratory, Batavia, P.O. Box 500, IL, USA
A. Nobrega	Fermi National Accelerator Laboratory, Batavia, P.O. Box 500, IL, USA
C. Noels	CERN, Accelerator & Technology Sector, CH-1211, Geneva, Switzerland
E. Nolan	STFC, Daresbury Laboratory, Warrington WA4 4AD, UK
Y. Nosochkov	SLAC National Accelerator Laboratory, 2575 Sand Hill Road, Menlo Park California 94025 USA
L. Oberli	CERN, Accelerator & Technology Sector, CH-1211, Geneva, Switzerland
T. Ogitsu	KEK, Oho, Tsukuba, 305-0801, Japan
K. Ohmi	KEK, Oho, Tsukuba, 305-0801, Japan
R. Olave	Old Dominion University, 5115 Hampton Boulevard, Norfolk, VA 23529, USA
T. Otto	CERN, Accelerator & Technology Sector, CH-1211, Geneva, Switzerland
L. Palumbo	University of Rome “La Sapienza”, Rome, Italy
Y. Papaphilippou	CERN, Accelerator & Technology Sector, CH-1211, Geneva, Switzerland
C. Parente	CERN, Accelerator & Technology Sector, CH-1211, Geneva, Switzerland
S. Paret	LBNL, Lawrence Berkeley National Laboratory, Berkeley, CA 94720, USA
H. Park	Old Dominion University, 5115 Hampton Boulevard, Norfolk, VA 23529, USA
S. Pattalwar	ASTeC, STFC, Daresbury Laboratory, Warrington WA4 4AD, UK
J. Payet	CEA/SACLAY, DSM/Irfu/SACM – 91191 Gif-sur-Yvette – France

G. Pechaud	CERN, Accelerator & Technology Sector, CH-1211, Geneva, Switzerland
J.C. Perez	CERN, Accelerator & Technology Sector, CH-1211, Geneva, Switzerland
J. Perez Espinos	CERN, Accelerator & Technology Sector, CH-1211, Geneva, Switzerland
A. Perillo Marcone	CERN, Accelerator & Technology Sector, CH-1211, Geneva, Switzerland
T. Peterson	Fermi National Accelerator Laboratory, Batavia, P.O. Box 500, IL, USA
T. Pieloni	CERN, Accelerator & Technology Sector, CH-1211, Geneva, Switzerland
M. Pojer	CERN, Accelerator & Technology Sector, CH-1211, Geneva, Switzerland
H. Prin	CERN, Accelerator & Technology Sector, CH-1211, Geneva, Switzerland
J. Qiang	LBNL, Lawrence Berkeley National Laboratory, Berkeley, CA 94720, USA
E. Quaranta	CERN, Accelerator & Technology Sector, CH-1211, Geneva, Switzerland
H. Rafique	UHUD, University of Huddersfield, Huddersfield, UK
I.L. Rakhno	Fermi National Accelerator Laboratory, Batavia, P.O. Box 500, IL, USA
D. Ramos Duarte	CERN, Accelerator & Technology Sector, CH-1211, Geneva, Switzerland
A. Ratti	Fermi National Accelerator Laboratory, Batavia, P.O. Box 500, IL, USA
S. Redaelli	CERN, Accelerator & Technology Sector, CH-1211, Geneva, Switzerland
T. Renaglia	CERN, Accelerator & Technology Sector, CH-1211, Geneva, Switzerland
J.M. Rifflet	CEA/SACLAY, DSM/Irfu/SACM – 91191 Gif-sur-Yvette – France
T. Rijoff	CERN, Accelerator & Technology Sector, CH-1211, Geneva, Switzerland
L. Rivkin	EPFL, Lausanne, Switzerland
S. Roesler	CERN, Accelerator & Technology Sector, CH-1211, Geneva, Switzerland
I. Romera Ramirez	CERN, Accelerator & Technology Sector, CH-1211, Geneva, Switzerland
L. Rossi	CERN, Accelerator & Technology Sector, CH-1211, Geneva, Switzerland
G. Rumolo	CERN, Accelerator & Technology Sector, CH-1211, Geneva, Switzerland
G.L. Sabbi	LBNL, Lawrence Berkeley National Laboratory, Berkeley, CA 94720, USA
T. Sahrner	CERN, Accelerator & Technology Sector, CH-1211, Geneva, Switzerland
B. Salvant	CERN, Accelerator & Technology Sector, CH-1211, Geneva, Switzerland
I. Santillana	CERN, Accelerator & Technology Sector, CH-1211, Geneva, Switzerland
C. Santini	Politecnico of Milan, Italy
K. Sasaki	KEK, Oho, Tsukuba, 305-0801, Japan
F. Savary	CERN, Accelerator & Technology Sector, CH-1211, Geneva, Switzerland
M. Schaumann	CERN, Accelerator & Technology Sector, CH-1211, Geneva, Switzerland
J. Schmalzle	BNL, Brookhaven National Laboratory, Upton, NY 11973, USA
H. Schmickler	CERN, Accelerator & Technology Sector, CH-1211, Geneva, Switzerland
R. Schmidt	CERN, Accelerator & Technology Sector, CH-1211, Geneva, Switzerland
M. Segreti	CEA/SACLAY, DSM/Irfu/SACM – 91191 Gif-sur-Yvette – France
M. Serluca	UMAN, The University of Manchester and the Cockcroft Institute, UK
E. Shaposhnikova	CERN, Accelerator & Technology Sector, CH-1211, Geneva, Switzerland
D. Shatilov	BINP, Novosibirsk, Russia
A. Siemko	CERN, Accelerator & Technology Sector, CH-1211, Geneva, Switzerland
J. Skarita	BNL, Brookhaven National Laboratory, Upton, NY 11973, USA
E. Skordis	CERN, Accelerator & Technology Sector, CH-1211, Geneva, Switzerland
D. Smekens	CERN, Accelerator & Technology Sector, CH-1211, Geneva, Switzerland
Z. Sobiech	CERN, Accelerator & Technology Sector, CH-1211, Geneva, Switzerland
B. Spataro	INFN-LNF, Via E. Fermi 40, 00044 Frascati, Rome, Italy

G. Spiezia	CERN, Accelerator & Technology Sector, CH-1211, Geneva, Switzerland
G. Stancari	Fermi National Accelerator Laboratory, Batavia, P.O. Box 500, IL, USA
G. Steele	CERN, Accelerator & Technology Sector, CH-1211, Geneva, Switzerland
M. Sugano	KEK, Oho, Tsukuba, 305-0801, Japan
A. Szeberenyi	CERN, Accelerator & Technology Sector, CH-1211, Geneva, Switzerland
M. Taborelli	CERN, Accelerator & Technology Sector, CH-1211, Geneva, Switzerland
C. Tambasco	CERN, Accelerator & Technology Sector, CH-1211, Geneva, Switzerland
L. Tavian	CERN, Accelerator & Technology Sector, CH-1211, Geneva, Switzerland
B. Teissandier	CERN, Accelerator & Technology Sector, CH-1211, Geneva, Switzerland
N. Templeton	STFC, Daresbury Laboratory, Warrington WA4 4AD, UK
M. Therasse	CERN, Accelerator & Technology Sector, CH-1211, Geneva, Switzerland
H. Thiesen	CERN, Accelerator & Technology Sector, CH-1211, Geneva, Switzerland
A. Toader	UHUD, University of Huddersfield, Huddersfield, UK
E. Todesco	CERN, Accelerator & Technology Sector, CH-1211, Geneva, Switzerland
R. Tomás	CERN, Accelerator & Technology Sector, CH-1211, Geneva, Switzerland
F. Toral	CIEMAT, Madrid, Spain
R. Torres-Sanchez	CERN, Accelerator & Technology Sector, CH-1211, Geneva, Switzerland
I.S. Tropin	Fermi National Accelerator Laboratory, Batavia, P.O. Box 500, IL, USA
J. Tuckmantel	CERN, Accelerator & Technology Sector, CH-1211, Geneva, Switzerland
J. Uythoven	CERN, Accelerator & Technology Sector, CH-1211, Geneva, Switzerland
A. Valishev	INFN-LNF, Via E. Fermi 40, 00044 Frascati, Rome, Italy
E. Van Weelden	CERN, Accelerator & Technology Sector, CH-1211, Geneva, Switzerland
F. Velotti	CERN, Accelerator & Technology Sector, CH-1211, Geneva, Switzerland
S. Verdu Andres	BNL, Brookhaven National Laboratory, Upton, NY 11973, USA
A. Verweij	CERN, Accelerator & Technology Sector, CH-1211, Geneva, Switzerland
N. Vittal Shetty	CERN, Accelerator & Technology Sector, CH-1211, Geneva, Switzerland
V. Vlachoudis	CERN, Accelerator & Technology Sector, CH-1211, Geneva, Switzerland
G. Volpini	INFN-LASA, Milan, Italy
U. Wagner	CERN, Accelerator & Technology Sector, CH-1211, Geneva, Switzerland
P. Wanderer	BNL, Brookhaven National Laboratory, Upton, NY 11973, USA
M.H. Wang	SLAC National Accelerator Laboratory, 2575 Sand Hill Road, Menlo Park California 94025 USA
X. Wang	LBNL, Lawrence Berkeley National Laboratory, Berkeley, CA 94720, USA
R. Wanzenberg	Deutsches Elektronen-Synchrotron Notkestr. 85, 2000 Hamburg 52, Germany
R.V. Weelden	CERN, Accelerator & Technology Sector, CH-1211, Geneva, Switzerland
S. Weisz	CERN, Accelerator & Technology Sector, CH-1211, Geneva, Switzerland
J. Wenninger	CERN, Accelerator & Technology Sector, CH-1211, Geneva, Switzerland
W. Weterings	CERN, Accelerator & Technology Sector, CH-1211, Geneva, Switzerland
S. White	CERN, Accelerator & Technology Sector, CH-1211, Geneva, Switzerland
G. Willering	CERN, Accelerator & Technology Sector, CH-1211, Geneva, Switzerland
D. Wollmann	CERN, Accelerator & Technology Sector, CH-1211, Geneva, Switzerland
A. Wolski	University of Liverpool, Liverpool L69 7ZE, UK
Q. Wu	BNL, Brookhaven National Laboratory, Upton, NY 11973, USA
B. Xiao	BNL, Brookhaven National Laboratory, Upton, NY 11973, USA

L. Xiao	SLAC National Accelerator Laboratory, 2575 Sand Hill Road, Menlo Park California 94025 USA
Q. Xu	KEK, Oho, Tsukuba, 305-0801, Japan
Y. Yakovlev	Fermi National Accelerator Laboratory, Batavia, P.O. Box 500, IL, USA
Y. Yang	University of Southampton, Southampton SO17 1BJ, UK
M. Yu	Fermi National Accelerator Laboratory, Batavia, P.O. Box 500, IL, USA
I. Zacharov	EPFL, Lausanne, Switzerland
O. Zagorodnova	Deutsches Elektronen-Synchrotron Notkestr. 85, 2000 Hamburg 52, Germany
C. Zannini	CERN, Accelerator & Technology Sector, CH-1211, Geneva, Switzerland
C. Zaroni	CERN, Accelerator & Technology Sector, CH-1211, Geneva, Switzerland
M. Zerlauth	CERN, Accelerator & Technology Sector, CH-1211, Geneva, Switzerland
F. Zimmermann	CERN, Accelerator & Technology Sector, CH-1211, Geneva, Switzerland
A. Zlobin	Fermi National Accelerator Laboratory, Batavia, P.O. Box 500, IL, USA
M. Zobov	INFN-LNF, Via E. Fermi 40, 00044 Frascati, Rome, Italy

# Chapter 1

## High Luminosity Large Hadron Collider HL-LHC

*G. Apollinari<sup>1</sup>, O. Brüning<sup>2</sup>, T. Nakamoto<sup>3</sup> and L. Rossi<sup>2\*</sup>*

<sup>1</sup>Fermi National Accelerator Laboratory, Batavia, USA

<sup>2</sup>CERN, Accelerator & Technology Sector, Geneva, Switzerland

<sup>3</sup>KEK, Tsukuba, Japan

### 1 High Luminosity Large Hadron Collider HL-LHC

#### 1.1 Introduction

The Large Hadron Collider (LHC) was successfully commissioned in 2010 for proton–proton collisions with a 7 TeV centre-of-mass energy and delivered 8 TeV centre-of-mass proton collisions from April 2012 to the end of 2013. The LHC is pushing the limits of human knowledge, enabling physicists to go beyond the Standard Model. The announcement given by CERN on 4 July 2012 about the discovery of a new boson at about 125 GeV, the long-awaited Higgs particle, is the first fundamental discovery, hopefully the first of a series that LHC can deliver.

It is a remarkable era for cosmology, astrophysics and high energy physics and the LHC is at the forefront of attempts to understand the fundamental nature of the universe. The discovery of the Higgs boson in 2012 is undoubtedly a major milestone in the history of physics. Beyond this, the LHC has the potential to go on and help answer some of the key questions of the age: the existence, or not, of supersymmetry; the nature of dark matter; the existence of extra dimensions. It is also important to continue to study the properties of the Higgs – here the LHC is well placed to do this in exquisite detail.

Thanks to the LHC, Europe has decisively regained world leadership in High Energy Physics (HEP), a key sector of knowledge and technology. The LHC can continue to act as catalyst for a global effort unrivalled by any other branch of science: out of the 10000 CERN users, more than 7000 are scientists and engineers using the LHC, half of which are from countries outside the EU.

The LHC will remain the most powerful accelerator in the world for at least the next two decades. Its full exploitation is the highest priority of the European Strategy for particle physics. This strategy has been adopted by the CERN Council, and is a reference point for the Particle Physics Strategy of the US and, to a certain extent, Japan. To extend its discovery potential, the LHC will need a major upgrade in the 2020s to increase its luminosity (and thus collision rate) by a factor of five beyond its design value. The integrated luminosity design goal is an increase by a factor of ten. As a highly complex and optimized machine, such an upgrade must be carefully studied. The necessary developments will require about 10 years to prototype, test and realize. The novel machine configuration, the High Luminosity LHC (HL-LHC), will rely on a number of key innovative technologies representing exceptional technological challenges. These include among others: cutting-edge 11–12 T superconducting magnets; very compact with ultra-precise phase control superconducting cavities for beam rotation; new technology for beam collimation; and long high-power superconducting links with zero energy dissipation.

---

\* Corresponding author: [Lucio.Rossi@cern.ch](mailto:Lucio.Rossi@cern.ch)

HL-LHC federates the efforts and R&D of a large international community towards the ambitious HL-LHC objectives and contributes to establishing the European Research Area (ERA) as a focal point of global research cooperation and a leader in frontier knowledge and technologies. HL-LHC relies on strong participation from various partners, in particular from leading US and Japanese laboratories. This participation will be required for the execution of the construction phase as a global project. In particular, the US LHC Accelerator R&D Program (LARP) has developed some of the key technologies for the HL-LHC, such as the large-aperture niobium–tin ( $\text{Nb}_3\text{Sn}$ ) quadrupoles and the crab cavities. The proposed governance model is tailored accordingly and should pave the way for the organization of the construction phase.

## 1.2 HL-LHC in a nutshell

The LHC baseline programme until 2025 is shown schematically in Figure 1-1. After entering into the nominal energy regime of 13–14 TeV centre-of-mass energy in 2015, it is expected that the LHC will reach the design luminosity of  $1 \times 10^{34} \text{ cm}^{-2} \text{ s}^{-1}$ . This peak value should give a total integrated luminosity of about  $40 \text{ fb}^{-1}$  per year. In the period 2015–2022 the LHC will hopefully further increase the peak luminosity. Margins in the design of the nominal LHC are expected to allow, in principle, about two times the nominal design performance. The baseline programme for the next ten years is depicted in Figure 1-1, while Figure 1–2 shows the possible evolution of peak and integrated luminosity.

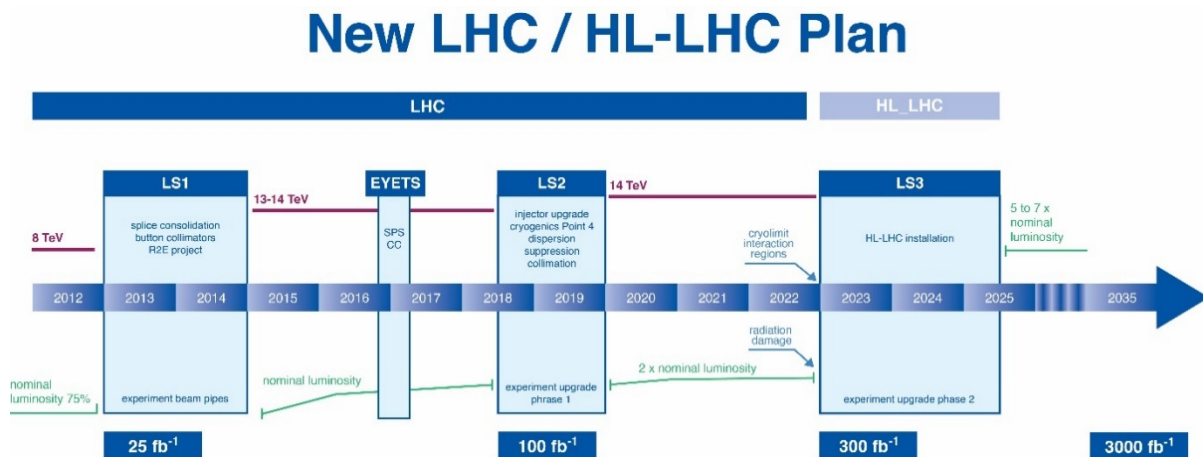


Figure 1-1: LHC baseline plan for the next decade and beyond showing the energy of the collisions (upper red line) and luminosity (lower green lines). The first long shutdown (LS1) in 2013–2014 will allow the design parameters of beam energy and luminosity to be reached. The second long shutdown (LS2) in 2018–2019, will consolidate luminosity and reliability as well as the upgrading of the LHC injectors. After LS3, 2023–2025, the machine will be in the High Luminosity configuration (HL-LHC).

After 2020 the statistical gain in running the accelerator without a significant luminosity increase beyond its design value will become marginal. The running time necessary after 2020 to halve the statistical error in measurements will be more than ten years. Therefore, to maintain scientific progress and to explore its full capacity, the LHC will need to have a decisive increase of its luminosity. This is why, when the CERN Council adopted the European Strategy for particle physics in 2006 [1], its first priority was agreed to be ‘to fully exploit the physics potential of the LHC. A subsequent major luminosity upgrade, motivated by physics results and operation experience, will be enabled by focused R&D’. The European Strategy for particle physics has been integrated into the European Strategy Forum on Research Infrastructures (ESFRI) Roadmap of 2006, as has the update of 2008 [2]. The priority to fully exploit the potential of the LHC has recently been confirmed as the *first priority* among the ‘High priority large-scale scientific activities’ in the new European Strategy for particle physics – Update 2013 [3]. This update was approved in Brussels on 30 May 2013 with the following wording: ‘Europe’s top priority should be the exploitation of the full potential of the LHC, including the high luminosity upgrade of the machine and detectors with a view to collecting ten times more data than in the initial design, by around 2030’.



The importance of the LHC luminosity upgrade for the future of high energy physics has been also recently re-affirmed by the May 2014 recommendation by the Particle Physics Project Prioritization Panel (P5) to the High Energy Physics Advisory Panel (HEPAP), which in turn advises the US Department of Energy (DOE) [4]. The recommendation, a critical step in the updating of the US strategy for HEP, states the following: ‘Recommendation 10: The LHC upgrades constitute our highest-priority near-term large project’.

In Japan, the 2012 report of a subcommittee in the HEP community concluded that an  $e^+e^-$  linear collider and a large-scale neutrino detector would be the core projects in Japan, with the assumption that the LHC and its upgrade are pursued de facto. The updated KEK roadmap in 2013 states that ‘The main agenda at LHC/ATLAS is to continually participate in the experiment and to take a proactive initiative in upgrade programmes within the international collaboration at both the accelerator and detector facilities.’ Following these supports, The ATLAS-Japan group has undertaken intensive R&D on the detector upgrades and the KEK cryogenic group has started the R&D upon the LHC separation dipole magnet.

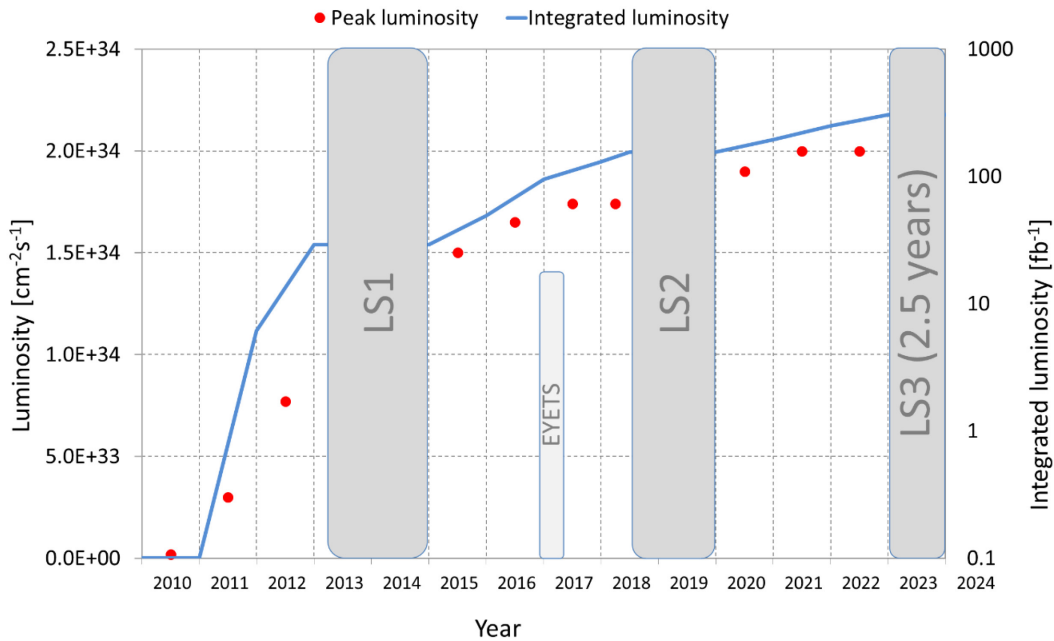


Figure 1-2: LHC luminosity plan for the next decade, both peak (red dots) and integrated (blue line). Main shutdown periods are indicated.

In this context, at the end of 2010 CERN created the High Luminosity LHC (HL-LHC) project [5]. Started as a design study, and after the approval of the CERN Council of 30 May 2013 and the insertion of the budget in the CERN Medium Term Plan approved by Council in June 2014, the HL-LHC has become CERN’s major construction project for the next decade.

The main objective of the High Luminosity LHC design study is to determine a set of beam parameters and the hardware configuration that will enable the LHC to reach the following targets:

- A peak luminosity of  $5 \times 10^{34} \text{ cm}^{-2} \text{ s}^{-1}$  with levelling, allowing:
- An integrated luminosity of  $250 \text{ fb}^{-1}$  per year with the goal of  $3000 \text{ fb}^{-1}$  in about a dozen years after the upgrade. This integrated luminosity is about ten times the expected luminosity reach of the first twelve years of the LHC lifetime.

The overarching goals are the installation of the main hardware for the HL-LHC and the commissioning of the new machine configuration during LS3, scheduled for 2023–2025, while taking all actions to assure a high efficiency in operation until 2035.

Actually, during the last year, the necessity emerged of aiming at an enhanced goal in terms of annual integrated luminosity. If the target of  $3000 \text{ fb}^{-1}$  should be reached by around 2035, as inferred by the European Strategy Update, the nominal goal of  $250 \text{ fb}^{-1}/\text{year}$  as fixed above is probably not adequate. However, since all equipment is being designed with a margin of 50%, regarding reaching the required luminosity, we are defining the concept of *ultimate parameters*. By using these margins we should be able to push our machine to about  $7\text{--}7.5 \times 10^{34} \text{ cm}^{-2} \text{ s}^{-1}$  of peak, levelling luminosity, therefore of course increasing the total pile-up in the detectors up to 200. This luminosity level should enable the collect of up to  $300\text{--}350 \text{ fb}^{-1}/\text{year}$ . Also, in terms of total integrated luminosity, we think we can define an ultimate value of about  $4000 \text{ fb}^{-1}$ . It must be said that while at first examination there is no showstopper for these performances, the ultimate parameters are not yet consolidated as the nominal parameters. Therefore, they will be thoroughly scrutinized and consolidated for the next version of the technical design report.

All of the hadron colliders in the world before the LHC have produced a combined total integrated luminosity of about  $10 \text{ fb}^{-1}$ . The LHC delivered nearly  $30 \text{ fb}^{-1}$  by the end of 2012 and should reach  $300 \text{ fb}^{-1}$  in its first 13–15 years of operation. The High Luminosity LHC is a major, extremely challenging, upgrade. For its successful realization, a number of key novel technologies have to be developed, validated, and integrated. The work was initiated quite early: ideas were circulating at the beginning of LHC construction [6] and this continued throughout construction [7]. From 2003, LARP (see Section 1.3.2) has been the main and continuous motor for technological development devoted to the LHC upgrade. After a period during which the upgrade was conceived in two phases, all studies were unified in 2010 under the newly formed High Luminosity Project. The first step consisted in launching a Design Study under the auspices of EC-FP7 with the nickname ‘HiLumi LHC’, which, following approval by the EC in 2011, has been instrumental in initiating a new global collaboration for the LHC matching the spirit of the worldwide user community of the LHC experiments. The High Luminosity LHC project is working in close collaboration with the CERN project for the LHC Injector complex Upgrade (LIU) [8], the companion ATLAS and CMS upgrade projects of 2018–2019 and 2023–2025 and the upgrade foreseen in 2018–2019 for both LHCb and Alice.

### 1.2.1 Luminosity

The (instantaneous) luminosity  $L$  can be expressed as:

$$L = \gamma \frac{n_b N^2 f_{\text{rev}}}{4\pi \beta^* \varepsilon_n} R; \quad R = 1 / \sqrt{1 + \frac{\theta_c \sigma_z}{2\sigma}} \quad (1-1)$$

where  $\gamma$  is the proton beam energy in unit of rest mass;  $n_b$  is the number of bunches per beam: 2808 (nominal LHC value) for 25 ns bunch spacing;  $N$  is the bunch population.  $N_{\text{nominal } 25 \text{ ns}}$ :  $1.15 \times 10^{11}$  p ( $\Rightarrow 0.58$  A of beam current at 2808 bunches);  $f_{\text{rev}}$  is the revolution frequency (11.2 kHz);  $\beta^*$  is the beam beta function (focal length) at the collision point (nominal design 0.55 m);  $\varepsilon_n$  is the transverse normalized emittance (nominal design:  $3.75 \mu\text{m}$ );  $R$  is a luminosity geometrical reduction factor (0.85 at a  $\beta^*$  of 0.55 m of, down to 0.5 at 0.25 m);  $\theta_c$  is the full crossing angle between colliding beam (285  $\mu\text{rad}$  as nominal design); and  $\sigma$ ,  $\sigma_z$  are the transverse and longitudinal r.m.s. sizes, respectively (nominally  $16.7 \mu\text{m}$  and  $7.55 \text{ cm}$ , respectively)

With the nominal parameter values shown above, a luminosity of  $1 \times 10^{34} \text{ cm}^{-2} \text{ s}^{-1}$  is obtained, with an average pile-up (number of events in the same bunch crossing) of  $\mu = 27$  (although  $\mu = 19$  was the original forecast at LHC approval due to uncertainties in the total proton cross-section at higher energies).

### 1.2.2 Present luminosity limitations and hardware constraints

There are various expected limitations to an increase in luminosity, either from beam characteristics (injector chain, beam impedance and beam–beam interactions in the LHC) or from technical systems. Mitigation of potential performance limitations arising from the LHC injector complex are addressed by the LIU project mentioned above, which should be completed in 2019 (after LS2). Any potential limitations coming from the LHC injector complex aside, it is expected that the present LHC will reach a performance limitation from the beam current, from cleaning efficiency with 350 MJ beam stored energy, from e-clouds effects, from the

maximum available cooling in the triplet magnets, from the magnet aperture ( $\beta^*$  limit) and from the acceptable pile-up level. The ultimate value of bunch population with the nominal LHC should enable a peak luminosity of around  $2 \times 10^{34} \text{ cm}^{-2} \text{ s}^{-1}$  to be reached. Any further performance increase of the LHC will require significant hardware and beam parameter modifications with respect to the design LHC configuration.

Before discussing the new configuration it is useful to recall the systems that need to be changed, and possibly improved, because they become vulnerable to breakdown and accelerated aging, or because they may become a bottleneck for operation in a higher radiation environment. This goes well beyond the ongoing basic consolidation.

- Inner triplet magnets. After about  $300 \text{ fb}^{-1}$  some components of the inner triplet quadrupoles and their corrector magnets will have received a dose of 30 MGy, entering into the region of possible radiation damage. The quadrupoles may withstand a maximum of  $400 \text{ fb}^{-1}$  to  $700 \text{ fb}^{-1}$ , but some corrector magnets of nested type are likely to have already failed at  $300 \text{ fb}^{-1}$ . Actual damage must be anticipated because the most likely failure mode is through sudden electric breakdown, entailing serious and long repairs. Thus the replacement of the triplet magnets must be envisaged before damage occurs. Replacement of the low-beta triplet is a long intervention, requiring a one- to two-year shutdown and must be coupled with major detector upgrades.
- Cryogenics. To increase intervention flexibility and machine availability it is planned to install a new cryogenics plant for a full separation between superconducting RF (SCRF) and magnet cooling. In the long term, the cooling of the inner triplets and matching section magnets must be separated from the arc magnets. This would avoid the need to warm-up an entire arc in the case of triplet region intervention.
- Collimation. The collimation system has been designed for the first operation phase of the LHC. The present system was optimized for robustness and will need an upgrade that takes into account the need for the lower impedance required for the planned increased beam intensities. A new configuration will also be required to protect the new triplets in IR1 and IR5.
- Also requiring special attention are the dispersion suppressor (DS) regions, where a leakage of off-momentum particles into the first and second main superconducting dipoles has been already identified as a possible LHC performance limitation. The most promising concept is to substitute an LHC main dipole with dipoles of equal bending strength ( $\sim 120 \text{ T}\cdot\text{m}$ ) obtained by a higher field (11 T) and shorter length (11 m) than those of the LHC dipoles (8.3 T and 14.2 m). The room gained is sufficient for the installation of special collimators.
- Radiation to electronics (R2E) and superconducting links for the remote powering of cold circuits. Considerable effort is being made to study how to replace the radiation-sensitive electronics boards of the power converter system with radiation-hard cards. A complementary solution is also being pursued for special zones. This would entail removal of the power converters and associated electrical feedboxes (DFBs), delicate equipment presently in line with the continuous cryostat) out of the tunnel, possibly to the surface. LHC availability should be improved. In particular in LHC P7, where a set of 600 A power converters are placed near the betatron cleaning collimators, removal will be to a lateral tunnel because the surface is not accessible. Displacement of power converters to distant locations is possible only thanks to a novel technology: superconducting links (SCLs) made from YBCO or Bi-2223 High Temperature Superconductors (HTS) or  $\text{MgB}_2$  superconductors.
- Quench Protection System (QPS), machine protection and remote manipulation. Other systems will potentially become problematic, along with the aging of the machine and the radiation level that comes with higher performance levels of  $40 \text{ fb}^{-1}$  to  $60 \text{ fb}^{-1}$  per year:
  - o QPS for the superconducting magnets, based on a design that is almost 20 years old.
  - o Machine protection: improved robustness to mis-injected beams, kicker sparks and asynchronous dumps will be required. The kicker system is, with collimation and the injection beam stopper, the

main shield against severe beam-induced damage. The kicker systems, along with the system will need renovation after 2020.

- Remote manipulation: the level of activation from 2020 onwards, and perhaps even earlier, requires careful study and the development of special equipment to allow the replacement of collimators, magnets, vacuum components, etc., according to the ‘as low as reasonably achievable’ (ALARA) principle. While full robotics is difficult to implement, given the conditions on the ground, remote manipulation, enhanced reality and supervision are the key to minimizing the radiation doses sustained during interventions.

### 1.2.3 Luminosity levelling, availability

Both the consideration of energy deposition by collision debris in the interaction region magnets, and the necessity to limit the peak pile-up in the experimental detector, impose an a priori limitation upon peak luminosity. The consequence is that HL-LHC operation will have to rely on luminosity levelling. As shown in Figure 1-3(a), the luminosity profile without levelling quickly decreases from the initial peak value due to ‘luminosity burn’ (protons consumed in the collisions). The collider is designed to operate with a constant luminosity at a value below the virtual maximum luminosity. The average luminosity achieved is almost the same as that without levelling, see Figure 1-3(b). The advantage, however, is that the maximum peak luminosity is lower.

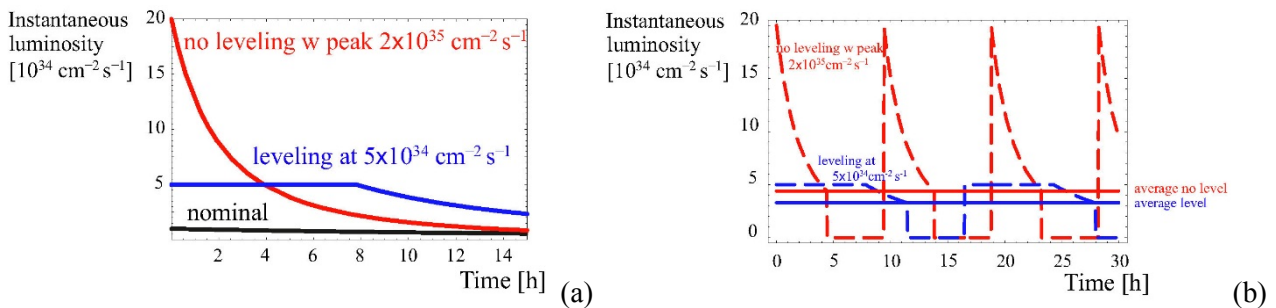


Figure 1-3: (a) Luminosity profile for a single long fill: starting at nominal peak luminosity (black line), with upgrade no levelling (red line), with levelling (blue line). (b) Luminosity profile with optimized run time, without and with levelling (blue and red dashed lines), and average luminosity in both cases (solid lines).

Because of the levelled luminosity limit, to maximize the integrated luminosity one needs to maximize the fill length. This can be achieved by maximizing the injected beam current. Other key factors for maximizing the integrated luminosity and obtaining the required  $3 \text{ fb}^{-1}/\text{day}$  (see Figure 1-4) are a short average machine turnaround time, an average operational fill length that exceeds the luminosity levelling time, and good overall machine efficiency. The machine efficiency is essentially the available time for physics after downtime for fault recovery is taken into account. Closely related is the physics efficiency – the fraction of time per year spent actually providing collisions to the experiments. For integrated luminosity the efficiency counts almost as much as the virtual peak performance.

The HL-LHC with 160 days of physics operation a year needs a physics efficiency of about 40%. The overall LHC efficiency during the 2012 run, without luminosity levelling, was around 37%. The requirement of an efficiency higher than the one of the present LHC, with a (levelled) luminosity five times that of nominal, will be a real challenge. The project must foresee a vigorous consolidation for the high intensity and high luminosity regime: the High Luminosity LHC must also be a high availability LHC.

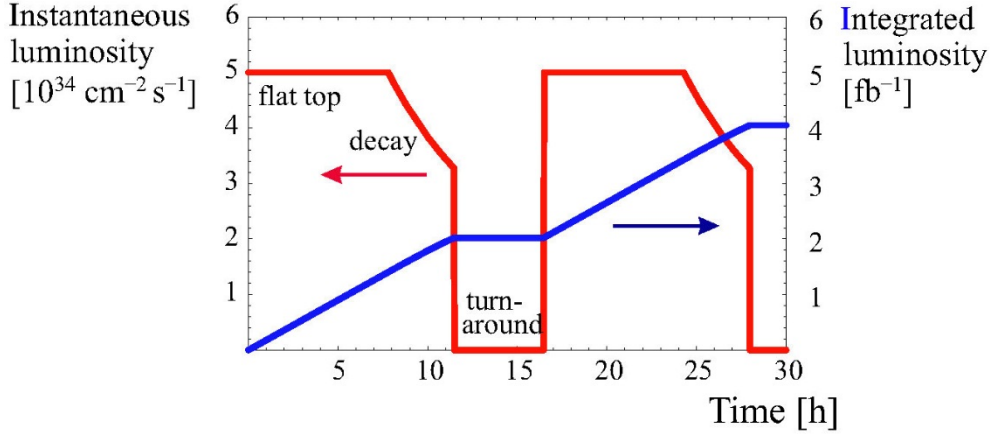


Figure 1-4: Luminosity cycle for HL-LHC with levelling and a short decay (optimized for integrated luminosity).

#### 1.2.4 HL-LHC parameters and main systems for the upgrade

Table 1-1 lists the main parameters foreseen for high luminosity operation. The 25 ns bunch spacing is the baseline operation mode; however, 50 ns bunch spacing is kept as a possible alternative in case the e-cloud or other unforeseen effects undermine 25 ns performance. A slightly different parameter set at 25 ns (batch compression and beam merging scheme (BCMS)) with very small transverse beam emittance is also shown and might be interesting for HL-LHC operation in case operation with high beam intensities results in unforeseen emittance blow-up.

Table 1-1: High Luminosity LHC parameters

Parameter	Nominal LHC (design report)	HL-LHC 25 ns (standard)	HL-LHC 25 ns (BCMS)	HL-LHC 50 ns
Beam energy in collision [TeV]	7	7	7	7
$N_b$	$1.5 \times 10^{11}$	$2.2 \times 10^{11}$	$2.2 \times 10^{11}$	$3.5 \times 10^{11}$
$n_b$	2808	2748	2604	1404
Number of collisions in IP1 and IP5	2808	2736*	2592	1404
$N_{\text{tot}}$	$3.2 \times 10^{14}$	$6 \times 10^{14}$	$5.7 \times 10^{14}$	$4.9 \times 10^{14}$
Beam current [A]	0.58	1.09	1.03	0.89
Crossing angle [ $\mu\text{rad}$ ]	285	590	590	590
Beam separation [ $\sigma$ ]	9.4	12.5	12.5	11.4
$\beta^*$ [m]	0.55	0.15	0.15	0.15
$\varepsilon_n$ [ $\mu\text{m}$ ]	3.75	2.50	2.50	3
$\varepsilon_L$ [eVs]	2.50	2.50	2.50	2.50
r.m.s. energy spread	$1.13 \times 10^{-4}$	$1.13 \times 10^{-4}$	$1.13 \times 10^{-4}$	$1.13 \times 10^{-4}$
r.m.s. bunch length	$7.55 \times 10^{-2}$	$7.55 \times 10^{-2}$	$7.55 \times 10^{-2}$	$7.55 \times 10^{-2}$
IBS horizontal [h]	80–106	18.5	18.5	17.2
IBS longitudinal [h]	61–60	20.4	20.4	16.1
Piwinski parameter	0.65	3.14	3.14	2.87
Geometric loss factor $R_0$ without crab cavity	0.836	0.305	0.305	0.331
Geometric loss factor $R_1$ with crab cavity	(0.981)	0.829	0.829	0.838
Beam–beam/IP without crab cavity	$3.1 \times 10^{-3}$	$3.3 \times 10^{-3}$	$3.3 \times 10^{-3}$	$4.7 \times 10^{-3}$
Beam–beam/IP with crab cavity	$3.8 \times 10^{-3}$	$1.1 \times 10^{-2}$	$1.1 \times 10^{-2}$	$1.4 \times 10^{-2}$
Peak luminosity without crab cavity [ $\text{cm}^{-2} \text{ s}^{-2}$ ]	$1.00 \times 10^{34}$	$7.18 \times 10^{34}$	$6.80 \times 10^{34}$	$8.44 \times 10^{34}$
Virtual luminosity with crab cavity, $L_{\text{peak}} \times R_1/R_0$ [ $\text{cm}^{-2} \text{ s}^{-2}$ ]	$(1.18 \times 10^{34})$	$19.54 \times 10^{34}$	$18.52 \times 10^{34}$	$21.38 \times 10^{34}$

Events/crossing without levelling and without crab cavity	27	198	198	454
Levelled luminosity [ $\text{cm}^{-2} \text{s}^{-2}$ ]	-	$5.00 \times 10^{34\dagger}$	$5.00 \times 10^{34}$	$2.50 \times 10^{34}$
Events/crossing (with levelling and without crab cavities for HL-LHC)	27	138	146	135
Peak line density of pile-up event [event/mm] (maximum over stable beams)	0.21	1.25	1.31	1.20
Levelling time [h] (assuming no emittance growth)	-	8.3	7.6	18.0
Number of collisions in IP2/IP8	2808	2452/2524 <sup>‡</sup>	2288/2396	0 <sup>**</sup> /1404
$N_b$ at SPS extraction <sup>††</sup>	$1.20 \times 10^{11}$	$2.30 \times 10^{11}$	$2.30 \times 10^{11}$	$3.68 \times 10^{11}$
$n_b$ /injection	288	288	288	144
$N_{\text{tot}}$ /injection	$3.46 \times 10^{13}$	$6.62 \times 10^{13}$	$6.62 \times 10^{13}$	$5.30 \times 10^{13}$
$\varepsilon_n$ at SPS extraction [ $\mu\text{m}$ ] <sup>‡‡</sup>	3.40	2.00	<2.00 <sup>***</sup>	2.30

\*Assuming one less batch from the PS for machine protection (pilot injection, Transfer line steering with 12 nominal bunches) and non-colliding bunches for experiments (background studies, etc.). Note that due to RF beam loading the abort gap length must not exceed the 3  $\mu\text{s}$  design value.

<sup>†</sup>For the design of the HL-LHC systems (collimators, triplet magnets, etc.), a margin of 50% on the stated peak luminosity (corresponding to the ultimate levelled luminosity) has been agreed.

<sup>‡</sup>The total number of events/crossing is calculated with an inelastic cross-section of 85 mb (also for nominal), while 100 mb is still assumed for calculating the proton burn off and the resulting levelling time.

<sup>\*\*</sup>The lower number of collisions in IR2/8 compared to the general-purpose detectors is a result of the agreed filling scheme, aiming as much as possible at a democratic sharing of collisions between the experiments.

<sup>††</sup>An intensity loss of 5% distributed along the cycle is assumed from SPS extraction to collisions in the LHC.

<sup>‡‡</sup>A transverse emittance blow-up of 10–15% on the average H/V emittance in addition to that expected from intra-beam scattering (IBS) is assumed (to reach 2.5  $\mu\text{m}$  of emittance in collision for 25 ns operation).

<sup>\*\*\*</sup>For the BCMS scheme emittances down to 1.7  $\mu\text{m}$  have already been achieved at LHC injection, which might be used to mitigate excessive emittance blow-up in the LHC during injection and ramp. An upgrade should provide the potential for performance over a wide range of parameters, and eventually the machine and experiments will find the best practical set of parameters in actual operations.

Beam current and brightness: the total beam current may be a hard limit in the LHC since many systems are affected by this parameter: RF power system and RF cavities, collimation, cryogenics, kickers, vacuum, beam diagnostics, QPS, etc. Radiation effects aside, all systems have been designed in principle for  $I_{\text{beam}} = 0.86$  A, the so-called ‘ultimate’ beam current. However the ability to go to the ultimate limit is still to be experimentally demonstrated and the HL-LHC will need to go 30% beyond ultimate with 25 ns bunch spacing.

For the HL-LHC there is a need to increase the beam brightness, a beam characteristic that must be maximized at the beginning of beam generation and then preserved throughout the entire injector chain and in LHC itself. The LIU project has as its primary objective increasing the number of protons per bunch by a factor of two above the nominal design value while keeping emittance at the present low value.

$\beta^*$  and cancelling the reduction factor R. A classical route for a luminosity upgrade is to reduce  $\beta^*$  by means of stronger and larger aperture low- $\beta$  triplet quadrupoles. However a reduction in  $\beta^*$  values implies not only larger beam sizes in the triplet magnets but also an increase in crossing angle. The increased crossing angle in turn requires even larger aperture triplet magnets, a larger aperture D1 (first separation dipole) and further modifications to the matching section. It also reduces the luminous region size and thus the gain in peak luminosity.

Stronger chromatic aberrations coming from the larger  $\beta$ -functions inside the triplet magnets may furthermore exceed the strength of the existing correction circuits. The peak  $\beta$ -function is also limited by the possibility to match the optics to the regular beta functions of the arcs. A previous study has shown that in the nominal LHC the practical limit for  $\beta^*$  is 30 cm to 40 cm cf. the nominal 55 cm. However, a novel scheme called Achromatic Telescopic Squeeze (ATS) uses the adjacent arcs as enhanced matching sections. The increase of the beta-functions in these arcs can boost, at constant strength, the efficiency of the arc correction circuits. In this way a  $\beta^*$  value of 15 cm can be envisaged, and flat optics with a  $\beta^*$  as low as 5 cm in the plane

perpendicular to the crossing plane could be realized. For such a  $\beta^*$  reduction the triplet quadrupoles need to double their aperture, and require a peak field 50% above the present LHC. This implies the use of new, advanced, superconducting technology based on Nb<sub>3</sub>Sn.

The drawback of very small  $\beta^*$  is that it requires a larger crossing angle. This causes a reduction of the geometrical luminosity reduction factor R. In Figure 1-5 the reduction factor is plotted vs.  $\beta^*$  values.

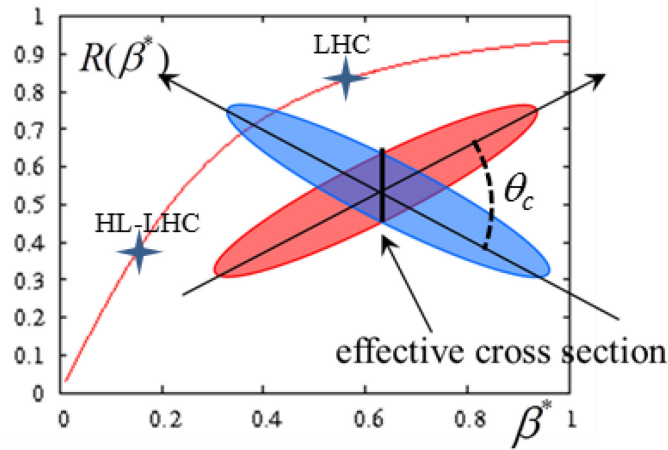


Figure 1-5: Behaviour of geometrical luminosity reduction factor vs.  $\beta$  for a constant normalized beam separation with the indication of two operational points: nominal LHC and HL-LHC. The bunch crossing sketch shows the reduction mechanism.

Various methods can be employed to at least partially counteract this effect. The most efficient and elegant solution for compensating the geometric reduction factor is the use of special superconducting RF crab cavities, capable of generating transverse electric fields that rotate each bunch longitudinally by  $\theta_c/2$ , such that they effectively collide head on, overlapping perfectly at the collision points, as illustrated in Figure 1-6. Crab cavities allow access to the full performance of the small  $\beta^*$  values offered by the ATS scheme and the larger triplet quadrupole magnets. While the primary function of the crab cavities is to boost the virtual peak luminosity, they can also be used in combination with dynamic  $\beta^*$  variation during the fill. This would allow optimization of the size of the luminous region and thus the pile-up density through the fill. Finally, the crab cavities can be used to tilt the bunches in a direction perpendicular to the plane of crossing, providing pile-up control and an additional handle for luminosity levelling through the so-called ‘crab-kissing’ scheme.

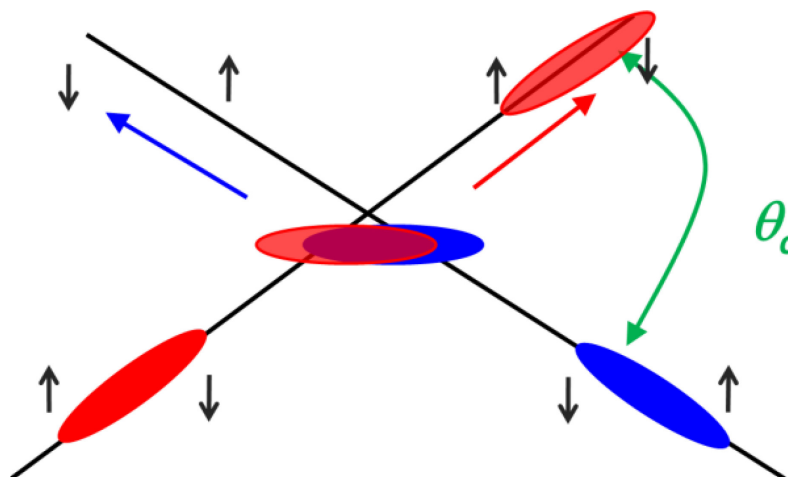


Figure 1-6: Effect of the crab cavity on the beam (small arrows indicate the torque on the bunch generated by the transverse RF field).

The layout and main hardware modifications required to produce the parameters listed in Table 1-1 are described in Chapter 2 of this report.

Given the yearly and long-term operations schedule, the targets of  $250 \text{ fb}^{-1}$  per year and  $3000 \text{ fb}^{-1}$  by the mid-2030s are very challenging. If the performance of the HL-LHC can go beyond the design levelled luminosity value of  $L_{\text{peak}} = 5 \times 10^{34} \text{ cm}^{-2} \text{ s}^{-1}$  then these targets become more reasonable. Indeed, all systems will be designed with some margin. If the behaviour of the machine is such as to allow the utilization of these margins, and if the upgraded detectors will accept a higher pile-up, up to 200, then the performance could eventually reach  $7.5 \times 10^{34} \text{ cm}^{-2} \text{ s}^{-1}$  with levelling. With a performance of  $300 \text{ fb}^{-1}/\text{year}$ , this would allow almost  $4000 \text{ fb}^{-1}$  to be obtained by 2037, as shown in Figure 1-7.

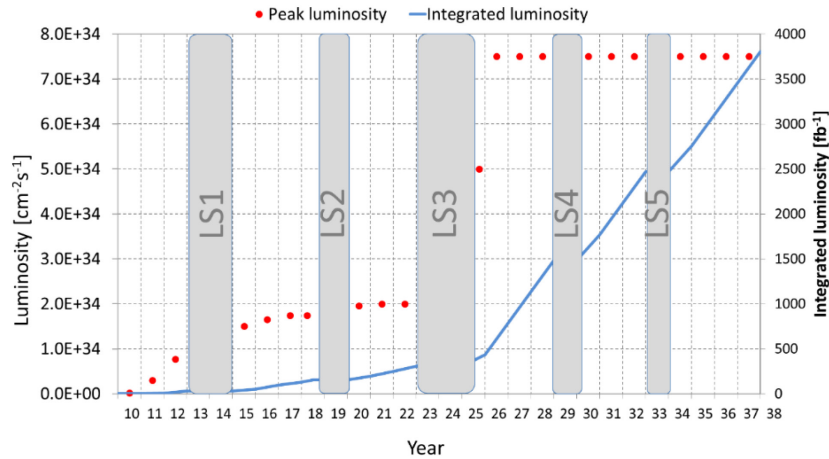


Figure 1-7: Forecast for peak luminosity (red dots) and integrated luminosity (blue line) in the HL-LHC era, for the case of ultimate HL-LHC parameters. Note that for the sake of simplicity there is no learning curve for luminosity after LS3.

### 1.2.5 Planning and costings

The HL-LHC schedule aims at the installation of the main HL-LHC hardware during LS3, together with the final upgrade of the experimental detectors (the so-called Phase II upgrade). However, a few items like the new cryogenic plant for P4, the 11 T dipole for DS collimation in P2 (for ions) and the SC links in P7 would be installed during LS2.

The HL-LHC schedule is based on the following milestones:

- 2014: Preliminary Design Report (PDR);
- 2015: End of design phase, release of the first Technical Design Report (TDR);
- 2016: Proof of main hardware components on test benches;
- 2017: Testing of prototypes (including crab cavity test in SPS) and release of TDR v1;
- 2017–2021: Construction and test of long-lead hardware components (e.g. magnets, crab cavities, SC links, collimators);
- 2018–2019: LS2 – Installation of cryo-plant P4, DS collimators (11 T) in P2, SC link in P7;
- 2020–2022: String test of inner triplet;
- 2023–2025: LS3 – Main installation (new magnets, crab cavities, cryo-plants, collimators, absorbers, etc.) and commissioning.





Figure 1-8: Schematic representation of the main HL-LHC milestones

The preliminary cost-to-completion (CtC) of the full HL-LHC project amounts to about 830 MCHF for materials (CERN accounting). A coarse evaluation of personnel requirements amounts to more than 1000 fulltime equivalent (FTE) years. The cost-to-completion does not include the civil engineering works for the underground infrastructures (presently under evaluation) and non-baseline systems such as the long-range beam-beam compensators, the RF harmonic system, and the related infrastructure. The budget profile is shown in Figure 1-9.

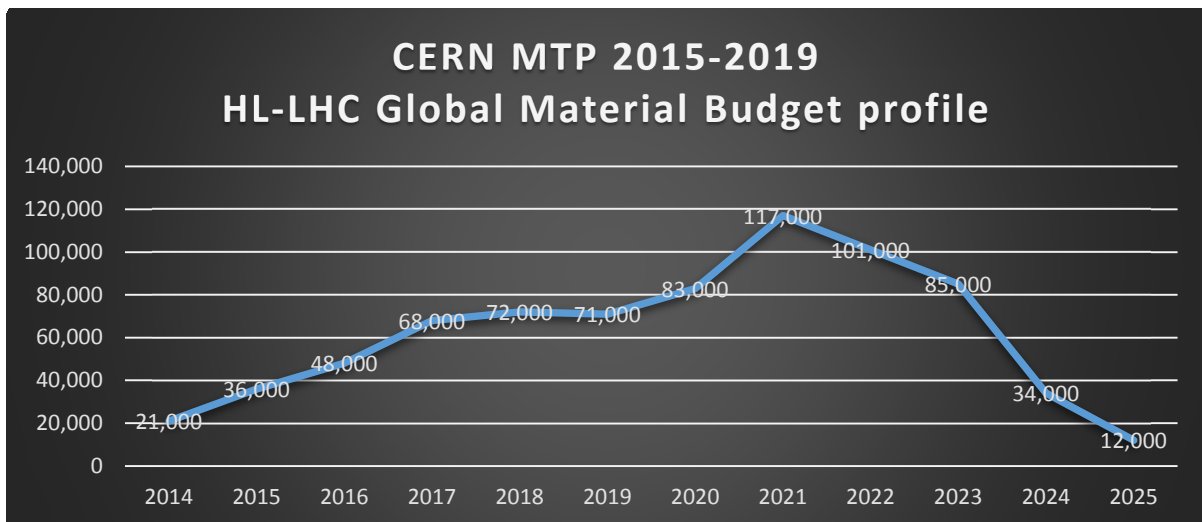


Figure 1-9: Budget allocation 2015 to 2025

Today the CERN draft budget attributes about 750 MCHF for the HL-LHC project until 2025, with certain assumptions of in-kind contributions from both the US and Japan. The discrepancy is not critical at this stage, since the modifications of certain systems are not yet fully defined. LHC operation at full energy and intensity will give important indications. The thorough investigation of potential synergy with the LHC consolidation project, together with various studies, should allow savings without compromising performance. Additional in-kind contributions to the hardware baseline would help alleviate the cost discrepancy and would also bring more personnel into the project.

A further possibility is to stage the project by using LS4, see Figure 1-7. Indeed the performance ‘forecast’ shown in Figure 1-7 is somewhat theoretical: there will be certainly a learning curve to pass from  $2 \times 10^{34} \text{ cm}^{-2} \text{ s}^{-1}$  to (levelled)  $5 \times 10^{34} \text{ cm}^{-2} \text{ s}^{-1}$ , naturally favouring a staged approach. However, the  $250 \text{ fb}^{-1}$  annual integrated luminosity goal can only be attained, and possibly even surpassed, when installation of all equipment is completed.

### 1.3 The collaboration

The LHC Luminosity Upgrade was conceived from the beginning as being even more international than the construction of the LHC machine, since US laboratories started to work on it with considerable resources well before CERN. In 2002–2003 collaboration between the US laboratories and CERN established the route for a machine upgrade [7]. The LARP programme was then setup and approved by the US Department of Energy (DOE). In the meantime, CERN was totally engaged in LHC construction and commissioning: it could only participate in Coordinated Accelerator Research in Europe (CARE), an EC-FP6 programme, in 2004–2008. CARE contained a modest programme for the LHC upgrade. Then two EC-FP7 programmes (SLH-PP and EuCARD) helped to reinforce the design and R&D work for the LHC upgrade in Europe, although still at a modest level. KEK in Japan, in the framework of the permanent CERN-KEK collaboration, from 2008 also engaged in activities for the LHC upgrade. LARP remained, until 2011, the main R&D activity in the world for the LHC upgrade.

Finally, with the approval of the EC-FP7 Design Study *HiLumi LHC* in 2011, and the maturing of the main project lines, the HL-LHC collaboration took its present form. It is worth noticing that FP7-HiLumi covers only the design of a few systems, given the limited amount of funding in such a programme. It has, however, allowed the formation and structuring of a European participation to the LHC Upgrade from the very beginning of the project. In 2014, CEA (Saclay, France), INFN (Milan and Genova, Italy) and CIEMAT (Madrid, Spain) have signed a further collaboration agreement to carry out design, engineering and prototyping work for HL-LHC magnets in addition to the FP7-EC commitment. In all three cases the CERN funding for the activities is approximately 50%, the rest being supported by the collaborating institutes. In Figure 1–10 a schematic indicating the various collaborating branches is shown.

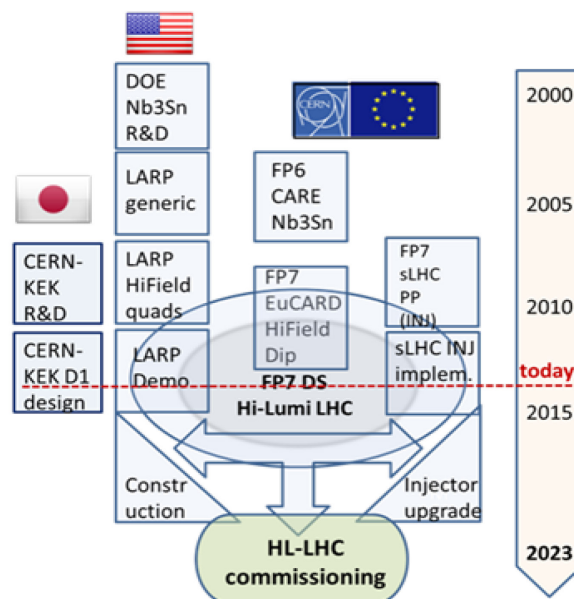


Figure 1-10: Timeline of the various collaboration branches, converging toward the LHC luminosity upgrade.

#### 1.3.1 FP7-Hilumi LHC

The ‘FP7 High Luminosity Large Hadron Collider Design Study’ (FP7-HiLumi LHC) proposal was submitted in November 2010 to the EC Seventh Framework Programme. Approved with a full score of 15/15 it has been fully funded by the EC. The contract was signed by the fifteen partners (beneficiaries). KEK is a partner without EC funding – all of their funding is internal. The US laboratories were part of the proposal, without EC funding, but then for various reasons (mainly related to Intellectual Property issues) they could not sign

the FP7-HiLumi LHC Consortium Agreement, thus they are external associates with no formal obligations. In practice LARP is excellently coordinated with FP7-HiLumi (see Section 1.3.2) and the project heavily relies on LARP to reach the project goals.

The workings of FP7 are such that each of the thirteen European institutions that are members of HiLumi LHC have to match the EC contribution with their own funding. In the case of FP7-HiLumi the matching funds equal the EC funds: each EU Institute receives 50% of the total cost (including overheads). The exception is CERN, which receives only 17% of its total costs, mainly for management and coordination. In Figure 1-11 the funding mechanism is explained. Given the success of the evaluation, see above, the project was ranked first in its category and was fully financed, with a EU contribution of M€4.9 against a request of M€4.97.

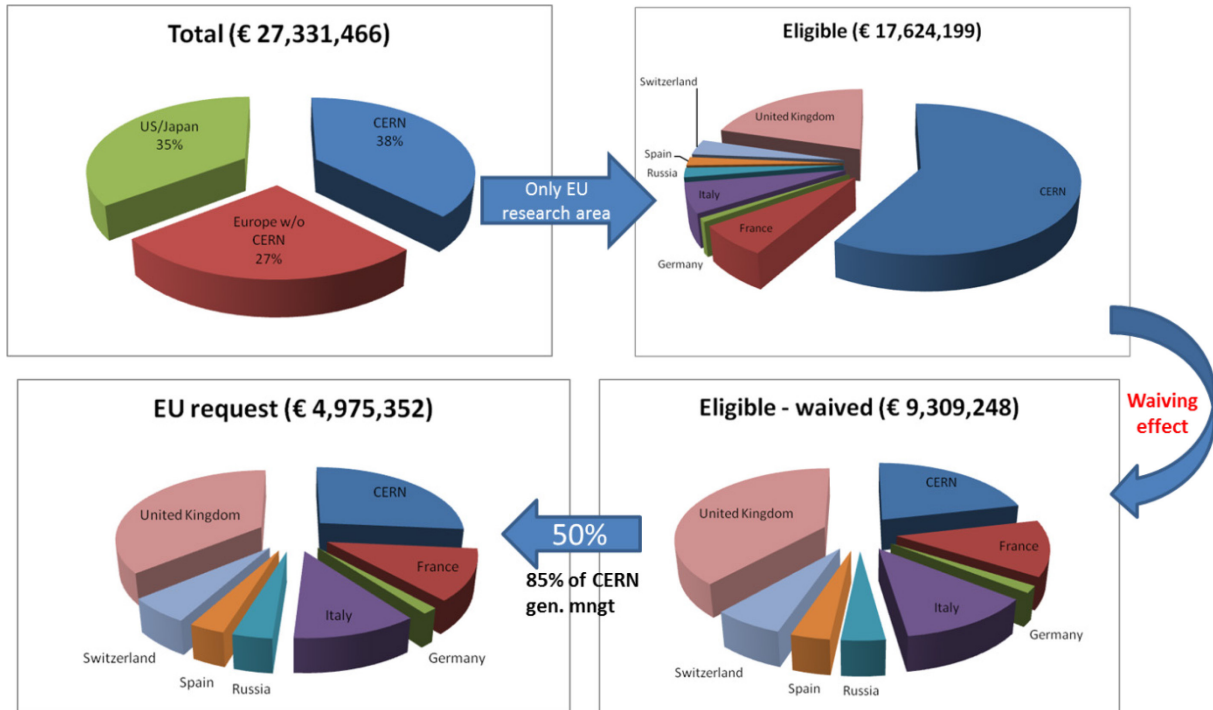

















Figure 1-11: (a) Total estimation of the cost of the design study, subdivided by the US and Japan, EU institutes and CERN. (b) Total cost with the US and Japan removed (i.e. only costs that are eligible for funding by the EC). (c) Effect of CERN waiving the cost for technical works (recognizing that the HL-LHC is part of the core CERN programme financed via the normal budget), while keeping the extra cost generated by the management and coordination of the project. This is the total cost declared to the EC. (d) Cost claimed from the EC: 50% of the declared cost (eligible cost reduced by CERN waiving action).

In Figure 1-12 a list of the 15 FP7-HiLumi institutes is given, followed by a list of the five US collaborating institutes.

Short Name	Country	Logo	Short Name	Country	Logo
<a href="#">CERN</a>	Geneva Switzerland		<a href="#">STFC*</a>	<del>Daresbury</del> United Kingdom	 Science & Technology Facilities Council
<a href="#">CEA</a>	<del>Saclay</del> France		<a href="#">ULANC*</a>	Lancaster United Kingdom	
<a href="#">DESY</a>	Hamburg Germany		<a href="#">UNILIV*</a>	Liverpool United Kingdom	
<a href="#">INFN</a>	<del>Erascati</del> Italy		<a href="#">UNIMAN*</a>	Manchester United Kingdom	
<a href="#">CSIC</a>	Madrid Spain		<a href="#">HUD</a>	Huddersfield United Kingdom	
<a href="#">EPFL</a>	Lausanne Switzerland		<a href="#">KEK</a>	Tsukuba Japan	
<a href="#">SOTON</a>	Southampton United Kingdom		<a href="#">BINP</a>	Novosibirsk Russia	
<a href="#">RHUL</a>	London United Kingdom		*Members of Cockcroft Institute		

(a)

Short Name	Country	Logo	
<a href="#">BNL</a>	Upton, NY USA		
<a href="#">FNAL</a>	Batavia, IL USA		
<a href="#">LBNL</a>	Berkeley, CA USA		
<a href="#">SLAC</a>	Menlo Park, CA USA		
<a href="#">ODU</a>	Norfolk, VA USA		

(b)

Figure 1-12: (a) Table showing the 15 members ('beneficiaries') of the FP7 HiLumi LHC design study and (b) the five LARP laboratories that are associated with the project.

### 1.3.2 LHC Accelerator R&D Program (LARP)

The LARP programme was initiated by the US Department of Energy (DOE) in 2003 to participate in the commissioning of the US-built interaction region triplets by bringing together and coordinating resources from the four US HEP laboratories (BNL, FNAL, LBNL and SLAC) with the inclusion of some universities as the programme evolved. By 2003 it was already recognized, based on the Tevatron experience, that an increase in LHC luminosity would become necessary after a decade of LHC operation to reduce the 'halving time', i.e. the time needed to reduce statistical errors by a factor of two. Consequently the programme focused – from the very beginning – on the design of improved focusing quadrupoles for the LHC low- $\beta$  insertion regions, finding a synergy with the various DOE high-field magnet (HFM) R&D programmes at the participating laboratories. The conductor of choice for this R&D programme was selected to be Nb<sub>3</sub>Sn and therefore LARP became synergetic with another DOE programme, the Conductor Development Program (CDP), initiated in 1998 with the goal of improving the performance of Nb<sub>3</sub>Sn. The LARP, CDP, and other US labs' HFM activities interacted in an extremely constructive way, achieving a substantial increase in the critical current performance of Nb<sub>3</sub>Sn superconductors (Figure 1-13) and defining the assembly technique for accelerator quality high-field Nb<sub>3</sub>Sn magnets in different kinds of configuration and with different apertures.

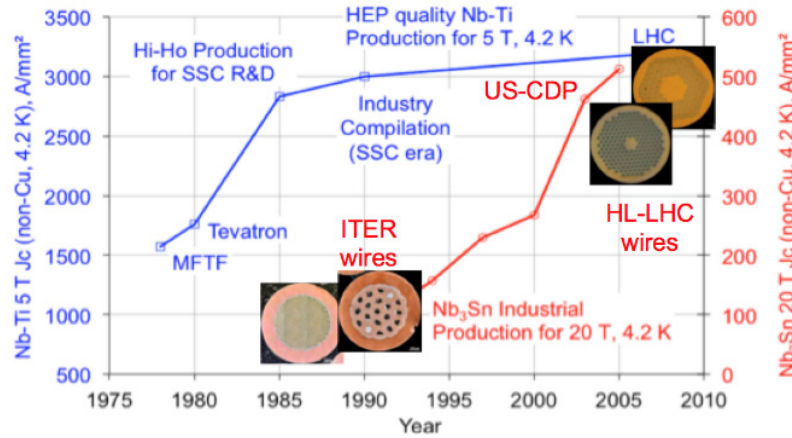
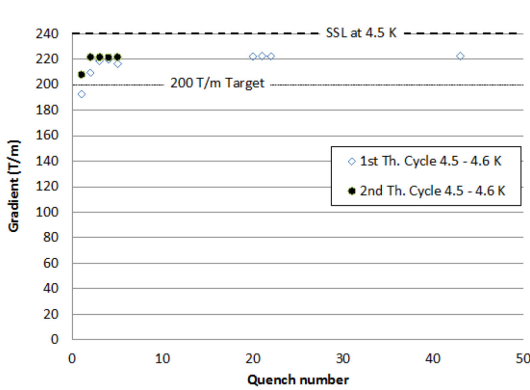
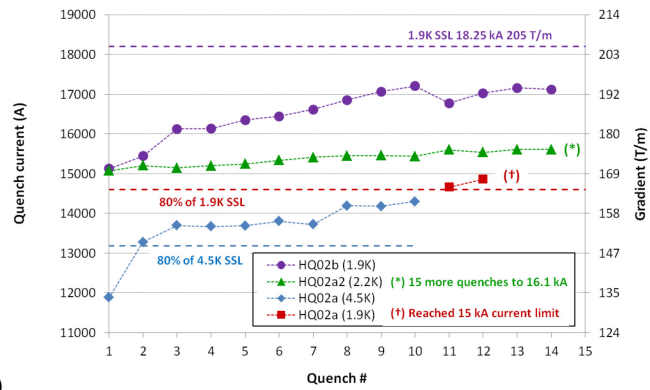


Figure 1-13: Left: Improvement in  $J_c$  (current density) in  $Nb_3Sn$  superconductor during the last three decades compared with  $Nb-Ti$   $J_c$  performance.

The LARP effort was funded at approximately \$12–13 million/year, with 50% of the funding going directly to magnet development. Several magnets developed by LARP reached and surpassed the design field as shown in Figure 1-14(b) for one of the latest models (HQ02, a 120 mm aperture quadrupole assembled in 2014 and tested at FNAL and CERN). Additionally, LARP has demonstrated the scale-up of the  $Nb_3Sn$  technology (i.e. the performance of the technology for magnets as long as 3 m) as shown in Figure 1-14(a) for the 90-mm aperture long quadrupole (LQ). The achievements of the US programmes, in particular LARP, but also of the general R&D high-field magnet programme, have led to the adoption of the  $Nb_3Sn$  superconductor solution as the baseline for the HL-LHC’s new focusing system and 11 T magnets.



(a)



(b)

Figure 1-14: (a) Quench performance of the long quadrupole (LQ), the first quadrupole demonstrating the scale-up of  $Nb_3Sn$  technology to lengths of interest for LHC applications ( $\sim 3$  m), (b) quench performance of HQ02 (120 mm aperture) after several re-assemblies, showing that in all cases the magnet achieved and passed the target (80% of the short sample limit (SSL)).

In addition to contributions to LHC commissioning and magnet development-related activities, LARP was also tasked with the support and promotion of accelerator physics R&D activities at the LHC accelerator. An additional very important aspect of this commitment was the institution of the Toohig Fellowship (<http://www.interactions.org/toohig/>) to support young accelerator physicists and engineers wishing to pursue research at the LHC in the early years of their career.

Recently, LARP has leveraged the superconducting RF capabilities and resources available at US laboratories and universities to focus on the development of crab cavities (Chapter 4), achieving transverse fields meeting the technical specifications for this system. In addition, a wide band feedback system is being researched and developed within LARP with the goal of mitigating transverse instabilities in the SPS and, possibly, in the LHC.

The DOE and CERN will negotiate the deliverables from the US in the coming years. In the CY15–CY17 period, LARP will concentrate on prototyping the elements needed by the HL-LHC project in which US national laboratories and universities have demonstrated excellent capabilities. In particular – subject to funding availability – LARP plans to build two short (1m) and three long (4 m) QXF magnet models to demonstrate the final design and reduce the risk during the construction period. In addition, LARP plans to deliver four fully-dressed SCRF crab cavities and a wide band feedback system prototype for tests in the SPS. This phase is expected to continue until the start of construction in the period 2018–2021.

### 1.3.3 KEK

Within the framework of the CERN-KEK collaboration, KEK has conducted Nb<sub>3</sub>Al superconductor R&D for the high-field magnets aimed at the future LHC upgrade from the early 2000s in collaboration with the National Institute of Materials Science (NIMS) in Japan. The Nb<sub>3</sub>Al superconductors are made by the rapid-heating, quenching transformation (RHQT) process, which was invented by NIMS. These superconductors have shown better critical current density and less strain dependence, and have been considered to be one of the promising candidates for high-field accelerator magnet applications. Nevertheless, KEK and NIMS faced technical difficulties in long wire production and it was judged in 2011 that the Nb<sub>3</sub>Al superconductor was unfortunately not ready for industrialization for the HL-LHC upgrade anticipated around 2022.

KEK has officially participated in the FP7 HiLumi LHC design study since 2011 in the context of enhancing the Japanese contribution to the physics outcome from the ATLAS experiment. Following the suppression of research activities on the development of the Nb<sub>3</sub>Al superconductor, the main effort was redirected to the conceptual design study for the beam separation dipole magnet, D1, situated immediately after the low-beta insertion quadrupoles in the HL-LHC machine. While the conceptual design study has been pursued dominantly by KEK, close collaboration with CERN and other partners has strengthened the success of the design study. The D1 magnet is based on the mature Nb-Ti technology. Design challenges are the tight control of the field quality with the large iron saturation, and the accommodation of the heat load and the radiation dose. The research engagement includes development of the 2 m long model magnet and testing at 1.9 K. KEK has also contributed to the HiLumi LHC design study through beam dynamics studies and the cooperative work associated with the crab cavity.

Aside from the FP7-HiLumi LHC, KEK has also participated in the LHC Injectors Upgrade (LIU) project. The main collaboration items have been consolidation and upgrade of PS Booster RF systems using Finemet-FT3L technology and development of the longitudinal damper system.

### 1.3.4 Other collaborations

In 2014, CEA (Saclay, France), INFN (Milan and Genova, Italy), and CIEMAT (Madrid, Spain), have each signed a further collaboration agreement to carry out design, engineering, and prototype work for HL-LHC magnets in addition to their FP7-HiLumi commitments. In all three cases, the CERN funding is about 50%, the rest being charged to the collaborating institutes.

#### 1.3.4.1 CEA

The CEA agreement concerns ‘Research and Development for future LHC Superconducting Magnets’. It has six technical work packages, covering R&D for the HL-LHC and for post-LHC magnets. Among them, the following are of HL-LHC interest.

- Design and construction of a single aperture, 1 m long, full-size coil model magnet for the first quadrupole of the matching section, Q4. The magnet is based on classical Nb-Ti technology but has a very large aperture (90 mm) in a two-in-one cold mass, and thus presents a number of design challenges.
- Completion of the 13 T, large-aperture dipole Fresca2 (a technological HL-LHC work package that has served to promote Nb<sub>3</sub>Sn at CERN).

- Studies on Nb<sub>3</sub>Sn thermal properties and a finite element model of Nb<sub>3</sub>Sn cable.

### 1.3.4.2 INFN (Milan and Genova)

The INFN agreement is also related to R&D on superconducting magnets for the HL-LHC and concerns two main items:

- Design and construction of a prototype of each of the six high-order corrector magnets for the inner triplet, all with a single aperture of 150 mm. The work is based on Nb-Ti superferric technology and is carried out at INFN-LASA in Milano. An option based on the MgB<sub>2</sub> superconductor is also being considered by INFN.
- Engineering Design of the superconducting recombination dipole magnet, D2, the first Two-in-One magnet, at the end of the common beam pipe. The work is based on Nb-Ti technology, with design challenges coming from the large aperture and the relatively high fields that have a parallel direction in both apertures. The work is being carried out at INFN-Genova.

### 1.3.4.3 CIEMAT (Madrid)

The CIEMAT agreement concerns the design and construction of a 1 m long prototype of the 150 mm aperture nested orbit corrector dipole for the inner triplet. It features two dipoles coils, rotated by 90° for simultaneous horizontal and vertical beam steering, in the same aperture. The main challenges are the mechanical structures to withstand the large torque, and the unusual force distribution arising when both field directions are needed.

## 1.4 Governance and project structure

Given the fact that the application for the FP7-HiLumi LHC Design Study marked the start of the project in its present form, the structure and terminology are borrowed from the typical FP7 style. To avoid any duplication the governance of the whole HL-LHC project is conceived as an extension of the governance that has been instituted for the governance of the FP7-HiLumi LHC.

As noted above, the FP7-HiLumi LHC covers only a few work packages (WPs), although they are the backbone of the upgrade. The WP structure, with tasks arranged in a tree-like structure, is the basic arrangement of the project. LARP is a parallel structure, independently funded, associated with FP7 with connections both at project management level as well as at WP/task level to maximize synergy. KEK is a direct member of FP7-HiLumi. It is worth noting that HiLumi LHC is the term indicating the part of the HL-LHC that is covered by FP7 funds, even if in practice it has become a popular name for the whole project. In Figure 1-15 the general governance of the project is shown. Each body contains the FP7 part and the part that is not covered by FP7. The Steering Committee is the main managing body: it meets regularly every two months and all WPs are represented there, with the addition of the LARP representatives. It oversees the progress of the technical work and planning, approving the milestones and deliverables. The Steering Committee usually meets in its 'enlarged' form, including the WPs not covered by FP7 and including the LARP leadership. The Collaboration Board is the highest-level governance body with representation from each institute.

In the case of approval of formal FP7 acts, only the FP7-WP coordinators and FP7 Institutes can vote. It is worth noting that the collaboration is based on a consortium agreement, signed by the 15 members (in FP7 terminology, beneficiaries) of FP7-HiLumi LHC. The US laboratories are not members of FP7-HiLumi LHC, however representatives of each US laboratory, including the LARP director, are co-opted onto the enlarged Collaboration Board. The formal link with the US laboratories is assured by the recently signed CERN-DOE Protocol II concerning the LHC and its upgrades. Given the fact that CERN is responsible for the LHC machine, the CERN director general, through his representative in the Collaboration Board, the project coordinator, has the right of veto.

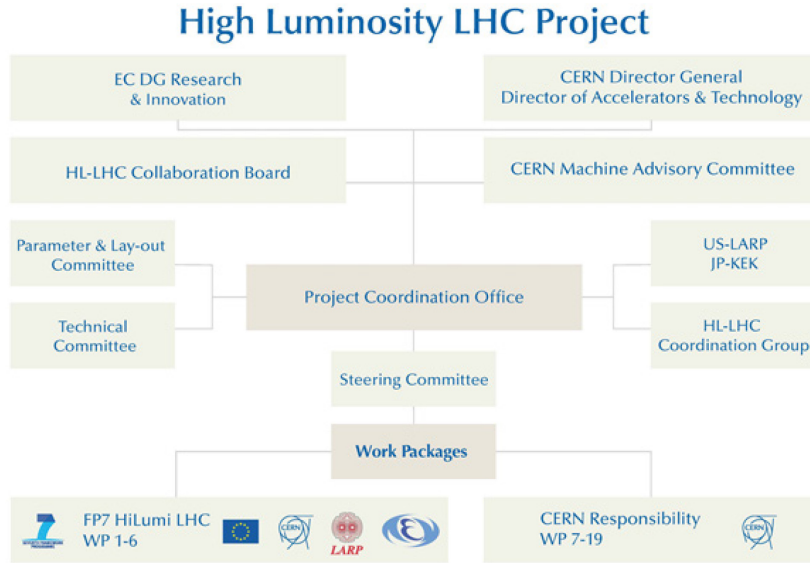


Figure 1-15: The general governance scheme of FP-7 HiLumi LHC, used for the whole HL-LHC project (see text for details)

The Parameter and Layout Committee and the Technical Committee have mainly technical functions inside the project. The Coordination group, chaired by the HL-LHC leader, constitutes the meeting point between CERN Management, HL-LHC, LIU and Detector Management.

A new structure, more suited to a project that is passing from the design study phase to construction project status, is under study and will be operative from November 2015 when the FP7 consortium agreement comes to an end.

In Figure 1-16 the project structure, with all WPs and their coordinators, as well as the main collaborators, is shown. Typically, each WP is assigned three to six tasks. The tasks are the core of the technical work.

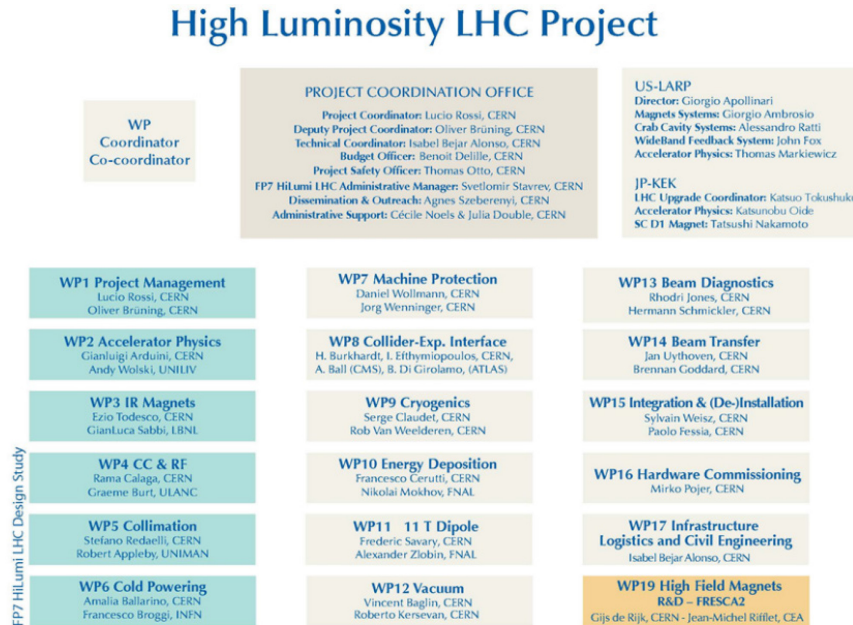


Figure 1-16: HL-LHC project structure, with FP7 part indicated in dark green. The orange box refers to the high-field magnets work package, which was started before the HL-LHC in the framework of generic R&D for the LHC upgrade.



## 1.5 References

- [1] The European Strategy for Particle Physics, adopted by the CERN Council at a special session at ministerial level in Lisbon in 2006, CERN (2006).  
<http://cern.ch/council/en/EuropeanStrategy/ESParticlePhysics.html>
- [2] European Strategy Forum for Research Infrastructures, ESFRI (2014). <http://ec.europa.eu/research/esfri>
- [3] The European Strategy for Particle Physics Update 2013, CERN-Council-S/106, adopted at a special session in Brussels on 30 May 2013, CERN (2013).  
<http://cern.ch/council/en/EuropeanStrategy/ESParticlePhysics.html>
- [4] Building for Discovery: Strategic Plan for U.S. Particle Physics in the Global Context, US DOE (2014).  
<http://science.energy.gov/hep/hepap/reports/>
- [5] L. Rossi, LHC Upgrade Plans: Options and Strategy, Proc. IPAC2011, San Sebastián, Spain, 2011, p. 908.
- [6] O. Brüning, R. Capi, R. Garoby, O. Grobner, W. Herr, T. Linnekar, R. Ostojic, K. Potter, L. Rossi, F. Ruggiero (editor), K. Schindl, G. Stevenson, L. Tavian, T. Taylor, E. Tsesmelis, E. Weisse and F. Zimmermann, LHC Luminosity and Energy Upgrade: A Feasibility Study. CERN-LHC-Project-Report-626, CERN (2002).
- [7] J. Strait, M. Lamm, P. Limon, N.V. Mokhov, T. Sen, A.V. Zlobin, O. Brüning, R. Ostojic, L. Rossi, F. Ruggiero, T. Taylor, H. ten Kate, A. Devred, R. Gupta, M. Harrison, S. Peggs, F. Pilat, S. Caspi, S. Gourlay and G. Sabbi, Towards a New LHC Interaction Region Design for a Luminosity Upgrade <http://accelconf.web.cern.ch/AccelConf/p03/PAPERS/MOPA006.PDF> 20th IEEE Particle Accelerator Conference, Portland, OR, USA, 12 - 16 May 2003, pp.42-4.
- [8] R. Garoby, S. Gilardoni, B. Goddard, K. Hanke, M. Meddahi, M. Vretenar, Plans for the upgrade of the LHC injectors. 2nd International Particle Accelerator Conference, San Sebastian, Spain, 4 - 9 Sep 2011, pp.WEPS017.



# Chapter 2

## Machine Layout and Performance

*D. Angal-Kalinin<sup>1</sup>, R. Appleby<sup>2</sup>, G. Arduini<sup>3\*</sup>, D. Banfi<sup>4</sup>, J. Barranco<sup>4</sup>, N. Biancacci<sup>3</sup>, D. Brett<sup>2</sup>, R. Bruce<sup>3</sup>, O. Brüning<sup>3</sup>, X. Buffat<sup>3</sup>, A. Burov<sup>5</sup>, Y. Cai<sup>6</sup>, R. Calaga<sup>3</sup>, A. Chance<sup>7</sup>, M. Crouch<sup>2</sup>, B. Dalena<sup>7</sup>, H. Day<sup>3</sup>, R. de Maria<sup>3</sup>, J. Esteban Muller<sup>3</sup>, S. Fartoukh<sup>3</sup>, M. Fitterer<sup>3</sup>, O. Frasciello<sup>8</sup>, M. Giovannozzi<sup>3</sup>, W. Herr<sup>3</sup>, W. Höfle<sup>3</sup>, B. Holzer<sup>3</sup>, G. Iadarola<sup>3</sup>, J.M. Jowett<sup>3</sup>, M. Korostelev<sup>9</sup>, K. Li<sup>3</sup>, E. McIntosh<sup>3</sup>, E. Métral<sup>3</sup>, A. Mostacci<sup>10</sup>, N. Mounet<sup>3</sup>, B. Muratori<sup>1</sup>, Y. Nosochkov<sup>6</sup>, K. Ohmi<sup>11</sup>, Y. Papaphilippou<sup>3</sup>, S. Paret<sup>12</sup>, J. Payet<sup>7</sup>, T. Pieloni<sup>3</sup>, J. Qiang<sup>12</sup>, T. Rijoff<sup>3</sup>, L. Rossi<sup>3</sup>, G. Rumolo<sup>3</sup>, B. Salvant<sup>3</sup>, M. Schaumann<sup>3</sup>, E. Shaposhnikova<sup>3</sup>, D. Shatilov<sup>13</sup>, C. Tambasco<sup>3</sup>, R. Tomás<sup>3</sup>, A. Valishev<sup>5</sup>, M.-H. Wang<sup>6</sup>, R. Wanzenberg<sup>14</sup>, S. White<sup>3</sup>, A. Wolski<sup>9</sup>, O. Zagorodnova<sup>14</sup>, C. Zannini<sup>3</sup>, F. Zimmermann<sup>3</sup> and M. Zobov<sup>8</sup>*

<sup>1</sup>ASTeC, STFC, Daresbury Laboratory, Warrington, UK

<sup>2</sup>UMAN, The University of Manchester and the Cockcroft Institute, Warrington, UK

<sup>3</sup>CERN, Accelerator & Technology Sector, Geneva, Switzerland

<sup>4</sup>EPFL, Lausanne, Switzerland

<sup>5</sup>FNAL, Fermi National Accelerator Laboratory, Batavia, USA

<sup>6</sup>SLAC, National Accelerator Laboratory, Menlo Park, USA

<sup>7</sup>CEA/SACLAY, DSM/Irfu/SACM, Gif-sur-Yvette, France

<sup>8</sup>INFN-LNF, Rome, Italy

<sup>9</sup>University of Liverpool, Liverpool, UK

<sup>10</sup>University of Rome “La Sapienza”, Rome, Italy

<sup>11</sup>KEK, Tsukuba, Japan

<sup>12</sup>LBNL, Lawrence Berkeley National Laboratory, Berkeley, USA

<sup>13</sup>BINP, Novosibirsk, Russia

<sup>14</sup>DESY, Deutsches Elektronen-Synchrotron, Hamburg, Germany

## 2 Machine layout and performance

### 2.1 Performance goals (nominal scheme)

The goal of the High Luminosity upgrade of the LHC is to deliver an integrated luminosity of at least 250 fb<sup>-1</sup> per year in each of the two high-luminosity general-purpose detectors, ATLAS and CMS, located at the interaction points (IP) one and five, respectively. The other two experiments, ALICE and LHCb with detectors located at IP2 and IP8 respectively, are expecting to collect integrated luminosities of 100 pb<sup>-1</sup> per year (of proton–proton data) and 5 fb<sup>-1</sup> to 10 fb<sup>-1</sup> per year, respectively [1]. No operation for forward physics experiments is expected after the upgrade.

The ATLAS and CMS detectors will be upgraded to handle an average number of pile-up events per bunch crossing of at least 140, corresponding to an instantaneous luminosity of approximately  $5 \times 10^{34}$  cm<sup>-2</sup> s<sup>-1</sup> for operation with 25 ns beams at 7 TeV, for a visible cross-section  $\sigma_{vis} = 85$  mb. The detectors are also expected to handle a line density of pile-up events of 1.3 events per mm per bunch crossing. ALICE and LHCb will be upgraded to operate at instantaneous luminosities of up to  $2 \times 10^{31}$  cm<sup>-2</sup> s<sup>-1</sup> and  $2 \times 10^{33}$  cm<sup>-2</sup> s<sup>-1</sup>, respectively.

The HL-LHC upgrade project aims to achieve a ‘virtual’ peak luminosity that is considerably higher than the maximum imposed by the acceptable event pile-up rate, and to control the instantaneous luminosity

---

\* Corresponding author: [Gianluigi.Arduini@cern.ch](mailto:Gianluigi.Arduini@cern.ch)

during the physics fill (‘luminosity levelling’) so that the luminosity production can be sustained over longer periods to maximize the integrated luminosity.

A simplified but realistic model of the luminosity evolution has been developed [2] taking into account the beam population  $N_{\text{beam}}$  reduction due to the collisions (the so called ‘burn-off’) in  $n_{\text{IP}}$  collision points with instantaneous luminosity  $L_{\text{inst}}$ ,

$$\frac{dN_{\text{beam}}}{dt} = -n_{\text{IP}}\sigma_{\text{tot}}L_{\text{inst}}, \quad (2-1)$$

where  $\sigma_{\text{tot}}$  is the total hadron cross-section (here assumed to be 100 mb). No other sources of intensity reduction or emittance blow-up are considered in this model. Figure 2-1 shows the expected yearly integrated luminosity as a function of the ‘virtual’ peak luminosity for three different values of the luminosity at which levelling is performed (see Section 1.2.3). In this figure the corresponding optimum fill length  $T_{\text{fill}}$  (i.e. the length of time for each fill that will maximize the average luminosity production rate) is also shown. In order to estimate the annual integrated luminosity, we assume a minimum turnaround time  $T_{\text{turnaround}}$  of 3 hours (see Chapter 16), a scheduled physics time  $T_{\text{physics}}$  for luminosity production of 160 days per year, with  $N_{\text{fills}}$  successful physics fills of duration  $T_{\text{fill}}$ , and a performance efficiency of 50% (this was 53.5% in 2012) where [3]:

$$\eta = N_{\text{fills}} \frac{T_{\text{turnaround}} + T_{\text{fill}}}{T_{\text{physics}}} \times 100\% \quad (2-2)$$

In order to reach the goal of integrating 250 fb<sup>-1</sup>/year levelling must be performed at luminosities larger than  $5 \times 10^{34} \text{ cm}^{-2} \text{ s}^{-1}$  and peak virtual luminosities of more than  $20 \times 10^{34} \text{ cm}^{-2} \text{ s}^{-1}$ . Furthermore, the performance efficiency must be at least 50% and the typical fill length must be comparable with the estimated optimum fill length (for comparison the average fill length during the 2012 run was 6.1 hours). In this respect, levelling to higher luminosities will be beneficial because it would make it easier to reach and even exceed the integrated luminosity goal, with fill lengths comparable to the fill lengths of the 2012 run.

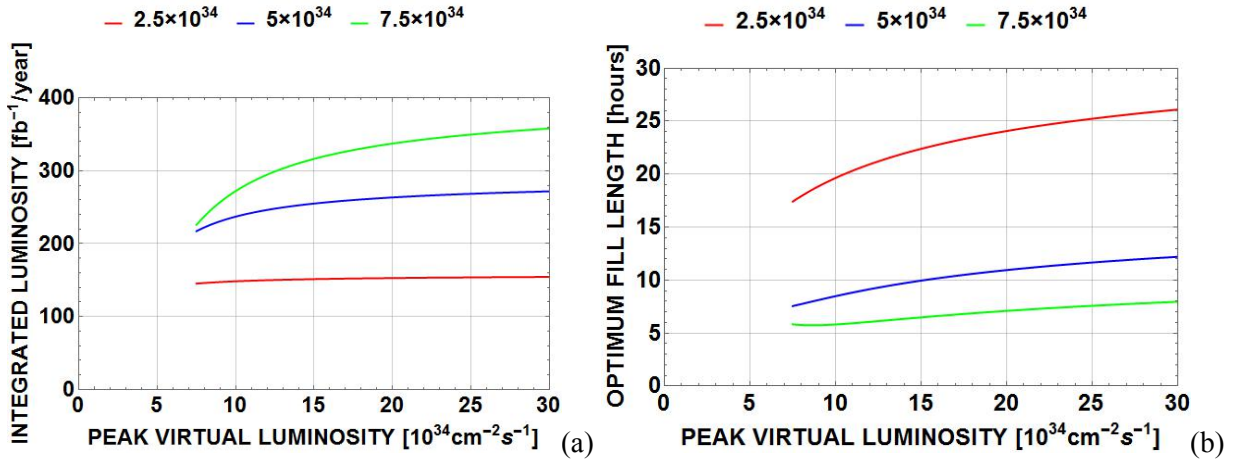


Figure 2-1: (a) Expected annual integrated luminosity; (b) optimum fill length as a function of the ‘virtual’ peak luminosity for three different values of the luminosity at which levelling is performed. A circulating current of 1.1 A (corresponding to  $N_{\text{beam}} = 6.1 \times 10^{14}$  p), a minimum turnaround time of 3 hours and a performance efficiency  $\eta$  of 50% have been assumed. Only burn-off for a total hadron cross-section of 100 mb has been considered for the estimate of the beam population and virtual luminosity evolution. Two high-luminosity interaction points have been assumed.

### 2.1.1 Parameter space and basic parameter choices

The instantaneous luminosity  $L$  is given by

$$L = \frac{n_b N^2 f_{\text{rev}} \gamma}{4\pi \beta^* \epsilon_n} R(\beta^*, \sigma_z, d_{\text{bb}}) \quad (2-3)$$

The r.m.s. normalized emittance  $\varepsilon_n$  in collision is assumed here to be equal for the two beams and for the horizontal and vertical planes. The Twiss beta function  $\beta^*$  in collision at the IP determines, together with the normalized emittance, the r.m.s. beam size  $\sigma^* = \sqrt{\varepsilon_n \beta^* / \gamma}$  at the IP (assuming that the contribution to the beam size due to the dispersion and the momentum spread of the beam can be neglected). Here and below it is assumed that the relativistic factor  $\beta = 1$ .

A crossing angle is needed to separate bunches immediately upstream and downstream of the collision point. This leads to a reduced geometric overlap between the colliding beams, and hence to a reduction in luminosity. The crossing angle needs to be increased when reducing the  $\beta^*$  in order to maintain a sufficiently large normalized beam–beam separation  $d_{bb}$ . The luminosity is also reduced by the ‘hourglass effect’ that arises from the increase of the beta function upstream and downstream of the interaction point along the bunch longitudinal distribution. The hourglass effect is enhanced by a reduction in  $\beta^*$  and by an increase in bunch length. The luminosity reduction factor  $R$  in Eq. (2-3) takes both the crossing angle and the hourglass effect into account.

Equation (2-3) shows the parameters that can be varied to maximize the instantaneous luminosity. The considerations that constrain their values are briefly discussed below [4, 5]:

- The maximum number of bunches  $n_b$  is limited by the minimum time interval between bunch crossings at the IP that can be handled by the detectors: this is limited to 25 ns. The maximum number of bunches that can be injected in the LHC is also limited by the following.
  - o The maximum number of bunches that can be transferred safely from the SPS to the LHC due to the maximum energy that can be deposited on the injection protection absorber (TDI) in case the LHC injection kicker is not firing. The present limitation for the TDI is considered to be a maximum of 288 bunches per SPS extraction for the ultimate bunch population [6].
  - o The rise-time of the injection kickers in the SPS and LHC, extraction kickers in the PS and SPS, and abort gap kicker in the LHC.
  - o The need for injecting one train consisting of a few bunches (typically 12 nominal bunches for 25 ns spacing) before injecting one nominal train for machine protection considerations [7]. For the same reason the last train must have the maximum number of bunches.
  - o The constraints imposed by the experiments: the need for non-colliding bunches for background evaluation, and a sufficient number of collisions for lower luminosity experiments [1].
- The maximum bunch population  $N$  is limited in the LHC by the onset of the single bunch transverse mode coupling instability (TMCI), expected to occur at  $3.5 \times 10^{11}$  p/bunch [8].
- The total current of the beam circulating in the LHC,  $I_{beam} = en_b N f_{rev}$  (where  $e$  is the proton charge), is expected to be limited to 1.1 A by the cryogenic power available to cool the beam screen. This assumes that a secondary electron yield (SEY) as low as 1.3 can be reached in the beam screen, to limit the heat load due to the electron cloud in the arcs, and additional cryogenic plants are installed in Points 1, 4 and 5 [4, 9].
- The beam brightness  $B \equiv N/\varepsilon_n$  is limited by the following considerations [4].
  - o The total head-on beam–beam tune shift  $\Delta Q_{bbho} \propto N/\varepsilon_n$  is expected to be limited to 0.02–0.03 based on experience gained (from operations and dedicated experiments) during LHC Run 1. Its value is reduced in a similar fashion to the luminosity in the presence of a crossing angle [10].
  - o Intra-beam scattering induces transverse and longitudinal emittance blow-up, particularly at injection (low energy) but also in the acceleration, squeeze, and collision phases. The evolution of the beam emittances can be described by the equations,

$$\frac{1}{\tau_H} = \frac{1}{\varepsilon_{nH}} \frac{d\varepsilon_{nH}}{dt} \text{ and } \frac{1}{\tau_L} = \frac{1}{\varepsilon_L} \frac{d\varepsilon_L}{dt} \text{ with } \frac{1}{\tau_d} \propto \frac{N}{\gamma \varepsilon_{nH} \varepsilon_{nV} \varepsilon_L} \text{ and } d = H, L, \quad (2-4)$$

where  $\varepsilon_{nH,V}$  are the r.m.s. normalized horizontal and vertical emittances. Here we assume that vertical dispersion and coupling are negligible so that the vertical emittance blow-up can be neglected.

The minimum  $\beta^*$  is limited by [5]:

- The aperture at the triplet, taking into account that the maximum  $\beta$  function  $\beta_{\max}$  at the triplet increases in inverse proportion to  $\beta^*$ , and that the crossing angle  $\theta_c$  required to maintain a sufficiently large normalized beam–beam separation  $d_{bb}$  to minimize the long-range beam–beam tune spread  $\Delta Q_{bbLR}$  is  $\theta_c = d_{bb}\sqrt{\varepsilon_n/\gamma\beta^*}$ ;
- The maximum  $\beta$  function at the triplet that can be matched to the regular optics of the arcs within the distance available in the matching section between the triplets and the arcs;
- The strengths of the arc sextupoles available to correct the chromaticity generated by the triplets (proportional to  $\beta_{\max}$ ) and, in general, the nonlinear chromaticities and off-momentum beta beating.

For a round optics (i.e. with equal  $\beta^*$  in the horizontal and vertical planes) in the presence of a crossing angle and at constant normalized long-range beam–beam separation  $d_{bb}$ , the increase in luminosity saturates for values of  $\beta^* < \sigma_z$ , as shown in Figure 2-2, because of the corresponding reduction of the luminosity reduction factor  $R$ . The effect of the geometric reduction due to the crossing angle can be counteracted by means of crab cavities operated at the LHC main RF frequency [11] as shown in Figure 1-6. The comparison of the two plots of Figure 2-2 also shows that the effect of crab cavities in enhancing the peak virtual luminosity becomes negligible, for  $\beta^*$  greater than 30–40 cm.

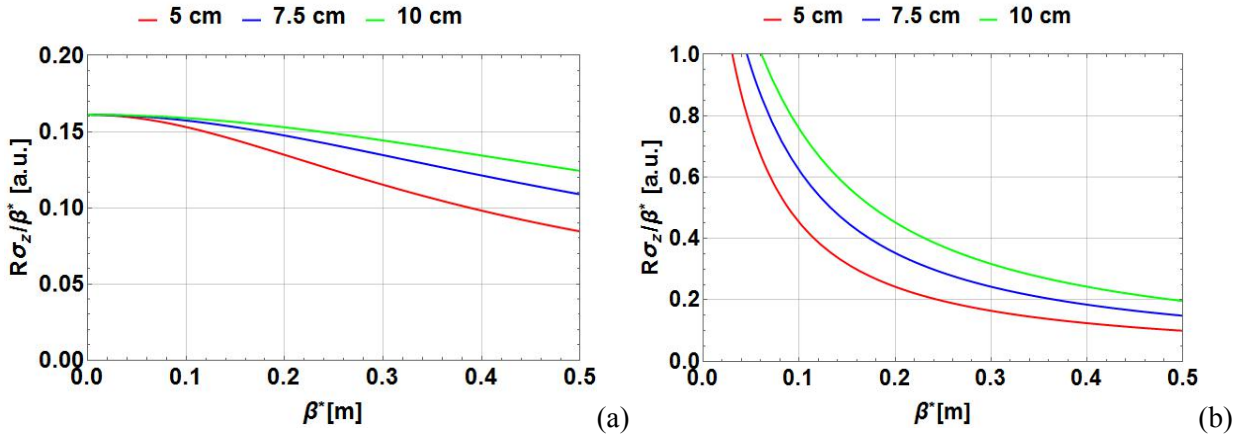


Figure 2-2: Parameter  $R\sigma_z/\beta^*$  vs.  $\beta^*$  for different bunch lengths for a round optics and constant normalized long-range beam–beam separation  $d_{bb}$  (a) without crab cavities and (b) with crab cavities. The small effect of RF curvature in the crab cavities is not included.

Even after their planned upgrades, the injectors will also constrain the parameters of the beam that can be expected in the LHC in collision. First, there is a maximum current  $I_{RF} \approx 2N_{SPS} e/T_{bb}$  (where  $N_{SPS}$  is the bunch population in the SPS and  $T_{bb}$  is the bunch spacing) that can be accelerated per SPS cycle due to RF power limitations in the power amplifiers, power couplers and feeder lines of the main 200 MHz RF system. This maximum current is 2.6 A corresponding to  $N_{SPS} = 2.0 \times 10^{11}$  particles at SPS extraction [12, 13]. The total number of bunches is also limited to 288 due to the thermal load on the power lines. Second, the brightness of the LHC beam in the injectors is expected to be limited by space charge effects at injection in the PSB, PS, and SPS. From present experience it is expected that the maximum brightness of the LHC beams after the full injector upgrade will be  $B_{SPS} \sim 1.5 \times 10^{11}$  p/ $\mu\text{m}$  [13].

Table 2-1 shows the beam parameters at collision, selected on the basis of the above considerations [3, 14]. The parameters in the table are consistent with the above constraints with the exception of the requested bunch population that can be delivered within the longitudinal acceptance of the LHC at injection. To avoid longitudinal instabilities in the SPS, a controlled longitudinal emittance blow-up needs to be applied for high bunch population, which would lead to bunches that are longer than acceptable for clean capture in the LHC with the main 400 MHz RF system (even with the maximum 200 MHz RF voltage available in the SPS at extraction). The identification of the elements contributing to the longitudinal impedance in the SPS and the reduction of their impedance might allow for this limit to be increased. In that case, the requirements in terms of bunch population for the HL-LHC could be met.

Table 2-1: HL-LHC nominal parameters for 25 ns operation [14] for two production modes of the LHC beam in the injectors described in Ref. [3].

Parameter	Nominal LHC (design report)	HL-LHC (standard)	HL-LHC (BCMS)
Beam energy in collision [TeV]	7	7	7
Particles per bunch, $N$ [ $10^{11}$ ]	1.15	2.2	2.2
Number of bunches per beam	2808	2748	2604
Number of collisions in IP1 and IP5*	2808	2736	2592
$N_{\text{tot}}$ [ $10^{14}$ ]	3.2	6.0	5.7
Beam current [A]	0.58	1.09	1.03
Crossing angle in IP1 and IP5 [ $\mu\text{rad}$ ]	285	590	590
Normalized long-range beam–beam separation [ $\sigma$ ]	9.4	12.5	12.5
Minimum $\beta^*$ [m]	0.55	0.15	0.15
$\varepsilon_n$ [ $\mu\text{m}$ ]	3.75	2.50	2.50
$\varepsilon_L$ [eVs]	2.50	2.50	2.50
r.m.s. energy spread [0.0001]	1.13	1.13	1.13
r.m.s. bunch length [cm]	7.55	7.55	7.55
IBS horizontal [h]	105	18.5	18.5
IBS longitudinal [h]	63	20.4	20.4
Piwinski parameter	0.65	3.14	3.14
Total loss factor $R_0$ without crab cavity	0.836	0.305	0.305
Total loss factor $R_1$ with crab cavity	(0.981)	0.829	0.829
Beam–beam/IP without crab cavity	0.0031	0.0033	0.0033
Beam–beam/IP with crab cavity	0.0038	0.011	0.011
Peak luminosity without crab cavity [ $10^{34} \text{ cm}^{-2} \text{ s}^{-1}$ ]	1.00	7.18	6.80
Virtual luminosity with crab cavity $L_{\text{peak}} \times R_1/R_0$ [ $10^{34} \text{ cm}^{-2} \text{ s}^{-1}$ ]	(1.18)	19.54	18.52
Events/crossing without levelling and without crab cavity	27	198	198
Levelled luminosity [ $10^{34} \text{ cm}^{-2} \text{ s}^{-1}$ ]	-	5.00 <sup>†</sup>	5.00 <sup>†</sup>
Events/crossing (with levelling and crab cavities for HL-LHC) <sup>‡</sup>	27	138	146
Maximum line density of pile-up events during fill [event/mm]	0.21	1.25	1.31
Levelling time [h] (assuming no emittance growth) <sup>‡</sup>	-	8.3	7.6
Number of collisions in IP2/IP8	2808	2452/2524 <sup>**</sup>	2288/2396 <sup>**</sup>
$N$ at LHC injection [ $10^{11}$ ] <sup>††</sup>	1.20	2.30	2.30
Maximum number of bunches per injection	288	288	288
$N_{\text{tot}}$ /injection [ $10^{13}$ ]	3.46	6.62	6.62
$\varepsilon_n$ at SPS extraction [ $\mu\text{m}$ ] <sup>**††</sup>	3.40	2.00	<2.00 <sup>***</sup>

\*Assuming one less batch from the PS for machine protection (pilot injection, Transfer line steering with 12 nominal bunches) and non-colliding bunches for experiments (background studies, etc.). Note that due to RF beam loading the abort gap length must not exceed the 3  $\mu$ s design value.

†For the design of the HL-LHC systems (collimators, triplet magnets, etc.), a margin of 50% on the stated peak luminosity (corresponding to the ultimate levelled luminosity) has been agreed.

‡The total number of events/crossing is calculated with an inelastic cross-section of 85 mb (also for nominal), while 100 mb is still assumed for calculating the proton burn off and the resulting levelling time.

\*\*The lower number of collisions in IR2/8 compared to the general-purpose detectors is a result of the agreed filling scheme, aiming as much as possible at a democratic sharing of collisions between the experiments.

††An intensity loss of 5% distributed along the cycle is assumed from SPS extraction to collisions in the LHC.

\*\*A transverse emittance blow-up of 10–15% on the average H/V emittance in addition to that expected from intra-beam scattering (IBS) is assumed (to reach 2.5  $\mu$ m of emittance in collision for 25 ns operation).

\*\*\*For the BCMS scheme emittances down to 1.7  $\mu$ m have already been achieved at LHC injection, which might be used to mitigate excessive emittance blow-up in the LHC during injection and ramp.

## 2.2 Proposed systems upgrades and improvements

The high luminosity configuration requires upgrades of numerous systems. In some cases, existing systems would not be able to face the increasingly harsh conditions that the highest luminosity performance will generate. Accelerated wear and radiation damage are serious concerns. Many changes will be necessary just in order to allow the machine to continue to run in a regime of nominal or ultimate luminosity. For certain systems, replacements could be made with equipment achieving better performance, rather than with spares of the same specification. This performance ‘improvement’ goes well beyond the basic consolidation that is already planned for the LHC.

For other systems, replacement, although triggered by technical reasons, is the chance to carry out a complete change of layout or performance and may be considered to be a real upgrade. The most striking example is the replacement of the inner triplet magnets with new magnets of different technology based on a Nb<sub>3</sub>Sn superconductor. This will constitute the backbone of the upgrade. Another case is the replacement of a good part of the present collimation system with an improved design with lower impedance jaws.

In other cases, new equipment not included in the present LHC layout will be installed in order to increase performance, either in terms of peak luminosity or availability. The most important example is the superconducting RF crab cavities, which are of a compact design as required for the HL-LHC, comprising a completely new development and a first for a proton collider. A further example is the installation of a collimation system in the continuous cryostat in the dispersion suppressors.

In this section, we compile a list of the systems that will require an upgrade or at least a serious improvement in performance, to face the ambitious challenge of the High Luminosity LHC.

### 2.2.1 Insertion region magnets

It is expected that the LHC will reach an integrated luminosity of approximately 300 fb<sup>-1</sup> by 2022, resulting in doses of up to 30 MGy to some components in the high luminosity interaction regions. The inner triplet quadrupoles should withstand the radiation resulting from 400 fb<sup>-1</sup> to 700 fb<sup>-1</sup>, but some nested-type corrector magnets could fail at around 300 fb<sup>-1</sup>. The most likely failure mode is sudden electric breakdown, entailing serious and long repairs. Replacement of the triplet must be anticipated before radiation damage reaches the level where serious failure is a significant possibility.

The replacement can be coupled with an increase in the quadrupole aperture to allow room for an increase in the luminosity via a lower  $\beta^*$ . However, larger aperture inner triplet (IT) quadrupoles and the increased luminosity, with consequent higher radiation levels, imply the redesign of the whole interaction region (IR) zone. This redesign includes larger D1 and D2 dipoles, a new electrical feedbox (DFBX), and much better access to various components for maintenance. In addition, larger aperture magnets in the matching sections will be required, as well as a redesign of the collimation system in the high luminosity insertions.

To maximize the benefit of such a long shutdown, this work must be complemented by a series of improvements and upgrades for other systems, and must be coupled with a major upgrade of the experimental



detectors. Both the machine and the detectors must be partially redesigned in order to withstand the expected level of integrated luminosity. The upgrade should allow the delivery of  $3000 \text{ fb}^{-1}$ , i.e. one order of magnitude greater than the nominal LHC design goal.

It is clear that the change of the inner triplets in the high luminosity insertions is the cornerstone of the LHC upgrade. The decision for the HL-LHC has been to rely on the success of the advanced  $\text{Nb}_3\text{Sn}$  technology, which provides access to magnetic fields well beyond 9 T, allowing the maximization of the aperture of the IT quadrupoles. A 15-year-long study led by the DOE in the US under the auspices of the US LARP programme (see Chapter 1, Section 1.3.2), and more recently by other EU programmes, has shown the feasibility of  $\text{Nb}_3\text{Sn}$  accelerator magnets. For the HL-LHC, some 24 IT  $\text{Nb}_3\text{Sn}$  quadrupoles are needed: they all feature a 150 mm aperture and an operating gradient of 140 T/m, which entails more than 12 T peak field on the coils. The Q1 and Q3 quadrupoles each consist of a pair of 4 m long magnets, while Q2a and Q2b each consist of a single unit almost 7 m long (see Chapter 3, Section 3.2). The same  $\text{Nb}_3\text{Sn}$  technology will be used to provide collimation in the DS, which will be achieved by replacing a number of selected main dipoles with two shorter 11 T  $\text{Nb}_3\text{Sn}$  dipoles (see Chapter 11 Section 11.3). A collimator will be installed between the shorter dipoles (see, for example, Ref. [15] and references therein).

In addition to the IT quadrupoles, there are four new D1/D2 separation/recombination dipole pairs, a number of matching section (MS) quadrupoles, not only in IR1 and IR5, but also in IR6, and a smaller number of lattice sextupoles that can be made using well-known Nb-Ti technology (see Tables 2-3 and 2-4). These magnets will feature a larger aperture and will be exposed to higher radiation doses if not properly protected, and thus will be more challenging than the present LHC equivalents (see Chapter 3).

The corrector packages in the IT and in the MS regions need to be significantly upgraded to increase aperture and (where needed) strength. Some 70 corrector magnets of various orders (from dipole for orbit correction to dodecapole skew correctors) and typology (from superferric to nested cos theta) have to be installed with the new larger IR magnets.

### 2.2.2 TAXS/TAXN absorbers

The change of the IT aperture will require replacement of the TAS, the first absorber on either side of the high luminosity interaction points. The TAS protects the downstream magnets from collision debris. Its aperture roughly scales with the IT aperture. The new absorber, named TAXS, will have an aperture of 54 mm (compared with 30 mm in the present TAS), and will have to withstand a flux of particles five times larger than in the present nominal design. In the current LHC, the TAS is probably the most highly activated component of the whole machine. The baseline choice at present is to replace the TAS with the TAXS during LS3 (see Chapter 8).

Given the fact that the experimental detectors have reduced the size of the vacuum chamber by nearly 50% (from 55 mm down to about 35 mm) it is clear that all challenges at the machine–detector interface are increased. This includes keeping background radiation in the detectors at acceptable levels.

### 2.2.3 Crab cavities

Superconducting (SC) RF crab cavities (CC) in the HL-LHC are needed in order to compensate for the geometric reduction factor, thus making the very low  $\beta^*$  fully useful for luminosity. HL-LHC crab cavities are beyond the state-of-the-art in terms of their unconventional, compact design, which cannot be achieved with the well-known geometry of an elliptical cavity. They also demand a very precise control of the phase of the RF (to better than  $0.001^\circ$ ) so that the beam rotation given before collision is exactly cancelled on the other side of the interaction point (IP). The crab cavities will also pose new challenges for machine protection. Compact crab cavities will be installed on both sides of IP1 and IP5 without additional magnetic doglegs (as in IP4 for the accelerating cavities). Each cavity is designed to provide a transverse kick voltage of 3.4 MV. There are four crab cavities per beam on each side of the IP. They will be assembled in cryomodules, each containing two cavities. All four cavities may be used to rotate the beam in the crossing plane; alternatively, a single

cryomodule (two cavities) can be used for this task, with the cavities in the second cryomodule providing a deflection in the orthogonal plane, enabling the so-called crab kissing scheme for reducing the pile-up density [16]. At present, the baseline is to use all crab cavities for geometric compensation, i.e. rotation in the crossing plane.

The first-generation, proof-of-principle, compact crab cavities have recently been tested successfully (see Chapter 4). However, a second generation with machine-oriented characteristics are now under construction by LARP, CERN, and UK institutions (Lancaster University, STFC, and the Cockcroft Institute). A full cryomodule will be tested in the SPS before LS2, to investigate experimentally the effect on a proton beam and to gain the necessary experience in view of LHC operation.

#### 2.2.4 Collimation

The collimation system has been designed for the first phase of LHC operation. It is currently operating according to design. However, the impedance of the collimation system may need to be reduced if beam instabilities are triggered at intensities close to, or just above, nominal. Hints of this behaviour have been already seen during Run 1: only operation near nominal conditions can dismiss or validate this hypothesis.

Safe handling of a beam of 1 A or more, with beta functions at collision beyond the design value, will constitute new territory. The triplet must remain protected during the large change of the collision beam parameters ( $\beta^*$  transition from 6 m to 10–15 cm). This will be one of the most critical phases of HL-LHC operation: just the beam halo itself could be beyond the damage limit. An upgrade of the collimation system is thus required. The main additional needs associated with the upgrade are a better precision in alignment and materials capable of withstanding higher power.

A second area that will require special attention in connection with the collimation system is the dispersion suppressor (DS), where leakage of off-momentum particles into the first and second main superconducting dipoles has already been identified as a possible LHC performance limitation. The most promising concept is to substitute an LHC main dipole with a dipole of equal bending strength (120 T·m) obtained by a higher field (11 T) and shorter magnetic length (11 m) than those of the LHC dipoles (8.3 T and 14.2 m). The space gained is sufficient for the installation of special collimators. This system is already needed for Run 3 ion operation in the DS region around IP2 following the upgrade of ALICE in LS2. It might also be needed in the DS around IP7 for HL-LHC operation. The requirements in other insertion regions have yet to be assessed.

#### 2.2.5 New cold powering

While a considerable effort is under way to study how to replace the radiation-sensitive electronics boards with radiation-hard cards, another solution is also being pursued for special zones: removal of the power converters and electrical feedboxes (DFBs), delicate equipment associated with the continuous cryostat, out of the tunnel. Besides improving LHC availability (fewer interruptions, faster interventions without the need for tunnel access), radiation dose to personnel would be reduced as well.

Removal of power converters and DFBs to locations far from the beam line, and possibly to the surface, is only possible through the use of a novel technology: superconducting links (SCLs) made out of high-temperature superconductors (YBCO or Bi-2223) or  $\text{MgB}_2$  superconductors. Regions where this radical solution will be needed because of the high radiation load on electronics, and/or the ‘as low as reasonably achievable’ principle (ALARA), have been identified.

- The long straight section of IP7 where a 500 m cable rated at 20 kA is needed.
- The high luminosity insertion regions IR1 and IR5, where much higher current cables (150 kA and 164 kA) are needed for the IT magnets and the magnets in the MS region (i.e. from D2 to Q6). In this latter case, the superconducting cable will link the magnets with power converters on the surface, with

significant challenges to the cryogenics and system integration resulting from the 100 m or so difference in altitude.

### 2.2.6 Enhanced machine protection and remote handling

Various systems will become a bottleneck with aging of the machine and higher performance beyond the  $40 \text{ fb}^{-1}$  to  $60 \text{ fb}^{-1}$  per year envisaged in the original LHC design. One such system is the quench protection system (QPS) of the superconducting magnets. The QPS should:

- i) become fully redundant in case of power loss;
- ii) allow low energy discharge on quench heaters and easy adaption of the detection thresholds;
- iii) provide an interlock for the quench heater discharge based on a sensor for quench heater integrity.

In general, the QPS will need a complete renovation after 2020.

Machine protection will have to be improved, and not just because of the higher beam energy and energy density: it will have to cope with very fast events generated, for example, by crab cavities and by a possible increase of the events generated by falling particles (UFOs).

The LHC has not been designed specifically for remote handling. However, the level of activation from 2020, and even earlier, requires careful study and development of special equipment to allow replacement of collimators, magnets, vacuum components, etc. according to the ALARA principle. While full robotics are difficult to implement given the conditions, remote manipulation, enhanced reality, and supervision are the key to minimizing the radiation dose to personnel.

### 2.2.7 New cryogenics plants and distribution

To increase the flexibility for intervention and rapid restoration of availability (i.e. to minimize loss of integrated luminosity) it will be useful to install a new cryogenics plant in P4 for a full separation between superconducting RF and magnet cooling. This should be done during LS2, to avoid a possible weak zone for Run 3. The new plant should also be able to provide cooling to new cryogenic equipment under consideration for IP4, i.e. a new SCRF harmonic system and the hollow e-lens for halo control, which requires a superconducting solenoid. For the time being, these two systems are not in the baseline; however, they constitute interesting options under study.

A further consolidation that is deemed necessary in the long term is the separation between the cooling of the inner triplets and the few stand-alone superconducting magnets in the MS from the magnets of the arc. The present coupling of IR and arc magnets means that an intervention in the triplet region requires warm-up of the entire sector (an operation of three months, not without risk).

New power plants will be needed to cope with higher heat deposition from the high luminosity points. In particular, given the luminosity-driven heat load in the cold magnets, and the cooling of superconducting crab cavities at 1.9 K, the power (at 4.2 K) of the new cryo-plant in IP1 and IP5 will have to be in the 15–18 kW range. The cooling scheme includes separation, with possible interconnection, between arc and IR cryogenics to gain in flexibility.

### 2.2.8 Enhanced beam instrumentation

Improving beam instrumentation is a continuous task during routine operation of an accelerator. The HL-LHC will require improved or new equipment to monitor and act on proton beams with more challenging parameters than those of the LHC. A short illustrative list includes the following.

- New beam loss monitors for the IT quadrupoles.
- A radiation-tolerant Application-Specific Integrated Circuit (ASIC) for the beam loss monitoring system.

- A new beam position monitoring system, including a high-resolution orbit measurement system, and high-directivity strip-line pick-ups for the insertion regions.
- Emittance measurement: while improving the present system, a new concept-based beam gas vertex emittance monitor is envisaged for the HL-LHC.
- Halo diagnostics to control the halo in order to minimize losses (and especially loss peaks) in the presence of a beam with a stored energy close to 0.7 GJ. Synchrotron radiation imaging, and possibly wire scanners, appear to be the only candidates for halo monitoring in the HL-LHC.
- Diagnostics for crab cavities: electromagnetic pick-ups and streak cameras are being studied for beam shape monitoring.
- Luminosity measurements with new radiation-hard devices (located in the new TAXN) capable of withstanding the radiation level, which will be ten times higher.

### 2.2.9 Beam transfer and kickers

The higher beam current significantly increases the beam-induced power deposited in many elements, including the injection kicker magnets in the LHC ring. New designs for several components in the dump system devices will probably be needed because of the increased energy deposition in the case of direct impact, and because of an increased radiation background, which could affect the reliability of this key machine protection system.

A non-exhaustive list of the elements that could need an improvement or a more radical upgrade (based on the experience from Run 2) is given below.

- Injector kicker magnets (better cooling of the magnets to cope with beam-induced heating, different type of ferrites with higher critical temperature, coating of ceramic tubes to reduce SEY to suppress e-cloud effects).
- Beam dump block TDE with its N<sub>2</sub> overpressure system and window VDWB: if these are not compatible with HL-LHC intensities, extension of the dilution pattern may be the only practical and safe solution, implying the installation of additional dilution kicker systems MKB (up to 50%).
- Injection absorber, auxiliary protection collimators, protection masks.
- Beam dump absorber system.

## 2.3 Baseline optics and layout

### 2.3.1 Basic optics and layout choices for the High Luminosity insertions

The current baseline optics design (HLLHCV1.1) has evolved from the previous LHC Upgrade Phase I project [17–19]. A realistic, cost-efficient and robust (achromatic) implementation of low  $\beta^*$  collision optics requires the deployment of the Achromatic Telescopic Squeeze (ATS) scheme, together with the installation of insertion magnets of larger aperture [20–24]. Successful validation tests of the ATS with beam were achieved in 2011–2012 [25–29] in very specific conditions (low intensity, no crossing angle to save aperture, etc.). The corresponding number, type, and specifications of the new magnets to reach low  $\beta^*$  [20, 21] were then endorsed by the project (see, for example, [30] and references therein).

The historical development of the optics design is summarized in Ref. [31]; here, only the last three parts of this long chain are mentioned, namely the so-called SLHCV3.1b [32], HLLHCV1.0 [33], and HLLHCV1.1 (current baseline) optics. SLHCV3.1b uses ATS optics based on 150 T/m Nb<sub>3</sub>Sn triplets and displacement of D2 for crab cavity integration [32]. HLLHCV1.0 is similar to SLHCV3.1b, but with a new triplet layout based on 140 T/m Nb<sub>3</sub>Sn triplets [33]. HLLHCV1.1, the new baseline, is based on HLLHCV1.0, but with some modifications to take into account the results of design studies for D2, energy deposition studies for the passive

protection of the superconducting elements, hardware integration studies, and updated naming conventions [34, 35], and corresponding optical configurations.

Table 2-2 presents an overview of the main features of the three layouts and of the corresponding optical configurations.

Table 2-2: Main HL-LHC optics variants currently under study. The baseline collision optics corresponds to  $\beta^* = 15$  cm in both transverse planes (round optics) with a full crossing angle of 590  $\mu$ rad. Other collision optics are available, round or flat, for dedicated studies.

	SLHC V3.1b	HLLHCV1.0	HLLHCV1.1 (Baseline)
Collision $\beta^*$ IP1, IP5	Round: 15cm, (10 cm, 33 cm, 40 cm). Flat: 30/7.5cm, (20/5 cm) with HV, VH crossing.	Round: 15cm, (10 cm). Flat: 30/7.5cm, (20/5 cm) with HV, VH crossing. Complete squeeze.	
Pre-squeeze $\beta^*$ IP1, IP5	40 cm, (2 m)	44 cm, (3 m) transition strengths.	44 cm
Injection $\beta^*$ IP1, IP5	5.5 m (11 m)	6 m, (11 m, 18 m)	6 m (15 m)
Triplet gradient	150 T/m	140 T/m	140 T/m
Triplet magnetic length	Q1–Q3: 7.685 m Q2: 6.577 m	Q1–Q3: 4.002 m $\times$ 2 Q2: 6.792 m	Q1–Q3: 4.00 m $\times$ 2 Q2: 6.8 m
Triplet corrector package	Nested triplet nonlinear corrector package with new $a_5$ , $b_5$ , $a_6$ corrector coils	Superferric, non-nested, nonlinear corrector package.	
Insertion region dipoles	D2 moved towards the IP by 15 m. For version HLLHCV1.1 the magnetic length of D1 [40] and D2 has been shortened.		
Insertion region quadrupoles	MQYY type for Q4 in IR1, IP5. Q5 moved towards arc by 11 m.  MQYL type for Q5 in IR1, IR5, IR6.  Additional MS in Q10 of IR1 and IR5.	MQYY type for Q4 in IR1, IR5. Q5 moved towards the arc by 11 m.  MQYL type for Q5 in IR1, IR5, IR6.  Additional MS in Q10 of IR1 and IR5.	MQYY type for Q4 in IR1, IR5. Q5 moved towards arc by 11 m. Q4 moved towards arc by 8 m. MQY at 1.9 K type for Q5 in IR1, IR5. Double MQY for Q5 in IR6. Additional MS in Q10 of IR1 and IR5.
Crab cavities	3		4

The current baseline layout incorporates various optimizations, and in particular has been made compatible with the latest hardware parameters and constraints. The magnetic elements in the region between the IP and Q4 (Figure 2-3) have been positioned to optimize the strength requirements for the magnets and for ancillary equipment. For instance, moving the Q4 quadrupole changes the value of the beta functions at the location of the crab cavities, thus improving their efficiency.

In the triplet region (Figure 2-3, which is in the range of approximately 20 m to 80 m) the Q1 and Q3 magnets are split into two and the dipole corrector magnets (used to create the crossing and separation schemes) are implemented in a nested configuration for both planes. The corrector package close to Q3 consists of superferric magnets. The specifications and performance of the non-linear correctors (used to compensate the field quality effects of the triplets and D1 separation dipoles on both sides of the IP) are reported in Refs. [36, 37]. Detailed numerical simulations indicate that additional corrector types are needed to cope with the pushed

performance of the HL-LHC, so the layout of the correctors will not be a simple carbon copy of the existing layout. Inclusion of the field quality of the D2 separation dipole has been considered, but is not trivial, due to the two-in-one structure of the D2.

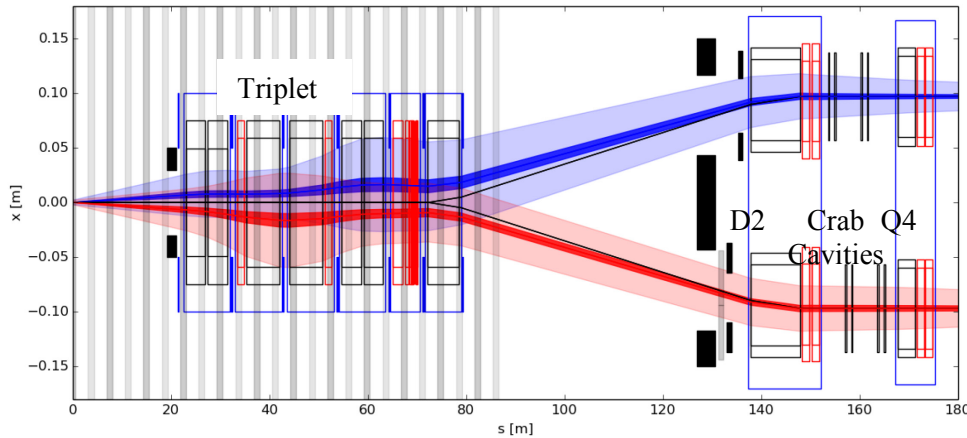


Figure 2-3: Overall layout of the insertion region between the IP and Q4. The dark blue and red areas represent the  $2\sigma$  beam envelope. The light regions correspond to a  $12\sigma$  value of the beam envelope for an emittance of  $3.5\ \mu\text{m}$  with a tolerance of 20% for beta-beating and 2 mm of closed orbit distortion. The shaded grey areas in the triplet region represent the locations of the parasitic beam-beam encounters.

The block of two separation dipoles has been changed with respect to the nominal LHC layout, decreasing their separation. The D2 area is particularly delicate for several reasons. First, there are space constraints because of the need for protection devices such as the absorber for neutral debris from the collisions. Second, the transverse separation is not yet optimal, leading to a reduction in the amount of iron between the two apertures of the D2, as well as to reduced beam and mechanical apertures because of the large values of the beta functions at this point. Downstream of D2, the situation is not much easier, as the crab cavities impose tight constraints on the space between D2 and Q4, as well as on the values of the beta functions.

Detailed work has been performed to specify the strengths of dipole orbit correctors in the triplets and the D2 and Q4 magnets [38, 39]. Initially, the required strength needed too long correctors, mainly because of the need to close the bumps at the D2 dipole in order to avoid a non-zero closed orbit at the location of the crab cavities. Detailed analysis of the RF aspects allowed the tight constraints to be relaxed (0.5 mm of closed orbit distortion can be tolerated at the crab cavities when operating and 2–3 mm when the cavities are made transparent to the beam). The design now includes a correction scheme with magnets that are 1.5–2.5 m long. This makes it possible to close the orbit bumps further downstream from the D2 separation dipoles, thus reducing their overall strength. In the current layout, Q4 is a new magnet with a larger aperture, MQYY, while Q5 is a MQY-type (the Q4 of the present LHC) operating at 1.9 K to provide the required gradient.

The implementation of the ATS scheme in the HLLHC V1.0 requires hardware changes in other parts of the LHC ring. In particular, an additional lattice sextupole (MS) magnet should be installed in Q10 in IR1 and IR5. Moreover, Q5 in IR6 should be upgraded. The current baseline layout envisages the installation of a second MQY-type quadrupole close to each existing Q5.

Table 2-3 lists the key parameters of the quadrupoles (new or refurbished) to be installed in IR1 and IR5, while Table 2-4 gives the corresponding parameters for the separation dipoles and orbit correctors. Table 2-5 gives the parameters for the multipolar correctors.

Table 2-3: New or refurbished quadrupoles for HL-LHC, all operating at 1.9 K. The orientation of the rectellipse aperture ( $R$ ) [40] can be changed to optimize the mechanical aperture.

	Inner triplet (single aperture)			Matching section (two-in-one)		
	Q1	Q2	Q3	Q4	Q5	Q6
Magnet	Q1	Q2	Q3	Q4	Q5	Q6
Number	2	2	2	1	1	1
Type	MQXFA	MQXFB	MQXFA	MQYY	MQY	MQML
Magnetic length [m]	4.0	6.8	4.0	3.8	3.4	4.8
Gradient [T/m]	140	140	140	115	200	200
Coil aperture [mm]	150	150	150	90	70	56
Aperture separation [mm]	-	-	-	194	194	194
Beam screen (BS) shape	Octagon	Octagon	Octagon	Rectellipse	Rectellipse	Rectellipse
BS aperture (H/V) [mm]	98/98	118/118	118/118	64/74	44/57.8	35.3/45.1
Mechanical tolerances (R/H/V) [mm] [41]	0.6/1/1	0.6/1/1	0.6/1/1	0.84/1.26/0.6	0.84/1.26/0.6	As built

Table 2-4: New dipole magnets for HL-LHC, all operating at 1.9 K. The orientation of the rectellipse ( $R$ ) aperture can be changed to optimize the mechanical aperture. The orbit correctors can be nested or consecutive as indicated.

	Separation/recombination dipoles		Orbit correctors			
	D1	D2	Corrector package	Q2	D2	Q4
Assembly	D1	D2	Corrector package	Q2	D2	Q4
Number per side per insertion	1	1	1 [HV nested]	2 [HV nested]	2 [HV consec.]	2 [HV consec.]
Type	MBXF	MBRD	MCBXFA	MCBXFB	MCBRD	MCBYY
Magnetic length [m]	6.27	7.78	2.2	1.2	1.5	1.5
Integrated field [T m]	35	35	4.5	2.5	4.5	4.5
Coil aperture [mm]	150	105	150	150	100	100
Aperture separation [mm]	n/a	188	-	-	194	194
BS shape	Octagon	Octagon	Octagon	Octagon	Octagon	Rectellipse
BS aperture (H/V) [mm]	118/118	84/84	118/118	118/118	79/79	64/74
Mechanical tolerances (R/H/V) [mm]	0.6/1/1	0.84/1.36/1	0.6/1/1	0.6/1/1	0.84/1.36/1	0.84/1.26/0.6

Table 2-5: New multipolar superferric correctors for HL-LHC, all operating at 1.9 K.

Number	1	1	1	1	1	1	1	1	1
Number of poles	4	12	12	10	10	8	8	6	6
Normal/skew	Skew	Normal	Skew	Normal	Skew	Normal	Skew	Normal	Skew
Type	MQSXF	MCTXF	MCTSXF	MCDXF	MCDSXF	MCOXF	MCOSXF	MCSXF	MCSSXF
Magnetic length [m]	0.807	0.43	0.089	0.095	0.095	0.087	0.087	0.111	0.111
Integrated field [mT·m] at 50 mm	1000	86	17	25	25	46	46	63	63
Coil aperture [mm]	150	150	150	150	150	150	150	150	150
BS shape	Octagon	Octagon	Octagon	Octagon	Octagon	Octagon	Octagon	Octagon	Octagon
BS aperture (H/V) [mm]	118/118	118/118	118/118	118/118	118/118	118/118	118/118	118/118	118/118
Mechanical tolerances (R/H/V) [mm]	0.6/1/1	0.6/1/1	0.6/1/1	0.6/1/1	0.6/1/1	0.6/1/1	0.6/1/1	0.6/1/1	0.6/1/1

As already mentioned, protection devices are required for the new layout of the IR1 and IR5 regions. The current LHC layout has only a TAS in front of Q1, to protect this magnet from collision debris, and a TAN to protect D2 from the neutrals produced at the IP. For the HL-LHC, these two devices will have to be upgraded to withstand much larger luminosities. Furthermore, additional masks are envisaged to protect other magnets in the matching section. A summary of the characteristics of these devices can be found in Table 2-6.

Table 2-6: New absorbers for HL-LHC, all operating at 1.9 K. The orientation of the rectellipse aperture can be changed to optimize the mechanical aperture.

	Inner triplet (single aperture)	Matching section (two-in-one)			
		TAN	Mask D2	Mask Q5	Mask Q6
Absorber	TAS	TAN	Mask D2	Mask Q5	Mask Q6
Aperture	1	2	2	2	2
Type	TAXS	TAXN	TCLMA	TCLMB	TCLMC
$L$ [m]	1.8	3.5	0.5	1.0	1.0
Aperture separation [mm]	n/a	149–159	188	194	194
Aperture (H/V) [mm]	54/54	80/80	84/84	44/57.8	35.3/45.1
Mechanical tolerances (R/H/V) [mm]	2/0.5/0.5	0.6/1/1	0.6/1/1	0.6/1/1	0.6/1/1

Figure 2-4 shows example optics configurations for injection and collision. Several configurations can be provided apart from the nominal (i.e. round) optics.

Table 2-7 gives the main sets of  $\beta^*$  values (including the optical parameters corresponding to the ion runs). Since IR2 and IR8 are running with increased strength of the triplets at injection, a so-called pre-squeeze has to be applied at top energy to reduce the strength of the triplets at constant value of beta function at the IP.

The transition between the various optical configurations has been studied in detail [42, 43]. The sequence of gradients during the squeeze is available, and will be used to perform first estimates of the hysteresis effects. Moreover, it will be possible to evaluate the time required to accomplish the squeeze, which is essential information to determine specifications for the required power converters. Work is in progress to address these two points; results are expected in the coming months.

Finally, it is worth mentioning additional studies that have looked at alternative layouts. Options have been studied based on triplets using 120 T/m and 170 T/m gradients [44, 45], and an additional Q7 for crab



cavity kick enhancements [46] without upgrading the matching section layout [47]. The latest results can be found in Ref. [48].

There are numerous constraints on the layout of components, arising from various considerations. The constraints and the associated issues are described in Chapter 15.

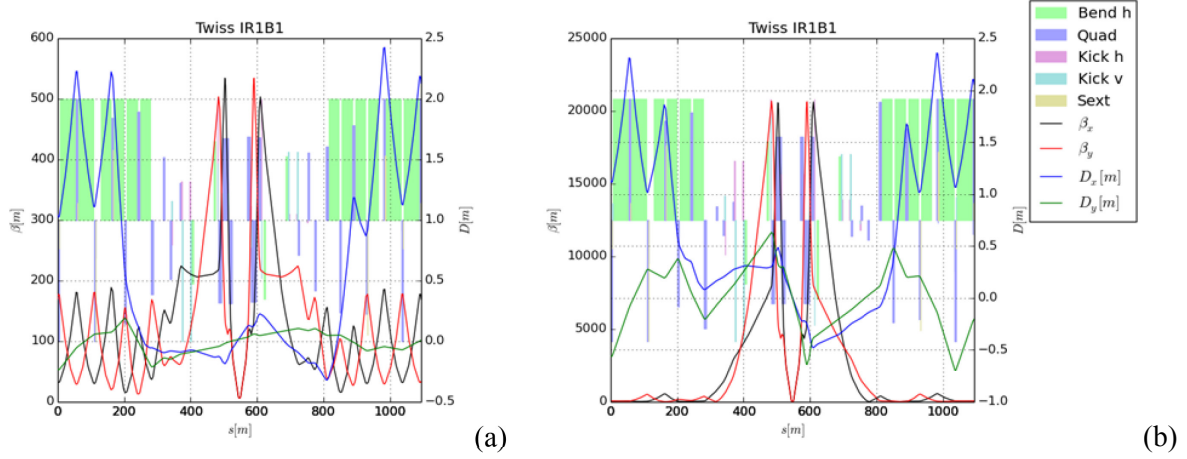


Figure 2-4: Optical functions at (a) injection and (b) collision. Note the different vertical scales: at collision, the beta functions in the triplets are large, to provide the low  $\beta^*$  at the IP.

Table 2-7: Available optical configurations for the baseline layout. IR3 and IR7 are not reported here as they have static optics from injection to collision and do not take part in the ATS scheme. Some alternative configurations (other than the nominal) are also shown.

Optics	IR1	IR5	IR2	IR8	IR4	IR6
Injection	$\beta^* = 6$ m, inj.	$\beta^* = 6$ m, inj.	$\beta^* = 10$ m, inj.	$\beta^* = 10$ m, inj.	Inj.	Inj.
End of ramp	$\beta^* = 6$ m	$\beta^* = 6$ m	$\beta^* = 10$ m	$\beta^* = 10$ m	Inj.	Inj.
Pre-squeeze	$\beta^* = 44$ cm	$\beta^* = 44$ cm	$\beta^* = 10$ m	$\beta^* = 3$ m	Inj.	Inj.
Collision round	$\beta_{ATS}^* = 15$ cm	$\beta_{ATS}^* = 15$ cm	$\beta^* = 10$ m, ATS (3 $\times$ , 3 $\times$ )	$\beta^* = 3$ m, ATS (3 $\times$ , 3 $\times$ )	ATS (3 $\times$ , 3 $\times$ )	ATS (3 $\times$ , 3 $\times$ )
Collision ions	$\beta^* = 44$ cm	$\beta^* = 44$ cm	$\beta^* = 50$ cm	$\beta^* = 50$ cm	Inj.	Inj.
Collision VDM	$\beta^* = 30$ m	$\beta^* = 30$ m	In preparation	In preparation	Inj.	Inj.
<b>Alternative configurations</b>						
Collision Flat	$\beta_{ATS}^* = 7.5/30$ cm	$\beta_{ATS}^* = 30/7.5$ cm	$\beta^* = 10$ m, ATS (6 $\times$ , 1.5 $\times$ )	$\beta^* = 3$ m, ATS (6 $\times$ , 1.5 $\times$ )	ATS (1.5 $\times$ , 6 $\times$ )	ATS (1.5 $\times$ , 6 $\times$ )
Collision FlatHV	$\beta_{ATS}^* = 30/7.5$ cm	$\beta_{ATS}^* = 7.5/30$ cm	$\beta^* = 10$ m, ATS (1.5 $\times$ , 6 $\times$ )	$\beta^* = 3$ m, ATS (1.5 $\times$ , 6 $\times$ )	ATS (6 $\times$ , 1.5 $\times$ )	ATS (6 $\times$ , 1.5 $\times$ )
Collision sRound	$\beta_{ATS}^* = 10$ cm	$\beta_{ATS}^* = 10$ cm	$\beta^* = 10$ m, ATS (4.5 $\times$ , 4.5 $\times$ )	$\beta^* = 3$ m, ATS (4.5 $\times$ , 4.5 $\times$ )	ATS (4.5 $\times$ , 4.5 $\times$ )	ATS (4.5 $\times$ , 4.5 $\times$ )
Collision sFlat	$\beta_{ATS}^* = 5/20$ cm	$\beta_{ATS}^* = 20/5$ cm	$\beta^* = 10$ m, ATS (9 $\times$ , 4.5 $\times$ )	$\beta^* = 3$ m, ATS (9 $\times$ , 4.5 $\times$ )	ATS (4.5 $\times$ , 9 $\times$ )	ATS (4.5 $\times$ , 9 $\times$ )
Collision sFlatHV	$\beta_{ATS}^* = 20/5$ cm	$\beta_{ATS}^* = 5/20$ cm	$\beta^* = 10$ m, ATS (4.5 $\times$ , 9 $\times$ )	$\beta^* = 3$ m, ATS (4.5 $\times$ , 9 $\times$ )	ATS (9 $\times$ , 4.5 $\times$ )	ATS (9 $\times$ , 4.5 $\times$ )

### 2.3.2 Target field quality and dynamic aperture

The dynamic aperture (DA) has been used since the initial steps of the design of the LHC [40] to determine the required field quality of the various magnet classes. For computation of the DA in the HL-LHC, particles are tracked over  $10^6$  or  $10^5$  turns, depending on whether beam–beam effects are included or neglected, respectively. The initial momentum co-ordinate is set to two-thirds of the bucket height ( $2.7 \times 10^{-4}$  and  $7.5 \times 10^{-4}$  for collision and injection energy, respectively). Sixty implementations of the random components in the magnets, corresponding to sixty realizations of the LHC lattice, are considered in the numerical

simulations. Eleven phase space angles have routinely been used (although for special studies up to 59 values have been probed), while thirty particle-pairs per  $2\sigma$  amplitude step have been used. All these parameters have been specified during the design stage of the LHC. Since then, the amount of available computing power has increased, thanks to the increased CPU power of the CERN batch system and because of the use of volunteer-based computing resources [49]: this has enabled an increase of the number of directions considered in the studies, making the DA estimate more accurate. Note that the number of turns and random seeds affects the accuracy of the DA calculation, which is at least  $0.1\sigma$  in this case.

For reference, the multipole expansion used to describe the magnetic field is given as [40]:

$$B_y + iB_x = B_{\text{ref}} \sum_{n=1}^{\infty} (b_n + ia_n) \left( \frac{x+iy}{r_0} \right)^{n-1}, \quad (2-5)$$

where  $B_x$ ,  $B_y$ , and  $B_{\text{ref}}$  are the transverse magnetic field components and the reference field, respectively. The coefficients  $a_n$ ,  $b_n$  are the skew and normal field components, and  $r_0$  is a reference radius. In the framework of the LHC studies the magnetic errors are split into three components, namely mean ( $S$ ), uncertainty ( $U$ ), and random ( $R$ ), such that a given multipole is obtained by:

$$b_n = b_{n_S} + \frac{\xi_U}{1.5} b_{n_U} + \xi_R b_{n_R}, \quad (2-6)$$

where  $\xi_U$ ,  $\xi_R$  are Gaussian-distributed random variables cut at  $1.5\sigma$  and  $3\sigma$ , respectively. The  $\xi_U$  variable is the same for all magnets of a given class, but changes from seed to seed and for the different multipoles. On the other hand,  $\xi_R$  also changes from magnet to magnet.

The target value of the DA differs between injection and collision energies. At injection, where the beam–beam effects can be safely neglected, the focus is on the impact of magnetic field quality. For the LHC design [40], a target value of  $12\sigma$  (for a normalized emittance of  $3.75\mu\text{m}$ ) was assumed. The best model of the LHC, including the measured field quality of the magnets and the sorting of magnets, provides a DA slightly lower than  $11\sigma$  [50]. No signs of issues due to DA limitations have been observed during operation or dedicated studies in Run 1, although operation at high intensity has been conducted with beams with an emittance smaller than nominal ( $2\text{--}2.5\mu\text{m}$  rather than  $3.75\mu\text{m}$ ).

At top energy, beam–beam effects cannot be neglected and the DA has to be evaluated, including both magnetic field imperfections and head-on and long-range beam–beam phenomena (see Section 2.4.2). Hence, the approach taken consists of probing the impact on DA of the field quality of the new magnets, asking that all new magnets have an impact on the DA that is in the shadow of the triplet quadrupoles. Eventually, the beam–beam effects are also included, providing the final DA value.

Studies for the field quality of the new magnets started from the top energy configuration and with an earlier version of the layout, namely the so-called SLHCV3.1b [32]. This allowed first estimates of the required field quality to be derived, which were then improved by including consideration of the injection energy, where the beam size reaches its maximum and the field quality is worse, due to the persistent current effect. The newer layout HLLHCV1.0 [33] has been used following its release.

In the numerical simulations consideration is made of the machine as built, i.e. the best knowledge of the measured magnetic errors is assigned to the magnets as installed, while, for the magnets that will be replaced according to the upgrade plans, the expected error table, with statistical assignment of errors, is used. This is the baseline configuration of the LHC ring to which magnetic field errors of other classes of magnets can be selectively added.

In these studies the acceptable minimum DA was set to about  $10.5\sigma$  at top energy, based on experience from the LHC. The DA calculation was performed using long-term tracking in SixTrack [51, 52], neglecting beam–beam effects. Determination of the required field quality based on DA computations is intrinsically a non-linear problem. The field quality obtained from electromagnetic simulations is used as an initial guess. Then, optimization of the field quality essentially involves determining the Jacobian of the DA as a function of the multipoles around the initial value of field quality. For this reason, it is of paramount importance to have

a reliable estimate of the expected field quality from detailed electromagnetic simulations and measurements (see Chapter 3). The resulting error tables can be found in the official optics repositories [53, 54] and are also collected in Ref. [55].

The previous IT specifications at 7 TeV [56] were updated to take into account the additional IT correctors for  $a_5$ ,  $b_5$ ,  $a_6$  errors. It is worth mentioning that in all the studies reported in this document, the IT correctors have been considered as ideal devices, i.e. exactly correcting the field quality of the IT and D1 magnets, without any error due to uncertainty in the transfer function of the correctors. These specifications will be referred to as IT\_errortable\_v66. An estimate of the D1 field quality is based on magnet design and referred to as D1\_errortable\_v1 [57]. Due to the evolution of the D2 dipole design, three versions of the D2 field quality were used in the study: these are referred to as D2\_errortable\_v3, \_v4 [58], and \_v5 [59]. The D2 low-order terms at 7 TeV are shown in Table 2-8. Estimates for the Q4 and Q5 magnets are based on a scaling of the measured field of the existing MQY quadrupole and referred to as Q4\_errortable\_v1 and Q5\_errortable\_v0, respectively.

Table 2-8: Evolution of low order terms of the estimated D2 field quality at 7 TeV ( $r_0 = 35$  mm).

$n$	$a_{nS}$	$a_{nU}$	$a_{nR}$	$b_{nS}$	$b_{nU}$	$b_{nR}$
<b>D2_errortable_v3</b>						
2	0.0	0.679	0.679	65.0	3.000	3.000
3	0.0	0.282	0.282	-30.0	5.000	5.000
4	0.0	0.444	0.444	25.0	1.000	1.000
5	0.0	0.152	0.152	-4.0	1.000	1.000
6	0.0	0.176	0.176	0.0	0.060	0.060
<b>D2_errortable_v4</b>						
2	0.0	0.679	0.679	25.0	2.500	2.500
3	0.0	0.282	0.282	3.0	1.500	1.500
4	0.0	0.444	0.444	2.0	0.200	0.200
5	0.0	0.152	0.152	-1.0	0.500	0.500
6	0.0	0.176	0.176	0.0	0.060	0.060
<b>D2_errortable_v5</b>						
2	0.0	0.679	0.679	1.0	1.000	1.000
3	0.0	0.282	0.282	1.0	1.667	1.667
4	0.0	0.444	0.444	-3.0	0.600	0.600
5	0.0	0.152	0.152	-1.0	0.500	0.500
6	0.0	0.176	0.176	2.0	0.060	0.060

The SLHCV3.1b collision optics features  $\beta^* = 15$  cm. The desired minimum DA (among all seeds and phase angles) at collision energy is about  $10 \sigma$ . Tracking simulations performed with the error table IT\_errortable\_v66 and without the D1, D2, Q4 and Q5 magnetic errors give  $DA_{\min} = 10.4 \sigma$ , which is acceptable. Note that  $DA_{\min}$  stands for the minimum DA over all seeds and angles, while  $DA_{\text{ave}}$  represents the minimum over all angles of the DA averaged over the seeds.

As a next step, the impact on DA of the field quality in the D1, D2, Q4 and Q5 magnets was verified. The Q4 and Q5 estimated magnetic errors produced negligible effect on the DA, hence their field quality is acceptable. Impact of the D1 estimated errors is mostly due to the relatively large allowed multipoles  $b_{nS}$ . It is found that the largest DA reduction is caused by  $b_{7S}$  and  $b_{9S}$ . The low-order D1 errors have negligible effect since they are compensated for by the included IT correctors of order  $n$  between 3 and 6. To reduce the impact of  $b_{7S}$  and  $b_{9S}$  while keeping them realistic, it is proposed to reduce them by a factor of 2 (to 0.2 and  $-0.295$ , respectively) relative to D1\_errortable\_v1.

Two versions of the estimated D2 field quality were used for the SLHCV3.1b tracking: D2\_errortable\_v3 and D2\_errortable\_v4. These tables were produced during successive iterations of the field quality optimization. The  $b_2$  to  $b_4$  terms are rather large due to field saturation. These terms showed a strong impact on the DA. The  $b_2$  affected the linear optics by increasing  $\beta^*$ , thus resulting in a too optimistic DA value. To avoid this effect,

the  $b_2$  was set to zero for subsequent tracking campaigns, on the assumption that it can be reduced by appropriate design and that  $\beta^*$  will be corrected after measurements. It is found that the D2  $b_3$  and  $b_4$  have a strong effect on the DA. Effects of feed-down due to the orbit in the straight D1 and D2 magnets were found to be very small. To maintain the  $DA_{\min}$  close to  $10\sigma$ ,  $b_3$  and  $b_4$  must be reduced by an order of magnitude relative to D2\_errortable\_v3. These terms had been, indeed, much improved in the updated error table, D2\_errortable\_v4 (see Table 2-8). Following the tracking results, the proposed further adjustment for D2\_errortable\_v4 is to reduce  $b_2$  to about 1 unit and  $b_{35}$  from 3.0 to 1.5. The resulting  $DA_{\min}$  and  $DA_{\text{ave}}$  at 7 TeV, with all new magnet errors and adjustments, are  $9.90\sigma$  and  $11.64\sigma$ , respectively, which is still acceptable.

The  $\beta^*$  for SLHCV3.1b lattice at 450 GeV is 5.5 m, with peak beta functions in the IR magnets lower by a factor of 35 than those in the collision optics. Beam sizes in these magnets are also reduced even though the emittance is larger by a factor of 16. Therefore, the impact of field errors of the new magnets will be much smaller, and the use of the IT correctors is a priori not needed: these results are confirmed by tracking studies. Hence, their field quality at injection based on the present estimates is acceptable. The resulting  $DA_{\min}$  and  $DA_{\text{ave}}$  with all errors are  $10.16\sigma$  and  $10.5\sigma$ , respectively, and are also acceptable. Another option of the injection optics, with  $\beta^*$  of 11 m, was verified and showed very similar DA.

The injection DA, however, is about  $1\sigma$  smaller than the DA of the nominal LHC. Since it is not limited by the IR magnets, other improvements (e.g. in the arcs) may need to be considered. Possible options include a larger integer tune split and adjustment of the working point. Tune scans indicate an effect of the 7th order horizontal resonance close to the current tune (62.28, 60.31). Reducing the horizontal and vertical tunes by about 0.01 would increase the DA by about  $0.5\sigma$ .

HLLHCV1.0 is the latest version of the HL-LHC lattice that has been considered in numerical simulations so far. Some of the differences relative to the SLHCV3.1b include: a longer IT with a lower gradient of 140 T/m and higher peak beta function (7%) at collision, adjusted orientation of magnets in the cryostat, new IT corrector positions, and different phase advance between IP1 and IP5. Using the previously optimized field quality of the new magnets, the collision DA of the HLLHCV1.0 lattice is reduced by about  $1\sigma$  relative to the SLHCV3.1b, i.e. with  $DA_{\min}$  and  $DA_{\text{ave}}$  of  $8.8\sigma$  and  $10.4\sigma$ , respectively. A stronger impact of the D2  $b_3$  and  $b_4$  terms of the previously adjusted D2\_errortable\_v4 was noticed. Since  $b_{35}$  had been already reduced in this table, the next step was to reduce  $b_{45}$  by half. This improved the DA to  $DA_{\min} = 9.1\sigma$  and  $DA_{\text{ave}} = 11.1\sigma$ . Further improvement was achieved when using the most recent D2 field estimate D2\_errortable\_v5 [59] (see Table 2-8), where the  $b_2$  and  $b_3$  terms are reduced at the expense of somewhat larger higher-order terms. In this case,  $DA_{\min} = 9.8\sigma$  and  $DA_{\text{ave}} = 12.5\sigma$ , as shown in Figure 2-5(a), which is acceptable and rather comparable to the DA of the SLHCV3.1b. The reasons for such noticeable improvement will need to be further analyzed.

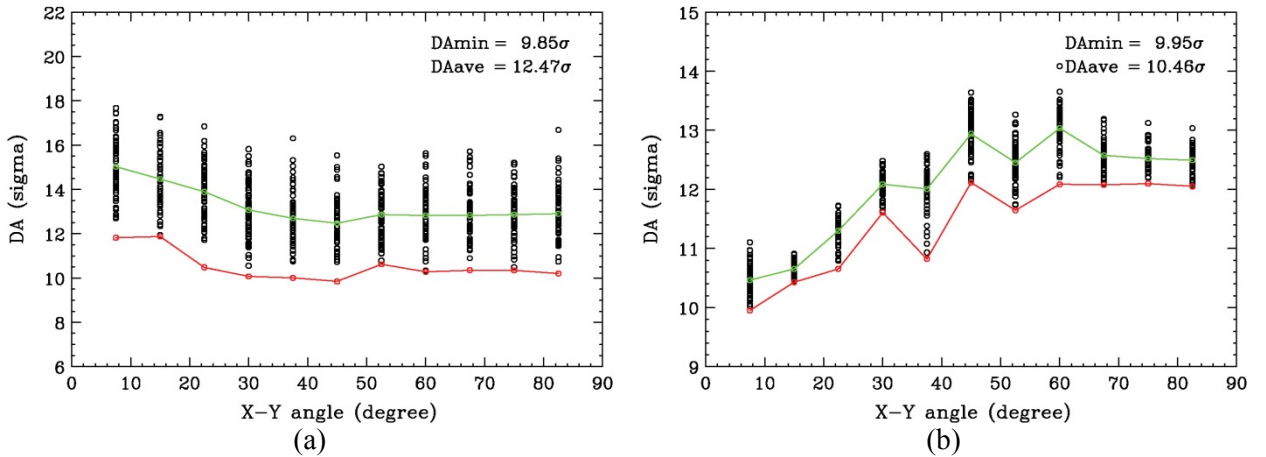


Figure 2-5: DA of HLLHCV1.0. (a) DA at 7 TeV with adjusted estimated field quality of new magnets. (b) DA at 450 GeV with estimated field quality of new magnets. The r.m.s. beam size is that corresponding to a normalized emittance of  $3.75\mu\text{m}$ .

The  $\beta^*$  at injection for HLLHC V1.0 is 6.0 m, comparable to SLHC V3.1b. The impact of the field errors in the new magnets on the DA was verified and found to be insignificant (similar to SLHC V3.1b). The resulting DA with all errors ( $DA_{\min} = 9.9 \sigma$  and  $DA_{\text{ave}} = 10.5 \sigma$ ) is acceptable, see Figure 2-5(b).

Field quality and dynamic aperture studies will be pursued in the future along several lines, including:

- dedicated studies to assess the impact of field quality of IT, D1, D2, Q4 and Q5 on linear optics, knowing that the distortion of the optical parameters can stem from both the  $b_2$  component and the feed-down from  $b_3$  and  $a_3$  via the crossing scheme bumps;
- dedicated studies (ongoing) to assess the maximum tolerable ripple in the power converters of the IT quadrupoles and magnets in the matching section [60];
- specification of crab cavity field quality: preliminary results [61–64] seem to indicate that the estimated field quality should be good enough to prevent any impact on the DA;
- assessment of the impact of fringe fields for the large aperture magnets, including the new IT quadrupoles and the separation dipoles.

Regarding fringe fields, the quadrupolar component has already been considered and found non-problematic in Ref. [65]. Preliminary analytical results [66] indicate that, albeit small, the detuning with amplitude induced by the fringe fields is not completely negligible, thus calling for a second level of study. This should include long-term numerical simulations to study the non-linear effects generated. This opens the wide field of symplectic integration as, in the presence of 3D magnetic fields, the standard approach based on multipoles cannot be applied. Work is underway to study the best integration schemes and their implementation [67, 68], before starting the real numerical work.

## 2.4 Performance

### 2.4.1 Beam stability

The impedance in the HL-LHC, shown in Figure 2-6 [69], is not dramatically higher than in the LHC. Molybdenum-coated secondary collimators could decrease the total impedance by more than a factor of 2. However, special caution should be given to devices in high beta regions and unshielded elements.

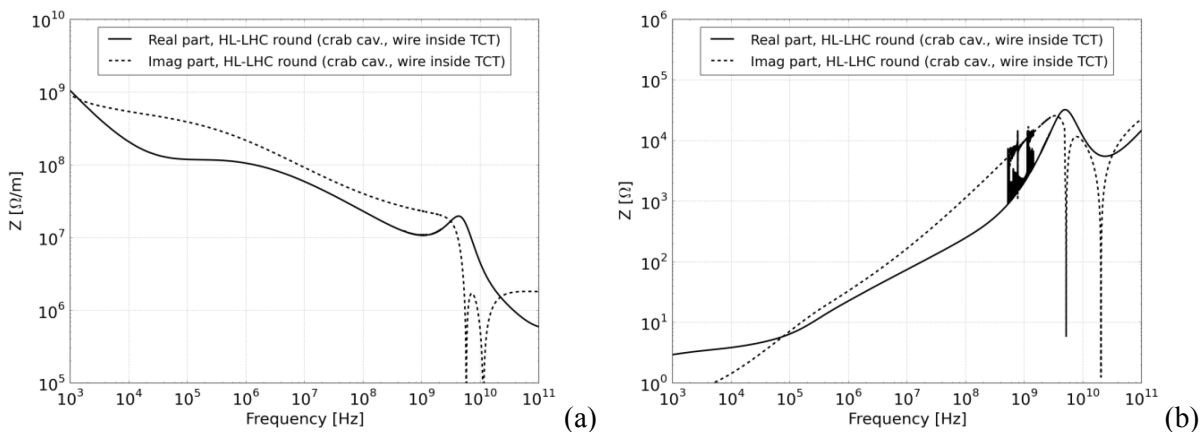


Figure 2-6: (a) First estimate of the horizontal dipolar impedance of HL-LHC, including both crab cavities and beam–beam wire compensators. The vertical dipolar impedance is similar to the horizontal. (b) Longitudinal impedance.

Longitudinal instabilities are not expected to be an issue in the HL-LHC [70]. Single bunch measurements in the LHC at 4 TeV showed an intensity threshold at  $1 \times 10^{11}$  p/b, for an RF voltage of 12 MV and a longitudinal emittance of 1 eVs (4  $\sigma$  bunch length of 0.8 ns, scaled from the measurement of the full

width at half maximum). Scaling to HL-LHC parameters (16 MV, 2.5 eVs) leads to an intensity threshold of  $\sim 3.4 \times 10^{11}$  p/b. A double RF system is therefore not needed for beam stability in the longitudinal plane. However, a high harmonic RF system [71–77] in bunch shortening mode could provide an additional margin for longitudinal stability; in bunch lengthening mode, by flattening the bunch profile, a high harmonic RF system could reduce intra-beam scattering (IBS) emittance growth rates, beam-induced heating, and pile-up density. A preliminary cavity design for the 800 MHz RF system exists [78]. Recently, the use of a low harmonic RF system in the LHC (200 MHz) as the fundamental RF system has been suggested [79] since:

- it would allow to accept larger longitudinal emittance and therefore larger bunch population from the SPS after its upgrade;
- it could help to reduce IBS, beam-induced heating, and e-cloud effects;
- together with the existing 400 MHz RF system, it could be used for luminosity and pile-up levelling;
- it also has a beneficial effect for ions and the momentum slip-stacking scheme in the SPS [80].

A new design has been proposed for a compact superconducting cavity [81]. The compatibility of this scheme with 400 MHz crab cavities or the possibility of installing 200 MHz crab cavities needs to be studied further if this scenario is to be considered. Finally, the expected benefits of a double RF system should be weighed against the impedance increase and the possible reduced reliability.

Transverse instabilities are a concern based on the experience of the LHC Run 1, during which a transverse instability at the end of the betatron squeeze could not be cured [70]. While transverse mode coupling instabilities (TMCI) thresholds well exceed the nominal HL-LHC bunch population both at injection and at high energy, to achieve transverse single-beam stability the collimators will need to be coated with 5  $\mu\text{m}$  of molybdenum [70], and the transverse damper must be able to damp coupled-bunch instabilities up to the maximum frequency (20 MHz). Figure 2-7 shows the expected HL-LHC single-beam stability limits for different scenarios with a transverse damper. If the instabilities observed in 2012 are mainly single-bunch (and therefore beyond the range of the damper), we will not be able to stabilize the HL-LHC beams in the case of the standard material collimators and RF dipole crab cavities. However, beam stability could be recovered with molybdenum-coated collimators. This assumes that the transverse damper can damp all coupled-bunch modes otherwise we will not be able to stabilize the HL-LHC beams for any scenario. It is thus clear that the operation of the transverse damper is vital for HL-LHC. The situation improves with the negative polarity of the Landau octupoles but the results are qualitatively the same.

In Figure 2-7, stability thresholds are plotted versus transverse emittance, assuming the fully squeezed ATS optics (with 15 cm  $\beta^*$  in both planes) [25]. The high beta functions greatly enhance the impedance contribution from crab cavities compared to the un-squeezed flat-top situation. The design of the crab cavities has to be carefully evaluated and optimized with regard to the high-order modes (HOMs), to minimize the contribution to the coupled-bunch instabilities. The coupled-bunch modes will have to be stabilized by the transverse damper; the damper specifications will therefore have to be finalized once the design of the crab cavities is more advanced (at present, the impedance model of the crab cavities is quite coarse and needs to be improved). During the squeeze, the tune spread (providing Landau damping) could be increased if the ATS can be implemented starting from  $\beta^* = 2$  m, thanks to the enhanced beta functions in the arcs. This effect would improve very significantly the situation in terms of stability. In reality, the situation will be even less critical because of luminosity levelling, as the smallest  $\beta^*$  will be reached only at a lower intensity. All these effects should be studied in more detail in the future.

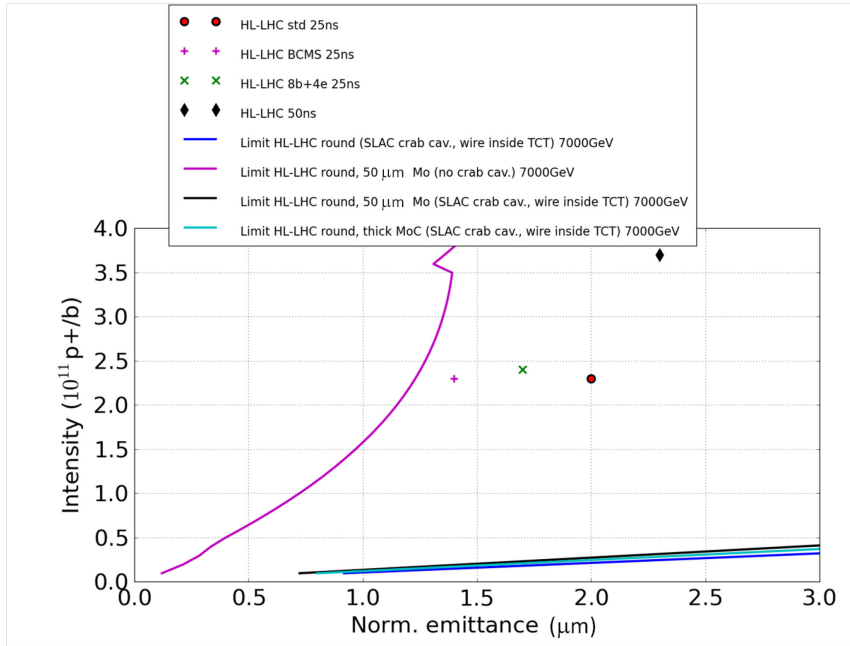


Figure 2-7: Single-beam (25 ns) intensity limit vs. transverse emittance with transverse damper (50-turn damping time) at top energy, for a chromaticity  $Q' \sim 15$  for the two extreme cases (CFC collimators with ODU/SLAC crab cavities and Mo-coated collimators without crab cavities) and for positive polarity of the Landau octupoles.

With an additional 800 MHz RF system, the bunch-shortening mode should be preferred from the point of view of transverse beam stability as, even at low chromaticity, beam stability could be reached [70]. However, the operating mode that has been envisaged until now is bunch lengthening to create flat bunches; for that reason alternative scenarios (e.g. bunch flattening by band-limited RF phase noise on the main 400 MHz system) should be studied.

The effect of the electron cloud on beam stability still needs to be assessed. Induced heat loads from the electron cloud are discussed in Section 2.4.3.

Based on experience from LHC Run 1, the interplay between impedance, Landau octupoles, and beam-beam is expected to play an important role in defining the stability limits. A first estimate of the stability diagram for the fully squeezed optics ( $\beta^* = 15$  cm) in the presence of both octupoles and long-range beam-beam can be found in Ref. [82]. The stable region with octupoles only increases for  $\beta^*$  below 40 cm, and is about 2.5 times larger with the ATS compared to the nominal optics, due to the larger beta functions at the octupoles. As is the case for the LHC, negative octupole polarity (negative amplitude detuning) is preferred for single-beam stability. On the other hand, compensation between negative amplitude detuning from the octupoles and positive amplitude detuning from long-range beam-beam leads to a reduction of the stable region during the squeeze [83]. Below a certain beam-beam separation, positive octupole polarity starts to give larger stable regions and is therefore preferred. Some details of the simulation still need to be checked. However, the proposed operational scenario for the HL-LHC is first to bring the beams into collision, and then to squeeze. By taking advantage in this way as soon as possible of the large amount of Landau damping provided by head-on beam-beam interactions, this should remove possible instability issues arising from long-range beam-beam during the betatron squeeze, while keeping negative octupole polarity (which is better for single-beam stability).

#### 2.4.2 Beam-beam effects

The beam-beam interaction is known to be an important factor limiting the performance reach of present particle colliders. Two of the most significant effects of beam-beam interactions are: (i) the induced particle

losses that decrease the beam lifetime, create a high background load for physics experiments, and elevated heat and radiation load on the collimation system; and (ii) the degradation of beam quality manifesting itself through the beam size blow-up that decreases the luminosity delivered to particle physics experiments.

Owing to the extensive theoretical and simulation campaign during the design of the LHC collider, the beam–beam effects in the present machine are well controlled [84]. However, the HL-LHC represents a quantitative as well as a qualitative leap into unknown territory with respect to beam–beam effects. The baseline configuration makes use of some novel concepts that have not so far been used to their full extent in hadron colliders, and thus require careful evaluation. The concepts related to beam–beam effects are: (i) luminosity levelling by variation of the beta function at the IPs; (ii) tilting bunches in the main IPs with the use of RF crab cavities; (iii) significantly high value of the head-on beam–beam tune shift.

Hence, the expected impact of beam–beam interactions on HL-LHC machine performance has been evaluated in order to provide an insight into possible limitations. The studies were mostly performed with the use of the weak–strong approximation and employed the SixTrack and Lifetrack codes, which have been successfully used for the design and optimization of past and existing colliders [85, 86]. Both codes are capable of calculating the area of stable motion in phase space (the dynamic aperture), and hence a direct comparison of the results is possible. The performance reach for weak–strong codes is a few million turns, which is equivalent to a few minutes of machine time. Where necessary, strong–strong simulations with BeamBeam3D, COMBI and a code by K. Ohmi [87–99] were carried out.

In the evaluation of the HL-LHC, the criteria used for establishing satisfactory beam dynamics behaviour were the same as in the LHC design study. In particular, the target value for the one-million turn DA was  $6\sigma$  (for the nominal HL-LHC emittance of  $2.5\ \mu\text{m}$ ) or more. The motivation for the choice of such a margin is explained in Ref. [85]. In short, the beam–beam driven diffusion at small amplitudes is quite slow, and the  $10^6$  turns of tracking typically does not represent the real long-term stability boundary. In the majority of studies, the  $6\sigma$  DA corresponds to a true stability boundary of about  $4\sigma$  with the appearance of chaotic spikes [85]. Benchmarking of the simulations with machine studies seem to indicate that losses and reduction of beam lifetime start to appear only at values of the crossing angle for which the simulated dynamic aperture is as low as  $4\sigma$  [89, 90]. However, it must be noted that other studies indicate that the simulations of the dynamic aperture of the installed LHC overestimate the dynamic aperture by 20–30% [94].

In the baseline HL-LHC scenario (25 ns spacing), bunches will begin colliding with  $2.2 \times 10^{11}$  p/b and transverse normalized emittance of  $2.5\ \mu\text{m}$ . The bunches will be tilted by crab cavities at each of the two main IPs to ensure head-on collisions despite the trajectories crossing at an angle. The luminosity will be levelled at the constant value of  $5 \times 10^{34}\ \text{cm}^{-2}\ \text{s}^{-1}$  by varying the beta function from  $\sim 69$  cm at the beginning of the fill to 15 cm at the end, in the case of constant crossing angle of  $590\ \mu\text{rad}$ . Assuming negligible transverse emittance growth, the separation of beams at parasitic crossings will thus vary from  $26\sigma$  at the beginning of the fill to  $12.5\sigma$  at the end. Hence, from the point of view of beam–beam effects, three stages can be distinguished over the course of a fill.

- Beginning of fill ( $\beta^* = 69$  cm,  $N = 2.2 \times 10^{11}$  p/b): weak long-range interactions ( $26\sigma$  separation) and strong head-on interactions, characterized by beam–beam tune shift  $\xi = 0.031$  (assuming head-on collisions in LHCb), determined by beam brightness  $B \sim N/\epsilon$ . Since optics with  $\beta^* = 69$  cm were not readily available, simulations were performed with  $\beta^* = 40$  cm, which, with the nominal initial intensity, corresponds to a significantly enhanced beam–beam effect (worst-case scenario). The bunch intensity at the specified levelled luminosity is  $N = 1.7 \times 10^{11}$  p/b.
- Middle of fill ( $\beta^* = 33$  cm,  $N = 1.5 \times 10^{11}$  p/b): appreciably large long-range and head-on interactions.
- End of fill ( $\beta^* = 15$  cm,  $N = 1.1 \times 10^{11}$  p/b): weak head-on ( $\xi = 0.015$  due to the particle burn-off in collisions) and relatively strong long-range ( $12.5\sigma$  separation).

All simulations were performed with lattice version SLHCV3.1b. In addition to IR1 and IR5, the beams also collide with a finite angle at IR8 (LHCb), which further enhances the negative impact of the head-on



beam–beam effects on the dynamics. The long-range effects are weaker thanks to the beneficial effects of the  $\beta^*$  levelling [92]. Multipole errors in the IR magnets were included in the simulations as specified in Ref. [94]. A parametric study was performed to establish the robustness of the baseline HL-LHC scenario [93] and in order to determine the optimal crossing angle. Figure 2-8 shows the dependence of the minimum DA value on the crossing angle at IP1 and IP5 for different bunch intensities. The dashed lines indicate the minimum target DA and the nominal crossing angle. For the operational cases described above, the DA is always largely above  $6\sigma$ .

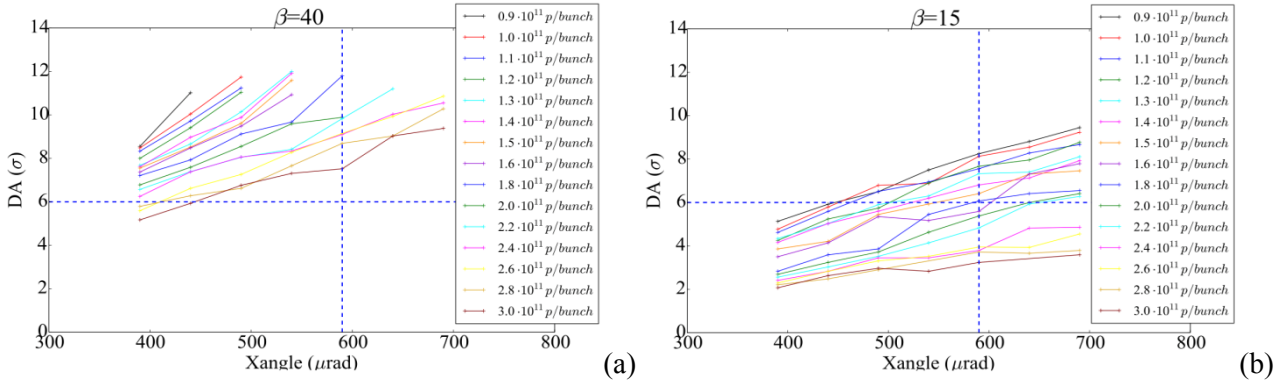


Figure 2-8: Minimum DA for (a)  $\beta^* = 40$  cm optics and (b)  $\beta^* = 15$  cm optics as a function of crossing angle for different bunch intensities. The r.m.s. beam size corresponds to a normalized emittance of  $2.5 \mu\text{m}$ .

Pacman effects [95, 97] have been evaluated and shown not to have a significant impact on DA and luminosity. The pacman effects are expected to be strongest at the end of the fill ( $\beta^* = 15$  cm), and will be weaker than the nominal LHC case due to a larger beam–beam separation ( $12.5\sigma$  compared to  $9.5\sigma$ ). With an intensity of  $N = 1.1 \times 10^{11}$  p/b and a long-range beam–beam separation of  $12.5\sigma$  one expects a maximum offset at IP1 and IP5 of about  $0.15\sigma$ . The spread over the bunch train is of the same order,  $0.1$ – $0.2\sigma$ . The long-range variations at IP1 and IP5 result in a very small asymmetry in the tune footprint, and no impact on long-term tracking has been noticed [93].

The results of weak–strong simulations confirm the robustness of the baseline HL-LHC scenario with respect to beam lifetime and particle losses, and suggest that a significant margin exists that would allow either a decrease of the crossing angle to approximately  $450 \mu\text{rad}$ , or operation at higher values of levelled luminosity [95].

Beam–beam effects can induce beam emittance growth and related luminosity lifetime degradation via a variety of mechanisms. Weak–strong simulations of multi-particle bunches were used to evaluate the emittance growth due to beam–beam related betatron resonances. The results predict that the luminosity lifetime due to beam–beam effects will be more than 80 h even in the worst case [98]. A more significant mechanism of emittance degradation can be related to the interplay between the nonlinearity of the beam–beam interaction and various sources of noise. In particular, the phase errors of crab cavities and the ripple of dipole magnet power supplies lead to fluctuations in beam–beam separation. Strong–strong beam–beam simulations have been carried out for the HL-LHC parameters with a large crossing angle and crab cavity compensation [99, 100]. A detailed damper model was included in the simulations. Both  $\beta^*$  levelling and crab cavity levelling were simulated including crab cavity noise and dipole power supply ripple [100]. For white random phase noise in the crab cavities, simulations suggest that the r.m.s. noise amplitude should be kept around the level of  $3 \times 10^{-5}$  rad in order to maintain a luminosity lifetime of 24 h. This tolerance limit might over-estimate the crab cavity phase noise level since the real phase error will have some spectral distribution different from white noise. For the present studies the spectrum was sampled at a number of frequencies near the betatron frequency. Simulations suggest that strong emittance growth would occur with noise frequencies near the fractional tune of 0.30 and 0.31. The phase errors with those frequencies should be kept as small as possible. The 600 Hz dipole noise was found to have negligible effect on the beam emittance

### 2.4.3 Beam-induced heat load on the cryogenic system

Both impedance and the e-cloud induce heat loads on the cryogenic system [70]. The impedance-induced heat loads with the HL-LHC beam parameters [14] for several key systems are summarized in Table 2-9. In the analysis it is assumed that no forward physics detectors (e.g. ALFA and TOTEM) will be installed during the HL-LHC era. The impedance-induced heat loads for the different types of beam screens vs. temperature are summarized in Table 2-10.

Electron cloud effects should be mitigated by beam-induced scrubbing in the arcs (experience from Run 2 will be vital in that respect) and by low secondary emission yield (SEY) coatings and/or clearing electrodes in the new insertion regions, intended to keep the heat loads within the cooling capacity [70]. Similar actions will be required for the beam screen of the triplets/D1 in IR2 and IR8.

Figure 2-9 shows the heat load from the e-cloud vs. bunch intensity for both an arc dipole and an arc quadrupole, for different SEYs. Provided that a low SEY is achieved, the increased bunch intensity should be acceptable for heat load, but the effect on the beam stability still needs to be assessed. The aim of the scrubbing run is to reach a SEY of  $\sim 1.3$  in the arc main magnets: this applies for both LHC and HL-LHC, because the dependence of the SEY threshold on bunch intensity in the dipoles is weak. It is worth noting that the quadrupoles have a threshold below 1.1, which cannot be reached by scrubbing. The detrimental effects of the electron cloud in the LHC (heat load in cold regions and emittance blow-up) can be partly mitigated by using specially conceived filling patterns. The underlying idea is to use the flexibility of the injector complex to build bunch trains in LHC with long enough gaps interspersed, to prevent the build-up of an electron cloud along the beam. An alternative scenario (referred to as 8b+4e) based on beams with 25 ns spacing has been conceived to reduce the electron cloud effects in the HL-LHC, if needed, in its initial phase of operation following the upgrade [101] and has been considered as part of the HL-LHC operational scenarios [3]. Operation with a 200 MHz main RF system would allow for longer bunches and would have a positive impact also on the e-cloud [79]. The impact of the bunch length on the e-cloud will be studied experimentally during the coming Run 2 (e.g. to reduce emittance blow-up at low energy).

Table 2-9: Summary of the impedance-induced heat load computations for several key systems

Element	Expected heat load [W]	Conclusion/comment
Equipment with RF fingers [102]	Negligible for conforming RF fingers.	Robust mechanical and quality control required during the installation phase.
Experimental beam pipes (resonant modes) [103–107]	ATLAS: no significant mode expected. ALICE: potentially* more than 1 kW. CMS: potentially* more than 350 W. LHCb: potentially* more than 250 W.	During Run 2, the temperature should be closely monitored in the large-diameter regions of ALICE, CMS, and LHCb. The impact of these potential expected heat loads on hardware integrity and outgassing should be assessed.
All types of beam screens [104] and Table 2-10	See Table 2-10, where the power losses have been computed vs. temperature (between 20 K and 70 K).	The effects of the beam screen longitudinal weld, the two counter-rotating beams, and the magneto-resistance have been taken into account. Decoupling of the cryogenics for the IR elements and the RF will provide more margin for acceptable heat load in the arcs.
Triplet beam position monitors [109]	$\sim 0.2$ W/m for the (most critical) 50 ns beam.	This assumes no interferences between the two beams' electromagnetic fields (worst case) and copper coating.
New collimators with integrated BPMs and ferrites [110]	$\sim 100$ W (of which $\sim 5$ W to 7 W would be dissipated in the ferrites, and $\sim 4$ W to 6 W in the RF fingers).	More thorough simulation studies as well as bench measurements are under way to confirm these results. This should be acceptable.
Injection kickers (MKIs) [111, 112]	Between $\sim 125$ W/m and $\sim 191$ W/m (based on measurements of 9 MKIs)	It is of the order of heat loads estimated with pre-LS1 parameters for the old MKI8D (i.e. before the third

	upgraded to have the full complement of 24 screen conductors). For comparison, most of the MKIs before LS1 had a power deposition of ~ 70 W/m (which did not limit LHC operation).	Technical Stop of 2012) which had a 90° twist in the screen conductors and that had a power deposition of ~160 W/m, based on measurements of impedance during LS1. This required significant time to cool-down after physics fills. For the HL-LHC we are looking at: (i) further reducing the power deposition; (ii) improving the cooling; (iii) using high Curie point ferrites.
Crab cavities [113]	In the multi kW range if the longitudinal modes overlap with beam harmonic frequencies.	The design should allow detuning the longitudinal modes from multiples of 20 MHz by ~0.5 MHz.
Injection protection dump (TDI) [106]	The present design already suffers from beam-induced heating (in the kW range for the injection settings) with nominal LHC parameters due to inefficient cooling.	The present design of the TDI is not compatible with the HL-LHC parameters and a new design is being studied, with installation foreseen for LS2.
Synchrotron radiation monitor (BSRT) [114]	The power deposited in the ferrite absorbers (heated at ~ 250°C to 350°C according to simulations and measurements) during 2012 operation could not be efficiently transferred, leading to damage.	A new design is being studied and installed during LS1. The usability of this design for HL-LHC will need to be assessed after LS1.

\*If the longitudinal modes overlap with beam harmonic frequencies.

Table 2-10: Impedance-induced heat loads for the different types of beam screens (including the effects of the longitudinal weld, two counter-rotating beams, and the magneto-resistance) vs. temperature: values are given for the 25 ns beam and for the 50 ns beam (in parentheses).

Power loss [W/m]	20 K	30 K	40 K	50 K	60 K	70 K
Q1 (49 mm, 6.9 T)	0.23 (0.28)	0.24 (0.31)	0.28 (0.35)	0.34 (0.43)	0.40 (0.51)	0.47 (0.59)
Q2-Q3 (59 mm, 8.3 T)	0.19 (0.24)	0.20 (0.26)	0.23 (0.29)	0.28 (0.35)	0.33 (0.42)	0.38 (0.49)
D1 (59 mm, 5.6 T)	0.17 (0.22)	0.19 (0.24)	0.22 (0.28)	0.27 (0.34)	0.32 (0.41)	0.38 (0.48)
D2 (42 mm, 4.5 T)	0.25 (0.32)	0.27 (0.34)	0.32 (0.40)	0.39 (0.50)	0.47 (0.59)	0.54 (0.69)
Q4 (32 mm, 3.7 T)	0.34 (0.43)	0.37 (0.47)	0.44 (0.56)	0.54 (0.68)	0.64 (0.81)	0.74 (0.94)
Q5 (22 mm, 4.4 T)	0.59 (0.74)	0.63 (0.80)	0.72 (0.91)	0.86 (1.09)	1.01 (1.28)	1.16 (1.46)
Q6 (17.7 mm, 3.5 T)	0.79 (0.99)	0.84 (1.06)	0.96 (1.22)	1.14 (1.44)	1.32 (1.68)	1.51 (1.91)
Q7 (17.2 mm, 3.4 T)	0.82 (1.03)	0.87 (1.11)	1.00 (1.26)	1.18 (1.49)	1.37 (1.74)	1.56 (1.98)

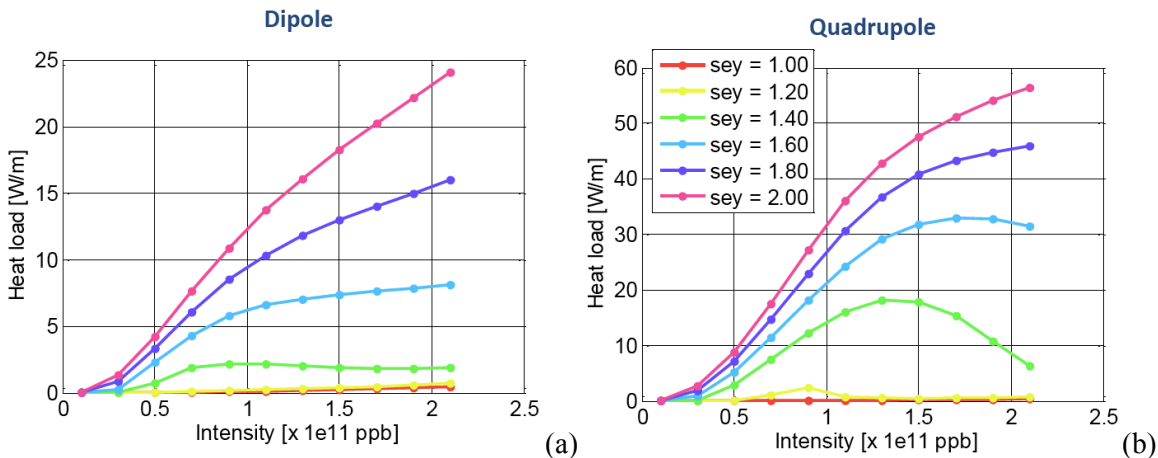


Figure 2-9: Heat load from e-cloud in the arc main magnets as a function of bunch intensity and SEY

Figure 2-10 shows the expected heat load along the triplet in IP1 and IP5 for different SEY values. The least efficient build-up (lower heat load) occurs at the locations of the long-range encounters (vertical dashed

lines). Note that the values in the D1 dipole are comparable to or higher than the values in the quads. The comparison of the heat load from the e-cloud for the current LHC and the future HL-LHC triplets shows that the larger bunch population and larger chamber size lead to a larger heat load by a factor  $\sim 3$ , for the HL-LHC [69] (for the same SEY, a similar energy of multipacting electrons, and a larger number of impacting electrons). For IP2 and IP8, scaling the results also leads to an increase of the heat load from the e-cloud by a factor  $\sim 3$ , but detailed simulations remain to be done. Unlike IP1 and IP5, the cryostats in IP2 and IP8 already include D1 (about 10 m long).

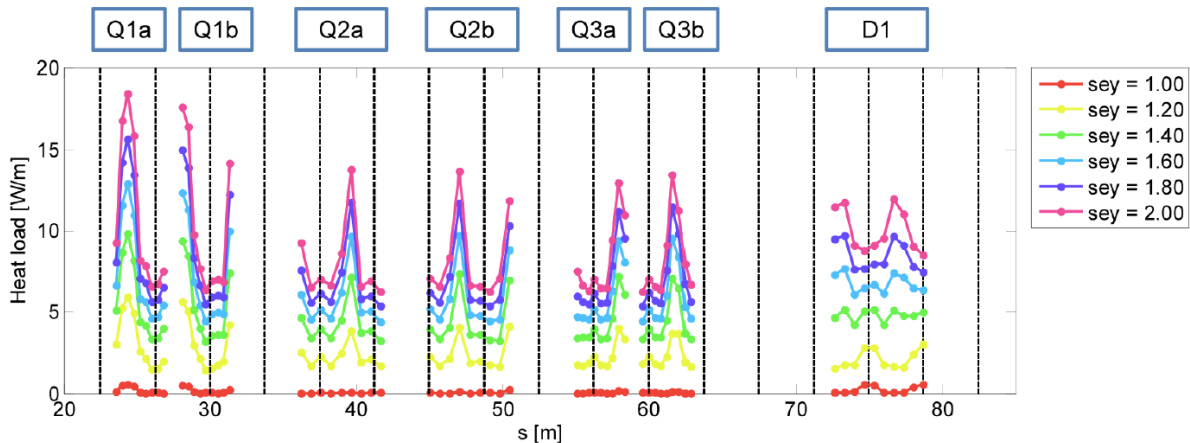


Figure 2-10: Heat load from the e-cloud along the future HL-LHC triplets

Understanding e-cloud build-up in the matching section requires the study of a large number of configurations (beam screen shape and dimensions, magnetic field configuration, beam size, beam position, etc.). Parametric studies will be performed to assess which of these dependencies strongly impact e-cloud build-up. Some preliminary simulations revealed that the beam size and the magnetic field have a small but non-negligible impact. The next step will be to try and disentangle these two effects. The effect of the beam position will then have to be studied in detail.

#### 2.4.4 Luminosity performance

The peak performance at 7 TeV has been estimated in Table 2-1. The estimate of the integrated luminosity requires determining the luminosity evolution during a fill. The beam intensity evolution has been evaluated taking into account burn-off due to luminosity considering a total cross-section of 100 mb [115, 116], and an additional (unknown) source of intensity loss with a lifetime of 200 h (based on experience during 2012 [117]).

The emittance evolution has been determined including: intra-beam scattering (IBS) (based on Run 1 experience, no coupling has been assumed); radiation damping; and an additional (unknown) source of vertical emittance blow-up with a lifetime of 40 h (based on observations during Run 1). A finite difference method in steps of 5 min has been implemented to model the intensity evolution and the evolution of the IBS lifetime as a function of the bunch population. Figure 2-11, Figure 2-12 and Figure 2-13 show the evolution of the main parameters for two cases of levelling, corresponding to a pile-up of 140 and 210, for the standard filling scheme with parameters listed in Table 2-1. In the estimates the worst case scenario (with respect to the head on beam-beam tune spread) of  $\beta^*$  levelling in IP1, IP5, and IP8 has been considered. Full compensation of the crossing angle by crab cavities has been included for IP1 and IP5. The crossing angle is assumed to be constant during the fill. Alternative (or complementary) luminosity levelling scenarios include:

- crossing angle variation to increase the geometric reduction factor at the beginning of the fill;
- crab cavity RF voltage variation to have a partial crossing angle compensation at the beginning of the fill;
- dynamic bunch length reduction;
- controlled variation of the transverse separation of the two colliding beams.

Options 1 and 2 have the disadvantage of increasing the line pile-up density at the start of the fill.

The performance estimates for the two cases considered (pile-up 140 and 210) are listed in Table 2-11. The parameters used for the estimates of the HL-LHC integrated performance are listed in Table 2-12. The operation at the higher pile-up limit is appealing because it allows higher integrated luminosity while keeping the optimum fill length to values already obtained in 2012; however, in this case, the maximum pile-up density exceeds the target pile-up density limit of 1.3 events/mm/crossing. This could be reduced by increasing the bunch length. A more elegant solution could be provided by the crab-kissing scheme [16] and/or by the implementation of flat-beam optics with a smaller crossing angle (provided that long-range effects can be kept under control, perhaps by the implementation of long-range compensation schemes). These alternative scenarios will be described below.

Table 2-11: Integrated performance estimate for levelling scenarios at pile-up levels of 140 (PU 140) and 210 (PU 210) events/crossing, respectively.

	Levelling time [h]	Optimum fill length [h]	Integrated Lumi [ $\text{fb}^{-1}/\text{y}$ ] for $\eta = 50\%$ , optimum fill length IP1/IP5/IP8/IP2	Maximum mean pile-up density [events/mm/crossing] in IP1/IP5	Maximum mean pile-up [events/crossing] in IP1/IP5
PU 140	8.1	9.4	261/8.9/0.105	1.25/140	140
PU 210	4.25	6	331/7.8/0.092	1.81/210	210

Table 2-12: Parameters assumed for HL-LHC performance estimate

<b>Scheduled physics time for p-p luminosity production/year (<math>T_{phys}</math>) [days]</b>	<b>160</b>
Minimum turnaround time [h]	3
Performance efficiency – goal [%]	50
Pile-up limit IP1/IP5 [events/crossing]	140/200
Pile-up limit IP8 [events/crossing]	4.5
Pile-up density limit – IP1/IP5 [events/mm/crossing]	1.3
Visible cross-section IP1/IP2/IP5 [mb]	85
Visible cross-section IP8 [mb]	75 [118]

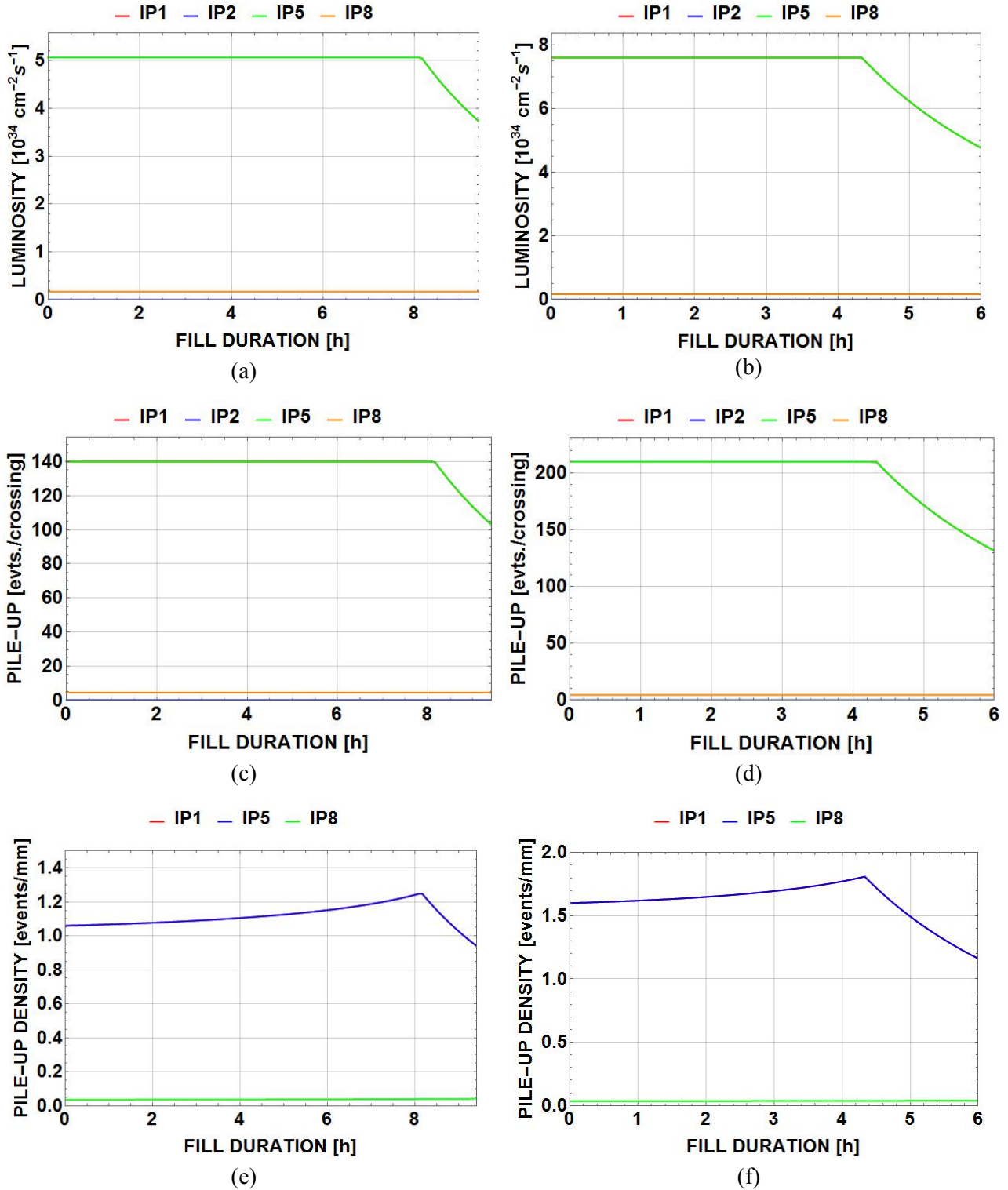


Figure 2-11: Evolution of Luminosity, pile-up and pile-up density assuming levelling at 140 events/crossing (a, c, e) and 210 events/crossing (b, d, f) in IP1 and IP5. The small effects of RF curvature in the crab cavities is not included.

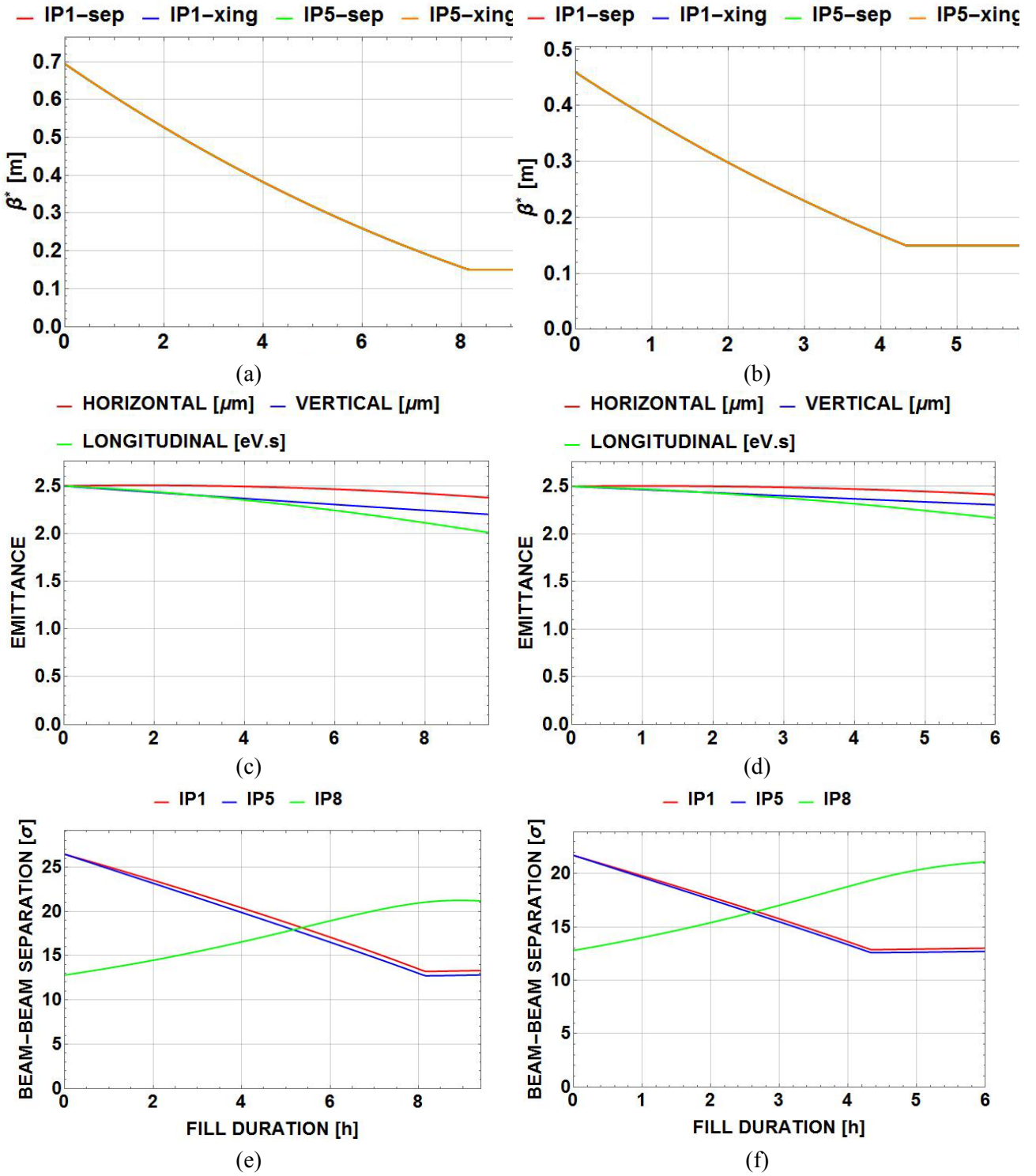


Figure 2-12: Evolution of  $\beta^*$ , emittance and long-range beam-beam normalized separation ( $d_{bb}$ ) for levelling at 140 (a, c, e) and at 210 events/crossing (b, d, f) in IP1 and IP5.

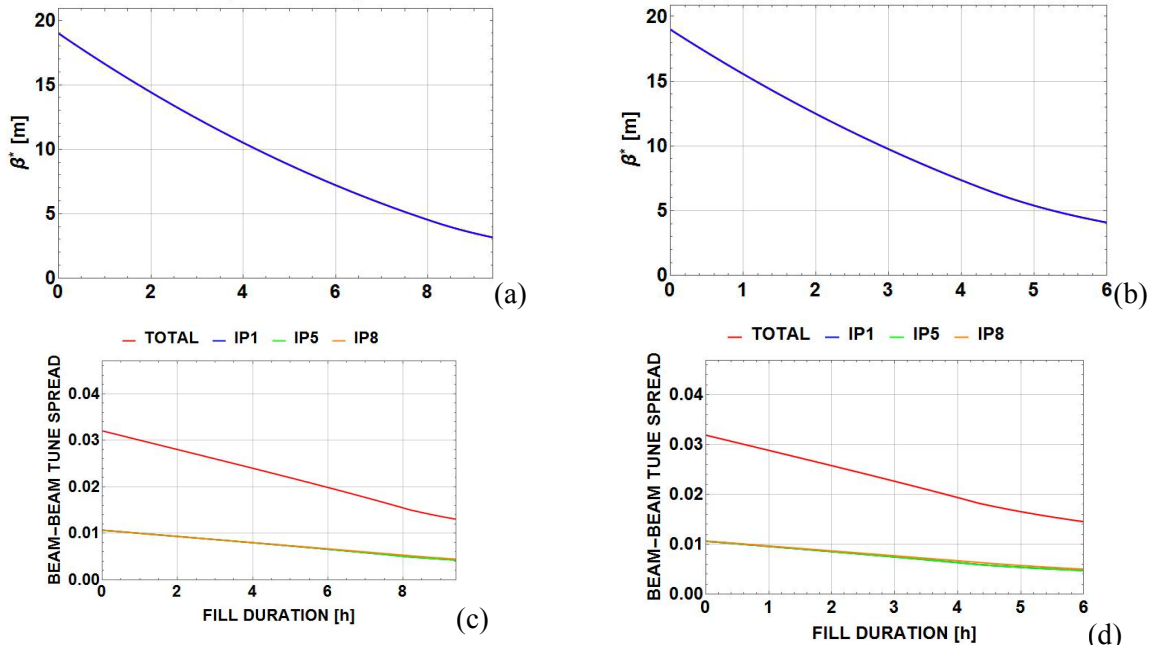


Figure 2-13: Evolution of  $\beta^*$  in IP8, head-on beam-beam tune spread assuming levelling at 140 events/crossing (a, c) and at 210 events/crossing (b, d) in IP1 and IP5.

### 2.5 Variants and options

The HL-LHC project includes the study of various alternatives to the present baseline configuration with the aim either of improving the potential performance of the machine or of providing options for addressing possible limitations or changes in parameters (see Figure 2-14).

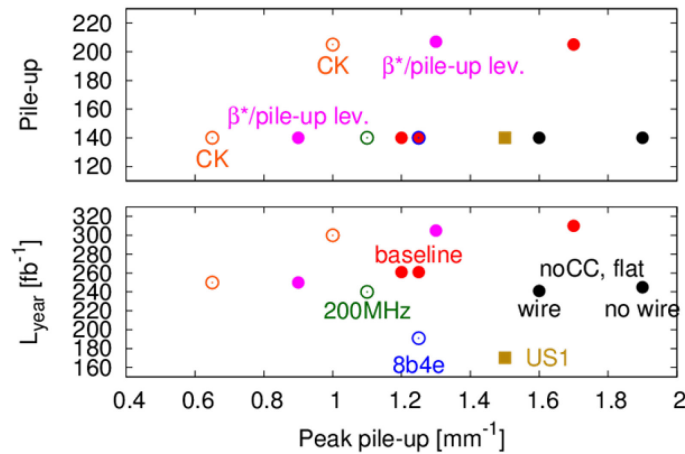


Figure 2-14: Performance expectation of different alternatives. The red markers represent the baseline scenarios (flat or round) for different target of total pile-up (140 and 200 events per crossing). In the case of the crab cavities are absent (black marker) annual integrated luminosity could be recovered by using flat optics for an increase of the peak pile-up density that can be limited with long-range compensators. The crab-kissing scheme (magenta markers) on the other hand offers the target annual luminosity with the means to control the pile-up density and to reduce it considerably with respect to the nominal scheme. Peak pile-up density can also be levelled with  $\beta^*$  (magenta markers). If e-cloud effects needs to be mitigated, a 200 MHz RF system or the 8b+4e filling schemes (green and blue markers) could be deployed.



### 2.5.1 Pile-up density management

The crab-kissing scheme ([16, 119] and references therein) would allow either improvement of the data quality by reducing the peak pile-up density at a constant integrated luminosity, or an increase of the integrated luminosity at constant total pile-up or levelled luminosity (see orange markers in Figure 2-14). At present, implementation of the crab-kissing scheme would require changes to the layout of the crab cavities, to allow bunch deflections in different planes. Also, a flat optics with beam–beam long-range compensator would need to be implemented. These changes are not completely compatible with the nominal scheme because the crab cavity voltage is insufficient to provide the required deflections in both planes; however new optics solutions are being explored to keep the crab-kissing scheme and the nominal configuration mutually compatible.

If crab kissing is not available it would still be possible to level peak pile-up density using  $\beta^*$  with different total pile-up targets (see magenta markers in Figure 2-14). In this scenario a flat longitudinal profile is assumed to be reachable through use of a second harmonic RF system or phase modulation as in the case of crab kissing. In the absence of flat longitudinal profiles one could expect an increase in the peak pile-up of about 10%.

### 2.5.2 Alternative scenarios

A compact 200 MHz RF system could be installed ([79] and references therein) in the LHC, potentially allowing an increase in the injected intensity from the SPS, although further studies are needed to confirm what could be achieved. Such a system, together with a 400 MHz system, could offer the means to increase the bunch length (e.g. 15 cm) to reduce electron cloud effects, reduce IBS growth rates, and provide flat longitudinal bunch charge density (see green markers in Figure 2-14).

If the e-cloud severely limits the beam current with 25 ns bunch spacing, the 8b+4e [79] filling scheme would allow comparable beam current at the cost of lower levelled luminosity with constant total pile-up. The 8b+4e scheme can provide about  $2.3 \times 10^{11}$  p/b with 1900 bunches [3], halfway between the corresponding 50 ns and 25 ns configurations, and therefore resulting in a performance reach between those two extremes (see blue markers in Figure 2-14).

In the absence of crab cavities, it may still be possible to implement some measures to limit the loss of performance [20]. By increasing  $\beta^*$  in the crossing plane and decreasing it in the separation plane, one could limit the impact of the geometric reduction factor thanks to the reduction of the necessary crossing angle (see rightmost black marker in Figure 2-14). However, a large crossing angle in units of  $\sigma$  is still needed ( $12 \sigma$  for the lower  $\beta^* = 30$  cm) because of the partial loss of the IR1/IR5 long-range beam–beam (LRBB) interaction compensation (i.e. passive compensation from the non-symmetric alternating crossing between IP1 and IP5). However, an LRBB compensator could potentially allow  $10 \sigma$  separation, therefore restoring the luminosity compared to the nominal scenario at the cost of some increase in pile-up density (see the leftmost black marker in Figure 2-14). Similarly, a staged upgrade scenario for which the replacement of the matching section is postponed (see Refs. [120, 47] and references therein) could still benefit from flat beam optics, although with a limited reach of  $\beta^*$  in the non-crossing plane (about 20 cm) but with the potential of reaching about  $170 \text{ fb}^{-1}$  per year (see dark yellow markers in Figure 2-14). In this context, a design for a movable TAXN that could be adapted to different  $\beta^*$  values would offer the best radiation protection for the downstream elements in all these scenarios, regardless of the chosen optics configurations.

## 2.6 The HL-LHC as a nucleus–nucleus collider

The LHC’s second major physics programme provides nucleus–nucleus collisions to ALICE, CMS and ATLAS, and proton–nucleus collisions to these three experiments and, in addition, to LHCb. The overall goal of the programme is ultimately to accumulate  $10 \text{ nb}^{-1}$  of Pb–Pb luminosity during the whole LHC operating period after Run 2 [80, 121]. The p–Pb requirement will be for approximate equivalence in terms of integrated nucleon-pair luminosity [80, 122, 123]. The heavy-ion programme may also require short p–p runs at specific energies to provide reference data; the luminosity requirement will be similar (see 16.6). Nuclei other than

$^{208}\text{Pb}^{82+}$  have not been requested by the experiments but remain as possible options with potential performance to be evaluated.

The heavy-ion luminosity upgrade aims at increasing integrated rather than peak luminosity and is therefore focused mainly on injecting the maximum beam current possible. With the expected upgrade to remove the event rate limit of the ALICE experiment, luminosity levelling will no longer be a necessity but may be employed to mitigate the rapid luminosity decay due to the large electromagnetic cross-sections [80, 124]. Low values of  $\beta^*$  are required at three or four interaction points so the ATS will not be used. The main elements of the heavy-ion luminosity upgrade should be in place a few years before those of the proton–proton part of the project.

Upgrades to the heavy-ion injector chain [125] would normally aim to increase the number of bunches and the intensity per bunch, but these two quantities are not independent. Injecting long trains from the SPS lengthens the injection plateau in the SPS, subjecting some bunches to higher losses from the effects of intra-beam scattering, space charge, and RF noise [126]. On the other hand, injecting a larger number of short trains from the SPS increases the average bunch intensity but leaves more gaps in the LHC bunch train and increases the LHC’s injection time, reducing overall efficiency and subjecting some bunches to more emittance growth at LHC injection. In all cases, there is a broad distribution of bunch parameters in collision in the LHC. Optimization of the injection and filling schemes has to take all these interdependencies into account [126] and will likely have to be done anew each year as a function of injector performance.

The present performance estimates are nevertheless based on an injection scheme that assumes that the maximum 12 PS batches of four bunches are assembled into a batch in the SPS, with a 50 ns bunch spacing achieved by slip-stacking. This is repeated 26 times to assemble a train of 1248 bunches in the LHC (practical filling scheme details will reduce this by some percent, depending on the experiment) and yielding a distribution of individual bunch-pair luminosities at the start of colliding beams as shown in Figure 2-15. Simulation of the evolution of these individual bunches, taking into account luminosity burn-off, IBS, and radiation damping [126] leads to the total luminosity shown in Figure 2-16. Depending on the turnaround time (between beam dump and the next declaration of stable beams for physics), the fill length can be optimized to give the ideal average daily luminosity shown.

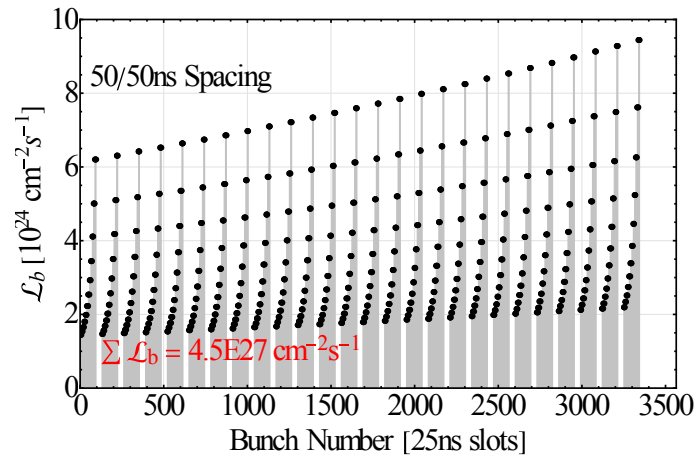


Figure 2-15: Initial luminosity for each colliding bunch pair along the full train in the LHC

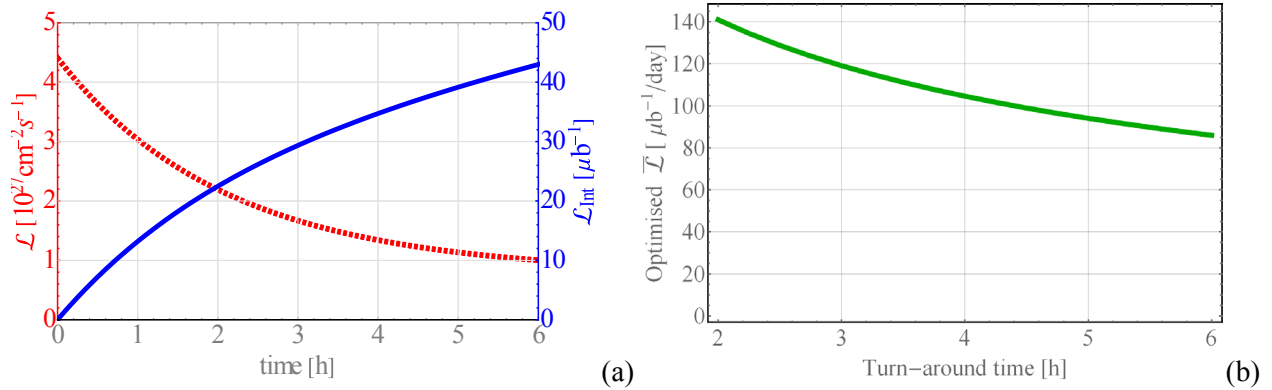


Figure 2-16: (a) Total luminosity (red) and integrated luminosity (blue) during a fill starting with the bunch-pair luminosities shown in Figure 2-15. (b) Average luminosity per day as a function of turnaround time (dump to next stable beams) when fill lengths are optimized, with lengths varying between 3 h and 6 h, with the luminosity dependence shown in the left plot.

The rapid luminosity decay is due to the large cross-sections of electromagnetic processes in the collisions [126, 127]. The peak luminosity is expected to be substantially above the quench limit from losses due to the bound-free pair-production process; and new collimators are foreseen in the dispersion suppressors to absorb these secondary beams emerging from the interaction points (see Chapter 5, Section 5.2). Intensity limitations may also arise from losses due to collimation inefficiency, which is higher for ion beams, due to the more complicated nuclear interactions with collimators [128, 129].

The 50 ns bunch spacing introduces close parasitic beam-beam encounters near to the ALICE experiment, which may require the half-crossing angle to be increased beyond the 60  $\mu\text{rad}$  limit imposed for optimum operation of the zero-degree calorimeters. The minimum acceptable at the low Pb bunch charge will be determined empirically [80]. The crossing angles for ATLAS and CMS are unrestricted and can be taken over from proton operation.

The principal beam parameters determining the luminosity are summarized in Table 2-13. Other parameters will be similar to those given in Ref. [130]. Further potential gains in luminosity may come from improved injector performance and, possibly, a cooling system [131] in the LHC.

Table 2-13: Average values of principal beam parameters at start of physics

Parameter	Value
Number of bunches per beam	1248
Normalized transverse emittance (average)	1.6 $\mu\text{m}$
Optical function at interaction point	0.5 m
Crossing angle at ALICE experiment	60 $\mu\text{rad}$
Bunch population (average)	$1.04 \times 10^8$
Bunch length	0.1 m
Peak luminosity	$4.5 \times 10^{27} \text{ cm}^{-2} \text{ s}^{-1}$

## 2.7 Acknowledgements

The volunteers of the LHC@home project are warmly acknowledged for their generous contribution of CPU time for the numerical simulations of dynamic aperture. Furthermore, we would like to express our gratitude to E. McIntosh for his continuous support for the numerical simulations and the SixTrack code.

## 2.8 References

- [1] R. Jacobsson, Future wishes and constraints from the experiments at the LHC for the proton-proton programme, ICFA Mini-Workshop on Beam-Beam Effects in Hadron Colliders (BB2013), CERN,

- Geneva, Switzerland, 18 - 22 Mar 2013, Eds. W. Herr and G. Papotti, CERN-2014-004 (2014), p. 167–176.
- [2] O.S. Brüning and F. Zimmermann, Parameter space for the LHC High Luminosity Upgrade, Proc. 3rd International Particle Accelerator Conf., New Orleans, 20–25 May 2012, Eds. C. Petit-Jean-Genaz and J. Corbett, p. 127–129.
- [3] G. Arduini, O. Brüning, R. De Maria, R. Garoby, S. Gilardoni, B. Goddard, B. Gorini, M. Meddahi, G. Rumolo and R. Tomás, Beam parameters at LHC injection, CERN-ACC-2014-0006 (2014).
- [4] O.S. Brüning, HL-LHC parameter space and scenarios, Proc. Chamonix 2012 Workshop on LHC Performance, Chamonix, France, 6–10 Feb 2012, Ed. C. Carli, CERN-2012-006 (2012), p. 315–324.
- [5] S. Fartoukh and F. Zimmermann, The accelerator physics challenges CERN-ACC-2014-0209 (2014).
- [6] V. Kain, Concerns with low emittance beams operation, LHC Performance Workshop, Chamonix, France, 22–25 September 2014,  
<http://indico.cern.ch/event/315665/session/5/contribution/22/material/slides/0.pdf>
- [7] V. Kain *et al.*, Injection protection – Are we taking it seriously? How can we make it safer?, Proc. 2nd Evian Workshop on LHC Beam Operation, Evian, France, 7–9 December 2010, Ed. B. Goddard, p. 143–149.
- [8] E. Métral, Pushing the limits: Beam, Proc. Chamonix 2011 Workshop on LHC Performance, Chamonix, France, 24–28 January 2011, Ed. C. Carli, CERN-ATS-2011-005, p. 252–260.
- [9] R.W. Assmann, Implications of higher intensities in the LHC, Proc. Chamonix 2011 Workshop on LHC Performance, Chamonix, France, 25–29 January 2010, Ed. C. Carli, CERN-ATS-2010-026, p. 328–333.
- [10] X. Buffat, R. Giachino, W. Herr, G. Papotti, T. Pieloni, R. Calaga and S.M. White, Observation of coherent beam-beam effects in the LHC, Proc. 2nd International Particle Accelerator Conf., San Sebastian, Spain, 4 - 9 Sep 2011, pp.TUPZ029 .
- [11] R. Calaga, R. Tomas and F. Zimmermann, LHC Crab-Cavity Aspects and Strategy, Proc. 1st International Particle Accelerator Conf., Kyoto, Japan, 23–28 May 2010, Eds. A. Noda, C. Petit-Jean-Genaz, V. Schaa, T. Shirai and A. Shirakawa, p. 1240–1242.
- [12] E. Shaposhnikova, E. Ciapala and E. Montesinos, Upgrade of the 200 MHz RF System in the CERN SPS, CERN-ATS-2011-042, Proc. 2nd International Particle Accelerator Conf., S. Sebastian, Spain, 4–9 September 2011, Eds. C. Petit-Jean-Genaz, A. Blanco, I. Etxebarria, F. Perez, A. Wolski and V. Schaa, p. 214–216.
- [13] H. Bartosik, G. Iadarola, Y. Papaphilippou, G. Rumolo and E. Shaposhnikova, Can we ever reach the HL-LHC requirements with the injectors?, Review of LHC and Injector Upgrade Plans Workshop, Archamps, 29–31 October 2013.  
<https://indico.cern.ch/event/260492/session/4/contribution/18/material/paper/0.pdf>
- [14] HL-LHC Parameter and Layout Committee Parameter table v 4.1.0 (27/8/2014).  
[https://espace.cern.ch/HiLumi/PLC/\\_layouts/xlviewer.aspx?id=/HiLumi/PLC/SiteAssets/Parameter%20Table.xlsx](https://espace.cern.ch/HiLumi/PLC/_layouts/xlviewer.aspx?id=/HiLumi/PLC/SiteAssets/Parameter%20Table.xlsx)
- [15] R. Bruce, A. Marsili and S. Redaelli, Cleaning performance with 11 T dipoles and local dispersion suppressor collimation at the LHC, 5th International Particle Accelerator Conference, Dresden, Germany, 15 - 20 Jun 2014, pp.MOPRO042.
- [16] S. Fartoukh, Pile-up density management at HL-LHC and the crab-kissing scheme, HL-LHC brainstorming coordination meeting, July 2013.  
<http://indico.cern.ch/conferenceDisplay.py?confId=263083>

- [17] S. Fartoukh, Optics challenges and solutions for the LHC insertion upgrade phase I, Workshop on LHC Performance, Chamonix, France, 25–29 January 2010, CERN-sLHC-PROJECT-Report-0038, pp. 262–290.
- [18] S. Fartoukh, Layout and optics solution for the LHC Insertion Upgrade Phase I, 1st International Particle Accelerator Conference, Kyoto, Japan, 23 - 28 May 2010, pp.THPE018.
- [19] S. Fartoukh, R. Tomás and J. Miles, Specification of the closed orbit corrector magnets for the new LHC inner triplet, CERN-sLHC-PROJECT-Report-0030 (2009).
- [20] S. Fartoukh, Towards the LHC Upgrade using the LHC well-characterized technology, CERN-sLHC-PROJECT-Report-0049 (2010).
- [21] S. Fartoukh, Breaching the phase I optics limitations for the HL-LHC, CERN-sLHC-PROJECT-Report-0053 (2011).
- [22] S. Fartoukh, An achromatic telescopic squeezing (ATS) scheme for the LHC upgrade, 2nd International Particle Accelerator Conference, San Sebastian, Spain, 4 - 9 Sep 2011, pp.WEPC037.
- [23] S. Fartoukh, B. Goddard, W. Höfle, M. Lamont, R. de Maria, R. Miyamoto, G. Müller, L. Ponce, S. Redaelli, R. Steinhagen, M. Strzelczyk, R. Tomás, G. Vanbavinckhove and J. Wenninger, The achromatic telescopic squeezing scheme: Basic principles and first demonstration at the LHC, 3rd International Particle Accelerator Conference 2012, New Orleans, LA, USA, 20 - 25 May 2012, pp.1978.
- [24] S. Fartoukh, Achromatic telescopic squeezing scheme and application to the LHC and its luminosity upgrade, *Phys. Rev. Spec. Top. Accel. Beams* **16** (2013) 111002.
- [25] S. Fartoukh, G. Vanbavinckhove, M. C. Alabau Pons, R. Alemany Fernandez, R. Assmann, A. Butterworth, M. Giovannozzi, B. Goddard, P. Hagen, W. Höfle, D. Jacquet, R. de Maria, R. Miyamoto, G. Müller, S. Redaelli, R. Steinhagen, M. Strzelczyk, R. Suykerbuyk, E. Todesco, R. Tomás, W. Venturini, J. Wenninger and F. Zimmermann, The achromatic telescopic squeezing (ATS) MD part I, CERN-ATS-Note-2011-033 MD (2011).
- [26] S. Fartoukh, M. Lamont, R. De Maria, R. Miyamoto, G. Müller, L. Ponce, S. Redaelli, M. Strzelczyk, R. Tomás, G. Vanbavinckhove, J. Wenninger, M. Albert, R. Giachino, M. Giovannozzi, B. Goddard, P. Hagen, W. Höfle, V. Kain, A. Macpherson, L. Normann, G. Papotti, R. Steinhagen, D. Valuch and D. Wollman, The achromatic telescopic squeezing (ATS) MD part II, CERN-ATS-Note-2011-060 MD (2011).
- [27] S. Fartoukh, R. Tomás, B. Goddard, W. Höfle, D. Jacquet, G. Kruk, M. Lamont, R. de Maria, R. Miyamoto, G. Müller, M. Pojer, L. Ponce, S. Redaelli, N. Ryckx, R. Steinhagen, M. Strzelczyk, G. Vanbavinckhove and J. Wenninger, The achromatic telescopic squeezing (ATS) MD part III, CERN-ATS-Note-2011-132 MD (2011).
- [28] S. Fartoukh, V. Kain, Y. Levinsen, E. Maclean, R. de Maria, T. Persson, M. Pojer, L. Ponce, P. Skowronski, M. Solfaroli, R. Tomás and J. Wenninger, The 10 cm beta\* ATS MD, CERN-ATS-Note-2013-004 MD (2013).
- [29] S. Fartoukh, First demonstration with beam of the Achromatic Telescopic Squeezing (ATS) scheme, 2012 Workshop on LHC Performance, Chamonix, France, 6–10 February 2012, pp. 128–134.
- [30] E. Todesco, H. Allain, G. Ambrosio, G. Arduini, F. Cerutti, R. De Maria, L. Esposito, S. Fartoukh, P. Ferracin and H. Felice *et al.*, A first baseline for the magnets in the High Luminosity LHC insertion regions, CERN-ACC-2014-0036 (2014).
- [31] S. Fartoukh and R. De Maria, Database of baseline scenarios and variants: Milestone: MS17, CERN-ACC-2014-0069 (2014).

- [32] S. Fartoukh and R. De Maria, Optics and layout solutions for HL-LHC with large aperture Nb<sub>3</sub>Sn and Nb-Ti inner triplets, 3rd International Particle Accelerator Conference 2012, New Orleans, LA, USA, 20 - 25 May 2012, pp.145.
- [33] R. De Maria, S. Fartoukh, A. Bogomyagkov and M. Korostelev, HLLHCv1.0: HL-LHC layout and optics models for 150 mm Nb<sub>3</sub>Sn Triplets and local crab-cavities, 4th International Particle Accelerator Conference, Shanghai, China, 12 - 17 May 2013, pp.1358.
- [34] R. Calaga and R. De Maria *et al.*, 9th HL-LHC PLC meeting (2014).  
<https://indico.cern.ch/event/315418/>
- [35] M. Giovannozzi *et al.*, Optics and layout update, 3rd Joint HiLumi LHC– 22nd LARP Collaboration Meeting, 7–8 May 2014, BNL, USA. <https://indico.bnl.gov/conferenceDisplay.py?confId=730>
- [36] M. Giovannozzi, S. Fartoukh and R. De Maria, Specification of a system of correctors for the triplets and separation dipoles of the LHC upgrade, 4th International Particle Accelerator Conference, Shanghai, China, 12 - 17 May 2013, pp.2612.
- [37] M. Giovannozzi, S. Fartoukh and R. De Maria, Initial models of correction systems, CERN-ACC-2014-0010 (2014).
- [38] M. Fitterer, Budget for HL-LHC Orbit Correctors, HSS meeting 14 April 2014. [http://ab-dep-abp.web.cern.ch/ab-dep-abp/HSS/HSS\\_meetings/2014/20140414/HSSMeeting14042014.pdf](http://ab-dep-abp.web.cern.ch/ab-dep-abp/HSS/HSS_meetings/2014/20140414/HSSMeeting14042014.pdf)
- [39] M. Fitterer and R. De Maria, IT BPM tolerances for HL-LHC orbit correction, HSS meeting 26 May 2014. [http://ab-dep-abp.web.cern.ch/ab-dep-abp/HSS/HSS\\_meetings/2014/20140526/HSSMeeting26052014.pdf](http://ab-dep-abp.web.cern.ch/ab-dep-abp/HSS/HSS_meetings/2014/20140526/HSSMeeting26052014.pdf)
- [40] O. S. Brüning, P. Collier, P. Lebrun, S. Myers, R. Ostojic, J. Poole and P. Proudlock (Eds.), LHC Design Report, v.1: The LHC Main Ring, CERN-2004-003-V-1 (2012).
- [41] J.-B. Jeanneret, Geometrical tolerances for the qualification of LHC magnets, LHC Project Report 1007 (2007).
- [42] M. Korostelev, A. Wolski, R. De Maria and S. Fartoukh, Optics Transition between Injection and Collision Optics for the HL-LHC Upgrade Project, 4th International Particle Accelerator Conference, Shanghai, China, 12 - 17 May 2013, pp.1460.
- [43] M. Korostelev, Transition between injection optics and collision optics (including ATS squeeze), 3rd Joint HiLumi LHC-LARP Annual Meeting, 11–15 November 2013.  
<https://indico.cern.ch/event/257368/session/11/contribution/31>
- [44] R. De Maria, Parametric study of optics options for the HL-LHC project, 3rd International Particle Accelerator Conference 2012, New Orleans, LA, USA, 20 - 25 May 2012, pp.142.
- [45] B.J. Holzer, R. De Maria, S. Fartoukh, A. Chancé, B. Dalena, J. Payet, A. Bogomyagkov, R. B. Appleby, S. Kelly, M. B. Thomas, L. Thompson, M. Korostelev, K. M. Hock, A. Wolski, C. Milardi, A. Faus-Golfe and J. Resta Lopez, Optics design and lattice optimisation for the HL-LHC, 4th International Particle Accelerator Conference, Shanghai, China, 12 - 17 May 2013, pp.1385.  
<https://cds.cern.ch/record/1558908>
- [46] B. Dalena, J. Payet and A. Chancé, R. De Maria, S. Fartoukh, High Luminosity LHC matching section layout vs crab cavity voltage, 4th International Particle Accelerator Conference, Shanghai, China, 12 - 17 May 2013, pp.1328.
- [47] M. Fitterer, R. Bruce, R. De Maria and S. Fartoukh, Optics Considerations for PIC and US1 scenarios for HL-LHC in the framework of the RLIUP review, CERN-ACC-NOTE-2014-0031 (2014).
- [48] B. Dalena, J. Payet, A. Chancé and R. De Maria, Alternative high luminosity LHC matching section layout, 5th International Particle Accelerator Conference, Dresden, Germany, 15 - 20 Jun 2014, pp.990.
- [49] M. Giovannozzi *et al.*, LHC@Home: A Volunteer computing system for Massive Numerical Simulations of Beam Dynamics and High Energy Physics Events, 3rd International Particle Accelerator Conference 2012, New Orleans, LA, USA, 20 - 25 May 2012, pp.505.

- [50] S. Fartoukh and M. Giovannozzi, Dynamic aperture computation for the as-built CERN Large Hadron Collider and impact of main dipoles sorting, *Nucl. Instrum. Methods Phys. Res.*, A **671** (2012) 10–23.
- [51] F. Schmidt, SixTrack – Version 4.2.16 – Single particle tracking code treating transverse motion with synchrotron oscillations in a symplectic manner – Users’ reference manual, CERN/SL/94-56 (AP) update (2012).
- [52] SixTrack web site <http://sixtrack-ng.web.cern.ch/sixtrack-ng/>
- [53] <https://espace.cern.ch/HiLumi/WP2/task4/SitePages/Home.aspx> and [afs/cern.ch/eng/lhc/optics/SLHCV3.1b/errors/](https://afs.cern.ch/eng/lhc/optics/SLHCV3.1b/errors/)
- [54] <https://espace.cern.ch/HiLumi/WP2/task4/SitePages/Home.aspx> and [/afs/cern.ch/eng/lhc/optics/HLLHCV1.0/errors/](https://afs.cern.ch/eng/lhc/optics/HLLHCV1.0/errors/)
- [55] R. de Maria, S. Fartoukh, M. Giovannozzi, E. McIntosh, Y. Nosochkov, Y. Cai and M.-H. Wang, HiLumi LHC Deliverable Report: Magnet Field Quality Specifications, CERN-ACC-2014-0295 (2014).
- [56] Y. Nosochkov, Y. Cai, M.-H. Wang, R. de Maria, S. Fartoukh, M. Giovannozzi and E. McIntosh, Optimization of Triplet Quadrupoles Field Quality for the LHC High Luminosity Lattice at Collision Energy, 4th International Particle Accelerator Conference, Shanghai, China, 12 - 17 May 2013, pp.1364.
- [57] <https://espace.cern.ch/HiLumi/WP3/SitePages/MBXF.aspx>
- [58] <https://espace.cern.ch/HiLumi/WP3/SitePages/D2.aspx>
- [59] E. Todesco, private communication (2014).
- [60] M. Fitterer, R. De Maria and M. Giovannozzi, Powering requirements for HL-LHC triplet, WP2 task leader meeting 18 July 2014. <https://indico.cern.ch/event/323862/contribution/2/material/slides/1.pdf>
- [61] Yi-Peng Sun, R. Assmann, J. Barranco, R. Tomás, T. Weiler, F. Zimmermann, R. Calaga and A. Morita, Beam dynamics aspects of crab cavities in the CERN Large Hadron Collider, *Phys. Rev. ST Accel. Beams* **12** (2009) 101002.
- [62] J. Barranco García *et al.*, Study of multipolar RF kicks from the main deflecting mode in compact crab cavities for LHC, 3rd International Particle Accelerator Conference 2012, New Orleans, LA, USA, 20 - 25 May 2012, pp.1873.
- [63] D. R. Brett *et al.*, Comparison of Taylor maps with RF multipoles in a thin lens 6D tracking code, Proc. 4<sup>th</sup> International Particle Accelerator Conference, Shanghai, China, 12 - 17 May 2013, Eds. Z. Dai, C. Petit-Jean-Genaz, V. Schaa, C. Zhang, pp. 2687-2689.
- [64] R. Appleby *et al.*, Modelling and long term dynamics of crab cavities in the LHC, 5th International Particle Accelerator Conference, Dresden, Germany, 15 - 20 Jun 2014, pp.1578.
- [65] S. Kelly, M.B. Thomas, R. Appleby, L. Thompson, B. Holzer, R. De Maria and S. Russenschuck, Study of the impact of fringe fields of the large aperture triplets on the linear optics of the HL-LHC, 4th International Particle Accelerator Conference, Shanghai, China, 12 - 17 May 2013, pp.2642.
- [66] A. Bogomyagkov *et al.*, Analysis of the non-linear fringe effects of large aperture triplets for the HL LHC project, Proc. 4th International Particle Accelerator Conference, Shanghai, China, 12 - 17 May 2013, pp.2615.
- [67] B. Dalena *et al.*, Fringe fields modelling for the High Luminosity LHC large aperture quadrupoles, 5th International Particle Accelerator Conference, Dresden, Germany, 15 - 20 Jun 2014, pp.993.
- [68] S. Jones, D. Newton and A. Wolski, Initial estimate of fringe field effects in HL-LHC using frequency map analysis, 5th International Particle Accelerator Conference, Dresden, Germany, 15 - 20 Jun 2014, pp.1067.
- [69] E. Métral, Initial estimate of machine impedance, CERN-ACC-2014-0005 (2014).
- [70] E. Métral, Initial estimates of intensity limitations, CERN-ACC-2014-0074 (2014).
- [71] O. Brüning *et al.*, LHC luminosity and energy upgrade: A feasibility study, LHC Project Report 626 (2002).

- [72] F. Ruggiero and F. Zimmermann, Luminosity optimization near the beam-beam limit by increasing the bunch length or crossing angle, CERN-SL-2002-005-REV (AP) (2002).
- [73] F. Ruggiero and F. Zimmermann, Possible scenario for an LHC upgrade, Proc. HHH 2004 Workshop, Geneva, November 2004, CARE-Conf-05-002-HHH.
- [74] T. Linnekar and E. Shaposhnikova, An RF system for Landau damping in the LHC, LHC Project Note 394 (2007).
- [75] C. Bhat, Bunch shaping in the LHC: A quick look, CERN 97th LMC meeting, 22 June 2011.
- [76] T. Mertens *et al.*, Emittance growth, debunching and integrated luminosity in the LHC with a higher harmonic RF system, CERN-AT-Note-2011-071 PERF (2011).
- [77] D. Shatilov and M. Zobov, On the possibility of utilizing flat longitudinal beam profiles to increase the luminosity in collisions with large Piwinski angle, 14 April 2012, unpublished note.  
[https://espace.cern.ch/HiLumi/WP2/task4/Shared%20Documents/flat\\_long\\_en.docx](https://espace.cern.ch/HiLumi/WP2/task4/Shared%20Documents/flat_long_en.docx)
- [78] L. Ficcadenti *et al.*, Summary of the 800 MHz RF design, CERN meeting on High Harmonic RF System Review, 27 May 2013. <https://indico.cern.ch/event/254151/>
- [79] R. Tomas *et al.*, HL-LHC: Exploring alternative ideas, Review of LHC and Injector Upgrade Plans Workshop (RLIUP), Archamps, France, 29–31 October 2013.
- [80] J.M. Jowett *et al.*, Future heavy-ion performance of the LHC, Review of LHC and Injector Upgrade Plans Workshop (RLIUP), Archamps, France, 29–31 October 2013.
- [81] R. Calaga *et al.*, A proposal for a compact 200 MHz SC-RF system for the LHC.
- [82] C. Tambasco *et al.*, Beam-beam and octupoles stability diagrams in the betatron squeeze for HL-LHC optics, CERN Beam-Beam meeting, 21 August 2014, CERN-ACC-SLIDES-2014-0089.
- [83] S. Fartoukh, The sign of the LHC octupoles, CERN LMC meeting, 11 July 2012.  
[https://espace.cern.ch/lhc-machine-committee/Presentations/1/lmc\\_141/lmc\\_141h.pdf](https://espace.cern.ch/lhc-machine-committee/Presentations/1/lmc_141/lmc_141h.pdf)
- [84] W. Herr, Observations of beam-beam effects in the LHC in 2011, Chamonix 2012 Workshop on LHC Performance (2012).
- [85] Y. Luo and F. Schmidt, Dynamic aperture studies for LHC optics Version 6.2 at Collision, LHC Project Note 310 (2003).
- [86] A. Valishev *et al.*, Simulation of beam-beam effects and Tevatron experience, *JINST* **7** (2012) P12002.
- [87] J. Qiang *et al.*, A parallel particle-in-cell model for beam–beam interaction in high energy ring colliders, *J. Comp. Phys.* **198** (2004) 278.
- [88] T. Pieloni, Ph.D. thesis, EPFL, 2008.
- [89] W. Herr, X. Buffat, R. Calaga, R. Giachino, G. Papotti, T. Pieloni and D. Kaltchev, Long range beam-beam effects in the LHC, CERN-2014-004, pp. 87–92 (2014).
- [90] T. Pieloni, X. Buffat, D. Banfi, J. Barranco, G. Arduini, E. Mounet, N. Mounet, S.M. White and J. Qiang, Two beam effects, Proc. 5th EVIAN workshop, Evian, France, 2–4 June 2014. Eds. B. Goddard, S. Dubourg, CERN-ACC-2014-0319 (2014), pp. 69-79.
- [91] T. Pieloni, Levelling Scenarios: present and future perspectives, LARP-HiLumi Meeting INFN Frascati, Frascati, Italy, 14–16 November 2012. <https://indico.cern.ch/event/183635/session/10/contribution/100>
- [92] X. Buffat, D. Banfi, G.R. Coombs, W. Herr and T. Pieloni, Beam-Beam Effects in Different Luminosity Levelling Scenarios for the LHC, Proc. 5<sup>th</sup> International Particle Accelerator Conference, Dresden, Germany, 15 - 20 June 2014, Eds. C. Petit-Jean-Genaz, G. Arduini, P. Michel and V.R.W. Schaa, pp. 1061-1063.
- [93] D. Banfi, J. Barranco, T. Pieloni and A. Valishev, Weak-Strong Beam-Beam Simulations for the HL-LHC, Proc. 5<sup>th</sup> International Particle Accelerator Conference, Dresden, Germany, 15 - 20 June 2014, Eds. C. Petit-Jean-Genaz, G. Arduini, P. Michel and V.R.W. Schaa, pp. 3079-3081.



- [94] M. Giovannozzi, Dynamic Aperture: Simulations vs. Experiments and first DA results in the LHC, 14th HiLumi WP2 Task Leader Meeting, 27 August 2013.  
<https://indico.cern.ch/getFile.py/access?contribId=2&resId=0&materialId=slides&confId=267840>.
- [95] T. Pieloni *et al.*, Beam-beam effects and limitations in the HL-LHC, LARP-HiLUMI Collaboration Meeting, 7–9 May 2014, Brookhaven National Laboratory.
- [96] M. Giovannozzi *et al.*, Dynamic aperture performance for different collision optics scenarios for the LHC luminosity upgrade, Proc. 4<sup>th</sup> International Particle Accelerator Conference, Shanghai, China, 12 - 17 May 2013, Eds. Z. Dai, C. Petit-Jean-Genaz, V. Schaa, C. Zhang, pp. 2609-2611.
- [97] T. Pieloni *et al.*, Preliminary studies of beam-beam long-range effects: Orbit, tune, chromaticity for HL-LHC, 35th HiLumi WP2 Task Leader Meeting, 10 October 2014.
- [98] A. Valishev *et al.*, Preliminary estimates of beam-beam effects, HiLumi LHC Milestone Report, CERN-ACC-2014-0066 (2014).
- [99] K. Ohmi, Beam-beam effects under the influence of external noise, CERN-2014-004 (2014) pp. 69–74 (2014).
- [100] J. Qiang *et al.*, Strong-strong beam-beam simulation for LHC upgrade, Proc. 5<sup>th</sup> International Particle Accelerator Conference, Dresden, Germany, 15 - 20 June 2014, Eds. C. Petit-Jean-Genaz, G. Arduini, P. Michel and V.R.W. Schaa, pp. 1006-1009.
- [101] H. Damerau, LIU: Exploring Alternative Ideas, Review of LHC and Injector Upgrade Plans workshop (RLIUP), Archamps, France, 29–31 October 2013.
- [102] E. Métral *et al.*, Lessons learnt and mitigation measures for the CERN LHC equipment with RF fingers, Proc. 4<sup>th</sup> International Particle Accelerator Conference, Shanghai, China, 12 - 17 May 2013, Eds. Z. Dai, C. Petit-Jean-Genaz, V. Schaa, C. Zhang, pp. 1802-1804.
- [103] R. Veness *et al.*, Specification of new vacuum chambers for the LHC experimental interactions, Proc. 2<sup>nd</sup> International Particle Accelerator Conference, San Sebastian, Spain, 4 - 9 Sep 2011, Eds. C. Petit-Jean-Genaz, A. Blanco, I. Etxebarria, F. Perez, A. Wolski and V. Schaa, pp. 1584-1586.
- [104] B. Salvant *et al.*, RF Analysis of ALICE, LHCb and AFP, 10th CERN LEB Technical Meeting, 15 June 2012.
- [105] R. Wanzenberg and O. Zagorodnova, Calculation of wakefields and higher order modes for the new design of the vacuum chamber of the CMS experiment for the HL-LHC, CERN-ATS-Note-2013-018 TECH (2013).
- [106] B. Salvant *et al.*, Heat load from impedance on existing and new hardware in the LHC era, Joint HiLumi LHC-LARP Annual Meeting, Daresbury, UK, 11–15 November 2013.
- [107] B. Salvant *et al.*, Impedance of new ALICE beam pipe, CERN internal TREX meeting, 31 July 2014.
- [108] E. Métral and C. Zannini, Temperature effects on image current losses in the HL-LHC triplets – Part 2, 33<sup>rd</sup> HiLumi WP2 Task Leaders Meeting, CERN, 5 September 2014.  
<https://indico.cern.ch/event/323863/>
- [109] N. Mounet *et al.*, Impedance considerations for the design of the triplet/D1 beam screen, Technical Meeting on Vacuum for HL-LHC, CERN, 5 March 2014.
- [110] E. Métral *et al.*, Expected impedance and heat load of the present design of the HL- LHC BPMs, 28th HiLumi WP2 Task Leaders Meeting, CERN, 23 May 2014.
- [111] H. Day *et al.*, TCTP summary of power loss and heat load calculations (with attention paid to the heat load of the ferrite damping material), LHC collimation working group, 1 October 2012.
- [112] H. Day, Ph.D. thesis, Manchester University, 2013.
- [113] B. Salvant *et al.*, Impedance aspects of crab cavities, HiLumi-LHC/LARP Crab Cavity System External Review, BNL, USA, 5–6 May 2014.
- [114] M. Wendt, Wakefield analysis of the LHC BSRT mirror holder, CERN Internal Impedance Meeting, 9 September 2013.

- [115] G. Antchev *et al.*, Luminosity-independent measurements of total, elastic and inelastic cross sections at  $\sqrt{s}=7$  TeV, CERN-PH-EP-2012-353 (2012).
- [116] G. Antchev *et al.*, Luminosity-independent measurements of the proton–proton total cross section at  $\sqrt{s}=8$  TeV, CERN-PH-EP-2012-354 (2012).
- [117] G. Arduini *et al.*, PICS: What do we gain in beam performance, Review of LHC and Injector Upgrade Plans Workshop, Archamps, 29–31 October 2013.  
<https://indico.cern.ch/event/260492/session/3/contribution/16/material/slides/7.pdf>
- [118] R. Jacobsson, private communication (2014).
- [119] S. Fartoukh, Pile up management at the High Luminosity LHC and introduction to the crab-kissing concept, CERN-ACC-2014-0076 (2014).
- [120] O. Brüning *et al.*, HL-LHC: How to achieve upgrade scenario 1 goals in the LHC? Proc. Review of LHC and Injectors Upgrade Plans Workshop, Archamps, France, 2013.
- [121] J.M. Jowett, R. Alemany-Fernandez, R. Assmann, P. Baudrengnien, G. Bellodi, S. Hancock, M. Lamont, D. Manglunki, S. Redaelli, M. Sapinski, M. Schaumann, M. Solfaroli, R. Versteegen, J. Wenninger and D. Wollmann, Heavy ions in 2012 and the programme up to 2022, Proc. Chamonix 2012 Workshop on LHC Performance, CERN-2012-006 (2012).
- [122] C.A. Salgado, J. Alvarez-Muniz, F. Arleo, N. Armesto and M. Botje *et al.*, Proton–nucleus collisions at the LHC: Scientific opportunities and requirements, *J. Phys.* **G39** (2012) 015010.
- [123] J.M. Jowett, R. Alemany-Fernandez, P. Baudrengnien, D. Jacquet, M. Lamont, D. Manglunki, S. Redaelli, M. Sapinski, M. Schaumann, M. Solfaroli, Camillocci, R. Tomas, J. Uythoven, D. Valuch, R. Versteegen and J. Wenninger Proton nucleus collisions in the LHC, Proc. 4<sup>th</sup> International Particle Accelerator Conference, Shanghai, China, 12 - 17 May 2013, Eds. Z. Dai, C. Petit-Jean-Genaz, V. Schaa, C. Zhang, pp.49-51.
- [124] R. Bruce, D. Bocian, S. Gilardoni and J.M. Jowett, Beam losses from ultraperipheral nuclear collisions between  $^{208}\text{Pb}^{82+}$  ions in the large hadron collider and their alleviation, *Phys. Rev.ST Accel. Beams* **12** (2009) 071002.
- [125] M. Bodendorfer, Ions: Baseline, Studies Plan and Strategy for Pending Options, Proc. Chamonix 2014 Workshop on LHC Performance, Chamonix, France, 22–25 September 2014, Ed. M. Draper, CERN–2015–002, pp. 192-197.
- [126] M. Schaumann, Semi-empirical model for optimising future heavy-ion luminosity of the LHC, Proc. 5<sup>th</sup> International Particle Accelerator Conference, Dresden, Germany, 15 - 20 June 2014, Eds. C. Petit-Jean-Genaz, G. Arduini, P. Michel and V.R.W. Schaa, pp. 1033–1035.
- [127] J.M. Jowett, H.-H. Braun, M.I. Gresham, E. Mahner and A.N. Nicholson, *et al.*, Limits to the performance of the LHC with ion beams, Proc. 9<sup>th</sup> European Particle Accelerator Conference, Lucerne, Switzerland, 5 – 9 July 2004, Eds. J. Chrin, C. Petit-Jean-Genaz, J. Poole, C. Prior, H.-A. Sytal, pp. 578–580.
- [128] H.-H. Braun, R.W. Assmann, A. Ferrari, J.-B. Jeanneret, J.M. Jowett and I.A. Pshenichnov, Collimation of heavy ion beams in LHC, Proc. 9<sup>th</sup> European Particle Accelerator Conference, Lucerne, Switzerland, 5 – 9 July 2004, Eds. J. Chrin, C. Petit-Jean-Genaz, J. Poole, C. Prior, H.-A. Sytal, pp. 551–553.
- [129] H.-H. Braun, A. Fassò, A. Ferrari, J.M. Jowett, P.R. Sala and G.I. Smirnov, Hadronic and electromagnetic fragmentation of ultrarelativistic heavy ions at LHC, *Phys. Rev. ST Accel. Beams* **17** (2014) 021006.
- [130] O. S. Brüning, P. Collier, P. Lebrun, S. Myers, R. Ostojic, J. Poole and P. Proudlock (Eds.), LHC Design Report, v.1: The LHC Main Ring, CERN-2004-003-V-1 (2012) Chapter 21. “The LHC as a Lead Ion Collider”, Tables 21.1-21.3.
- [131] M. Schaumann *et al.*, Potential of stochastic cooling of heavy ions in the LHC, Proc. 5<sup>th</sup> International Particle Accelerator Conference, Dresden, Germany, 15 - 20 June 2014, Eds. C. Petit-Jean-Genaz, G. Arduini, P. Michel and V.R.W. Schaa, pp. 76–78.

# Chapter 3

## Insertion Magnets

*G. Ambrosio<sup>1</sup>, M. Anerella<sup>2</sup>, R. Bossert<sup>1</sup>, D. Cheng<sup>3</sup>, G. Chlachidze<sup>1</sup>, D. Dietderich<sup>3</sup>, D Duarte Ramos<sup>4</sup>, P. Fabbri<sup>5</sup>, S. Farinon<sup>5</sup>, H. Felice<sup>3</sup>, P. Ferracin<sup>4</sup>, P. Fessia<sup>4</sup>, J. Garcia Matos<sup>6</sup>, A. Ghosh<sup>2</sup>, P. Hagen<sup>4</sup>, S. Izquierdo Bermudez<sup>4</sup>, M. Juchno<sup>4</sup>, S. Krave<sup>1</sup>, M. Marchevsky<sup>3</sup>, T., Nakamoto<sup>7</sup>, T. Ogitsu<sup>7</sup>, J.C. Perez<sup>4</sup>, H. Prin<sup>4</sup>, J.M. Rifflet<sup>8</sup>, G.L. Sabbi<sup>3</sup>, K. Sasaki<sup>7</sup>, J. Schmalzle<sup>2</sup>, M. Segreti<sup>8</sup>, M. Sugano<sup>7</sup>, E. Todesco<sup>4\*</sup>, F. Toral<sup>6</sup>, G. Volpini<sup>9</sup>, P. Wanderer<sup>2</sup>, X. Wang<sup>3</sup>, R.V. Weelderen<sup>4</sup>, Q. Xu<sup>7</sup> and M. Yu<sup>1</sup>*

<sup>1</sup>FNAL, Fermi National Accelerator Laboratory, Batavia, USA

<sup>2</sup>BNL, Brookhaven National Laboratory, Upton, USA

<sup>3</sup>LBNL, Lawrence Berkeley National Laboratory, Berkeley, USA

<sup>4</sup>CERN, Accelerator & Technology Sector, Geneva, Switzerland

<sup>5</sup>INFN, Sezione di Genova, Genova, Italy

<sup>6</sup>CIEMAT, Madrid, Spain

<sup>7</sup>KEK, Tsukuba, Japan

<sup>8</sup>CEA/SACLAY, DSM/Irfu/SACM, Gif-sur-Yvette, France

<sup>9</sup>INFN-LASA, Milan, Italy

### 3 Insertion magnets

#### 3.1 Overview

The layout of the HL-LHC insertion magnets is shown in Figure 3-1 and compared to those of the LHC in Figure 3-2. The main technical choices can be summarized as follows [1, 2].

- Maintain the distance from the first magnet to the collision point at ~23 m. This allows preservation of the most critical interfaces with the detectors.
- Increase the triplet coil aperture from 70 mm to 150 mm to allow a smaller  $\beta^*$ . Nb<sub>3</sub>Sn technology has been selected for the quadrupoles [3], allowing an increase in the aperture while keeping the magnet length at acceptable values. The choice of a large coil width (about 36 mm, arranged in two layers of 18 mm wide cable) aims at reaching maximum performance in terms of gradient [1, 4]. At the same time, the operational current is set at 80% of the load line, which is a good compromise between risk and performance [5, 6]. In these conditions, Nb<sub>3</sub>Sn can generate an operational field of 140 T/m [7], corresponding to a triplet length of ~35 m, compared to ~25 m in the LHC with an operational gradient of 200 T/m.
- To recover the 10 m of additional space allocated to the triplet, and gain further space for inserting the crab cavities (see Chapters 2 and 4), three steps are taken.
  - o Increase the strength of the separation/recombination dipoles from 26 T·m to 35 T·m, thus reducing the D1–D2 distance to 70 m and recovering 15 m.
  - o Replacing the 20 m long normal conducting magnet D1 operating at 1.28 T with a superconducting 6.27 m long magnet, operating at 5.5 T [8], thus recovering ~14 m.
  - o The power feed for the triplet and D1 is not made through a module placed between D1 and the triplet as in the LHC (indicated by DFB in Figure 3-2), but through a service module on the D2 side

---

\* Corresponding author: [Ezio.Todesco@cern.ch](mailto:Ezio.Todesco@cern.ch)

of D1 (not shown in Figure 3-1). This allows the shifting of D2 towards the IP by a few metres, at the price of having the power feeding the triplet and corrector magnets through D1.

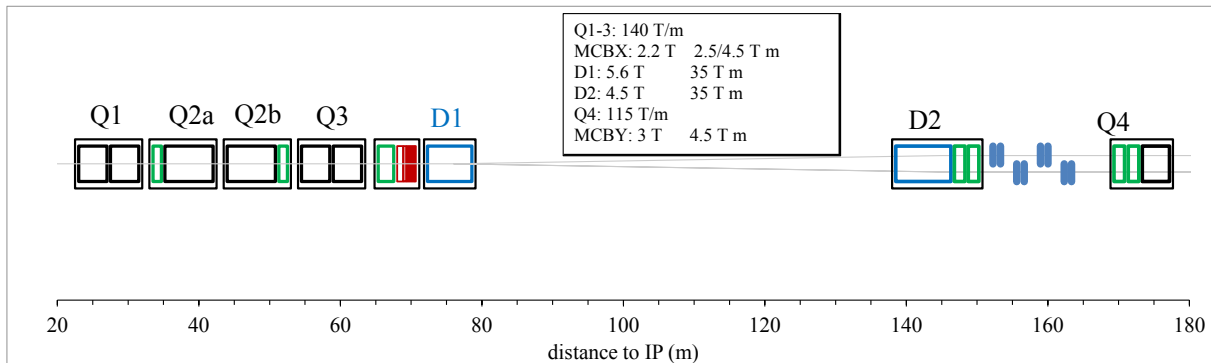


Figure 3-1: Conceptual layout of the IR region of HL-LHC. Thick boxes are magnets, thin boxes are cryostats.

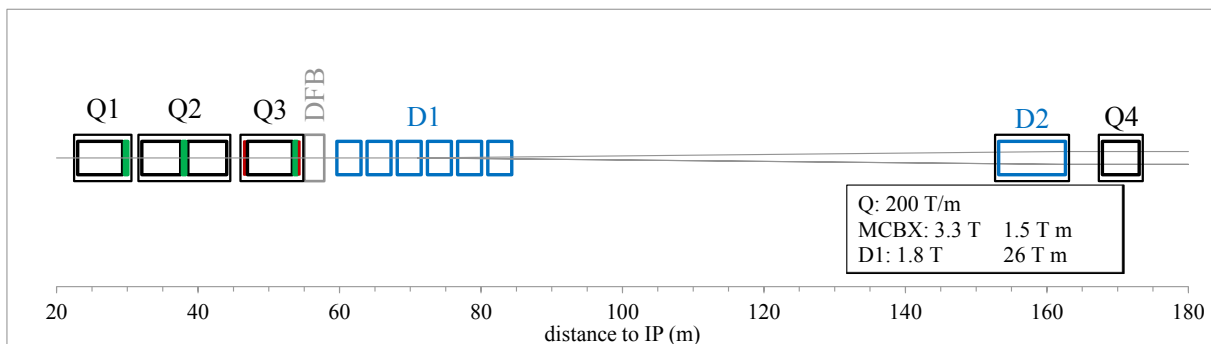


Figure 3-2: Schematic layout of the current IR region of the LHC. Thick boxes are magnets, thin boxes are cryostats.

- Q4 is also shifted by  $\sim 5$  m away from the interaction point (IP)
- The apertures of the magnets between the triplet and the dispersion suppressor have to be increased: D1 from 60 mm to 150 mm, D2 from 80 mm to 105 mm, Q4 from 70 mm to 90 mm, and Q5 from 56 mm to 70 mm. For all these magnets, Nb-Ti technology has been chosen [1, 2], since the potential performance improvement given by Nb<sub>3</sub>Sn is not sufficient to justify the additional cost and complexity. Since the size of the magnet is limited by the cryostat, and the aperture is enlarged, for D1, D2, and Q4 we selected a small coil width (15 mm) to have enough space for an appropriate iron yoke. We opted to reuse the LHC cable in a single-layer configuration to reduce the risks (the cable properties are well known), to ease the schedule (lengths are already available), and simplify protection (quench heaters can be replaced by a dump resistor), at the price of a larger operational current.
- All magnets operate at 1.9 K to have the maximum superconductor performance. This is an important change with respect to the LHC, where the D2, Q4, Q5, and Q6 operational temperature is 4.5 K.
- Three orbit correctors are required in the triplet. The strength is increased from 1.5 T·m (LHC value) to 2.5 T·m for the correctors close to Q2a/b, and to 4.5 T·m for the corrector close to Q3. The position is the same as in the LHC layout, with the exception of the corrector between Q2a and Q2b, which is moved to between Q2b and Q3.
- A skew quadrupole is used to correct the triplet tilt, as in the LHC. Non-linear correctors of the order 3, 4, 5, and 6 are required, both normal and skew. With respect to the LHC layout, normal and skew decapole correctors and a skew dodecapole corrector are added. Experience with LHC operation and field quality of the triplet short models will confirm whether these correctors are needed.

- With a nominal luminosity five times larger than the nominal design goal of the LHC, a newly designed absorber, using thick tungsten (W) shielding attached to the outer surface of the beam screen (Figure 3-3) is foreseen to reduce the effect of collision debris. The tungsten shielding will limit the radiation damage over the HL-LHC accumulated luminosity of  $3000 \text{ fb}^{-1}$  to a maximum of 30 MGy and the peak energy deposition to a maximum of  $4 \text{ mW/cm}^3$  [9]. These values are similar to the expected heat load and radiation doses for the nominal LHC [10]. The cryogenic system from the triplet to D1 has to absorb 1.2 kW steady-state at a nominal luminosity of  $5 \times 10^{34} \text{ cm}^{-2} \text{ s}^{-1}$ . Half of this is intercepted by the cold mass at 1.9 K and half by the beam screen, where heat is removed at 40–60 K. Note that the system has to be able to remove a 50% larger load, corresponding to the ultimate peak luminosity of  $7.5 \times 10^{34} \text{ cm}^{-2} \text{ s}^{-1}$ .

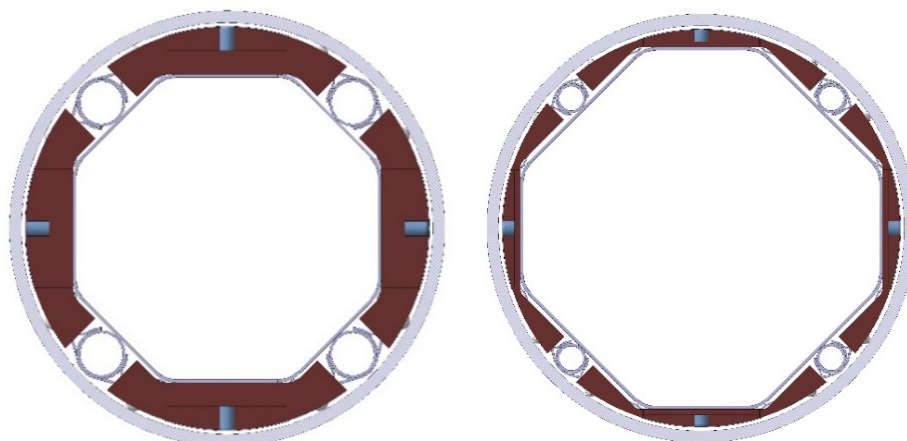


Figure 3-3: Beam screen (grey) with tungsten shielding (dark brown) and cooling tubes in Q1 (lefthand side) and in Q2-D1 (righthand side).

The main parameters of the magnets are listed in Table 3-1.

Table 3-1: Overview of the main parameters of the insertion magnets – see the text for definitions of footnotes

	Units	Triplet Q1/Q3 MQXFA	Triplet Q2a/b MQXFB	Short orbit corrector MCBXFB	Long orbit corrector MCBXFA	Separation dipole D1 MBXF	Recomb. Dipole D2 MBRD	Orbit corrector MCBR D	Large ap. 2-in-1 Q4 MQYY
Aperture <sup>1</sup>	[mm]	150	150	150	150	150	105	100	90
Field	[T]			2.10	2.10	5.58	4.50	3.00	
Gradient	[T/m]	140	140						115
Magnetic length <sup>2</sup>	[m]	4.00	6.80	1.20	2.20	6.27	7.78	1.5	3.83
Int field	[T m]			2.5	4.5	35.0	35.0	4.5	
Int gradient	[T]	560	952						440
Number of apertures		1	1	1	1	1	2	2	2
Distance between apertures <sup>1</sup>	[mm]						188	188	194
Number of circuits		4	4	16	8	4	4	32	8
Units needed		16	8	8	4	4	4	16	4
Spares		4	2	2	2	2	2	2	2
<b>Cable data</b>									
Material		Nb <sub>3</sub> Sn	Nb <sub>3</sub> Sn	Nb-Ti	Nb-Ti	Nb-Ti	Nb-Ti	Nb-Ti	Nb-Ti
Cable thick. in. <sup>3</sup>	[mm]	1.438	1.438	0.819	0.819	1.362	1.362	0.819	1.362
Cable thick. ou. <sup>3</sup>	[mm]	1.612	1.612	0.871	0.871	1.598	1.598	0.871	1.598
Cable width <sup>3</sup>	[mm]	18.15	18.15	4.37	4.37	15.10	15.10	4.37	15.10
Ins. thick radial <sup>4</sup>	[mm]	0.150	0.150	0.105	0.105	0.155	0.150	0.105	0.160
Ins. thick azimuth. <sup>4</sup>	[mm]	0.150	0.150	0.105	0.105	0.135	0.130	0.105	0.145
No. strands		40	40	18	18	36	36	18	36
Strand diameter <sup>3</sup>	[mm]	0.850	0.850	0.480	0.480	0.825	0.825	0.480	0.480
Cu/NonCu		1.20	1.20	1.75	1.75	1.95	1.95	1.75	1.75
Filling factor <sup>5</sup>		0.31	0.31	0.25	0.25	0.24	0.24	0.25	0.25

Coil design									
N. layers		2	2	1+1	1+1	1	1	1	1
N. turns/pole		50	50	74/88	74/88	44	31	52	14
Cable length/pole	[m]	430	710	220/240	380/430	600	500	310	110
	Units	Triplet Q1/Q3 MQXFA	Triplet Q2a/b MQXFB	Short orbit corrector MCBXFB	Long orbit corrector MCBXFA	Separation dipole D1 MBXF	Recomb. Dipole D2 MBRD	Orbit corrector MCBR D	Large ap. 2-in-1 Q4 MQYY
Operational parameters									
Peak field <sup>6</sup>	[T]	12.1	12.1	4.3	4.3	6.6	5.1	3.8	6.0
Temperature	[K]	1.9	1.9	1.9	1.9	1.9	1.9	1.9	1.9
Current	[kA]	17.46	17.46	2.42/2.14	2.42/2.14	11.80	12.00	3.20	15.65
j overall <sup>7</sup>	[A/mm <sup>2</sup> ]	486	486	331/290	331/290	438	448	662	573
Loadline fraction <sup>8</sup>	[adim]	0.80	0.80	0.60	0.60	0.75	0.65	0.5	0.80
Temperature margin	[K]	4.2	4.2	3.5	3.5	2.5	3.0		2.0
Stored energy/m	[MJ/m]	1.32	1.32	0.100	0.100	0.342	0.284	0.174	0.190
Inductance/m	[mH/m]	8.22	8.22	15.2 / 24.2	15.2 / 24.2	4.01	3.51		0.77
Stored energy <sup>9</sup>	[MJ]	5.28	8.98	0.122	0.223	2.15	2.21		0.73
Mechanical structure									
Forces x	[MN/m]	2.47	2.47	0.322	0.322	1.53	0.64		0.33
Forces y	[MN/m]	-3.91	-3.91	0.402	0.402	-0.64	-0.40		-0.47
F <sub>mag</sub> stress <sup>10</sup>	[MPa]	130	130	135	135	100	50		35
Protection									
Circuit inductance <sup>11</sup>	[mH]	132	112	18.3/29.1	33.5/53.2	25	27		2.9
Coil energy density <sup>12</sup>	[J/mm <sup>3</sup> ]	0.092	0.092	0.026/0.03	0.026/0.03	0.072	0.043		0.062
Dump resistor <sup>13</sup>	[mW]	50	50	300	300	70	70	250	50
Heater circuits <sup>14</sup>		12	12	0	0	4 or 0	4 or 0	0	0
Dose and heat load given by collision debris									
Coil peak power <sup>15</sup>	[mW/cm <sup>3</sup> ]	1.1/2.5	2.0/2.5	1.1/2.5	1.1	1.3	1.8	0.6	0.3
Heat load cold mass <sup>16</sup>	[W]	110/160	105/130		70	100	50	10	6
Heat load beam screen <sup>16</sup>	[W]	150/60	50/70		45	50	<5	<1	<1
Peak dose <sup>17</sup>	[MGy]	11/33	22/32	28	44	15	36	20	8

<sup>1</sup>Aperture is the coil inner diameter at room temperature, excluding ground insulation, cold bore, and beam screen; distance between apertures is given at 1.9 K.

<sup>2</sup>Magnetic length is given at 1.9 K.

<sup>3</sup>Strand/cable dimensions are given at room temperature, in the case of Nb<sub>3</sub>Sn before reaction.

<sup>4</sup>Insulation dimensions are given at room temperature.

<sup>5</sup>Filling factor is defined as the fraction of superconductor in the insulated cable.

<sup>6</sup>Peak field in the coil is given including the contribution of the strand where the peak is located (what is usually called self-field correction).

<sup>7</sup>Overall current density is the average over the whole cross-section of the insulated cable at 1.9 K (i.e. including voids or impregnation and insulation, but not copper wedges).

<sup>8</sup>Load line fraction is the ratio between the operational current and the short sample current on the load line.

<sup>9</sup>Stored energy is given for the whole magnet: in the case of independently powered apertures or nested magnets, stored energy is given for both circuits powered with maximum nominal current.

<sup>10</sup>Stress is an estimate given by the accumulation of the azimuthal Lorentz forces at nominal current divided by the coil radial width – the impact of the structure, preload, and bending is not considered.

<sup>11</sup>Circuit inductance is the differential inductance of the circuit at maximum nominal current.

<sup>12</sup>Energy density is given over the coil volume at 1.9 K, including insulation but not coil parts such as copper wedges and pole pieces.

<sup>13</sup>Dump resistor is estimated using a maximum voltage target of ~750 V.

<sup>14</sup>The number of heater circuits is the number of independent circuits for each magnet.

<sup>15</sup>Peak power is the maximum deposited power in the coil for a nominal luminosity of  $5 \times 10^{34} \text{ cm}^{-2} \text{ s}^{-1}$  (details on the binning and simulations are given in Chapter 10).

<sup>16</sup>Heat load is given for nominal luminosity  $5 \times 10^{34} \text{ cm}^{-2} \text{ s}^{-1}$ , separated between cold mass (this portion is absorbed at 1.9 K) and beam screen (where it is absorbed at 40–60 K); values for the short orbit correctors and for Q2a and Q2b are given together, in the Q2a Q2b column; the load on the interconnections is given in the text. For ultimate performance these values are 50% large.

<sup>17</sup>Peak dose is the same as the maximum dose in the magnet (for details of binning and simulations see Chapter 10).

### 3.2 Triplet

**Function and operational modes:** The triplet ramps with the energy of the LHC, with a nominal gradient of 9 T/m at 450 GeV, and 140 T/m at 7 TeV. During squeeze, its gradient is constant or decreases by not more than 10%. Q1 and Q3 will be operated in series, as will Q2a and Q2b. A 2 kA powering trim is acting on Q3: this is needed for special beam measurements requiring different power between Q1 and Q3. The quadrupoles of the triplet are developed by LARP and CERN.

**Cable:** A Nb<sub>3</sub>Sn cable based on 40 strands, with 0.85 mm diameter, has been chosen [7]. The main specifications are (i) the minimum non-copper critical current density of 1400 A/mm<sup>2</sup> at 15 T and 4.2 K, (ii) a strand RRR larger than 150, and (iii) a Cu/no Cu ratio of 1.2 (54.5% of copper in the strand). The cable has a S2 glass braided insulation, whose thickness is 150 μm at 5 MPa before reaction. The cable contains a 12-mm-wide, 25-μm-thick stainless steel core to control and reduce the dynamic effects.

**Coil, current density, and margin:** With two layers one can reach the operational gradient of 140 T/m at 0.80 of the short sample limit on the load line (i.e. 20% of load line margin). Each layer has a copper wedge to tune field quality.

**Lengths and transverse size:** The triplet is made of Q1 and Q3, each unit requiring magnetic length of 8 m; plus two units Q2a and Q2b, each one with a 6.8 m long magnetic length. The LARP collaboration, in charge of Q1 and Q3 construction, has proposed splitting both Q1 and Q3 into two parts, each resulting in 4 m long magnets separated by 0.5 m. The Q1, Q2, and Q3 cross-sections are identical, and make use of the same design, technologies, and components. The magnet cross-section has a 630 mm diameter, i.e. 60 mm more than the LHC dipoles, including the stainless steel vessel.

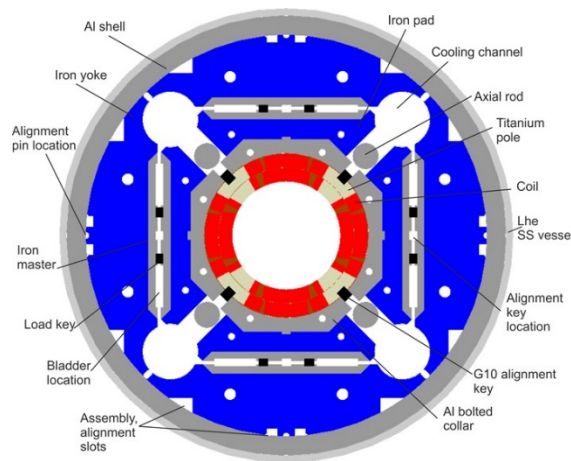


Figure 3-4: Sketch of triplet quadrupole magnet cross-section

**Mechanical structure:** The quadrupole makes use of a shell-based structure developed at LBNL and within the LARP collaboration [11]. The structure, scaled up to a length of 3.4 m, was demonstrated in the LARP LR and LQ quadrupole models [12], and features to assure alignment in operational conditions have been included in the 120 mm aperture quadrupole HQ [13]. The QXF cross-section is a scaling up of the HQ design. Coils are mainly prestressed by the Al shell during cool-down, acting as the structure to contain the Lorentz forces during powering up. The level of stress is fine-tuned during the loading of the coil, which is done at room temperature using water-pressurized bladders and interference keys. Typically one has ~70 MPa of azimuthal coil compression at room temperature, which becomes ~150 MPa at 1.9 K thanks to the interplay of the thermal contractions of the different components. The structure keeps the coil under compression up to the ultimate current, corresponding to 150 T/m (7% above nominal).

**Protection:** The energy density in the coil is ~0.1 mJ/mm<sup>3</sup>, about twice that of the Nb-Ti LHC magnets [14]. This makes quench protection particularly challenging. Since the circuit inductance is of the order of 100 mH, only a small fraction of the energy can be extracted on a dump resistor. Therefore we have to rely on

quench heaters on the outer layer of the coil, i.e. 25  $\mu\text{m}$  stainless steel strips with a 50  $\mu\text{m}$  polyamide layer to ensure proper insulation. The heaters will have heating stations of 40 mm length, separated by 120 mm sections with lower resistance due to a 10  $\mu\text{m}$  copper cladding (see Figure 3-5(a)). Since the width of the heating stations is 20 mm, two independently powered strips will cover the two blocks of the outer layer; a 6.8 m long magnet will have  $\sim 40$  heating stations. The typical time needed to quench the coil is of the order of 15–20 ms following heater firing [15]. Assuming 5 ms for detection time, a validation window of 10 ms and a few ms for switch opening, this brings the hotspot temperature to  $\sim 350$  K [16]. To reduce this value and to ensure some redundancy, we plan to also have heaters on the inner layer, and/or use the CLIQ system [17], recently developed at CERN, based on coil heating induced by fast current discharge in the magnet. For the inner layer, heating stations are also needed, with a more complex geometry since  $\sim 50\%$  of the surface must be left free for heat removal. A single strip slaloms between the two blocks, with 25 mm long heating stations and 40 mm long cladding (see Figure 3-5(b)). The CLIQ system has the interesting feature of acting rapidly on the inner layer, and is therefore complementary to the outer layer quench heaters. It requires an additional lead to bring the current between coil poles: the viability of this protection system in the case of more complex circuits (two magnets in series, with an additional trim) is to be carefully studied.

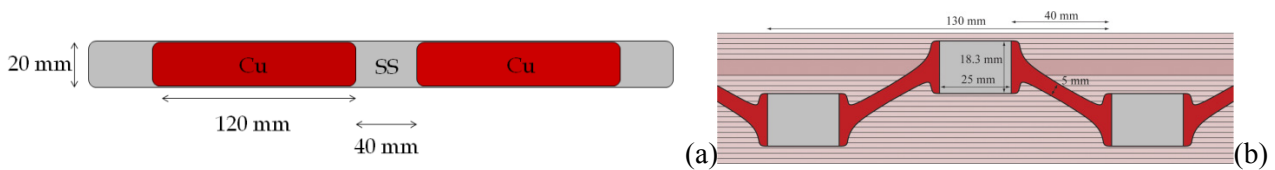


Figure 3-5: (a) Quench heaters for the outer layer; (b) a design for the inner layer. Stainless steel (SS) in grey and copper cladding in red.

**Field quality:** Allowed field harmonics ( $b_6$ ,  $b_{10}$ ) are optimized at high field, and will be below one unit in absolute value. Contributions from the coil ends have to be taken into account and optimized and/or compensated through the straight part [18]. Fine tuning of  $b_6$  can be done in the short model phase through small changes to the coil cross-section. Random components are estimated for a 25  $\mu\text{m}$  random error in the block positioning for non-allowed, and 100  $\mu\text{m}$  for allowed (see Table 3-2); most critical components are low-order harmonics ( $b_3$ ,  $a_3$ ,  $b_4$ ,  $a_4$ ). To minimize these components we opted for a strategy similar to that used in the RHIC magnets [19], with magnetic shims to be inserted in the bladder location [20]. This allows correcting (i)  $\pm 5$  units of  $b_3$ ; (ii)  $\pm 5$  units of  $a_3$ ; (iii)  $\pm 3$  units of  $b_4$ ; (iv)  $\pm 1$  units of  $a_4$ , for a maximum of two harmonics at the same time, through an asymmetric magnetic shimming.

Table 3-2: Expected systematic harmonics and random components in the triplet

Expected systematic harmonics					
	Geometric	Saturation	Persistent	Injection	High field
$b_6$	4.20	-3.80	-20.00	-15.80	0.40
$b_{10}$	-0.37	-0.02	4.00	3.63	-0.39
$b_{14}$	-0.60	-0.07	0.00	-0.60	-0.67

Random components		
Order	Normal	Skew
3	0.82	0.80
4	0.57	0.65
5	0.42	0.43
6	1.10	0.31
7	0.19	0.19
8	0.13	0.11
9	0.07	0.08

**Cooling:** The magnet is in a static bath of pressurized HeII, with a welded stainless-steel shell placed outside the Al structure acting as a helium vessel. Cooling is ensured via two heat exchangers of 68 mm inner diameter, in which saturated HeII circulates, housed in the 77 mm diameter holes of the iron located in the upper part, see Figure 3-4 [21]. This circuit cools the triplet and the short orbit correctors, with the separation dipole and corrector package on a different circuit (see Section 3.11 for more details). With this design, one can comfortably remove  $\sim 800$  W, and ultimately  $\sim 1000$  W, of heat load on the triplet, i.e. 500 W on the cold mass given by debris (see Table 3-1), plus a 100 W budget for other loads (among them the 25 W load on interconnections), with a 50% margin. For the Nb-Ti coils in the LHC, the peak heat deposition target was set



at  $4 \text{ mW/cm}^3$ ; this has a factor of 3 safety on  $12 \text{ mW/cm}^3$ , which was considered to be the hard limit. Later experience showed that the hard limit is a factor of two larger. In the HL-LHC, thanks to the tungsten shielding, we are always below the  $4 \text{ mW/cm}^3$  target. Considering that the  $\text{Nb}_3\text{Sn}$  superconductor is expected to have a three times larger margin, peak power in the HL-LHC will not be critical.

The heat loads from the coils and the beam-pipe area can only be evacuated to the two heat exchangers by means of pressurized HeII. To this end the cold mass design incorporates the required helium passages: 1.5 mm annular spacing between cold bore and inner coil-block, and free passage through the coil pole and subsequent G10 alignment key. The free passage needed through the coil pole and G10 alignment key in the transverse direction is estimated to be at least 4% (equivalent to 8 mm diameter holes repeated every 40 mm).

**Cryostat:** Independent cryostats are used for Q1, Q2a, Q2b, and Q3. The Q1 and Q3 cryostats contain two 4 m long magnets. The Q2a and Q2b cryostats contain the 6.8 m long magnet plus the orbit correctors described below. The cryostat size should be able to accommodate the cold mass, the shielding, and the cooling pipes. First estimates show that the standard size of 980 mm (including flanges) is a very tight fit for all of these components. Two options are being considered [22]: a 1050 mm diameter cryostat, and an elliptical cryostat (see Figure 3-6).

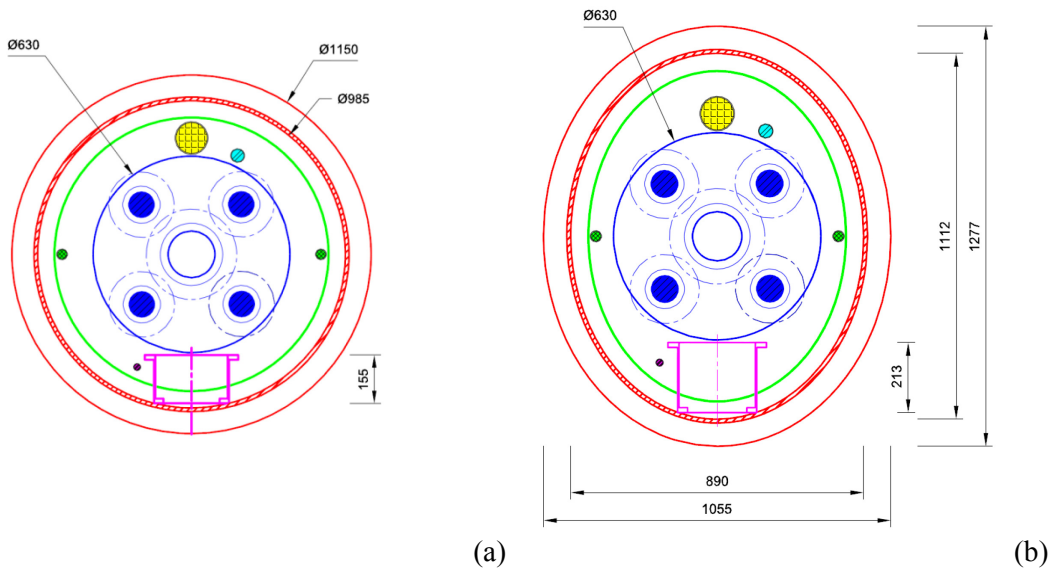


Figure 3-6: Possible cross-sections of the cryostat: (a) larger diameter and (b) elliptical solution

### 3.3 Orbit correctors

**Function and operational modes:** The orbit correctors are single-aperture magnets. Two versions are required, providing  $2.5 \text{ T}\cdot\text{m}$  and  $4.5 \text{ T}\cdot\text{m}$  integrated fields. To have a more compact layout, a nested design has been adopted, with the horizontal and vertical dipole coil in the same cross-section (see Figure 3-7). The field in each plane has been limited to 2.1 T, giving a maximum combined field of 3 T. Powering will be allowed in a square in the horizontal/vertical plane, with both positive and negative currents. These magnets are used to create the crossing angle and partially to correct quadrupole misalignment. Orbit correctors are being developed by CIEMAT [23].

**Cable:** The 4.5 mm wide Nb-Ti cable developed for the S-LHC corrector [24] has been adopted. This is based on a 0.48 mm diameter strand, arranged in a Rutherford cable with 18 strands.

**Coil, current density and margin:** With one layer per dipole direction, it can reach the operational field of 2.1 T simultaneously in both planes at 60% of the load line.

**Lengths and transverse size:** The magnetic length is 1.2 m for the short version (MCBXB) and 2.2 m for the long one (MCBXA). The magnet cross-section has a 570 mm diameter, including the stainless steel vessel, i.e. as in the LHC dipoles and D1. Cooling channels are shared with the quadrupoles for MCBXB, so the iron has 77 mm diameter holes at 45°. MCBXA will share cooling channels with D1, thus the iron has 60 mm diameter holes as in D1 (i.e. at 90° and 270°).

**Mechanical structure:** The magnet makes use of an iron shell support and collars. An aluminium shell is used to increase the rigidity of the assembly, applying a pre-stress through the iron that will increase during cool-down. Approximately 20 mm thick collars are used for keeping the inner coil, and the same for the outer coil. Due to the nested option, a complex collaring based on two steps (first the inner, then the outer) is needed. The inner collars are closed with two round pins; the outer ones will be kept in place by four prismatic keys. A difficulty is that when both horizontal and vertical coils are powered, Lorentz forces push the inner coil towards the centre of the aperture: this requires a structure between the inner coil and the cold bore to prevent movement. A titanium tube has been proposed as a solution, given that its contraction coefficient is lower than those of the other materials. All of these issues are being addressed at the time of writing.

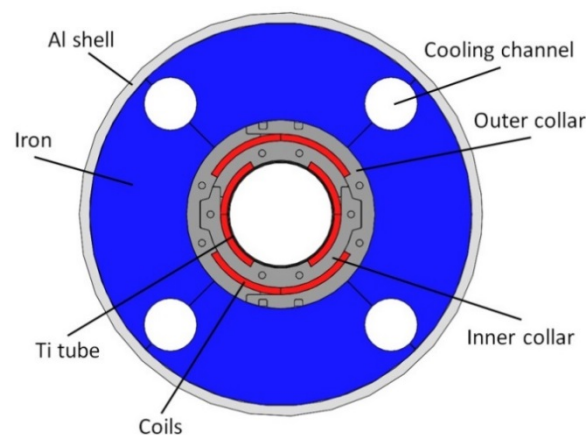


Figure 3-7: Sketch of orbit corrector cross-section (short version MCBXB, in the cold mass of the triplet magnets Q2a and Q2b).

### 3.4 High-order correctors

**Function, design and operational modes:** The high-order correctors (skew quadrupole, normal and skew sextupole, octupole, decapole, and dodecapole) are specified on the expected field quality and alignment errors (see Chapter 2), with a safety factor of 2 on the quadrupole, sextupole, and octupole, and 1.5 on the decapole and dodecapole. The magnets will operate with settings based on the measured field errors of the triplet and separation dipole. To ease operation a non-nested layout (see Figure 3-8) has been adopted, with a superferic technology, already developed for the S-LHC [25]. Nb-Ti racetrack coils provide the ampere-turns, with iron giving the required field shape. The aperture is 150 mm, as for the triplet and D1 (see Figure 3-9). The high-order correctors are being developed by INFN-Milano.

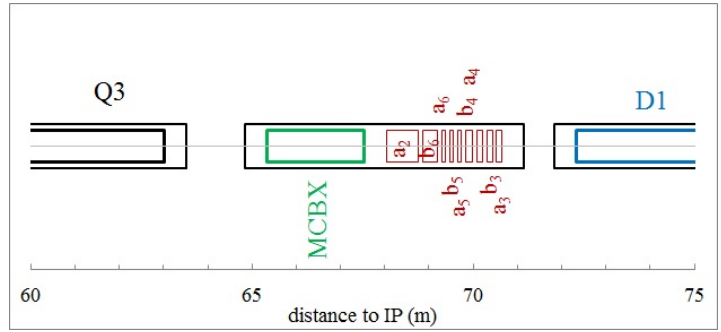


Figure 3-8: Layout of the corrector region

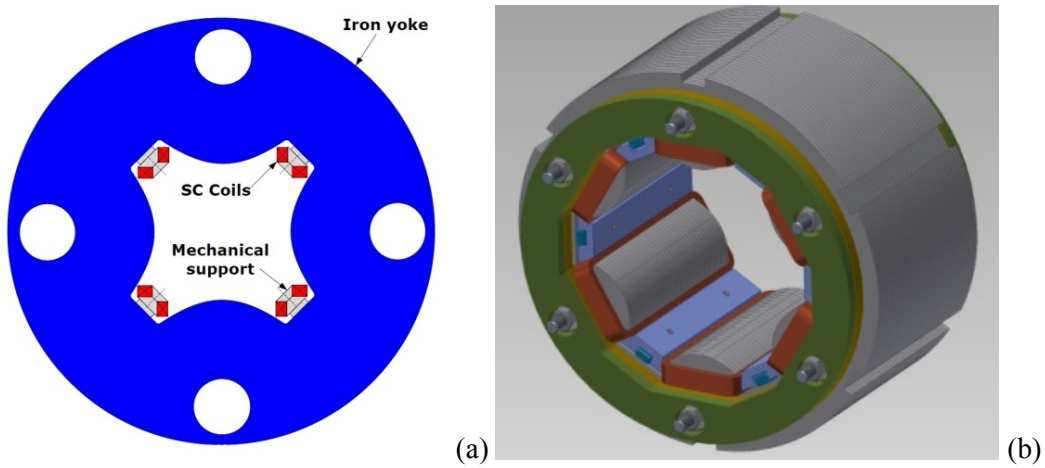


Figure 3-9: (a) Cross-section of the skew quadrupole; (b) 3D view of a sextupole

Cable: the cable is a single Nb-Ti strand, of 0.7 mm diameter for the quadrupole and of 0.5 mm diameter for the higher orders. Insulation is made with a 0.07 mm thick S2 glass. Further ground insulation is added on the external side of the coil.

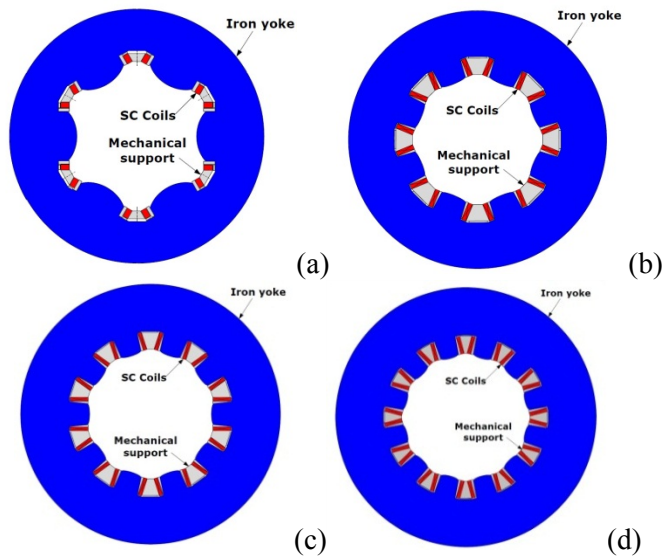


Figure 3-10: Sketch of nonlinear corrector cross-sections of (a) normal sextupole; (b) octupole; (c) decapole; (d) dodecapole correctors.

**Coil, current density, and margin:** We chose to operate at 40% on the load line. The optimization [26] provides a current density of the order of 300 A/mm<sup>2</sup>, with peak fields on the coil in the range 2.0–2.3 T for the nonlinear correctors and 3.0 T for the skew quadrupole (see Table 3-3). Coils are impregnated with CTD-101.

**Lengths and transverse size:** The magnet coil lengths are ~0.1 m for the sextupole, octupole, decapole, and skew dodecapole (see Table 3-3). The normal dodecapole and the skew sextupole require greater strengths, giving a coil length of ~0.45 m and ~0.84 m, respectively. The skew quadrupole needs a 460 mm diameter iron yoke that has to include the cooling holes for the D1 heat exchanger and orbit corrector. The nonlinear correctors can have an iron yoke diameter of 320 mm, which fits inside the cooling holes. Spacers are required to match the transverse size of the correctors to the same value of the MCBXA orbit correctors, and to maintain alignment within the cold mass. Heat exchangers will go through these spacers to cool the whole cold mass.

**Mechanical structure:** the mechanical support for the correctors coils are under study. The forces are of the order of 60 kN/m for the quadrupole and 10–30 kN/m for the other magnets.

The main parameters of the correctors are given in Table 3-3.

Table 3-3: Overview of the main parameters of the triplet corrector magnets

	Units	MCQSX	MCSX/MCSSX	MCOX/MCOSX	MCDX/MCDSX	MCTX	MCTSX
Order		2	3	4	5	6	6
Aperture	[mm]	150	150	150	150	150	150
Integrated strength <sup>1</sup>	[T m]	1	0.06	0.04	0.03	0.086	0.017
Coil length <sup>2</sup>	[mm]	841	123	99	107	449	102
Gradient	[T/m <sup>n-1</sup> ]	25	11	3690	50600	640000	613000
Number of apertures		1	1	1	1	1	1
Number of circuits		1	2	2	2	1	1
Units needed		4	8	8	8	4	4
Spares		2	2	2	2	2	2
<b>Cable data</b>							
Strand diameter	[mm]	0.700	0.500	0.500	0.500	0.500	0.500
Insulation thickness	[mm]	0.070	0.070	0.070	0.070	0.070	0.070
Cu/No_Cu		2.3	2.3	2.3	2.3	2.3	2.3
<b>Coil design</b>							
Material		Nb-Ti	Nb-Ti	Nb-Ti	Nb-Ti	Nb-Ti	Nb-Ti
N. turns/pole		320	214	344	256	154	172
Cable length/pole	[m]	604	79	88	67	144	42
<b>Operational parameters</b>							
Coil peak field	[T]	2.97	2.33	2.41	2.34	2.04	2.01
Temperature	[K]	1.9	1.9	1.9	1.9	1.9	1.9
Current	[A]	182	132	120	139	167	157
j overall <sup>3</sup>	[A/mm <sup>2</sup> ]	303	353	314	360	259	284
Loadline fraction		0.40	0.40	0.40	0.40	0.40	0.40
Differential inductance	[mH]	1247	118	152	107	229	52
Stored energy	[kJ]	24.6	1.24	1.41	1.39	4.35	0.92
<b>Dose and heat load</b>							
Heat load cold mass	[W]	70					
Heat load beam screen	[W]	45					
Peak dose	[MGy]	44					

<sup>1</sup>Integrated strength is defined as the field at the 50 mm reference radius times the magnetic length.

<sup>2</sup>Coil length refers to the physical coil length, and not to magnetic length.

<sup>3</sup>The overall current density includes 0.07 mm thick strand insulation and the coil ground insulation.

### 3.5 Separation dipole D1

**Function and operational modes:** The separation dipole is ramped with the energy of the LHC, and is constant during squeeze. Each magnet is independently powered. The separation dipole is being developed by KEK.

**Cable:** The 15 mm wide Nb-Ti cable used for the outer layer of the main LHC dipole is adopted (see Figure 3-10). The required unit length is smaller than the main LHC dipole outer cable unit length (780 m).

**Coil, current density and margin:** For the initial choice of 70% operational level, the magnet length was slightly longer than the KEK test station [8, 27]. We therefore fixed the operational current at 75% of the load line. This allows reaching an operational field of 5.58 T and a magnetic length of 6.27 m, fitting the vertical test station without significantly increasing the risk related to the lower margin.

**Lengths and transverse size:** The magnet cross-section has a 570 mm diameter, including the stainless steel vessel, i.e. the same as the LHC dipoles. A larger diameter has been excluded to be able to reuse the yoking tooling used for J-PARC at KEK.

**Mechanical structure:** Forces are kept by the iron yoke, with thin spacers between the iron and the coil, as the J-PARC [28], RHIC magnets [29], and LHC Q1/Q3 [30]. Here the prestress is given by the iron laminations, horizontally split, that are locked through keys (see Figure 3-11). A thin stainless-steel collar acts as a spacer between the coil and the iron yoke. An average prestress of 90 MPa is given at room temperature during the so-called ‘yoking’. During cool-down the prestress lowers to 70 MPa, which is enough to counteract the Lorentz forces during powering.

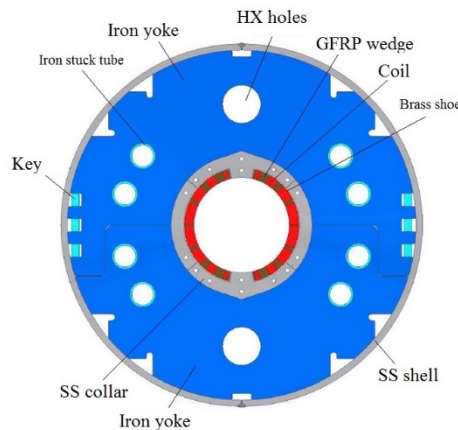


Figure 3-11: Sketch of separation dipole cross-section

**Protection:** The large cable and operational current of 12 kA (see Table 3-1) will probably allow safe operation with energy extraction at a dump and without quench heaters. Simulations show that with a 75 mΩ resistor the hotspot temperature in the adiabatic approximation is 220 K for the nominal current of 12 kA. Quench heaters or CLIQ [17] are still being considered to add a margin and redundancy.

**Field quality:** The main issue here is the saturation component [8], which is optimized via the iron shaping (see Table 3-4). Following the analysis given in Refs. [31, 32], the random components are estimated through random positioning of the coil block with different amplitudes for each family of harmonics, namely 40 μm for the allowed  $b_{2n+1}$ , 30 μm for the even skew  $a_{2n}$ , 15 μm for the odd skew  $a_{2n+1}$ , and 10 μm for the even normal multipoles  $b_{2n}$ .

**Cooling:** The magnet is in a static bath of pressurized HeII, with a stainless steel shell acting as a helium vessel. Cooling is ensured via two heat exchangers, of 49 mm inner diameter, housed in the 60 mm diameter holes through the iron.

**Cryostat:** The cryostat has the same geometry as the triplet cryostat (see Figure 3-6).

Table 3-4: Expected systematic harmonics and random components of D1

Expected systematic harmonics					
	Geometric	Saturation	Persistent	Injection	High field
b <sub>3</sub>	-1.80	0.90	-14.2	-16.00	-0.90
b <sub>5</sub>	0.50	-0.50	-1.00	-0.50	0.00
b <sub>7</sub>	1.60	-1.20	-0.70	0.90	0.40
b <sub>9</sub>	-0.68	0.09	0.02	-0.66	-0.59
b <sub>11</sub>	0.44	0.03	0.00	0.44	0.47

Random components		
Order	Normal	Skew
2	0.20	0.68
3	0.73	0.28
4	0.13	0.44
5	0.36	0.15
6	0.06	0.18
7	0.16	0.06
8	0.03	0.06
9	0.06	0.02
10	0.01	0.03
11	0.02	0.01

### 3.6 Recombination dipole D2

**Function and operational modes:** The recombination dipole is ramped with the energy of the LHC, and is constant during squeeze. Each magnet is independently powered, and the two apertures are in series. The fields point in the same direction in both apertures; this makes field quality control much more challenging than in the LHC dipole, where the field points in opposite directions. The design of the recombination dipole is being studied by INFN-Genova.

**Cable:** The 15 mm wide Nb-Ti cable used for the outer layer of the main LHC dipole is adopted. The required unit length is not larger than that of the LHC main dipole's outer layer unit length (780 m).

**Coil, current density and margin:** We selected a conservative margin, operating at 65% of the load line with a single layer 15 mm width coil, and an operational field of 4.5 T. In these conditions, the approach used in the current D2, using iron to magnetically decouple the two apertures, leads to large saturation effects. An alternative approach using left-right asymmetric coils was therefore adopted [33] to compensate for the cross-talk between the two apertures (see Figure 3-12). A very careful optimization is needed to find the best solution. After several iterations, a cross-section was found where the left-right asymmetry is only given by the angles of the blocks, but the number of cables per block is the same [34]. This allows for much simpler coil heads.

**Lengths and transverse size:** The magnetic length is 7.78 m. The magnet requires an adequate iron thickness to reduce the fringe field. An elliptical iron yoke is proposed, of 570 mm vertically and 630 mm horizontally.

**Mechanical structure:** The square design of the central aperture in the iron is imposed by field quality optimization, namely the reduction of the field harmonics due to saturation. The accumulation of Lorentz forces corresponds to a pressure in the midplane of about 40 MPa. A self-supporting stainless-steel twin collar, where the iron is only for alignment, has been shown to be viable, with a peak stress during collaring of the order of 100 MPa [35]. An alternative structure with separated stainless steel collars, allowing more flexibility in production, is also being considered.

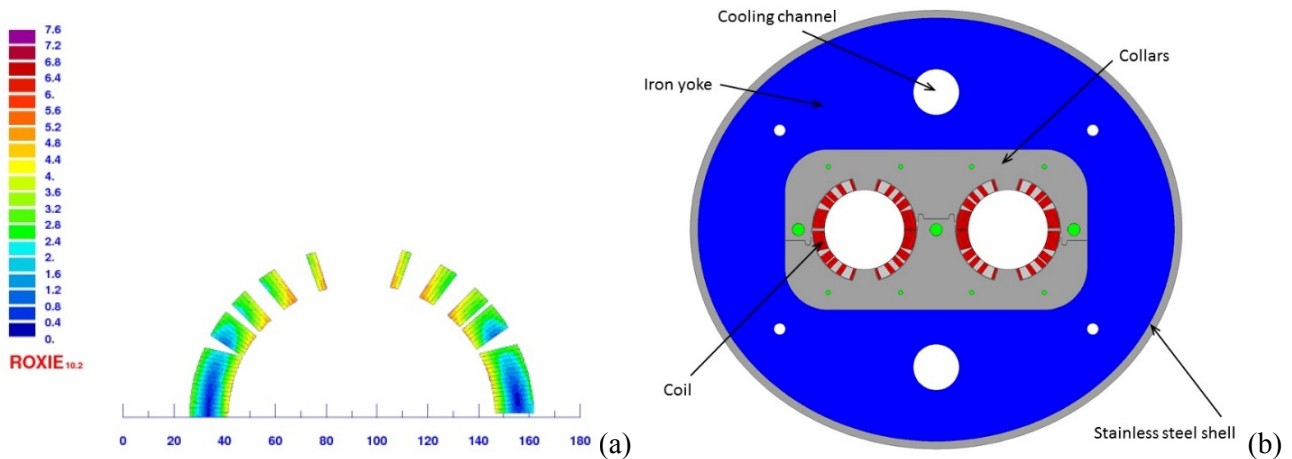


Figure 3-12: Sketch of recombination dipole cross-section. (a) Asymmetric coil; (b) magnet cross-section.

**Protection:** Protection will be probably based on quench heaters; studies are in progress at the time of writing.

**Field quality:** This is the main issue for this magnet. Cross-talk is optimized via the asymmetric cross-section, and the saturation through an iron shaping. Field quality tables are still in progress at the time of writing.

**Cooling:** The magnet is in a static bath of pressurized HeII. Cooling is ensured via two heat exchangers, of 51 mm diameter, housed in a 60 mm diameter hole in the iron, located in the upper part.

### 3.7 D2 and Q4 correctors

**Function and operational modes:** Both D2 and Q4 need orbit correctors for each beam and each plane (horizontal and vertical), with an integrated strength of 4.5 T·m. An aperture of 100 mm is required. In the preliminary layout, a field of 3 T for a magnetic length of 1.5 m has been allocated. These correctors are used to open the crossing angle and to correct the closed orbit, and therefore they should be powered in any configuration.

**Cable:** The 4.5 mm wide Nb-Ti cable used for the single aperture orbit corrector is considered.

**Coil, current density, and margin:** With one layer, one can reach the operational field of 3 T with a comfortable margin (~40%) on the load line.

**Field quality:** The challenge in these magnets is the cross-talk between the apertures. Since the beam distance is 194 mm, and the aperture is 100 mm, little space is left for the iron to decouple the two apertures [36]. No optimization can be made through the iron or the coil cross-section as is the case in D2, since these magnets have to be powered with any combination of currents. The solution is to keep the coil width as small as possible and to have thin collars to maximize the iron thickness. Requirements on field quality are stringent, especially on  $b_3$  where the tolerance is of the order of 1.5 units. Given these constraints, the operational field will probably have to be lowered to reduce the cross-talk. Special ferromagnetic laminations are also considered as an option for further decreasing the coupling between the apertures.

**Mechanical structure:** 15 mm thick collars would provide a self-supporting structure, allowing the iron to align the two modules, and to shield the fields.

**Cooling:** The magnets will share cooling with D2 and Q4, so will have heat exchangers in the same position.

### 3.8 Large aperture two-in-one quadrupole Q4

**Function and operational modes:** The Q4 quadrupole (MQYY) is ramped with the energy of the LHC. During the squeeze the gradient is lowered and a minimum operational current of 3% of nominal is required, to allow flexibility for the optics. The two apertures are independently powered, with a possible current unbalance up to 50%. The gradients shall have the same sign in both apertures, resulting in a focusing effect for one beam and defocusing for the other one. A Q4 short model, only, however, of single aperture, is being developed by CEA-Saclay.

**Cable:** The 15 mm wide Nb-Ti cable used for the outer layer of the main LHC dipole is adopted. The required unit length is much smaller than the LHC unit length (780 m), so short lengths of the production that could not be used in the dipoles can be employed, at zero cost, and not affecting the LHC dipole spares. Insulation is based on the enhanced scheme proposed in Ref. [37], allowing a direct path from the cooling bath to the strand.

**Coil, current density and margin:** With one layer, this can reach the operational gradient of 115 T/m at 80% of the load line [38].

**Lengths and transverse size:** The magnetic length is 3.83 m. The magnet cross-section has a 497.5 mm nominal diameter, including the stainless steel vessel, i.e. the same as the LHC main quadrupoles.

**Mechanical structure:** The quadrupole makes use of self-standing collars, the same as the main LHC quadrupoles [39] and MQXC [40] (Figure 3-13). Here, the prestress is given by the 25 mm thick collars, which are locked through keys. An average prestress of 80 MPa is given at room temperature after yoking. Thirty percent of prestress is then lost due to cable insulation creep, leading to 55 MPa. During cool-down the prestress lowers to 40 MPa, enough to counteract the Lorentz forces during powering. The iron is used to magnetically separate the two apertures, close the flux lines, and provide alignment. The shells will probably be welded with the quadrupole and the correctors, since an inertia tube would become too long (8 m) for the vertical assembly.

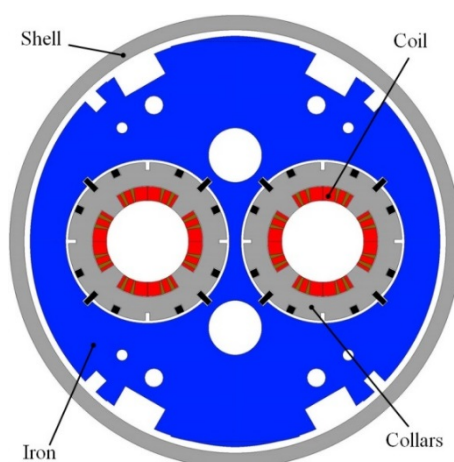


Figure 3-13: Sketch of Q4 cross-section

**Protection:** The large cable and operational current will allow safe operation, with energy extraction in a dump. Simulations show that with a 50 mΩ resistor the hotspot temperature in the adiabatic case is below 200 K.

**Field quality:** The coil has three blocks, allowing  $b_6$  and  $b_{10}$  to be within one unit and  $b_{14}$  to be within two units (see Table 3-5). Shimming on the pole and in the midplane is foreseen to allow the steering of  $b_6$  in the model/prototype phase. An estimate of the random component is given in Table 3-5.



**Cooling:** The magnet is in a static bath of HeII, with a stainless steel inertia tube acting as a helium vessel. Cooling is ensured via heat exchangers of 51 mm diameter, housed in the 60 mm diameter holes in the iron, located in the upper part.

**Cryostat:** The cryostat will include the quadrupole plus two orbit correctors (see the previous section), with a total length of about 8 m.

Table 3-5: Expected systematic harmonics and random components

Expected systematic harmonics						Random components		
	Geometric	Saturation	Persistent	Injection	High field	Order	Normal	Skew
b <sub>6</sub>	-0.45	0.40	-11.00	-11.45	-0.05	3	1.79	1.79
b <sub>10</sub>	0.00	0.00	1.00	1.00	0.00	4	1.16	1.16
b <sub>14</sub>	1.50	0.00	0.00	1.50	1.50	5	0.75	0.75
						6	1.93	0.48
						7	0.31	0.31
						8	0.20	0.20
						9	0.13	0.13
						10	0.34	0.08

### 3.9 Q5

For the Q5 magnet, the present baseline is to replace it with a 70 mm aperture MQY [41] (at the time of writing Q4 around IP1 and IP5), operating at 1.9 K. With an operational current of 4510 A, it reaches an operational gradient of 200 T/m. As for Q4, apertures are independently powered. There are seven available spares, plus four MQY that will be recovered from IP1 and IP5 in the Q4 position. An alternative option, requiring a larger aperture, is also under consideration. In this case the 90 mm aperture Q4 would be also used as Q5, with a longer length or with two units.

### 3.10 Powering

The baseline of the powering scheme of the triplet-corrector-separation dipole is shown in Figure 3-14. The powering is from the D2-side of D1, allowing a more compact layout with respect to the LHC, where this is done through a distribution feedbox taking a few metres between the triplet and D1. This choice improves performance at the price of having triplet and corrector cables going through (or along) the separation dipole. The second important choice is that magnets are fed by a superconducting link: therefore the transition from superconducting to resistive leads is shifted from the neighbourhood of the beam line. For the triplet, the baseline option is to have Q1 and Q3 in series, and Q2a and Q2b in series, with two 20 kA independent power converters, plus a 2 kA trim on Q3. This configuration provides a good compromise between cost and operation. Other options are under consideration at the time of writing.

- Power in series Q1 and Q2a, and Q2b and Q3: this configuration allows compensation of the power converter ripple between a couple of focusing/defocusing quadrupoles, at the price of a smaller flexibility in the optics.
- All four magnets in series, with a single 20 kA power converter. In this case a 2 kA trim is needed on Q1 and a second trim on Q3. This configuration minimizes the cost of the hardware, but is the more complex from the point of view of operation. It also provides the largest inductance per circuit, increasing the challenges related to the busbar and magnet protection.
- Four independent circuits for Q1, Q2a, Q2b, and Q3, with four 20 kA power converters. This solution provides the best flexibility for optics and operation, at a higher hardware cost. It also provides the lowest inductance per circuit, easing protection of the busbar and of the magnet.

Besides the triplet, one has one 13 kA circuit for D1, and six 3 kA circuits for the orbit correctors, plus the nine correctors rated at 200–300 A. In the baseline case, with 20 kA circuits for the triplet, one has a total

of  $\sim 70$  kA of current to bring in and out of the triplet–D1 area through the link (see Chapter 6). For the busbar the baseline is to place it inside the magnet (as in the LHC main cell), through the iron holes that are not used by the heat exchangers; two other options are also under study:

- busbar inside the cryostat, but outside the cold mass, in a separate line (as the M line in the LHC cell, carrying some correctors busbars);
- busbar outside the cryostat in a separate cryostat, in this case each magnet is fed by a bypass of the busbar cryostat.

The matching section is fed by a second superconducting link, bringing current to the recombination dipole D2, Q4, and the orbit correctors. Here we have one 13 kA circuit for D2, two 20 kA circuits for Q4, and four 3 kA circuit for the orbit correctors, with a total of 65 kA.

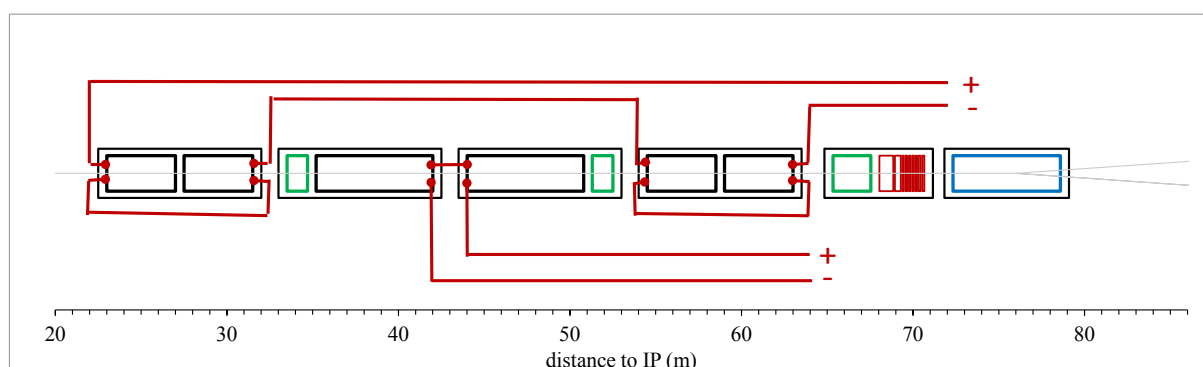


Figure 3-14: Sketch of baseline for triplet powering (trims not shown)

### 3.11 Cooling

The static heat load on the cold mass is mainly due to collision debris: 500 W on the triplet, and 70 W on the separation dipole. A factor of 1.5 has to be applied to these estimates to be compatible with the ultimate luminosity of  $7.5 \times 10^{34} \text{ cm}^{-2} \text{ s}^{-1}$ . The heat load on the triplet is removed via two 68 mm inner diameter heat exchangers, ultimately providing the ability to remove up to 1000 W (see Figure 3-15). To cope with these high heat loads, an additional low pressure pumping is added between Q2a and Q2b to keep the two-phase vapour flow velocity below 7 m/s, above which the HXs would not function correctly. These heat exchangers also cool the 1.2 m long orbit corrector. Simulations show that a solution with one (or more) heat exchangers cooling the whole string triplet–D1 is not viable. Therefore, a second system of heat exchangers is used to cool the corrector package and D1, which receive 50 W and 70 W, respectively at nominal luminosity. Here the baseline is to have two heat exchangers of 49 mm inner diameter, able to remove 250 W. One heat exchanger would provide only 125 W, barely enough to remove the 120 W due to collision debris, without the required 50% margin. Additional low pressure pumping is added between Q2a and Q2b.

The beam screen receives  $\sim 500$  W in the triplet–correctors–D1 region (see Table 3-1, including 80 W from the interconnections). Given a 50% margin to reach ultimate peak luminosity, and a 150 W budget for the residual effect of electron cloud, the system has to remove  $\sim 975$  W over 55 m, i.e.  $\sim 17$  W/m. Heat is removed at 40–60 K [42]. The cooling tubes inner diameter is kept at  $\sim 7$  mm due to an increase of the pressure of the helium to 18 bar. This choice is more challenging for the piping system but allows minimization of the space taken by the cooling pipes, which reduce the aperture available to the beam.

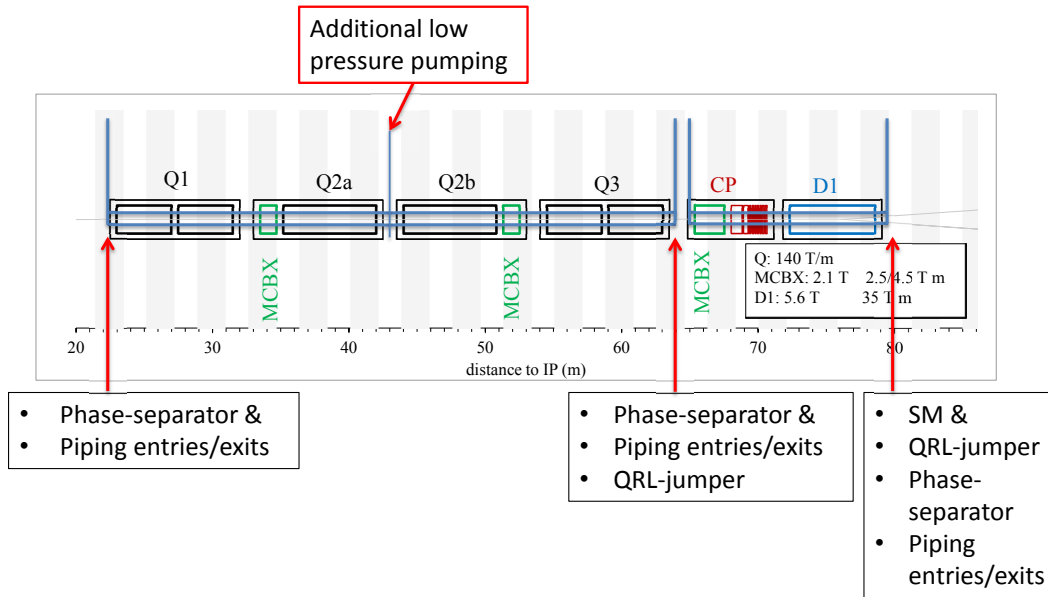


Figure 3-15: Sketch of the cooling system

For the stand-alone magnets, the jumper is located on the upper part of the slope, and the symmetry of the cryostat with respect to the interaction point is lost. This means that the left and right cryostats are not interchangeable, but the piping needed for the cooling system is simpler. This choice cannot be taken for the triplet, where there is no space for a jumper between the quadrupole and the interaction point. So the jumper is on the D1 side, requiring an additional return pipe.

### 3.12 Instrumentation

We give here a short summary of the instrumentation foreseen for the IR magnets.

- Quench protection requires voltage taps; for dipoles and quadrupoles we foresee the possibility of monitoring the voltage on each coil. Quench detection is therefore based on an analysis of the difference between signals of different coils, thus allowing cancelling of the inductive voltage.
- Beam loss monitors will be located inside the triplet cold mass to have the possibility of monitoring beam losses closer to the beam pipe and to the coil. Installation of special beam loss monitors in one of the iron holes not used by the heat exchangers or by the busbars is foreseen.
- Temperature sensors: one per cold mass, plus a spare, as in the LHC.
- Strain gauges: all quadrupoles based on the bladder and key structure will have strain gauges on the Al shell. Gauges will also be installed on the coil (winding pole) in the model and prototype phase, and possibly during production. One could consider having these signals extracted from the cryostat to have them available during operation. In the case of the LHC dipoles, strain gauges were used in the initial prototyping phase only.
- Beam position monitors will be placed in the interconnections between Q1 and Q2a, Q2b and Q3, Q3 and the corrector package, and between the corrector package and D1. Moreover they will be present at positions close to D2, Q4, and Q5.

### 3.13 Test

In general, magnets will be tested individually in a vertical test station, and then horizontally in the final cold mass assembly within the final cryostat. In some cases the first test will be possible in laboratories collaborating with CERN (for instance FNAL for Q1/Q3, and KEK for D1). The second test will be carried out at CERN. A string including the magnets from Q1 to D1 will be assembled in the CERN test facility (SM18) by 2019–

2020. Magnetic measurements at 1.9 K with the rotating coil technique will be carried for all main magnets and for all the low-order (dipole and quadrupole) correctors. For the high-order corrector the magnetic measurement strategy is still to be defined.

### 3.14 References

- [1] O. Bruning, L. Rossi, Eds. “The High Luminosity Large Hadron Collider”, Advances Series on Directions in High Energy Physics **24**, (World Scientific, Singapore 2015).
- [2] E. Todesco *et al.*, A first baseline for the magnets in the high luminosity LHC insertion regions, *IEEE Trans. Appl. Supercond.* **24** (2014) 4003305.
- [3] G. Sabbi, Nb<sub>3</sub>Sn IR Quadrupoles for the High Luminosity LHC, *IEEE Trans. Appl. Supercond.* **23** (2013) 4000707.
- [4] L. Rossi and E. Todesco, Electromagnetic design of superconducting quadrupoles, *Phys. Rev. STAB* **9** (2006) 102401.
- [5] A. Tollestrup *et al.*, The development of superconducting magnets for use in particle accelerators: from Tevatron to the LHC, *Rev. Sci. Accel. Tech.* **1** (2008) 185–210.
- [6] P. Ferracin *et al.*, Limits to high field magnets for particle accelerators, *IEEE Trans. Appl. Supercond.* **22** (2012) 4003106.
- [7] P. Ferracin *et al.*, Magnet design of the 150 mm aperture low-beta quadrupoles for the high luminosity LHC, *IEEE Trans. Appl. Supercond.* **24** (2014) 4002306.
- [8] Q. Xu *et al.*, Design optimization of the new D1 dipole for HL-LHC upgrade, *IEEE Trans. Appl. Supercond.* **24** (2014) 4000104.
- [9] L. Esposito *et al.*, Fluka energy deposition studies for the HL-LHC, IPAC (2013) 1379–1381. Conf. Proc. C130512 (2013) pp.TUPFI021
- [10] N. Mokhov *et al.*, Protecting LHC IP1/IP5 component against radiation resulting from colliding beam interactions, LHC project report 633 (2003) p. 55.
- [11] S. Caspi *et al.*, Test results of LARP Nb<sub>3</sub>Sn quadrupole magnets using a shell-based support structure (TQS), *IEEE Trans. Appl. Supercond.* **19** (2009) 1221–1225.
- [12] G. Ambrosio *et al.*, Test results of the First 3.7 m long Nb<sub>3</sub>Sn quadrupole by LARP and future plans, *IEEE Appl. Supercond.* **21** (2011) 1858–1862.
- [13] H. Felice *et al.*, Design of HQ – A high field, large bore, *IEEE Trans. Appl. Supercond.* **19** (2009) 1235–1239.
- [14] E. Todesco, Quench limits in the next generation of magnets, CERN Yellow Report 2013-006 (2013) 10–16.
- [15] T. Salmi *et al.*, Modeling heat transfer from quench protection heaters to superconducting cables in Nb<sub>3</sub>Sn magnets, *CERN Yellow Report* **2013-006** (2013) p. 30–37.
- [16] V. Marinuzzi *et al.*, Study of quench protection for the low  $\beta$  quadrupole for the LHC luminosity upgrade. Applied Superconductivity Conference 2014, Charlotte, NC, USA, 10 - 15 Aug 2014
- [17] E. Ravaioli *et al.*, New coupling loss induced quench protection system for superconducting accelerator magnets, *IEEE Trans. Appl. Supercond.* **24** (2014) 0500905.
- [18] S. Izquierdo Bermudez *et al.*, Coil end optimization of the low  $\beta$  quadrupole for the high luminosity LHC, Applied Superconductivity Conference 2014, Charlotte, NC, USA, 10 - 15 Aug 2014
- [19] R. Gupta, Tuning shims for high field quality in superconducting magnets, *IEEE Trans. Magn.* **32** (1996) 2069–2073.
- [20] P. Hagen, Study of magnetic shimming in triplet magnets, Milestone Report 36 of HiLumi project. <http://www.cern.ch/hilumi/wp3>
- [21] R. Van Weelden, Superfluid helium cooling, Milestone Report 42 of HiLumi project. <http://www.cern.ch/hilumi/wp3>

- [22] D. Duarte Ramos *et al.*, talk given at WP3 meeting on 28 January 2014. <https://espace.cern.ch/HiLumi/WP3/SitePages/Minutes%20and%20Presentations.aspx>
- [23] J. Garcia Matos *et al.*, talk given at WP3 meeting on 17 July 2014. <https://espace.cern.ch/HiLumi/WP3/SitePages/Minutes%20and%20Presentations.aspx>
- [24] M. Karppinen, Corrector magnets for the LHC upgrade phase-1, CERN EDMS doc. N. 1039976, and R. Ostojic *et al.*, Conceptual design of the LHC interaction region upgrade: Phase I, LHC Project Report **1163** (2008) p. 42.
- [25] F. Toral *et al.*, Development of radiation resistant superconducting corrector magnets for the LHC upgrade, *IEEE Trans. Appl. Supercond.* **23** (2013) 4101204.
- [26] G. Volpini *et al.*, Nb-Ti superferric corrector magnets for the LHC luminosity upgrade, submitted to *IEEE Trans. Appl. Supercond.*, presented at ASC 2014.
- [27] T. Nakamoto *et al.*, Model magnet development of D1 beam separation dipole for the HL-LHC upgrade, *IEEE Trans. Appl. Supercond.* **25** (2015) 4000505
- [28] T. Nakamoto *et al.*, Construction of superconducting magnet system for the j-PARC neutrino beam line, *IEEE Trans. Appl. Supercond.* **20** (2010) 208–213.
- [29] M. Anerella *et al.*, The RHIC magnet system, *Nucl. Instrum. Meths. A* **499** (2003) 280–315.
- [30] Y. Ajima *et al.*, The MQXA quadrupoles for the LHC low-beta insertions, *Nucl. Instrum. Meths. A* **550** (2005) 499–513.
- [31] B. Bellesia, J. P. Koutchouk and E. Todesco, Field quality in low-beta superconducting quadrupoles and impact on the beam dynamics for the Large Hadron Collider, *Phys. Rev. STAB* **10** (2007) 062401.
- [32] B. Bellesia, C. Santoni and E. Todesco, Random errors in superconducting dipoles, 10th European Particle Accelerator Conf. (2006) 2601–2603.
- [33] V. Kashikhin, *et al.*, Design study of 2-in-1 large aperture IR dipole (D2) for the LHC luminosity upgrade Particle Accelerator Conference (2007) 464–6, and G. Sabbi *et al.*, Conceptual Design Study of the High Luminosity LHC Recombination Dipole, 5th International Particle Accelerator Conf., (2014) 2712-4
- [34] P. Fabbriatore *et al.*, talk given at WP3 meeting on 17 September 2014. <https://espace.cern.ch/HiLumi/WP3/SitePages/Minutes%20and%20Presentations.aspx>
- [35] S. Farinon *et al.*, talk given at WP3 meeting on 17 September 2014. <https://espace.cern.ch/HiLumi/WP3/SitePages/Minutes%20and%20Presentations.aspx>
- [36] J. Rysti *et al.*, talk given at WP3 meeting on 17 September 2014. <https://espace.cern.ch/HiLumi/WP3/SitePages/Minutes%20and%20Presentations.aspx>
- [37] P. P. Granieri *et al.*, Thermally enhanced cable insulation for the Nb-Ti high luminosity LHC inner triplet model, *IEEE Trans. Appl. Supercond.* **22** (2012) 7700404.
- [38] M. Segreti *et al.*, A Nb-Ti 90 mm double aperture quadrupole for the high luminosity LHC upgrade, *IEEE Trans. Appl. Supercond.* **25** (2015) 4001905.
- [39] T. Tortschanoff *et al.*, The LHC main quadrupoles during series fabrication, *IEEE Trans. Appl. Supercond.* **16** (2006) 281.
- [40] G. Kirby *et al.*, LHC IR upgrade Nb-Ti, 120 mm aperture model quadrupole test results at 1.8 K, *IEEE Trans. Appl. Supercond.* **24** (2014) 4002405.
- [41] G. Kirby *et al.*, Performance of the 1-m model of the 70 mm twin aperture superconducting quadrupole for the LHC insertions, *IEEE Trans. Appl. Supercond.* **11** (2001) 1641.
- [42] V. Baglin *et al.*, Cryogenic beam screens for high energy particle accelerators, International Cryogenic Engineering Conf., CERN ATS-2013-006 (2013).



# Chapter 4

## RF Systems

*P. Baudrenghien<sup>1</sup>, G. Burt<sup>3</sup>, R. Calaga<sup>1</sup>, O. Capatina<sup>1</sup>, W. Hofle<sup>1</sup>, E. Jensen<sup>1</sup>, A. Macpherson<sup>1</sup>, E. Montesinos<sup>1</sup>, A. Ratti<sup>2</sup> and E. Shaposhnikova<sup>1</sup>*

<sup>1</sup>CERN, Accelerator & Technology Sector, Geneva, Switzerland

<sup>2</sup>FNAL, Fermi National Accelerator Laboratory, Batavia, USA

<sup>3</sup>University of Lancaster, Lancaster, UK and Cockcroft Institute Sci-Tech Daresbury, Warrington, UK

### 4 RF systems

#### 4.1 Introduction

The HL-LHC upgrade to enhance the integrated luminosity by a factor of 10 per year will need the following RF systems:

- deflecting (or crab) cavities for compensation of the effective geometric crossing angle at the IP to recover the luminosity loss due to increased crossing angle;
- a harmonic RF system for bunch manipulation and increased stability;
- a transverse damper upgrade for higher power, bandwidth, and low noise.

The above RF systems are described with relevant technical details below. The beam and machine parameters from Appendix A.1 are used to design the RF systems.

#### 4.2 Crab cavities

The LHC uses a 60 m common focusing channel plus 21 m common drift space and 20 m common dipole channel on each side of the interaction region (IR), where the two counter-rotating beams have to be separated transversely to avoid parasitic collisions. Separation is accomplished by introducing a crossing angle at the interaction point (IP), which needs to increase with the inverse of the transverse beam size at the collision point in order to maintain a constant normalized beam separation. The non-zero crossing angle implies an inefficient overlap of the colliding bunches. The luminosity reduction compared to that of a zero crossing angle, assuming a Gaussian distribution, can be conveniently expressed by a reduction factor,

$$R_{\Phi} = \frac{1}{\sqrt{1+\Phi^2}}, \quad (4-1)$$

where  $\Phi = \sigma_z \phi / \sigma_x$  is the aspect ratio of the longitudinal ( $\sigma_z$ ) to the transverse ( $\sigma_x$ ) beam sizes multiplied by the half crossing angle  $\phi$ , which is also known as the Piwinski angle [1]. Alternatively the reduction can be viewed as an increase in the transverse beam size at the collision point to effective beam size given by  $\sigma_{\text{eff}} = \sqrt{\sigma_x^2 + \sigma_z^2 \phi^2}$ . For HL-LHC beam parameters, the reduction compared to the case of a head-on collision can be 70% or larger. Therefore, the effective gain in luminosity by simply reducing the beam size at the collision point diminishes rapidly.

To recover the loss, an elegant scheme using RF deflectors (also known as crab cavities) on either side of the collision point was first proposed and used for electrons [2, 3]. The time-dependent transverse kick from

---

\* Corresponding author: [Rama.Calaga@cern.ch](mailto:Rama.Calaga@cern.ch)

an RF deflecting cavity is used to perform a bunch rotation, in the  $x$ - $z$  plane or  $y$ - $z$  plane depending on the crossing angle orientation, about the barycentre of the bunch (see Figure 4-1). The kick is transformed to a relative displacement of the head and the tail of the bunch at the IP to impose a head-on collision while maintaining the required beam separation to minimize parasitic collisions. The upstream RF deflector is used to reverse the kick to confine the bunch rotation to within the IR. The crab crossing scheme in a global compensation using only a single cavity per beam was successfully implemented at the  $e^+e^-$  collider at KEKB in Japan to achieve record luminosity performance [4].



Figure 4-1: Bunches colliding with (a) a crossing angle without crab crossing; (b) with the crab crossing

Since the luminosity gain is substantial, the crab crossing scheme is adopted as a baseline for the HL-LHC upgrade. The time-dependent transverse kick can equally be used to regulate the crossing angle at the IP and therefore allows for a natural knob to control the total number of events per crossing (luminosity levelling), a feature highly desired by the experiments. Levelling by means of collision offsets is already used at LHCb and ALICE. More sophisticated means of levelling to control the density of the events along the luminous region by means of crab cavities are under investigation [5].

#### 4.2.1 Beam and RF system parameters

The HL-LHC upgrade lattice requires crab cavities to provide a total voltage of 12–13 MV per beam per side of each collision point at a frequency of 400.79 MHz. Since the crossing plane in the two experiments is different, a local crab cavity system is a prerequisite. The nominal configuration will use a two-cavity cryomodule as the basic unit. Four such modules per IP side at P1 and P5 are required to perform the bunch rotation resulting in 16 modules (a total of 32 cavities). Four spare modules (eight cavities) are required. Two are designed for horizontal crossing and the other two for vertical crossing to perform crab crossing for P5 and P1, respectively. The low frequency is required to minimize the RF curvature for the long LHC bunches (see Appendix A.1). The machine constraints near the interaction region require cavities with a transverse dimension compatible with the location of the adjacent beam pipe. The RF and machine parameters directly relevant to the crab cavities are shown in Table 4-1.

An operating temperature of 2 K is chosen as a baseline. A pressure stability on the cavity surface should be minimized to less than 1 mbar. The static and dynamic heat load is expected to be approximately 30 W to the 2 K bath for a two-cavity module. A cavity vacuum level to better than  $10^{-10}$  mbar is required to assure stable performance.

The input RF power of 80 kW is available to power each of the eight cavities to their nominal voltage with sufficient margin to cope with beam loading caused by beam offset. The low level RF (LLRF) will include a regulation loop around the tetrode (to reduce the RF amplitude and phase noise in a band extending to a few tens of kHz), plus an RF feedback to control the vector sum precisely on the two sides of the interaction region. Longitudinal pickups (Pus) located close to the crab cavities (one per IP-side per beam) are used to regulate the slow drifts of the deflecting voltage with respect to the average bunch centre. To stay within the specified RF power limits, an orbit stability including mechanical tolerances must not exceed 1 mm with stable beams at flat-top. The cavity is kept on tune at all times. The resonant frequency should be precisely controlled by a tuning system to a level well below 0.5 kHz to be compatible with the RF power limits.



Table 4-1: Relevant RF parameters for HL-LHC crab cavities

Characteristics	Units	Value
Resonance frequency	[MHz]	400.79
Bunch length	[ns]	1.0 (4 $\sigma$ )
Maximum cavity radius	[mm]	$\leq 145$
Nominal kick voltage	[MV]	3.4
$R/Q$ (assumed, linac convention)	[ $\Omega$ ]	400
$Q_0$		$\geq 1 \times 10^{10}$
$Q_{\text{ext}}$ (fixed coupling range)		$3 \times 10^5 - 5 \times 10^5$
RF power	[kW]	80
Power coupler OD (50 $\Omega$ )	[mm]	62
LLRF loop delay	[ $\mu$ s]	$\approx 1$
Cavity detuning	[kHz]	$\approx 1.0$

#### 4.2.2 RF cavity design

In order to sustain the surface fields at the required kick gradient of 3.4 MV/cavity for the LHC, crab crossing superconducting technology is essential; space restrictions, voltage requirements, and impedance considerations strongly rule out a normally conducting option. ‘Conventional’ superconducting elliptical cavities, which have already been used at KEK, pose significant integration problems at the operating frequency of 400 MHz in the LHC due to their transverse size.

This led to the concept of ‘compact’ cavities. These cavities have unconventional geometries not widely used in superconducting technology. A few concepts with complex shapes exist primarily in the field of heavy ion acceleration. Such structures fit within the LHC constraints in the existing tunnel and reveal significantly better surface field characteristics than the conventional cavities for beam deflection. As a result of an intense R&D programme within the EuCARD and LARP programmes and with other external collaborators during the past four years, three compact designs at 400 MHz have emerged as potential candidates. Their topologies are shown in Figure 4-2. The three proposed designs are at least four times smaller in the plane of crossing compared to an elliptical cavity with a ratio of the kick gradient to the peak surface fields lower by a factor of 2.

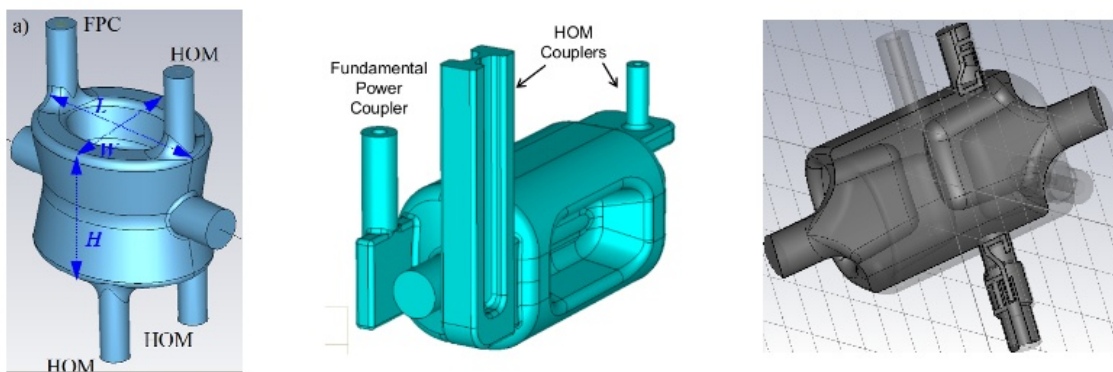


Figure 4-2: Compact cavities. (a): Double quarter wave cavity (DQW), courtesy of Brookhaven National Lab. (b) RF dipole cavity (RFD), courtesy of Old Dominion University. (c) Four-rod cavity, courtesy of Lancaster University.

As a part of the R&D phase, it was decided to prototype full-scale cavities for all three designs for a field validation at the nominal kick voltage. Following the recommendation by the Crab Cavity Advisory Panel a prototype module in a two-cavity configuration will be tested with beam in the SPS machine with LHC type beams [6]. These tests will help validate the cavity performance and operation with beam and understand the effects on protons as well as relevant machine protection aspects. The three cavities were fabricated in 2012–2013 and their performance validated at or beyond the nominal kick voltage [7–9]. The cavity designs including

the fundamental power coupler and higher order mode couplers have evolved significantly from the prototype to meet the impedance requirements of the LHC. Following the recommendation of the May 2014 technical review [10], only two of the cavity designs have been considered for SPS testing (DQW and RFD).

The development of a two-cavity cryomodule for the SPS tests in 2017 is at an advanced stage. An overview of crab cavity planning spanning approximately ten years until full installation in the LHC is shown in Table 4-2. A more detailed plan for the SPS and the LHC, including the pre-series and series production, can be found in Ref. [35].

Table 4-2: Overview of crab cavity planning from R&D to installation in the LHC

2013–2014	2015–2016	2017–2018	2019–2023	2023–2024
Cavity testing and prototype cryomodule	SPS cryomodule fabrication	SPS tests and LHC pre-series module	LHC cryomodule construction and testing	LHC installation

### 4.2.3 Beam loading and RF power

In deflecting cavities operated in the crabbing mode, the RF phase and the RF component of the beam current are in quadrature ( $\phi_s = 0$ , synchrotron convention). For a beam transversely centred, there is no beam loading: the RF generator does not pass power to the beam. With a superconducting cavity (negligible surface losses) the RF power required to maintain the cavity voltage decreases monotonically with  $Q_L$ . Therefore, with a perfectly centred beam, the choice of  $Q_L$  only requires sufficient bandwidth for unavoidable frequency transients due to external perturbations (see Section 4.2.10.4, Frequency tuning).

The situation is different for a beam circulating at an offset  $\Delta x$ . The beam-induced voltage due to an orbit offset is given by

$$\Delta V = I_b \cdot \frac{R_T}{Q_0} \cdot Q_L \cdot \Delta x, \tag{4-2}$$

where  $I_b$  is the average beam current,  $R_T/Q_0$ , is the transverse shunt impedance in  $\Omega$  and  $\Delta x$  is the offset. A sufficient bandwidth and the corresponding RF power are required to compensate for the unavoidable orbit offsets. Figure 4-3 shows the required forward power as a function of the  $Q_L$  for a beam that is centred (red) and off-centred by 1 mm (green) and 2 mm (blue). It is expected that the orbit will be kept within 0.5 mm for the entire energy cycle of the LHC; another 0.5 mm should be added for mechanical tolerances.

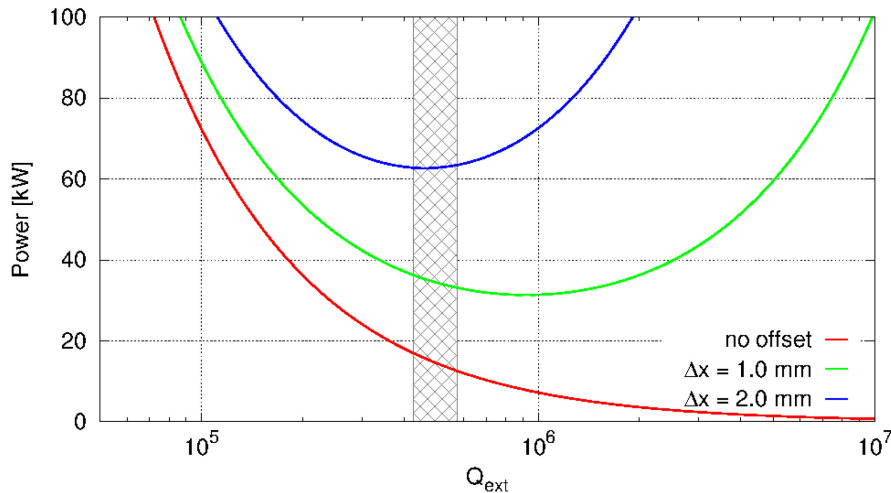


Figure 4-3: Forward power vs. cavity  $Q_L$  for centred (red), 1 mm offset (green), and 2 mm offset (blue) beams. Assumed  $R/Q = 400 \Omega$ , 3.4 MV RF, 1.1 A DC.

The required RF power has a broad minimum ( $\leq 40$  kW) from a  $Q_L$  of about  $3 \times 10^5$  to  $1.5 \times 10^6$ . Selection of an optimal  $Q_L$  value in the broad minimum is a compromise between the feasible tuning precision and the minimization of the field fluctuations from the

amplifier electronics. For larger bandwidth (leading to more stability), lower  $Q_L$  values are favoured – the cross-hatched area in Figure 4-3 was chosen as a compromise. A lower  $Q_L$  is also favourable for the tuning system as it relaxes the precision needed by a mechanical system and the power needed to compensate for fast frequency changes.

#### 4.2.4 RF power coupler

The RF power coupler was designed in view of the HL-LHC requirements; additional constraints (common platform) were introduced to limit the variances between the alternative designs in view of the SPS tests.

The crab cavity power coupler adopted will use a single coaxial disk-type window to separate the cavity vacuum and the air side. The antenna shape is specific to each cavity as the coupling mechanisms for the different cavities are not identical. However, a common platform starting from the cavity flange followed by the ceramic and double wall tube is imposed. To respect the common platform, the inner antenna is 27 mm diameter with an outer coaxial line of 62 mm diameter for a maximum power capability of approximately 200 kW. The inner line is made of a copper tube and the outer line is 316LN stainless steel with the inner surface coated with copper. The vacuum-to-air separation is achieved with a coaxial ceramic window ( $Al_2O_3$ ) with an outer flange made of titanium. The rest of the items are built from massive Oxygen Free Electronic (OFE) 3D forged copper blocks. The coupler body is made in a conical line to increase the ceramic region to limit arcing, with the primary aim of enlarging the air side to the maximum while keeping the 62 mm/27 mm dimensions for the input antenna on the vacuum side. A coaxial to waveguide transition is performed with a WR2300 half-height without a doorknob (see Figure 4-4 (a)).

The air side of the coupler will be air-cooled while the antenna itself will be water-cooled. The waveguide design includes the possibility of DC polarization in order to avoid multipacting effects. Each coupler is equipped with three ports for a vacuum gauge, electron monitoring, and arc detection devices. The vacuum gauge, which is mandatory to protect the window during conditioning as well as in operation, will be oriented along the air line in order to minimize the cryomodule flange size. Special test boxes to condition the couplers have also been designed (see Figure 4-4 (b)). The coupler ports are designed to come out on the top of the cryomodule, perpendicular to the beam axis for ease of integration with the WR2300 waveguide transition. The cavity's helium vessel is designed to withstand the weight of the couplers and the waveguide (approximately 35 kg). The alternating crossing angle scheme will require that the orientation of a coupler assembly be robust for horizontal and vertical deflections.

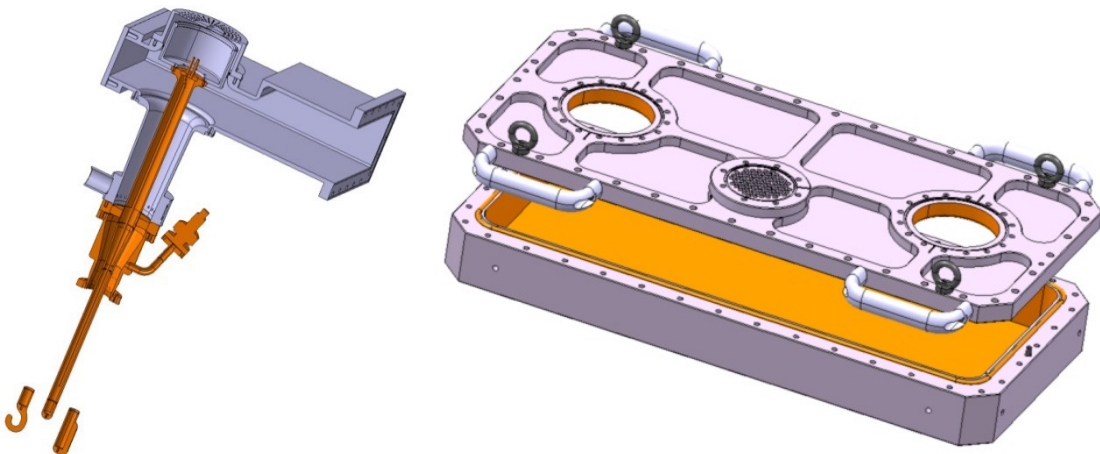


Figure 4-4: (a) Input coupler assembly; (b) test box for RF conditioning

#### 4.2.5 Coupled bunch instabilities

The crab cavities must cope with the various modes of the collider cycle: filling, ramping, and physics. During filling of the 2808 bunches into the LHC, ramping, or operation without crab cavities (crabbing off), the cavity

can be detuned; but a small field should be kept for the active tuning system. This is referred to as ‘parking’. Parking the cavity half the distance between two revolution frequency sidebands would be ideal for stability. Another possibility is to operate with ‘crabbing off’, which is possible since more than one cavity is used, namely counter-phasing to make the effective kick voltage zero while always keeping accurate control of the cavity field. This counter-phasing ensures both zero effective voltage and beam stability on tune – in fact, it has been found that this is the preferred scenario [11].

If detuning is used with a positive non-integer tune ( $Q_h = 64.3$ ), the cavity should be tuned above the RF frequency to make the mode  $l = -64$  stabilizing (see Ref. [11]). Although RF feedback is not mandatory for stability with a detuned cavity, it is preferred for accurate knowledge about, and control of, the cavity’s resonance frequency and field. Active feedback will also keep the beam-induced voltage zero if the beam is off-centred. The additional RF power is used as a measurement of beam loading to guide beam centring. The RF signal picked up through the HOM couplers might also be used.

On the flat-top detuning can be reduced (but keeping the total kick voltage initially at zero). The RF feedback keeps the cavity impedance small (beam stability) and compensates for beam loading as the cavity moves to resonance. Once the cavity detuning is reduced to zero, we drive counter-phasing to zero and use the functions to synchronously change the voltage in all crab cavities as desired (crabbing on). In a physics run, with crabbing on, the active RF feedback will continue to provide precise control of the cavity field. The RF feedback reduces the peak cavity impedance and transforms the high  $Q$  resonator to an effective impedance that covers several revolution frequency lines. The actual cavity tune has no big importance for stability anymore. The growth rates and damping rates are much reduced, and we have no more dominant mode as shown in Figure 4-5.

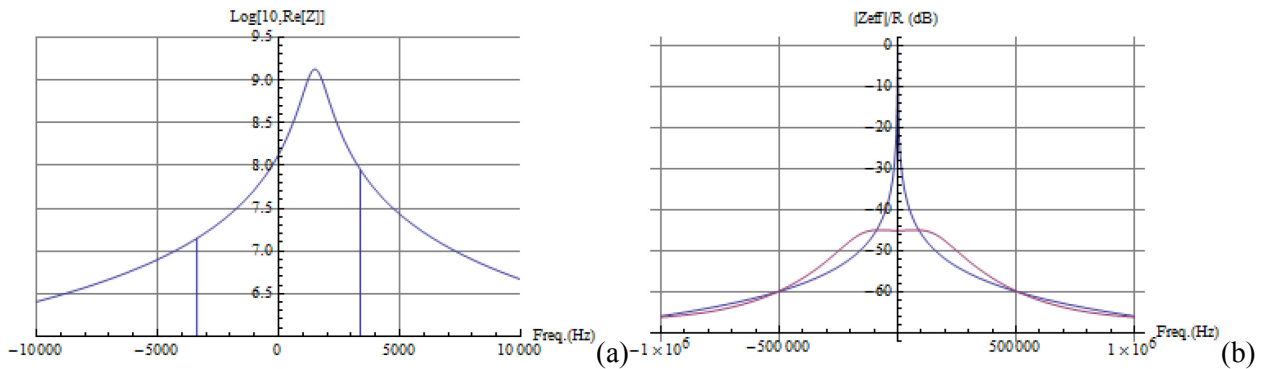


Figure 4-5: (a) Real part of the deflecting mode impedance with a detuning of 1.5 kHz from from 400 MHz. The vertical lines represent the difference in  $\Re\{Z\}$  evaluated at  $\pm 0.3 f_{\text{rev}}$  for the computation of damping rate (mode  $l = -64$ ). (b) Modulus of the cavity impedance seen by the beam with the RF feedback on (red) and off (blue) normalized to the cavity impedance at the fundamental mode.

#### 4.2.6 Impedance budget

On resonance, the large impedance of the fundamental deflecting (dipole) mode is cancelled between the positive and negative sideband frequencies, which are symmetric around  $\omega_{\text{RF}}$ . The active feedback will reduce the growth rates by a large factor.

For higher order modes (HOMs), both narrowband and broadband impedance should be minimized during the entire machine cycle as the LHC will accelerate and store beams of currents exceeding 1.1 A (DC). Tolerances are set from impedance thresholds estimated from Ref. [12].

The longitudinal impedance has approximately a quadratic behaviour vs.  $f$  in the region of interest with the minimum threshold value at 300–600 MHz. The total maximum allowed impedance from each HOM, summing over all cavities in one beam, assuming that the HOM falls exactly on a beam harmonic, is set at  $<200$  k $\Omega$ , so if all 16 cavities have identical HOM frequencies, the longitudinal impedance must not exceed

12.5 k $\Omega$  per cavity. For frequencies higher than 600 MHz, the threshold is higher ( $\propto f^{5/3}$ ), but the same threshold was imposed. Modes with frequencies above 2 GHz are expected to be Landau-damped due to natural frequency spread and synchrotron oscillations.

In the transverse plane, the impedance threshold is set by the bunch-by-bunch feedback system with a damping time of  $\tau_D = 5$  ms [12]. Assuming the pessimistic case that the HOM frequency coincides with the beam harmonic, the maximum impedance is set to be  $<4.8$  M $\Omega$ /m. Again, assuming 16 cavities per beam, the maximum allowed impedance per cavity is 0.3 M $\Omega$ /m. Analogous to the longitudinal modes, frequencies above 2 GHz are expected to be Landau-damped due to natural frequency spread, chromaticity, and Landau octupoles. It should be noted that there are nominally only eight cavities per transverse plane, so the threshold per cavity is higher, but 0.3 M $\Omega$ /m is given assuming that the crossing plane between the experiments could become the same as a worst case scenario.

Due to the very tight impedance thresholds, the distribution of HOM frequencies due to manufacturing errors can help relax the tolerances. The beam power deposited in the longitudinal HOMs can become significant when the frequencies coincide with bunch harmonics. The HOM couplers were dimensioned to accept a maximum of 1 kW to be able to cope with HL-LHC beams [13].

#### 4.2.7 Higher order mode couplers

The first design goal of the HOM filter is to block the transmission of the main deflecting mode, while transmitting all remaining HOMs. Several HOM coupler designs were developed and optimized for different cavity geometries. Two high-pass filter designs, incorporating a notch filter at the fundamental frequency, are shown in Figure 4-6 with both HOMs using hook-like antennae to couple to the HOMs.

Simulations show that the HOM coupler must have a superconductive surface due to the high fields of the fundamental mode. A second design constraint requires that HOM couplers be able to efficiently remove the power in the HOMs (up to 1 kW) and the heat dissipated by the fundamental mode in the inner part of the HOM coupler from the cavity. High purity bulk niobium with sufficient cooling can ensure this. The required cooling may be possible by conduction, but the possibility of actively cooling with superfluid liquid helium or immersion in a small He tank is also under study.

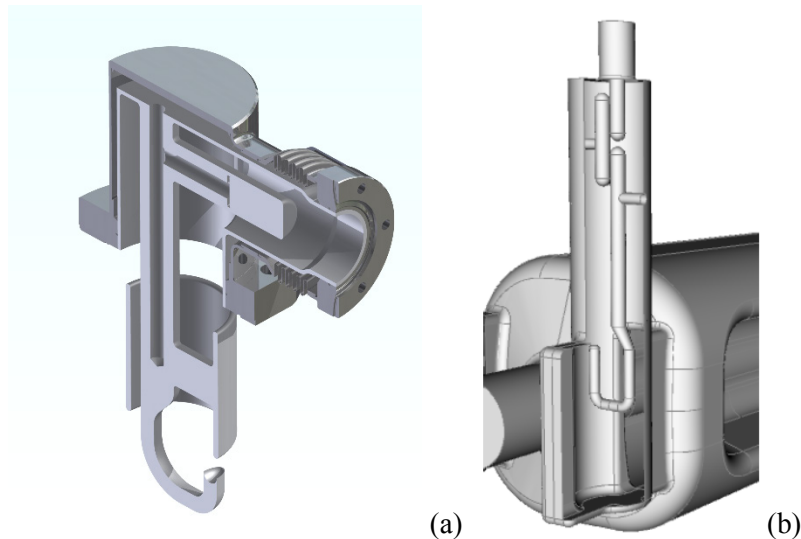


Figure 4-6: HOM filter for (a) DQW; (b) RFD

#### 4.2.8 RF multipoles

The crab cavity designs presently considered are such that they lack axial symmetry. Therefore, they can potentially exhibit all higher order components of the main deflecting field. Due to the placement of the cavities at high beta-function locations, the higher order components of the main deflecting mode can affect long-term particle stability. RF multipole components  $b_n$  of the RF deflecting field can be approximated and hence expressed in a similar fashion to magnets:

$$b_n = \int_0^L \frac{1}{qc} F_{\perp}^n dz \quad [\text{T m}^{2-n}]. \quad (4.1)$$

The quadrupolar component  $b_2$  is zero in the case of perfect symmetry; due to fabrication errors and ancillary components it is non-zero – it must be smaller than 10 units leading to a tune shift in the order of  $\Delta Q \approx 10^{-4}$ . The first systematic multipole is the sextupolar component,  $b_3$ . Long-term simulations with the optical functions of the HL-LHC indicate that the  $b_3$  component should be limited to approximately  $1000 \pm 10\%$  units, which results in an acceptable degradation of the dynamic aperture below  $1 \sigma$  for orbit offsets of 1.5 mm [1]. No specifications are yet provided for higher order terms, but it is expected that they be controlled to smaller values than the neighbouring D2 dipole magnet.

For  $n \geq 4$ , assuming a very approximate scaling of the additional kick from an orbit offset via  $b_n$ , the  $b_n$  must be kept  $< O(10^n)$ . Better estimates are pending; results from long-term tracking are needed.

#### 4.2.9 Lorentz force detuning and multipacting

When the cavity contains RF fields there is a Lorentz force on the cavity surface resulting from the high radiation pressure on the cavity walls. This results in a detuning of the cavity frequency. The Lorentz force detuning is kept small ( $\leq 0.6$  kHz) at the nominal field.

Another common problem in complex RF structures is multipactor. This is a resonant electron phenomenon where an electron follows a regular trajectory in the RF fields, where it strikes the surface with energy such that the number of secondaries produced is statistically likely to be greater than one. If these secondaries follow the same trajectory then the process will repeat causing an exponential growth in the number of secondaries. The electrons will absorb RF power, limiting the field to a finite level and depositing additional heat load in the walls. Initially the cavity surface may have an oxidized layer that will increase the secondary emission yield (SEY). However, multipactor also conditions the surface, removing this layer. If the multipactor disappears after processing or if sufficient power is available to overcome the multipactor it is termed a ‘soft’ barrier; otherwise it is termed a ‘hard’ barrier.

Multipactor was modelled in all cavities and couplers using two codes using different methodologies to identify multipactor. CST Particle Studio uses particle tracking with accurate secondary emission models to simulate the growth in electrons with time, while Track3P tracks a single particle in the RF fields and looks for resonant trajectories.

In CST three SEY models were used to look at the effect of surface cleanliness. The models were for wet treated, baked, and processed niobium surfaces. While multipactor in all cavities was found for the wet-treated and baked models, no multipacting trajectories were found for the processed surface, suggesting that any multipactor would be soft and easily processed through. Similarly, Track3P found multipactor at low field. This is in good agreement with the results from the prototype tests, where multipactor was observed and could be processed away easily.

#### 4.2.10 Cryomodule and integration

##### 4.2.10.1 Temperature choice

The BCS resistance of niobium at 4.5 K and 400 MHz is around 50 n $\Omega$ , which is more than 10 times larger than the value at 2 K. The complex shapes of the cavities may also be susceptible to microphonics caused by

liquid He boil-off, hence operation below the lambda point of He is preferred. For these reasons operation at 2 K is baseline. This will require the provision of liquid He at 2 K to the crab cavity location in the LHC. The current heat load limits for the LHC are not currently known, but are likely to be around 3 W of dynamic load per cavity at 2 K.

**4.2.10.2 Cavity interfaces and cold mass**

Following the recommendation of the May 2014 technical review [10], only two cavity designs are considered for the engineering design towards the SPS tests (DQW and RFD). The mechanical design of the cavities ensures their safe use under maximum loading condition during their entire life-cycle. The cavity was dimensioned to cope with several mechanical constraints: ensure elastic deformation during maximum pressure as well as during all transport and handling conditions; maximize tuning range; minimize sensitivity to pressure fluctuation; avoid buckling due to external pressure; and maximize the frequency of the first mechanical natural mode. The final mechanical design of the cavities including all external interfaces is shown in Figure 4-7.

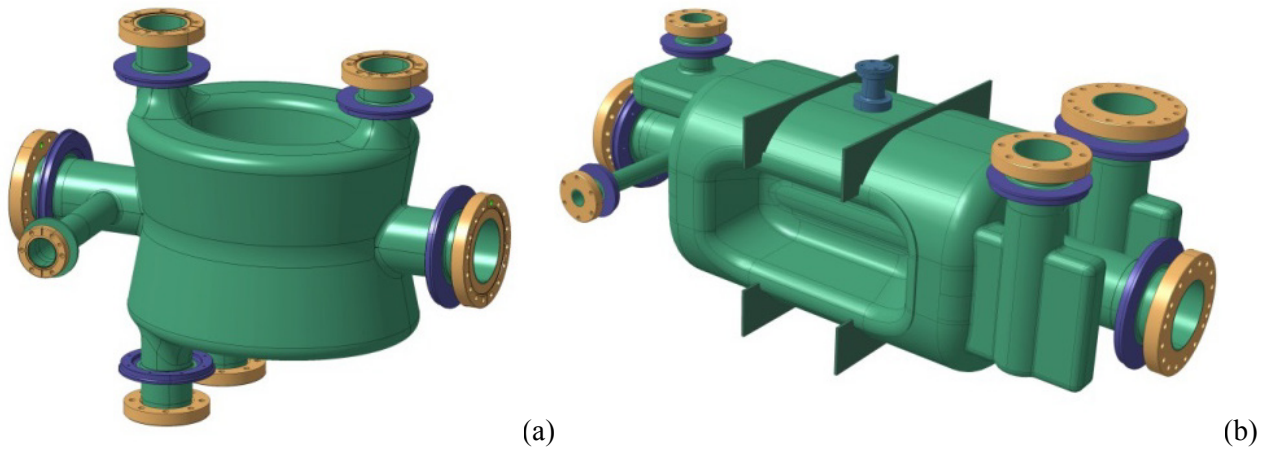


Figure 4-7: Schematic view of the cavity with interfaces (a) DQW; (b) RFD

The superconducting resonators are fabricated from bulk niobium sheets by electron-beam welding of deep-drawn parts. A final thickness of 4 mm was calculated to be acceptable in order to cope with all the mechanical constraints as well as minimizing the cost of cavity production. The cavities are bath-cooled by saturated superfluid helium at 2 K. Each cavity is equipped with: a helium tank, a tuning system, a fundamental RF power coupler, a field probe, and two or three HOM couplers. A functional specification including all tolerances for the cavity with its interfaces to develop manufacturing drawings for the DQW and the RFD are shown in Figure 4-8 and Figure 4-9, respectively.

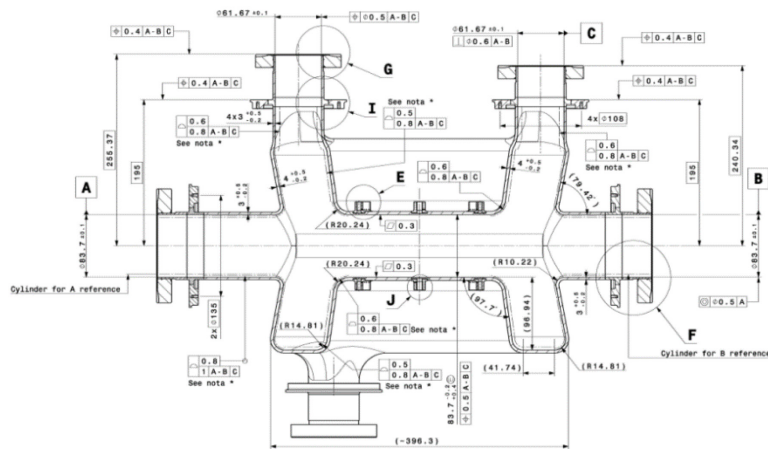


Figure 4-8: Dimensional plot with tolerances of the DQW cavity

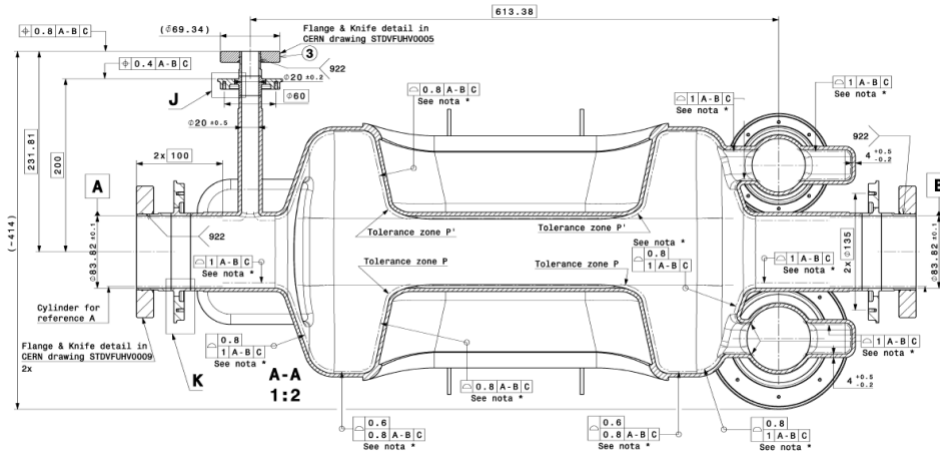


Figure 4-9: Dimensional plot with tolerances of the RFD cavity

### 4.2.10.3 Helium vessel and dressed cavity unit

The helium tank will contain saturated superfluid helium at 2 K, cooling the cavity and allowing the extraction of the heat dissipated in the cavity and adjacent cold components. Superfluid helium is an excellent thermal conductor for small heat flux. Above a critical heat flux, the temperature increases drastically and eventually superfluidity is lost. The geometry of the helium tank has been determined to allow this maximum heat extraction while optimizing the quantity of the helium to be used.

Two choices of material have been studied for the helium tank: stainless steel and titanium. Titanium has the advantage of the same thermal contraction as niobium (in the order of 1.5 mm/m from ambient temperature to 2 K), while the thermal contraction of stainless steel is twice as large, leading to larger thermal stresses. The advantage of stainless steel is the manufacturability and thus the cost. However, for the unconventional geometries of the crab cavities, titanium grade 2 was chosen as the optimum material for the helium tank, allowing for rigid connection of cavity ports to the helium vessel.

The helium tank has a structural role, and its rigid connection to the cavity ports ensures optimum boundary conditions for the cavity during mechanical loading, in particular during maximum pressure loading and tuning. The helium tank geometry was chosen to limit the maximum stress on the cavity to tolerable values [12]. Figure 4-10 shows a qualitative stress distribution in the cavity wall during maximum pressure. The red colour indicates only small areas of high stress, which are tolerable. This distribution, as well as the maximum values, are directly influenced not only by the cavity geometry but also by the helium tank configuration.

A major concern for the mechanical design were the transitions from the helium tank to all of the adjacent components, in particular the main coupler, HOM couplers, and the flanges for connection to the beam pipes and helium pipes. All flange connections are stainless steel to stainless steel connections. Due to its proximity, the second beam pipe had to be integrated inside the helium vessel and consequently will be at 2 K; it is proposed to use a niobium beam pipe. A schematic view of the DQW and RFD cavities inside their helium tanks and equipped with the required ancillary equipment are shown in Figure 4-11 and Figure 4-12.



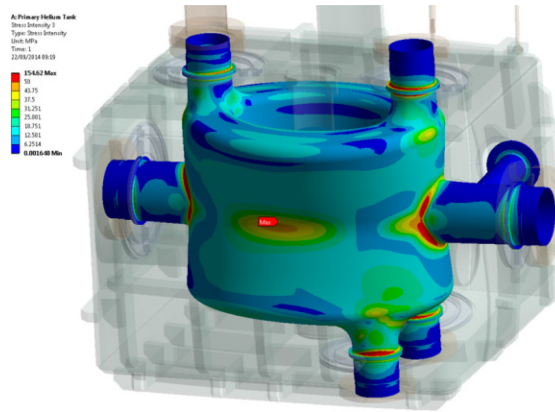


Figure 4-10: Mechanical stress induced by maximum pressure on the DQW cavity inside its helium tank. Red indicates regions with highest stress, which can be tolerated if confined to small areas.

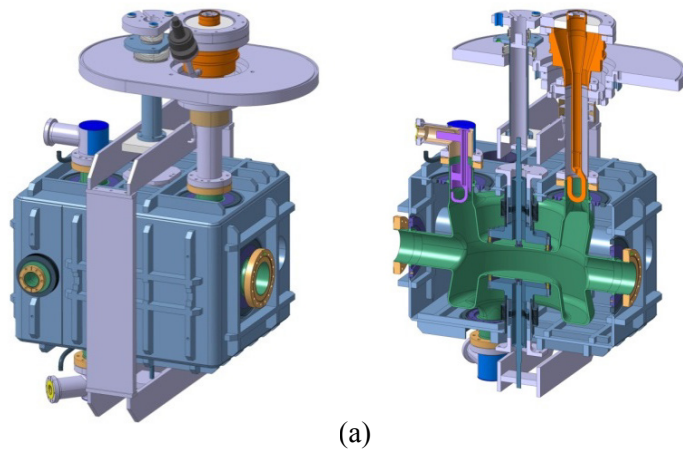


Figure 4-11: (a) The DQW cavity inside its helium tank with the field probe port (front), beam port (right) and tuner frame around. (b) Sectional view of the DQW cavity inside its helium tank with the power coupler (top right, orange), HOM coupler (left, top and bottom), and tuner (centre, top, and bottom).

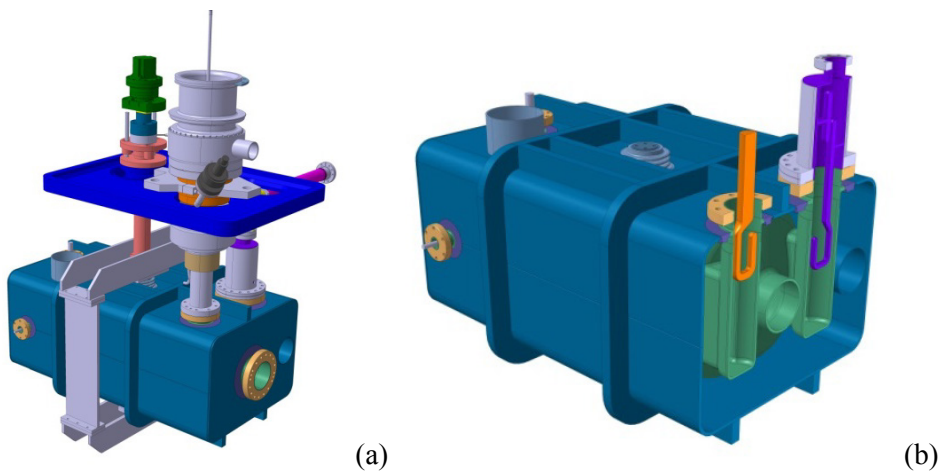


Figure 4-12: (a) The RFD cavity inside its helium tank with the field probe port (centre left), beam port (centre right), tuner frame around helium vessel and tuner actuation (top centre). (b) Schematic sectional view of the RFD cavity inside its helium tank with the power coupler (orange) and HOM coupler (violet).

#### 4.2.10.4 Frequency tuning

The final resonance frequency of the cavity will depend on a number of fabrication and handling steps and cool-down (hundreds of kHz). A ‘slow’ mechanical tuning system is required to compensate for the uncertainties of the above steps by altering the cavity shape – this will dominate the tuner requirement. At 2 K, it must be possible to tune the cavity to  $f_{\text{res}} = f_{\text{operation}} \pm \Delta f_{\text{LFD}}$ , where  $\Delta f_{\text{LFD}}$  denotes Lorentz force detuning occurring during cavity filling. The operating frequency can vary by an additional 60 kHz (cf. Section 4.2.18.5). Despite the large resulting tuning range ( $\approx \pm 200$  kHz) the resolution of the tuner should allow at least four steps inside the cavity bandwidth ( $\approx 800$  Hz); backlash and hysteresis must be small.

The tuning system, similar for both cavities (DQW and RFD), is shown in Figure 4-11 and Figure 4-12. It consists of an actuation system that is placed outside the cryomodule, and operated at room temperature and at atmospheric pressure, which makes it accessible and thus maintainable. The actuation system consists of a stepper motor, a harmonic gearbox, a roller screw, and linear guide bearings. The concept is based on a design developed and already in use at JLAB. The details of the prototype actuation system are shown in Figure 4-13. Since the cavity will be operated in continuous wave (CW) mode and frequency variations are expected to be small, active tuning with piezoelectric actuators may not be needed in the final design. A piezo is, however, foreseen for the first cavity tests to validate this assumption.

Actuation induces a relative movement between two titanium cylinders. The inner cylinder is directly connected to the top of the cavity, the outer cylinder to the bottom via a titanium frame. A symmetric deformation is thus applied simultaneously to the top and bottom of the cavity.

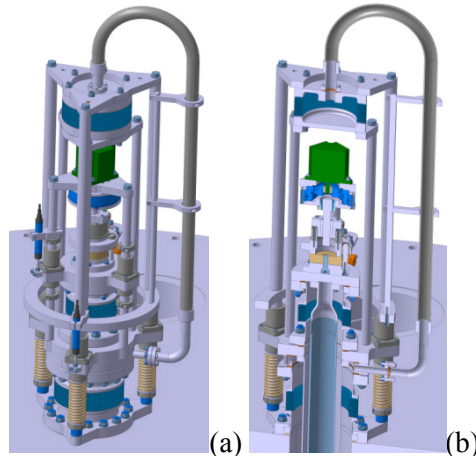


Figure 4-13: (a) Actuation system of the prototype tuning system for DQW and RFD cavities. (b) Cross-section.

The estimated mechanical resolution of the tuning at the connection to the cavity is estimated to be in the order of  $0.1 \mu\text{m}$ , which is equivalent to a few tens of Hz for both cavities, allowing for at least 10 micro-steps inside the cavity RF frequency bandwidth.

Low frequency mechanical resonances (below 150 Hz) should be avoided to minimize cavity perturbation due to both helium pressure fluctuations  $\mathcal{O}(1 \text{ mbar})$  and external noise sources. Resonances above 150 Hz are considered to be benign. If fast-acting tuners (piezos) are deemed necessary, they should be able to compensate for deformations of  $\leq 10\text{--}20 \mu\text{m}$  to reduce the RF power overhead (see Figure 4-14).

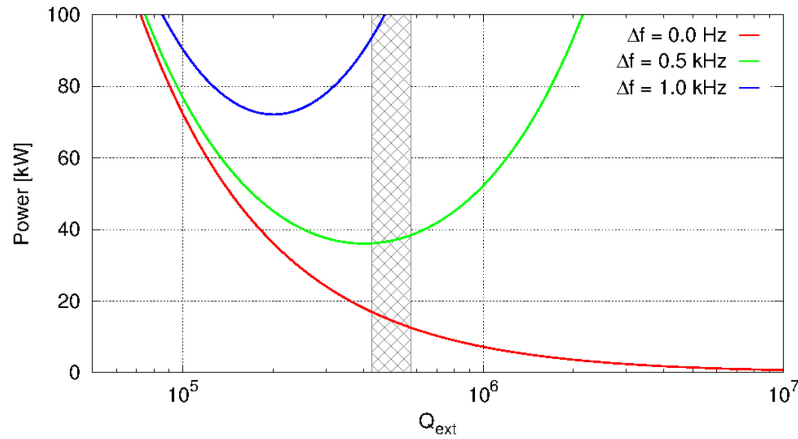


Figure 4-14: Forward power requires a function of  $Q_{\text{ext}}$  for different detuning of the cavity. The cross-hatched area indicates the nominal range of  $Q_{\text{ext}}$ .

#### 4.2.10.5 Space, modularity, and the second vacuum chamber

Machine architecture and integration studies for the LHC led to the choice of housing two individual cavities in stand-alone cryomodules, individually connected to a cryogenic distribution line cryostat running in parallel with the main line. The nominal configuration will use a two-cavity cryomodule as a basic unit. As a consequence, a total of eight cold-to-warm transitions for the beam tube and four connections to the cryogenic distribution line are required for one side of an LHC interaction region (Figure 4-15).

The length of the cryomodule depends on the cavity type and, for the longest cavity, results in a total of 13.4 m for eight cavities (four cryomodules) per side of the LHC interaction region for both beams including gate valves from the interconnection plane, as shown in Figure 4-15. For each two-cavity module, two gate valves inside the cryomodule vacuum (see Figure 4-16) and two valves outside at ambient temperature are foreseen.

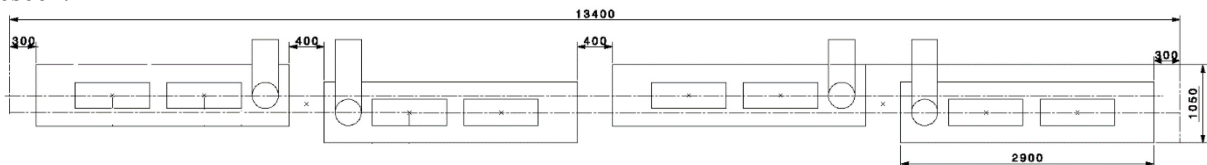


Figure 4-15: Cryomodule layout for one side of the interaction region in the LHC

A detailed view of the cryomodule containing two DQW and RFD cavities is illustrated in Figure 4-16. The fixed RF coaxial coupler, with a single ceramic window, providing 80 kW average power, is mounted onto the cavity via a ConFlat™ flange assembly equipped with a specific vacuum/RF seal designed at CERN and widely used elsewhere.

The RF coupler is mounted on the cavity in the clean-room, constraining the assembly of subsequent components of the cryomodule due to its size. The vacuum vessel was designed in three parts and uses a lateral assembly procedure for the cavity string inside the vessel [16]. This allows the possibility of cavity alignment with optical devices (laser trackers, for example) while making fine adjustments through the adjustable supports before closing the cryomodule lateral covers.

The cavity supporting concept uses the external conductor of the RF coupler as the main mechanical support of the dressed cavities. An additional supporting point to keep cavity alignment stability within requirements is obtained by the inter-cavity support. In the RFD cavity, the power coupler is transversely offset from the cavity axis, which requires additional vertical support, as shown in Figure 4-16(b).

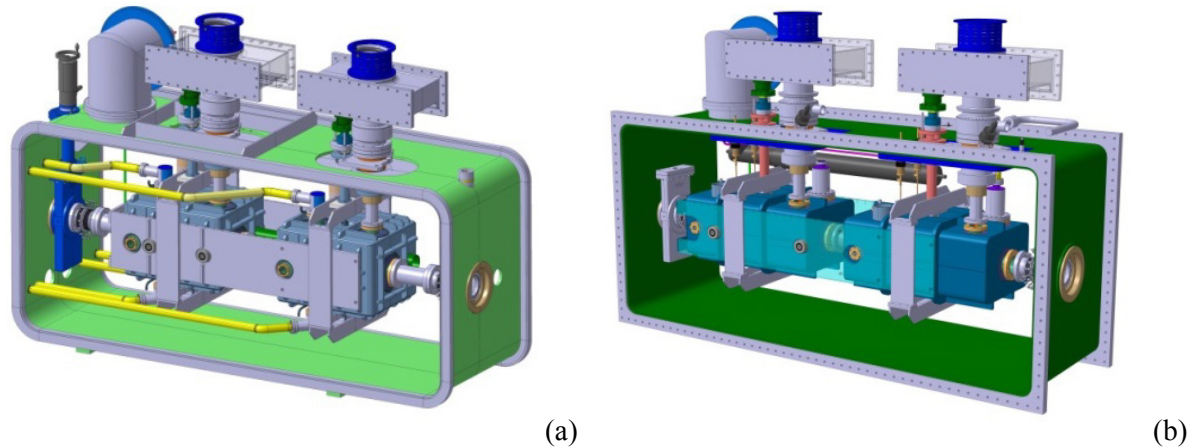


Figure 4-16: Cryomodules for (a) DQW cavity; (b) RFD cavity

For the LHC cryomodule, two options are considered. The baseline consists of four cryomodules per side per IP, each with two cavities similar to the SPS test prototype cryomodule. This would have the advantage of a topology similar to that having been tested in the SPS. The overall design would probably become simpler than for the SPS test prototype cryomodule. As a second option, a single eight-cavity cryomodule could be considered, optimized for LHC operation requiring less access and minimizing cold-to-warm transitions.

Currently only the SPS test cryomodule exists with full technical specifications. The cryomodules are designed to have a rectangular outer vacuum vessel with removable side panels such that the dressed cavities are side-loaded into the vessel [16]. All external connections except the beam pipes are on the top of the cryomodule. The cavities are supported by the power couplers. This allows easy access, as required for a prototype. This design requires several stiffening ribs to keep the stress within reasonable limits when placed under vacuum pressure and during cool-down. The designs for both cavity variants are kept as similar as possible.

#### 4.2.10.6 Magnetic and thermal shielding

Assuming a cavity geometric factor of  $G \approx 100 \Omega$ , the additional surface resistance due to trapped flux  $R_{mag}$  required to be below 1–2 n $\Omega$  to stay in the shadow of the total surface resistance specification of 10 n $\Omega$ . To achieve this, magnetic shielding in the cryostat should reduce the external magnetic field on the outer surface of the cavity by a factor of at least 100 (reducing the earth's magnetic field to <1  $\mu$ T).

The external warm magnetic shield is made of 3 mm thick mu-metal and will be directly attached to the vacuum vessel. Due to the large apertures in the shielding for couplers and beam pipes, this layer on its own is not sufficient to completely shield the earth's magnetic field to the required level with sufficient safety margin. Figure 4-17(b) shows the magnetic field amplitude inside a two-cavity cryomodule without an internal shield for an applied external shield of 60  $\mu$ T in the longitudinal direction. To meet the magnetic field requirements a second shield is required close to the cavity. In order to reduce the size of the holes in the internal shield the cold magnetic shielding will be integrated inside the helium vessel, as presented in Figure 4-17(a). The internal shield is 1 mm thick and will be made from Cryoperm or Aperam Cryophy. Magnetization of both materials is adversely affected due by stress. Hence, degradation of the shielding material during assembly and handling should be carefully studied and monitored. Effects of weight and thermal stresses were modelled in ANSYS, as shown in Figure 4-17. The simulations indicate that while the maximum stress is 439 MPa in the titanium supports, the stress on the shield is kept to less than 150 MPa. It is possible that this may affect the magnetization locally, but the effect is comparable to that of a small hole in the shield. Simulation results from OPERA, assuming the worst case field orientation, show that the use of the proposed two-layer shielding solution to achieve magnetic fields well below 1  $\mu$ T is feasible, as shown in Figure 4-17(b) [17].

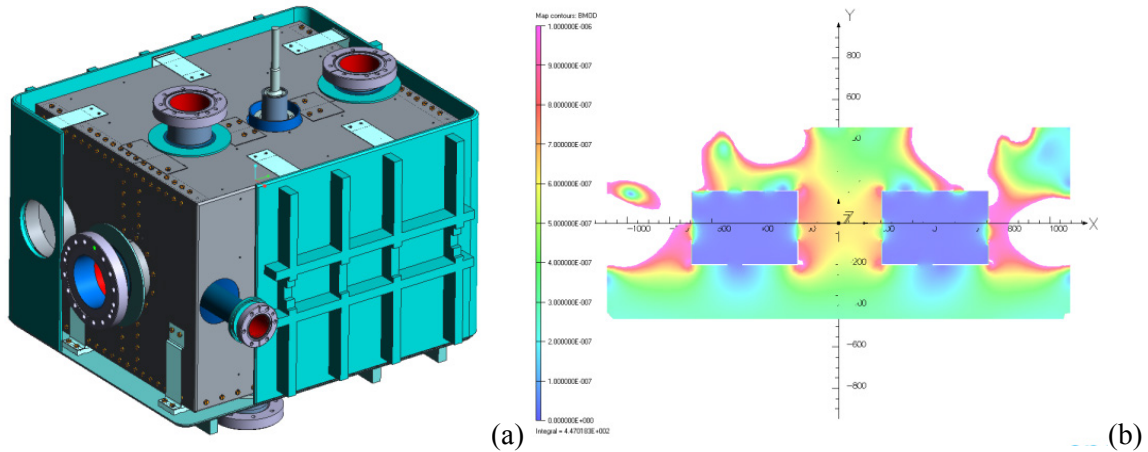


Figure 4-17: (a) Cold magnetic shielding inside the helium vessel; (b), magnetic field amplitude inside the two-cavity CM without the second internal cold magnetic shield, scale 0 to 1  $\mu\text{T}$ . An external field of 60  $\mu\text{T}$  in the direction parallel to X (longitudinal) is used.

The thermal shield is made of rolled aluminium sheets. The shield is suspended from the vacuum vessel via flexible guides made from titanium alloy that also copes, through angular movements, with its thermal contractions. The absence of mechanical contact between the shield and the string of cavities eliminates the risk of interference with the alignment of the cavities induced by differential contractions and cooling transients. The cryomodule contains a single thermal shield, actively cooled in the LHC at about 50 K by a cryogenic cooling line containing pressurized helium gas. For the SPS tests, this active cooling will be done with pressurized liquid nitrogen. A 30-layer prefabricated Multi-Layer Insulation (MLI) blanket protects the thermal shield whereas a 10-layer blanket is mounted around each helium vessel.

#### 4.2.11 RF powering and control architecture

The overall architecture and approximate volume of the RF infrastructure is shown schematically in Figure 4-18. Near P1 and P5, the existing caverns closest to the cavity (RR caverns) are approximately 80 m away, while requiring a large space in the tunnel to pass the RF transmission lines along this distance. Radiation concerns rule out the installation of highly sensitive RF electronics in those caverns. Therefore, two remaining options are under study.

- RF gallery near crab cavities. The longitudinal range would be approximately 155 m from IP1 and IP5 on either side in a gallery parallel to the LHC tunnel. Access to the gallery is required with RF on and field in the cavity, but without circulating beam.
- Surface option. The longitudinal range is similar to that given above, preferably above the crab cavity locations on the surface on either side of IP1 and IP5. To minimize the high power RF transmission line dimensions, the circulator and load are assumed to be in an extended tunnel alcove close to the cavity.

An independent powering system using LEP-type 400 MHz tetrodes (or an equivalent Inductive Output Tube, aka IOT) of 40–80 kW is assumed. Recent advances in solid-state technology could eventually lead to power sources in the required power range and may provide a cheaper and more robust platform. The tetrodes provide adequate power overhead in a compact footprint. This scheme would also allow for fast and independent control of the cavity set point voltage and phase to ensure accurate control of the closed orbit and the crossing angle in the multi-cavity scheme. Most importantly, fast control of the cavity fields will minimize the risk to the LHC during an abrupt failure of one of the cavities, ensuring machine protection before the beams can be safely extracted. For such fast and active feedback, a short overall loop delay between the RF system and the cavity is required [11].

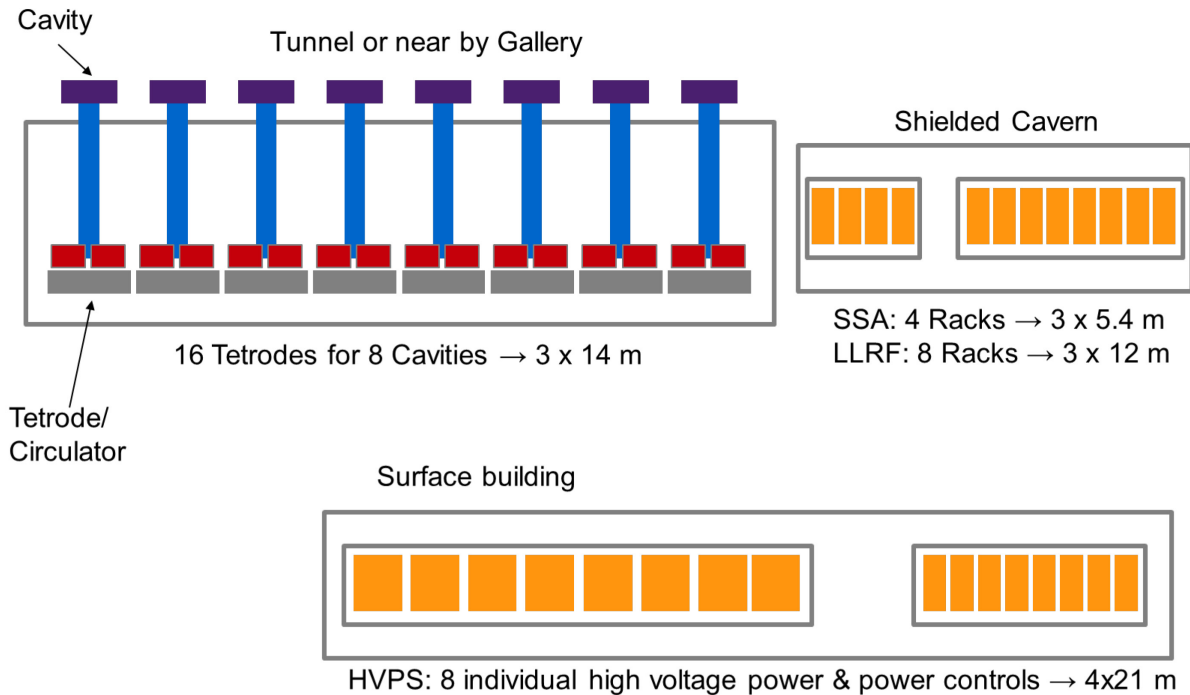


Figure 4-18: Schematic of the RF system layout in (a) the LHC tunnel; (b) the electronics racks in a shielded cavern close to the cavities; (c) the surface building. Note that these are only estimated values of space requirements.

To provide strong feedback, the low-level RF system requires the total loop delay to be approximately  $1\text{--}2\ \mu\text{s}$ . This includes the group delay from the driver, amplifier, circulator, and cable delays. Therefore, a distance of less than 100 m is desired for the separation between the amplifier, electronics, and the cavity in the tunnel. Such a short delay is already in place for the ACS main RF system in P4 (650 ns loop delay) with a service gallery running parallel to the tunnel.

The controls and driver electronics are required to be located in a radiation-minimized zone. Assuming two tetrode amplifiers per cavity to provide 80 kW and electronics racks required for drivers, PLC, LLRF, and fast interlocks for eight cavities per IP side, an area of approximately  $100\ \text{m}^2$  is needed near the cavities. The high-voltage power supplies and the power controls would need an additional  $85\ \text{m}^2$ , which will nominally be placed on the surface. If all high- and low-power RF and controls are placed on the surface, an equivalent of  $185\ \text{m}^2$  will be required there. The proximity of the circulator and RF loads to the cavity will allow for smaller RF transmission lines from the surface to the tunnel.

A total height of approximately 6 m is estimated for the high-power RF, controls, and services, distributed over two levels. This allows a minimum space of 3 m for the equipment racks, amplifiers, etc. while leaving 3 m height directly underneath cooling pumps, cabling, and services, see Figure 4-19. Alternatively, additional volume adjacent to the building to accommodate the pumps, ventilation and other required units for high power amplifiers can be envisioned to limit the height. All 'surface' buildings could actually be underground and would not occupy any surface area. The required electrical interfaces are specified in Ref. [18]. A study is ongoing to determine the feasibility of the civil engineering with minimal perturbation affecting the LHC [19].

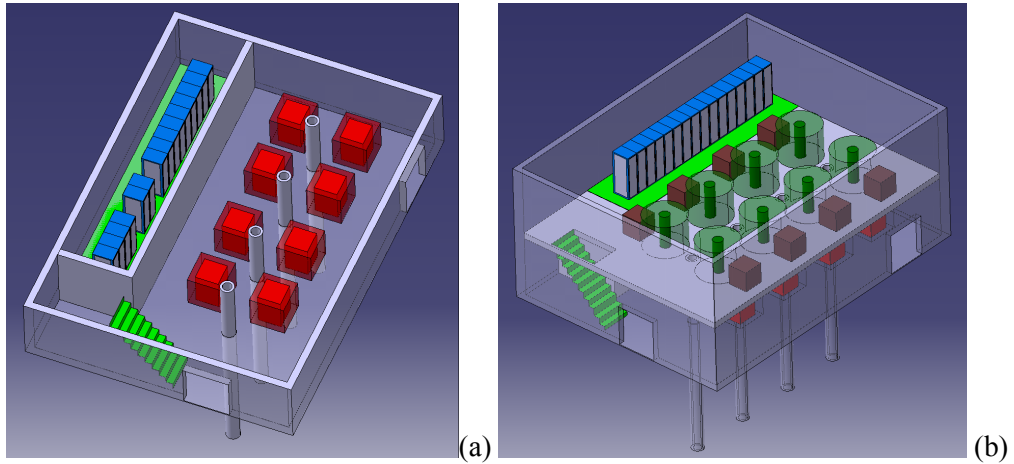


Figure 4-19: Preliminary sketch of a high-power RF, controls and LLRF layout in a surface building, distributed over two levels. (a) Lower level containing pumps and general services; (b) upper level containing RF amplifiers and equipment racks. Courtesy of C. Magnier and P. Fessia.

4.2.12 Low level RF architecture and operational scenarios

The RF control system, also commonly referred as the low level RF system (LLRF), includes several functionalities. First, a tuning control is required to keep the cavity resonant frequency on-tune with the beam during the crabbing operation. If required, the LLRF also has to ensure that the cavity is safely parked at an optimal detuned position during filling, ramping, and collisions without crabbing. This system also synchronizes the phase of the RF kicks with the exact passage of the bunches for both beams. The LLRF includes a regulation loop around the amplifier (to reduce the RF amplitude noise and phase noise in a band extending to a few tens of kHz), plus an RF feedback to control the cavity field precisely. The feedback loop consists of both a local loop around the cavity-amplifier and a global loop regulating the vector sum of voltages on the two sides of the interactions’ region. The global loop will reduce beam perturbation following a single cavity trip, by quickly reducing the field in the companion cavities to track the uncontrolled voltage in the faulty cavity. The beam dump system has a three-turn (270  $\mu$ s) response delay.

For each ring, the eight accelerating cavities (ACS) are driven from a single reference generated in a surface building above IP4. These two signals must be sent over phase-compensated links to IP1 (ATLAS) and IP5 (CMS). The eight crab cavities of a given ring at each IP are coupled with an 8-in, 8-out multi-cavity feedback (MFB). Figure 4-20 shows the proposed architecture.

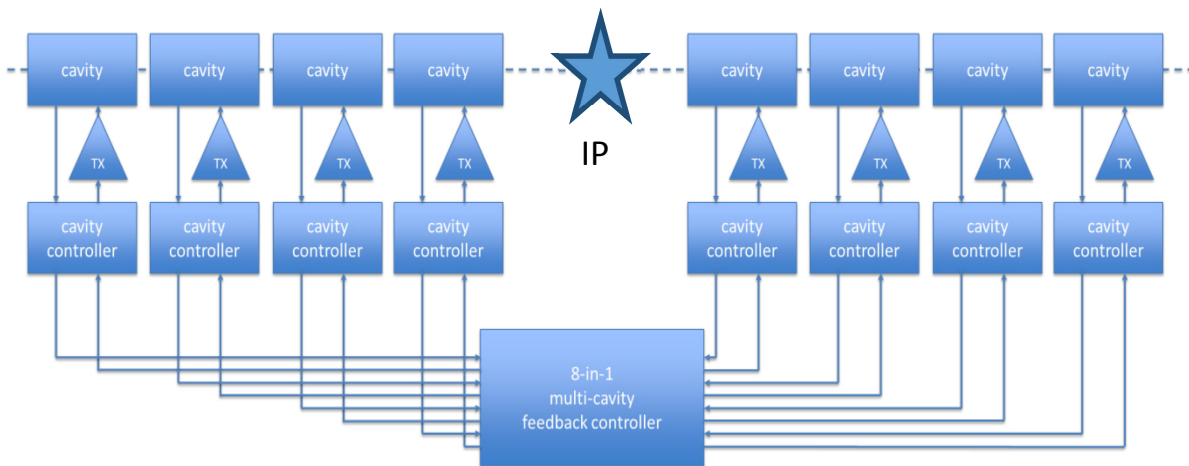


Figure 4-20: Proposed LLRF architecture for one ring at one IP

A central controller receives measurements from all relevant cavities on each ring and IP, and makes corrections to the drive of each individual TX. If the field starts changing in a cavity, the MFB will adjust the field in the other cavities on both sides of the IP, such that the orbit distortions remain local. As described in Section 4.2.5 on flat-top, counter-phasing is nulled while keeping the voltage set point small. The RF feedback keeps the cavity impedance small (beam stability) and compensates for beam loading as the cavity moves to resonance. The voltage set points are ramped to synchronously change the voltage in all crab cavities as desired. Any levelling scheme is possible. With a circulator between amplifier and cavity, the TX response is not affected by the cavity tune.

At present the spacing between LHC bunches within a batch is strictly constant along the ring. A large amount of RF power is used in the ACS system to fully compensate the transient beam loading caused by the 3  $\mu$ s long abort gap and the smaller gaps required for the injection kicker ('half detuning'). This scheme cannot be extended into the HL-LHC era as it would require excessive RF power. The power required is minimized by optimally detuning the cavity ('full detuning') and adapting the cavity set-point phases bunch by bunch. It results in bunch arrival time modulation of up to  $\pm 42$  ps [20]. This may be acceptable given the 1 ns bunch length. There is no effect on the luminosity as the modulation is identical in both beams, only the vertex position is modulated around the nominal vertex by a maximum of 1  $\mu$ m over one turn. The bunch-to-bunch variation within a batch is at least an order of magnitude smaller. If not, the LLRF must synchronize the bunch-by-bunch crabbing field with the actual phase modulation.

#### 4.2.13 Cavity failure scenarios

Crab cavity failures can lead to a fast voltage and/or phase change with a fast time constant. This can lead to large, global head-tail oscillations, or coherent betatron oscillations with a change in transverse beam trajectories of  $1.7 \sigma$  for a single cavity failure; the effect is cumulative with the number of failing cavities. These failures can be broadly classified into two categories.

- Fast failures, single or few turns. For example, a sudden cavity quench or breakdown.
- Slow failures, several tens of turns or greater (caused by vacuum degradation, voltage and phase drifts, or similar).

Due to the relatively high quality factor in the superconducting cavity, the stored energy inside the cavity can typically only be extracted with a time constant determined by  $Q_L$ , which results from the strong coupling to the cavity via the power coupler. The stored energy will decay with a time constant  $\tau = 2Q_L/\omega_0$ . For  $Q_L = 5 \times 10^5$ , the time constant is approximately 400  $\mu$ s. The three turn delay time (267  $\mu$ s) for a beam dump trigger is an important consideration during a RF source failure, where the cavity field decays to roughly half its value before the beam can be safely aborted. In the case of a quench, the time constant of field decay may be dominated by the quench dynamics rather than  $Q_L$ . The situation is similar due to strong and sudden electron loading due to multipacting or other phenomena.

The cavity quench mechanism described above and measurements from KEKB crab cavities [21] indicate that typically a quench is a slow thermal process (typically of the order of several milliseconds). Once the temperature of a sufficiently large area exceeds the critical temperature of niobium, the quench can propagate very quickly to completely quench or cause RF breakdown. However, any change in cavity quality factor well before reaching a critical temperature limit could be easily detected from the requested forward power (fast) or changes in the cavity temperature bath (slow). An interlock on the forward power, except due to induced orbit excursion, can cut the RF to slow down or stop quench propagation. A beam abort, if required, can be triggered simultaneously (a few  $\mu$ s) for machine protection.

#### 4.2.14 Failure scenario mitigation

The choice of low operating temperature (2 K) and moderate surface field levels allow operation with an ample margin over quench temperature and field limits. The significantly better thermal conductivity of superfluid helium should also improve the thermal performance and stability of the cavity. Additional measures in the



cryomodule design are being considered to dimension the helium enclosures with sufficient margin for heat flux. The cavity thermal and RF stability will be thoroughly tested in the SM18 test facility and during the SPS beam tests.

To minimize the perturbation on the beam during a cavity failure, the MFB will adjust the field in the other cavities on both sides of the IP, such that the orbit distortion remains local. Figure 4-21 shows the cavity control of two cavities across the IP with one cavity failure and the RF controller to adjust the second cavity to follow. The rapid change in field will also result in a detuning of the cavity; however, the mechanical tuning system is unable to adjust the tune within 400  $\mu\text{s}$ . Since a rapid breakdown of a failed cavity may become unpredictable, it is probably safest to ramp down the cavities synchronously. However, small and slow changes in one of the cavities can be adjusted for without aborting the beam.

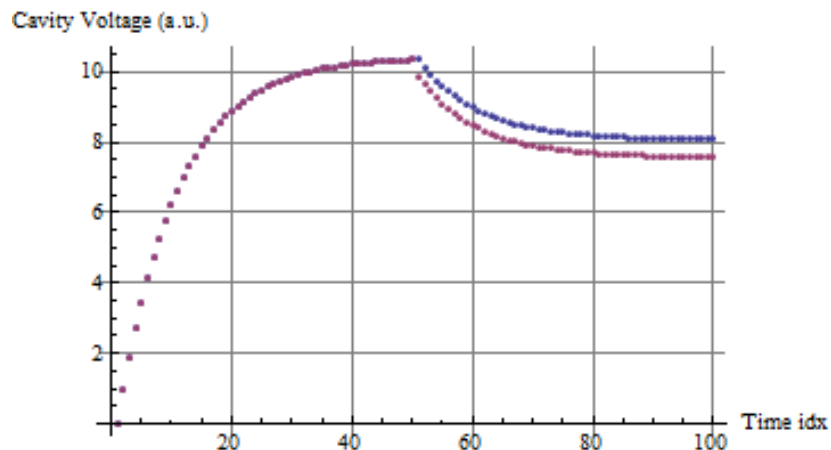


Figure 4-21: Voltage response with strongly coupled cavities across the IP as a function of time [ $\mu\text{s}$ ]. At 50  $\mu\text{s}$ , one cavity trips (red trace) and the other one is forced by the RF controller to follow (blue trace).

The cavities can be equipped with a fast tuning system such as a piezo mechanism. If the speed of such tuning devices is sufficient, it could compensate for Lorentz force detuning during transients and thus keep the tune within the bandwidth of the feedback system.

An additional mitigation to avoid large beam losses (and hence deposited energy) in the case of single or multiple cavity failure is a robust measurement and interlocking of the tail population and eventual head–tail oscillations. This could be achieved with new equipment such as a hollow electron lens for cleaning of the bunch tails and interlocking with improved diagnostics like fast head–tail monitors and/or fast beam loss monitors (e.g. Diamond monitors).

#### 4.2.15 Heat loads and cryogenics

The cavities are housed in individual titanium helium tanks connected by a 100 mm diameter two-phase He pipe placed above the cavities. This pipe ensures that liquid is fed to the cavities by gravity, and is also used as a pumping line for gaseous helium. A saturated helium bath maintains the cavities operating temperature at 2 K. Liquid helium is supplied to the two-phase pipe through a capillary. It is proposed to fill from one single point at one extremity of the two-phase pipe, and control just the He level in the phase separator. The static plus dynamic heat loads are expected to be approximately 30 W to the 2 K bath for a two-cavity module. The cryogenic limits in the LHC are not precisely known at this time. However, the 15 W per cavity heat load at 2 K is small compared to the LHC heat load capacity; the total heat load of the LHC crab cavity systems is estimated at 0.5 kW at 2 K.

#### 4.2.16 Vacuum system

The crab cavity system has three independent types of vacuum systems: the cavity vacuum, the adjacent beam pipe, and the cryostat. The two-cavity common vacuum is pumped at room temperature with two ion pumps mounted at each end of the modules. However, at 2 K, the cryogenic pumping of the cavity walls is the dominating feature, with a pumping speed of 10 000 L/s. The background pressure without RF is expected to be much better than  $10^{-10}$  mbar and likely limited by the measurement devices such as Penning gauges. Pressure signals provided for RF control are a hardware interlock from the ion pumps to cut the high voltage and readout from the Penning gauges, one per coupler, to limit the RF power. The cavity vacuum can be isolated by two all-metal valves at the ends of each module, to maintain vacuum during transport and installation.

The second beam pipe for the counter-rotating beam has to pass through the cavity helium vessel due to its proximity. It is planned that this will be made of niobium and will remain superconducting at close to 2 K to preserve the same surface conditions as in the cavity. The use of carbon coating in the warm regions near the crab cavities to reduce the pressure and to avoid electron cloud effects is currently not considered; this would risk contamination of the cavities.

The insulation vacuum is less demanding in terms of pressure, the modules being pumped to  $10^{-5}$  mbar before being cooled down. When cold, the insulation vacuum also benefits from the cryogenic pumping of the cold surfaces and the operating pressure will decrease to  $10^{-7}$  mbar. Turbo molecular pumps are used and pressures are measured using Penning gauges. Intense gamma radiation could be produced during cavity RF conditioning and operation of high fields.

#### 4.2.17 Interlocks for machine protection

Due to the immense stored energy ( $>700$  MJ), the transient behaviour of the crab cavities is of concern. The crab cavity system will be equipped with several levels of interlocks both for machine protection and to protect the RF system itself. Slow and fast interlocks, including specific RF interlocks (reflected power, signal level, arc detection, etc.) will ensure safe operation under all conditions and cope with transients; the interlock system will be fully embedded in the overall machine interlock system. All RF systems, including amplifiers, circulators, and loads are designed to withstand full reflection in the case of a malfunction in the RF chain.

#### 4.2.18 SM18 and SPS beam tests

The addition of crab cavities to the LHC should ensure robust functioning through the entire sequence of the LHC physics cycle. Since crab cavities of this type have yet to be realized and used with hadrons, beam tests with a prototype two-cavity cryomodule are a prerequisite to identifying potential risks from the technology to safe and reliable operation of the LHC. Therefore, an essential milestone for a crab cavity in the SPS is to demonstrate machine protection and cavity transparency. All RF manipulations and cavity-beam interactions will first be validated and commissioned in the SPS with the prototype module. The beam tests are planned as machine development studies during the run 2017–2018. Successful validation of the crab cavities in the SPS is a prerequisite for installation in the LHC.

##### 4.2.18.1 Tests before installation

The two cavity cryomodule will be assembled in SM18 with the cold masses (cavities, helium vessels, HOMs, and tuner) provided by the LARP collaboration. The cold masses are tested and qualified in the US to their final specification and delivered under vacuum to the SM18 facility. Only the assembly of the power coupler in SM18 is foreseen, due to the risk associated with damage during transport.

The assembled SPS cryomodule in its final assembly, along with all of the other major components, will be tested for vacuum integrity, RF performance, and operational reliability in the SM18 horizontal bunker to their nominal specifications prior to installation in the SPS. The RF control and interlock system will also be validated in SM18.

#### 4.2.18.2 SPS environment

The SPS ring is equipped in LSS4 (currently used for the COLDEX experiment) with a special bypass (Y-chamber) with mechanical bellows that allows for horizontal displacement. This allows for a test module to be moved out of the beam line during regular operation of the SPS and only moved into the beam line during the periods dedicated to studying the crab cavity test module with beam. This setup is essential both due to aperture limitations of the crab cavities and the risk associated with leaving the cavities in the beam line with different modes of operation in the SPS. The cryomodule is placed on a movable table that can be moved sideways by 510 mm (see Figure 4-22). A special working group (crab cavity technical coordination) has been set up to follow up the various integration issues including the RF and cryogenic systems.

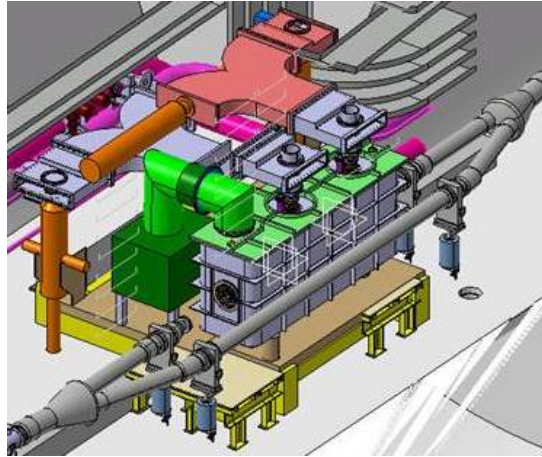


Figure 4-22: 3D integration of the cryomodule, RF assembly, and the cryogenics in the SPS

The relevant cryomodule envelope dimensions for the SPS tests is given in Table 4-3. In general, the SPS constraints are tighter than those of the LHC.

Table 4-3: Cryomodule envelope dimensions

Description	Distance [mm]
Cryomodule length (gate valve to gate valve)	3000
Horizontal distance cavity axis to inner edge of cryomodule volume	420
Vertical distance, floor to cavity axis	1200
Maximum height above cavity axis	1200
Inner diameter of cavity beam pipe	84
Horizontal distance cavity axis to bypass beam pipe axis	510

#### 4.2.18.3 SPS RF system and operation

Specially designed WR2300 will feed the RF power from the tetrode amplifiers to the respective cavity (see Figure 4-23). Placement of the amplifiers on the movable table will depend on the full integration of the cryomodule, transmission lines, and circulator. An LHC-type circulator, although over-dimensioned, is preferred for reasons of maintenance and spares policy. A 3D integration of the cryomodule and the RF assembly in the LSS4 region is shown in Figure 4-22.

In the LHC, the four cavities per IP side are always powered on tune, initially with a small voltage (10%–15% of the nominal) and counter-phased with active feedback to guarantee maximum beam stability during the entire cycle. Therefore, beam injection with counter-phased cavities with low voltage requires testing in the SPS. Other issues related to beam loading and transient effects with and without RF feedback and slow orbit control will be studied to evaluate the stability and tolerances required from the feedback systems. Induced RF trips and their effects on the beam will be studied in detail to guarantee machine protection

and to devise appropriate interlocks. Long-term effects with crab cavities on coasting beams at various energies will also be tested.

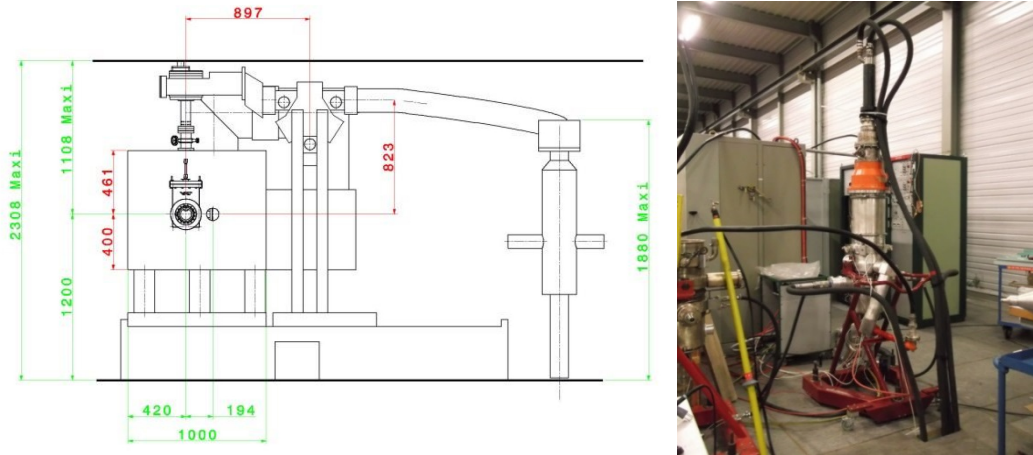


Figure 4-23: (a) Cryomodule and RF system layout in the LSS44 cavern; (b) a 400 MHz tetrode amplifier under test.

#### 4.2.18.4 SPS cryogenics requirements

The SPS-LSS4 region is currently equipped with the TCF20 cryogenic box. It was originally planned to upgrade the existing cold box to deliver 2 K helium for the operation of the crab cavities [15]. Due to the very limited capacity available in the SPS TCF20 refrigerator, the total losses (static and dynamic) are limited to a maximum of 25 W (at 2 K). The heat load of the two-cavity cryomodule, however conservative, is at least 15% higher than the TCF20 capacity. A replacement for the TCF20, increasing the capacity to approximately 40 W, is planned to be put in place for the SPS tests [15]. Despite the plan to increase the capacity, a strong effort is being made to minimize the heat load of all cavity elements and cryomodule interfaces to ensure a successful beam test in the SPS prior to any installation in the SPS.

#### 4.2.18.5 SPS tuning requirements

For beam tests in the SPS a slow mechanical tuner system is required to bring the cavity on resonance in the energy range of the SPS (0–60 kHz). In addition the tuner must allow detuning of the cavity to its parking position, and it has to be precise enough to work together with the RF feedback. Table 4-4 summarizes the potential energies at which the SPS can be operated for crab cavity tests and their corresponding RF frequencies compared with that of LHC operation.

Table 4-4: Detuning ranges for the LHC and SPS

Parameter	Unit	LHC	SPS		
Energy	[GeV]	450–7000	120	270	450
Frequency	[MHz]	400.79	400.73	400.78	400.79
$\Delta F_0$	[kHz]	0	-58.2	12.2	-2.4
Bandwidth	[kHz]	0.4–4	0.4–4	0.4–4	0.4–4
Detuning	[Hz]	$\pm 5.5$	$\pm 21.7$		

The detuning required to tune the cavity in its parking position (between betatron lines) is approximately  $\pm 21.7$  kHz in the SPS. The detuning requires a resolution of at least one-quarter of the final cavity bandwidth due to available power limits. Additional studies have to be carried out to verify if a tuning speed higher than that possible with the mechanical tuner is required if limitations arise from feedback and/or orbit control.

#### 4.2.18.6 SPS test objectives

The test programme objectives in the SPS are given below.

- Demonstration of cavity deflecting field with proton beam including injection, energy ramp, and coast at energies ranging from 26–450 GeV.
- Verification and control of cavity field (amplitude and phase), frequency, tuning sensitivity, input coupling, power overhead, and HOM signals. Establish and test operational cycle with crab cavities.
- Demonstrate the possibility to operate without crab cavity action (make them invisible) by both counter-phasing the two cavities or by appropriate detuning (to parking position) at energies ranging from 26–450 GeV.
- Measurements of beam orbit centring, crab dispersive orbit, and bunch rotation with available instrumentation such as BPMs and head–tail monitors.
- Demonstrate MFB operation.
- Demonstrate non-correlated operation of two cavities in a common cryomodule – trigger quench in one cavity without inducing quench in the other.
- Define and implement interlock hierarchy. Verification of machine protection aspects and functioning of slow and fast interlocks.
- Test HOM coupler operation with high beam currents, different filling schemes, and associated power levels. Measurement of impedance and instability thresholds for nominal mode and HOMs.
- Measure emittance growth induced by the crab cavities as far as possible.

#### 4.2.18.7 Outline of an SPS test programme

- Initial RF commissioning with the cryomodule in out-of-beam position (no dedicated MD required).
- RF commissioning with low-intensity beam, single bunch to a few bunches. Establish the proper RF parameters, including cavity tune, operating frequency, amplitude, and phase. Verify crab cavity active and invisible.
- High intensity single bunches to trains of bunches to investigate the effect of cavity performance, impedance, and machine protection; and characterize the transient behavior of the crab cavity system as a function of beam current. Verify cavity stability over many hours (as relevant for LHC physics fill).
- Long-term behavior of coasting beams in the SPS with relatively low intensity to study the effects of emittance growth and possibly non-linear effects such as RF multipoles

### 4.3 Harmonic systems

The harmonic cavity systems are presently not part of the HL-LHC baseline. Two categories of harmonic systems are proposed [20], [22].

- A higher harmonic (800 MHz) system can be used either for changing the bunch profile (in bunch lengthening mode (BL)) or for increasing the synchrotron frequency spread (in BL or bunch shortening mode (BS)). Depending on the mode of operation, this RF system can help to reduce the beam-induced heating, effect intra-beam scattering, improve longitudinal beam stability, and in some scenarios increase or level luminosity.
- A sub-harmonic (200 MHz) system could either completely replace the existing main RF system or work jointly with the 400 MHz RF system, which in this case will act as the second harmonic. The lower harmonic RF system will improve the capture efficiency for longer SPS bunches with very high

intensity. The benefits of the combined 200 MHz and 400 MHz system are similar to the above double-harmonic system but with the primary aim of luminosity improvement.

For the higher harmonic system (800 MHz), a maximum of 8 MV longitudinal voltage can be provided from approximately four to ten cavities depending on the mode of operation [20]. Relevant RF parameters are listed in Table 4-5. This is a maximum of 300 kW input power assumed to be feasible [23]. The BS mode, with the full-detuning scheme in the fundamental 400 MHz cavities, requires significantly lower RF power. Therefore, a four-cavity system is more than adequate to provide the required 8 MV with a maximum power of 300 kW per cavity. In the BL mode, the required RF power at 1 MV already exceeds 300 kW. Therefore, approximately 10 cavities are needed to provide for the 8 MV required to stay below the RF power limit.

Table 4-5: Relevant RF parameters for 800MHz RF cavities

Characteristics	Units	Value
Resonance frequency	[MHz]	801.58
Total accelerating voltage	[MV]	8
Number of Cavities		4 (BS) to $\approx 10$ (BL)
Residual resistance $R_s$	[n $\Omega$ ]	$\approx 250$
$R/Q$	[ $\Omega$ ]	$\approx 45$
$Q_0$		$\geq 1 \times 10^9$
$Q_{\text{ext}}$	-	N/A
RF power per cavity	[kW]	$10^5$ (BS), $\approx 10^4$ (BL)
Operating temperature	[K]	4.5

Replacing the existing acceleration system with a sub-harmonic system (200 MHz) will require a minimum of 3 MV of longitudinal voltage to capture, accelerate, and store the HL-LHC beams [24]. This can be provided from two to four compact quarter wave cavities, where the number of cavities also depends on power requirements and technology constraints [20]. Some relevant RF parameters for the 200 MHz cavities are listed in Table 4-6.

Table 4-6: Relevant RF parameters for 200 MHzc RF cavities

Characteristics	Units	Value
Resonance frequency	[MHz]	200.4
Total accelerating voltage	[MV]	3–6
Residual resistance $R_s$	[n $\Omega$ ]	$\leq 10$
$R/Q$	[ $\Omega$ ]	$\approx 50$
$Q_0$		$\geq 1 \times 10^{10}$
$Q_{\text{ext}}$	-	N/A
RF power (assumed)	[kW]	500
Operating temperature	[K]	4.5

The total static and dynamic heat load for either system has to be evaluated in detail during the engineering phase of the cryomodule. A cryogenic sectorization of two cavities per cryomodule is assumed for modularity, maintenance, and reliability. For 200 MHz, a preliminary estimate of 120 W for a two-cavity module at 4.5 K can be assumed where each cavity operates at 3 MV. The cavity technology (bulk niobium or Nb-coated copper cavities) can play a role in the final quality factor of the cavity and hence the heat loads at the operating gradient.

For the 800 MHz system, the frequency dependence of the surface resistance gives 250 n $\Omega$  leading to approximately 50 W at 4.5 K due to dynamic RF losses. This is only 1 W at 2 K. A geometric factor of 230  $\Omega$  and a cavity voltage of 2 MV are assumed. Therefore, it is preferable to operate the 800 MHz system at 2 K to both take advantage of the lower surface resistance and superior properties of superfluid helium. Assuming a baseline of 4.5 K, approximately 200 W can be assumed as an upper limit for a two-cavity module.

#### 4.4 Transverse damper (ADT) upgrade

The LHC requires a transverse feedback to damp injection oscillations and provide stability for impedance-driven transverse instabilities, thus guaranteeing preservation of beam intensity and emittance [25]. The existing coupled bunch feedback system ADT, installed in P4 of the LHC, was fully commissioned in 2010 [26]. It damps transverse instabilities within a bandwidth of 20 MHz, correcting the oscillations of the centre of gravity of the individual bunches about their orbit.

For the upgrade of the ADT system, three possible routes have been identified in the past [27]: increase of kick strength, reduction of noise, and increase of bandwidth. A space reservation of approximately 5 m on each side was made in the original design of the LHC to install more kickers adjacent to the existing ADTs in P4 [28].

Following the experience of the LHC Run 1, priority was given to an upgrade of the pick-up and signal processing systems aimed at reducing the noise floor, one of the options already foreseen in 2006. This includes new electronics and a doubling of the number of pick-ups, from two to four per beam and plane, with commissioning foreseen after LS1 [29]. The experience of Run 1 has also shown that an increase in kick strength may not be required, as injection errors are on average more than a factor of 4 smaller than originally assumed, and fast damping times of less than 20 turns for the injection errors can be achieved with the existing system. During Run 1, improvements in ADT signal processing were tested to address single bunch oscillations observed, which were different in nature from the coupled bunch oscillations typically driven by the resistive wall impedance, which falls off in frequency towards 20 MHz. The nature of some of these observed instabilities was not entirely unravelled during Run 1, and new diagnostics such as the multiband instability monitor (MIM) were added to the LHC to better characterize these instabilities [30]. Improvements in ADT signal processing tested during Run 1 permit running with a flat frequency response of up to approximately 20 MHz [31]. Beyond 20 MHz, the kicker and ADT power amplifier system cannot be used.

For the HL-LHC, a transverse kicker system with a larger bandwidth than 20 MHz would be an asset in view of the high bunch intensity.

In the SPS a development was started in 2008 to design a high bandwidth transverse feedback system [32, 33] that aims at damping intra-bunch motion. The system consists of pick-ups, kickers, power amplifiers, and signal processing. Both slot-line and strip-line kickers are studied for this system; slot-line kickers could offer broadband response of up to 1.2 GHz [34]. The system can also be used to damp and attenuate intra-bunch motion caused by the electron cloud, impedance-driven instabilities, or other perturbations driven, for example, by beam–beam effects or crab cavities. With its generic approach the results of the SPS development are relevant to other accelerators, including the LHC and other large colliders.

At 1 GHz four slotlines, as developed for the SPS LIU project [34], with 2 kW amplifier power per coupling port can develop a transverse voltage of 37 kV. Consequently the beam can be kicked by 82 nrad at 450 GeV and 5 nrad at 7 TeV. Assuming a reference beta function value of 180 m, at pick-up and kicker, the kick strength corresponds to removing 15  $\mu\text{m}$  of oscillation at 450 GeV and 0.9  $\mu\text{m}$  at 7 TeV, within a single turn. As a feedback system with a gain corresponding to 500 turns damping time, saturation would occur at 3.7 mm at 450 GeV and 225  $\mu\text{m}$  at 7 TeV.

#### 4.5 References

- [1] A. Piwinski, *Nucl. Instr. Meth.* **81** (1970) 199.
- [2] R. Palmer, Energy scaling, crab crossing and the pair problem, SLAC-PUB-4707 (1988).
- [3] K. Oide, K. Yokoya, The crab crossing scheme for storage-ring colliders, SLAC-PUB-4832 (1989).
- [4] Y. Funakoshi, Operational experience with crab cavities at KEKB. <http://arxiv.org/pdf/1410.4036>
- [5] S. Fartoukh, Pile up management at the High Luminosity LHC and introduction to the crab kissing concept, CERN-ACC-2014-0076 (2014).
- [6] G. Arduini *et al.*, Summary of the LHC-CC11 Crab Cavity Workshop, CERN-ATS-2012-055 (2011).

- [7] S. De Silva *et al.*, Compact Superconducting RF-dipole Cavity Designs for Deflecting and Crabbing Applications, in the proceedings of IPAC 2013, <http://accelconf.web.cern.ch/AccelConf/IPAC2013/>, Shanghai (2013).
- [8] B. Hall *et al.*, Analysis of the Four Rod Crab Cavity for HL-LHC, in the proceedings of IPAC12, New Orleans, 2012; G. Burt *et al.*, Manufacture of a Compact Prototype 4R Crab Cavity for HL-LHC, in the proceedings of IPAC 2013, <http://accelconf.web.cern.ch/AccelConf/IPAC2013/>, Shanghai (2013).
- [9] R. Calaga *et al.*, A Double Quarter-Wave Deflecting Cavity for the LHC, in the proceedings of IPAC 2013, <http://accelconf.web.cern.ch/AccelConf/IPAC2013/>, Shanghai (2013); Q. Wu *et al.*, Mechanical Study of 400 MHz Double Quarter Wave Crab Cavity for LHC Luminosity Upgrade, in the proceedings of IPAC 2013, <http://accelconf.web.cern.ch/AccelConf/IPAC2013/>, Shanghai (2013).
- [10] A. Yamamoto *et al.*, Crab cavity system external review report, CERN-ACC-2014-0093 (2014).
- [11] P. Baudrenghien, LLRF for Crab Cavities, presented at the 2nd HiLumi Meeting, Frascati, 2012.
- [12] P. Baudrenghien *et al.*, Functional specification of the LHC prototype crab cavity system, CERN-ACC-Note-2013-003 (2013).
- [13] R. Calaga and B. Salvant, Comments on crab cavity HOM power, (unpublished).
- [14] M. Navarro-Tapia, R. Calaga and A. Grudiev, RF Multipolar Characterization of the Latest LHC Deflecting Cavities, 4th International Particle Accelerator Conference, Shanghai, China, 12 - 17 May 2013, pp.2402.
- [15] K. Brodzinski, S. Claudet, Private communication.
- [16] S. Pattalwar *et al.*, Key Design Features of Crab-Cavity Cryomodule for HiLumi LHC, 5th International Particle Accelerator Conference, Dresden, Germany, 15 - 20 Jun 2014, pp.WEPR1045.
- [17] T. Jones *et al.*, Crab cavity manufacturing readiness meeting, <https://indico.cern.ch/event/334041/>, CERN, 2014.
- [18] L. Arnaudon *et al.*, Conceptual specification of the crab cavity RF system, EDMS 1363181.
- [19] P. Fessia *et al.*, Private communication.
- [20] R. Calaga, Chamonix 2014, in the proceedings of the LHC Performance Workshop, Chamonix 2014
- [21] K. Nakanishi *et al.*, Beam Behaviour due to Crab Cavities Break down, in the proceedings of IPAC10, Kyoto, 2010.
- [22] R. Calaga *et al.*, Conceptual specification of the LHC RF harmonic system, EDMS 1363179, 2014.
- [23] E. Montesinos, private communication.
- [24] E. Shaposhnikova, Harmonic system for the LHC, presented at the 4th HiLumi Meeting, KEK, 2014
- [25] O. Bruning *et al.*, (Ed.), LHC Design Report, CERN-2004-003 (2004) 140–142.
- [26] W. Hofle and D. Valuch, Transverse feedback: High intensity operation, AGC, IGC, lessons for 2012, LHC Beam Operation Workshop, Evian, December 2011, CERN-ATS-2012-083 (2012) 97–100.
- [27] W. Hofle, Transverse feedback systems in LHC and its injectors: Projected performance and upgrade paths, 3rd CARE-HHH-APD Workshop, LHC-Lumi-06, Valencia, 16–20 October 2006, CERN-2007-002 (2007) 177–179.
- [28] CERN CDD Drawing LHCLJ4GA0007 AH, March 2007.
- [29] W. Hofle, G. Kotzian, T. Levens and D. Valuch, Transverse feedback, 5th Evian Workshop, 2–4 June 2014, CERN (2014).
- [30] R.J. Steinhagen, M.J. Boland and T.G. Lucas, A multiband-instability-monitor for high-frequency intra-bunch beam diagnostics, Proc. IBIC 2013, Oxford, (2013), pp. 327–330.
- [31] W. Hofle, F. Dubouchet, G. Kotzian and D. Valuch, Performance of the LHC transverse damper with bunch trains, Proc. IPAC 2013, Shanghai (2013), pp. 3022–3024.
- [32] J.R. Thompson *et al.*, Initial simulation of damping system for electron cloud driven instabilities in the CERN SPS, Proc. PAC 2009, Vancouver (2009), <http://accelconf.web.cern.ch/AccelConf/PAC2009/>, pp. 4713–4715.



- [33] J.D. Fox *et al.*, First results and analysis of the performance of a 4 GS/s intra-bunch vertical feedback system at the SPS, Proc. IPAC 2013, <http://accelconf.web.cern.ch/AccelConf/IPAC2013/>, Shanghai (2013), pp. 3070–3072.
- [34] J.M. Cesaratto *et al.*, SPS wideband transverse feedback kicker: Design report, SLAC-R-1037, SLAC (2013); M. Cesaratto *et al.*, A wideband slotted kicker design for the SPS transverse intra-bunch feedback, Proc. IPAC 2013, <http://accelconf.web.cern.ch/AccelConf/IPAC2013/> Shanghai (2013), pp. 3073–3075.
- [35] R. Calaga and A. Ratti, 4th HiLumi Meeting, <https://indico.cern.ch/event/326148>, KEK, 2014.



# Chapter 5

## Collimation System

*R.B. Appleby<sup>1</sup>, R. Barlow<sup>2</sup>, A. Bertarelli<sup>3</sup>, R. Bruce<sup>3</sup>, F. Carra<sup>3</sup>, F. Cerutti<sup>3</sup>, L. Esposito<sup>3</sup>, A. Faus-Golfe<sup>4</sup>, H. Garcia Morales<sup>5</sup>, L. Gentini<sup>3</sup>, S. M. Gibson<sup>5</sup>, P. Gradassi<sup>3</sup>, J.M. Jowett<sup>3</sup>, R. Kwee-Hinzmann<sup>5</sup>, L. Lari<sup>6</sup>, A. Lechner<sup>3</sup>, T. Markiewicz<sup>7</sup>, A. Marsili<sup>3</sup>, J. Molson<sup>1</sup>, L.J. Nevay<sup>5</sup>, E. Quaranta<sup>3</sup>, H. Rafique<sup>2</sup>, S. Redaelli<sup>3\*</sup>, M. Serluca<sup>1</sup>, E. Skordis<sup>3</sup>, G. Stancari<sup>8</sup>, G. Steele<sup>3</sup> and A. Toader<sup>2</sup>*

<sup>1</sup>UMAN, The University of Manchester and the Cockcroft Institute, Warrington, UK

<sup>2</sup>UHUD, University of Huddersfield, Huddersfield, UK

<sup>3</sup>CERN, Accelerator & Technology Sector, Geneva, Switzerland

<sup>4</sup>IFIC, Instituto de Física Corpuscular, Valencia, Spain

<sup>5</sup>URHL, Royal Holloway, London, UK

<sup>6</sup>IFIC, Instituto de Física Corpuscular, Valencia, Spain (now ESS European Spallation Source, Lund, Sweden)

<sup>7</sup>SLAC National Accelerator Laboratory, Menlo Park, USA

<sup>8</sup>FNAL, Fermi National Accelerator Laboratory, Batavia, USA

## 5 Collimation system

### 5.1 LHC multi-stage collimation system

#### 5.1.1 Motivation

A variety of processes can cause unavoidable beam losses during normal and abnormal operation. Because of the high stored energy above 700 MJ, the beams are highly destructive. Even a local beam loss of a tiny fraction of the full beam in a superconducting magnet could cause a quench, and large beam losses could cause damage to accelerator components. Therefore, all beam losses must be tightly controlled. For this purpose, a multistage collimation system has been installed [1–8] to safely dispose of beam losses. Unlike other high-energy colliders, where the main purpose of collimation is to reduce experimental background, the LHC and the HL-LHC require collimation during all stages of operation to protect its elements.

The HL-LHC imposes increased challenges for the collimation system. For the same collimation cleaning and primary beam loss conditions as in the LHC, the factor  $\sim 2$  increase in total stored beam energy foreseen from the HL-LHC parameters requires a corresponding improvement of cleaning performance to achieve the same losses in cold magnets. Total losses might also exceed the robustness limit of collimators. The LHC system was designed to safely withstand beam lifetime drops down to 0.2 h during 10 s, corresponding to peak losses of up to 500 kW. As mentioned above, these loss levels scale with the total beam intensity so they will increase by about a factor of 2 for the HL-LHC parameter set. The collimation system must be upgraded to cope with these higher loss levels. It is clear that the lifetime control and optimization of beam halo losses will be crucial for the LHC upgrade (see also Section 5.4 Other collimators of the present system required in the HL-LHC). The larger stored energy, together with smaller beam sizes achieved through higher brightness beams, also imposes more severe challenges for collimator robustness against design loss scenarios for cleaning. In the case of single-turn beam failures, brighter beams significantly increase thermo-mechanical loads on collimator materials and components. The higher peak luminosity challenges entail the definition of new concepts for physics debris cleaning and an overall redesign of the IR collimation layouts. For example, in the present LHC layout, the inner triplet represents the IR aperture bottleneck and is protected

---

\* Corresponding author: [Stefano.Redaelli@cern.ch](mailto:Stefano.Redaelli@cern.ch)

by two dedicated tertiary collimators per plane per beam. Future optics scenarios might add critical aperture restrictions at magnets further away from the IP, requiring additional cleaning and protection.

To meet the new challenges, the HL-LHC collimation system therefore builds on the existing LHC collimation system, with the addition of several upgrades.

### 5.1.2 Collimation system inherited from the LHC

The backbone of the HL-LHC collimation system will remain, as for the current LHC, the betatron (IR7) and momentum (IR3) cleaning systems installed in two separated warm insertions [1]. A very efficient halo cleaning, as required to operate the LHC with unprecedented stored beam energies in a superconducting collider, is achieved by very precisely placing blocks of materials close to the circulating beams, while respecting a pre-defined collimator hierarchy that ensures optimum cleaning in a multi-stage collimation process. This is illustrated schematically in Figure 5-1. Most collimators consist of two movable blocks referred to as ‘jaws’, typically placed symmetrically around the circulating beams. The present system deployed for LHC operation between 2010 and 2013 provided a cleaning efficiency of above 99.99% [2], i.e. it ensured that less than  $10^{-4}$  of the beam losses are lost in superconducting magnets.

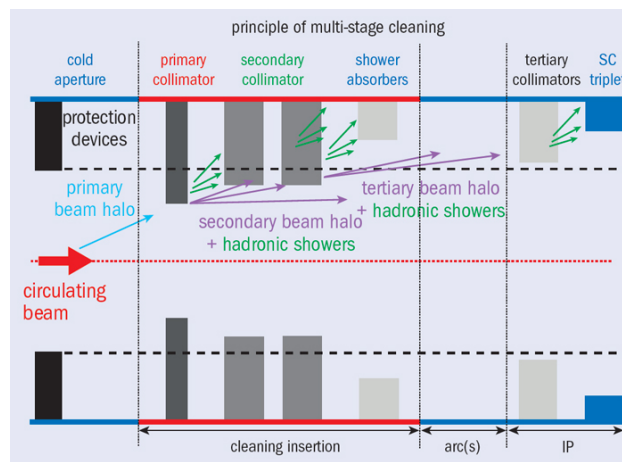


Figure 5-1: Schematic illustration of multi-stage collimation cleaning at the LHC. Primary and secondary collimators (darkest grey) are the devices closest to the circulating beam and are made of robust carbon-fibre composites. Shower absorbers and tertiary collimators (lighter grey) sit at larger apertures and are made of a tungsten alloy to improve absorption. Collimators of different families are ordered in a pre-defined collimation hierarchy that must be respected in order to ensure the required system functionalities. The collimator hierarchy is ensured by defining collimator settings in units of local beam size at the collimator location.

The LHC collimators are built as high-precision devices with beam sizes as small as 200 microns, in order to ensure the correct hierarchy of devices along the 27 km ring. Details of the collimator design can be found in Ref. [9]. Key features of the design are (i) a jaw flatness of about 40 microns along the 1 m long active jaw surface; (ii) a surface roughness below 2 microns; (iii) a 5 micron positioning resolution (mechanical, controls); (iv) an overall setting reproducibility below 20 microns [10]; (v) a minimal gap of 0.5 mm; and (vi) evacuated heat loads of up to 7 kW in a steady-state regime (1 h beam lifetime) and of up to 30 kW in transient conditions (0.2 h beam lifetime). Two photographs of the present LHC collimator are given in Figure 5-2, where a horizontal collimator and a 45° tilted collimator are shown. An example of the tunnel installation layout for an IR7 collimator is given in Figure 5-3. The complete list of collimators, including injection protection collimators in the transfer lines, is given in Table 5-1. For completeness, the injection protection TDI blocks and the one-side beam dump collimator TCDQ (considered to be part of beam transfer rather than of the LHC collimation system, but designed with a similar concept) are also listed (see Chapter 14). The full system comprises 118 collimators, 108 of which are movable.

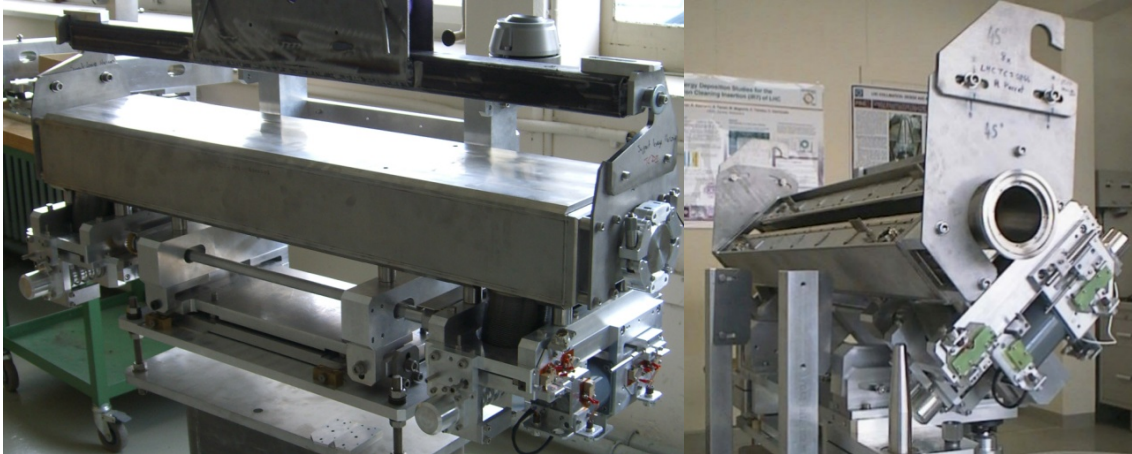


Figure 5-2: (a) horizontal LHC collimator; (b) skew LHC collimator. The latter has the vacuum tank open to show the two movable CFC jaws.

Since the collimator jaws are close to the beam (e.g. the minimum collimator gap in 2012 was 2.1 mm, i.e. jaws were 1.05 mm from the circulating beam), the collimation system also has a critical role in the passive machine protection in case of beam failures that cannot be counteracted by active systems. Primary and secondary collimators in IR7 are the closest to the beam; their jaws are mainly made of robust carbon-fibre carbon composites (CFC), and are designed to withstand beam impacts without significant permanent damage from the worst failure cases such as impacts of a full injection batch of  $288 \times 1.15 \times 10^{11}$  protons at 450 GeV and of up to  $8 \times 1.15 \times 10^{11}$  protons at 7 TeV [11]. However, they contribute significantly to the machine impedance, which is particularly critical at top energy, because of the low electrical conductivity of the CFC. Impedance constraints determine the smallest gaps that can be used in IR3 and IR7 and hence the minimum  $\beta^*$  in the experiment [3]. Other absorbers and tertiary collimators are positioned at larger gaps in units of the local beam size. They can be less robust, in term of resistance to impact of the beam, than primary and secondary collimators because they are less exposed to beam losses. Thus, metal-based jaws that are more effective in absorbing particles can be used.



Figure 5-3: Photograph of the active absorber TCLA.B6R7.B1 as installed in the betatron cleaning insertion.

The initial collimator design has been improved by adding two beam position monitors (BPMs, known as ‘buttons’) on both extremities of each jaw [12]. Eighteen collimators (16 TCTP and 2 TCSP) have been already upgraded with this new design during LS1. This concept allows for fast collimator alignment as well as a continuous monitoring of the beam orbit at the collimator, while the BLM-based alignment can only be performed during dedicated low-intensity commissioning fills. The BPM buttons will improve significantly

the collimation performance in terms of operational flexibility and  $\beta^*$  reach [3]. The BPM collimator design is considered to be the baseline for future collimation upgrades, and the BPM design is equally applicable to all collimators regardless of the jaw material. The concept has been tested extensively at the CERN SPS with a collimator prototype with BPMs [13–15]. An example of a CFC jaw prototype with in-jaw BPMs is shown in Figure 5-4.

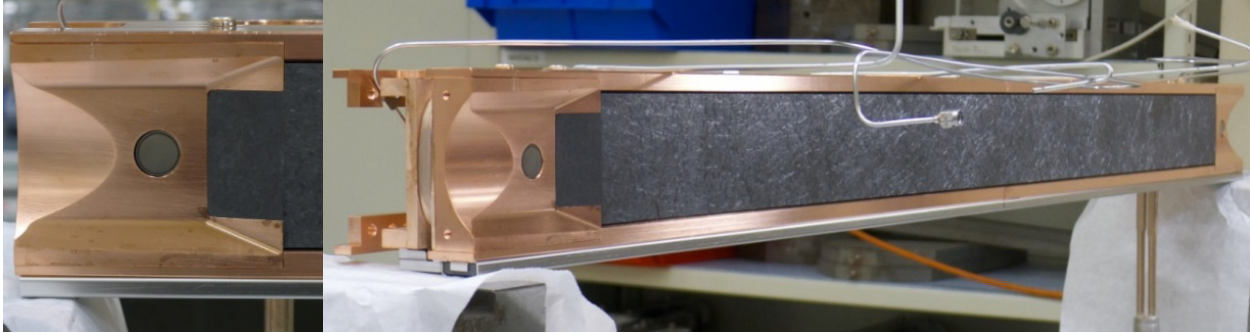


Figure 5-4: New carbon/carbon collimator jaw with integrated BPMs at each extremity ('buttons') to be installed as the secondary collimator in the dump insertion IR6. A detail of the BPM is given on the left hand side. A variant of this design, made with a Glidcop support and tungsten inserts on the active jaw part, will be used for the tertiary collimators in all IRs.

In addition to beam halo cleaning, the collimation system has other important roles.

- Passive machine protection: the collimators are the closest elements to the circulating beam and represent the first line of defense in case of various normal and abnormal loss cases. Due to the damage potential of the LHC beams, this functionality has become one of the most critical aspects for LHC operation and commissioning. In particular, it must be ensured that the triplet magnets in the experiments are protected during the betatron squeeze [3].
- Active cleaning of collision debris products: this is achieved with dedicated (TCL) collimators located on the outgoing beams of each high luminosity experiment, which catch the debris produced by the collisions. These collimators keep losses below the quench limit of the superconducting magnets in the matching sections and dispersion suppressors close to the interaction points.
- Experiment background optimization: this is one of the classical roles of collimation systems in previous colliders like the ISR, the SppS, and the Tevatron. For the LHC, the contribution to background from beam halo has always been expected to be small, due to effective IR7 collimation cleaning that induces only limited losses close to the experiments. The initial run confirmed this expectation [4].
- Concentration of radiation losses: for high power machines, it is becoming increasingly important to be able to localize beam losses in confined and optimized 'hot' areas rather than having a distributed activation of equipment along the machine. This is an essential functionality to allow easy access for maintenance in the largest parts of the machine.
- Local protection of equipment and improvement of lifetime: dedicated movable or fixed collimators are used to shield equipment. For example, eight passive absorbers are used in the collimation insertions in order to reduce the total dose to warm dipoles and quadrupoles that otherwise would have a short lifetime in the high-radiation environment foreseen during nominal LHC operation.
- Beam halo scraping and halo diagnostics: collimator scans in association with the very sensitive LHC beam loss monitoring system proved to be a powerful way to probe the population of beam tails [5, 6], which were otherwise too small compared to the beam core to be measured by conventional emittance measurements. Thanks to their robustness, the present primary collimators can also be efficiently used to scrape and shape the beams, as in Ref. [7].

In order to fulfil all these functionalities, the LHC collimation system features an unprecedented complexity compared to the previous state-of-the-art in particle accelerators. The Run 1 system required managing about 400° of freedom for collimator movements [8]. As a comparison, the Tevatron collimation system had less than 30° of freedom. For this reason, the possibility of reliably operating the collimation system has always been considered to be a major concern for LHC performance. Upgrade scenarios must address improved operational aspects, as the HL-LHC goal relies on machine availability.

Table 5-1: Collimators for the LHC Run 2, starting in 2015. For each type, acronyms, rotation plane (horizontal, vertical or skew), material and number of devices, summed over the two beams, are given. For completeness, movable injection and dump protection devices are also listed. In addition, the collimation system comprises 10 fixed-aperture absorbers in IR3 and IR7 to reduce total doses to worm magnets of the cleaning insertions.

Functional type	Name	Plane	Number	Material
Primary IR3	TCP	H	2	CFC
Secondary IR3	TCSG	H	8	CFC
Absorber IR3	TCLA	H, V	8	Inermet 180
Primary IR7	TCP	H, V, S	6	CFC
Secondary IR7	TCSG	H, V, S	22	CFC
Absorber IR7	TCLA	H, V, S	10	Inermet 180
Tertiary IR1/IR2/IR5/IR8	TCTP	H, V	16	Inermet 180
Physics debris absorbers IR1/IR5	TCL	H	12	Cu, Inermet180
Dump protection IR6	TCDQ	H	2	CFC
	TCSP	H	2	CFC
Injection protection (transfer lines)	TCDI	H, V	13	C
Injection protection IR2/IR8	TDI	V	2	hBN, Al, Cu/Be
	TCLI	V	4	C, CFC
	TCDD	V	1	Copper

**5.2 Baseline upgrades to the LHC collimation system**

To cope with the increased challenges in the HL-LHC, several of the functionalities of the LHC collimation system must be upgraded. We discuss how to improve the cleaning performance, the impedance, and the collimation in the experimental IRs.

**5.2.1 Upgrades for cleaning improvement**

**5.2.1.1 Upgrades of the IR7 system**

Protons and ions interacting with the collimators in IR7 emerge from the IR with a modified magnetic rigidity. This represents a source of local heat deposition in the cold dispersion suppressor (DS) magnets downstream of IR7, where the dispersion starts to increase (see Ref. [16] and references therein): these losses are the highest cold losses around the ring. This may pose a certain risk for inducing magnet quenches, in particular in view of the higher intensities expected for the HL-LHC.

A possible solution to this problem is to add local collimators in the dispersion suppressors, which is only feasible with a major change of the cold layout at the locations where the dispersion start rising. Indeed, the present system’s multi-stage cleaning is not efficient at catching these dispersive losses. Clearly, the need

for local collimation depends on the absolute level of losses achieved in operation and the quench limit of superconducting magnets. In this design phase, where the quench limits and the operational performance are not yet known accurately enough at beam energies close to 7 TeV, it is important to take appropriate margins to minimize the risk of being limited in the future (LHC operation at beam intensity above nominal design, and even more in the HL-LHC era).

A strategy to eliminate any risk of quench is the installation of DS collimators (target collimator long dispersion suppressors (TCLDs)). As shown below, two collimators per side of IR7, one per beam on each side, would be sufficient to effectively intercept the protons or ions that would otherwise hit the DS magnets. In order to make space for the new collimators, it is envisaged to replace, for each TCLD, an existing main dipole with two shorter 11 T dipoles with the TCLD in between, as shown in Figure 5-5. This is a modular solution that can actually be applied to any dipole without additional changes to the adjacent superconducting magnets or other cold elements, should a space in the continuous cryostat be needed for any reason in the future [17].

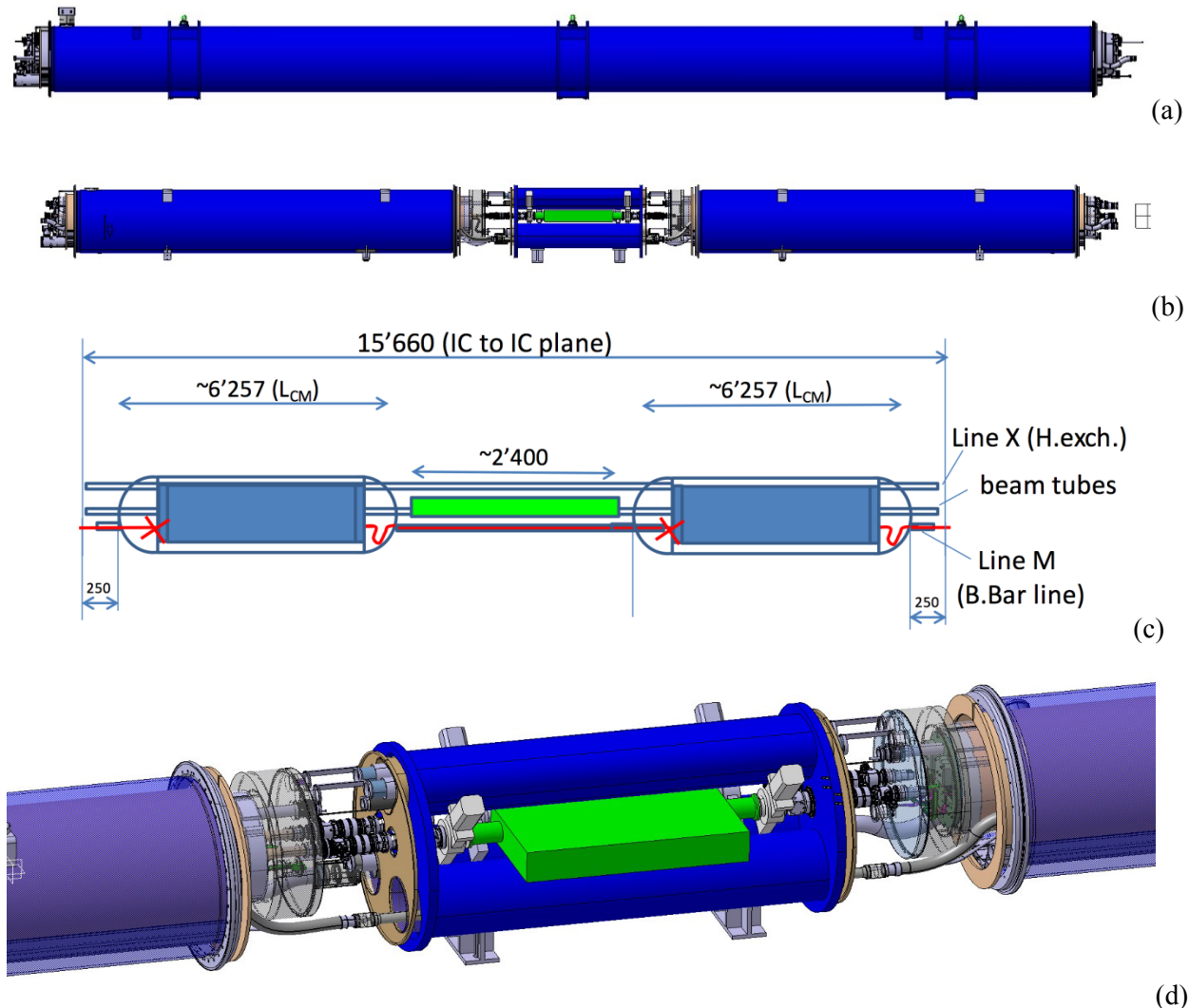


Figure 5-5: (a–c) Schematic view of the assembly of two shorter 11 T dipoles with a collimator in between, which can replace one standard main dipole. (Courtesy of V. Parma.) (d) Preliminary 3D model of a TCLD assembly showing the collimator (in green), the two short dipole cryostats and the connection cryostat. Note the very tight space constraints for the collimator unit.

Extensive tracking and energy deposition simulations have been performed to assess the effect of the TCLDs [18–22], based on the assumption that the dipoles MB.B8R7 and MB.B10R7 are substituted for



cleaning B1, and MB.B8L7 and MB.B10L7 for cleaning B2. This layout makes room for two TCLDs per beam. For example, the simulated energy deposition profile of the DS magnets for the case of 0.2 h lifetime in the nominal LHC beam is illustrated in Figure 5-6. It can be seen that the presence of local DS collimators reduces the peak energy deposition by about a factor of 10 compared to the present layout with standard dipoles.

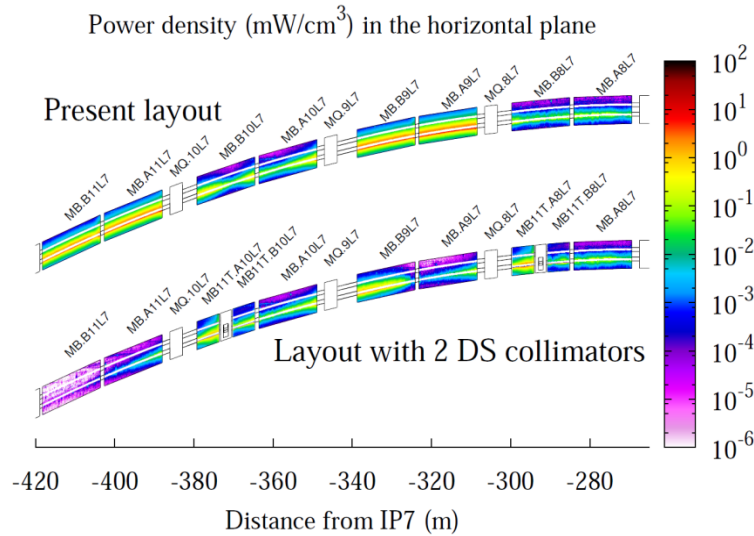


Figure 5-6: Simulated power density map in the horizontal plane of DS dipoles for nominal 7 TeV operation and a beam lifetime of 0.2 h ( $4.5 \times 10^{11}$  protons lost per second). The map makes a comparison between the present layout and a layout with two TCLDs. Results correspond to relaxed collimator settings. Beam direction is from the right to the left. From Ref. [19].

TCLD collimators also make the cleaning performance more robust against various errors of the collimation system, of the optics, and of the orbit [22], as they remove the off-momentum particles at the first high-dispersion location downstream of IR7. This is of particular concern for the ATS optics, which require modified optics in the cold arcs. Indeed, for the HL baseline optics, this solution almost eliminates losses around the ring coming from the telescopic squeeze. Should the total intensity be limited by collimation cleaning, the factor of 10 quoted above would translate into the same gain factor for the total stored beam energy.

Furthermore, the improvement in cleaning could be very beneficial for LHC operation even if this is not limited by the collimation losses. For example, a better cleaning performance might allow relaxation of the opening of some secondary collimators with a subsequent reduction of machine impedance. It should also be noted that the DS collimation solution might also mitigate issues related to radiation damage to cold magnets protected by the TCLD collimators and the activation of near-by components.

The real need for this gain can only be addressed after having accumulated beam experience at higher energies during post-LS1 operation (including beam tests of quench limits at energies close to 7 TeV). On the other hand, a recent collimation project review recommended that the preparation of DS collimation in IR7 be pursued with a high priority [23].

Even if the full performance improvement provided by the DS collimation solution in IR7 relies on two TCLD collimators per side, alternative solutions based on one single unit are being considered for possible ‘staged’ deployment in IR7, in case performance limitations during high-intensity proton operation are made apparent by the post-LS1 operation experience.

The TCLD collimators’ design is derived from one of the standard LHC collimators [24]. In particular, it incorporates the latest design improvements, such as in-jaw BPMs. TCLD collimators require a reduced set of control cables because each jaw will be moved by a single motor; though they still require cooling water and baking equipment. The key parameters are listed in Table 5-2. Although some design features are less

demanding, which is also due to lower losses compared to other collimators, integration design aspects are much more complicated due to their location between cold elements.

Table 5-2: Key parameters of TCLD collimators

Characteristics	Units	Value
Jaw active length	[mm]	80
Jaw material	-	Inermet 180
Flange-to-flange distance	[mm]	1080
Number of jaws	-	Two
Orientation	-	Horizontal
Dipole replaced by 11 T dipole/TCLD	-	MB.B10
Number of BPMs per jaw	-	Two
RF damping	-	RF fingers or ferrite
Cooling of the jaw	-	Yes
Cooling of the vacuum tank	-	No
Minimum gap	[mm]	<2
Maximum gap	[mm]	>45
Stroke across zero	[mm]	>4
Number of motors per jaw	-	One
Angular adjustment	-	No
Transverse jaw movement (fifth axis)	-	No

The new baseline that relies on shorter 11 T dipoles has been reviewed from the integration point of view [25]. Space is restricted, and the length of all components and transitions must be carefully optimized. The present baseline is that the TCLD will have an active jaw length of 80 cm, which has proved to be sufficient to improve cleaning in all relevant cases. Tungsten heavy alloy is assumed for the material because the TCLD will rarely be exposed to a large beam load, so there is no need at this stage to consider advanced materials. From the RF view point, designs with transverse RF fingers (as in the present system) as well as with ferrite blocks to absorb high-order modes (as in the collimators with BPMs) are being comparatively assessed. A possible design is shown in Figure 5-7, where a detail of the collimator jaw extremity is given.

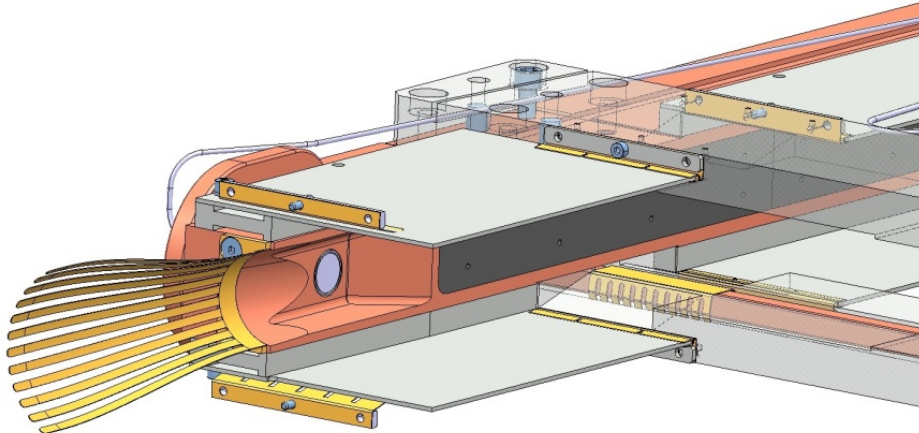


Figure 5-7: Detail of one corner of the TCLD collimator to be installed in the DS between two new 11 T dipoles. The present design foresees an 80 cm long jaw made of tungsten (the first of four 20 cm tungsten tiles is shown) and will have two jaws. Designs with transverse RF fingers or ferrite tiles are being comparatively assessed to reduce the detrimental effects of trapped RF modes.

5.2.1.2 Upgrades for improved cleaning of physics debris close to experiments

Collision products emerging from the interaction points might be lost in the matching sections and the dispersion suppressors (DS) around the experiments. In particular, protons that changed their magnetic rigidity represent a source of local heat deposition in the first DS cells where the dispersion function starts rising. These physics debris losses may pose a certain risk of inducing magnet quenches.

Mechanisms with similar effects also occur during heavy-ion operation [25–28]. Secondary ion beams with a changed magnetic rigidity are created when ions undergo ultra-peripheral interactions at the collisions. The dominating processes are bound-free pair production (BFPP), where electron–positron pairs are created and an electron is caught in a bound state by one (BFPP1) or both (BFPP2) nuclei, thus changing their charge, and 1- or 2-neutron electromagnetic dissociation (EMD1 and EMD2) where one of the colliding ions emits one or two neutrons, respectively, thus changing mass. Further photo-induced processes also take place, but the four mentioned here have the higher cross-sections. An example of ion beams produced in collisions of  $^{208}\text{Pb}^{82+}$  nuclei in IR2 is given in Figure 5-8.

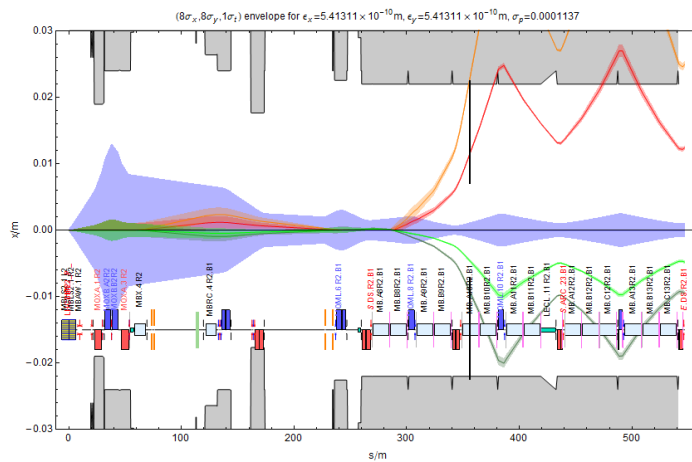


Figure 5-8:  $1\sigma$  envelope of the main  $\text{Pb}^{82+}$  beam (violet) together with the dispersive trajectories of ions undergoing BFPP1 (red), BFPP2 (orange), EMD1 (light green), and EMD2 (dark green), coming out of the ALICE experiment in nominal optics. The DS collimator appears as a black line. Varying its opening allows different secondary beams to be intercepted (note that the orange BFPP2 beam carries energies well below the quench limit).

As can be seen, these secondary beams are lost very locally due to the big and sudden change of magnetic rigidity, and may pose a risk of inducing magnet quenches [16, 28]. For the LS2 ALICE upgrade, aiming at a peak luminosity of  $6 \times 10^{27} \text{cm}^{-2} \text{s}^{-1}$  (about six times higher than the nominal one), the dominant BFPP1 beam can carry about 150 W, resulting in a power load in the coils of the MB.B10 dipole of about  $50 \text{ mW/cm}^3$  [29], in the DS regions on both sides of ALICE. This is a factor of about 2 above the quench limit according to figures presented at a recent collimation review [23]. Similar losses also occur in the DS regions around ATLAS and CMS during ion operation.

A strategy to eliminate any risk of quenches in the experimental IRs, both for proton and heavy-ion runs, is the installation of TCLD collimators in the DS to catch ions beams before they reach the magnets, as shown schematically in Figure 5-8. For heavy-ion operation, one collimator per side of the experiment would be sufficient to effectively intercept the secondary beams from the most dominant processes in a location where these ions are well separated from the main beam.

Extensive energy deposition simulations in the DS around ALICE, where MB.A10 is substituted by a pair of 11 T magnets and a TCLD collimator, confirm this assumption [16, 29]. The proposed TCLD collimator installation, with a jaw based on 80 cm of a tungsten heavy alloy, is expected to reduce by more than a factor of 100 the peak power density in the new 11 T dipoles compared to the power density in cold dipoles with the

present layout with old dipoles and no TCLD collimators [29]. DS collimation around IR2 is therefore considered to be necessary for the full exploitation of the ALICE detector upgrade.

Different jaw lengths and materials have been comparatively addressed for the specific case of ions in IR2 by using, as an advantageous comparison, the reduction factor of losses in the DS dipoles [29]. Simulations show that 50 cm of copper would suffice (see, for example, the results presented at the collimation review [23]). However, in order to minimize design effort and production works both for the collimator and for the design of the cryo bypass, the same length of 80 cm adopted for the TCLD in IR7 (see Table 5-2) is also used as a baseline for the TCLD collimators in the experimental IRs. For the jaw material, the tungsten alloy Inermet 180 is used as a baseline for IR7. Should the copper design be easier/less costly, it could be considered for implementation around P2.

For high intensity proton operation, the losses observed around IR1 and IR5 can be reduced with two TCLD collimators per IR side. The need for such implementation depends on the dipole quench limits and on the effectiveness of the physics debris collimation with TCL collimators. Layouts based on TCL collimators only (positioned in the straight section of IR1 and IR5 where the local dispersion from the collision point is low) might be sufficient but this requires further studies with the latest HL-LHC layouts that will estimate the peak energy deposited in the DS magnets. If required the TCLDs would then complement the present system with TCLs.

### 5.2.2 Upgrades for impedance improvement

The LHC impedance budget is largely dominated by the contribution of the LHC collimators. For this reason, the present collimation system has been conceived in a way that it can be easily upgraded to reduce the impedance [30]: every secondary collimator slot in IR3 and IR7 features a companion slot for the future installation of a low-impedance secondary collimator. A total of 22 slots (IR7) and eight slots (IR3) are already cabled for a quick installation of new collimators – referred to as TCSMP in the present database naming convention – that can either replace the present TCSGs or be used together with them. Partial preparation of these slots is ongoing in LS1.

The importance of minimizing the machine impedance for the HL-LHC has been emphasized in Refs. [31–33] and also in a recent LHC collimation review [23]. We therefore foresee that, by the time of the full HL-LHC implementation (LS3), some or all of the available TCSMP slots might be equipped with advanced collimators using new materials, and possibly coatings, to reduce the impedance. A staged installation using the various technical stops and shutdowns after LS1 is possible according to actual needs.

Secondary collimators in the betatron cleaning insertion (IR7) also have a crucial role in LHC machine protection and might be exposed to large beam losses. Therefore, new material choices and designs must also be robust against beam failure (at the least those exposed to horizontal losses). The driving requirements for the development of new materials are thus: (i) low resistive-wall impedance to avoid beam instabilities; (ii) high cleaning efficiency; (iii) high geometrical stability to maintain the extreme precision of the collimator jaw during operation despite temperature changes; and (iv) high structural robustness in case of accidental events like single-turn losses.

The present baseline for the upgraded secondary collimators relies thus on molybdenum carbide-graphite (MoGr) composites, possibly coated with pure molybdenum (Figure 5–9). Other lower  $Z$  refractory coatings are presently under study. The molybdenum coating under consideration would reduce the surface resistivity by about a factor of 10 to 20 compared to Mo-Gr and by more than a factor of 100 compared to CFC. The benefit on the impedance budget of the collimation system would be significant: in the relevant frequency range, impedance would be reduced to 10% of that of the CFC jaws [34], as illustrated in Figure 5-10.

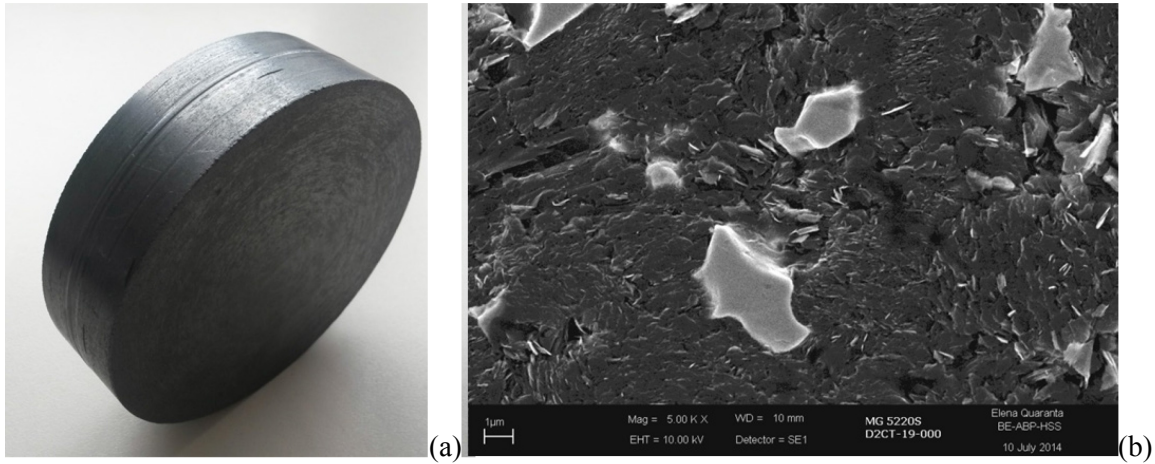


Figure 5-9: (a) Mo-Gr plate recently produced by Brevetti Bizz, Italy. Dimensions of the plate: 90 mm diameter and 24.3 mm thickness. It is a massive piece prepared in view of the production of the LHC collimator jaw inserts. (b) A detail of the microstructure, where the graphite flakes matrix well sintered with the carbon fibers is visible together with a few molybdenum carbide ‘islands’ of about 5 μm length.

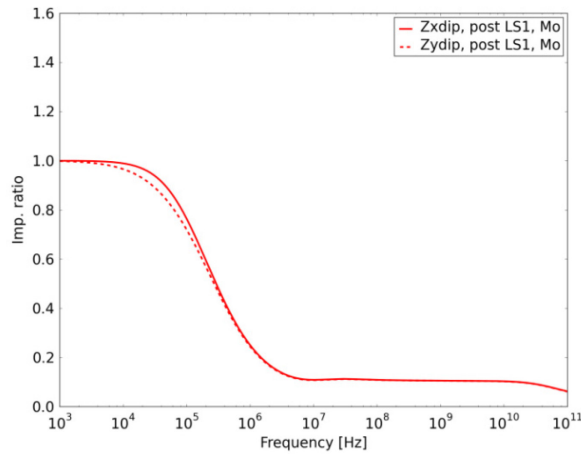


Figure 5-10: Collimation impedance versus frequency: impedance ratio between Mo coating on Mo-Gr (50 μm layer) and present CFC jaw for the real (solid) and imaginary (dotted) parts. A secondary collimator is considered. Courtesy of N. Mounet.

On the other hand, the new design and materials [35] must be validated for operation. Material properties and the coating options have to be validated for operation in the LHC. For these purposes, a rich programme of validation is in progress, involving:

- tests at HiRadMat, covering both material samples as well as full jaw validation;
- mechanical engineering prototyping;
- beam tests at the LHC, planned for 2016 (collimation installation in the 2015 shutdown).

In addition to the impedance improvements, the new TCSPM also feature a number of improvements in the mechanical design (Figure 5-11) [35]. They incorporate the BPM button design. The key hardware parameters are listed in Table 5-3.

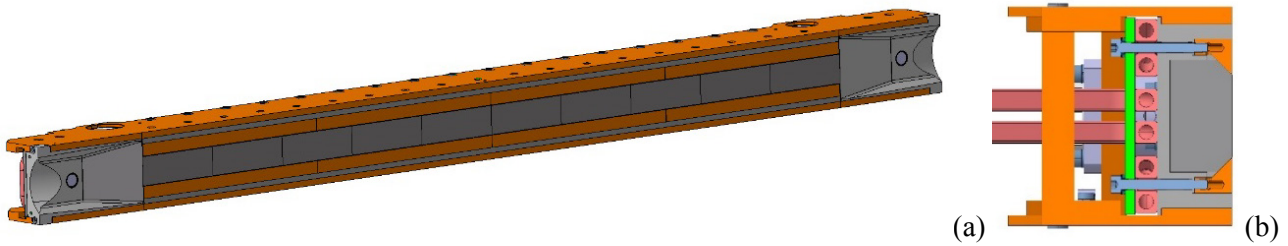


Figure 5-11: Preliminary design of the TCSMP jaw (a) and of its cross-section (b). The jaw assembly features 10 MoGr blocks. Also note that the jaw tapering is lengthened, further reducing its contribution to HOM RF instabilities in the geometrical transition zones

Table 5-3: Parameters of TCSMP collimators

Characteristics	Units	Value
Jaw active length	[mm]	1000
Jaw material	-	MoGr
Flange-to-flange distance	[mm]	1480
Number of jaws	-	2
Orientation	-	Horizontal, vertical, skew
Number of motors per jaw	-	Two
Number of BPMs per jaw	-	Two
RF damping	-	Fingers
Cooling of the jaw	-	Yes
Cooling of the vacuum tank	-	Yes
Minimum gap	[mm]	<1
Maximum gap	[mm]	60
Stroke across zero	[mm]	5
Angular adjustment	-	Yes
Jaw coating	-	Mo (to be confirmed)
Transverse jaw movement (fifth axis)	[mm]	±10

### 5.2.3 Upgrades to the collimation of the incoming beam in the experimental IRs

The LHC Run 1 operation period has shown that protection of the IR superconducting magnets and experiments is a key asset for machine performance: the available aperture, to be protected in all operational phases, determines the collimation hierarchy. The present tertiary collimators (target collimator tertiary with pick-up (TCTP)) are located at positions that protect the triplet and are made of a heavy tungsten alloy (Inermet 180). They effectively protect the elements downstream but are not robust against high beam losses, in particular during very fast beam failures that might occur if the beam dumping system does not trigger synchronously with the abort gap (an asynchronous beam dump). Settings margins are added to the collimator hierarchy to minimize the risk of exposure of these collimators to beam losses in case of such failures [3]. A design with improved robustness would allow the reduction of these margins and, as a result, push further the  $\beta^*$  performance of the LHC, in particular for the HL optics baseline (ATS) that features an unfavourable phase between dump kickers and triplet magnets.

In addition to improvements from increased robustness, the HL-LHC layout has additional aperture constraints [2, 3] because the aperture of the magnets up to Q5 is now smaller than in the present layout. Thus, up to four more tertiary collimators might be required in IR1/IR5 to protect the Q4 and Q5 quadrupole magnets, in addition to those installed to protect the triplet (two TCTP collimators – one horizontal and one vertical). The present baseline under study includes also a pair of new collimators in front of Q5. Ongoing studies are addressing: (i) the need for additional Q4 protection; and (ii) the need to keep tertiary collimators at the present locations in case additional tertiaries are added upstream.

A new design of tertiary collimators, referred to as target collimator tertiary with pick-up metallic (TCTPM), is under study to address the new challenges. This design will be based on novel materials to improve collimator robustness while ensuring adequate absorption, adequate cleaning, and protection of the elements downstream. The TCTPM design and material choice must also take impedance constraints under consideration to keep the collimator impedance under control. A summary of the technical key parameters are given in Table 5-4.

The experimental experience of beam impacts on collimator material samples at HiRadMat [4, 5] indicates that a molybdenum-graphite (Mo-Gr) composite can improve the TCTP robustness by a factor of several hundreds. Note that the present Inermet design is expected to undergo severe damage requiring a collimator replacement if hit by one single LHC nominal bunch of  $10^{11}$  proton at 7 TeV. Other advanced materials are being studied as possible alternatives to further improve the robustness. The HL beam parameters with bigger charge and smaller emittance pose additional challenges in terms of beam damage potential.

Despite being less critical because of the larger  $\beta^*$  values, upgraded TCTP's are under consideration also for IR2/8 because various luminosity scenarios in there IRs require the usage of tertiary collimators, although at relaxed settings compared to IR1 and IR5.

Table 5-4: Equipment parameters of the TCTPM

Characteristics	Units	Value
Jaw active length	[mm]	1000
Jaw material	-	Mo-Gr (to be decided)
Flange-to-flange distance	[mm]	1480 (to be reviewed)
Number of jaws	-	Two
Orientation	-	Horizontal, vertical
Number of motors per jaw	-	Two
Number of BPMs per jaw	-	Two
RF damping	-	Fingers
Cooling of the jaw	-	Yes
Cooling of the vacuum tank	-	Yes
Minimum gap	[mm]	<1
Maximum gap	[mm]	>60 (to be reviewed)
Stroke across zero	[mm]	>5
Angular adjustment	-	Yes
Jaw coating	-	No
Transverse jaw movement (fifth axis)	[mm]	$\pm 10$ mm (at least)

### 5.3 Advanced collimation concepts

In this section we discuss new, more advanced, collimation concepts that still require R&D and are therefore not in the baseline. However, depending on the results of Run 2, some of these concepts may become an important asset for the LHC and the HL-LHC.

#### 5.3.1 Halo diffusion control techniques

The 2012 operational experience indicates that the LHC collimation would profit from halo control mechanisms. These mechanisms were used in other machines like HERA and Tevatron. The idea is that, by controlling the diffusion speed of halo particles, one can act on the time profile of the losses, for example by reducing rates of losses that would otherwise take place in a short time, or simply by controlling the static population of halo particles in a certain aperture range. These aspects were recently discussed at a collimation review on the possible usage of the hollow e-lens collimation concept at the LHC [36], where it was concluded that hollow e-lenses could be used at the LHC for this purpose. In this case, a hollow electron beam runs parallel to the proton or ion beam that is on the axis of the cylindrical layer of electron. This hollow beam

produces an electromagnetic field only affecting halo particles above a given transverse amplitude, changing their transverse speed. The conceptual working principle is illustrated in Figure 5-12(a). A solid experimental basis achieved at the Tevatron indicates this solution is promising for the LHC ([37] and reference therein).

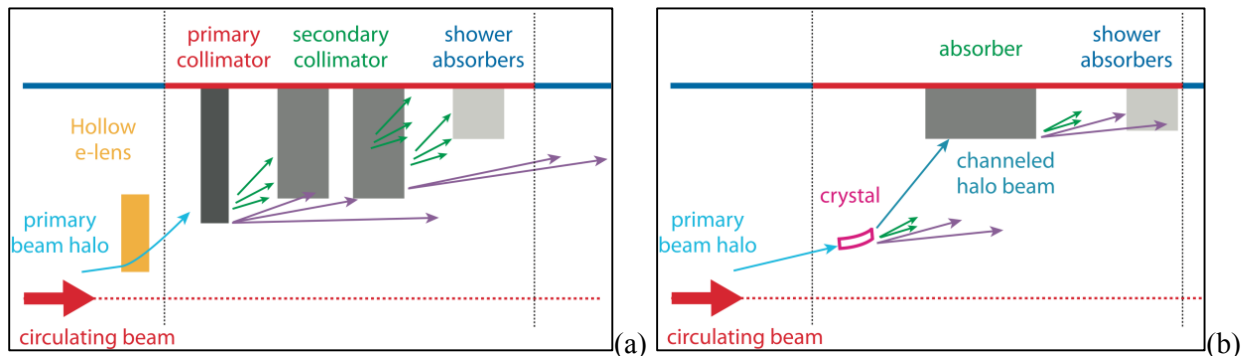


Figure 5-12: Illustrative view (a) of the collimation system with integrated hollow e-lens or equivalent halo diffusion mechanism; (b) an ideal crystal-based collimation. A simplified collimator layout to that in Figure 5-1 is adopted to show the betatron cleaning functionality only (one side only). Halo control techniques are used to globally change the diffusion speed of halo particles, and rely on the full collimation system remaining in place. Crystals entail a change of concept where the whole beam losses are concentrated, ideally, in one single beam absorber per plane.

The potential advantages of the electron lens collimation are several.

- Control of the primary loss rates, with potential mitigation of peak loss rates in the cold magnets, for a given collimation cleaning. Peak power losses on the collimators themselves can be optimized as well.
- Controlled depletion of beam tails, with beneficial effects in case of fast failures.
- Reduction of tail populations and therefore peak loss rates in the case of orbit drifts.
- Beam scraping at very low amplitudes ( $>3\sigma$ ) without the risk of damage, as for bulk scrapers.
- Tuning of the impact parameters on the primary collimators with a possible improvement in cleaning efficiency.

Since the main beam core is not affected, hollow electron beam (HEB) operation should in theory be transparent for the luminosity performance if this technique works as designed. This was demonstrated at the Tevatron for DC powering of the electron beams.

The use of HEB requires the collimation system to be in place in order to dispose of the tail particles expelled in a controlled way. No losses occur at the HEB location and the tail control mechanism can be put in place in any ring location. Larger beam size locations are favourable as they entail reduced alignment accuracy for the hollow beam. IR4 is considered to be the best candidate for two HEB devices due to the larger than standard inter-beam distance (which eases integration of the device on the beam), cryogenics availability, low-radiation environment, and quasi-round beam.

While the functionality of HEB will provide clear benefits for LHC operation, the real need for such a scheme at the LHC and the HL-LHC has to be addressed after gaining sufficient operational experience at energies close to 7 TeV on quench limits, beam lifetime, and loss rates during the operational cycle and collimation cleaning. Fast failure scenarios for the crab cavities require a low tail population above about 4 beam  $\sigma$ : HEB is the only technique solidly validated experimentally in other machines that could in this case ensure safe operation.



The HEB is targeted at enabling active control of beam tails above 3 beam  $\sigma$ , with tail depletion efficiencies of the order of 90% over times of tens of seconds, in all phases of the operational cycle, specifically before and after beams are put into collision.

The HEB implementation should ensure: (i) the possibility of pulsing the current turn-by-turn (as required to drive resonances in the linear machine before beams are in collision); (ii) a train-by-train selective excitation (leaving ‘witness’ trains with populated halos for diagnostics and machine protection purposes).

The main systems/components of a HEB can be summarized as:

- electron beam generation and disposal: electron gun and collector, with the required powering;
- several superconducting and resistive magnets: solenoids, dipoles, and correctors to stabilize and steer the electron beam;
- beam instrumentation for the optimization of the electron beam.

The parameters listed here are extracted from the conceptual design document [38] compiled by colleagues from FNAL who worked on this topics within the LARP collaboration. A detail engineering design is now ongoing at CERN. The first goal will be to define the volumes for a full integration into the LHC.

Table 5-5: Hollow electron beam equipment parameters

Parameter	Value or range
<i>Beam and lattice</i>	
Proton kinetic energy, $T_p$ [TeV]	7
Proton emittance (rms, normalized), $\epsilon_p$ [ $\mu\text{m}$ ]	3.75
Amplitude function at electron lens, $\beta_{x,y}$ [m]	200
Dispersion at electron lens, $D_{x,y}$ [m]	$\leq 1$
Proton beam size at electron lens, $\sigma_p$ [mm]	0.32
<i>Geometry</i>	
Length of the interaction region, $L$ [m]	3
Desired range of scraping positions, $r_{mi}$ [ $\sigma_p$ ]	4–8
<i>Magnetic fields</i>	
Gun solenoid (resistive), $B_g$ [T]	0.2–0.4
Main solenoid (superconducting), $B_m$ [T]	2–6
Collector solenoid (resistive), $B_c$ [T]	0.2–0.4
Compression factor, $k \equiv \sqrt{B_m/B_g}$	2.2–5.5
<i>Electron gun</i>	
Inner cathode radius, $r_{gi}$ [mm]	6.75
Outer cathode radius, $r_{go}$ [mm]	12.7
Gun perveance, $P$ [ $\mu\text{perv}$ ]	5
Peak yield at 10 kV, $I_e$ [A]	5
<i>High-voltage modulator</i>	
Cathode-anode voltage, $V_{ca}$ [kV]	10
Rise time (10%–90%), $\tau_{\text{mod}}$ [ns]	200
Repetition rate, $f_{\text{mod}}$ [kHz]	35

Source: Ref. [38]

At the collimation review [36], it became clear that, if loss spikes were limiting LHC performance after LS1, the hollow e-lens solution would not be viable because it could only be implemented in the next long

shutdown at the earliest (driven by the time for integration into the cryogenics system). It is therefore crucial to work on viable alternatives that, if needed, might be implemented in an appropriate time scale. Two alternatives are presently being considered:

- tune modulation through a ripple in the current of lattice quadrupoles;
- narrow-band excitation of halo particles with the transverse damper system.

Though very different from the hardware point of view, both these techniques rely on exciting tail particles through resonances induced in the tune space by appropriate excitations. This works on the assumption of the presence of a well-known and stable correlation between halo particles with large amplitudes and corresponding tune shift in tune space (de-tuning with amplitude). Clearly, both methods require a solid experimental verification in a very low noise machine like the LHC, in particular to demonstrate that this type of excitation does not perturb the beam core emittance. Unlike hollow e-lenses, which act directly in the transverse plane by affecting particles at amplitudes above the inner radius of the hollow beam, resonance excitation methods require a good knowledge of the beam core tune even in dynamic phases of the operational cycle, so the possibility of using these techniques at the LHC remains to be demonstrated. For this purpose, simulation efforts are ongoing with the aim of defining the required hardware interventions during LS1 that might enable beam tests of these two halo control methods early on in 2015. Ideally, these measurements would profit from appropriate halo diagnostic tools. We are, however, confident that conclusive measurements could be achieved in Run 2 with the techniques described, for example in Ref. [5].

### 5.3.2 Crystal collimation

Highly pure bent crystal can be used to steer high-energy particles that get trapped by the potential of parallel lattice planes. Equivalent bending fields of up to hundreds of tesla can be achieved in crystals with a length of only 3–4 mm, which allows in principle steering of halo particles to a well-defined point. As opposed to a standard collimation system based on amorphous materials, requiring several secondary collimators and absorbers to catch the products developed through the interaction with matter (Figure 5-1), one single absorber per collimation plane is in theory sufficient in a crystal-based collimation system [39]. This is shown in the scheme in Figure 5-12(b). Indeed, nuclear interactions with well-aligned crystals are much reduced compared to a primary collimator, provided that high channelling efficiencies for halo particles can be achieved (particles impinging on the crystal to be channelled within a few turns). This is expected to significantly reduce the dispersive beam losses in the DS of the betatron cleaning insertion (IR7) compared to the present system, which is limited by the leakage of particles from the primary collimators. Simulations indicate a possible gain of between 5 and 10 [40], even for a layout without an optimized absorber design. The crystal collimation option is particularly interesting for collimating heavy-ion beams thanks to the reduced probability of ion dissociation and fragmentation compared to the present primary collimators. SPS test results are promising [41].

Another potential advantage of crystal collimation is a strong reduction of machine impedance due to the facts that: (i) only a small number of collimator absorbers are required; and that (ii) the absorbers can be set at much larger gaps thanks to the large bending angle from the crystal (40–50  $\mu\text{rad}$  instead of a few  $\mu\text{rad}$  from the multiple-Coulomb scattering in the primary collimator). On the other hand, an appropriate absorber design must be conceived in order to handle the peak loss rates in case of beam instabilities: the absorber must withstand continuous losses of up to 1 MW during 10 s while ensuring the correct collimation functionality. This is a change of paradigm compared to the present system, where such losses are distributed among several collimators. Other potential issues concern the machine protection aspects of this system (such as the implications of a crystal not being properly aligned and therefore channelling a large fraction of the total stored energy to the wrong place) and the operability of a system that requires mechanical angular stability in the sub- $\mu\text{rad}$  range to be ensured through the operational cycle of the LHC (injection, ramp, squeeze, and collision).

Promising results have been achieved in dedicated crystal collimation tests at the SPS performed from 2009 within the UA9 experiment [41–43]. On the other hand, some outstanding issues about the feasibility of the crystal collimation concept for the LHC can only be addressed by dedicated beam tests at high energy in the LHC. For this purpose, a study at the LHC has been proposed [44]: two goniometers housing crystals have been installed in IR7 during LS1 for horizontal and vertical crystal collimation tests. The main purpose of beam tests at the LHC is to demonstrate the feasibility of the crystal-collimation concept in the LHC environment, in particular to demonstrate that such a system can provide a better cleaning of the present high-performance system throughout the operational cycle. Until a solid demonstration is achieved, crystal collimation schemes cannot be considered for future HL-LHC baseline scenarios.

### 5.3.3 Improved optics scenarios for collimation insertions

Alternative optics concepts in IR7 can be conceived in order to improve some present collimation limitations without major hardware changes. For example, non-linear optics schemes derived from the linear collider experience [45] were considered for IR7. The idea is that one can create a ‘non-linear bump’ that deforms the trajectories of halo particles and effectively increases their transverse amplitudes in a way that allows opening the gaps of primary and secondary collimators. These studies are well advanced from the optics point of view but at the present time it is not possible to easily find a layout solution providing the same cleaning as the present system [46]. These studies, and others aimed at increasing the beta functions at the collimators, are ongoing.

### 5.3.4 Rotatory collimator design

The rotatory collimator design developed at SLAC under the LARP effort proposes a ‘consumable collimator’ concept based on two round jaws with 20 flat facets that can be rotated to offer to the beam a fresh collimator material in case a facet is damaged [47]. This design features a low impedance and is based on standard non-exotic materials. It was conceived for high-power operation, with a 12 kW active cooling system to withstand the extreme power loads experienced by the secondary collimators in IR7. A photograph of this device before closing the vacuum tank is given in Figure 5-13, where the rotatory glidcop (a copper alloy) jaws are visible. The first full-scale prototype of this advanced collimator concept has recently been delivered to CERN [48] and is being tested in preparation for beam tests. The ultimate goal is to validate the rotation mechanism after high intensity shock impacts at the HiRadMat facility, aimed at demonstrating that the concept of consumable collimator surfaces can indeed work for the LHC beam load scenarios. The precision accuracy of this prototype and the impedance are also being tested together with its vacuum performance. The vacuum measurements indicated that the SLAC prototype is suitable for installation in the SPS or even the LHC. An optimum strategy for beam tests is being established based on these new results.

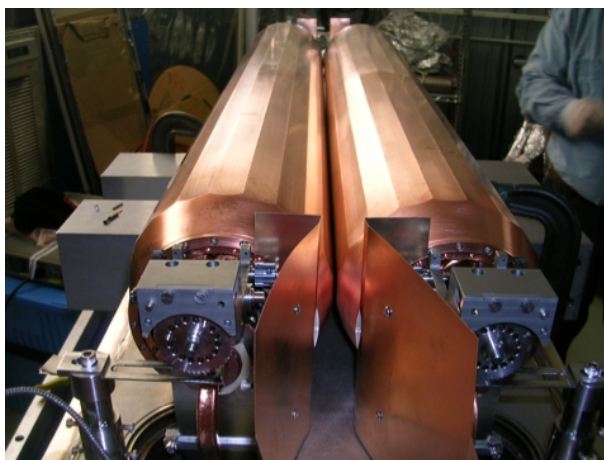


Figure 5-13: Photograph of the SLAC rotatory collimator prototype jaws before assembly in the vacuum tank. Courtesy of T. Markiewicz (SLAC, LARP).

## 5.4 Other collimators from the present system required in the HL-LHC

It is important to realize that more than 60% of the LHC collimators, which are not to be modified or replaced in the present collimation upgrade baseline described above, must remain reliably operational for the HL-LHC era. Even devices whose design is deemed adequate for the HL-LHC parameters can hardly survive for the lifetime of the LHC machine without appropriate maintenance, substitution, or revamping. A long-term strategy must be put in place in order to ensure that the LHC collimation system can meet the performance and availability challenges of the HL-LHC project. In this section, the present LHC collimators that will also be needed for the HL-LHC, possibly with improved design and features, are described.

### 5.4.1 IR3 and IR7 primary collimators (target collimator primary and TCP with pick-up)

Carbon-based primary collimators, the target collimator primary (TCP), are used in the LHC to define the primary beam halo cut in the momentum (IR3) and betatron (IR7) cleaning insertion. One TCP collimator per beam is used in IR3 (horizontal orientation) whereas three collimators per beam are used in IR7 (horizontal, vertical, and skew orientations) for a total of eight primary collimators in the LHC. Since these collimators are closest to the circulating beams, their jaws are built with a robust carbon-fibre composite (CFC) that is designed to withstand the design LHC failure scenarios at injection (full injection train of 288 bunches impacting on one jaw) and at 7 TeV (up to eight bunches impacting on one jaw in the case of an asynchronous dump) [1]. The need to improve the TCP collimator design in view of the updated beam parameters for the HL-LHC design is being assessed.

The LHC primary collimator might needed to be upgraded for the HL-LHC if the present design:

- proves to not be adequate to cope with the design LHC failure scenarios updated for the upgraded HL-LHC beam parameters (larger bunch intensity and smaller emittances);
- proves to not be adequate for standard operational losses with a larger stored beam energy in the HL-LHC: for the same assumed minimum beam lifetime in operation, the total loss rates expected on the collimators might be up to a factor of 2 larger for the HL-LHC than for the LHC;
- can be improved in a way that the HL-LHC could profit from, e.g. improved materials or alignment features (integrated BPMs) for a more efficient operation.

The primary collimators are a fundamental element of the LHC multi-stage collimation hierarchy and are required in all operational conditions with beam in the machine. These are therefore high-reliability devices that must be compatible with operation in very high radiation environments and withstand standard operational losses and relevant failure cases without permanent damage that could jeopardize their functionality.

Note that a design with BPM-integrated jaw for primary collimators is currently being studied. This design, referred to as TCP with pick-up (TCPP) currently uses the same CFC materials for the jaw but provides greatly improved operational features in terms of alignment speed and beam position monitoring. This design is also being considered for HL upgrades.

### 5.4.2 IR3 and IR7 secondary collimators (target collimator secondary graphite)

Carbon-based secondary collimators (target collimator secondary graphite (TCDG)) are used in the LHC for the secondary stage of the beam halo cut in the momentum (IR3) and betatron (IR7) cleaning insertion. Four secondary collimators per beam are used in IR3 whereas 11 collimators are used in IR7 for a total of 30 TCSG collimators in the LHC. Horizontal, vertical, and skew orientations are used in different locations. Since these collimators are among the closest to the circulating beams, their jaws are built with a robust CFC that is designed to withstand the same design LHC failure scenarios at injection and at 7 TeV as the primary collimators.

The present baseline for the HL-LHC is that new secondary collimators, TCSPM, based on advanced robust and low-impedance materials will be added in IR3 and IR7, using existing TCSM slots [2]. In this scenario, the need to maintain the operability of the present CFC secondary collimators remains to be assessed.

This depends, for example, on whether the new TCSPM collimators will be able to withstand the injection failure scenario. These aspects are presently under study.

#### 5.4.3 IR3 and IR7 active shower absorbers collimators (target collimator long absorber)

Tungsten-based shower absorbers collimators (target collimator long absorber (TCLA)) are used in the LHC for the third or fourth stage of cleaning of beam halos in the momentum (IR3) and betatron (IR7) cleaning insertion. Four TCLA collimators per beam are used in IR3 whereas five collimators are used in IR7, with a total of 18 TCLA collimators in the LHC. Horizontal and vertical orientations are used depending on the location. Operationally, these collimators are not supposed to intercept primary or secondary beam losses. They are therefore built using a heavy tungsten alloy that maximizes efficiency in cleaning but which is not robust with respect to a beam impact of considerable power. The need to improve the TCLA collimator design in view of the updated beam parameters for the HL-LHC design is being assessed.

As for the previous case, the upgrade of the LHC shower absorber collimators might be needed for the HL-LHC if the present design proves to not be adequate for the standard operational losses with a larger stored beam energy in the HL-LHC and/or if it can be improved in a way from which the HL-LHC could profit (improved materials, BPM features).

The TCLA collimators are an important element of the LHC multi-stage collimation hierarchy and are required in all operational conditions with beam in the machine. Operation might continue temporarily in the case of isolated TCLA failures, but we assume here that HL operation for physics without TCLA collimators will not be possible. These are therefore high-reliability devices that must be compatible with operation in very high radiation environments and withstand standard operational losses and relevant failure cases without permanent damage that could jeopardize their functionality.

A joint study by the collimation team and the beam dump team has indicated the addition of two TCLA collimators per beam in IR6 in order to improve the protection of the Q4 and Q5 magnets immediately downstream of the dump protection devices [49]. The results indicate that this improvement was not necessary for post-LS1 operation. The requirements for HL will be reviewed in 2015.

#### 5.4.4 IR6 secondary collimators with pick-up (target collimator secondary with pick-up)

Carbon-based secondary collimators with pick-up buttons (target collimator secondary with pick-up (TCSP)) are used in the LHC IR6 insertion as a part of the LHC protection system. Two collimators are used in the LHC, one per beam, as auxiliary dump protection devices in the horizontal plane. In LS1, the TCSG design without integrated beam position monitors (BPMs) was replaced with the new one with BPMs for improved alignment and local orbit monitoring. Since these collimators are among the closest to the circulating beams, and are expected to be heavily exposed to beam losses in case of asynchronous dumps, their jaws are built with a robust CFC that is designed to withstand the design LHC failure scenarios at injection (full injection train of 288 bunches impacting on one jaw) and at 7 TeV (up to eight bunches impacting on one jaw in case of an asynchronous dump). The need to improve the IR6 TCSP collimator design in view of the updated beam parameters for the HL-LHC design is being assessed.

#### 5.4.5 Passive absorbers in IR3 and IR7 (TCAPA, TCAPB, TCAPC, TCAPD)

Tungsten-based passive shower absorbers collimators (target collimator absorber passive (TCAP)) are used in the LHC as fixed-aperture collimators in the momentum (IR3) and betatron (IR7) cleaning insertion to reduce radiation doses to the warm quadrupole and dipoles in these insertions. Two TCAP collimators per beam are used in IR3 whereas three collimators are used in IR7 for a total of 10 TCAP collimators in the LHC. Four variants of these collimators exist to match the dimensions and orientations of the aperture of the adjacent warm magnets: TCAPA, TCAPB, TCAPC, TCAPD. Operationally, these collimators are not supposed to intercept primary or secondary beam losses but rather to absorb shower products generated by halo particles impinging on primary and secondary collimators. They are built using a heavy tungsten alloy that maximizes

shower absorption, surrounded by copper. The need to improve the TCAP collimator design in view of the updated beam parameters for the HL-LHC design is being assessed.

The TCAP collimators ensure that doses on warm magnets in the cleaning insertions are minimized. Doses are determined by the integrated luminosity and therefore the possibility to improve the warm magnet protection must be envisaged for the HL-LHC luminosity goal. The upgrade of the passive absorber collimators might be needed for the HL-LHC if the present design proves not to be adequate for HL-LHC operational loss cases and/or if it can be improved by increasing the lifetime of warm magnets due to radiation wear (e.g. new materials or improved layouts/designs).

#### 5.4.6 Tertiary collimators with pick-up in the experimental regions (target collimator tertiary with pick-up)

As discussed above, tungsten-based tertiary collimators with pick-up buttons (target collimator tertiary with pick-up (TCTP)) are used in the LHC to protect the superconducting triplets and the experiments in each experimental insertion against horizontal (TCTPH) and vertical (TCTPV) beam losses. A complete re-design of IR1 and IR5 collimation is imposed by the layout changes foreseen in the HL-LHC for LS3. The need to improve the present TCTP collimators in IR1/IR5 in view of the updated beam parameters for the HL-LHC design is also being assessed. In particular, consideration is being given to the possibility of replacing the TCTPs with more robust ones based on novel materials, at least in the horizontal plane, which is affected by beam dump failures.

#### 5.4.7 Physics debris collimators in the experimental regions (Target Collimators Long - TCL)

Physics debris absorbers are used in IR1 and IR5 to protect the matching sections and the dispersion suppressor from beam losses caused by collision product. The LHC IR layouts as of 2015 feature three horizontal TCL collimators per beam and per IR, for a total of 12 TCL collimators, installed in cells 4, 5, and 6. Their jaws are made of copper (TCLs in cells 4 and 5) and Inermet 180 (cell 6), as the latter were installed by recuperating tertiary collimators replaced in LS1 with the new TCTPs. Indeed, the tungsten based TCT can serve as TCL without design changes. The present baseline foresees changing all TCLs for HL by adding the BPM feature. If it is proven that this new feature is not mandatory, the present TCL collimators might be re-used for the HL-LHC by being moved to new layout positions. Mechanical and radiation hardware should be studied for this scenario.

## 5.5 References

- [1] O. Brüning (Ed.) *et al.*, LHC Design Report Vol. 1, CERN-2004-003-V-1 (2004).
- [2] R. Assmann *et al.*, The final collimation system for the LHC, Proc. EPAC2006, Edinburgh, 2006. Conf. Proc. C060626 (2006) 986-988. Also as CERN-LHC-PROJECT-REPORT-919 (2006).
- [3] R. Bruce *et al.*, LHC beta\* reach in 2012, LHC Operation Workshop, Evian, 2011.  
<http://indico.cern.ch/event/155520>
- [4] R. Bruce *et al.*, Sources of machine-induced background in the ATLAS and CMS detectors at the CERN Large Hadron Collider, *Nucl. Instrum. Methods Phys. Res. A* **729** (2013) 825–840.
- [5] G. Valentino *et al.*, Beam diffusion measurements using collimator scans at the LHC, *Phys. Rev. Spec. Top. Accel. Beams* **16** (2013) 021003.
- [6] K.H. Mess and M. Seidel, Collimators as diagnostic tools in the proton machine of HERA, *Nucl. Instrum. Meth.* A351 (1994) 279–285.
- [7] H. Burkhardt, S. Redaelli, B. Salvachua and G. Valentino, Collimation down to 2 sigmas in special physics runs in the LHC, Proc. IPAC2013, Shanghai. Conference: [C13-05-12](#), TUPFI037. Also as CERN-ACC-2013-0144 (2013).
- [8] S. Redaelli *et al.*, LHC collimator controls for a safe LHC operation, Proc. ICALEPSC2011, Grenoble, 2011. <http://accelconf.web.cern.ch/AccelConf/icalepcs2011/papers/wepmu020.pdf>

- [9] A. Bertarelli *et al.*, The mechanical design for the LHC collimators, Proc. EPAC2004, Lucern, EPAC-2004-MOPLT008. <http://accelconf.web.cern.ch/accelconf/e04/papers/moplt008.pdf>
- [10] S. Redaelli *et al.*, Final implementation and performance of the LHC collimator control system, Proc. PAC09, Vancouver (CA). ). Conference: [C09-05-04](#), FR5REP007.
- [11] A. Bertarelli *et al.*, Mechanical design for robustness of the LHC collimators, Proc. PAC2005, Knoxville. <http://accelconf.web.cern.ch/AccelConf/p05/PAPERS/TPAP004.PDF>
- [12] F. Carra *et al.*, LHC collimators with embedded beam position monitors: A new advanced mechanical design, Proc. IPAC2011, San Sebastian, IPAC-2011-TUPS035 (2011).
- [13] D. Wollmann *et al.*, First beam results for a collimator with in-jaw beam position monitors, Proc. IPAC2011. <http://accelconf.web.cern.ch/AccelConf/IPAC2011/papers/thpz027.pdf>
- [14] D. Wollmann *et al.*, Experimental verification for a collimator with in-jaw beam position monitors, Proc. HB2012. <http://accelconf.web.cern.ch/AccelConf/HB2012/papers/mop242.pdf>
- [15] G. Valentino *et al.*, Successive approximation algorithm for BPM-based LHC collimator alignment, PRST-AB (2013) Phys. Rev. ST Accel. Beams 17, 021005..
- [16] HiLumi-WP5 deliverable document 5.4. <http://hilumilhc.web.cern.ch/science/deliverables>. Also available on the collimation page <https://lhc-collimation-upgrade-spec.web.cern.ch/lhc-collimation-upgrade-spec/HiLumi.php>
- [17] Web site: Review of 11 T dipoles and cold collimation. <https://indico.cern.ch/event/155408>
- [18] A. Marsili, R. Bruce, L. Lari, S. Redaelli, Simulated cleaning for HL-LHC layouts with errors, [http://indico.cern.ch/event/257368/session/30/contribution/59/attachments/451994/626718/HiLumiLHC\\_error\\_models\\_2.pdf](http://indico.cern.ch/event/257368/session/30/contribution/59/attachments/451994/626718/HiLumiLHC_error_models_2.pdf). Presentation at the 3rd Joint HiLumi LHC-LARP Annual Meeting, Daresbury (UK), 2013. Event web site: <http://indico.cern.ch/event/257368>
- [19] A. Lechner, *et al.*, Energy deposition with cryo-collimators in IR2 (ions) and IR7, [http://indico.cern.ch/event/257368/session/14/contribution/57/attachments/451997/626723/2013\\_13\\_1\\_1\\_endepdscoll.pdf](http://indico.cern.ch/event/257368/session/14/contribution/57/attachments/451997/626723/2013_13_1_1_endepdscoll.pdf). Presentation at the 3rd Joint HiLumi LHC-LARP Annual Meeting, Daresbury (UK), 2013. Event web site: <http://indico.cern.ch/event/257368>
- [20] R. Bruce, A. Marsili, S. Redaelli, Cleaning performance with 11 T dipoles and local dispersion suppressor collimation at the LHC, IPAC2014, Dresden, (2014). <http://accelconf.web.cern.ch/AccelConf/IPAC2014/papers/mopro042.pdf>
- [21] A. Lechner *et al.*, Power deposition in LHC magnets with and without dispersion suppressor collimators downstream of the betatron cleaning insertion, IPAC2014, Dresden, (2014). <http://accelconf.web.cern.ch/AccelConf/IPAC2014/papers/mopro021.pdf>
- [22] A. Marsili, R. Bruce, S. Redaelli, Collimation cleaning for HL-LHC optics with error models, IPAC2014, Dresden, (2014). <http://accelconf.web.cern.ch/AccelConf/IPAC2014/papers/mopro040.pdf>
- [23] Recommendation of 2013 Collimation Project review panel. <https://indico.cern.ch/event/251588/>
- [24] L. Gentini, presentation at the 30th meeting of the Collimation Upgrade Specification working group. <http://indico.cern.ch/event/278104/>
- [25] 2013 Collimation Project Review. <http://indico.cern.ch/event/251588>
- [26] LHC Collimation Review 2009. <http://indico.cern.ch/conferenceDisplay.py?confId=55195>
- [27] J.M. Jowett *et al.*, Heavy ion beams in the LHC, Proc. PAC 2003, Portland (2003). <http://accelconf.web.cern.ch/AccelConf/p03/PAPERS/TPPB029.PDF>
- [28] R. Bruce *et al.*, Beam losses from ultraperipheral nuclear collisions between  $^{208}\text{Pb}^{82+}$  ions in the Large Hadron Collider and their alleviation, *Phys. Rev. ST Accel. Beams* **12** (2009) 071002.
- [29] G. Steele *et al.*, Heat load scenarios and protection levels for ions, presentation at the 2013 LHC Collimation Project review. <http://indico.cern.ch/event/251588>
- [30] R. Assmann *et al.*, Collimation chapter of the LHC Design Report, Eds. O. Brüning *et al.* <http://ab-div.web.cern.ch/ab-div/Publications/LHC-DesignReport.html>

- [31] HiLumi WP2 deliverable document D2.1. <https://cds.cern.ch/record/1557082/files/CERN-ACC-2013-009.pdf>
- [32] HiLumi WP2 milestone document M29, Initial estimate of machine impedance. <https://cds.cern.ch/record/1644770/files/CERN-ACC-2014-0005.pdf>
- [33] HiLumi WP2 milestone document M31, Preliminary estimates of beam-beam effect. <http://cds.cern.ch/record/1709432/files/CERN-ACC-2014-0066.pdf>
- [34] N. Mounet, Transverse impedance in the HL-LHC era, presentation at the 3rd HiLumi Annual meeting, Daresbury, (2013). <https://indico.cern.ch/event/257368/>
- [35] F. Carra *et al.*, Mechanical engineering and design of novel collimators for HL-LHC, IPAC2014, Dresden, (2014). <http://accelconf.web.cern.ch/AccelConf/IPAC2014/papers/mopro116.pdf>
- [36] Review of hollow e-lens for the LHC collimation. <https://indico.cern.ch/event/213752>
- [37] G. Stancari, Progress towards the conceptual design of a hollow electron lens for the LHC, presentation at the 3rd Joint HiLumi LHC-LARP Annual Meeting, Daresbury, 2013. <http://indico.cern.ch/event/257368>
- [38] G. Stancari *et al.*, Conceptual design of hollow electron lenses for beam halo control in the Large Hadron Collider, FNAL note FERMILAB-TM-2572-APC (2014) and CERN ATS Report CERN-ACC-2014-0248 (2014).
- [39] W. Scandale, Crystal-based collimation in modern hadron colliders, *Int. J. Mod. Phys. A* **25S1** (2010) 70–85.
- [40] D. Mirarchi *et al.*, Layouts for crystal collimation tests at the LHC, Proc. IPAC2013, Shanghai. <https://cds.cern.ch/record/1573725?ln=en>
- [41] W. Scandale *et al.*, Comparative results on collimation of the SPS beam of protons and Pb ions with bent crystals, *Phys. Lett.* **B703** (2011) 547–551.
- [42] W. Scandale *et al.*, Optimization of the crystal-assisted collimation of the SPS beam, *Phys. Lett.* **B726** (2013) 182–186.
- [43] W. Scandale *et al.*, Strong reduction of the off-momentum halo in crystal assisted collimation of the SPS beam, *Phys. Lett.* **B714** (2012) 231–236
- [44] CERN EDMS document 1329235, LHC-TEC-EC-0001 (2013).
- [45] A. Faus-Golfe *et al.*, Non-linear collimation in linear and circular colliders, Proc. EPAC2006, Edinburgh. <http://accelconf.web.cern.ch/AccelConf/e06/PAPERS/WEXFI03.PDF>
- [46] L. Lari *et al.*, Studies for an alternative LHC non-linear collimation system, Proc. IPAC2012. <http://accelconf.web.cern.ch/AccelConf/IPAC2012/papers/moppd077.pdf>
- [47] J. Smith *et al.*, Design of a rotatable copper collimator for the LHC phase II collimation upgrade. EPAC2008, Genova (I). <http://accelconf.web.cern.ch/AccelConf/e08/papers/mopc096.pdf>
- [48] T. Markiewicz, Status of SLAC RC, presentation at the 3rd HiLumi annual meeting, Daresbury, 2013. <http://indico.cern.ch/event/257368>
- [49] Collimation Working group meeting. <https://indico.cern.ch/event/244412/>



# Chapter 6

## Cold Powering

*A. Ballarino<sup>1\*</sup>, J.P. Burnet<sup>1</sup>, D. Ramos<sup>1</sup>, U. Wagner<sup>1</sup>, S. Weisz<sup>1</sup> and Y. Yang<sup>2</sup>*

<sup>1</sup>CERN, Accelerator & Technology Sector, Geneva, Switzerland

<sup>2</sup>University of Southampton, Southampton, UK

### 6 Cold powering

#### 6.1 Overview

The electrical feed for the approximately 1700 superconducting (SC) circuits of the Large Hadron Collider (LHC) requires the transmission of more than  $\pm 1.5$  MA of current from the power converters to the magnets. This is done via conventional copper cables for the room temperature path between power converters and current leads, and high temperature superconducting (HTS) and resistive current leads for transfer to the 4.5 K liquid helium bath. Nb-Ti busbars operating in liquid helium at 4.5 K or in superfluid helium at 1.9 K provide the connection to the SC magnets. In the current LHC configuration, the power converters and the current leads are both located in underground areas, the former mainly in alcoves situated adjacent to the machine tunnel, and the latter in cryostats that are near the LHC interaction points and in line with the SC magnets. The 60 A power converters for the dipole orbit correctors are located in the tunnel, underneath the main dipole magnets. From each of the eight interaction points, power converters and current leads feed the magnets, occupying half of the two adjacent machine sectors. Some equipment in the tunnel is exposed to significant levels of radiation.

For the HL-LHC upgrade, novel superconducting lines (hereafter called ‘links’) are being developed to supply current to the magnets from remote locations [1]. The new electrical layout envisages the location of the power converters and current leads either in surface buildings or in underground areas, some hundreds of metres away from the tunnel. The transmission of the current to the magnets is performed via SC links containing tens of cables feeding different circuits. Each link would transfer in total up to about 150 kA. There are several benefits of remote powering via F and these can be summarized as follows.

- Access of personnel for maintenance, tests, and interventions on power converters, current leads, and associated equipment in radiation-free areas, in accordance with the principle of radiation protection that optimizes doses to personnel exposed to radiation by keeping them as low as reasonably achievable (ALARA).
- Removal of the current leads and associated cryostats from the accelerator ring, thus making space available for other accelerator components. In the baseline hardware layout of the HL-LHC interaction regions (IR) around P1 and P5, no space is available for current leads and cryostats in line with the magnets. Also, there is no space in the existing underground alcoves for locating the power converters feeding the HL-LHC circuits.
- Location of the power converters in radiation-free areas.

The ongoing programme focuses on the development of links to be integrated at LHC points P1, P5, and P7.

---

\* Corresponding author: [amalia.ballarino@cern.ch](mailto:amalia.ballarino@cern.ch)

### 6.1.1 Cold Powering Systems at LHC P1, P5, and P7

The Cold Powering System consists of the following.

- Power converters.
- Current leads, located as near as possible to the power converters in a radiation-free zone some hundreds of metres distance from the LHC tunnel. The leads are connected to the power converters via room temperature conventional cables.
- A dedicated cryostat (DFH), where the cold terminations of the leads are electrically connected to the cables in the link.
- A link, made of superconducting cables housed in a semi-flexible cryostat (DSH). The link electrically connects the leads to the magnet busbar.
- A cryostat (DF) in line with the magnets at the location where the link terminates in the LHC tunnel. In the DF cryostat, each cable of the link is connected to the Nb-Ti busbar feeding a magnet circuit. The helium cryogen required for the cooling of the Cold Powering System is supplied from this cryostat.
- Cryogenic instrumentation required for control, monitoring, and interlock functions as well as the electrical instrumentation needed for protection of superconducting components and current leads.

The Cold Powering System relies on cooling with helium gas, and the superconducting part of the system spans the temperature range from 4.2 K up to 35–50 K. The use of MgB<sub>2</sub> and HTS materials enables safe operation of the superconducting components, for which a temperature margin, intended as the increase of temperature that generates a resistive transition, of at least 10 K is guaranteed.

In the tunnel, vapour generated in the DF cryostat from a two-phase helium bath is conveyed inside the link cold mass [2]. The gas cools the SC cables in the link and warms up to about 17 K while absorbing the static heat load of the cryostat. The DSH cryostat includes a thermal shield actively cooled by forced flow of He gas taken from the tunnel at about 20 K. For the Cold Powering Systems at LHC P1 and P5, the two helium flows are mixed at the level of the DFH to produce the flow of He gas, at about 30 K, required for the cooling of the current leads. The system at LHC P7 does not need mixing – the helium flow in the superconducting link cold mass is sufficient for the cooling of the leads. The design of the current leads is such that the gas is recovered at room temperature at their warm end.

The development of the Cold Powering System for LHC P7 <sup>1</sup>is well advanced to date.

- Concepts [3] and prototype [4] SC cables have been developed and tested.
- Dedicated cabling machines conceived for production of long unit lengths of novel HTS or MgB<sub>2</sub> cables have been designed, assembled, and operated [5].
- A prototype Cold Powering System has been developed and tested [6].
- Integration studies in the LHC have been performed [7].
- New concepts of current leads and DFH cryostats optimized for easy transport and integration in the LHC underground areas have been elaborated. Detailed drawing activity for production of prototypes is being launched.

The design of the Cold Powering Systems minimizes the work done in the tunnel during installation of components. It also takes into account boundary conditions imposed by transport in the LHC underground areas. In particular, volumes of individual components have been minimized according to transport

---

<sup>1</sup> The SC link in P7 has recently been removed from the HL-LHC baseline; see LMC199 of 17 December 2014. However, the PDR refers to the baseline of October–November 2104, therefore we prefer to keep the description of the P7 SC link in this text. In addition this assures consistency with the first version of the PDR delivered to the FP7 office on 30 November 2014, and also avoids a revision of other parts of the PDR referring to the November 2014 baseline,

requirements, and the main components (link, i.e. DSH cryostat with the SC cables inside, current leads, and the DFH and DF cryostats) are integrated as complete and pre-tested assemblies. Activities after integration are limited to splicing between current leads and link and closure of the DFH cryostat; splicing between link and Nb-Ti busbar and closure of the DF cryostat; and connection of the conventional room temperature cables to current leads and power converters.

### 6.1.2 Superconducting link

The superconducting link is a semi-flexible transfer line, of a total length of up to about 500 m, which houses the SC cables connecting the cold end of the current leads to the Nb-Ti busbar of the magnet [1]. The transfer line consists of four corrugated concentric pipes that define the link cold mass, the actively cooled thermal shield, and the external vacuum insulation wall.

The number of SC cables contained inside the link and their operating current vary for the different Cold Powering Systems that are currently under study. Inside the cold mass of each link there are tens of cables rated at different DC currents ranging from a minimum of 120 A up to a maximum of 20 kA. The cables are grouped in the form of compact cable assemblies with a total current capability of up to about 150 kA.

At LHC P1 and P5 six superconducting links, three right and three left of each interaction point, are being considered for integration in the LHC machine:

- two links for the powering of the HL-LHC insertions (low- $\beta$  quadrupoles, D1 and corrector magnets);
- two links for the powering of the HL-LHC matching sections;
- two links for the powering of the LHC magnets in the arc<sup>2</sup>.

The associated Cold Powering Systems replace the LHC cryogenic feedboxes (DFBX, DFBL, and DFBA). New current leads and cryostats (DFHX, DFHM, and DFHA), connected to the link in a radiation-free area away from the tunnel, are being developed.

Work until now has been focused on the systems for the HL-LHC upgrade, but the development is directly applicable to the Cold Powering Systems that are intended to replace the DFBA. The present baseline electrical layout envisages the installation of the power converters and current leads in surface buildings. This calls for the development of superconducting links, about 300 m long, including a vertical section of about 80 m.

At LHC P7 it is proposed to move power converters and current leads to an underground radiation-free gallery, which serves as access to the LHC ring (TZ76 gallery). Two superconducting links, each about 500 m long, are needed to connect the DF cryostat in the tunnel to the DFH in the TZ76 (see Section 6.1). The SC link will contain all cables feeding the LHC 600 A circuits that are currently powered via the DFBA and DFBL at P7. The cable assembly in the SC link cold mass requires 48 cables rated at 600 A, for a total current-carrying capability of about 29 kA.

The need of the Cold Powering Systems for the LHC circuits that are not part of the HL-LHC upgrade, i.e. those feeding either the magnets in the arc at LHC P1 and P5 or the magnets at P7, is driven by the Radiation To Electronics (R2E) requirements of the power converters. Integration with the LHC machine will be decided at a later stage of the project.

The present baseline proposal envisages using MgB<sub>2</sub> conductor in the longest part of the Links (from 4.2 K to 20 K), and HTS material (YBCO or Bi-2223) in the temperature range 20 K to 35–50 K. The potential low cost of the MgB<sub>2</sub> conductor and the possibility of cooling the superconducting link cold mass with He gas

---

<sup>2</sup> SC links for the LHC magnet in the arc (change of DFBA) has been removed from the HL-LHC baseline (see LMC199 of 17 December 2104). However, for reason of coherence with the November 2014 baseline that is the reference for the present PDR (see previous footnote), the text has not been modified. The change will be recorded in the next version of the Technical Design Report due at the end of 2015.

enable the development of Cold Powering Systems with improved performance. There is a higher temperature margin, with the benefit of safer operation and lower total exergetic cost of the refrigeration, with no extra cost with respect to the conventional Nb-Ti solution. Figure 6-2 shows a cross-section through the superconducting cable assembly proposed for the links powering the HL-LHC insertions at LHC P1 and P5. The total current transferred by these 44 cables is 165 kA. Six 20 kA cables are required for powering the low- $\beta$  insertion Nb<sub>3</sub>Sn quadrupole magnets and the Nb-Ti separation dipole, while the other cables feed corrector and trim circuits. Details of the cable assemblies developed for other Cold Powering Systems are presented elsewhere [1].

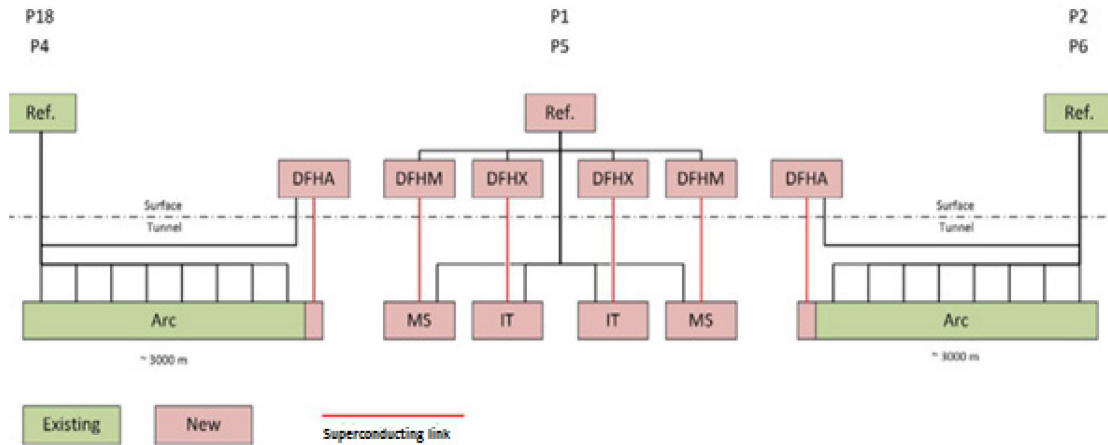


Figure 6-1: Superconducting links at LHC P1 and P5

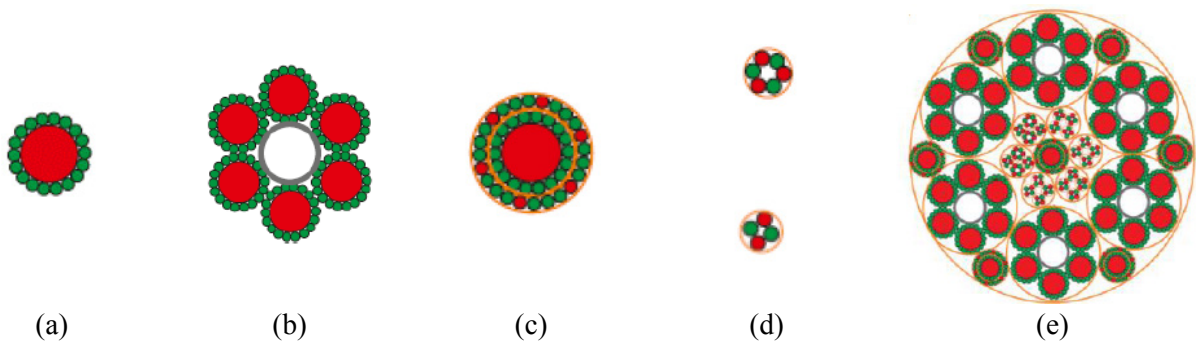


Figure 6-2: Cable assemblies for superconducting links at LHC P1 and P5. (a) Sub-unit of 20 kA cable,  $\Phi \sim 6.5$  mm; (b) 20 kA cable,  $\Phi \sim 19.5$  mm; (c) concentric  $2 \times 3$  kA cable,  $\Phi \sim 8.5$  mm; (d) 0.4 kA cable (top) and 0.12 kA cable (bottom),  $\Phi < 3$  mm; (e) 165 kA cable assembly for LHC P1 and P5 ( $6 \times 20$  kA,  $7 \times 2 \times 3$  kA,  $4 \times 0.4$  kA,  $18 \times 0.12$  kA),  $\Phi \sim 65$  mm. The cables are made of copper stabilizer (red) and MgB<sub>2</sub> wire (green).

The cable (twisted-pair superconducting tapes or wires) and cable assemblies developed for LHC P7 are optimized for the transport of current in the 1 kA range. Details of the cable concepts and results from tests performed under nominal operating conditions are presented elsewhere [4]. The cable assemblies are incorporated in a semi-flexible cryostat of the Cryoflex<sup>®</sup> type. The present baseline, which is to be confirmed through ongoing integration studies and tests, envisages integration in the LHC tunnel of the cryostat with the cable assemblies already pulled in at the surface. To limit the risks associated with high-current resistive joints operated in a helium gas environment, the cables are planned to be assembled in one single unit length with no splices between cables inside the link.

The main achievements to date are:

- the development of the first MgB<sub>2</sub> powder-in-tube (PIT) round wire with electrical and mechanical performance that permits its use in high-current cables – work done in collaboration between CERN and Columbus Superconductors, Genova;

## COLD POWERING

- the test of a 3 m long superconducting link of the type needed at LHC P7 [6];
- the design of a Cold Powering System optimized for integration at LHC P7 [6];
- the successful development and test of the first  $2 \times 20$  m long cable made from  $MgB_2$  round wire operated successfully up to 20 kA at 24 K [8].

Figure 6-3 shows the test station designed and successfully operated at CERN for the test of superconducting links up to 20 m long. As in the final configuration, the cables are cooled by the forced flow of helium gas operating at any temperature from about 5 K to 35 K. Temperatures of up to 70 K can be achieved, enabling appraisal of cables made from different types of conductor.

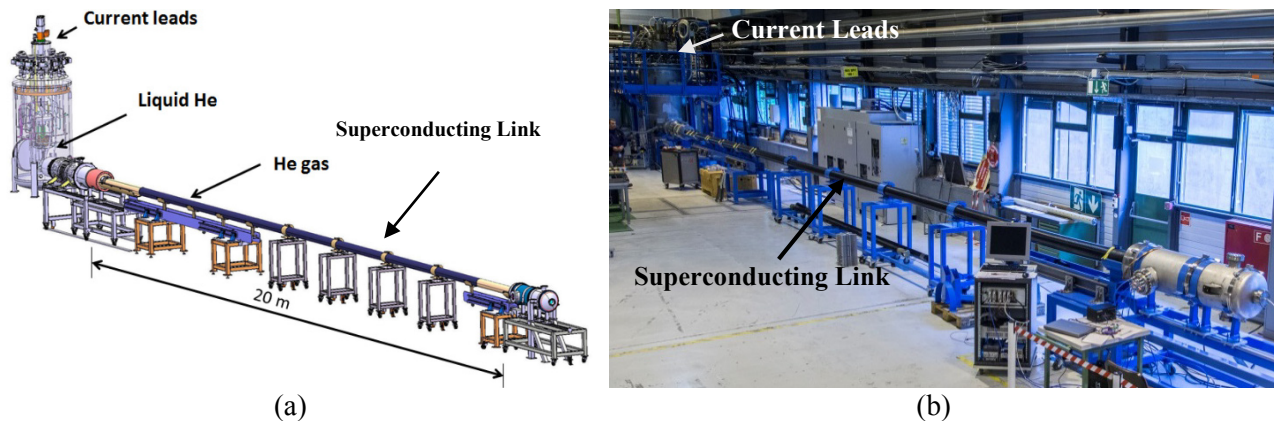


Figure 6-3: Two views of the test station designed and operated at CERN for the test of superconducting links up to 20 m long. The cables are cooled by forced flow of helium gas operating at any temperature from about 5 K to 35 K. Temperatures of up to 70 K can be achieved, enabling appraisal of cables made from different types of conductor.

### 6.2 Cold Powering System design

In essence the Cold Powering System for the powering of the LHC magnets by superconducting links is a semi-flexible cryostat extending over a few hundred metres. The novel design has to face several challenges never encountered previously.

#### 6.2.1 Cryostat for the superconducting link

The superconducting link cryostat (DSH) must maintain a stable and well-defined cryogenic environment within which the superconducting cables are cooled by the forced flow of helium gas. Unlike the liquid helium-cooled superconducting busbars in the LHC machine, the cryogenic stability of the superconducting cables depends more critically on the cooling efficiency in a helium gas environment within the superconducting link cold mass. The basic cryostat structure consists of an inner vessel surrounded by an actively cooled thermal shield and enclosed by an outer vessel as room temperature vacuum envelope. At present the reference design of the cryostat is analogous to Nexans' four-tube coaxial Cryoflex<sup>®</sup> transfer line, which can be manufactured and delivered in one continuous length compatible with the cold powering requirements. It is essential to minimize the number of splices between cables inside the SC link cold mass due to their multiple circuit complexity and cooling challenges for high-current resistive joints cooled by gaseous helium. While cryostat flexibility is a crucial design aspect, it is recognized that the mechanical support to the vertical section at LHC P1 and P5 requires additional consideration. As part of the HL-LHC design studies, pre-prototype cryostats in 5 m and 20 m lengths have been procured from Nexans and tested at CERN [8] and at the University of Southampton [6]. The working experiences have been positive so far and a 60 m long cryostat will be procured in the coming months for integration tests in configurations similar to those in the LHC underground areas and for horizontal and vertical evaluation.

The gaseous helium in the cold mass of the link provides cooling for (i) steady-state heat load of the radial heat in-leak (conduction and radiation) from the surrounding thermal shield and heat conduction along the link and the inner vessel wall from the warmer end at 20 K; and (ii) transient heat load due to local disturbances in the link and/or thermal/vacuum instability in the cryostat. Under nominal operating conditions, the radial heat in-leak is dominant, estimated conservatively at below 0.2 W/m for a thermal shield temperature of  $\sim 60$  K without multilayer insulation. The thermal shield will be actively cooled by flowing helium gas with an inlet temperature at 20 K. Further discussions on the cooling requirement can be found in Ref. [2].

### 6.3 Interfaces to the superconducting link

The link has a colder (4.2 K) interface to the LHC machine at one end and a warmer (20 K) interface to the current leads at the level of the DFH cryostat. The two interfaces are an integral part of the Cold Powering System due to electrical continuity and synergy in the cooling arrangements.

The present LHC current leads consist of a self-cooled HTS section and a 20 K helium gas-cooled resistive copper section [9]. The former is connected to the Nb-Ti busbar in helium and the latter extends from the warm end of the HTS at 50 K to room temperature. The Cold Powering System design seeks the integration of the different helium gas flows at the interface of the superconducting link and current leads.

#### 6.3.1 Electrical interface between the superconducting link and the current leads

Each of the multiple cables inside the superconducting link is spliced and connected to its corresponding current lead inside the DFH interconnection cryostat. The cryostat must allow easy access for making the electrical connections after the deployment of the superconducting link cable assembly in the semi-flexible DSH cryostat. The primary design focus is the reliable and secure handling of the SC cables via robust tooling and procedures. In addition, the design ensures in situ completion of low resistance joints between the SC cables in the link and the current leads. Effective cooling of the resistive joints via the helium gas inside the link also requires integrated heat transfer features.

There are additional considerations to address specific circumstances for the systems at P1, P5, and P7. For example, the SC link at P7 terminates in the TZ76 underground gallery. The present configuration of TZ76 imposes stringent space restrictions for component transportation and installation. These constraints have been satisfied in the present baseline design where a stand-alone interconnection cryostat is connected to twelve discrete units of four  $\times$  600 A current lead assemblies via HTS cables housed in twelve slim transfer-line type cryostats. A prototype of the Cold Powering System at LHC P7 will be manufactured and tested in the SM18 in 2015. The existing test station incorporating the 20 m Cryoflex<sup>®</sup> line (see Figure 6-3) will be used for this purpose.

#### 6.3.2 Cryogenic interface between the superconducting link and the current leads

The interface between the superconducting link and the current leads involves several cryogenic aspects. First of all, the continuation of the helium gas from the superconducting link into the current leads and its mixing with additional cooling gas if necessary will be assured. The present cooling proposal for the systems at P1 and P5 [2] uses the warm exit of the helium gas cooling the SC link thermal shield as the supplementary coolant for the current leads. Since the exit temperature of the shield cooling gas always exceeds the warm boundary condition of 20 K for the SC cable in the link, this option implicitly imposes hydraulic separation of the helium spaces of the link and the leads. This is likely to be the scenario for P1 and P5, where the superconducting link cold mass requires  $\sim 1$  g/s while the current leads require  $\sim 10$  g/s for a total transfer of about 150 kA.

The cooling requirements for the SC link and current leads at P7 are well matched, with 1.5 g/s for the DSH cold mass and 1.4 g/s for the DFH. Therefore, there is a compelling case for using only the helium gas from the SC link cold mass for cooling the current leads. The elimination of hydraulic separation/re-mixing is an attractive proposition for aspects of both assembly and installation.

It is envisaged that the superconducting link cryostat (DSH) and current leads share a common vacuum space. A Paschen scenario will be avoided by ensuring that all of the high-tension side is surrounded by helium cooling gas at about 1 bar.

### 6.3.3 Control

The stable operation of the Cold Powering System relies on maintaining two temperature boundary conditions, i.e. 20 K at the splice terminations between the superconducting link and the current leads and about 35 K to 50 K at the cold end of the resistive section of the current leads. The former is controlled by a heater to generate the required helium boil-off from the DF cryostat in the LHC tunnel while the latter is controlled by a valve at the helium warm exit of each current lead. If a single helium flow is adopted for P7, then an appropriate override should be devised for the two controllers to work correctly in tandem. Specifically, if more flow is required by the current leads, the boil-off heater must allow the temperature in the DF to drift below the set value of 20 K. Conversely, if higher boil-off is necessary for the cooling of the interconnections, a pressure-controlled cold bleed will be used to discharge the excess in order to avoid over-cooling of the current leads.

## 6.4 Interface to the LHC machine

### 6.4.1 General

The DF cryostat interfacing the superconducting link to the magnets cold mass performs the role of electrical, cryogenic, and mechanical interface. It includes:

- the required connections to the LHC cryogenic distribution line (QRL);
- a saturated liquid helium bath for the electrical splices between the cables in the link and the Nb-Ti cables;
- a hydraulic separation with respect to the superfluid helium bath cooling the magnets;
- the instrumentation required for cryogenic process control.

Different variants of DF cryostats are necessary for the Cold Powering Systems under study. The DF cryostats are vacuum-insulated and equipped with an actively cooled thermal shield wrapped in multilayer insulation. Vacuum barriers are foreseen to separate the insulation vacuum of the DF cryostat from that of the link, in order to allow interventions on either piece of equipment without the need for vacuum conditioning of the full system.

### 6.4.2 Interface cryostat for the HL-LHC insertions

A continuous cryostat of approximately 60 m in length is foreseen to house the magnets from Q1 to D1 in a common insulation vacuum, with the interface cryostat to the link (DFX) located at its non-IP extremity, after D1. This being the most suitable location from the machine optics point of view, it implies on the other hand that the DFX vacuum vessel and respective supports must be designed to withstand an axial force of up to 10 tonnes, which is induced by unbalanced atmospheric pressure. The DFX will include a jumper to the QRL with helium piping for the supply of both the superconducting link and part of the continuous cryostat.

The DFX may either be designed as an independent cryostat or as a service module integrated in the D1 cryostat. The choice between these two configurations will be made not only on the basis of integration and engineering considerations, but most importantly taking into account the need for minimizing the residual radiation doses to personnel during specific interventions that may occur in the lifetime of the HL-LHC machine, such as the exchange of a magnet.

### 6.4.3 Interface cryostat for the matching sections

The most compact solution for the Cold powering System of the matching sections is to include the connection to the link in the service module of the magnet cryostat (QQS). From there, a first link cooled by supercritical

helium is routed up to the DFM cryostat that replaces the present LHC DFL feedbox. All cables are then gathered inside the DFM into a main link connecting the DFM to the current leads at the surface. The supercritical helium arriving from the link in the tunnel is expanded inside the DFM to generate liquid for the splices and gas for the cooling of the SC link joining the surface. As such, this concept does not require a connection to the QRL at the level of the DFM.

#### 6.4.4 Interface cryostat for the arcs

The DFBA LHC feedboxes comprise the so-called current modules, housing the current leads, and a shuffling module that serves as an interface to the Q7; all being supported in a stiff beam which spreads the axial force from atmospheric pressure to the tunnel floor. The most cost effective approach consists in exchanging the existing current module with a new DFA cryostat, profiting from the existing interfaces to the arc cryostat and the QRL. In this way, no interventions are required on the shuffling module and on the support beam. The DFA includes the connection to the QRL and provides the helium supply for the link. The DFA also contains two 13 kA current leads, used for energy extraction of the main dipole circuit, which will remain in their current location. Because they require a precise control of the liquid helium level, these leads will be cooled by a separate helium bath. In the particular case of LHC P7, a supercritical helium cooled link connects the Q6 to the DFA.

### 6.5 Integration of the Cold Powering Systems in the LHC machine

The constraints for integration of the Cold Powering Systems at LHC P7, P1, and P5 are very different, and each of these cases requires a specific analysis:

- P7 is below the border between France and Switzerland, near the Lycée International of Ferney Voltaire, and surface buildings cannot be envisaged in this environment;
- P1 is equipped with a large service shaft and the LHC tunnel is enlarged in the corresponding straight section;
- P5 underground conditions are very restrictive, with a service shaft that is small and off-centre, and with standard LHC tunnel around the collision region.

The following sections summarize the solutions presently retained for installing the Cold Powering Systems in these different areas.

#### 6.5.1 Integration of the Cold Powering Systems at LHC P7

The insertion at P7 houses the betatron collimation system, where a large fraction of the beam losses is intercepted. This induces a radiation level that is a long-standing issue regarding single event upset in the electronics devices installed in the area. Additional shielding to protect the RR was installed in 2008 [10]. The uninterruptible powering system (UPS) was also relocated in 2008 [11]. All sensitive elements were relocated out of UJ76 during Long Shutdown 1 (LS1) [12]. The power converters located in the service caverns RR73 and RR77 are the next source of concern as both the energy and intensity of the circulating beam will increase in the future. The solutions envisaged require either to increase the radiation tolerance or to relocate these power converters, and the Cold Powering System provides a practical solution for the second option.

As mentioned above, the geographical situation of P7 strongly constrains the installation of surface buildings, and this is the reason why the access shaft, which dates from the LEP construction era, is located about 400 m from the machine tunnel. Figure 6-4 gives an overview of the corresponding underground premises. The long gallery TZ76, which was already used to relocate equipment originally installed in the UJ76 cavern, provides a radiation-free area to install the power converters after their removal from RR73 and RR77. The red and yellow lines in Figure 6-4 indicate the routing of the Cold Powering Systems associated with arc 6–7 and arc 7–8, respectively. The total length of each line is about 500 m, with 250 m along the beam



line in the LHC tunnel. Section 6.5.2 presents the integration of the Cold Powering System along the different portions of these routings, starting from the RR toward the TZ service gallery.

The RR73/R77 alcoves contain the LHC DFBAM/N feedboxes that provide the warm to cold transition via the current leads. These DFBs will be replaced by the DFAM/N interfaces between the SC link and the Nb-Ti busbar of the magnets.

The links and the helium gas warm recovery lines can be installed close to the ceiling of the LHC tunnel in the long straight sections R74 and R771.

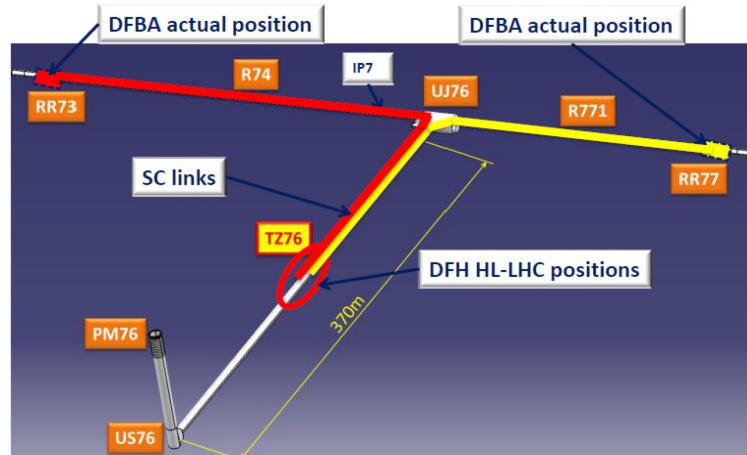


Figure 6-4: Underground layout at LHC P7

The passage of the links from the LHC tunnel to the TZ76 service gallery is the most delicate area regarding the installation of the Cold Powering Systems at LHC P7. Two alternatives are presently under consideration. The first involves a large number of rather sharp bends of the SC link to comply with the geometry of the UJ76 junction area (see Figure 6-5). The second relies on the drilling of two long ducts (each ~19 m long) to simplify the routing of the SC link (see Figure 6-6). A 60 m long cryostat should become available in spring 2015 to test the handling and installation of a SC link in order to decide between these two options.

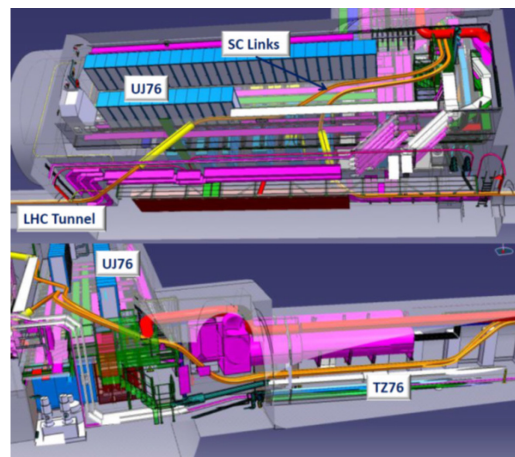


Figure 6-5: Passage through UJ76 with routing of the links in the UJ76 area

The two links and the two He return lines can be installed on the upper part of the TZ76 service gallery as shown on Figure 6-7(b). The routing in this configuration would be about 500 m until one reaches an equipment-free area where the current leads and the relocated power converters can be installed. Figure 6-7(a) gives a schematic view. The precise dimension and shape of the DFH cryostats are being defined. Space has been allocated for the power converters and their associated cooling units.

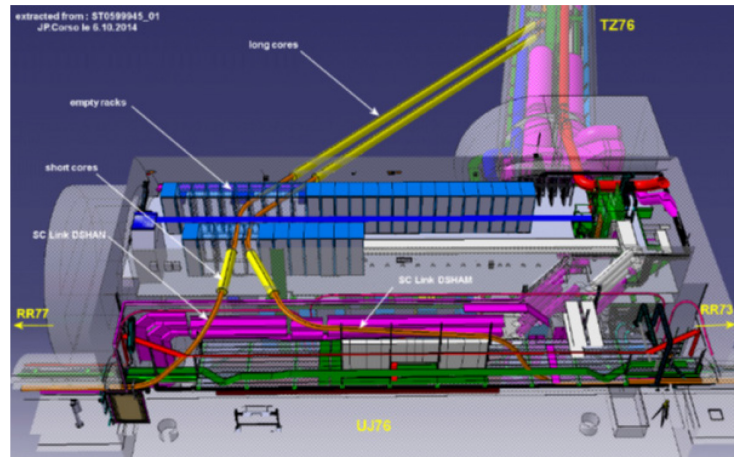


Figure 6-6: Passage of links through UJ76 with additional ducts

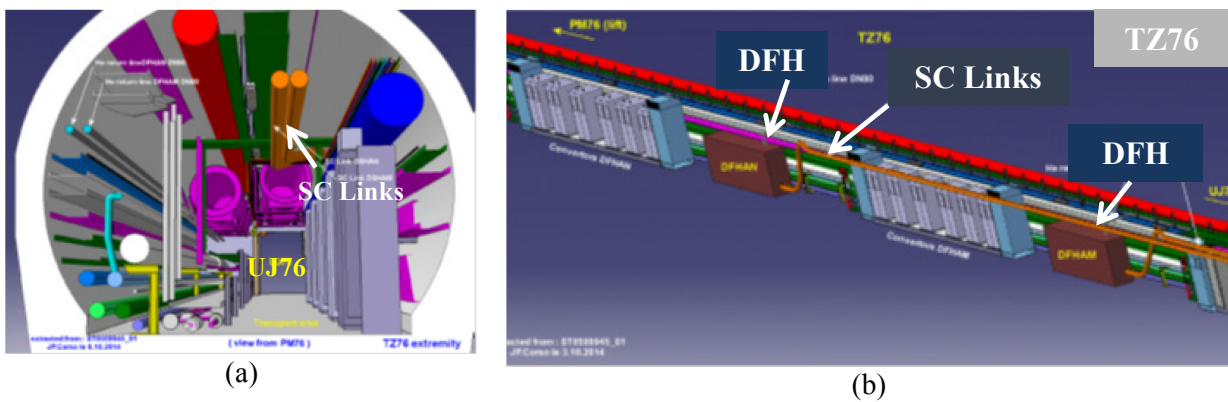


Figure 6-7: (a) Routing of the two links and the two He return lines in the service gallery. (b) Installation of the DFH and of the power converters in TZ76.

### 6.5.2 Integration of the Cold Powering Systems at LHC P1

P1 houses high luminosity insertions that are totally redesigned to meet the HL-LHC performance requirements. The inner triplet quadrupoles, the D1–D2 separation dipoles, and the matching sections will be replaced. Much higher current will be required to power the new magnets. The present underground premises at P1 do not provide enough space for the corresponding power converters; and the objective of the Cold Powering System is to allow the installation of these new power converters at the surface. There is a large service shaft (PM15) at P1 that can be used to route several SC links, and those powering the new low- $\beta$  triplets and D1 have a quite simple path as shown in Figure 6-8.

The D2 separation dipole and the stand-alone quadrupoles of the matching section are presently powered through a Nb-Ti superconducting link with distribution feedboxes (DFBLA and DFBLB) and power converters located in the alcoves located at about 250 m distance from the tunnel on both sides of IP1 (RR13 and RR17). The new Cold Powering Systems include DFM cryostats between the Nb-Ti magnet busbars and the MgB<sub>2</sub> cables that would be installed in place of the present DFBLA and DFBLB. The links will then be routed along the beam lines in the long straight sections until reaching the junction caverns (UJ13 and UJ17, left and right, respectively, of IP1) and then running to the surface as shown in Figure 6-8. The precise position of the links in the long straight section is not defined yet as they will need to pass across the crab cavities area that is still being designed. However, as the LHC tunnel is enlarged to a 4.4 m diameter around P1, no space difficulties are expected.

The RR13 and RR17 also house feedboxes (DFBAA and DFBAB) and power converters for arcs 8-1 and 1-2, respectively. Radiation levels in these areas will increase with luminosity and may become an issue. Moreover, the HL-LHC involves new equipment in the high luminosity insertions that, in turn, will require additional space. While the impact of the radiation level and the need for shielding are being assessed, there are clear incentives to relocate as many as possible of the present power converters from RR13/RR17 to the surface. If this is the case, the removal of the DFBA would free space for the installation of new DFA cryostats, with the current leads for energy extraction of the main dipole circuit and the connections to the QRL remaining at their current locations. The links would then follow the same path to the surface as those discussed above for D2 and the matching section quadrupoles.

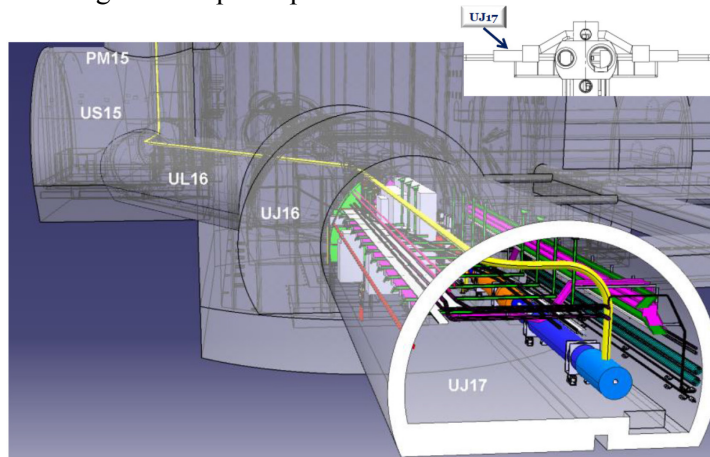


Figure 6-8: Routing of the links to surface for the low- $\beta$  triplet right of LHC P1

The detailed integration of the power converters in a surface building is not yet available, but it will involve an extension of the SD15 building at the top of PM15 with a total size that has to account for the total number of relocated power converters and for other additional HL-LHC related equipment.

### 6.5.3 Integration of the Cold Powering Systems at LHC P5

The elements of the Cold Powering Systems to be installed for HL-LHC at P5 are the same as those for P1. However, the environment at P5 is different. The tunnel diameter in the straight sections is 3.8 m, and nearly all of the space is already allocated. The service shaft (PM56), located to the right of P5, is a small shaft dedicated to personnel access only. Therefore, a totally different routing to the surface must be envisaged for the links compared with the solution retained for P1.

Vertical shafts would allow routing the links from the LHC machine to the surface. They can be done with a standard excavation method (auger drilling) providing a 0.4 m internal diameter duct that is sufficient for housing one SC link and its supporting system. As it is a top-down drilling technique, there is a tolerance of about 0.5 m on the position of the shaft when it reaches the LHC level some 90 m below ground. This would be problematic if the target is the narrow machine tunnel, but it is acceptable if the shaft has to reach enlarged areas as the RRs or UJs, which are 10.40 m and 8.40 m wide, respectively. The position of these enlarged areas at P5 is indicated in Figure 6-9. Vertical shafts above the UJ53 and the UJ57 would be allocated to the links for the new low- $\beta$  triplets and D1 separation dipoles. Those above the RR53 and the RR57 would be allocated to the links for the stand-alone magnets of the matching sections. If the power converters for the arcs are also relocated to the surface, shafts would be drilled above the RR53 and the RR57 for the corresponding links.

New surface buildings will be required to house the power converters. The optimization process between small local buildings or larger ones, connected through trenches to regroup the power converters, has yet to be done. A global optimization should take account of all new equipment required for the HL-LHC. The crab cavity system is facing a similar problem and it should be mentioned that a study is ongoing for new underground premises to cope with the space requirements of the cryogenics cold boxes, the crab cavities, and the powering equipment.

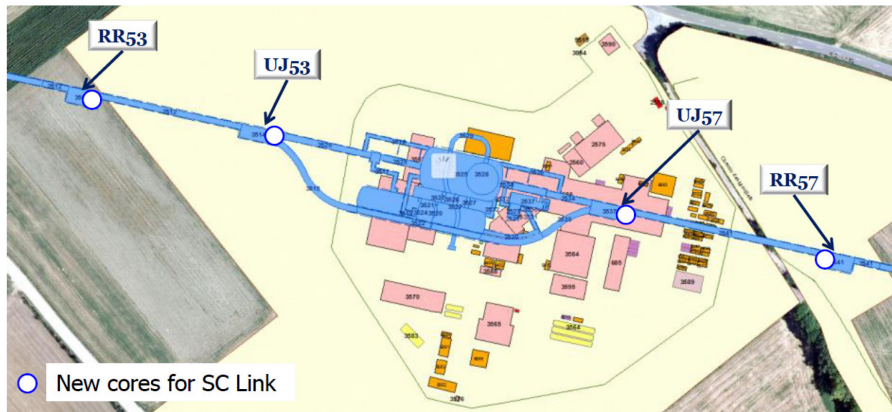


Figure 6-9: Layout of underground premises and of surface buildings at P5

## 6.6 Powering layout

Figure 6-10 shows the powering layout of the present LHC inner triplets. This powering scheme consists of a nested circuit with three power converters and free-wheeling protection circuits [13].

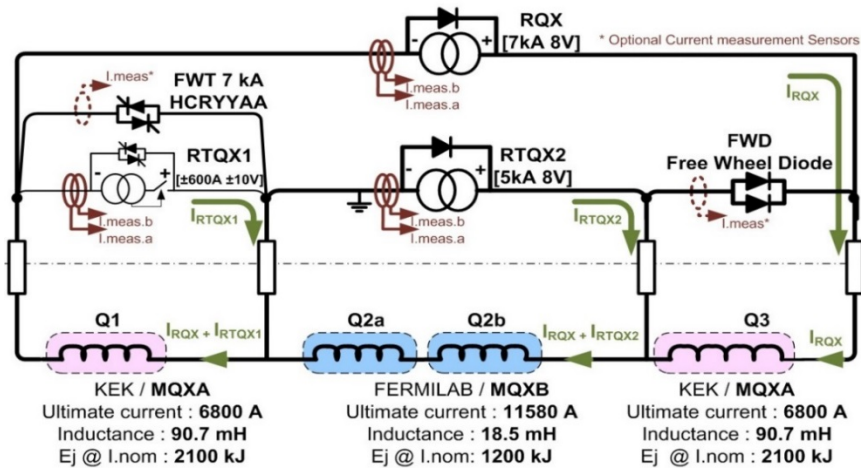


Figure 6-10: Powering layout of the present LHC inner triplets

It requires a dedicated control system to decouple the control of the power converters [14]. At the beginning of the LHC operation, this specificity generated longer downtimes with respect to the other electrical circuits. Thanks to the experience gained and the development of diagnostic tools, the system has currently reached a good level of reliability. It should be noted that the ramp-down time of these circuits, which defines the minimum time before a beam injection, had to be slowed down with respect to that obtained with the free-wheeling process. This was done in order to avoid trips of the power converters generated by the nested configuration.

The baseline powering layout of the HL-LHC inner triplets is shown in Figure 6-11. The low- $\beta$  quadrupoles (Q1, Q2, and Q3) are powered via two main circuits, each equipped with one trim power converter. The two Q2 units are powered in series with a 200 A trim converter on Q2b. Q1 and Q3 are powered in series with a 2 kA trim converter on Q3. The separation dipole (D1) and the corrector magnets are individually powered. This layout: i) provides maximum flexibility for beam optics; ii) simplifies the powering scheme with respect to the layout in Figure 6-10 with the advantage of a reduction of the mean time to repair (MTTR) for interventions on the power converters. It should be noted that the total current transferred for feeding each triplet increases from about 40 kA in the present LHC scheme to above 150 kA for the HL-LHC configuration.

The possibility of powering all low- $\beta$  quadrupoles in series, with dedicated trims, was considered. However, the layout in Figure 6-11 was preferred because of the smaller inductance per circuit and therefore reduced challenges for magnet quench protection. The powering of each low- $\beta$  quadrupole magnet via a separate circuit was also not retained because of the related higher cost of the powering equipment – power converters and Cold Powering System.

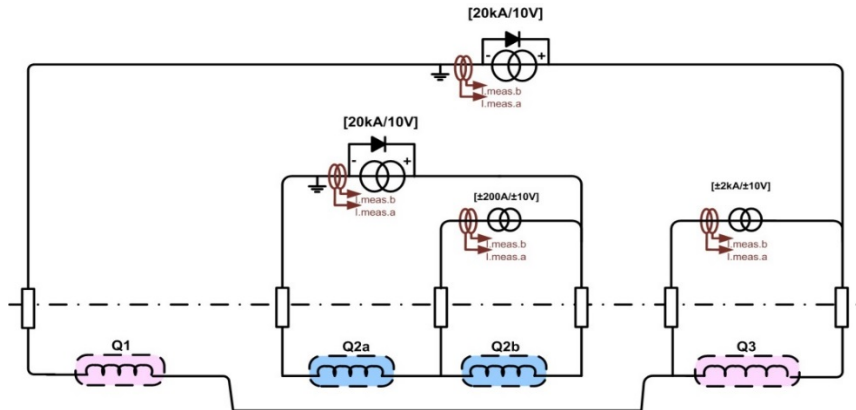


Figure 6-11: Powering layout of the HL-LHC inner triplets

The powering layout of the HL-LHC matching sections has also been reviewed. In the present LHC matching sections, the quadrupole magnets for Beam 1 and Beam 2 have a common return current lead. This choice was made in order to reduce the number of current leads from four – for individually powered magnets – to three. This electrical coupling puts constraints on the current settings of both circuits with the consequence of reducing the flexibility for different beam optics configurations. For this reason, in the HL-LHC matching sections it is proposed that quadrupoles Q4, Q5, and Q6 are individually powered with two current leads per circuit.

In the present LHC matching sections one-quadrant power converters are used for all of the quadrupoles. The decrease of the magnet current is done with a free-wheeling process, and the ramp rate depends on the time constant of the circuit, which is in turn defined mainly by the inductance of the circuit. With the present configuration, the beam squeeze process takes up to 20 minutes – and for the HL-LHC, the squeeze process would be even longer due to the wider range of  $\beta^*$ . The use of two-quadrant power converters (with bipolar voltage) is being considered for Q5. This would allow a faster decrease of the quadrupole current and therefore a reduced time for the beam squeeze process.

## 6.7 Power converters

The LHC was built with modular power converters to facilitate maintenance and integrate the redundancy principle [15] – redundancy was included in all LHC power converters rated at currents above 600 A. This has proven to be a real asset during operation. The  $n + 1$  redundancy allows the power converters to be run even with one module in fault. The advantages are the following: i) in the case of a fault, only one sub-converter is not operational and, in most cases, the fault does not generate a beam dump; ii) the LHC can run with some faulty sub-converters in the machine and all interventions for repair can be performed during a machine technical stop. With the exception of the dipole magnets, switch-mode technology was chosen for the LHC power converters in order to minimize their size and assure low output voltage ripple. All LHC power converters rated at currents above 120 A are water-cooled, with the advantage of a reduced size of the hardware. All these design principles will be maintained for the new power converters of the HL-LHC magnets.

### 6.7.1 Performance of the power converters

The HL-LHC power converters will be regulated in a closed current loop. Those for Q1, Q2, and Q3 will be of the highest precision class, like the LHC main dipole circuits. The stability of the low- $\beta$  power converters will be at the level of  $1 \times 10^6$  ( $10^{-6}$  of nominal current) – with an uncertainty of  $\pm 1$  ppm [16]. The stability of

the other power converters will be of the order of  $10 \times 10^6$ . The achievement of this level of stability does not require any new developments. All hardware developed for the LHC power converters will be re-used, e.g. for the 20 kA DCCT and 22 bits  $\Sigma\Delta$  ADC.

For the control of the power converters, the powerful function generator and controller (FGC) system, which allows control of all LHC power converters with the same hardware and software [17], is proposed. Its limitation is within the WORLDFIP bus, which has a speed that is limited to 2.5 Mbits/s. The replacement of this bus by an Ethernet type bus is being considered.

### 6.7.2 Location of the power converters

The present LHC power converters are installed in underground areas. Of the 1710 total units, 1065 are exposed to radiation. During machine operation up to 2013, the power converters generated a number of beam dumps due to single event effect (SEE). The faults due to SEE represented about 20% of the total power converter faults. A R2E programme was launched in 2010 to mitigate radiation issues for the whole LHC machine. In this framework, all power converters connected to the present DFBX were relocated to reduce their exposure to radiation. More shielding was added inside the RR alcoves to reduce particles fluences. A new radiation-tolerant version of the FGC system, called FGClite, was developed for integration in the machine in 2016. The 600 A 4 kA, 6 kA, and 8 kA power converters are being redesigned to be radiation-tolerant. After the full deployment of this programme – presently foreseen for 2018 – all power converters will be able to operate in the RR alcoves and withstand the radiation levels foreseen for the HL-LHC.

According to the present baseline, the power converters for the powering of HL-LHC magnets will be installed in surface buildings. The ongoing development of radiation-tolerant power converters aims at operating the power converters for the circuits fed via the DFBA in the RR alcoves, where they are currently located.

### 6.7.3 Power converters for the HL-LHC

The list of power converters for HL-LHC is reported in Table 6-1. The list of magnets and corresponding power converters needed for HL-LHC is reported in Table 6-2. In the present LHC machine, 8kA, 600A, and 120A power converters are already in operation.

Table 6-1: List of new power converters for inner triplet and matching section magnets

Power Converter	Current [kA]	Voltage [V]	Quadrant	Quantity IP side	Spare	Total quantity
Type 1	20	<20	1	4	2	18
Type 2	18	<20	1	2	2	10
Type 3	14	<20	1	2	2	10
Type 4	8	< $\pm 10$	2	4	2	18
Type 5	$\pm 4$	< $\pm 10$	4	15	6	66
Type 6	$\pm 600$	< $\pm 10$	4	1	2	6
Type 8	$\pm 200$	< $\pm 10$	4	9	6	42
Type 9	$\pm 120$	< $\pm 10$	4	8	6	38
Total				45	28	208

The HL-LHC will require the development of two types of new power converters: i) the one-quadrant converter 20 kA/10 V, which will be based on an extension of the 8 kA LHC power converter family; ii) the four-quadrant converter  $\pm 4$  kA/ $\pm 10$  V, which will be based on the present topology of 600 A LHC power converters.

The HL-LHC could require new topologies of two-quadrant power converters rated at 8 kA/ $\pm 10$  V. This development is mandatory if the squeeze time process needs to be reduced.

Also, by replacing the present 13 kA/18 V power converters of the main quadrupole circuits with two-quadrant power converters 13 kA/±18 V, the ramp down of the machine can be reduced by about 30 minutes. This upgrade would increase the global availability of the machine by about 4%.

Table 6-2: Magnets at each side of LHC P1 and P5

Optics	Magnet	Operating current [kA]	Inductance [mH]	Power converters [kA]	Uncertainty ppm of max current with weekly calibration	½ hour stability ppm of max current
MQXF Q1-Q3	MQXF	17.46	170	20	±1ppm	±1ppm
Q3	Trim Q3	±2	85	±3.2	±10ppm	±5ppm
Q2a-Q2b	MQXF	17.46	145	20	±1ppm	±1ppm
Q2b	Trim Q2	±0.3	72.5	±0.8	±100ppm	±10ppm
CP	MCBX	±2.42	25	±3.2	±10ppm	±5ppm
	MQSXF	0.182	1600	±0.2	±100ppm	±10ppm
	MCTSXF	0.167	600	±0.2	±100ppm	±10ppm
	MCTSXF	0.157	150	±0.2	±100ppm	±10ppm
	MCDXF	0.139	300	±0.2	±100ppm	±10ppm
	MCDSXF	0.139	300	±0.2	±100ppm	±10ppm
	MCOXF	0.12	400	±0.2	±100ppm	±10ppm
	MCOSXF	0.12	400	±0.2	±100ppm	±10ppm
	MCSXF	0.132	180	±0.2	±100ppm	±10ppm
MCSSXF	0.132	180	±0.2	±100ppm	±10ppm	
D1	MBXF	11.8	36	14	±10ppm	±5ppm
D2	MBRD	12	37	14	±10ppm	±5ppm
	MCBRD	±3.2	12	±4	±10ppm	±5ppm
Q4	MQYY	15.65	6	18	±10ppm	±5ppm
	MCBYY	±3	12	±4	±10ppm	±5ppm
Q5	MQY	4.21	74	8	±10ppm	±5ppm
	MCBY	0.088		±0.12	±100ppm	±10ppm
Q6	MQML	5.39	21	8	±10ppm	±5ppm
	MCBC	0.1		±0.12	±100ppm	±10ppm

## 6.8 Radiation-tolerant power converters

The power converters currently in the RR alcoves will be replaced with radiation-tolerant converters. This development concerns the 600 A and the 4 kA, 6 kA, and 8 kA families. The replacement is planned to take place during Long Shutdown 2 (LS2). The new power converters will be able to withstand the doses and the fluences expected after the HL-LHC upgrade.

The present 60 A converters will not withstand the doses estimated during HL-LHC operation. They were designed for tolerating a maximum total dose of about 50 Gy, and the power converters placed in or close to the matching sections will receive a dose of up to 32 Gy/year. These converters will be replaced with new ones designed for withstanding a total dose of 200 Gy. This target corresponds to the maximum dose that can be tolerated by a design based on commercial off-the-shelf (COTS) components. A rotation between highly exposed and less exposed power converters is also foreseen. Development of 120 A radiation-hard power converters is also required.

## 6.5 Power converters and LHC machine availability

Global machine availability is affected by the pre-cycle needed to degauss the magnets and by the magnets ramp-down time. In the present LHC, the most limiting circuits are those of the inner triplet quadrupoles and

of the main quadrupoles. All of these circuits are powered via one-quadrant converters, which are the cause for the long ramp-down time. Two upgrades can be envisaged if machine availability needs to be improved: i) replacement of these power converters with two-quadrant converter types; ii) use of external dump resistors to accelerate the discharge. As an illustration, by replacing the present 13 kA/18 V power converters of the main quadrupole circuits with two-quadrant 13 kA/±18 V power converters, the ramp down of the machine can be reduced by 30 minutes. As mentioned in Section 6.3, it is estimated that the replacement of both power converters powering the inner triplet quadrupole and main quadrupole circuits will increase the global availability of the machine by about 4%.

## 6.9 Reference

- [1] A. Ballarino, Development of superconducting links for the LHC Machine, *Supercond. Sci. Tech.* **27** (2014) 044024.
- [2] U. Wagner, A. Ballarino and Y. Yang, Cryogenic scenarios for the cold powering system, HiLumi LHC Milestone Report, FP7 High Luminosity Large Hadron Collider Design Study, CERN-ACC-2014-0065 (2014).
- [3] A. Ballarino, Alternative design concepts for multi-circuit HTS link systems, *IEEE Trans. Appl. Supercond.* **21** (2011) 980–984.
- [4] A. Ballarino, J. Fleiter, J. Hurte, M. Sitko and G. Willering, First tests of twisted-pair HTS 1 kA range cables for use in superconducting links, *Physics Procedia* **36** (2012), EuCARD-CON-2011-062.
- [5] A. Ballarino, M7.5.1: Final design report HTS link, EuCARD-REP-2012-017 (2012).
- [6] Y. Yang, E. A. Young, W. O. S. Bailey, C. Beduz and A. Ballarino, Development of superconducting links for the Large Hadron Collider machine, *Supercond. Sci. Tech.* **27** (2014). DOI [10.1088/0953-2048/27/4/044024](https://doi.org/10.1088/0953-2048/27/4/044024).
- [7] J. P. Corso, HL-LHC Integration SC links Point 7, CERN Engineering and Equipment Data Management Service, EDMS N. 1419773 (2014).
- [8] <http://phys.org/news/2014-04-cern-world-record-current-superconductor.html>
- [9] A. Ballarino, Large capacity current leads, *Physica C* **468** (2008) 2143–2148.
- [10] S. Weisz, Mobile shielding for RR73/77, LHC-LC-EC-0021, CERN Engineering and Equipment Data Management Service, EDMS N° 985313.
- [11] S. Weisz, Protection of equipment located in UJ76, LHC-LJ-EC-0019, CERN Engineering and Equipment Data Management Service, EDMS N° 977085.
- [12] A-L. Perrot, Protection of equipment located in UJ76, LHC-LJ-EC-0030, CERN Engineering and Equipment Data Management Service, EDMS N° 1260765.
- [13] F. Bordry and H. Thiesen, LHC Inner triplet powering strategy, 19th IEEE Particle Accelerator Conference, Chicago, IL, USA, 18 - 22 Jun 2001, pp.e-proc. 633 (2001).
- [14] F. Bordry, D. Nisbet, H. Thiesen and J. Thomsen, Powering and control strategy for the main quadrupole magnets of the LHC inner triplet system. 13th European Conf. on Power Electronics and Applications (EPE'2009), Barcelona, CERN/ATS 2010-022 (2009).
- [15] F. Bordry, V. Montabonnet and H. Thiesen, Soft switching (ZVZCS) high current, low voltage modular power converter (13 kA, 16 V), 9th European Conference on Power Electronics and Applications, Graz, Austria, 27 - 29 Aug 2001, pp.9.
- [16] H. Thiesen, M. Cerqueira-Bastos, G. Hudson, Q. King, V. Montabonnet, D. Nisbet and S. Page, High precision current control for the LHC main power converters, 1st International Particle Accelerator Conference, Kyoto, Japan, 23 - 28 May 2010, pp.WEPD070 (2010).
- [17] I. Barnett, D. Hundzinger, Q. King and J.G. Pett, Developments in the high precision control of magnet currents for LHC, 18th Biennial Particle Accelerator Conference, New York, NY, USA, 29 Mar - 2 Apr 1999, pp. e-proc. 3743 (1999).



# Chapter 7

## Machine Protection, Interlocks and Availability

A. Apollonio, T. Baer, K. Dahlerup-Petersen, R. Denz, I. Romera Ramirez, R. Schmidt, A. Siemko, J. Wenninger, D. Wollmann\* and M. Zerlauth

CERN, Accelerator & Technology Sector, Geneva, Switzerland

### 7 Machine protection, interlocks and availability

#### 7.1 Machine protection with a 700 MJ beam

The combination of high intensity and high energy that characterizes the nominal beam in the LHC leads to a stored energy of 362 MJ in each of the two beams. This energy is more than two orders of magnitude larger than in any previous accelerator. For the HL-LHC it will increase by another factor of two as shown in the comparisons in Figure 7-1. With intensities expected to increase up to  $2.3 \times 10^{11}$  p/bunch with 25 ns bunch spacing and  $3.7 \times 10^{11}$  p/bunch with 50 ns bunch spacing [1], an uncontrolled beam loss at the LHC could cause even more severe damage to accelerator equipment than at today's nominal beam parameters. Recent simulations that couple energy deposition and hydrodynamic simulation codes show that the nominal LHC beam can already penetrate fully through a 20 m long block of copper if the entire beam is accidentally deflected. Such an accident could happen if the beam extraction kickers deflect the beam at an incorrect angle. Hence, it becomes necessary to revisit many of the damage studies in light of the new beam parameters [2]. In addition, new failure scenarios will have to be considered following the proposed optics changes and the installation of new accelerator components such as crab cavities and hollow electron beam lenses. Special care is required to find a trade-off between equipment protection and machine availability in view of the reduced operational margins (e.g. decreasing quench limits and beam loss thresholds versus increased beam intensity and tighter collimator settings, UFOs at higher energies, reduced bunch spacing, etc.)

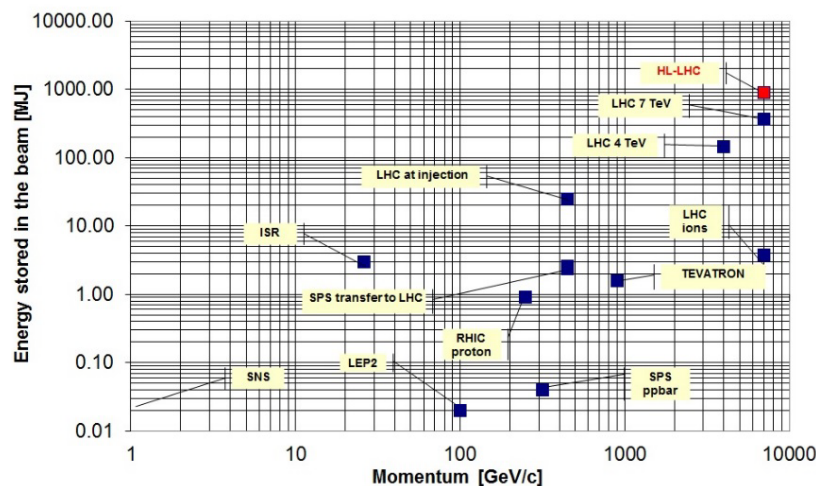


Figure 7-1: Stored beam energy as a function of HL-LHC beam momentum in comparison with other particle accelerators.

\* Corresponding author: [daniel.wollmann@cern.ch](mailto:daniel.wollmann@cern.ch)

Safe operation of the LHC currently relies on a complex system of equipment protection. The machine protection system (MPS) is designed for preventing the uncontrolled release of energy stored in the magnet system and damage due to beam losses, with very high reliability. An essential element of the active MPS system is the early detection of failures within the equipment. In addition, the beam parameters are monitored with fast and reliable beam instrumentation. This is required throughout the entire cycle, from injection to collisions. Once a failure is detected by any of the protection systems, the information is transmitted to the beam interlock system (BIS), which triggers the extraction of the particle beams via the LHC beam dumping system (LBDS). It is essential that the beams are always properly extracted from the accelerator via 700 m long transfer lines into large graphite dump blocks. These are the only elements of the LHC that can withstand the impact of the full beams.

The current machine protection architecture is based on the assumption of three types of failure scenarios [3].

- Ultra-fast failures: failures within less than three turns, e.g. during beam transfer from the SPS to the LHC, beam extraction into the LHC beam dump channel, or the effect of missing beam–beam deflection during beam extraction (1 LHC turn = 88.9  $\mu$ s). In the case of these failures, passive protection elements are required to intercept the beams and protect the accelerator equipment from damage, as no active protection is possible.
- Fast failures: a timescale of several LHC turns (less than a few milliseconds) as a result of equipment failures with a rapid effect on particle trajectories. The active extraction of the beams is completed within up to three turns after the detection of the failure and hence provides protection against such failures.
- Slow failures: multi-turn failures on timescales equal to or more than a few milliseconds, e.g. powering failures, magnet quenches, RF failures, etc.

## 7.2 Protection against uncontrolled beam losses

Equipment failures or beam instabilities appearing on the timescale of multiple turns allow for dedicated protection systems to mitigate their effects on the circulating beams. Figure 7-2 shows a comparison of the failure detection times of different protection systems. As shown in the figure, the LHC beam loss monitoring system (BLM) has the fastest detection time of 40  $\mu$ s. The BLM system is complemented with fast interlocks on the beam position in IR6, fast magnet current change monitors (FMCM) and a beam lifetime monitor (currently under development by the beam instrumentation group at CERN). All of these systems feature similar failure detection times in the 100  $\mu$ s to 1 ms range, providing diverse redundancy to the BLM system.

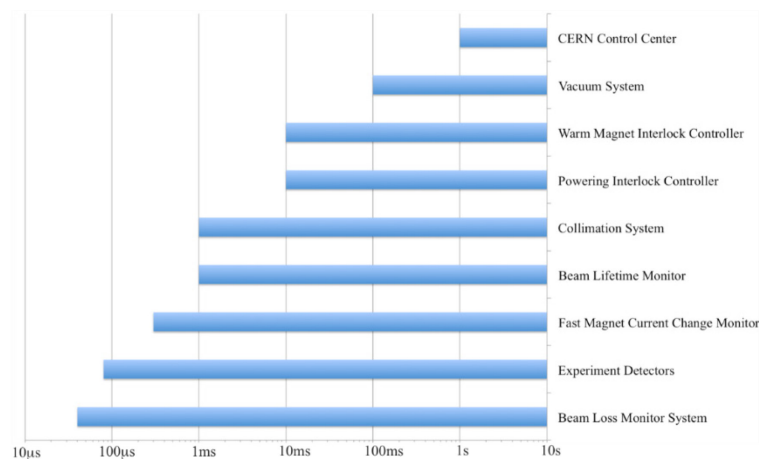


Figure 7-2: Some failure detection times at the LHC. The shortest failure detection time is currently assured by the BLM system, with a fastest integration time of 40  $\mu$ s, which is equivalent to half a LHC turn.

Adding the additional time required to transmit the detected failure through the LHC beam interlock system, the time required to synchronize the firing of the beam dump kickers with the abort gap as well as the time needed to completely extract the beam from the LHC leads to an equivalent worst case MPS response time of three LHC turns after the failure detection as depicted in Figure 7-3.

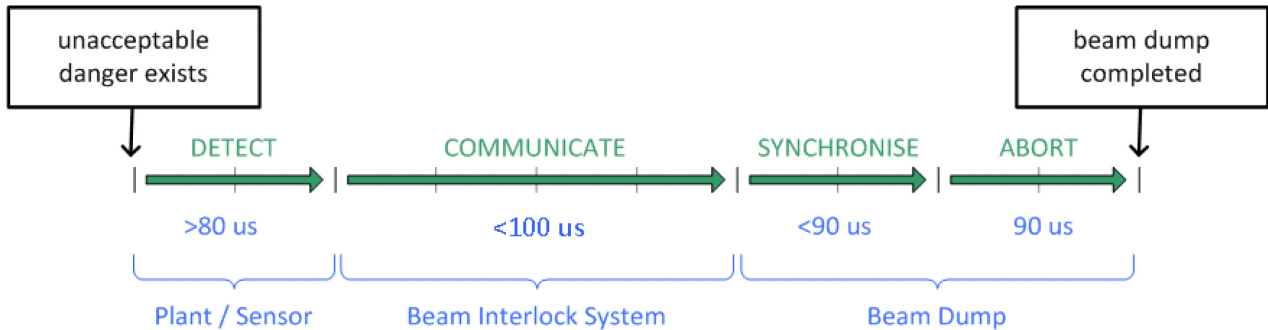


Figure 7-3: Current MPS response time from failure detection to completion of beam dump

This reaction time is sufficient in the absence of failures occurring on timescales below 10 LHC turns. A failure of the normal conducting separation dipole D1 in IP1 and IP5 is currently considered the fastest possible failure with circulating beam. Therefore, this was the basis for the design of the current MPS system. Due to their location in areas with high beta functions and the fast decay of magnet current in the case of a magnet powering failure, these normal conducting magnets can induce fast changes of the particle trajectory. These changes lead to rapidly increasing beam losses in the LHC betatron cleaning insertion (IR7), which define the smallest aperture in the LHC. At nominal energy and intensity the losses after that special failure can reach collimator damage levels within just ten turns. Therefore, a dedicated protection system – the so-called fast magnet current change monitors (FMCM) – has been very successfully deployed on critical magnets in the LHC and its transfer lines in 2006 [4].

With the HL-LHC upgrade, the optics in the insertion regions will significantly change. For certain types of ATS optics the  $\beta$ -function at the D1 separation dipole magnets in IR1 and IR5 will increase up to  $\sim 17\,000$  m, which will enhance its effect on the beam trajectory. The replacement of the D1 separation dipole magnets by a superconducting magnet would significantly increase the time constants of these circuits, practically mitigating the potential of fast failures originating from these magnets.

For HL-LHC operation, the use of crab cavities will introduce failures that can affect the particle beams on timescales well below the fastest failures considered so far [5]. Studies of different failure scenarios are still underway. These studies require consideration of details of the design eventually to be adopted for the crab cavity and the corresponding low-level RF system. Both have a significant impact on the effect on the circulating beams following, e.g. cavity quenches or trips of the RF power generator. In addition, detailed measurements of the quench and failure behaviour of the chosen design have yet to be conducted. First experience with similar devices at KEK, however, shows that certain failures can happen within just a few turns, as depicted in Figure 7-4.

While protection against failures with time constants  $>15$ ms is not expected to be of fundamental concern, voltage and/or phase changes of the crab cavities will happen with a time constant  $\tau$ , which is proportional to  $Q_{\text{ext}}$ . For a 400 MHz cavity with a  $Q_{\text{ext}} = 1 \times 10^6$  this will result in a time constant as low as 800  $\mu$ s. The situation becomes even more critical for cavity quenches, where the energy stored in the cavity can be dissipated in the cavity walls on ultra-fast timescales. Failures believed to be quenches observed in cavities at KEKB show a complete decay of the cavity voltage within 100  $\mu$ s, accompanied by an oscillation of the phase by  $50^\circ$  in only 50  $\mu$ s. Such crab cavity failures can imply large global betatron oscillations, which could lead to critical beam losses for amplitudes above about  $1 \sigma_{\text{nom}}$ . Highly overpopulated transverse tails compared with Gaussian beams were measured in the LHC. Based on these observations the energy stored in the tails beyond  $4 \sigma$  are expected to correspond to  $\sim 30$  MJ for HL-LHC parameters. These levels are significantly beyond the specification of the collimation system, capable of absorbing up to 1 MJ for very fast accidental beam losses.

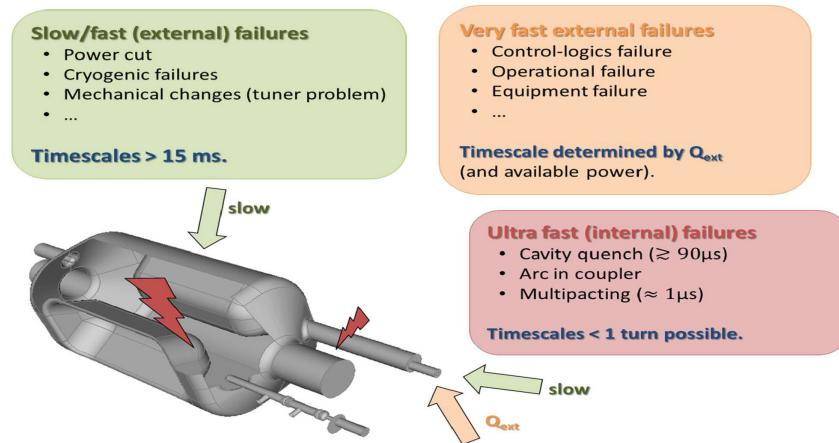


Figure 7-4: Schematic overview of crab cavity failure categories [5]

Therefore, mitigation techniques have to include a fast, dependable, and redundant detection and interlocking of a crab cavity failure on these timescales. Appropriate measures must be taken when designing the cavity and associated RF control to increase as much as possible the failure time constants.

- Avoid correlated failures of multiple cavities (on one side of an IP) through mechanical and cryogenic separation of the individual modules and appropriate design of the low-level RF [6].
- Investigate the use of fast failure detection mechanisms such as RF field monitor probes, diamond beam loss detectors, power transmission through input coupler and head–tail monitors.
- Ensure the partial depletion of the transverse beam tails to reduce the energy stored in the beam halo, which would potentially be deflected onto the collimation system beyond the design value of 1 MJ. For the current baseline this would correspond to an area of  $1.7 \sigma_{\text{nom}}$  (before reaching the closest primary collimator) as the possible transverse beam trajectory perturbation following an ultra-fast failure of a single crab cavity. It is important to note that the partial depletion of the beam halo may have a negative effect on the available time to detect a failure with other machine protection systems like BLMs. The consequences of this need to be studied carefully.
- Decrease the reaction time of the MP system for such ultra-fast failures by, e.g. increasing the number of abort gaps, accept the triggering of asynchronous beam dumps with potential local damage, add direct links to the beam dumping system in IR6, and consider the installation of disposable absorbers.

### 7.2.1 Beam interlock system

The beam interlock system (BIS) is a highly dependable fast interlock system and a key element of the accelerator machine protection. It is currently used in the LHC, SPS, and parts of the injector chain at CERN. Its primary objective is to provide a highly reliable link between users requesting a beam abort and the beam dumping system. The hardware implementation of the system is based on custom-made electronics, as industrial solutions have not been found to be adequate for the specific requirements of the system, e.g. in terms of reaction time combined with the geographical distribution of the system. Due to the obsolescence of electronics components and potential problems with the optical links the present system will need to be upgraded. To fulfil the requirements of the HL-LHC, the system will be equipped with additional input channels to connect more user interfaces and to provide more flexibility in the configuration of the various user inputs. The number of required channels is subject to a future functional specification to be provided by the SPS and LHC machine protection panel (MPP). The possibility of implementing very fast interlock channels and direct links between the crab cavities and the LHC beam dumping system will be studied but the feasibility cannot yet be confirmed. The new system will be equipped with advanced diagnostic features for all optical links allowing pre-emptive maintenance, e.g. in the case of degraded performance due to the enhanced radiation load in some underground areas.

### 7.2.1.1 Equipment performance objective

The upgraded system is supposed to reach the same performance level in terms of reliability as the present system, which corresponds to safety integrity level (SIL) 3. The safety critical part of the BIS hardware architecture will be based on well-proven principles and solutions but adapted to state-of-the-art electronics components and assemblies. It is therefore probably possible to reuse a major part of the safety critical code, which is very well tested and fully validated. Considering the system's complexity and dimensions, and the experience gained so far, it is expected that system performance will hardly affect LHC availability, e.g. not producing more than one spurious beam abort per year.

The new BIS could be equipped with a new hardware controls interface, replacing obsolete architectures for communication busses and simplifying maintenance and potential upgrades. The BIS hardware will also feature advanced diagnostic tools for the system hardware and the optical links.

All of the proposed changes will require a major revision of the high-level supervision and controls software and be adapted to the accelerator controls environment then in place.

### 7.2.2 Fast magnet current change monitor

The main task of the fast magnet current change monitors (FMCM) is to monitor fast current changes in electrical circuits with normal conducting magnets. A fast current change can be caused by sudden powering failures or perturbations on the supply network, which change the particle trajectories leading to fast beam losses. These monitors are required for electrical circuits with a short decay time constant and magnets installed in regions with high beta functions. Each monitor delivers a permit signal to the beam interlock system to request the extraction of particle beams before losses occur. Therefore, the FMCM provides a redundant protection to the beam loss monitors (BLM). A total of 26 monitors are presently installed to protect the LHC and SPS-LHC transfer lines.

#### 7.2.2.1 Objectives for HL-LHC machine performance

The installation of FMCMs is required to ensure machine protection against powering failures in critical magnetic elements during all operational phases. Twelve monitors are currently installed in the LHC, namely for dump septa magnets in IR6, collimation insertion regions in IR3/IR7, Alice compensator circuits in IR2, and main separation dipoles D1 in IR1 and IR5 [6]. Additional input from WP3 (magnets) and WP2 (accelerator physics) is required to clarify the necessity of additional FMCM units for the protection of the new magnet powering in the high luminosity insertion regions IR1 and IR5 and the HL-LHC optics. In addition, new failure modes derived from the introduction of new elements (such as crab cavities) need to be studied to understand the machine protection requirements and to estimate the number of monitors required to protect the accelerator equipment in the HL-LHC.

#### 7.2.2.2 Equipment performance objective

FMCMs have successfully operated in the LHC and the SPS-LHC transfer lines for many years, and no missed dump has been identified since the start of operation. For the protection of the electrical circuits in the HL-LHC the use of the same design is recommended. However, a review of the system needs in view of the HL-LHC requirements, followed by a corresponding reproduction of additional units, will be required. The review and potential redesign of the hardware is a mandatory step due to the aging and obsolescence of the electronics parts used in the current system.

The aim of the upgrade of the FMCM will be to improve the maintainability of the system and to comply with the requirements of the HL-LHC.

### 7.3 Magnet powering protection

During operation at 7 TeV the energy stored in the main dipole circuits of each sector reaches  $\sim 1$  GJ. This illustrates that the LHC magnet system needs to be protected against damage due to failures in magnet powering or quenches.

Therefore, the superconducting circuits, busbars, and future superconducting links must be equipped with a quench protection system (QPS) that detects changes in the superconducting state and activates quench heaters and/or the energy extraction systems (EE) to safely extract the magnetic energy stored in the circuit.

Furthermore, the correct powering conditions have to be ensured for each circuit by a powering interlock system (PIC), which will interlock the powering of the circuit via the power converter in the case of problems and potentially request a beam dump. Therefore, the PIC is interfacing the quench protection systems, power converters, cryogenic systems, and technical services such as uninterruptible power supplies (UPS), emergency stop buttons (AUG), and controls.

The protection of the normal conducting magnets in the LHC and its injector complex is ensured by the warm magnet interlock system (WIC), which collects signals from thermo switches installed on the magnets and status signals from the associated power converters.

As a failure in the magnet system will also impact the stored particle beam, these systems have to interface the magnet powering systems with the BIS and initiate a beam dump in case of a failure.

#### 7.3.1 Quench protection system

The HL-LHC will incorporate new superconducting elements requiring dedicated protection systems. The upgrade of the QPS will provide this functionality, including the related data acquisition systems, monitoring the state of the protection systems and the protected elements.

The enhanced luminosity of the HL-LHC will increase the radiation levels in certain underground areas like the dispersion suppressors to levels no longer compatible with the operation of radiation-tolerant electronics based on COTS currently installed in those areas. Based on the progress in electronics, it is probably feasible to re-locate a major part of the protection electronics to low radiation zones or, eventually, to surface buildings and use long instrumentation cables or optical fibres to link to the protected elements.

The proposed upgrade will also include new communications links for supervision and data acquisition (DAQ) superseding the then obsolete classic fieldbus networks. At the same time, advanced tools for remote diagnostics and maintenance will be provided.

##### 7.3.1.1 Equipment performance objective

The QPS is a highly complex system incorporating a large amount of electronics components and assemblies. As for the existing system, a particular design effort will be necessary to achieve the very demanding level of system dependability required for successful LHC operation. The number of accesses to LHC underground areas needs to be minimized for personnel protection and machine availability.

The protection parameter settings will be subject to a functional specification to be issued by the LHC magnet circuits, powering and performance panel (MP3) based on the input of equipment specialists.

The request for very fast magnet protection systems with reaction times in the order of some milliseconds will be addressed in a feasibility study, but a potential implementation will rely strongly on the proper instrumentation of the protected element (magnet, superconducting link) and the adapted reaction time of other protection systems such as energy extraction systems and the powering interlock system.

The hardware capabilities of the DAQ and related communication links will be enhanced to allow higher data transmission rates and advanced maintenance. All of the proposed changes will require a major revision of the high-level supervision and controls software, which also needs to be adapted to the accelerator controls environment then in place.

### 7.3.2 Energy extraction system

Energy extraction systems (EE) are an integrated part of the safety-critical quench protection systems, which are widely used in the existing LHC machine with a total of 234 installed facilities (202 for the 600 A corrector circuits and 32 13 kA systems for the main dipole and quadrupole circuits). The systems are strongly circuit-specific, tailor-made for a particular set of requirements, and adapted to the local infrastructure.

The current mechanical energy extraction switches will have to be replaced for the HL-LHC era. To allow for faster reaction times, which may be required by future superconducting magnets, the development of fast switches based on semiconductors (IGCTs, IGBTs) is currently ongoing. Alternatively, slower (~20 ms) hybrid systems, where an electromechanical switch is connected in parallel to a semiconductor switch, are under study. Furthermore, for slow switching times, classical mechanical switches in combination with large snubber capacitor banks could be used.

The new design of the extraction resistors (DQR) will be significantly different from those developed and built for the present LHC main circuits. The pursued characteristics and properties of these new energy absorbers are very fast recovery (cooling) times, compact design (minimized volume), and easily changeable resistance values.

#### 7.3.2.1 Equipment performance objectives

The new energy extraction equipment for the HL-LHC will use a new generation of switches, incorporate the newest technology for high-current transmission, benefit from built-in features for facilitating diagnostics and maintenance, offer systems that will minimize intervention time for accessing all parts of the facilities, and profit from the experience gained with the operation of the existing LHC EE facilities.

### 7.3.3 Powering interlock system

The powering interlock system (PIC) ensures the correct powering conditions for the different electrical circuits with superconducting magnets in the LHC. At the same time, it guarantees the protection of the magnet equipment by interfacing quench protection systems, power converters, cryogenics, and technical services such as uninterruptable power supplies (UPS), emergency stop buttons (AUG), and controls. The PIC is a distributed system currently consisting of 36 individual powering interlock controllers, which manage the powering of each of the 28 powering subsectors [7].

#### 7.3.3.1 Objective for HL-LHC machine performance

Magnet interlocks are required to guarantee safe magnet powering during all phases of operation from injection to collisions. In order to achieve this protection while maintaining the time constraints required for equipment protection, interlock electronics are usually installed close to the main clients (QPS and power converters) such as the UA, UJ, and RR alcoves. At the design luminosity for HL-LHC ( $5 \times 10^{34} \text{ cm}^{-2} \text{ s}^{-1}$ ) the thermal neutron and high-energy hadron fluencies in the areas close to the tunnel will increase considerably with respect to the values for which the existing PIC has been designed. Additional changes and requirements from the new quench protection system will have to be reflected in the upgraded interlock system to assure the dependability of the system during the HL-LHC era. For these reasons, a new design for the distributed I/O modules is required to cope with the increment of particle flux in the most sensitive areas. In addition, an upgrade of the industrial components used will very likely become necessary due to the changing of the low-level I/O components used.

#### 7.3.3.2 Equipment performance objectives

The PIC was installed during 2006 and has been operating since the start of LHC operation in 2008. By the time the HL-LHC starts operation the system will have been running for more than 15 years. Therefore, some of the electronics components will reach the end of their life expectancy, which can have an impact on the availability of the system. In addition, obsolescence of electronics parts needs to be addressed since some of

the critical components of the system can no longer be purchased on the open market, affecting its maintainability. Furthermore, the increased radiation dose in certain areas will affect the most sensitive components of the PIC.

The upgrade of the PIC will address the issues mentioned above to adapt to HL-LHC requirements. In addition, the system will be reviewed to provide enhanced diagnostics of the safety-critical hardwired loops in line with the upgrades foreseen for the quench protection system. The implementation of triple redundancy in combination with two-out-of-three voting is considered for the quench loop.

#### 7.3.4 Warm magnet interlock system (WIC)

The warm magnet interlock system (WIC) assures the protection of normal conducting magnets in the LHC and its injector complex. It collects signals from thermo switches installed on the magnets and status signals from the associated power converters. Based on these input signals a programmable logic controller (PLC) calculates and transmits fast abort signals to interlock the power converter of a given electrical circuit in case of powering failures. In addition, it initiates a beam dump in case a circuit relevant for beam operation of the given machine is not operating in nominal conditions [8].

##### 7.3.4.1 Objective for the HL-LHC machine performance

Magnet interlocks are required to guarantee safe magnet powering during all phases of operation from injection to collisions and to abort beam operation avoiding inevitable beam losses in case of powering failures. In addition, interlock systems provide remote diagnostic features to allow an efficient and precise identification of faulty equipment. As normal conducting magnets in the LHC are concentrated around the IPs, a single industrial controller installed in a radiation-free area is required to manage the protection of powering equipment in a given IR. The main objective for the HL-LHC era is a consolidation of the existing system, along with an upgrade to accommodate changes and new requirements for the magnet powering system in the different insertion regions.

##### 7.3.4.2 Equipment performance objectives

The WIC – consisting of eight industrial controllers and several I/O crates – has been installed in the LHC since 2006 and has been continuously operating since the start of LHC operation in 2008. No failures have been observed in the WIC system throughout the whole of Run 1. Nevertheless, by the time the HL-LHC starts operation the WIC system will have been running for more than 15 years, requiring an upgrade of the electronics and industrial components to assure the current level of dependability throughout the full HL-LHC period. Furthermore, the increased radiation dose in certain areas will affect the most sensitive components of the WIC (mostly the magnet and remote test interconnection boxes) for which a new design and production has to be envisaged.

#### 7.4 Availability requirements to achieve HL-LHC goals for integrated luminosity

The challenging goals in terms of integrated luminosity require a high level of accelerator availability and operational efficiency. The estimated integrated luminosity as a function of machine availability is analyzed below. There are three important figures to be considered when evaluating LHC availability.

- The stable beams time: the time for beam collisions. This quantity must be optimized by operators as a function of the observed distributions of turnaround time and fault time. Stable beam optimization will be particularly relevant for levelled operation.
- The turnaround time: the time to go from a beam dump at the end of stable beams to the next stable beams, when no faults occur. This quantity has a minimum value imposed by the injection process and the ramp time of superconducting magnets. Efforts must be devoted to reaching this lower value. Parallelizing/combining machine modes (e.g. collide and squeeze) is one possibility to optimize the turnaround time.



- The fault time: the time to clear machine faults and recover operational conditions for beam injection. It includes the time for expert diagnostics and intervention, eventually requiring access to the LHC tunnel.

For the following extrapolations, the 2012 LHC run is taken as a reference, being the most stable and reproducible year of the first LHC run [9]. In 2012 the average turnaround time was 5.5 h, but the energy was limited to 4 TeV, requiring current ramps of only 13 min. For HL-LHC operation, the reference energy will be 7 TeV, resulting in an increased average turnaround time, estimated to be 6.2 h. Making predictions of the fault time distribution for HL-LHC operation is not trivial, as many factors will play a role in this respect. The increased energies and intensities will result in higher radiation levels, which could have a direct impact on the observed number of single event effects (SEE) per year and on long-term effects on components due to the total integrated dose (TID). Mitigations to these effects have been deployed during LS1, with a major relocation of sensitive equipment in protected areas of the LHC tunnel. Nevertheless, future radiation levels will have to be measured for a final assessment of the expected increase in beam dumps due to radiation effects in electronics components (R2E). It is already foreseen that a new generation of electronics systems will be designed before the HL-LHC era. New designs should cope with such radiation levels. The increased energy and intensities will also have a direct impact on the observed UFO-induced beam dumps due to localized losses. Current extrapolations assume a significant increase of UFO events that are large enough to provoke a beam dump, if 2012-like BLM thresholds are to be kept. A balance between the tolerated number of UFO dumps and the possibility of having beam-induced quenches should be found, by the definition of suitable threshold and, eventually, BLM relocation. On the equipment side, components will operate closer to design limits and partially reach their end-of-life.

A Monte Carlo model [10, 11] of LHC availability was used to qualitatively assess the combined impact of all these factors. A sensitivity analysis has been carried out with respect to the average fault time and machine failure rate, defined as the ratio between fills to stable beams followed by failures and the total number of physics fills. The results for 200 days of HL-LHC operation are presented in Figure 7-5. Nominal HL-LHC parameters ( $5 \times 10^{34} \text{ s}^{-1} \text{ cm}^{-2}$  levelled luminosity,  $2.19 \times 10^{35} \text{ s}^{-1} \text{ cm}^{-2}$  virtual peak luminosity, 4.5 h average luminosity lifetime, 7 TeV) and the same duration of intensity ramp-up as 2012 were assumed.

The results show that, assuming 2012 figures for average fault duration (6.9 h) and machine failure rate (70%), 260  $\text{fb}^{-1}$  could be produced in 200 days of HL-LHC operation. To reach the goal of 300  $\text{fb}^{-1}$  per year, a reduction of 10% of the machine failure rate, combined with a reduction of the average fault time of around 25%, are necessary (HL1). As an alternative for reaching 300  $\text{fb}^{-1}$ , the sensitivity analysis shows that a further reduction of the machine failure rate to 50% would keep the same average system fault time as observed in 2012 (HL2). These requirements in particular need to be considered during the design of future electronics equipment.

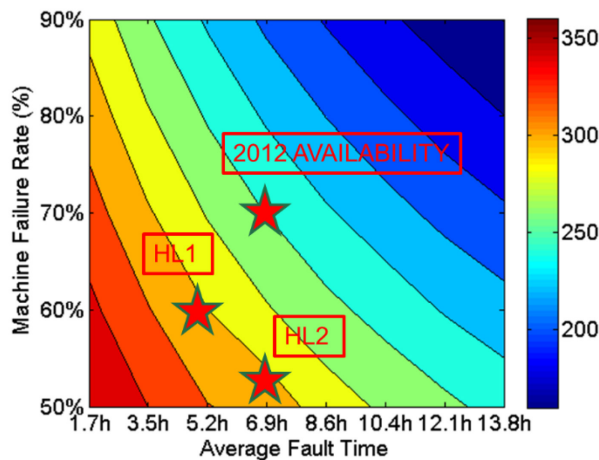


Figure 7-5: Sensitivity analysis of integrated luminosity to the machine failure rate and average fault time.

## 7.5 References

- [1] O.S. Bruning, HL-LHC Parameter space and scenarios, Proc. Chamonix 2012 workshop on LHC Performance, CERN-2012-006 (2012) p. 315.
- [2] N.A. Tahir, J.B. Sancho, A. Shutov, R. Schmidt and A.R. Piriz, Impact of high energy high intensity proton beams on targets: Case studies for Super Proton Synchrotron and Large Hadron Collider, *Phys. Rev. ST accel. Beams* **15** (2012) 051003.
- [3] R. Filippini, B. Goddard, M. Gyr, V. Kain, R. Schmidt, J. Uythoven and J. Wenninger, Possible causes and consequences of serious failures of the LHC machine protection systems, 9th European Particle Accelerator Conf., Lucerne, Switzerland, 5–9 July 2004, p. 620.
- [4] M. Werner, Einrichtung zur Bestimmung der Stärke des Magnetfeldes eines Elektromagneten, Patent DE102005045537B3 28.12.2006, September 2005.
- [5] T. Baer et al., Very fast crab cavity failures and their mitigation, Proc. IPAC'12, May 2012, pp. 121–123, MOPPC003.
- [6] M. Werner, M. Zerlauth, A. Dinius and B. Puccio: Requirements for the fast magnet current change monitors (FMCM) in the LHC and SPS-LHC transfer lines, LHC-CIW-ES-0002, EDMS 678140.
- [7] R. Schmidt, B. Puccio, M. Zerlauth: The hardware interfaces between the powering interlock system, power converters and quench protection system', LHC-D-ES-0003, EDMS 368927.
- [8] P. Dahlen, R. Harrison, R. Schmidt and M. Zerlauth, The warm magnet interlock system for the LHC ring, LHC-CIW-ES-0003, EDMS 653548.
- [9] B. Todd *et al.*, Workshop on Machine Availability and Dependability for Post-LS1 LHC, Proc. Workshop, CERN (2013).
- [10] A. Apollonio *et al.*, HL-LHC: Integrated luminosity and availability, TUPFI012, Proc. IPAC'13 Shanghai, China, 2013, 1352-1354.
- [11] A. Apollonio *et al.*, Update on predictions for yearly integrated luminosity for HL-LHC based on expected machine availability, TUPRO015, Proc. IPAC'14, Dresden, 1036-1038.

# Chapter 8

## Interface with Experiments

*H. Burkhardt and I. Efthymiopoulos\**

CERN, Accelerator & Technology Sector, Geneva, Switzerland

### 8 Interface with experiments

#### 8.1 Introduction

The machine upgrade for high luminosity requires major changes on the machine side. Key ingredients for the luminosity increase are larger apertures in the focusing sections around the experiments and higher beam intensities. The experiments are upgraded for reduced inner beam pipes with more powerful vertex detectors. This is important for physics and essential for the increased pile-up.

Other key design considerations for the upgraded LHC detectors include longevity at increased radiation levels and minimization of activation. The definition of the machine-experiment interface issues and its timeline is described in the M18 document [1].

#### 8.2 Interaction regions

Figure 8-1 shows the schematic layout of the LHC with its four interaction regions.

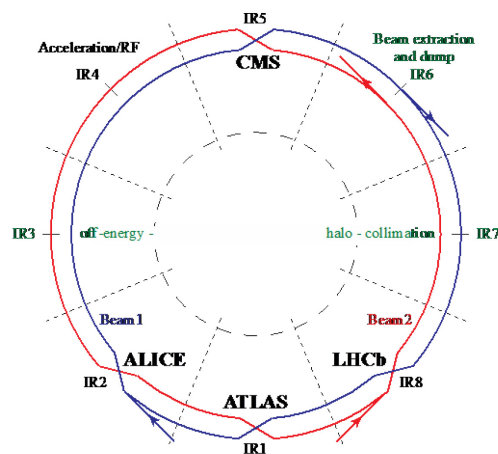


Figure 8-1: Schematic layout of the LHC with the four interaction regions that house the ALICE, ATLAS, CMS, and LHCb experiments.

The HL-LHC design is for four experiments: the two high luminosity experiments ATLAS and CMS at IR1 and IR5, respectively; ALICE at IR2; and LHCb at IR8.

Table 8-1 shows the target luminosities for the experiments in proton–proton operation for the original LHC design and for the high luminosity upgrade. Operation at so-called ‘ultimate’ parameters with peak luminosity of  $7.5 \times 10^{34} \text{ cm}^{-2} \text{ s}^{-1}$  is considered. With levelling, this would lead to around  $4000 \text{ fb}^{-1}$  by 2037.

\* Corresponding author: [ilias.efthymiopoulos@cern.ch](mailto:ilias.efthymiopoulos@cern.ch)

Table 8-1 Target luminosities for p–p operation for the HL-LHC. The luminosities for LHC Run 2 are also included for comparison. Total target integrated luminosity in CMS and ATLAS is 3000 fb<sup>-1</sup> after 12 years of operation.

Experiment	IP	Peak levelled luminosity [cm <sup>-2</sup> s <sup>-1</sup> ]	
		HL-LHC	LHC
ATLAS	1	$5 \times 10^{34}$	$2 \times 10^{34}$
CMS	5	$5 \times 10^{34}$	$2 \times 10^{34}$
ALICE	2	$1 \times 10^{31}$	$1 \times 10^{31}$
LHCb	8	$2 \times 10^{33}$	$4 \times 10^{32}$

The main luminosity upgrade is for interaction regions IR1 and IR5, and will be implemented in the long shutdown LS3. The ALICE and LHCb experiments installed in IR2 and IR8 will have their most significant detector upgrades during LS2 scheduled for 2018/2019 and will continue to run after LS3. LHCb has requested a luminosity increase up to  $2 \times 10^{33}$  cm<sup>-2</sup> s<sup>-1</sup>. This is possible without changes to the magnet layout in IR8, and the required detector and vacuum beam pipe upgrades can be implemented in long shutdown LS2. It should be accompanied by improved shielding (including a minimal TAN upstream of D2), to minimize the impact of the increase in radiation and heating of cold machine elements. The low target luminosity for ALICE in p–p operation will require collisions with large transverse offsets.

The experimental programmes of other smaller experiments (LHCf, TOTEM) do not at present extend beyond LS3. Should these or other experimental proposals appear in the future, they will need to adapt to the HL-LHC beam conditions and installed hardware planned for the straight sections. The HL-LHC will be more constrained towards high luminosity/low  $\beta$  operation than the present LHC. Very high  $\beta^*$  running will have to end with LS3. The upper limit for  $\beta^*$  for physics at top energy is expected to be reduced to about 30 m.

For HL-LHC operation, the machine layout in IR1 and IR5 will change significantly. The most relevant machine modification for the experiments will be the installation of the new large aperture triplet magnets Q1–Q3 in IR1 and IR5. Details are described in Chapter 3. What is important for the layout of the interface with the experiments is that the distance of the first quadrupole magnet (Q1) from the IP will remain the same (23 m) as before the upgrade. As a result, no modifications to the forward shielding of the experiments need to be implemented to accommodate changes in the accelerator layout. The inner coil diameter of the triplet magnets however will increase by roughly a factor of two from 70 mm to 150 mm. This implies that the inner beam pipe radius will have to increase between the triplet and the experiment. In particular, the passive absorbers (TAS) installed at 19 m from the interaction points will have to be replaced by a new larger aperture absorber (TAXS).

### 8.3 Experimental beam pipes

A key upgrade of the ATLAS and CMS experiments for HL-LHC operation is to the inner tracker detectors. The change to a smaller radius beam pipe was already made during LS1 [3, 4]. This is important for the detectors to deal with high pile-up and will be kept for HL-LHC operation. The ALICE and LHCb experiments also plan modifications to their experimental beam pipe to a reduced inner radius. The present and foreseen experimental beam apertures are summarized in Table 8-2.

The LHCb VELO is movable. It is only closed in stable physics to the value shown in the table, and retracted to 30 mm otherwise.

Table 8-2: Original and reduced inner beam pipe radii at the IPs

IP	Experiment	When	Original $r_{\min}$ [mm]	Reduced $r_{\min}$ [mm]
1	ATLAS	LS1	29	23.5
2	ALICE	LS2	29	18.2
5	CMS	LS1	29	21.7
8	LHCb, VELO	LS2	5	3.5

## 8.4 The passive forward absorbers

The high luminosity regions of LHC at IP1 and IP5 are equipped with passive absorbers for charged (TAS) [5, 6] and neutral (TAN) [7] particles. The TAS is installed on either side of the interaction region at the transition of the experimental caverns to the LHC tunnel. TAS's and TAN's primary function is to protect the superconducting quadrupoles in the straight section from the collision debris coming from the interaction region. The TAS primarily shields the inner triplet quadrupoles Q1–Q3; TAN shields the D2 and Q4 quadrupoles. In parallel the TAS completes the forward shielding of the experiments and both the TAS and TAN participate in the reduction of background to the experiments.

For HL-LHC operation the following modifications are foreseen.

- New TAS and TAN absorbers on either side of IP1 and IP5, called TAXS and TAXN, respectively, should replace the existing ones. The protection must be extended to D1 magnets that in the HL-LHC will be superconducting (these are normally conducting in the present LHC). The new absorbers must have an aperture adapted to HL-LHC beam optics and operation, and should be designed to cope with the increased energy deposition.
- A new TAXN absorber is planned for IP8, designed to operate at the foreseen five times higher luminosity operation. The installation of a TAXS absorber around IP8 is not required.
- The new absorbers will be designed to operate at the ultimate luminosity conditions during the HL-LHC era as defined above.

### 8.4.1 The charged particle passive absorber – TAXS

The TAXS absorber is located approximately 19 m from the interaction point on either side of IP1 or IP5. Its core is a 0.5 m diameter and 1.8 m long copper cylinder traversed on its axis by a constant aperture beam pipe. The design of the new TAXS absorbers for the HL-LHC for IP1 and IP5 is based on that of the presently installed TAS absorbers, with the following modifications and improvements:

- the beam pipe aperture increases to 54 mm in diameter from the present 34 mm;
- the cooling power increases to dissipate approximately 780 W deposited in the TAXS during HL-LHC ultimate beam operation conditions, including a safety margin;
- the overall design of the TAXS remains compatible with the mechanical and envelope constraints from the surrounding shielding of the experiments.

Improvements in the alignment mechanism and vacuum exchange should be incorporated in the new design in view of the need for optimized maintenance operations and exposure to radiation. The change from the TAS to TAXS is to happen during LS3 after a few months (at least) of cool-down. The overall procedure must be optimized so as to minimize the exposure of personnel to radiation in compliance with the ALARA principle and the overall planning of the activities in the LHC tunnel and experimental caverns.

### 8.4.2 The neutral particle passive absorber – TAXN

The TAXN absorber is designed to absorb the flux of forward high-energy neutral particles produced at the interaction region of IP1 and IP5. There is a TAXN absorber installed in either side of IP1 and IP5, located between the separation/recombination dipole pair D1 and D2, containing the transition from the single common beam pipe to the two separate pipes for the incoming/outgoing beams.

The design of the new TAXN absorbers for IP1 and IP5 is based on that of the presently installed TAN, with the following modifications and improvements.

- The position of the TAXN is different by a few metres (towards the IP) with respect to the present position.

- The overall design and layout is to be adapted to the available space constraints while maintaining the correct shielding efficiency.
- The vacuum chamber layout is efficiently adapted to the new geometry for protection of the adjacent quadrupoles and optimization of the background conditions of the experiment. The TAXN vacuum pipes have a fixed aperture that, combined with a specially designed TCL collimator with movable jaws just downstream towards D2, provides the maximum protection efficiency at all beam optics scenarios for the HL-LHC.
- Active water cooling will be required to dissipate approximately 1.5 kW of power from the beam, expected during ultimate operation during the HL-LHC era.

Improvements in the mechanical design of the absorber should be incorporated in the design to allow optimized installation and maintenance activities. The locations for beam instrumentation for luminosity monitoring and experimental detectors will be maintained unless they impose important constraints in the TAXN design and maintenance.

In IP8 new TAXN absorbers should be installed on either side of the IR in available slots upstream of D2.

## 8.5 References

- [1] Interface Machine-Experiments: Definition and Time Plan, Milestone MS18 CERN-ACC-2014-0304. <https://cds.cern.ch/record/1973060/files/CERN-ACC-2014-0304.pdf>
- [2] The High Luminosity Large Hadron Collider: the new machine for illuminating the mysteries of Universe. Rossi, Lucio (ed.) ; Brüning, Oliver (ed.), Hackensack, NJ : World Scientific, 2015
- [3] M. Gallilee, CMS Central chamber diameter reduction, LHC-VC5-EC-0001, EDMS 1230176.
- [4] M. Gallilee, Reduction of ATLAS VI Diameter, LHC-VC11-EC-0001, EDMS 1230222.
- [5] E. Hoyer *et al.*, Interface specification LHC IP1/IP5, front quadrupole absorbers (TAS), LHC-TAS-ES-0003, EDMS 111998.
- [6] E. Hoyer *et al.*, Functional specification LHC IP1/IP5 front quadrupole absorbers (TAS), LHC-TAS-ES-0001, EDMS 101559.
- [7] E. Hoyer *et al.*, LHC IP1/IP5 neutral beam absorbers (TAN), LHC-TAN-ES-0100, EDMS 108093.

# Chapter 9

## Cryogenics for the HL-LHC

*S. Claudet\* and L. Tavian*

CERN, Accelerator & Technology Sector, Geneva, Switzerland

### 9 Cryogenics for the HL-LHC

#### 9.1 Introduction

The upgrade of the cryogenics for the HL-LHC will consist of the following:

- The design and installation of two new 1.9 K cryogenic plants at P1 and P5 for high luminosity insertions. This upgrade will be based on a new sectorization scheme aimed at separating the cooling of the magnets in these insertion regions from the arc magnets, and on a new cryogenic architecture based on electrical feedboxes located at ground level and vertical superconducting links.
- The design and installation of a new 4.2 K cryogenic plant at P4 for the Superconducting Radio Frequency (SRF) cryomodules and other future possible cryogenic equipment (e-lens, RF harmonic system).
- The design of new cryogenic circuits at P7 for the HTS links and displaced current feedboxes.
- Cryogenic design support for the 11 T dipoles.

Figure 9-1 shows the overall LHC cryogenic layout, including the upgraded infrastructure.

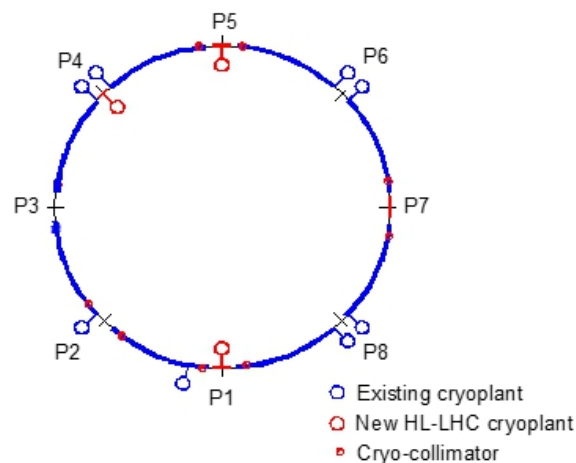


Figure 9-1: Overall LHC cryogenic layout, including the upgraded infrastructure

\* Corresponding author: [Serge.Claudet@cern.ch](mailto:Serge.Claudet@cern.ch)

## 9.2 LHC machine upgrades

### 9.2.1 Upgraded beam parameters and constraints

The main parameters impacting on the cryogenic system are given in Table 9-1. With respect to the nominal beam parameters, the beam bunch population will double and the luminosity in the detectors of the high luminosity insertions at P1 and P5 will be multiplied by a factor 5.

Table 9-1: LHC upgraded beam parameters for 25ns bunch spacing

Parameter	Units	Nominal	Upgrade
Beam energy, $E$	[TeV]	7	7
Bunch population, $N_b$	[protons/bunch]	$1.15 \times 10^{11}$	$2.2 \times 10^{11}$
Number of bunches per beam, $n_b$	-	2808	2748
Luminosity, $L$	[ $\text{cm}^{-2} \text{s}^{-1}$ ]	$1 \times 10^{34}$	$5 \times 10^{34}$
Bunch length	[ns]	1.04	1.04

These upgraded beam parameters will introduce new constraints to the cryogenic system.

- The collimation scheme must be upgraded by adding collimators to the continuous cryostat close to P2 and P7, and possibly also P1 and P5. The corresponding integration space must be created by developing shorter but stronger 11 T dipoles. As the new collimators will work at room temperature, cryogenic bypasses are required to guarantee the continuity of the cryogenic and electrical distribution. Figure 9-2 shows the nominal and upgraded layouts of the continuous cryostat. Halo control for the HL-LHC may require the installation of hollow electron lenses at P4, making use of a superconducting solenoid. While not yet in the HL-LHC baseline, this device may be the best option for controlling particle diffusion by depopulating the halo of the high-power hadron beams, thereby avoiding uncontrolled losses during critical operations such as the squeeze. Figure 9-3 shows the nominal and upgraded layouts of the P4 insertion region (IR4), anticipating the installation of an e-lens and a new SRF system.
- The increase of the level of radiation to the electronics could possibly require relocating power convertors and related current feedboxes to an access gallery at P7 and at ground level at P1 and P5. New superconducting links will be required to connect the displaced current feedboxes to the magnets. Figure 9-4 and Figure 9-5 show the nominal and upgraded layouts of IR1, IR5, and IR7.
- To better control the bunch longitudinal profile, reduce heating and improve the pile-up density, new cryomodules of 800 MHz RF cavities could be added to the existing 400 MHz cryomodules at P4 creating a high-harmonic RF system (see Figure 9-3). Actually, discussions are underway to see if a better scheme would be the installation of a new 200 MHz SRF system, rather than the 800 MHz. From the cryogenic point of view the requests are similar, so we will consider below the 800 MHz system that is in an advanced phase of study.
- To improve the luminosity performance by addressing the geometric luminosity reduction factor and possibly allowing the levelling of the luminosity, cryomodules of crab cavities (CC) will be added at P1 and P5 (see Figure 9-5).
- Finally, the matching and final focusing of the beams will require completely new insertion assemblies at P1 and P5 (see Figure 9-5).



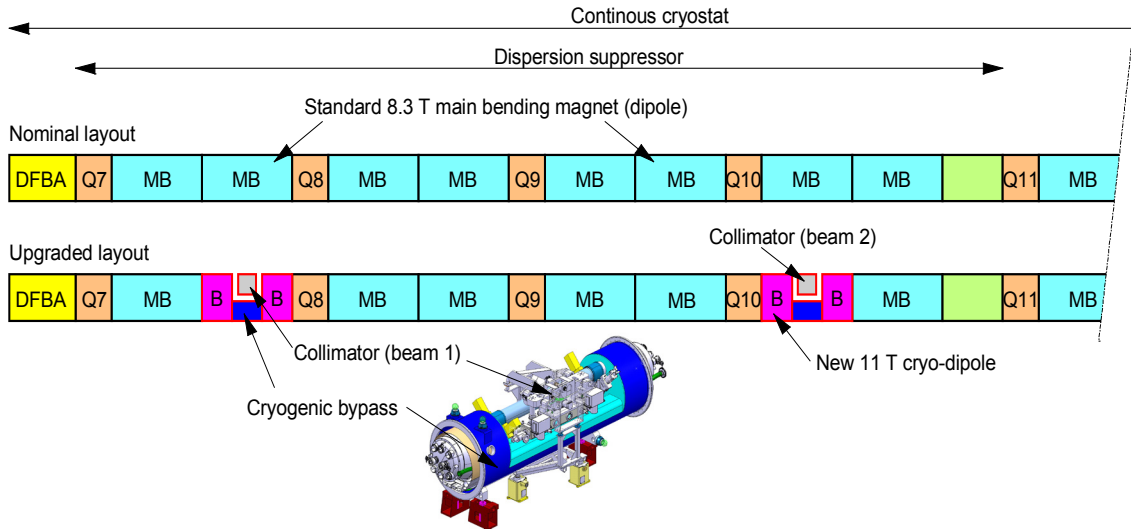


Figure 9-2: Upgraded layout of the continuous cryostat at P2 (as well at P1, P5, and P7)

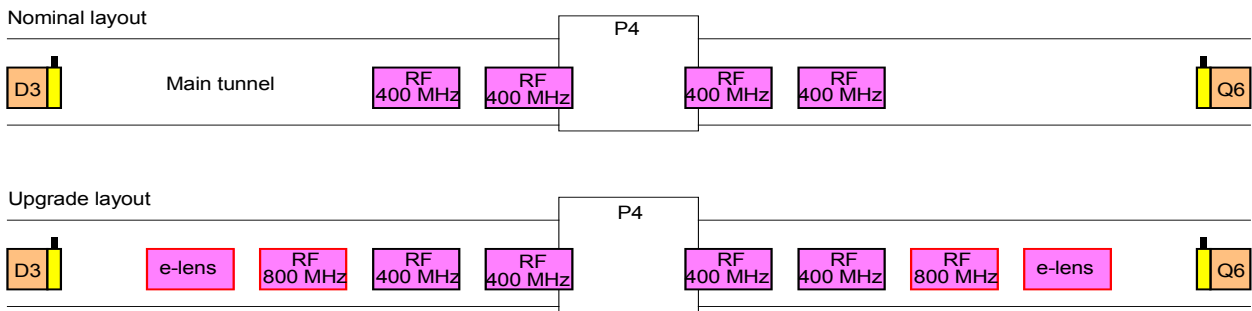


Figure 9-3: Possible upgraded layout of the P4 insertion region

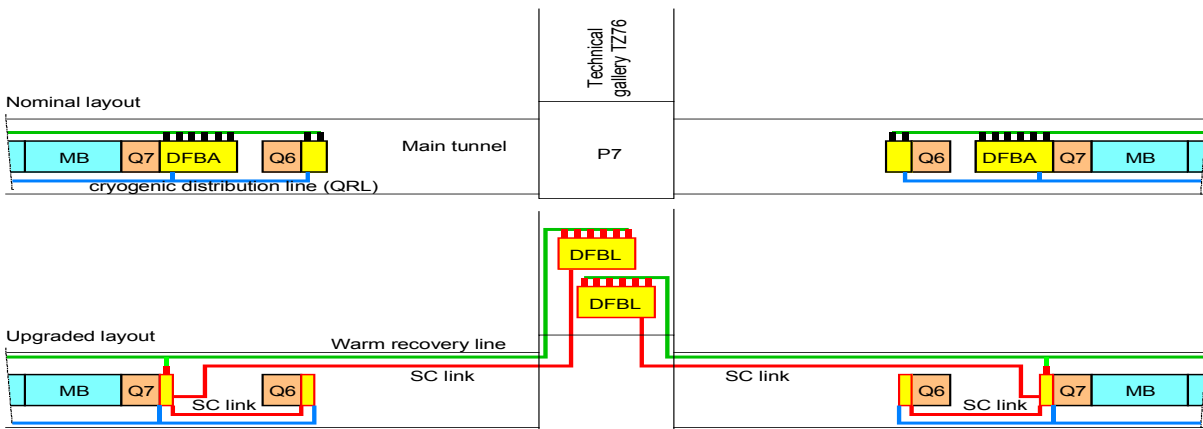


Figure 9-4: Upgraded layout of the P7 insertion region

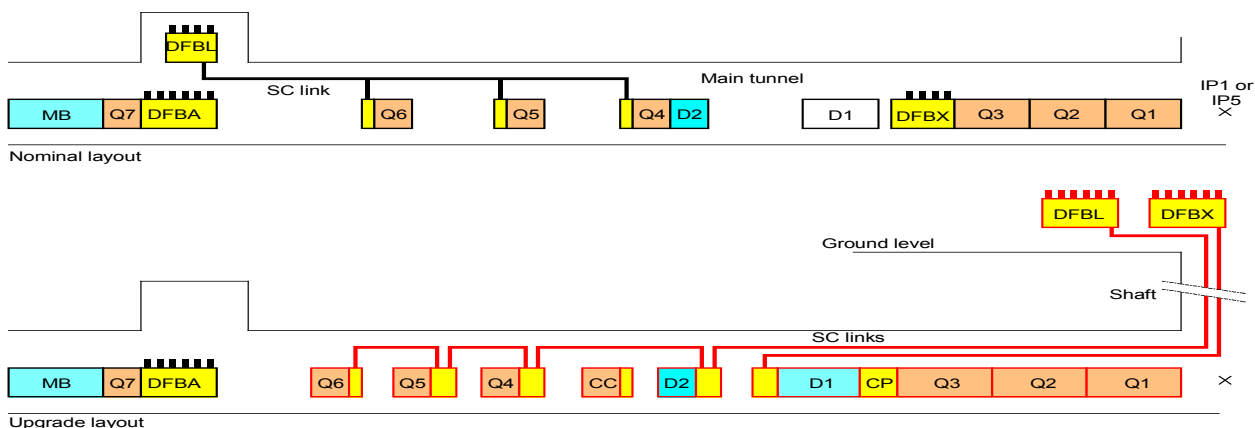


Figure 9-5: Upgraded layout of the P1/P5 insertion region (half insertion)

### 9.3 Temperature level and heat loads

Heat loads to the cryogenic system have various origins and uncertainties. As done for the LHC and clearly described in the design report, two categories of heat loads are considered: static heat loads ( $Q_{static}$ ) to be compensated just to reach the desired temperature level, and dynamic heat loads ( $Q_{dynamic}$ ) due to energising or circulating beams. These heat loads are primarily considered without contingency to avoid piling-up margins. However, the cooling capacity to be installed has to include margins that vary for the static and dynamic heat loads to properly allow the nominal beam scenario. This margin vanishes for the ultimate beam scenario.

In Table 9-2 the static heat in-leaks are reported, for different temperature levels. For new equipment, the thermal performance of supporting systems, radiative insulation and thermal shields is considered identical to that of existing LHC equipment.

Table 9-2: Static heat in-leaks of HL-LHC machine (without contingency)

Temperature [k]	Equipment	Unit	Nominal	Upgrade
4.6–20	Beam screen circuit (arc + DS)	[mW/m]	140	140
	Beam screen circuit (IT)	[mW/m]	125	125
	Beam screen circuit (MS)	[mW/m]	578	578
1.9	Cold mass (arc + DS)	[mW/m]	170	170
	Cold mass (IT)	[mW/m]	1250	1250
	Crab cavities	[W per module]	0	25
4.5	Cold mass (MS)	[mW/m]	3556	3556
	400 MHz RF module	[W per module]	200	200
	800 MHz RF module	[W per module]	0	120
	Electron-lens	[W per module]	0	12
20–300	Current lead	[g/s per kA]	0.035	0.035

Table 9-3 gives the dynamic heat loads expected for the HL-LHC. The main concern is electron-cloud impingement on the beam screens, which can only be reduced by efficient beam scrubbing (dipole off) of the beam screens. This remains to be demonstrated. Without efficient beam scrubbing (dipole on), the e-cloud activity will remain high (more than 4 W/m and per beam) in the arcs and dispersion suppressors (DS). This heat deposition corresponds to about twice the local cooling limitation given by the hydraulic impedance of the beam screen cooling circuits. In addition, the corresponding integrated power over a sector (more than 25 kW) is not compatible with the installed capacity of the sector cryogenic plants. For e-cloud deposition in the arcs and dispersion suppressors, efficient (dipole off) or inefficient (dipole on) beam scrubbing is considered.

Table 9-3: Dynamic heat loads on HL-LHC machine (without contingency)

Temperature [k]	Equipment	Unit	Nominal	Upgrade
4.6–20	Synchrotron radiation (arc + DS)	[mW/m per beam]	165	310
	Image current (arc + DS + MS)	[mW/m per beam]	145	522
	Image current (IT low-luminosity)	[mW/m]	475	1698
	Image current (IT high luminosity)	[mW/m]	166	596
	E-clouds (arc + DS) (dipole off)	[mW/m per beam]	271	41
	E-clouds (arc + DS) (dipole on)	[mW/m per beam]	4264	4097
	E-clouds (IT high luminosity)	[mW/m]	5500	9455
	E-clouds (IT low-luminosity)	[mW/m]	5500	5500
	E-clouds (MS)	[mW/m per beam]	2550	383
	Secondaries (IT beam screen P1 and P5)	[W per IT]	0	650
1.9	Beam gas scattering	[mW/m per beam]	24	45
	Resistive heating in splices	[mW/m]	56	56
	Secondaries (IT cold mass P1 and P5)	[W per IT]	155	630
	Secondaries (DS cold mass P1 and P5)	[W per DS]	37	185
	SCRF crab cavities	[W per module]	0	24
4.5	SCRF 400 MHz	[W per module]	101	366
	SCRF 800 MHz	[W per module]	0	183
	E-lens	[W per module]	0	2
20–300	Current lead	[g/s per kA]	0.035	0.035

The beam screens of the new inner triplets at P1 and P5 will be protected by tungsten shielding that will be able to absorb about half of the energy deposited by collision debris escaping the high luminosity detectors. For simplicity at this stage, beam screen loads were considered to be between 4.6 K and 20 K as for the current LHC. However, the large dynamic power to be extracted could force consideration of the next possible temperature range compatible with beam vacuum requirements, i.e. the range 40 K to 60 K. Despite this thick W-shielding, the 1.9 K load, i.e. the energy that collision debris deposited onto the magnet coil and cold mass, increases by four times with respect to the nominal LHC case. The W-shielding, in any case, reduces the overall refrigeration cost and increases the lifetime of the inner-triplet coils.

#### 9.4 Impact on existing sector cryogenic plants

With new cryogenic plants dedicated to the cooling of cryogenic equipment in P1, P4, and P5, the cooling duty of the existing sector cryogenic plants will be reduced and more equally distributed. Figure 9-6 shows the required cooling capacities for the different temperature levels and compares them to the nominal cooling requirements and to the installed capacities. The low-load sectors equipped with upgraded ex-LEP cryogenic plants have lower installed capacity than the four cryogenic plants specially ordered for the LHC’s high-load sectors. For the HL-LHC, sufficient capacity margin still exists providing that the beam scrubbing of dipole beam-screens is efficient (dipole off).

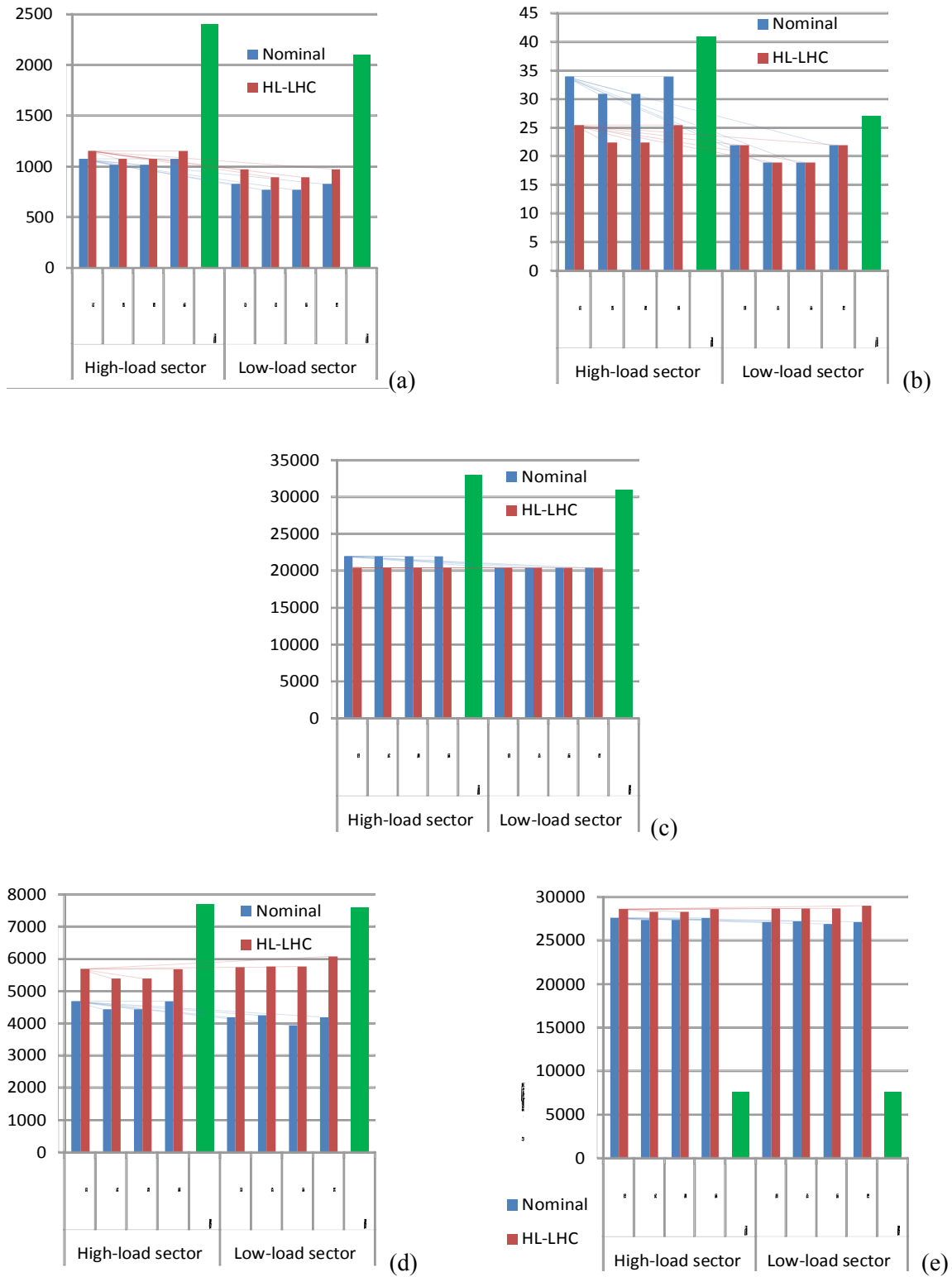


Figure 9-6: Cooling capacity requirement of sector cryogenic plants. (a) Cold mass; (b) current leads; (c) thermal shields; (d) beam screen (dipole off); (e) beam screen (dipole on).

**9.5 New cryogenics for Point 4 insertion**

Figure 9-7 shows the cryogenic architecture of the upgraded P4 insertion consisting of:

- a warm compressor station (WCS) located in a noise-insulated surface building and connected to a helium buffer storage;
- a lower cold box (LCB) located in the UX45 cavern and connected to a cryogenic distribution valve box (DVB), also located in the UX45 cavern;
- main cryogenic distribution lines connecting the cryomodules to the distribution valve box;
- auxiliary cryogenic distribution lines interconnecting the new infrastructure with the existing QRL service modules (SM) and allowing redundancy cooling with adjacent-sector cryogenic plants;
- a warm-helium recovery line network.

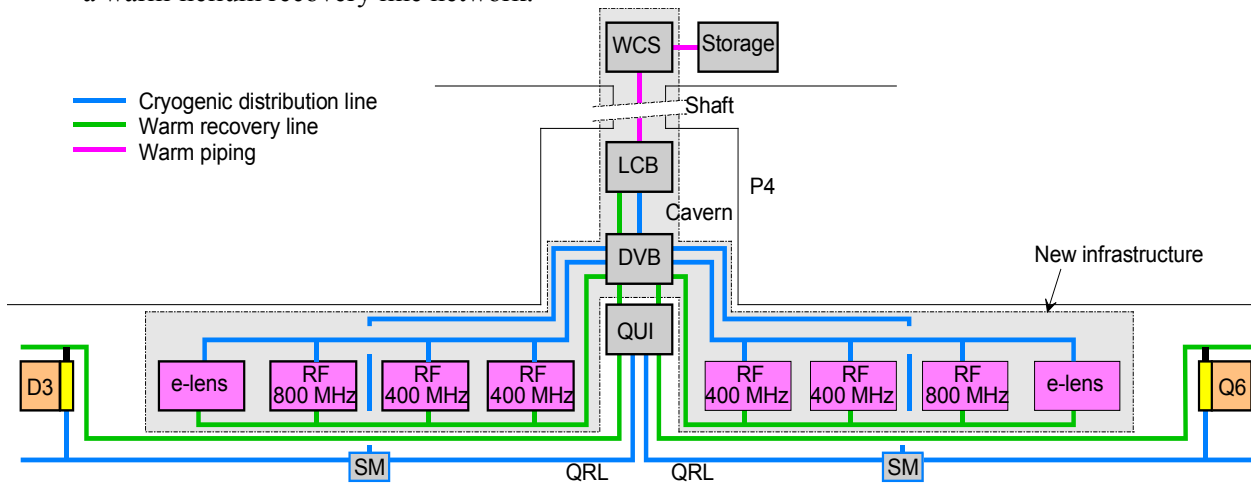


Figure 9-7: Upgraded cryogenic architecture at P4

Concerning the planned installed capacity ( $Q_{\text{installed}}$ ) of the new cryogenic plant, some uncertainty ( $f_u$ ) and overcapacity ( $f_o$ ) margins have to be introduced as shown in Eq. 9.1:

$$Q_{\text{installed}} = f_o \times (Q_{\text{static}} \times f_u + Q_{\text{dynamic}}), \tag{9-1}$$

where  $f_o = 1.5$  and  $f_u = 1.5$ .

Table 9-4 gives the installed capacity of the P4 cryogenic plant required at different temperature levels. The P4 cryogenic plant will require an equivalent capacity of about 6 kW at 4.5 K.

This is considered as the present baseline, with the evaluation of an alternative scenario for the refrigeration part. The alternative scenario would consist of an upgrade of one of the existing refrigerator of P4 to fulfil the required cooling capacity of existing SRF modules with sufficient margin, while keeping the baseline new distribution scenario. This modular and staged approach would allow the installation at a later stage of a new and dedicated refrigerator adapted to the loads presently under definition.

Table 9-4: Installed capacity requirements of the new cryogenic plant at P4

Temperature level [K]	Static [W]	Dynamic [W]	Installed [W]	Equivalent installed capacity at 4.5 K [kW]	
4.5	1144	1736	5223	5.6	5.8
50–75	1000	0	2250	0.2	5.8

### 9.6 New cryogenics for high luminosity insertions at Point 1 and Point 5

Figure 9-8 shows the proposed cryogenic architecture of the P1 and P5 high luminosity insertions consisting of:

- a warm compressor station (WCS) located in a noise-insulated surface building and connected to a helium buffer storage;
- an upper cold box (UCB) located in a ground-level building;
- a quench buffer (QB) located at ground level;
- one or two cold compressor boxes (CCB) in an underground cavern;
- two main cryogenic distribution lines (one per half-insertion);
- two interconnection valve boxes with existing QRL cryogenic line allowing redundancy with the cryogenic plants of adjacent sectors.

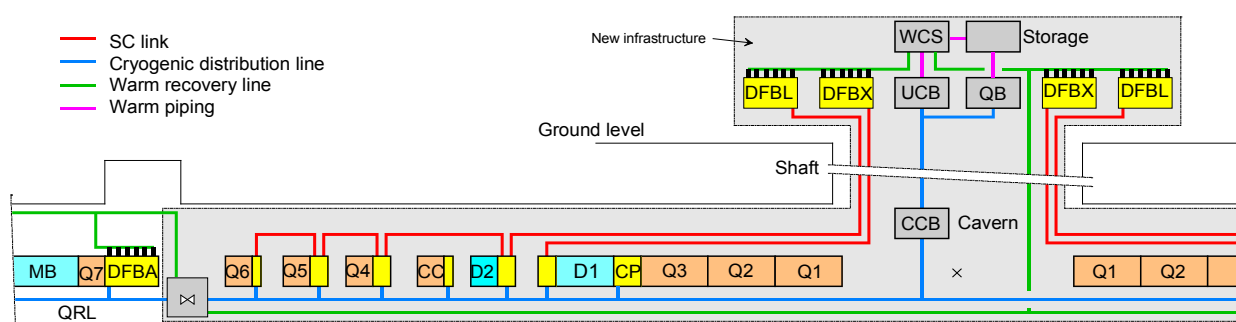


Figure 9-8: Upgraded cryogenic architecture at P1 and P5

Table 9-5 gives the installed capacity of the proposed P1 and P5 cryogenic plants required at the different temperature levels and using the same uncertainty and overcapacity margins as those used for P4. The cryogenic plants will require an equivalent capacity of about 18 kW at 4.5 K, including 3 kW at 1.8 K.

Table 9-5: Installed capacity requirements of the new cryogenic plants at P1 and P5

Temperature level [K]	Units	Static	Dynamic	Installed	Equivalent installed capacity at 4.5 K [kW]	
1.9	[W]	433	1380	3045	12	18
4.5	[W]	196	8	452	0.5	18
4.6–20	[W]	154	2668	4348	2.4	18
50–75	[W]	4900	0	7350	0.5	18
20–300	[g/s]	16	16	59	2.6	18

At P1 and P5 the superconducting magnets of the ATLAS and CMS detectors are cooled by dedicated cryogenic plants. A possible redundancy with detector cryogenic plants could be interesting in the event of a major breakdown of the detector cryogenic plants. The corresponding power requirements are about 1.5 kW at 4.5 K for CMS and 3 kW at 4.5 K for ATLAS.

The cooling capacity of 3 kW at 1.8 K is higher than the 2.4 kW installed capacity of an LHC sector, which corresponds to the present state-of-the-art for the cold compressor size. Consequently:

- larger cold compressors have to be studied and developed;
- or parallel cold compressor trains have to be implemented (one 1.5 kW train per half insertion);
- or duplication of the first stage of cold compression to keep the machine within the available size.

### 9.7 Building and general service requirement

Table 9-6 gives the buildings and general services at P1, P4, and P5 required by the cryogenic infrastructure. At P4, the required surface and volume for the warm compression station and for the cold box are respectively available in the existing SUH4 building and in the UX45 cavern.

Table 9-6: Building and general service requirement

Cryogenic system			P1 and P5	P4
Warm compressor building	Surface	[m <sup>2</sup> ]	700	400
	Crane	[t]	20	20
	Electrical power	[MW]	4.6	2.0
	Cooling water	[m <sup>3</sup> /h]	540	227
	Compressed air	[Nm <sup>3</sup> /h]	30	20
	Ventilation	[kW]	250	100
	Type	-	Noise-insulated (~108 dB_A)	
Surface SD building	Surface	[m <sup>2</sup> ]	30 × 10	N/A
	Height	[m]	12	N/A
	Crane	[t]	5	N/A
	Electrical power	[kW]	50	N/A
	Cooling water	[m <sup>3</sup> /h]	15	N/A
	Compressed air	[Nm <sup>3</sup> /h]	90	N/A
Cavern	Volume	[m <sup>3</sup> ]	200	300
	Local handling	[t]	2	2
	Electrical power	[kW]	100	20
	Cooling water	[m <sup>3</sup> /h]	20	20
	Compressed air	[Nm <sup>3</sup> /h]	40	30

### 9.8 Conclusions

The HL-LHC project will require a major cryogenic upgrade. The main challenges are given below.

- Cooling circuits for large heat deposition.
  - o Up to 13 W/m on 1.9 K cold masses for heat extraction from SC cables and sufficient quench energy margin. Accurate heat flow calculation in coil and yoke cross-section must be developed.
  - o Up to 23 W/m on inner-triplet beam screens possibly with a different operating range (40–60 K) and with a large dynamic range that will require specific cryogenic plant adaptation studies.
- Cooling of HTS SC links and current feedboxes.
- Cooling and pressure relief of crab cavities.
- Validation tests on SC link, crab cavities, magnets, beam screens, etc.
- Reactivation of the Heat Load Working Group.
- Quench containment and recovery.
- Larger 1.8 K refrigeration capacities beyond the present state-of-the-art.
- Large capacity (1500 W/3000 W) sub-cooling heat exchangers.
- Larger turndown capacity factor (up to 10) on the 1.8 K refrigeration cycle.





# Chapter 10

## Energy Deposition and Radiation to Electronics

*A. Bignami<sup>1</sup>, F. Broggi<sup>1</sup>, M. Brugger<sup>2</sup>, F. Cerutti<sup>2\*</sup>, L.S. Esposito<sup>2</sup>, A. Lechner<sup>2</sup>, N.V. Mokhov<sup>3</sup>, I.L. Rakhno<sup>3</sup>, C. Santini<sup>4</sup>, E. Skordis<sup>2</sup> and I.S. Tropin<sup>3</sup>*

<sup>1</sup>INFN-LASA, Milan, Italy

<sup>2</sup>CERN, Accelerator & Technology Sector, Geneva, Switzerland

<sup>3</sup>FNAL, Fermi National Accelerator Laboratory, Batavia, USA

<sup>4</sup>Politecnico of Milan, Italy

### 10 Energy deposition and radiation to electronics

#### 10.1 Characterization of the radiation source

Proton–proton inelastic collisions taking place in the LHC inside its four detectors generate a large number of secondary particles with average multiplicities of approximately 100 (120) per single proton–proton interaction with 3.5 (7) TeV beams, but with very substantial fluctuations over different events. Moving away from the interaction point (IP), this multiform population evolves, even before touching the surrounding material, because of the decay of unstable particles (in particular neutral pions decaying into photon pairs). Figure 10-1 illustrates the composition of the debris at 5 mm from the point of a 14 TeV centre of mass collision, featuring a ~30% increase in the number of particles, due to the aforementioned decays, and a clear prevalence of photons (almost 50%) and charged pions (~35%).

Most of these particles are intercepted by the detector and its forward region shielding, releasing their energy within the experimental cavern. However, the most energetic particles, emitted at small angles with respect to the beam direction, travel farther in the vacuum and reach the accelerator elements, causing a significant impact on the magnets along the insertion regions (IRs), in particular the final focusing quadrupoles and the separation dipoles. Figure 10-1 also shows the breakdown of the debris components going through the aperture of the target absorber secondaries (TAS) absorber, a protection element consisting of a 1.8 m long copper core located 20 m from the IP and representing the interface between the detector and the accelerator. The TAS absorbers are only installed each side of the high luminosity detectors, ATLAS in P1, and CMS in P5, since their protection role, which is in fact limited to the first quadrupole, is not needed for luminosities up to  $0.2 \times 10^{34} \text{ cm}^{-2} \text{ s}^{-1}$  [1].

Despite the fact that the number of particles per collision leaving the TAS aperture is more than one order of magnitude lower than the total number of debris particles, they carry about 80% of the total energy, implying that 40% of the released energy at the IP exits on each side of the experiments. At the nominal HL-LHC luminosity ( $5 \times 10^{34} \text{ cm}^{-2} \text{ s}^{-1}$ ), this represents about 3800 W per side that is inevitably impacting upon the LHC elements and consequently dissipated in the machine and in the nearby equipment (e.g. electronics, racks, etc.) and in the tunnels walls.

It is fundamental to study how these particles are lost in order to implement the necessary protections for shielding sensitive parts of the LHC magnets and the machine. For these purposes, Monte Carlo simulations of particle interactions with matter play an essential role, relying on a detailed implementation of physics models and an accurate 3D description of the region of interest.

---

\* Corresponding author: [Francesco.Cerutti@cern.ch](mailto:Francesco.Cerutti@cern.ch)

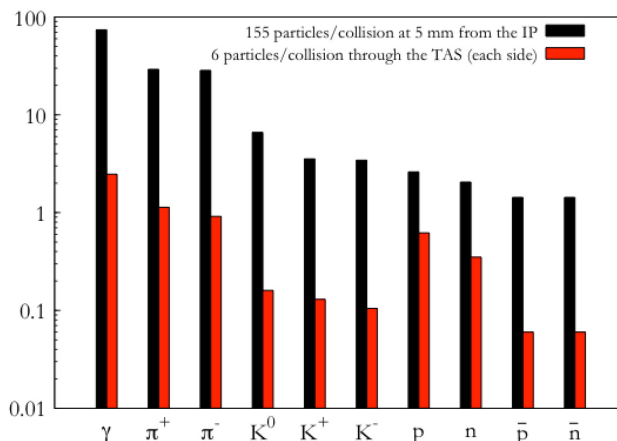


Figure 10-1: Number of debris particles per single proton–proton inelastic interaction at 5 mm from the interaction point (black) and at the exit of each 60 mm TAS aperture (red).

In addition to the luminosity debris, which dominates energy deposition in the vicinity of the collision points, regular and accidental beam losses represent other relevant sources of radiation. In particular, beam halo particles caught in the collimators (see Chapter 5) initiate hadronic and electromagnetic showers, mainly in the betatron and momentum cleaning IRs. The same happens with injection and dumping protection devices (see Chapter 14). Moreover, secondary particle showers are also originated by beam interactions with the residual gas inside the vacuum chamber the length of the accelerator, as well as with dust fragments falling into the beam path.

## 10.2 Power and dose evaluations concerning the triplet-D1 region

The LHC upgrade includes replacement of the inner triplet (IT) 70 mm Nb-Ti quadrupoles in P1 and P5 with the 150 mm coil aperture Nb<sub>3</sub>Sn quadrupoles, along with the new 150 mm coil aperture Nb-Ti dipole magnet and orbit correctors. Moreover, a corrector package (CP) that includes a skew quadrupole and eight high-order magnets (from sextupole to dodecapole, normal and skew, based on Nb-Ti technology) will be located between the triplet and D1.

As the first studies of radiation loads in the LHC upgrades have shown [2, 3], one could provide the operational stability and adequate lifetime of the IR superconducting magnets by using tungsten-based inner absorbers in the magnets. The goals are: i) reduce the peak power density in the inner Nb<sub>3</sub>Sn cable to below the quench limit with a safety margin; ii) keep the 3000 fb<sup>-1</sup> lifetime peak dose in the innermost layers of insulation and radiation loads on inorganic materials in the hottest spots of the coils below the known radiation damage limits; iii) keep the dynamic heat load to the cold mass at a manageable level.

### 10.2.1 FLUKA–MARS modeling

To design such a system in a consistent and confident way, coherent investigations have been undertaken with two independent Monte Carlo codes benchmarked in the TeV energy region and regularly used in such applications: FLUKA at CERN [4–7] and MARS15 (2014) at Fermilab [8–10]. The studies were done for 7 + 7 TeV p–p-collisions with a 295  $\mu$ rad half-angle vertical crossing in IP1 (which had previously been found earlier to be the worst case) using DPMJET-III as the event generator.

An identical, very detailed geometry model was created and used in both codes with the same materials and magnetic field distributions in each of the components contained within the 80 m region from the IP through to the D1 dipole. An octagonal stainless steel beam screen, equipped with 6 mm tungsten absorbers on the mid-planes, is placed inside the cold bore along the triplet, the CP, and the D1, except in Q1, where the tungsten thickness is increased to 16 mm, compatible with the relaxed aperture requirements. The absorbers are between the beam screen and the 1.9 K beam pipe: they are supported by the beam screen, and thermally

connected to it, whereas they have negligible contact with the cold mass. Therefore, from the point of view of energy deposition, the beam screen function is two-fold:

- it shields the coils from the debris by reducing the energy deposited;
- it removes a sizable part of the heat load from the 1.9 K cooling system, intercepting it at a higher temperature.

The present HL-LHC layout foresees six cryostats on each side of the IP: four for the triplet quadrupoles (Q1, Q2A, Q2B, and Q3), one for CP and one for D1. The distance between the magnets in the interconnections is 1.5–1.7 m, and an interruption of the beam screen is necessary therein. As a reasonable baseline, we assume here a 500 mm interruption of the tungsten absorbers in the middle of the interconnects. Figure 10-2 and Figure 10-3 show a 3D view of the model and details in the inner parts of the quadrupoles and orbit correctors.

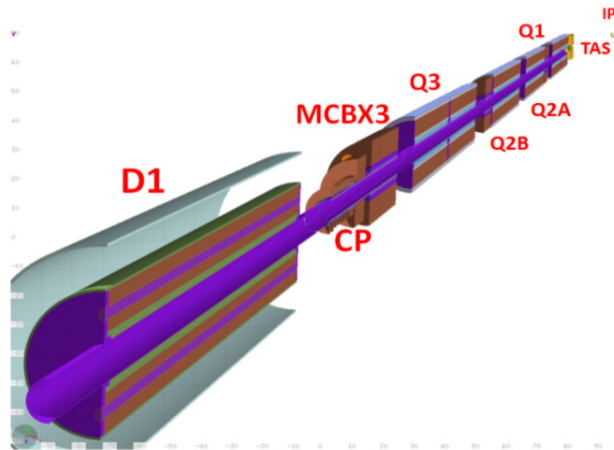


Figure 10-2: HL-LHC inner triplet with MCBX/CP correctors and D1 dipole

Fine-mesh distributions of power density as well as absorbed dose, neutron fluence, and displacements-per-atom (DPA), along with dynamic heat load in every IT component were calculated with FLUKA and MARS in high-statistics runs. The power density and dynamic heat load results are normalized to a luminosity of  $5 \times 10^{34} \text{ cm}^{-2} \text{ s}^{-1}$ , while all others are to  $3000 \text{ fb}^{-1}$  integrated luminosity, corresponding to  $\sim 10\text{--}12$  years of HL-LHC operation. Longitudinal scoring bins are 10 cm, and azimuthal ones are  $2^\circ$ . Radially, power density is averaged over the superconducting cable width, while dose, fluence, and DPA are scored within the innermost layer equal to 3 mm or its thickness, whichever is thinner.

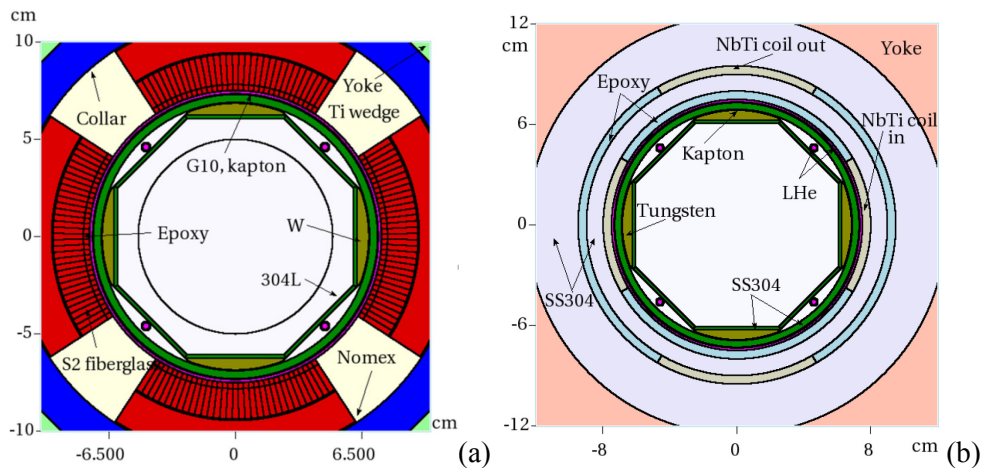


Figure 10-3: Details of the FLUKA–MARS model in the innermost regions of (a) the Q2–Q3 quadrupoles; (b) MCBX orbit correctors.

### 10.2.2 Operational radiation loads

Power density isocontours at the IP end of the cold mass of the Q2A quadrupole are shown in Figure 10-4(a). The longitudinal peak power density profile on the inner coils of the IT magnets at the azimuthal maxima is presented in Figure 10-4(b). Results from FLUKA and MARS are in excellent agreement, being observable discrepancies – which are naturally related to the use of fully independent tracking and scoring algorithms and physics models – largely within the safety margin to be recommended at the design stage. The peak value of  $2 \text{ mW/cm}^3$  in the quadrupoles is 20 times less than the assumed quench limit of  $40 \text{ mW/cm}^3$  in  $\text{Nb}_3\text{Sn}$  coils [2]. The peak value of  $\sim 1.5 \text{ mW/cm}^3$  in the Nb-Ti based coils of the correctors and D1 dipole is almost ten times less than the known quench limit of  $13 \text{ mW/cm}^3$  in such coils [11].

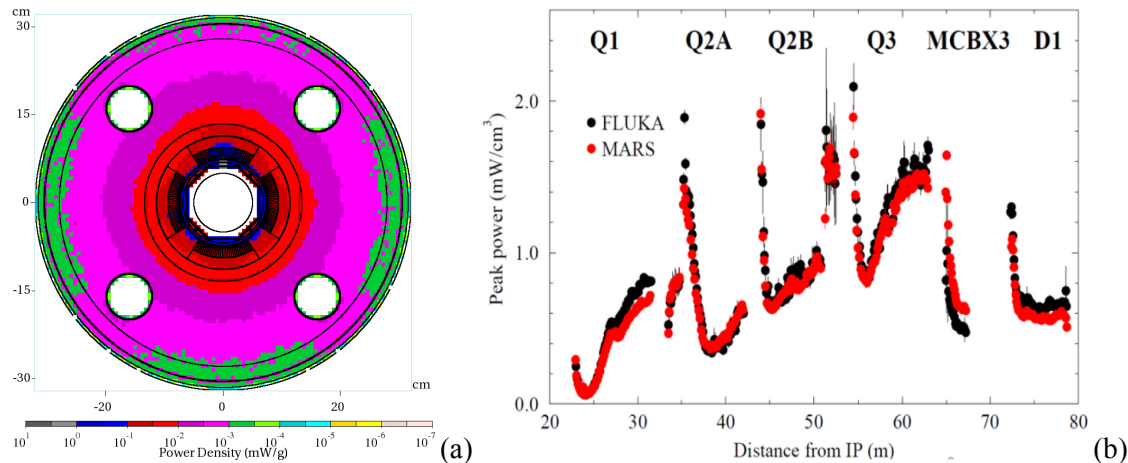


Figure 10-4: (a) Power density isocontours at the IP end of Q2A; (b) longitudinal peak power density profile on the inner coils of the IT magnets.

The total power dissipation in the inner triplet IT region from the IP1 collision debris splits roughly 50–50 between the cold mass and the beam screen with tungsten absorber, 630 W and 615 W, respectively, from the FLUKA calculations. MARS predicts values about 2% lower. For the 45 m effective length of the cold mass, the average dynamic heat load is  $\sim 14 \text{ W/m}$ .

### 10.2.3 Lifetime radiation loads

The peak dose and DPA – the quantities that define radiation damage and the lifetime of the insulators and non-organic materials of the IT magnets, respectively – are calculated at the azimuthal maxima in the innermost tiny layers of each IT component shown in Figure 10-2.

The longitudinal peak dose profiles on the inner coils and insulating materials are presented in Figure 10-5(a). The values in the MCBX orbit correctors (located in the Q1–Q2A, Q2B–Q3, and Q3–D1 regions) are given for the epoxy layer (FLUKA) and kapton layer (MARS); see Figure 10-3 for details. Results from FLUKA and MARS are again in good agreement. The larger aperture IT magnets and the simulated implementation of tungsten absorbers perform very well, reducing the peak values of both power density and absorbed dose in the HL-LHC IR to the levels that correspond to LHC nominal luminosity.

The maximum peak dose in the coils is about 25 MGy for quadrupoles and  $\sim 15 \text{ MGy}$  for the D1 dipole. The integrated peak dose in the IT magnet insulation reaches 30–36 MGy in the MCBX3 corrector, 28–30 MGy in the quadrupoles, and  $\sim 22 \text{ MGy}$  in the D1 dipole. This is at or slightly above the common limits for kapton (25–35 MGy) and CTD-101K epoxy (25 MGy).

Degradation of the critical properties of inorganic materials in the IT magnets –  $\text{Nb}_3\text{Sn}$  and Nb-Ti superconductors, copper stabilizer, and mechanical structures – is usually characterized not by absorbed dose but by integrated neutron fluence and by DPA accumulated in the hottest spots over the magnet's expected lifetime. DPA is the most universal way to characterize the impact of irradiation on inorganic materials. In

both FLUKA and MARS, all products of elastic and inelastic nuclear interactions as well as Coulomb elastic scattering (NIEL) of transported charged particles (hadrons, electrons, muons, and heavy ions) from  $\sim 1$  keV to TeV energies contribute to DPA using Lindhard partition function and energy-dependent displacement efficiency. For neutrons at  $<20$  MeV (FLUKA) and  $<150$  MeV (MARS), the ENDF-VII database with NJOY99 processing is used in both the codes.

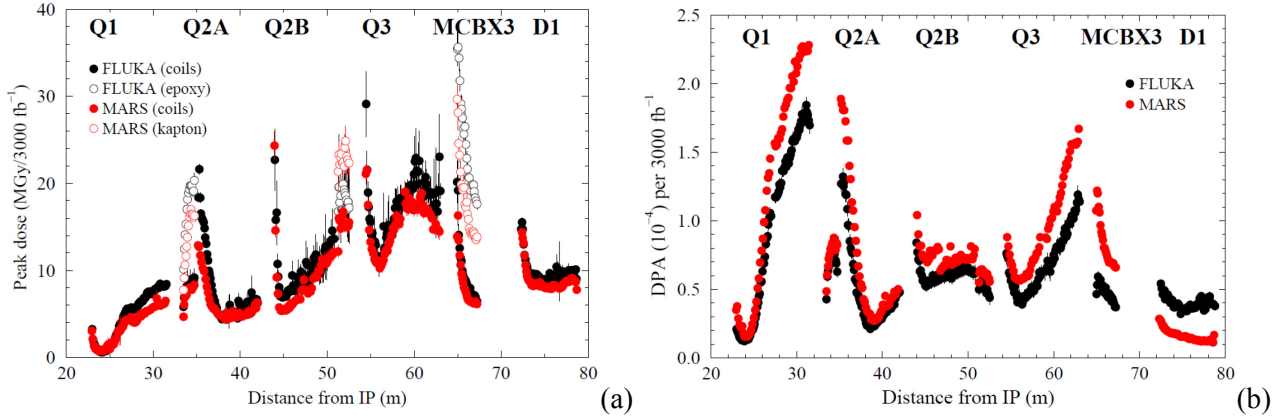


Figure 10-5: Longitudinal distributions of (a) peak dose on inner coils and nearby insulators; (b) peak DPA on inner coils.

The longitudinal peak DPA profiles on the IT magnet coils are presented in Figure 10-5(a). The peaks are generally observed at the inner coils; therefore, the data is given for these areas. With the vertical crossing in IP1, the MCBX3 orbit corrector is the exception with the peak in the outer coil in the vertical plane (see Figure 10-5). To see this effect, the MARS data in Figure 10-5(b) for MCBX3 is given for the outer coil, while FLUKA shows results for the inner coil as in all other magnets. Contrary to the power density and dose distributions driven by electromagnetic showers initiated by photons from  $\pi^0$  decays, DPA peaks at the non-IP end of the Q1B quadrupole. At that location, about 70% of DPA is from neutrons with  $E < 20$  MeV,  $\sim 25\%$  from transported nuclear recoils above 0.25 keV/A, and the rest is due to other transported particles and non-transported recoils. The thicker Q1 shielding, while assuring a very effective dose reduction, plays a clear role in enhancing neutron production.

The peak in the Q1B inner coil is about  $2 \times 10^{-4}$  DPA per 3000  $\text{fb}^{-1}$  integrated luminosity. In other IT components it is about  $(1 \pm 0.5) \times 10^{-4}$ . These numbers should be acceptable for the superconductors and copper stabilizer provided that there is periodic annealing during the collider shutdowns. Taking into account a good correlation of DPA with neutron fluence in the coils, one can also compare the latter with known limits. In the quadrupole coils, the peak fluence is  $\sim 2 \times 10^{17} \text{ cm}^{-2}$  which is substantially lower than the  $3 \times 10^{18} \text{ cm}^{-2}$  limit used for the  $\text{Nb}_3\text{Sn}$  superconductor. In the orbit corrector and D1 dipole coils, the peak fluence is  $\sim 5 \times 10^{16} \text{ cm}^{-2}$  which is again lower than the  $10^{18} \text{ cm}^{-2}$  limit used for the Nb-Ti superconductor. The integrated DPA in the magnet mechanical structures are 0.003 to 0.01 in the steel beam screen and tungsten absorber,  $\sim 10^{-4}$  in the collar and yoke, and noticeably less outside. These are to be compared to a  $\sim 10$  DPA limit for the mechanical properties of these materials. Neutron fluences in the IT mechanical structures range from  $3 \times 10^{16} \text{ cm}^{-2}$  to  $3 \times 10^{17} \text{ cm}^{-2}$ , compared to the  $10^{21} \text{ cm}^{-2}$  to  $7 \times 10^{22} \text{ cm}^{-2}$  limits.

Peak dose on the beam screen was found to be of the order of several hundred MGy after 3000  $\text{fb}^{-1}$  integrated luminosity (up to 700 MGy in D1), mostly carried by electromagnetic particles. Its impact on carbon coating has to be considered.

### 10.3 Critical dependencies

The beam screen equipped with tungsten absorbers represents the backbone element for the protection of the IR magnets. Therefore, the details of its design play a crucial role in determining its actual effectiveness.

After the preliminary studies described in the previous section, new estimates were necessary to include:

- the real absorber material, Inermet 180, which has a density of  $18 \text{ g cm}^{-3}$ , about 8% less than pure tungsten, implying a reduced shielding performance;
- the first prototype taking into account the machinability of Inermet and the required size of the cooling tubes as dictated by preliminary cryogenics estimates;
- the reduction of the beam screen thickness (from 2 mm to 1 mm) necessary to let the structure respond elastically to possible deformations occurring during a quench.

Figure 10-6(a) shows a transverse section of the beam screen model (BS#2) embedding the abovementioned modifications. It can be compared to the model (BS#1) used in the calculations reported in the previous section (see Figure 10-3). The longitudinal peak dose profile on the inner coils of the IR magnets is presented in Figure 10-7 for BS#1 (black points) and BS#2 (red points). In the latter case, the accumulated peak dose turns out to be systematically higher all along the IR magnets, almost doubling its value in Q3 and reaching about 55 MGy in the MCBX3 corrector. Along Q2, most of the impacting debris, which is positively charged, is pushed by the magnetic field from the crossing angle side to the opposite side, i.e. from top to bottom in the assumed crossing scheme, where the outgoing beam points upwards. This moves the energy deposition peak through different azimuthal regions, which in the revised design (BS#2) are no longer shielded by the beam screen absorbers, hence yielding the resulting substantial increase. To fix this problem, we considered a third version of the beam screen (BS#3), where the Inermet absorbers were extended as much as possible to cover the coils towards the poles (see Figure 10-6(b)). The estimated peak dose distribution (green points in Figure 10-7(a) shows a significant improvement in the Q3–CP region, when compared to the BS#2 case. It should also be noticed that, mainly due to the reduced absorber density, the sharing of the total deposited power between cold mass and beam screen gets unbalanced, moving to 55–45 and making the heat released in the cold mass approach 700 W (at  $5 \times 10^{34} \text{ cm}^{-2} \text{ s}^{-1}$ ).

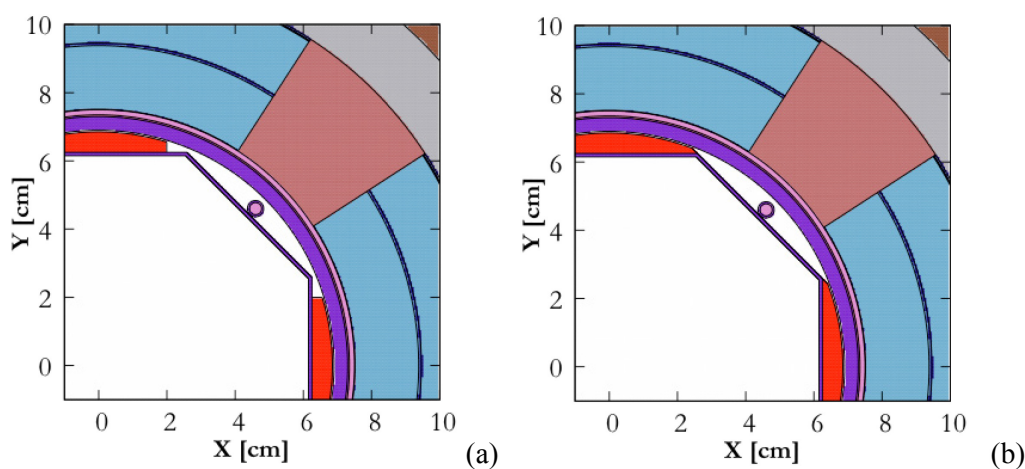


Figure 10-6: (a) Beam screen model as per the first conceptual design developed by WP12 (BS#2); (b) beam screen model with the modification of the absorbers driven by energy deposition considerations (BS#3).

Another crucial aspect is the longitudinal interruption of the beam screen and its absorbers, which is necessary between two consecutive cryostats in order to host a bellows and a BPM. As mentioned in the previous section, we initially assumed a 500 mm gap. Shorter gaps are possible if the BPMs are going to be equipped with absorber layers like those in the beam screen (see Chapter 12). To mimic this case, we looked at the effect of a 100 mm gap, which should be considered as the most optimistic case. The peak dose dependence on the gap length is presented in Figure 10-7(a) where the improvement achieved downstream of Q2A–Q2B, Q2B–Q3, and especially Q3–CP interconnects is visible, with a reduction from 55 MGy to 35 MGy in MCBX3 for the BS#2 design.

Therefore, the actual implementation of the absorber layers in the design of both the beam screen and the relevant BPMs considerably affects the maximum dose expected in the IT coils.

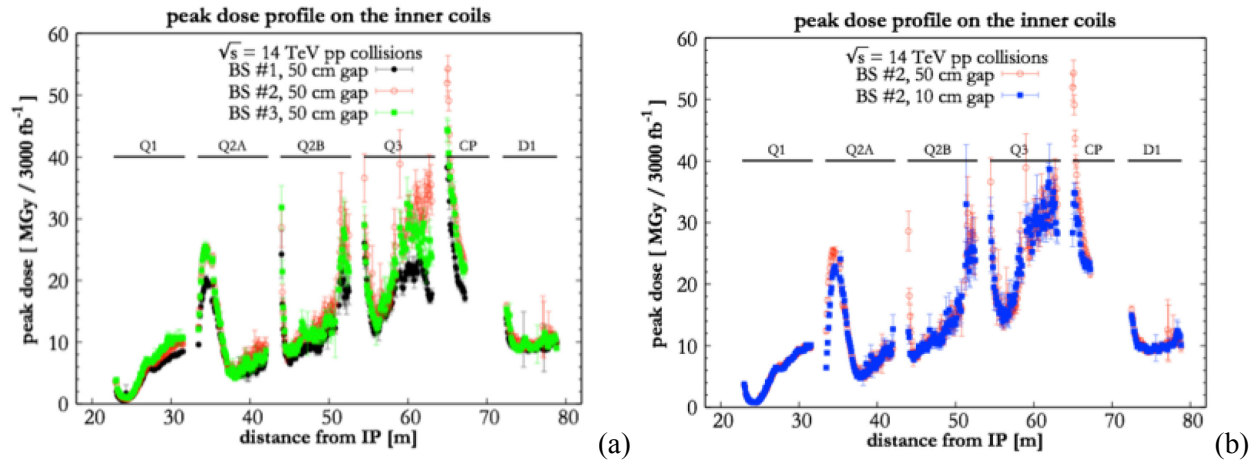


Figure 10-7: Longitudinal distributions of peak dose on the inner coils of the IR magnets referring to (a) different beam screen designs; (b) different lengths of the beam screen gap in the interconnects.

#### 10.4 Impact on the matching section and protection strategy

The HL upgrade foresees changes in the IR1 and IR5 matching section, implying a new target absorber neutral (TAN) absorber with larger apertures, a new recombination dipole D2 and Q4 (both with larger twin apertures, together with their respective correctors). The present baseline also foresees the Q5 replacement with the present Q4 (providing a larger aperture) and the installation of crab cavities. From Q6 onwards, no hardware modifications are expected inside the IRs.

With respect to the present LHC, the variation of three ingredients mainly impacts the energy deposition in the matching section elements. They are:

- the distance between the separation/recombination dipoles (reduced from 86 m to 67 m);
- the aperture of the upstream magnets (IT quadrupoles, CP correctors, and D1);
- the TAN design, which has to comply with larger beam separation and sizes.

As a consequence, the number of debris particles entering the matching section per primary collision is much larger than in the case of the current machine. This is illustrated in Figure 10-8, where the debris particle distributions at the exit of the TAN outgoing beam pipe are shown for the LHC (Figure 10-8(a)) and the HL-LHC (Figure 10-8(b)). The number of protons is increased by about 30% (from 0.12 to 0.16 protons/collision), while the number of photons and neutrons is about seven times higher (from 0.06 to 0.41 particles/collision). Note that in the case of the HL-LHC optics the beam size at this location is about twice as large as that of the LHC optics. Therefore, a collimator set at the same aperture in beam sigmas turns out to be less effective in intercepting debris particles, as clearly revealed in the figure by the number of particles left inside the beam envelope.

In the present LHC machine, a network of target collimator long physics debris (TCL) collimators secures the protection of the cold magnets in the matching section. There is one copper TCL in front of D2 (TCL4, installed during LS1), one copper TCL in front of Q5 (TCL5, the only one already present and operating during Run 1), and one tungsten TCL in front of Q6 (TCL6, whose installation during LS1 was triggered by specific Roman pot operation scenarios). However, at nominal luminosity not all TCLs are necessary to keep the heat load below the quench level. It was shown that the single TCL4 set at  $15\sigma$  is sufficient to maintain the peak power density below  $0.3 \text{ mW/cm}^3$  in all matching section magnets [12].

Conversely, in the case of the HL-LHC, all of the TCLs are indispensable for magnet protection. For the purposes of the estimates presented here, the jaws of all the collimators are assumed to be made of tungsten (Inermet 180) because of its greater absorption efficiency (higher density and atomic number than copper). Moreover, additional fixed target collimator long mask (TCLM) masks are required in order to further shield

the magnet aperture. The masks are supposed to be placed between the magnet cryostat and the TCL collimator (where present). Since the hottest spot is typically located on the IP side of each magnet, a shielding strategy based on a beam screen equipped with thick absorbers, as in the IT region, does not pay here. On the other hand, the masks, which have the same shape and aperture as the beam screen of the protected magnet and a radial thickness sufficient to shadow the downstream coils, can ensure an effective interception of the shower coming from the upstream elements. Sensitivity to mask presence and length has been investigated, and also aiming to comply with integration issues that are particularly challenging in the TAN–D2 region.

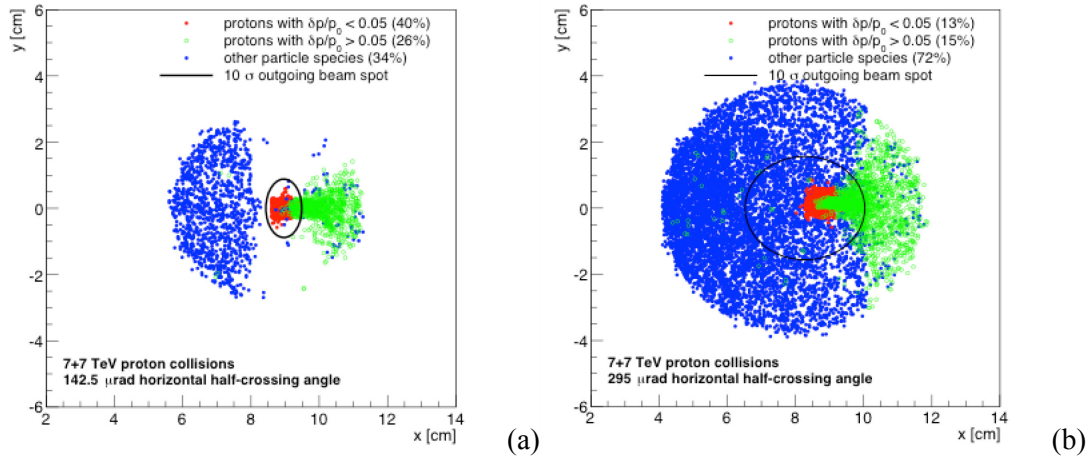


Figure 10-8: Debris particle distribution at the exit of the outgoing beam pipe of the TAN, (a) for the LHC; (b) for the HL-LHC. Red points indicate protons with magnetic rigidity within 5% with respect to beam protons and green points indicate protons with lower magnetic rigidity. Blue points indicate neutral particles (photons and neutrons). In both cases the same number of collision is simulated. The black ellipse shows the  $10\sigma$  outgoing beam spot.

Preliminary longitudinal profiles of the peak power density along D2, Q4, Q5, and Q6 are shown in Figure 10-9. All of the TCLs are set to  $10\sigma$ , but for TCL4 a  $20\sigma$  aperture is also explored. Dedicated masks turn out to be necessary for Q5 and Q6, while their need is less obvious for D2 and Q4, for which further studies are being carried out taking into account refined specifications concerning the TAN and TCL4 aperture and position. Considering lifetime issues, the installation of 50 cm masks in front of Q5 and Q6 keeps the respective peak dose values within  $20\text{ MGy}$  after  $3000\text{ fb}^{-1}$ .

The heat load due to collision debris on the most exposed crab cavity (the first one on the outgoing beam) was estimated to be about  $0.2\text{ W}$ . The maximum power density is located on the cavity internal plate and is about  $0.4\text{ mW/cm}^3$ . It corresponds to  $\sim 3\text{ MGy}$  after the target HL-LHC integrated luminosity. The contribution from beam–gas interactions is expected to be 10 times smaller, for a conservative residual gas density of  $10^{15}\text{ H}_2\text{-equivalent molecules/m}^3$ .



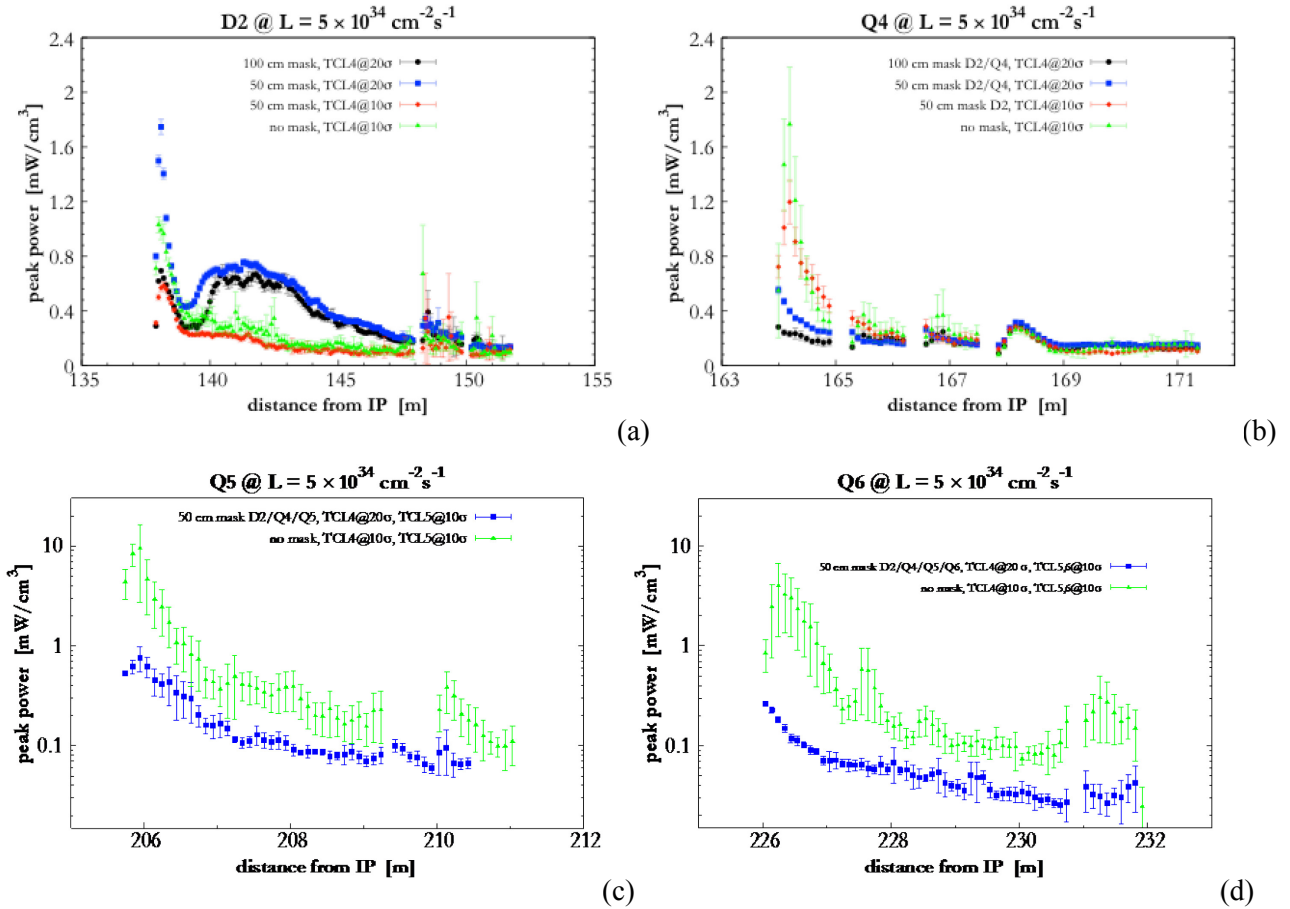


Figure 10-9: Longitudinal profile of peak power density along (a) D2; (b) Q4; (c) Q5, log scale; (d) Q6, log scale, at the HL-LHC target luminosity of  $5 \times 10^{34} \text{ cm}^{-2} \text{ s}^{-1}$ . Different layouts and settings are compared. Error bars indicate statistical uncertainties.

### 10.5 Exposure of the superconducting links

Cold powering of the HL-LHC magnets foresees moving the power converters to the surface [13]. The consequences of this new configuration are:

- safer long-term operation of powering equipment (power converters, current leads, and associated auxiliary devices), being located in a radiation-free environment;
- safer access of personnel to equipment for maintenance, repair, and diagnostic and routine test interventions;
- reduced time of interventions on power converters and current leads;
- more free space in the beam areas, which becomes available for other equipment.

The connecting lines will be made of  $\text{MgB}_2$ . The link cold mass contains SC cables that are connected at one end, in the tunnel, to the Nb-Ti magnet busbar operating in liquid helium; and the other end to the bottom end of the current leads maintained at a maximum temperature ( $T_{CL}$ ) of about 20 K in a helium gas environment, see Figure 10-10 [14].

The radiation impact on the  $\text{MgB}_2$  SC links is evaluated from different points of view. Boron consumption by thermal neutrons is not a concern. The total number of neutrons escaping from the first quadrupole of the new triplet is of the order of  $10^{21}$ , over an integrated luminosity of  $3000 \text{ fb}^{-1}$ . Considering the amount of  $^{10}\text{B}$  in the links, consumption can be estimated to be much less than 0.01%.

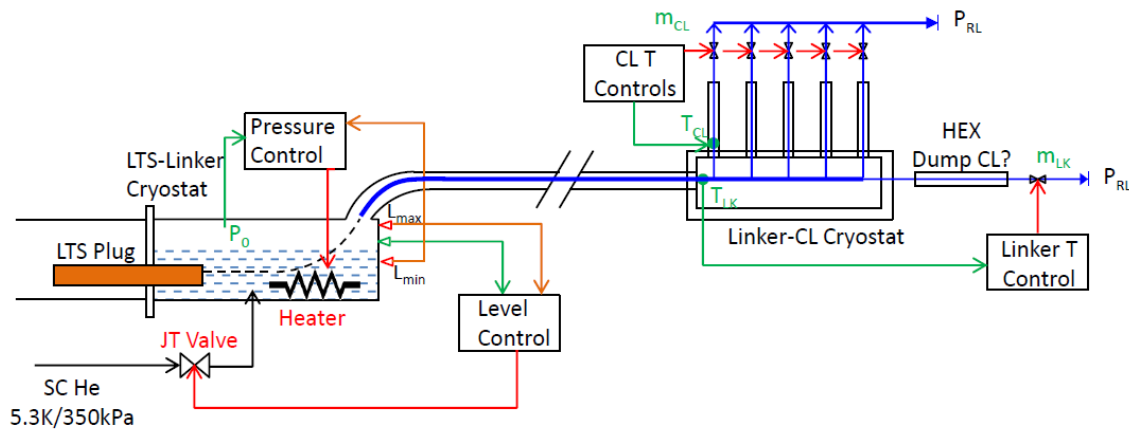


Figure 10-10: Cooling scheme of the cold powering system. Lefthand side: low temperature (LT) side, where there are the connections with the SC magnet cable. Righthand side: connection with the current leads (CL).

The links in P1 and P5 consist of a multi-cable assembly as shown in Figure 10-11(a). Its model as implemented in the FLUKA geometry is also shown in Figure 10-11(c).

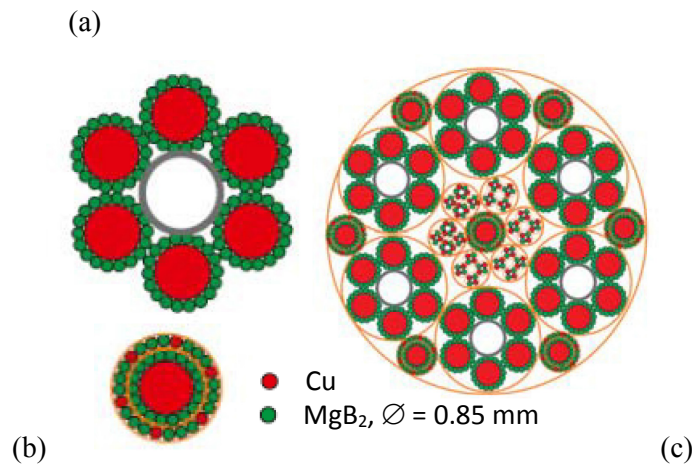


Figure 10-11: (a) 20 kA  $\text{MgB}_2$  cable,  $\varnothing = 19.5$  mm, two  $\text{MgB}_2$  concentric cables for 3 kA total current,  $\varnothing = 8.2$  mm. (b) 150 kA cable assembly for LHC P1 and P5 ( $6 \times 20$  kA,  $7 \times 3$  kA,  $4 \times 0.4$  kA,  $20 \times 0.12$  kA),  $\varnothing = 65$  mm. (c) The FLUKA model of the cable.

The calculated dose maps for the horizontal and vertical routing of the SC link inside the shuffling module in P1 are shown in Figure 10-12. The obtained values (up to about 1 MGy) are not expected to affect the link operation (provided that the chosen insulator is radiation resistant). The maximum DPA induced in the links is of the order of  $10^{-6}$ . Preliminary simulations for P5 indicate the same outcome as for P1.

The modelling of the cable in P7 is in progress; so, as a first approximation, the same cable as in P1 and P5 has been used in order to evaluate its level of exposure to radiation. In this case, the latter is originated by beam losses in the collimators, from which energetic particle showers develop. The link routing has been implemented at about 1 m above the beam. The hottest region is downstream of the primary collimators, close to the passive absorber that shields the warm dipoles. Assuming that the ratio between yearly losses in the collimators and accumulated luminosity does not get significantly worse than what was achieved with the present machine, the resulting maximum dose and DPA are again not of concern for the Link operation and long-term integrity.

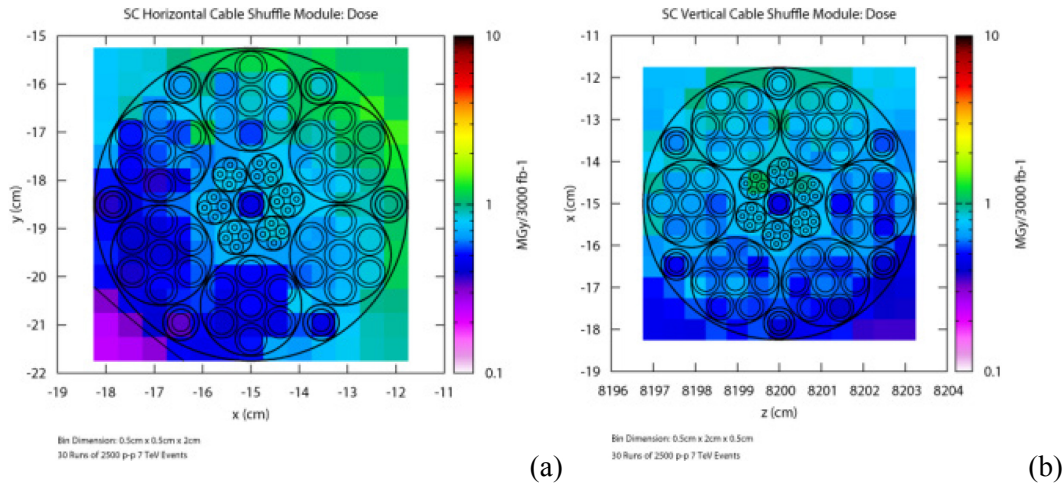


Figure 10-12: Maps of dose released in the SC Link in the P1 shuffling module. (a) Superconducting horizontal cable shuffle module dose; (b) Superconducting vertical cable shuffle module dose. Values (in MGy) are normalized to 3000 fb<sup>-1</sup>.

## 10.6 Radiation To Electronics

A specific problem is represented by the electronics' sensitivity to radiation. The above described particle debris emerging from the IP, together with the additional loss contribution from beam-gas interactions, will impact equipment present in the areas adjacent to the LHC tunnel (UJs, RRs). Installed (present or future) control systems are either fully commercial or based on COTS components, both possibly affected by radiation. This includes the immediate risk of SEE and a possible direct impact on beam operation, as well as in the long-term cumulative dose effects (impacting the component/system lifetime) that additionally have to be considered.

For the tunnel equipment in the existing LHC, radiation was only partially taken into account as a design criteria prior to construction, and most of the equipment placed in adjacent and partly shielded areas was not conceived nor tested for their actual radiation environment. Therefore, given the large amount of electronics being installed in these areas, during the past years a CERN-wide project called Radiation To Electronics (R2E) [15] has been initiated to quantify the danger of radiation-induced failures and to mitigate the risk for nominal beams and beyond to below one failure per week. The respective mitigation process included a detailed analysis of the radiation fields involved, intensities and related Monte Carlo calculations; radiation monitoring and benchmarking; the behaviour of commercial equipment/systems and their use in the LHC radiation fields; as well as radiation tests with dedicated test areas and facilities [15, 16].

In parallel, radiation-induced failures were analyzed in detail in order to confirm early predictions of failure rates, as well as to study the effectiveness of implemented mitigation measures. Figure 10-13 shows the actual number of SEE failures measured during 2011 and 2012 operations, the achieved improvement (please note that the failure rate measured during 2011 already benefitted from mitigation measures implemented during 2009 and 2010), as well as the goal for operation after LS1 and during the HL-LHC era.

Aiming for annual luminosities of up to 300 fb<sup>-1</sup>, it is clear that machine availability has to be maximized during the HL-LHC period in order to successfully achieve the physics goal. This implies that existing electronics control systems are either installed in fully safe areas, sufficiently protected by shielding, or are made adequately radiation tolerant.

The last statement implies that existing equipment, as well as any future equipment that may be installed in R2E critical areas, must be conceived in a specific way.

Radiation damage to electronics is often considered in space applications. However, it is important to note that the radiation environment encountered at the LHC, the high number of electronics systems and

components partly exposed to radiation, as well as the actual impact of radiation-induced failures, differ strongly from the context of space applications. While for the latter application design, test, and monitoring standards are already well defined, additional constraints, but in some cases also simplifications, have to be considered for the accelerator environment.

The mixed particle type and energy field encountered in the relevant LHC areas is composed of charged and neutral hadrons (protons, pions, kaons, and neutrons), photons, electrons, and muons ranging from thermal energies up to the GeV range. This complex field has been extensively simulated by the FLUKA Monte Carlo code and benchmarked in detail for radiation damage issues at the LHC [17, 18]. As discussed above, the observed radiation is due to particles generated by proton–proton (or ion–ion) collisions in the LHC experimental areas, distributed beam losses (protons, ions) around the machine, and to beam interacting with the residual gas inside the beam pipe. The proportion of the different particle species in the field depends on the distance and on the angle with respect to the original loss point, as well as on the amount (if any) of installed shielding material. In this environment, electronics components and systems exposed to a mixed radiation field will experience three different types of radiation damage: displacement damage, damage from the TID, and SEEs. The latter range from single or multiple bit upsets (SEUs or MBUs), transients (SETs) up to possible destructive latch-ups (SEIs), destructive gate ruptures, or burn-outs (SEGRs and SEBs).

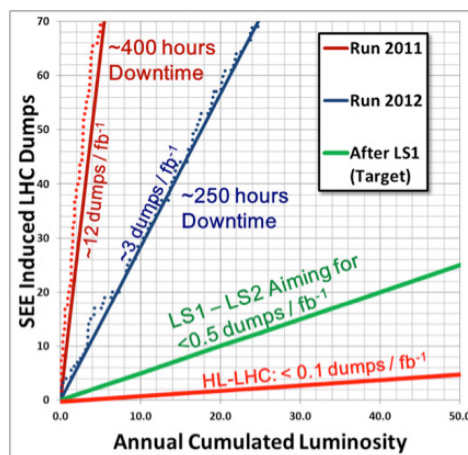


Figure 10-13: LHC beam dumps due to single-event effects against beam luminosity. Dots (2011 and 2012) refer to measurements, whereas lines show annual averages for both past and future operations.

The first two groups are of cumulative nature and are measured through TID and non-ionizing energy deposition (non-ionizing energy losses (NIEL), generally quantified through accumulated 1 MeV neutron equivalent fluence), where the steady accumulation of defects causes measurable effects that can ultimately lead to device failure. As for stochastic SEE failures, they form an entirely different group, since they are due to direct ionization by a single particle, and are able to deposit sufficient energy through ionization processes to perturb the operation of the device. They can only be characterized in terms of their probability of occurring as a function of accumulated high energy (>5–20 MeV) hadron (HEH) fluence. The probability of failure will strongly depend on the device as well as on the flux and nature of the particles. In the context of the HL-LHC, several tunnel areas close to the LHC tunnel, and partly not sufficiently shielded, are or are supposed to be equipped with commercial or not specifically designed electronics that are mostly affected by the risk of SEEs, whereas electronics installed in the LHC tunnel will also suffer from accumulated damage in the long term [19].

Three distinct areas are to be distinguished.

- The accelerator between the inner triplet and Q6: in this area no active electronics is installed and any future installation should clearly be avoided as radiation levels clearly exceed the usability domain of commercial components and also pose significant constraints to custom designs, including application specific integrated circuits (ASICs).

- The adjacent (shielded) areas: where the shielding has been maximized before and during LS1 and where radiation levels become acceptable for characterized and qualified custom electronics. The equipment and selected electronics components have to be qualified for both SEEs and TID. For the first, it is important that radiation tests are carried out in a representative radiation environment, or adequate safety margins have to be added. Fully commercial systems (COTS based) are still to be avoided in these areas. In case they are required, their failure impact and respective mitigation has to be studied in the context of accelerator operation.
- The dispersion suppressor area: given the fact that the magnets have to be protected against quenches, it is likely that the leakage into this area must not increase significantly with respect to nominal LHC operation. A detailed quantification is, however, needed to coherently design the required control electronics, again both for SEE effects as well as for their lifetime (TID) to comply with the stringent availability requirement, as shown in Figure 10-13.

During the first years of LHC operation, the radiation levels in the LHC tunnel and in the (partly) shielded areas have been measured using the CERN RadMon system [20], which is dedicated to the analysis of radiation levels possibly impacting installed electronics equipment. Table 10-1 summarizes the level of accumulated HEH fluence measured during 2012 for the most critical LHC areas where electronics equipment is installed and that are relevant for the HL-LHC project, together with the expected annual radiation levels for nominal LHC performance ( $50 \text{ fb}^{-1}/\text{y}$ ). The HEH fluence measurements are based on the RadMon reading of the SEUs of SRAM memories whose sensitivity has been extensively calibrated in various facilities [21]. The results obtained during 2012 LHC proton operation show that the measurements compare very well with previously performed FLUKA calculations, and that observed differences can actually be attributed to changes of operational parameters not considered in the calculations [22]. In a first approximation, the measured radiation levels can also be used to extrapolate towards the HL-LHC by purely scaling with annual luminosity (see the last two columns of Table 10-1); however, keeping in mind that operational and layout parameters (beam energy, crossing angle, TAN design, absorbers, etc.) can have a non-negligible impact on the final values, especially for the RRs close to the matching section. The resulting values clearly indicate that any equipment installed in the LHC tunnel will not only suffer SEE failures, but will also be heavily impacted by TID effects, thus limiting the equipment's lifetime.

Table 10-1: Predicted and measured annual HEH fluence in critical shielded areas for a cumulated ATLAS/CMS luminosity of  $15 \text{ fb}^{-1}$  during 2012 operations, then extrapolated based on the measurement to the expected nominal and HL-LHC performance ( $50 \text{ fb}^{-1}/\text{y}$  for nominal and  $300 \text{ fb}^{-1}/\text{y}$  for HL-LHC performance, except for P8 where 2012 can already be considered as almost nominal and HL-LHC refers to a five-fold increase). For the HL-LHC an estimate for corresponding annual TID levels is also given.

LHC area	Prediction (HEH/cm <sup>2</sup> )	Measured (HEH/cm <sup>2</sup> )	Nominal (HEH/cm <sup>2</sup> )	HL-LHC (HEH/cm <sup>2</sup> )	HL-LHC (Dose/Gy)
UJ14/16	$1.4 \times 10^8$	$1.6 \times 10^8$	$5 \times 10^8$	$3 \times 10^9$	6
RR13/17	$2.0 \times 10^8$	$2.5 \times 10^8$	$8 \times 10^8$	$5 \times 10^9$	10
UJ56	$1.6 \times 10^8$	$1.5 \times 10^8$	$5 \times 10^8$	$3 \times 10^9$	6
RR53/57	$2.0 \times 10^8$	$2.5 \times 10^8$	$8 \times 10^8$	$5 \times 10^9$	10
UJ76	$2.1 \times 10^7$	$6.0 \times 10^7$	$2 \times 10^8$	$1 \times 10^9$	2
RR73/77	$2.9 \times 10^7$	$5.0 \times 10^7$	$2 \times 10^8$	$1 \times 10^9$	2
UX85B	$4.3 \times 10^8$	$3.5 \times 10^8$	$4 \times 10^8$	$2 \times 10^9$	4
US85	$1.3 \times 10^8$	$8.8 \times 10^7$	$9 \times 10^7$	$4 \times 10^8$	1

A first calculation aimed to assess the radiation levels in the UJ/UL/UP areas close the new IT during HL-LHC operation was carried out, implementing the dedicated shielding presently in place. Figure 10-14

shows the expected annual HEH fluence, which confirms the order of magnitude of the respective extrapolation reported in the first row of Table 10-1.

Concerning the radiation in the RR area adjacent to the matching section, HL-LHC simulations are at this stage still premature due to the unknowns regarding optics and layout. Nevertheless, specific studies were performed for the present LHC, evaluating the contribution of the relevant source terms, which in this case include both the collision debris and the beam interactions with the residual gas, as shown in Figure 10-15. A significant effect in increasing the fluence levels – to be re-evaluated for the HL-LHC machine – is played here by the TCL6 collimator, due to its position.

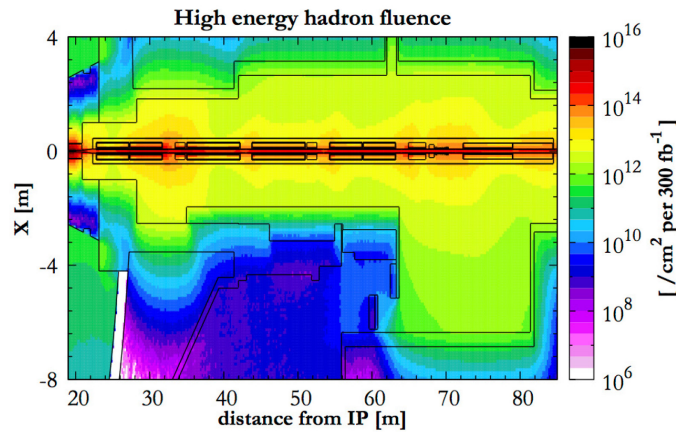


Figure 10-14: Annual HEH fluence expected in the IT region and in the adjacent UJ/UL/UP areas at P1 during the HL-LHC era (normalized to 300 fb<sup>-1</sup>).

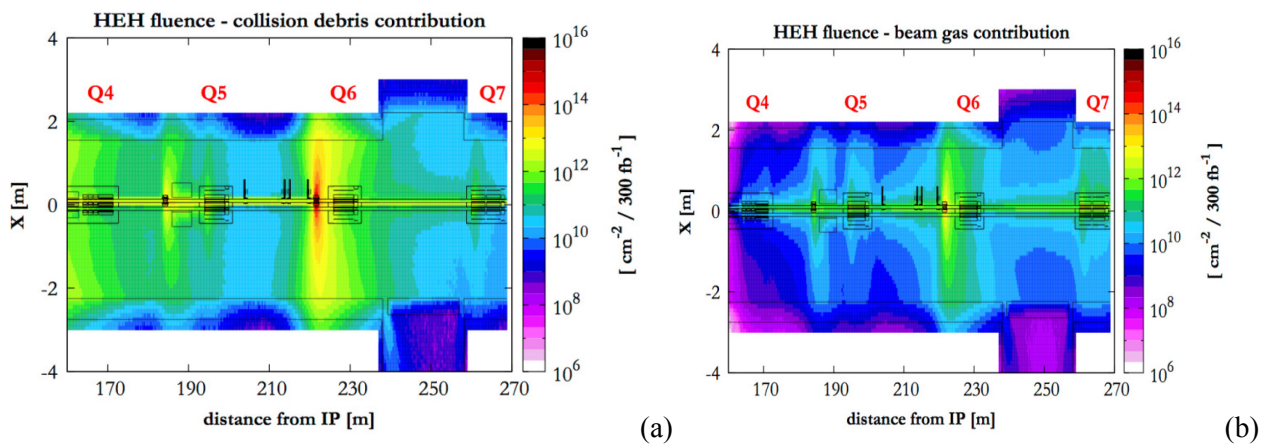


Figure 10-15: Cumulated HEH fluence expected in the matching section region and in the adjacent RR area at P5 for the operation of the present LHC at 7 TeV beam energy. (a) Contribution from the collision debris normalized to 300 fb<sup>-1</sup>. (b) Contribution from interactions of the outgoing beam (Beam 1) with the residual gas, normalized to nominal current over  $3 \times 10^7$  s (i.e. the time needed to accumulate 300 fb<sup>-1</sup> at nominal luminosity) and to a gas density of  $10^{15}$  H<sub>2</sub>-equivalent molecules/m<sup>3</sup>. TCL collimator settings: 15  $\sigma$  (TCL4), 35  $\sigma$  (TCL5), 10  $\sigma$  (TCL6).

Any control equipment (commercial or based on commercial components) to be installed in these areas clearly has to be proven to be sufficiently radiation tolerant. For comparison, as mentioned earlier, during the last years of operation we have already observed a number of radiation-induced failures of commercial equipment at radiation levels corresponding to  $10^8$ – $10^9$  cm<sup>-2</sup>/y (which is about 1 000–10 000 times more than what one would get at the surface due to cosmic radiation).

The analysis of the performed radiation tests, as well as the experience acquired during LHC Run 1 operation allowed the deduction of an acceptable limit of  $10^7 \text{ cm}^{-2} \text{ y}^{-1}$  annual radiation level, leading to the definition of so-called protected areas (in terms of overall risk of radiation-induced failures). Therefore, for the HL-LHC any installation of non-tested (and not specifically designed) electronics equipment in the UJs, part of the ULs, and RRs is clearly to be avoided or subjected to a detailed analysis process before an exceptional installation can be granted under the following conditions:

- the equipment is not linked to any safety system;
- the failure of the equipment will not lead to a beam dump;
- the failure of the equipment does not require quick access (thus lead to downtime);
- there is no any other operational impact (loss of important data, etc.).

In all other cases requiring installation in critical areas, a respective radiation-tolerant electronics development must be considered from a very early stage onward. Related expertise exists at CERN within the equipment groups, the R2E project, and a dedicated working group [23].

In a first approximation and limiting the total number of exposed systems, the above-mentioned annual radiation design level of  $10^7 \text{ cm}^{-2} \text{ y}^{-1}$  can also be chosen as acceptable, aiming to achieve an overall performance of less than one radiation-induced failure per one or two weeks of HL-LHC operation.

For operation critical equipment, the HL-LHC project already foresees radiation-tolerant developments at an early stage of the design phase, taking into account that:

- for the LHC-tunnel: in addition to SEEs cumulative damage also has to be considered for both existing and future equipment;
- for partly shielded areas (UJs, RRs, ULs): cumulative damage should be carefully analyzed but can most likely be mitigated by preventive maintenance (detailed monitoring mandatory); however, radiation-tolerant design is mandatory in order to limit SEE-induced failures;
- the knowledge of radiation-induced failures and radiation-tolerant development within the equipment groups and in the overall accelerator and technology sector has to be maintained and further strengthened;
- the access and availability of radiation test facilities (both inside CERN and outside) has to be ensured, providing efficient support to equipment groups;
- building on the experience obtained during the LHC R2E project and in view of the HL-LHC time-scale, it is important that the expertise of and support to radiation-tolerant developments (currently available through the Radiation Working Group [23]) are maintained and ensured from the early project stages onwards.

## 10.7 References

- [1] L.S. Esposito *et al.*, Power load from collision debris on the LHC Point 8 insertion magnets implied by the LHCb luminosity increase, IPAC2013, C130512 (2013), TUPFI022, p. 1382.
- [2] N.V. Mokhov and I.L. Rakhno, Mitigating radiation loads in Nb<sub>3</sub>Sn quadrupoles for the CERN Large Hadron Collider upgrades, *Phys. Rev. ST Accel. Beams* **9** (2006) 101001.
- [3] L.S. Esposito, F. Cerutti and E. Todesco, Fluka Energy Deposition Studies for the HL LHC, Conf. Proc. C130512 (2013) pp.TUPFI021, p. 1379.
- [4] G. Battistoni *et al.*, The FLUKA code: Description and benchmarking, AIP Conf. Proc. 896 (2007) 31–49.
- [5] A. Ferrari *et al.*, FLUKA: A multi-particle transport code (Program version 2005), CERN-2005-010. <http://www.fluka.org>

- [6] V. Vlachoudis, FLAIR: A powerful but user friendly graphical interface for FLUKA, Proc. Int. Conf. Mathematics, Computational Methods & Reactor Physics, Saratoga Springs, New York (2009) on CD-ROM, American Nuclear Society, LaGrange Park, IL (2009) 1-11.
- [7] A. Mereghetti *et al.*, The FLUKA LineBuilder and Element DataBase: Tools for Building Complex Models of Accelerator Beam Lines, IPAC2012, Conf. Proc. C1205201 (2012), WEPPD071, p. 2687.
- [8] N.V. Mokhov and C. James, The MARS Code System User's Guide. <http://www-ap.fnal.gov/MARS>
- [9] N.V. Mokhov and S.I. Striganov, MARS15 Overview, Proc. of Hadronic Shower Simulation Workshop, Fermilab, AIP Conf. Proc. **896** (2007) pp. 50–60.
- [10] N.V. Mokhov *et al.*, MARS15 code developments driven by the intensity frontier needs, *Prog. Nucl. Sci. Tech.* **4** (2014) 496–501.
- [11] N.V. Mokhov *et al.*, Protecting LHC IP1/IP5 components against radiation resulting from colliding beam interactions, CERN-LHC-Project-Report-633 17 Apr 2003. - 56 p..
- [12] L.S. Esposito and F. Cerutti, FLUKA simulations of collision debris with TCL6, presentation at LHC Collimation Working Group #163.  
<http://indico.cern.ch/event/267815/contribution/1/material/slides/0.pdf>
- [13] A. Ballarino, Development of superconducting links for the LHC machine, EEE/CSC & ESAS Superconductivity News Forum (global edition), October 2013.
- [14] A. Ballarino, Preliminary report on cooling options for the cold powering system, June 2013.  
<http://cds.cern.ch/record/1557215/files/CERN-ACC-2013-010.pdf>
- [15] R2E website, [www.cern.ch/r2e](http://www.cern.ch/r2e)
- [16] M. Brugger *et al.*, R2E Experience and outlook for 2012, Proc. LHC Performance workshop, Chamonix 2012.
- [17] K. Roed *et al.*, FLUKA simulations for SEE studies of critical LHC underground areas, *IEEE Trans. Nucl. Sci.* **58**, (2011) 932.
- [18] M. Brugger *et al.*, FLUKA capabilities and CERN applications for the study of radiation damage to electronics at high-energy hadron accelerators, *Prog. Nucl. Sci. Tech.* (2010) PNST10184-R1.
- [19] K. Roed, M. Brugger and G. Spiezia, An overview of the radiation environment at the LHC in light of R2E irradiation test activities, CERN publication, CERN-ATS-Note-2011-077 TECH (2011).
- [20] G. Spiezia *et al.*, The LHC accelerator Radiation Monitoring System – RadMON, *Proc. Science*, 2011, (RD11) 024.
- [21] D. Kramer *et al.*, LHC RadMon SRAM detectors used at different voltages to determine the thermal neutron to high energy hadron fluence ratio, *IEEE Trans. Nucl. Sci.* **58**, (2011) 1117.
- [22] G. Spiezia *et al.*, R2E Experience and Outlook, LHC Beam Operation Workshop, Evian, (2012).
- [23] CERN Radiation Working Group (RadWG), [www.cern.ch/radwg](http://www.cern.ch/radwg)



# Chapter 11

## 11 T Dipole for the Dispersion Suppressor Collimators

*M. Karppinen<sup>1</sup>, S. Izquierdo Bermudez<sup>1</sup>, A. Nobrega<sup>2</sup>, H. Prin<sup>1</sup>, D. Ramos<sup>1</sup>, S. Redaelli<sup>1</sup>, F. Savary<sup>1\*</sup>, D. Smekens<sup>1</sup> and A. Zlobin<sup>2</sup>*

<sup>1</sup>CERN, Accelerator & Technology Sector, Geneva, Switzerland

<sup>2</sup>FNAL, Fermi National Accelerator Laboratory, Batavia, USA

### 11 11 T dipole for the dispersion suppressor collimators

#### 11.1 Introduction

A pair of 11 T dipoles will replace some of the main dipoles (MB) in the dispersion suppressor (DS) regions of the LHC to create space for additional collimators, which are necessary to cope with beam intensities that are larger than nominal, such as in the High Luminosity LHC (HL-LHC) project [1].

A joint research and development (R&D) programme was initiated in October 2010 at the Fermi National Laboratory (FNAL) in the US, and in the middle of 2011 at CERN, with the goal of developing the necessary technology for the fabrication of a full-length two-in-one aperture Nb<sub>3</sub>Sn dipole prototype suitable for installation in the LHC [2]. After the design, fabrication, and test of a number of short models with a length of 1 m and 2 m, FNAL is now slowing down development, while CERN is gradually ramping up with the fabrication of 2 m long models and the preparation of the tooling for full-length prototypes. The design of the 11 T dipole described in this preliminary design report features the solutions developed in the framework of the CERN programme. Except for the pole loading concept, for the cable insulation scheme and for features specific to full-length magnets, the solutions used at CERN are largely based on the results of the R&D programme conducted at FNAL.

#### 11.2 The cryo-assembly

##### 11.2.1 Description

An MB cryo-assembly will be replaced with a string of three independently installed and aligned cryo-assemblies: two of these will each house a 6.252 m long 11 T dipole, referred to below as the MBH, with a bypass cryostat installed between them. The bypass cryostat ensures the continuity of the cryogenic and electrical circuits and comprises cold to warm transitions on the beam lines in order to create a room temperature vacuum sector for the collimator.

Figure 11-1 shows a schematic layout of the string of cryostats composing the 11 T cryo-assembly, which will replace an MB cryostat.

The cryostat for the MBH shall follow the same design and fabrication principles as the other arc cryostats; it shall comply with the static heat loads specified by the Heat Load Working Group [3]. Standard LHC cryostat performance in terms of alignment tolerances and geometrical stability shall be ensured.

---

\* Corresponding author: [Frederic.Savary@cern.ch](mailto:Frederic.Savary@cern.ch)

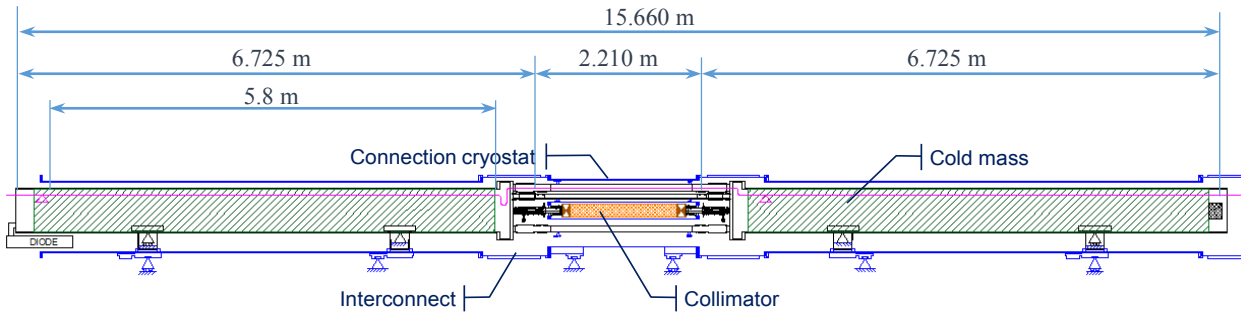


Figure 11-1: Longitudinal section of the 11 T cryo-assembly showing the collimator and the cold-to-warm transitions.

The design of the bypass cryostat shall be compatible with the integration of the collimator and also with the RF-shielded gate valves at the extremity of the cold-to-warm transitions. All cryogenic lines and powering busbars shall have their continuity ensured across the bypass cryostat.

In the present concept, independent installation and alignment of the three cryostats is foreseen. In addition, the TCLD collimator shall be supported directly by the tunnel floor so as not to be affected by deformations of the cryostat vacuum vessels due to alignment or pressure-induced forces.

### 11.2.2 Equipment parameters

The main parameters of the 11 T cryo-assembly are given in Table 11-1. The lengths are, for the present, provisional and may vary depending on the detail design of the MBH and on the details of collimator integration. The dimensions of the cryogenic pipes are equivalent to those of a standard LHC arc continuous cryostat.

Table 11-1: Main parameters of the 11 T cryo-assembly

Characteristics	Unit	Value
Total length including interconnects	[mm]	15 660
Upstream cryostat length between interconnect planes	[mm]	6 725
Downstream cryostat length between interconnect planes	[mm]	6 725
Bypass cryostat length between interconnect planes	[mm]	2 210
Beam line cold bore diameter (inner)	[mm]	50
Length of room temperature beam vacuum sector measured between cold-to-warm transition flanges	[mm]	1 550

The preliminary design of the 11 T cryo-assembly is based on the following assumptions.

- The interface between the cold beam lines of the MBH cryostats and the beam vacuum sector of the collimator requires sectorization by RF-shielded gate valves.
- As opposed to other collimators in the machine, residual radiation to personnel is assumed to be compatible with the removal and installation of the TCLD collimator without remote handling equipment. Given the integration constraints in the LHC dispersion suppressors, the design of a collimator compatible with remote handling is most likely not achievable.
- Radiation doses on the cryostat throughout the HL-LHC lifetime are compatible with the usage of LHC standard cryostat materials.
- Magnetic shielding is not required on the bypass cryostat. It is assumed that the magnetic field created by the busbar currents will not be detrimental to the accuracy of the TCLD instrumentation and controls.

### 11.3 The 11 T dipole

The design of the MBH is based on the two-in-one concept, i.e. the cold mass comprises two apertures in a common yoke and shell assembly. The MBH cold mass assembly has a length of 6.252 m between the datum planes C and L that are shown on the end covers, see Figure 11-2. The coils have a length of 5.415 m without the outermost end spacers (called saddles), and 5.573 m with the saddles, see Figure 11-3. A pair of MBHs is needed to produce an integrated field of 119 T m at 11.85 kA, which corresponds to the bending strength of the MB. The MBHs need to be compatible with the LHC lattice and its main systems. They will be connected

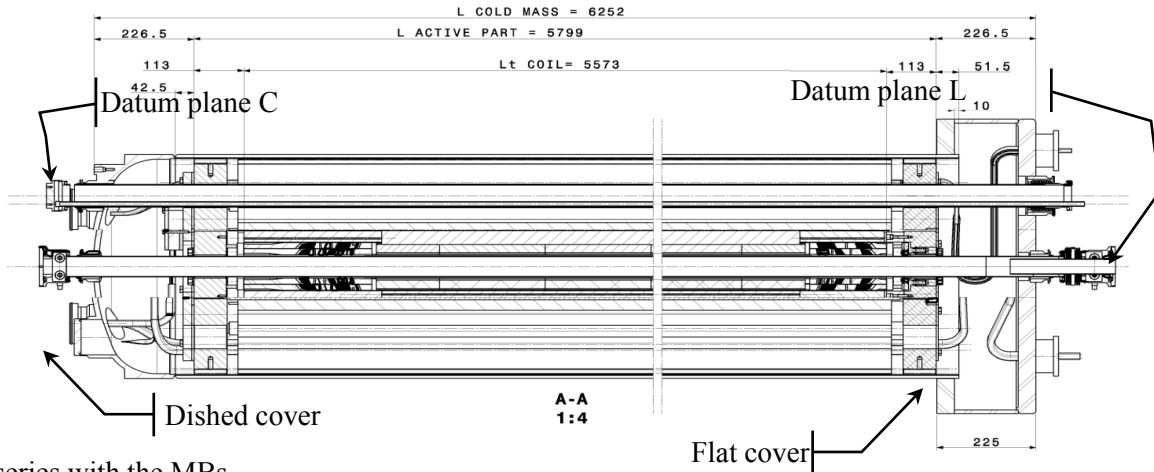


Figure 11-2: Longitudinal section of the cold mass assembly of the MBH

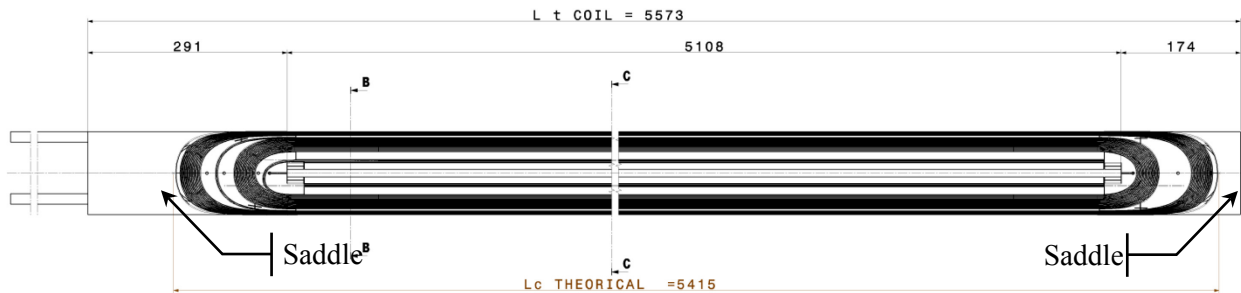


Figure 11-3: Longitudinal section of the coil

#### 11.3.1 Description

The coils of the MBH are made of two layers and six blocks with Nb<sub>3</sub>Sn keystone Rutherford-type cable as shown in Figure 11-4. Each coil comprises 56 turns, with 22 in the inner layer and 34 in the outer layer. There is no splice at the layer jump, i.e. the two layers are wound from the same cable unit length. The cable is made of 40 strands of 0.7 mm diameter. Two manufacturing routes are considered for the strand: the restacked rod (RRP) process and the powder-in-tube (PIT) process.

The mechanical structure comprises separate austenitic steel collars for each aperture to balance the electromagnetic forces, and a vertically split iron yoke surrounded by a welded stainless steel shrinking cylinder, which contributes to the overall rigidity of the assembly. The axial component of the electromagnetic forces is also transferred to the shrinking cylinder via thick end plates, which are welded to it, and bolts in contact with the saddles. The bolts are screwed into the end plates. The cold mass envelope is closed at the ends by a dished cover on the side of the assembly facing the existing MBs and by a flat cover of a larger diameter on the side of the assembly facing the collimator, see Figure 11-1. A larger diameter is needed on that side to allow the routing of the busbars across the bypass cryostat within the limits of the radial and longitudinal space available.

A cross-section through the MBH is shown in Figure 11-4, without the busbars, heat exchanger tube, support pads, and line N. The key parts of the collared coil are also shown in Figure 11-4.

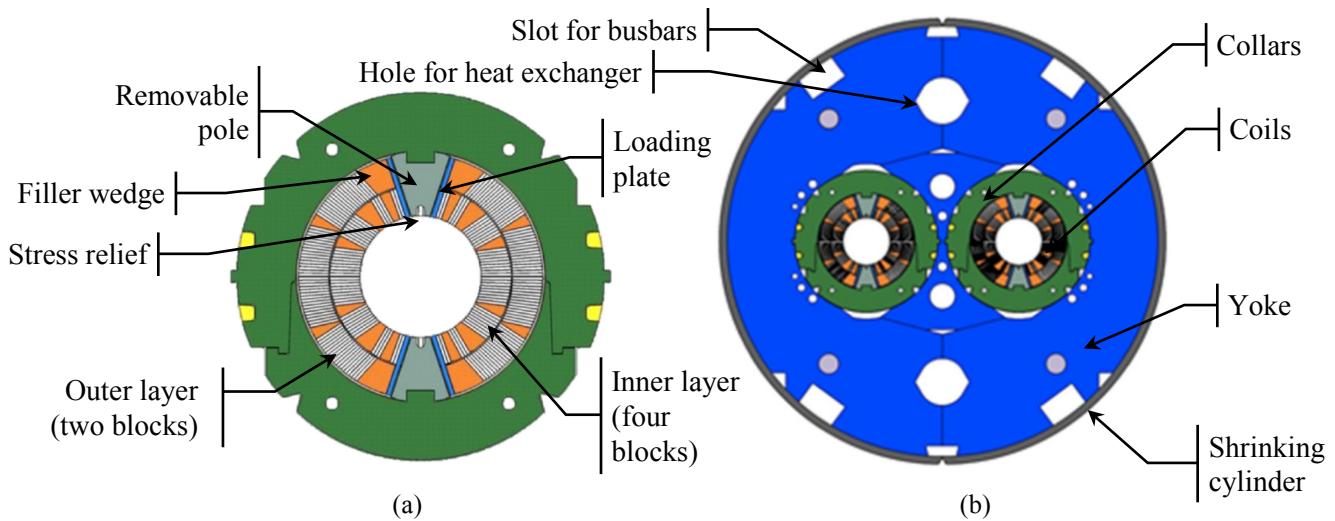


Figure 11-4: Cross-section through (a) the 11 T dipole collared coil; (b) cold mass assembly

To avoid deformation of the beam closed orbit, the integrated transfer function of a pair of MBHs shall be identical to that of the MB. However, this is not possible across the entire range of current during ramping up to nominal, as shown in Figure 11-5. The design is such that a pair of MBHs provides the same integrated field of 119 T m as a standard MB at the nominal current of 11.85 kA.

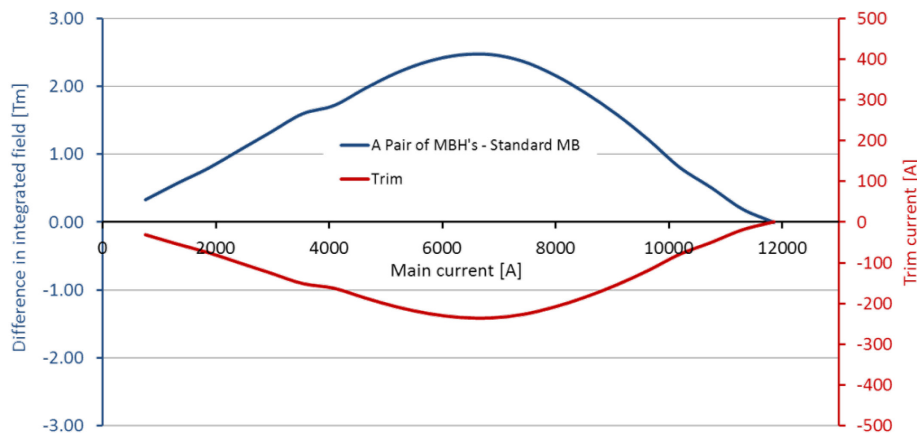


Figure 11-5: The blue line shows the difference in integrated field between a pair of MBHs and an MB, both delivering 119 T m at 11.85 kA. The red line shows the trim current needed to correct the difference at currents below 11.85 kA.

The MBH is stronger at lower currents (it has more turns) with a peak difference in integrated field around 6.5 kA. This can be mitigated by adding a dedicated trim power converter. In the absence of trim current, the resulting orbit distortion could be mitigated by means of the standard orbit correctors in the LHC lattice. However, a fully validated solution including machine protection, reliability, and availability is not currently available (for example, the operation of LHC would be compromised in the case of failure of an orbit corrector). The correction of the transfer function with a trim current is the preferred option as it would allow simpler and more transparent operation.

Unlike the MB, which is curved in the horizontal plane, the MBH will be straight because of the brittleness of Nb<sub>3</sub>Sn after reaction. Also, it will be equipped with the same cold bore tube and beam screen as the present curved MB, to facilitate integration. To mitigate for the corresponding reduction of mechanical

aperture, the two MBHs of a cryo-assembly will be assembled with an angle of 2.55 mrad relative to each other, and shifted by 0.8 mm towards the centre of the machine.

Depending on the location, the MB to be replaced may be of type A or type B, i.e. it will have both a magnet corrector sextupole (MCS) on the lyre side (i.e. downstream), and a nested magnet corrector decapole/octupole (MCDO) on the connection side (i.e. upstream), respectively, or only an MCS on the lyre side. The MBH, which is on the righthand side of the collimator for an observer looking at the machine from its centre, will have only an MCS on the lyre side. In the current stage of the project, it is also planned to install an MCDO on the connection side of the MBH that is installed on the lefthand side of the collimator. The MCDO may be connected, or not, depending on the installation location of the cryo-assembly.

### 11.3.2 Equipment parameters

A pair of MBHs will provide an integrated field of 119 T m at the nominal operation current of the MBs, 11.85 kA. This corresponds to a nominal magnetic flux density of 11.23 T at the centre of the bore. This goal shall be obtained with a margin of ~20% on the magnet load line [4].

The geometric field quality will be optimized to keep the low-order field errors below 1 unit. The different contributions to the field errors are given in Table 11-2. These include the contributions of the coil ends, cryostat, persistent currents, and eddy currents effects. The field errors shall be confirmed by magnetic measurements. The main parameters of the MBH are listed in Table 11-3.

Table 11-2: Field errors -  $R_{ref}=17$  mm

	Systematic					Uncertainty		Random	
Normal	Geometric	Saturation	Persistent	Injection	High field	Injection	High field	Injection	High field
2	0.000	-12.200	1.010	1.010	-12.200	1.930	1.930	1.9300	1.930
3	7.459	-0.279	-1.299	6.160	7.180	1.240	1.240	1.2400	1.240
4	0.000	-0.400	0.070	0.070	-0.400	0.600	0.600	0.6000	0.600
5	-0.014	0.514	6.594	6.580	0.500	0.310	0.310	0.3100	0.310
6	0.000	-0.020	0.000	0.000	-0.020	0.180	0.180	0.1800	0.180
7	-0.093	0.062	-0.688	-0.780	-0.030	0.110	0.110	0.1100	0.110
8	0.000	0.000	0.000	0.000	0.000	0.060	0.060	0.0600	0.060
9	0.912	0.028	1.024	1.936	0.940	0.030	0.030	0.0300	0.030
10	0.000	0.000	0.000	0.000	0.000	0.010	0.010	0.0100	0.010
11	0.450	0.000	-0.090	0.360	0.450	0.010	0.010	0.0100	0.010
12	0.000	0.000	0.000	0.000	0.000	0.000	0.000	0.000	0.000
13	-0.115	-0.006	-0.028	-0.143	-0.121	0.000	0.000	0.000	0.000
14	0.000	0.000	0.000	0.000	0.000	0.000	0.000	0.000	0.000
15	-0.032	-0.002	-0.008	-0.040	-0.034	0.000	0.000	0.000	0.000

	Systematic					Uncertainty		Random	
Skew	Geometric	Saturation	Persistent	Injection	High field	Injection	High field	Injection	High field
2	0.000	-0.261	0.000	0.000	-0.261	1.660	1.660	1.660	1.660
3	-0.130	0.050	0.000	-0.130	-0.080	1.000	1.000	1.000	1.000
4	0.000	-0.010	0.000	0.000	-0.010	0.640	0.640	0.640	0.640
5	0.080	0.000	0.000	0.080	0.080	0.380	0.380	0.380	0.380
6	0.000	0.000	0.000	0.000	0.000	0.200	0.200	0.200	0.200
7	0.030	0.000	0.000	0.030	0.030	0.090	0.090	0.090	0.090
8	0.000	0.000	0.000	0.000	0.000	0.050	0.050	0.050	0.050
9	0.000	0.000	0.000	0.000	0.000	0.030	0.030	0.030	0.030
10	0.000	0.000	0.000	0.000	0.000	0.020	0.020	0.020	0.020
11	0.000	0.000	0.000	0.000	0.000	0.010	0.010	0.010	0.010
12	0.000	0.000	0.000	0.000	0.000	0.000	0.000	0.000	0.000
13	0.000	0.000	0.000	0.000	0.000	0.000	0.000	0.000	0.000
14	0.000	0.000	0.000	0.000	0.000	0.000	0.000	0.000	0.000
15	0.000	0.000	0.000	0.000	0.000	0.000	0.000	0.000	0.000

Table 11-3: Main parameters of the MBH

Characteristics	Unit	Value
Aperture	[mm]	60
Number of apertures	-	2
Distance between apertures at room temperature/1.9 K	[mm]	194.52/194.00
Cold mass outer diameter	[mm]	580
Magnetic length	[m]	5.307
Coil physical length, as per magnetic design	[m]	5.415
Magnet physical length: active part (between the end plates)	[m]	5.799
Magnet physical length: cold mass (between datum planes C and L)	[m]	6.252
Cold mass weight	[tonne]	~8
Nominal operation current	[kA]	11.85
Bore field at nominal current	[T]	11.23
Peak field at nominal current (without strand self-field correction)	[T]	11.59
Operating temperature	[K]	1.9
Load line margin	(%)	19
Stored energy/m at $I_{nom}$	[MJ/m]	0.9663
Differential inductance/m at $I_{nom}$	[mH/m]	11.97
Number of layers	-	2
Number of turns (inner/outer layer)	-	56 (22/34)
Superconductor	-	Nb <sub>3</sub> Sn
Cable bare width before reaction	[mm]	14.7
Cable bare mid-thickness before reaction	[mm]	1.25
Keystone angle	[degree]	0.79
Cable unit length for the two layers (no layer jump splice)	[m]	~600
Strand diameter	[mm]	0.700 ± 0.003
Number of strands per cable	-	40
Cu to non-Cu ratio	-	1.15 ± 0.10
RRR, after reaction	-	>100
Minimum strand critical current, $I_c$ , without self-field correction (12 T, 4.222 K)	[A]	438
Minimum strand current density, $J_c$ , at 12 T, 4.222 K	[A/mm <sup>2</sup> ]	2560
Cable insulation thickness per side azimuthal, before/after reaction	[mm]	0.155/0.110
Heat exchanger hole diameter	[mm]	60
Heat exchanger distance from centre (same position as in the MB)	[mm]	180
Cold bore tube inner diameter/thickness (assuming the current CBT is used)	[mm]	50/1.5
Gap CBT to coil (assuming the current CBT and ground insulation are used)	[mm]	3

### 11.3.3 Protection

The MBH will be protected with quench heaters and a bypass diode operating at cold, integrated with the cold mass assembly. At the current stage of development, it is foreseen to use one bypass diode for the two MBHs of a cryo-assembly. However, this needs to be validated.

### 11.3.4 Radiation

The MBH will, inevitably, see a shower of particles from the collimator. The worst case currently is with ion operation at IP2, for which the peak dose in the coils is estimated to be around 1 MGy [5, 6]. The 11 T dipole cold mass will be designed with a reasonable margin, 5 MGy.

### 11.3.5 Installation and dismantling

The cold mass of the MBH will be equipped with standard features in the ends facing the existing MBs in the tunnel to facilitate the installation and connection, e.g. M-flanges and bellows, preparation of the busbar extremities with regard to splicing, end flanges on the X/V lines, etc. The ends facing the collimator need to be specific; however, standard elements will be used as much as possible.

## 11.4 Inventory of units to be installed and spare policy

Two full-length MBH prototypes will be fabricated to validate the design, the overall performance in nominal operation conditions (to be checked on horizontal test benches in building SM18 at CERN), and the different interfaces with the neighbour systems.

The cryo-assemblies to be installed in LHC are listed below.

- For LS2, around IP2, two cryo-assemblies to replace two main dipoles MB.A10L2 and MB.A10R2, i.e. 4 MBHs and two bypass cryostats.
- For LS3, around IP7, four cryo-assemblies to replace four main dipoles MB.B8L7, MB.B10L7, MB.B8R7, and MB.B10R7, i.e. eight MBHs and four bypass cryostats.
- For LS3, to be confirmed, around IP1 and IP5, up to a maximum of eight cryo-assemblies to replace eight main dipoles, location to be defined.

It is planned to fabricate at least two spare MBHs and one spare bypass cryostat. The prototypes may be used as spares, should they conform fully to the functional requirements.

## 11.5 References

- [1] L. Rossi, LHC Upgrade Plans: Options and Strategy, 2nd International Particle Accelerator Conference, San Sebastian, Spain, 4 - 9 Sep 2011, pp.TUYA02.
- [2] F. Savary *et al.*, Status of the 11 T Nb<sub>3</sub>Sn dipole project for the LHC. Applied Superconductivity Conference, USA, 10 – 15 Aug. 2014, DOI 10.1109/TASC.2014.2375914.
- [3] Heat Load Working Group, <http://lhc-mgt-hlwg.web.cern.ch/lhc-mgt-hlwg/default.htm>
- [4] M. Karppinen *et al.*, Design of 11 T twin-aperture Nb<sub>3</sub>Sn dipole demonstrator magnet for LHC upgrades, CERN-ATS-2013-025 (2013).
- [5] A. Lechner, private communication, 28 August 2014.
- [6] G. Steel *et al.*, Limits on collimator settings and reach in  $\beta^*$ , LHC Collimation Review 2013.



# Chapter 12

## Vacuum System

*V. Baglin\*, P. Chiggiato, P. Cruikshank, M. Gallilee, C. Garion and R. Kersevan*

CERN, Accelerator & Technology Sector, Geneva, Switzerland

### 12 Vacuum system

#### 12.1 Overview

The luminosity upgrade programme (HL-LHC) requires modifications of the present LHC's vacuum system, in particular in the triplets and experimental areas. Such modifications must follow guidelines, similar to those followed for the present machine. The increased stored current implies a higher thermal power in the beam screen from the image current moving along with the stored particles and stronger synchrotron radiation (SR) and electron cloud (EC) effects, which in turn translate into higher degassing rates.

One of the main tasks of the vacuum HL-LHC work package is to define the geometry of the vacuum equipment in the new superconducting (SC) triplet and Separation dipole D1 magnets. It is also necessary to define a strategy for assembling and inserting high-density shielding material into the SC IR magnets. This is mandatory for protecting the magnets from collision debris coming from the experiments' interaction points (IPs). A balance between cold bore size and vacuum pumping system will be defined based on experience gained with the present machine and recent advances on new materials. A number of new ideas have recently emerged – for example, the amorphous carbon coating for which validation is ongoing.

The change of the aperture of the triplets at IR1 and IR5 implies that the experimental vacuum chambers of CMS and ATLAS will require a review of aperture, impedance, and vacuum (dynamic and static) values. From preliminary analyses, the forward regions of CMS and ATLAS will need to be adapted to cope with the new beam geometry in IR1 and IR5. New materials will likely be needed to mitigate the additional activation from the increased luminosity. New access procedures will be needed to allow the minimization of the integrated dose to personnel. With the HL-LHC, less flexibility will be available for the optics of LHCb and ALICE; therefore, the vacuum chambers at IR2 and IR8 must be validated for ultimate running conditions to ensure that these chambers do not impose a limitation. Positions of mechanical supports, pumps, and gauges must be analyzed to ensure that layouts are optimized for the new machine configuration. Bake-out equipment will be redefined depending on activation and specific needs. All experimental chambers must be treated with Non-Evaporative Getter (NEG) or equivalent to minimize secondary electron yield (SEY), thus reducing electron cloud effects.

#### 12.2 Beam vacuum requirements

The HL-LHC beam vacuum system must be designed to ensure the required performance when beams with HL-LHC nominal parameters circulate. The system must be designed for HL-LHC ultimate parameters, without a margin.

The vacuum system must be designed to avoid pressure runaway induced by ion-stimulated desorption. It must also be designed to take into account the effects of synchrotron radiation, electron cloud, and ion-stimulated desorption from the walls. Heat load onto the beam vacuum chamber walls or flanges and beam impedance effects must also be taken into account [1].

---

\* Corresponding author: [Vincent.Baglin@cern.ch](mailto:Vincent.Baglin@cern.ch)

The system must be compatible with the global LHC impedance budget and the machine aperture.

The average gas density along the IR must satisfy the level defined by the 100 h vacuum lifetime due to nuclear scattering, i.e. less than  $1.2 \times 10^{15}$  H<sub>2</sub> molecules m<sup>-3</sup> in the LHC [2]. This limit decreases proportionally to the inverse of the beam current. Table 12-1 gives the molecular gas densities yielding a 100 h vacuum lifetime in the LHC and the HL-LHC assuming the presence of a single gas in the vacuum system. The average gas density along IR1, IR2, IR5, and IR8 must also ensure that the background to the LHC experiments is at a minimum [3, 4]. In the absence of specified values from the LHC experiments themselves, the LHC design value will be scaled to HL-LHC parameters.

Table 12-1: Single gas species molecular gas density (m<sup>-3</sup>) to satisfy 100 h vacuum lifetime in the LHC and the HL-LHC [2].

Machine	I [A]	H <sub>2</sub> [m <sup>-3</sup> ]	CH <sub>4</sub> [m <sup>-3</sup> ]	H <sub>2</sub> O [m <sup>-3</sup> ]	CO [m <sup>-3</sup> ]	CO <sub>2</sub> [m <sup>-3</sup> ]
LHC	0.58	$1.2 \times 10^{15}$	$1.8 \times 10^{14}$	$1.8 \times 10^{14}$	$1.2 \times 10^{14}$	$7.9 \times 10^{13}$
HL-LHC	1.09	$6.4 \times 10^{14}$	$9.6 \times 10^{13}$	$9.6 \times 10^{13}$	$6.4 \times 10^{13}$	$4.2 \times 10^{13}$

### 12.3 Vacuum layout requirements

The vacuum layout must ensure the vacuum requirements when beams with HL-LHC nominal parameters circulate. The system must be designed for the HL-LHC ultimate luminosity (i.e.  $7.5 \times 10^{34}$  cm<sup>-2</sup> s<sup>-1</sup>), without margin.

- All beam vacuum elements must be leak tight (leak rate less than  $10^{-11}$  mbar<sup>-1</sup>/s He equivalent) clean according to CERN vacuum standards and free of contamination.
- According to the LHC baseline [2], the vacuum system in the LSS must be sectorized with gated valves. The vacuum sectorization is delimited by cold-to-warm transitions, length of vacuum sectors, or specificity of components (fragility, maintenance, etc.) [5].
- Vacuum sector valves must be installed at each cold-to-warm transition in order to decouple the room temperature and cryogenic temperature vacuum systems during bake-out and cool-down phases.
- The distance between the vacuum sector valve and the cold-to-warm transition must be minimized in order to reduce the length of the beamline that is not baked-out in situ.
- Dedicated vacuum instrumentation must be provided close to and either side of each sector valve and along each vacuum sector.
- Sector valves must be remotely controlled and interlocked in order to dump the circulating beam in the case of malfunctioning. The LHC and HL-LHC vacuum sectorizations delimit two types of vacuum system:
  - room temperature vacuum system;
  - cryogenic temperature vacuum system.
- The vacuum system shall be integrated in the tunnel and cavern volumes with the permanent/mobile bake-out system, bake-out racks, quick flanges collars, mobile pumping systems, and diagnostics systems. The corresponding space must be reserved into the tunnel integration to allow a proper access and operation of the vacuum system.
- Integration studies must also be performed for installation and un-installation phases of equipment to identify potential conflicts.
- Integration and installation drawings must be circulated and validated before installation in the tunnel and caverns.

## VACUUM SYSTEM

- The vacuum chamber aperture is defined by the beam optics system, and by machine protection and background for experimental considerations. The aperture of the vacuum chamber must not be the limiting aperture.
- All components to be installed into the vacuum systems must be approved and their vacuum performance validated before installation.
- A maximum number of LHC beam vacuum components will be reused for the HL-LHC upgrade.
- High radiation areas along the LSS must be clearly identified at an early stage of the design, in particular to highlight positions where remote handling/tooling might be preferred and positions where instrumentation must be radiation resistant.
- When needed, irradiation tests of specific components (instruments, bake-out jackets, cables, electronics, O rings, etc.) must be conducted to meet the radiation dose specifications.
- The spares policy will follow the general A&T sector policy. A spares policy must be made available from early on during procurement to benefit from large quantity orders, in particular for highly specialized equipment such as beam screens, modules, etc.
- Cryogenic elements must be installed first; then room temperature vacuum sector valves, followed by completion of the room temperature vacuum sectors.
- Time, resources, and space to allow the temporary storage of LHC vacuum components, which need to be dismantled to allow HL-LHC infrastructure modifications and equipment installation, will be evaluated in the next phase of the project.

### 12.3.1 Room temperature vacuum system requirements

Standard vacuum chambers and vacuum modules connect the machine components.

In order to accommodate thermal expansion during bake-out and sustain ‘vacuum forces’ due to the differential pressure, each component containing a beam pipe must have a single fixed point. Other supporting points, if any, must be sliding.

All machine components operating at room temperature must be bakeable. The required bake-out temperature is  $230^{\circ}\text{C} \pm 20^{\circ}\text{C}$  for NEG coated vacuum chambers and  $300^{\circ}\text{C} \pm 20^{\circ}\text{C}$  for uncoated stainless steel beam pipes. To optimize the bake-out duration while minimizing the mechanical strength and radiation to personnel, the applied heating rate during bake-out is  $50^{\circ}\text{C/h}$ .

The vacuum system layout must be designed to fulfil the stated requirements throughout a full run. In particular, the impact of the outgassing rate of specific components, e.g. collimators, must be taken into account during the layout definition phase. No NEG coating re-activation can be foreseen during short stops to recover loss of pumping performance.

A vacuum module equipped with a bellows must be inserted between each machine component and vacuum chamber, and between the vacuum chambers themselves.

These vacuum modules must be screened by an RF bridge for impedance reasons.

For the sake of cost, reliability, spares policy, and standardization, the maximum number of vacuum module variants must be reduced with respect to the LHC baseline.

The warm vacuum chambers must be circular and bakeable. The current LHC variants are 80 mm, 100 mm, 130 mm, and 212 mm ID: any further variants needed for the HL-LHC will be kept to the minimum necessary.

Special chambers may be designed if needed but the quantity must be kept to a minimum. A typical case is that of the recombination chambers installed into the TAN absorber, which by definition is not circular.

Vacuum chamber transitions (VCT), which gives offsets and adaptation between pipe apertures, must be integrated at the early design stage into the concerned equipment by the equipment owners themselves, e.g. BTV, ACS, TCDQ, etc. in agreement with the vacuum group.

The vacuum chambers are aligned by TE-VSC within  $\pm 3$  mm accuracy. Better tolerance will require the installation of survey targets. Alignment of other equipment is the responsibility of the survey group.

The choice of the vacuum chamber material between Cu alloy and stainless steel (either Cu coated or bare) is dictated by beam impedance constraints. Aluminium alloys are preferred in high-radiation areas

Connections between equipment must be made by Conflat bolt technology unless radiation issues and/or remote handling require the use of quick-release flanges with, for example, chain clamps.

The vacuum system must be integrated in the tunnel with the permanent or mobile bake-out system, bake-out racks, quick-flange collars, mobile pumping systems, and diagnostics systems. The corresponding space must be reserved during the tunnel integration studies to allow proper operation of the vacuum system.

### 12.3.2 Cryogenic temperature beam vacuum system requirements

The cryogenic beam vacuum system must be tightly decoupled by sector valves from the room temperature vacuum system. Dedicated instruments must be provided close to the sector valves to allow roughing, monitoring, and safety of the vessel.

A cold-to-warm transition must be integrated into the cryogenic beam vacuum sector at each extremity of the cryogenic system.

A continuous cold bore, i.e. without penetrating welds between the beam vacuum and helium enclosure, ensures leak-tightness between the superfluid helium and beam vacuum along the cryogenic beam vacuum sector. The LHC nominal cold bore temperature is 1.9 K in the arcs.

A beam screen must be inserted into the cold bore to extract the beam-induced heat load at a temperature higher than 1.9 K. The beam screen must be perforated with slots (4% transparency) to allow pumping into the cold bore space [2]. The LHC beam screen operates from 5 K to 20 K. The HL-LHC beam screens of the IT + D1 will probably need to run at a higher temperature (between 40 K and 60 K) due to a much higher heat load. In situ heating of the beam screen up to 90 K, with cold bore  $< 3$  K, is required to flush the condensed gas present on the beam screen inner surfaces towards the cold bore. This heating cycle may be required after a long technical stop or even between physics fills. The HL-LHC beam screen perforation percentage will be scaled to HL-LHC parameters and therefore increased as compared to the LHC.

When a cold bore operates at 4.5 K, cryoabsorbers are installed outside the beam screen in order to provide hydrogen pumping speed and capacity.

In the LHC, the maximum length without beam screen is less than 1 m. This LHC design value will be scaled to HL-LHC parameters and therefore reduced.

For the HL-LHC, the beam screen aperture will be derived from beam optics and magnet aperture inputs.

## 12.4 Insulation vacuum requirements

The insulation vacuum system ensures the required performance of the cryogenic system by eliminating the heat losses due to gas convection. The insulation vacuum systems under the responsibility of TE-VSC include the cryogenic distribution line (QRL) and cryogenic machine components, but exclude transfer lines outside the LHC tunnel and those of the experimental cavern.

The requirements of the insulation vacuum system for the HL-LHC can be summarized as follows:

- the pressure must be below  $10^{-5}$  mbar;
- the helium leak rate, at the component level, must be below  $10^{-10}$  mbar L/s;

- it must be compatible with the LHC insulation vacuum system [2];
- it must be built with the same standards used for the LHC insulation vacuum system.

The QRL and the magnet cryostats are connected via jumpers. However, the insulation vacuum of the QRL and continuous cryostat is sectorized through vacuum barriers. There is no sectorization of the QRL in the LSS of the LHC. Sectorization of the HL-LHC cryostats shall ensure that longitudinal leak location techniques can be employed. Connection to cryo-plant or transfer lines outside the LHC tunnel shall be delimited by vacuum barriers.

The insulation vacuum relies on cryopumping in normal operation. Fixed turbomolecular pumping groups are used for pumping before cool-down. This system also mitigates the impact of helium leaks during operation. Such pumps are also used for the detection of helium or air leaks. Dedicated pumping ports are used for rough pumping groups, pressure gauges, pressure relief valves, longitudinal leak localization techniques, and additional pump placement in case of operational leaks. A bypass equipped with isolation valves is installed between subsectors. The standard for pumping ports is the ISO-K DN 100 flange. Each insulation vacuum volume has to be equipped with pressure relief valves. Elastomer seals (Viton, NBR) are used where system demountability is necessary (interconnections, instrumentations, etc.). The layout detailed design, testing, and final acceptance of the HL-LHC cryostats are subject to TE-VSC approval.

For the HL-LHC project, in the areas of expected high irradiation, specific seals (metals or hard-rad polymers) have to be installed on new equipment and be used to replace standard seals on any retained equipment.

Regular preventive maintenance will be carried out on turbomolecular pumping groups during technical stops.

### 12.5 Experimental vacuum system requirements

The experimental vacuum system is located between Q1L and Q1R of each interaction point. Similarly to the LSS, the vacuum layout of each experimental vacuum system must ensure the vacuum requirements when beams with HL-LHC nominal parameters circulate. The system shall be designed for HL-LHC ultimate parameters, without margin. Therefore, all constraints and requirements defined in Sections 12.3 and 12.3.1 apply in this section.

During long beam stops (>10 days), neon venting is needed to protect the fragile experimental vacuum chambers from deformations caused by mechanical shocks. The baseline is that there will be no work in the vicinity of the vacuum chambers while they are under vacuum.

The vacuum chamber supporting system must be compatible with standard activities performed in the experimental cavern during short stops (e.g. winter technical stops). In particular, no personnel are allowed in the vicinity of the beam pipe (<2 m radius) during these phases.

A vacuum sector valve is installed at each Q1 extremity. This vacuum sector valve, installed just after the cold-to-warm transition, ensures decoupling of the room temperature and cryogenic temperature vacuum systems during bake-out and cryogenic temperature transients. The Q1 sector valves are interlocked to the circulating beam.

A second vacuum sector valve is installed between Q1 and the TAXS on the lefthand and righthand sides of the ATLAS and CMS experiments. On the lefthand and righthand sides of the ALICE and LHCb experiments a sector valve is installed between Q1 and the cavern shielding. Such vacuum valves allow the decoupling of two delicate and complex beam vacuum sectors, i.e. the inner triplets' vacuum sector and the experimental vacuum sector, in areas that can be radioactive. They are blocked open during operation, i.e. they are out of the interlock chain.

A rupture disk is installed in the buffer zones in order to protect the experimental vacuum chambers in case of liquid helium inrush. Therefore, the Q1 sector valve located at the cold-to-warm transition position must be interlocked against possible helium inrush in case of a cryogenic accident inside the inner triplets.

As for the present LSS vacuum system, all machine components operating at room temperature must be bakeable and NEG coated.

Scheduled or accidental air venting in air for repair or maintenance of any of the vacuum sectors of the experimental vacuum system implies a complete NEG recommissioning of the beam pipes, i.e. two bake-out cycles, the first for the bake-out of the metallic part, the second for NEG activation.

An ultra-pure neon venting system is installed in the buffer zone (for ATLAS, CMS, and ALICE) or in the detector itself (i.e. the vertex locator, VELO) to allow remote venting of the experimental vacuum system during long stops (>10 days).

#### 12.5.1 High luminosity experiments: ATLAS and CMS

ATLAS and CMS vacuum layout drawings are described in Refs. [6, 7].

On both sides of ATLAS and CMS, a pumping system is installed in the buffer zone to allow pump-down and vacuum commissioning during NEG activation of the ATLAS and CMS experiment.

In the Q1-TAXS areas instrumentation must be minimized. The Q1 sector valve must remain in the interlock chain in order to protect the experimental area from gas contamination or liquid helium inrush.

The following are required to avoid personnel intervention in a high radiation area.

- A pumping and neon systems must be installed in the buffer zone on the righthand side of ATLAS to complement the lefthand side.
- Remote tooling must be foreseen to avoid personnel intervention. Quick type flanges are mandatory. Welds are preferred to flanges.
- Installed components must be robust: in particular, sliding fingers in RF bridges are forbidden.
- The bake-out system must be permanent and fully integrated with the other systems from the design phase.
- Detector modifications shall be designed taking into account movement and intervention of personnel. They shall also take into account the beam pipe system and flanges for detector movements. It must be ensured that standard interventions during technical stops and chamber replacements are thoroughly studied during the design phase with the aim of minimizing the radiation dose to personnel during the detector and chamber lifecycle.

ATLAS is equipped with a permanent bake-out system while CMS is not. However, the HL-LHC might require the use of permanent bake-out systems for both detectors due to radiation issues. In CMS, a specific design of the jackets, thermocouple, and cable layouts must also comply with radiation requirements.

The vacuum modules are not screened by sliding RF finger for access and space constraints, radiation protection reasons, and potential risk of aperture loss.

The alignment of the vacuum chambers shall be performed remotely with appropriate hardware.

The choice of the vacuum chamber material between Cu alloy and stainless steel (either Cu coated or bare) is dictated by beam impedance requirements. Al alloys are preferred in high-radiation areas.

The connection between equipment shall be done by Conflat bolted technology unless there are radiation issues and/or remote handling that requires the use of quick-release flanges.

It is assumed that the ATLAS central beam pipe inner diameter, as installed during LS1, remains the same until at least LS3 [8].

According to Ref. [8], that the following are assumed.

- The CMS central beam pipe inner diameter, as installed during LS1 remains the same until at least LS3.
- End cap, HF, CT2, and forward pipes of the CMS vacuum system must be upgraded to Al bulk material during LS2. No mechanical intervention between TAXS L and TAXS R is therefore expected during LS3.

Any new chamber to be installed in the future must be compatible with remote tooling, e.g. equipped with a 'quick flange' type system.

Since the TAS needs to be replaced during LS3, the vacuum system located inside the experimental cavern needs to be recommissioned, i.e. NEG activation even if no changes to the vacuum system inside the cavern are foreseen.

### 12.5.2 ALICE and LHCb experiments

On the righthand side of ALICE, a pumping system is installed in the buffer zone to allow pumpdown and commissioning during NEG activation of the beam pipes.

In the ALICE cavern, a manual valve, located on the lefthand side of the beryllium central beam pipe, allows the isolation of the detector vacuum sector from the RB24 vacuum sector. Consequently, the vacuum chambers in the RB24 area can be dismantled during long shutdowns if needed.

The ALICE vacuum layout drawing is described in Ref. [9].

The ALICE central beryllium beam pipe is not equipped with a permanent bake-out system. The beam pipes located in the RB26 area of the ALICE cavern (i.e. the righthand side of the IP) are equipped with a permanent bake-out system. From the left of the central beam pipe to the end of RB26 the vacuum modules are not screened by sliding RF fingers because of access and space constraints, radiation issues, and the potential risk of aperture loss.

In LHCb, the vertex locator (VELO) detectors are installed into a secondary vacuum system, which is isolated from the beam vacuum system by a thin RF shield. The RF shield mechanical integrity is protected during pumping and venting phase by an automatic gas balance system to maintain the pressure difference within a mechanically stable range.

At the VELO, an automatic pumping system is installed to allow pumpdown and commissioning during NEG activation while protecting the VELO RF shield.

At the VELO, an ultra-pure neon venting system is installed to allow remote venting of the LHCb with an automatic gas balance system while protecting the VELO RF shield during long stops (>10 days).

The LHCb beam pipes are not equipped with a permanent bake-out system. However, it is foreseen that part of the UX85/3 vacuum chamber in the region of the calorimeter will be equipped with permanent bake-out for LS2 [10].

The VELO beam pipe must be baked for 48 h at a minimum of 180°C to suppress the electron cloud.

From the righthand side of the VELO beam pipe to the end of UX85, the vacuum modules are not screened by sliding RF fingers because of access and space constraints, radiation issues, and the potential risk of aperture loss.

Wake-field suppressors are installed at the VELO beam pipe extremities for impedance reasons.

The LHCb vacuum layout drawing is described in Ref. [11].

According to Ref. [12], it is assumed that the ALICE central beam pipe inner diameter will be changed during LS2 and remains unchanged afterward.

According to Ref. [10], is the following are assumed that.

- The LHCb VELO beam pipe will be changed during LS2 and remains in the ring afterward [3].
- The 2 m long Cu-alloy vacuum chamber, VCDBV, located on the righthand side of the VELO will be replaced by an Al alloy beam pipe. This change will take place during LS2. No modification is expected afterward.
- Part of the UX85/3 vacuum chamber in the calorimeter region will be equipped with permanent bake-out jackets during LS2. It is also assumed that there will be no more installation of permanent bake-out jackets after LS2.

## 12.6 Beam screen requirements

Beam screens are inserted into cryogenic cold bores in order to guarantee vacuum performance. They are part of the LHC vacuum system baseline [1]. The requirements of the HL-LHC beam screen can be summarized as follows.

- The system lifetime must be longer than the HL-LHC lifetime, i.e. 40 years of operation and 50 quenches.
- The system must fulfil the required vacuum performance in terms of vacuum stability, vacuum lifetime, and background to the experiments.
- The shielded beam screen must be perforated (or be shadowing) in order to fulfil the vacuum performance in a way to allow the pumping of molecules onto the cold bore.
- The cold bore temperature must be held below 3 K to allow cryosorption of all molecules with the exception of helium.
- The shielded beam screen must be heatable to allow a transfer of the gas onto the shielded beam screen towards the cold bore during machine stops.
- The shielded beam screen must withstand the Lorentz forces induced by eddy currents during a quench.
- The temperature of the shielded beam screen must be actively controlled in a given temperature range.
- To minimize the heat load on the shielded beam screen due to the electron cloud, a coating, e.g. amorphous carbon or a clearing electrode system, must be studied, validated, and implemented. The e-cloud mitigation measures must be applied not only to the new high-luminosity insertion regions, IP1 and IP5, that will be renovated. They will be applied also to the interaction regions of IP2 and IP8. These are indeed low-luminosity insertions, however the beam pattern will be the same as in the high-luminosity insertions. This point is quite recent and mitigation measures are currently under investigation.
- The system must be compatible with the impedance budget.
- The system must be compatible with the machine aperture.
- The surface of the beam screen must withstand a dose of several hundred MGy during its lifetime.

In order to operate properly, the beam vacuum system must be evacuated for five consecutive weeks, at least, prior to cool-down to allow the outgassing rate of adsorbed water to be reduced to acceptable levels.

During cool-down of a cryogenic system, the cold bore must be cooled first in order to minimize gas condensation onto the beam screen.

In the case where gas condenses onto the beam screen during operation, e.g. after a magnet quench, a transfer of this gas towards the cold bore via beam screen heating is needed. This procedure should be carried out in a couple of days.

The HL-LHC beam screen must be inserted during the cryostating phase prior to tunnel installation. The surface of the beam screens must be kept clean during assembly. This implies that the beam screen is installed



at the last stage of cryostating. Without specific tooling and procedures, no probe or device can be inserted into the vacuum system once the beam screens are installed.

The cooling tubes must be dimensioned to allow a proper cooling of the system during operation within the limits defined above.

According to vacuum standards, full penetrating welds are forbidden in the vessel wall separating the beam vacuum and helium enclosures. However, given the limited number and length of new vacuum elements to be installed, this general rule might be revised in the case of compelling reasons, if compensated for by adequate measures of risk mitigation.

Depending on the location, two types of beam screens may exist: shielded and non-shielded beam screens. The shielded beam screens intercept part of the debris produced at the high luminosity IPs, thereby protecting the cold masses from radiation-induced damaged.

Amorphous carbon (a-C) coating is at present the baseline for the inner surface of the HL-LHC shielded and non-shielded beam screens. Due to a-C's properties, strong electron cloud suppression in these HL-LHC components is expected. Amorphous carbon coating will be applied to HL-LHC beam screens if needed for the reduction of heat load to cryogenic systems, reduction of background to experiment, and/or beam physics requirements.

A demonstration of the electron cloud suppression must be performed with a dedicated set up such as COLDEX in SPS LSS4. Studies will be held during SPS scrubbing runs and dedicated machine developments. Experimental results must be supported by theoretical expectations derived from simulations codes such as Ecloud or PyCloud.

Amorphous carbon coating should be the last step of beam vacuum preparation before lowering the magnet into the tunnel, avoiding any subsequent insertion of tooling or other devices into the beam vacuum line.

For IP2 and IP8, in situ coating of the present beam screen (or alternatively the placement of a clear electrode) must be studied and conducted during the long shutdown (LS2 or LS3). If in situ coating is not possible, removal of the magnet cryostat will be considered to allow beam screen exchange.

If needed, a sawtooth structure can be produced on the beam screen walls (dipoles and quadrupoles). The sawtooth must be designed to intercept the synchrotron radiation at perpendicular incidence and to reduce the forward scattering of light.

### 12.6.1 Shielded beam screen

HL-LHC shielded beam screens are to be inserted into HL-LHC D1 and IT of LSS1 and LSS5. These beam screens ensure the vacuum requirements, the shielding of the cold mass from physics debris, and the screening of the 1.9 K cold bore cryogenic system from beam-induced heating.

As a baseline, the shielded beam screen is assumed to fulfil the vacuum requirements with a-C coating operating at 40–60 K.

The shielded beam screen is estimated to operate in the 40–60 K  $\pm$ 10 K temperature range. The operating temperature range will be defined by the available cooling power, the expected beam-induced heat load, and compatibility with the vacuum requirements.

The selected shielding material is Inermet, a tungsten alloy. It is made of 40 cm long blocks, which must be accommodated on the beam screen structure [13].

### 12.6.2 Non-shielded beam screen

HL-LHC non-shielded beam screens are to be inserted into HL-LHC D2, Q4, Q5, and Q6 of LSS1 and LSS5 and, if needed, in D1, DFBX, and IT of LSS2 and LSS8. Such beam screens ensure the vacuum requirements together with screening of the 1.9 K cold bore from beam-induced heating.

As a baseline, the a-C beam screen is assumed to fulfil its vacuum requirements with a-C coating operating at 5–20 K.

In LSS1 and LSS5, the a-C beam screen is part of the new D2, Q4, Q5, and Q6 system for the HL-LHC, which will replace the present ones.

In LSS2 and LSS8, the a-C coated beam screens will replace part of the present beam screens. The dismantling of the D1, DFBX, and IT of LSS2 and LSS8 is needed unless the cryogenic system can be upgraded.

The a-C coated beam screen is estimated to operate in the 5–20 K  $\pm$ 3 K temperature range. The operating temperature range will be defined by the available cooling power, the expected beam-induced heat load and compatibility with the vacuum requirements.

The selected a-C coated beam screen material is P506 non-magnetic stainless steel. It is similar to that used for the present beam screens. Copper will be co-laminated for impedance reasons. The proposed thickness of the Cu layer is 60  $\mu$ m.

### 12.6.3 Vacuum beam line interconnection

HL-LHC shielded beam screens are to be inserted into HL-LHC D1 and IT of LSS1 and LSS5. Beam vacuum interconnections ensure the continuity of the beam vacuum envelope, a smooth transition between adjacent beam screens, and the electrical continuity of the image current. The beam screens are fixed on one side to the cold mass; on the other side, a compensation bellows between the beam screen extremity and the cold mass has to be integrated to cope with the differential thermal displacements between the beam screens and the cold mass.

The HL-LHC beam screens rely on cooling tubes larger than those currently used. The routing of these cooling tubes, in and out of the cold bore, requires exit pieces with significant longitudinal space. Trough-wall welds on the helium circuit are forbidden in the beam vacuum. Automatic welds have to be used in the insulation vacuum.

A bellows between two adjacent beam screens has to be integrated to allow thermal contraction as well as to compensate for the mechanical and alignment tolerances. In the transitions, collisions debris shielding with a circular aperture and non-sliding RF fingers are foreseen and are being studied.

The vacuum beamline interconnections in the triplets integrate BPM as well. They define the interconnection length. Therefore, iteration and optimization of the different elements are required to complete machine integration.

## 12.7 References

- [1] O. Grobner, Overview of the LHC vacuum system. *Vacuum* **60** (2001) 25–34.
- [2] LHC Design Report, CERN-2004-003 (2004).
- [3] A. Rossi, CERN LHC Project Report 783 (2004).
- [4] A. Rossi, Residual gas density estimations of the LHC experimental interaction regions. CERN LHC Project Report 674 (2003). EDMS 410413, 2003-11-19.
- [5] Model of LSS layout LHCLJV\_L0011. <https://edms.cern.ch/document/356208/AA>
- [6] ATLAS vacuum layout Q1/Q1. LHCVC1\_\_0007. <https://edms.cern.ch/document/1317281/0>
- [7] CMS vacuum layout Q1/Q1. LHCVC5\_\_0006. <https://edms.cern.ch/document/903240/AA>

- [8] M. Gallilee, TE-VSC & ATLAS work packages consolidation and upgrade of the beam vacuum systems. <https://edms.cern.ch/document/1065775> (2013).
- [9] ALICE vacuum layout Q1/Q1. LHCVC2\_\_0001. <https://edms.cern.ch/document/946914/0>
- [10] M. Gallilee, TE-VSC & LHCb work packages consolidation and upgrade of the beam vacuum systems. EDMS 1065775 (2013).
- [11] LHCb vacuum layout Q1/Q1. LHCVC8B\_0151. <https://edms.cern.ch/document/932121/0>
- [12] M. Gallilee, TE-VSC & ALICE work packages consolidation and upgrade of the beam vacuum systems. EDMS 1065775 (2013).
- [13] R. Kersevan *et al.*, 3rd Joint HiLumi LHC-LARP Annual meeting, 11–15 November 2013, Daresbury. <https://indico.cern.ch/event/257368/session/16/contribution/37>



# Chapter 13

## Beam Instrumentation and Long-Range Beam–Beam Compensation

*E. Bravin, B. Dehning, R. Jones\*, T. Lefevre and H. Schmickler*

CERN, Accelerator & Technology Sector, Geneva, Switzerland.

### 13 Beam instrumentation and long-range beam–beam compensation

#### 13.1 Introduction

The extensive array of beam instrumentation with which the LHC is equipped has played a major role in its commissioning, rapid intensity ramp-up, and safe and reliable operation. In addition to all of these existing diagnostics, the HL-LHC brings a number of new challenges in terms of instrumentation that are currently being addressed.

The beam loss system, designed to protect the LHC from losses that could cause damage or quench a superconducting magnet, will need a significant upgrade in order to be able to cope with the new demands of the HL-LHC. In particular, cryogenic beam loss monitors are under investigation for deployment in the new inner triplet magnets to distinguish between collision debris and primary beam losses. Radiation-tolerant integrated circuits are also under development to allow the front-end electronics to sit much closer to the detector, so minimizing the cable length required and reducing the influence of noise.

The use of crab cavities and possible use of long-range beam–beam compensators and hollow-electron lenses also implies new instrumentation in order to allow for optimization of their performance. Several additional diagnostic systems will therefore be considered. Very high bandwidth pick-ups and a streak camera installation to perform intra-bunch transverse position measurements are being investigated, along with new techniques for transverse beam size measurements such as a beam gas vertex detector.

An upgrade to several existing systems is also envisaged, including the beam position measurement system in the interaction regions and the addition of a halo measurement capability to synchrotron light diagnostics.

#### 13.2 Beam loss measurement

Monitoring of beam losses is essential for the safe and reliable operation of the LHC. The beam loss monitoring (BLM) system provides knowledge of the location and intensity of such losses, allowing an estimation to be made of the energy dissipated in the equipment along the accelerator. The information is used for machine protection, to qualify the collimation hierarchy, to optimize beam conditions, and to track the radiation dose to which equipment has been exposed. This is currently done using nearly 4000 ionization monitors distributed around the machine and located at all probable loss locations, with the majority mounted on the outside of the quadrupole magnets, including those in the inner triplet regions. Around one-third of the arc monitors have recently been relocated in order to optimize the system for protection against fast beam losses believed to be caused by dust particles falling into the vacuum pipe. While the existing system is believed to meet the needs of the HL-LHC for the arcs, this will no longer be the case for the high luminosity interaction points.

---

\* Corresponding author: [Rhodri.Jones@cern.ch](mailto:Rhodri.Jones@cern.ch)

In the HL-LHC high luminosity insertions the magnets will be subjected to a greatly enhanced continuous radiation level due to the increase in collision debris resulting from the higher luminosity. With the presently installed configuration of ionization chambers in this region the additional signal from any dangerous accidental losses would be completely masked by that coming from collision debris. This is a critical issue for LHC machine protection and therefore R&D has started to investigate possible options for placing radiation detectors inside the cryostat of the triplet magnets as close as possible to the superconducting coils. The dose measured by such detectors would then correspond much more precisely to the dose deposited in the coils, allowing the system to be used once again to prevent a quench or damage.

The quench level signals estimated for 7 TeV running are, for some detectors, very close to the noise level of the acquisition system. This is mainly determined by the length of cable required to bring the signal from the radiation hard detector to the more radiation-sensitive front-end electronics. Although qualified for use in the low radiation environments of the LHC arcs, the current electronics cannot be located close to the detectors in the higher radiation insertion regions. Development has thus started to implement these electronics in a radiation-hard application-specific integrated circuit (ASIC).

### 13.2.1 Beam loss monitors for the HL-LHC triplet magnets

Three detectors are currently under investigation as candidates for operation at cryogenic temperatures inside the cryostat of the triplet magnets [1]:

- single crystal chemical vapour deposition (CVD) diamond with a thickness of 500  $\mu\text{m}$ , an active area of 22  $\text{mm}^2$ , and gold as the electrode material;
- p<sup>+</sup>-n-n<sup>+</sup> silicon wafers with a thickness of 280  $\mu\text{m}$ , an active area of 23  $\text{mm}^2$  and aluminum as the electrode material;
- liquid helium ionization chambers.

Experiments have already been performed to observe the behaviour of such detectors in a cryogenic environment and on the radiation effects at such temperatures upon silicon and single crystal diamond. Irradiation at up to 2 MGy ( $0.8 \times 10^{14}$  protons/cm<sup>2</sup>) showed degradation in the charge collection efficiency for CVD diamond by a factor of 15 and for Si by a factor of 25 (see Figure 13-1). The major downside of silicon compared to diamond, its much higher leakage current when irradiated, has been observed to disappear at liquid helium temperatures, with the leakage current remaining below 100 pA at 400 V, even under forward bias for an irradiated diode. Further experiments combining irradiation with cryogenic temperatures will be necessary to optimize the final detector design. These experiments will be accompanied by tests of detectors mounted inside the cryostats of existing LHC magnets with the aim of gaining experience with the long-term performance of such detectors under operational conditions. The technology chosen will need to be able to withstand irradiation up to 20 MGy at 4.5K.

Up to six detectors will be installed inside the cold mass of each main triplet quadrupole magnet, which leads to a baseline procurement of 100 detectors (96 installed and four spares). If the option of equipping the 11 T dipole and all the spare triplet magnet assemblies is also taken into account, then a total procurement of 150 detectors would be required. They are foreseen to be housed in existing holes in the iron yoke within the cold mass of the magnet. Each detector will be equipped with a single semi-rigid coaxial cable that will provide the necessary high voltage (up to 1000 V) and extract the loss signal from each detector. Feedthroughs allowing a total of six coaxial cable connections will need to be integrated into each of the main triplet quadrupole cryostats with the location of the feedthrough chosen so as to minimize the cable length required.

As part of the machine protection system these components need to be highly reliable and maintenance-free. In the event that some of these monitors stop functioning the existing external BLM system should still provide adequate protection against damage due to excessive beam loss, but will probably not be able to distinguish quench provoking losses from the experimental background.

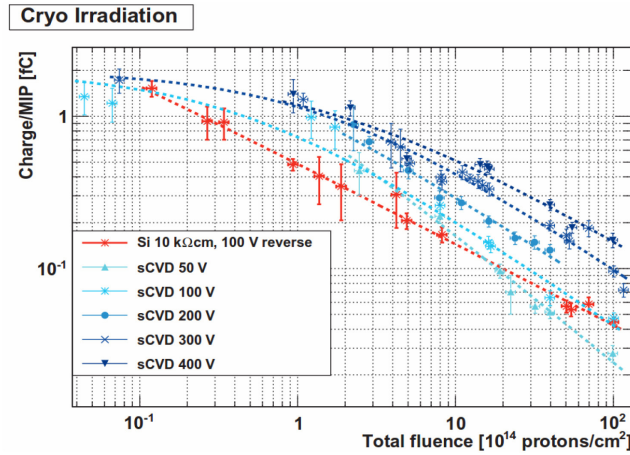


Figure 13-1: Charge collection efficiency for silicon and diamond detectors with increasing radiation fluence in a cryogenic environment.

13.2.2 A rad-tolerant application-specific integrated circuit for the HL-LHC beam loss monitoring system

The current front-end electronics for the LHC BLM system, while providing a 40 μs integration time, is limited in the dynamic range it can handle and is only radiation tolerant up to ~500 Gy. The latter implies the use of long cables in the higher radiation LSS regions, which further limits the dynamic range and in some cases brings the noise floor close to the quench level signal at 7 TeV. Instead of the discrete component currently used, an optimized ASIC is therefore under development. This is still based on the current-to-frequency conversion used in the existing system, but is packaged in a compact, radiation-tolerant form with an increased dynamic range. The technique employed allows the digitization of bipolar charge over a 120 dB dynamic range (corresponding to an electric charge range of 40 fC–42 nC) with a 40 μs integration time and a conversion reference provided by an adjustable, temperature-compensated current reference [2].

Figure 13-2 shows the block diagram of the integrated circuit. It is composed of a bipolar, fully-differential integrator that converts the charge received from the detector into a voltage input for a synchronous comparator system. A three-level digital-to-analog converter (DAC) drives the discharge current for the integrator and is connected in a feedback loop to the comparator output. The first logic block is used to select the gain in the integrator, the current step in the DAC, and the threshold in the comparators, while a second logic block encodes the output signal from the comparators. The results of both of these are used by a third block to assemble the final, correctly weighted, output word.

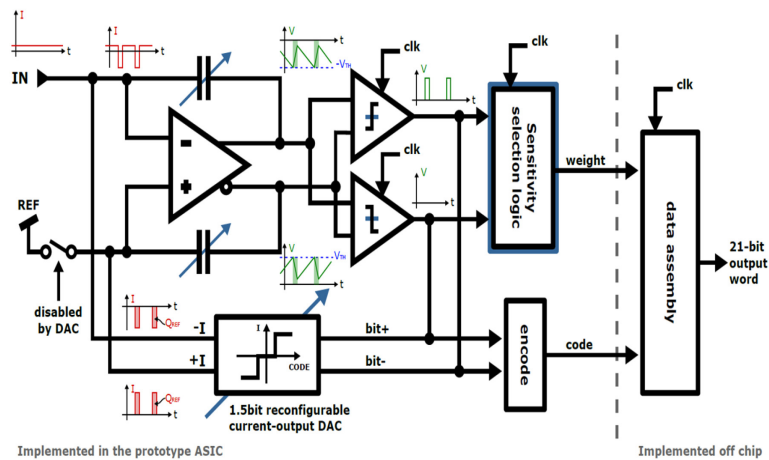


Figure 13-2: Schematic representation of the ASIC implementation currently under development

The prototype ASIC is designed with commercial CMOS technology and has two analog-to-digital (A/D) channels and a sensitivity selection logic that can be disabled to implement the circuitry externally. This strategy has been useful for testing the device and improving the algorithm. Its measured characteristics are listed in Table 13-1.

Table 13-1: Characteristics of the prototype HL-LHC BLM system ASIC

Parameter	Value
<b>A/D converter</b>	
Integration time	40 $\mu$ s
Input current range	-1.05–1.05 mA
Input charge range	-42–42 nC
Offset	<40 aC at 40 $\mu$ s integration, <1 pA
Default least significant bit step	50 fC $\pm$ 20%, adjustable
Dynamic range	120 dB
Linearity error	< $\pm$ 5%
Peak signal/noise ratio	53 dB
SFDR at 999 Hz, 1 mA	50 dB
Total ionizing dose	10 Mrad (Si)
Supply voltage	2.5 V
Clock	12.8 MHz
Power	40 mW
<b>Reference charge</b>	
Drift with TID	3% at 10 Mrad (Si)
Drift with temperature	<600 $\times$ 10 <sup>6</sup> /°C

The measured linearity is limited by transistor matching imperfections in the DAC, introducing an error at the transition between the sensitivities. However, overall the error is less than 5% and well inside specification (<10%).

Total ionizing dose (TID) effects on the ASIC have been investigated using an X-ray beam with 20 keV peak energy. The characteristics of the device were measured up to 100 kGy (Si), followed by a one-week annealing cycle at 100°C. From the beginning to the end of the irradiation cycles, the functionality was always preserved, with the conversion offset remaining below 1 least significant bit (LSB) and the value of the full-scale charge drifting by less than 3%. Development will now continue to address the issues found using the prototype and to implement more advanced logic blocks within the ASIC.

It is foreseen that a total of some 300 detectors, mainly located in the LSS regions, will be equipped with such a front-end ASIC.

### 13.3 Beam position monitoring

With its 1070 monitors, the LHC beam position monitor (BPM) system is the largest BPM system in the world [3]. Based on the wide band time normalizer (WBTN) principle, it provides bunch-by-bunch beam position over a wide dynamic range (~50 dB). Despite its size and complexity (3820 electronics cards in the accelerator tunnel and 1070 digital post-processing cards in surface buildings) the performance of the system during the last three years has been excellent, with greater than 97% overall availability.

#### 13.3.1 Current performance and limitations

The position resolution of the LHC arc BPMs has been measured to be better than 150  $\mu$ m when measuring a single bunch on a single turn and better than 10  $\mu$ m for the average position of all bunches. The main limitation on the accuracy of the BPM system is linked to temperature-dependent effects in the acquisition electronics, which can generate offsets of up to a millimetre over a timescale of hours. On-line compensation was



introduced to limit this effect during operation, and temperature-controlled racks are currently being installed with the hope of eliminating this limitation from Run 2 start-up in 2015.

The non-linearity of the BPMs located near the interaction points has also proven to be problematic, in particular for accurate measurements during the beta squeeze and during machine development periods. A new correction algorithm has therefore been developed, based on exhaustive electromagnetic simulations, with the aim of bringing down the residual error to below 20  $\mu\text{m}$  over most of the useable BPM area [4]. Developed to be able to distinguish between the positions of two counter-propagating beams in the same beam pipe, these BPMs also suffer from non-optimal decoupling between the beams, which is something that will need to be addressed for the HL-LHC.

### 13.3.2 A high resolution orbit measurement system for the HL-LHC

Originally developed to process signals from BPM buttons embedded in LHC collimator jaws, orbit measurement using a compensated diode detector scheme [5] has already been demonstrated to be simple and robust, and to provide a position resolution down to the nanometre level. A comparison of the orbit measured on a single BPM during a van der Meer scan by the current orbit system and the new diode orbit system is presented in Figure 13-3, where the resolution of the new system can be seen to be over 50 times better. All new LHC collimators will have BPMs using this acquisition system installed with them, with plans to also equip the BPMs in all four LHC interaction regions. It is important to note, however, that the new system does not provide the bunch-by-bunch measurement capability of the existing system.

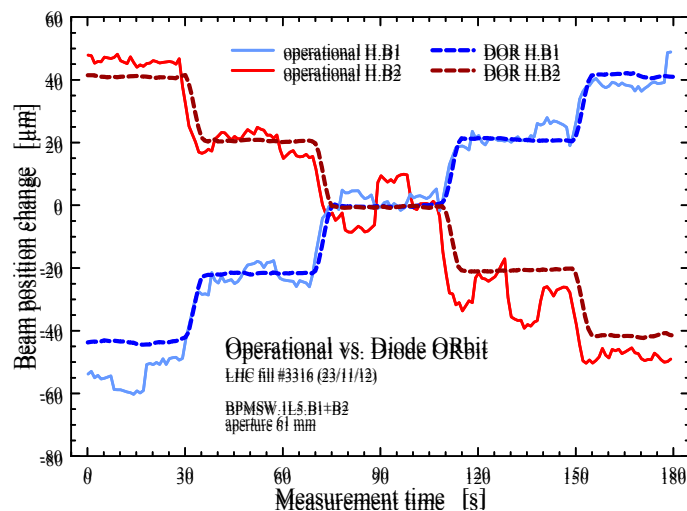


Figure 13-3: Comparison of the new LHC orbit system electronics with the existing system during a van der Meer scan.

At the start of the HL-LHC era the existing BPM system will have been operational for over 15 years, using components that are over 20 years old. It is therefore likely that a completely new system will need to be installed for HL-LHC operation. One candidate would be to extend the new diode orbit system to the whole machine for accurate global orbit measurements, and complement this with a system capable of providing the high-resolution bunch-by-bunch, turn-by-turn measurements required in particular for optics studies and the many other accelerator physics experiments that will be needed to understand and optimize HL-LHC performance.

With the higher bunch intensities foreseen, the dynamic range of the BPM system for the HL-LHC will need to be increased accordingly. The present system implements two sensitivity ranges, optimized for pilot and nominal bunch intensities. Issues have been observed in the first three years of operation with BPMs providing large errors when reaching the limit of their dynamic range. For the interlock BPMs located in P6, this can trigger false beam dumps, which clearly has an impact on machine availability. Although improvements have already been made to this interlock system for Run 2, any consolidation of the LHC BPM

system should include developing dedicated electronics for this system, optimized for both high reliability and availability.

### 13.3.3 High directivity strip-line pick-ups for the HL-LHC insertion regions

In the BPMs close to the interaction regions, the two beams circulate in the same vacuum chamber. Directional strip-line pick-ups are therefore used to distinguish between the positions of both beams. When the two beams pass through the BPM at nearly the same time, the two signals interfere due to the limited directivity of the strip-line that, in the present design, only gives a factor of 10 isolation between the wanted signal and that coming from the other beam. This effect can be minimized by installing the BPMs at a location where the two beams do not overlap temporally. This is a constraint included in both the present and future layout, but which cannot be satisfied for all BPM locations. The ideal longitudinal location corresponds to  $(1.87 + N \times 3.743)$  m from the IP where  $N$  is an integer. Any deviation from this will diminish the possibility of the system distinguishing one beam from the other.

For the HL-LHC BPMs in front of the Q2a and Q3 magnets and the triplet corrector magnet package, there is the additional constraint that tungsten shielding is required in the cold bore to minimize the heat deposition in these magnets. A mechanical re-design coupled with extensive electromagnetic simulations is therefore necessary to optimize the directivity under these constraints.

As part of the beam position system of the LHC these components need to be highly reliable and maintenance-free, while the system should be able to measure the beam position for each beam with a resolution of 1  $\mu\text{m}$  and a medium term (fill to fill) reproducibility of 10  $\mu\text{m}$ .

#### 13.3.3.1 Cold stripline beam position monitors

The HL-LHC high luminosity insertion regions will be equipped with two types of cold stripline BPMs, measuring simultaneously the position of both beams in both planes.

The BPMs located in the interconnect in front of the Q2b and Q3 magnets and the triplet corrector magnet package will be cold stripline BPMs, rotated by  $45^\circ$  to allow the insertion of tungsten shielding in the median planes of both horizontal and vertical axes.

The BPMs located in front of Q2a and before and after the D1 magnet will be cold stripline BPMs with orthogonally positioned electrodes and without tungsten shielding.

The signal from all of these BPMs will be extracted using eight semi-rigid, radiation-resistant coaxial cables per BPM. Two feedthroughs with four coaxial cable connections will be integrated into the Q2a, Q2b, and Q3 cryostats and into the cryostat of the triplet corrector magnet package, with four such feedthroughs integrated into the D1 cryostat. The outputs on these feedthroughs will be connected to standard  $\frac{1}{2}$ " coaxial cables taking the signal to the electronics in the UA/UJ.

A total of 12 stripline BPMs of each type will be installed, with three spares foreseen per type of BPM assembly.

#### 13.3.3.2 Warm stripline beam position monitors

The beam position monitor in front of Q1a will be a warm stripline BPM, simultaneously measuring the position of both beams in both planes. The signal will be extracted using eight semi-rigid, radiation-resistant coaxial cables, to a patch panel located in an area of lower radiation on the tunnel wall, where they will connect to eight standard  $\frac{1}{2}$ " coaxial cables taking the signal to the electronics in the UA/UJ.

A total of four such BPMs will be installed with two spares foreseen for this type of BPM assembly.

### 13.3.4 Collimator beam position monitors

All next-generation collimators in the LHC will have button electrodes embedded in their jaws for on-line measurement of the jaw-to-beam position [4]. This is expected to provide a fast and direct way of positioning the collimator jaws and subsequently allow constant verification of the beam position at the collimator location, improving the reliability of the collimation system as a whole. The design of such a BPM was intensively simulated using both electromagnetic (EM) and thermo-mechanical simulation codes. In order to provide the best accuracy, the BPM readings must be corrected for the nonlinearity coming from the varying geometry of the collimator jaws as they are closed and opened, for which a 2D polynomial correction has been obtained from EM simulations and qualified with beam tests using a prototype system installed in the CERN SPS.

The collimator BPM hardware, i.e. the button electrode located in the jaw, the cable connecting the electrode to the electrical feedthrough mounted on the vacuum enclosure, and the feedthrough itself have been chosen to withstand the radiation dose of 20 MGy expected during the lifetime of the collimator.

## 13.4 Beam profile measurements

The LHC is currently fitted with a host of beam size measurement systems used to determine beam emittance. These different monitors are required in order to overcome the specific limitation of each individual system. Wire scanners are used as the absolute calibration reference, but can only be operated with a low number of bunches in the machine due to intensity limitations linked to wire breakage. A cross-calibrated synchrotron light monitor is therefore used to provide beam size measurements, both average and bunch-by-bunch, during nominal operation. However, the small beam sizes achieved at 7 TeV, the multiple sources of synchrotron radiation (undulator, D3 edge radiation, and central D3 radiation), and the long optical path required to extract the light imply that the correction needed to extract an absolute value is of the same order of magnitude as the value itself. This requires an excellent knowledge of the error sources to obtain meaningful results. The third system installed is an ionization profile monitor, which is foreseen to provide beam size information for lead ions at injection, when there is insufficient synchrotron light. The monitor has also been used for protons, but suffers from significant space charge effects at energies above 2 TeV.

Whilst efforts are ongoing to improve the performance of all the above systems, alternative techniques to measure the transverse beam size and profile are also under study for the HL-LHC.

### 13.4.1 Fast wire scanners

The currently installed LHC linear wire scanners have a maximum scan speed of  $1 \text{ ms}^{-1}$ . This gives a limit on the total intensity that can be scanned at injection of  $\sim 2.7 \times 10^{13}$  protons for an emittance of  $\sim 2 \text{ } \mu\text{m}$ , or some 200 nominal bunches. Scanning at  $20 \text{ ms}^{-1}$  would allow systematic, average beam size measurements to be performed on the full physics beam at injection. A new fast, rotational wire scanner concept is therefore being explored to reach such speeds whilst achieving an accuracy of  $5 \text{ } \mu\text{m}$  on the beam width determination, i.e. an error of 5% or less for nominal emittance beams.

The mechanics will be based on the design currently being developed for the injector complex as part of the LHC Injector Upgrade project [6]. It eliminates the need for mechanical bellows by placing all moveable parts of the rotational scanner in the beam vacuum. These bellows have a limited lifetime that, due to their intensive use in the LHC, can be reached within a matter of years. The use of a magnetically coupled motor without the need for moving vacuum parts should significantly increase the MTBF of the mechanical system. In addition, the current shower detection acquisition will be replaced with a diamond-based sensor connected to high dynamic range acquisition electronics, which should considerably improve the operational ease-of-use of these devices.

Plans to install two horizontal and two vertical scanners for Beam 1 next to the existing scanners in 5R4 and two horizontal and two vertical scanners for Beam 2 next to the existing scanners in 5L4 are foreseen. One spare horizontal and one spare vertical unit will also be manufactured.

### 13.4.2 A Beam gas vertex profile monitor (BGV)

The VELO detector of the LHCb experiment has shown how beam–gas interactions can be used to reconstruct the transverse beam profile of the circulating beams in the LHC [7]. The new concept under study is to see whether a simplified version of such a particle physics tracking detector can be used to monitor the beams throughout the LHC acceleration cycle. This concept has, until now, never been applied to the field of beam instrumentation, mainly because of the high level of data treatment required. However, the advantages compared to the standard beam profile measurement methods listed above are impressive: high resolution profile reconstruction, single bunch measurements in three dimensions, quasi non-destructive, no detector equipment required in the beam vacuum, and high radiation tolerance of the particle detectors and accompanying acquisition electronics.

Such a beam shape measurement technique is based on the reconstruction of beam–gas interaction vertices, where the charged particles produced in inelastic beam–gas interactions are detected with high-precision tracking detectors. Using the tracks left in the detectors, the vertex of the particle–gas interaction can be reconstructed so, with enough statistics, building up a complete 2D transverse beam profile (Figure 13-4). The longitudinal profile could also be reconstructed in this way if relative arrival time information is additionally acquired by the system, which is not currently planned.

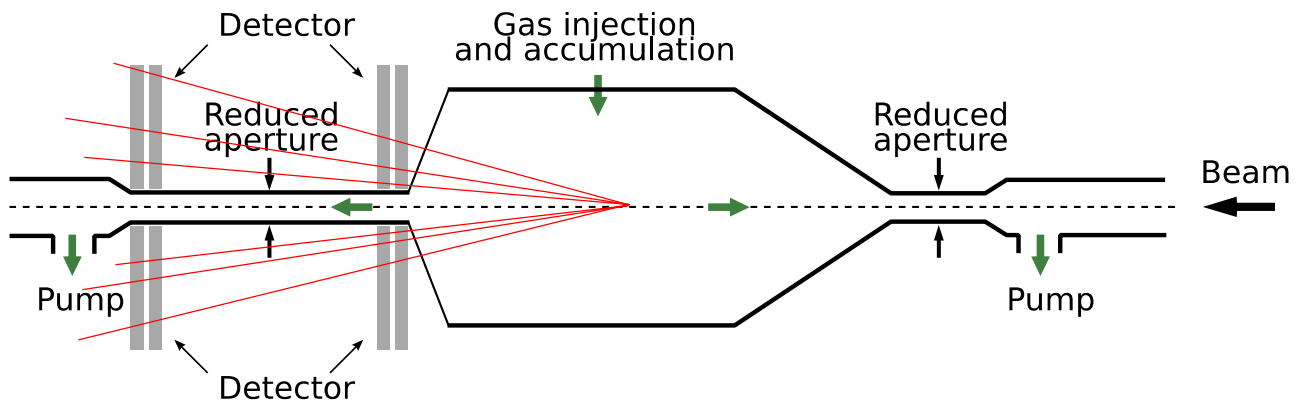


Figure 13-4: A sketch demonstrating the beam gas vertex measurement concept

Unlike LHCb, where the detector is placed very close to the beam and can therefore only be used during stable beams, the aim with the beam gas vertex profile monitor (BGV) detector is to design a robust instrument that can be used for beam size measurements throughout the LHC cycle. Its final specifications are to provide:

- transverse bunch size measurements with a 5% resolution within 1 minute;
- average transverse beam size measurements with an absolute accuracy of 2% within 1 minute.

The main subsystems are: a neon gas target at a pressure of  $6 \times 10^{-8}$  mbar, a thin aluminium exit window, tracking detector based on scintillating fibre modules read out by silicon photomultipliers, hardware and software triggers, and a readout and data acquisition system based on that used for LHCb. As the tracking detector is external to the vacuum chamber, no movable parts are needed. The final design of the prototype is shown in Figure 13-5.

A proof-of-principle demonstrator is foreseen for installation on the lefthand side of LHC IP4 on Beam 2 during LS1, with a second system for Beam 1 installed on the righthand side of IP4 in LS2. A full upgrade of these systems, to include a third detector layer and upgraded electronics, may be required in LS3 to reach the full design goals outlined above. This upgrade is currently not part of the HL-LHC baseline.

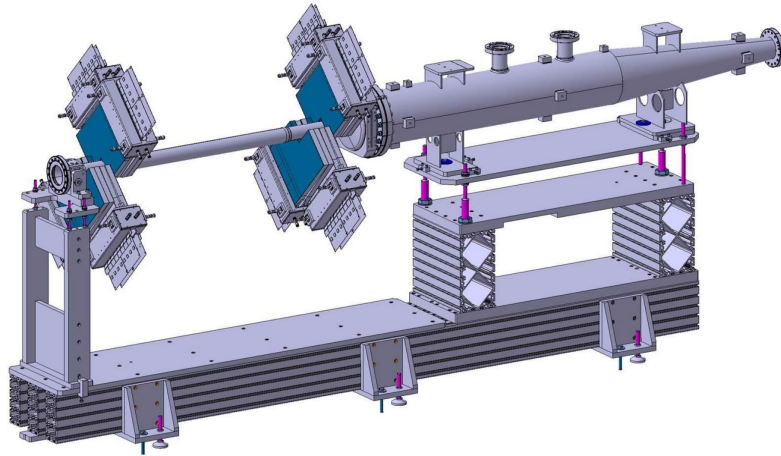


Figure 13-5: The demonstrator beam gas vertex detector installed in the LHC during LS1

### 13.5 Diagnostics for crab cavities

The crab cavities for the HL-LHC are proposed to counter the geometric reduction factor and so to enhance luminosity. These cavities will be installed around the high luminosity interaction points (IP1 and IP5) and used to create a transverse bunch rotation at the IP. The head and tail of each bunch is kicked in opposite directions by the crab cavities such that the incoming bunches will cross parallel to each other at the interaction point. These intra-bunch bumps are closed by crab cavities acting in the other direction on the outgoing side of the interaction region. If the bumps are not perfectly closed the head and tail of the bunch will follow different orbits along the ring. Monitors capable of measuring the closure of the head–tail bump and any head–tail rotation/oscillation outside of the interaction regions are therefore required.

#### 13.5.1 Bunch shape monitoring using electromagnetic pick-ups

Electromagnetic monitors for intra-bunch diagnostics are already installed in the LHC. These so-called ‘head–tail’ monitors mainly provide information on instabilities and have a bandwidth of approximately 2 GHz. To go to a higher resolution within the bunch a bandwidth of 10 GHz or more is desirable. This will be important to better understand instabilities in the HL-LHC and to help with the tuning of the crab cavities, with several of these systems foreseen for installation around the interaction points. In addition to studies aimed at improving the existing electromagnetic pick-ups, which include optimization of the pick-up design and the testing of faster acquisition systems, pick-ups based on electro-optical crystals in combination with laser pulses are also being considered [8]. Such pick-ups have already demonstrated fast time responses in the picosecond range [9]. Developed mainly for linear accelerators, this technology is now also being considered for circular machines, with a design for a prototype to be tested on the CERN SPS recently initiated.

#### 13.5.2 Bunch shape monitoring using streak cameras

The use of synchrotron light combined with a streak camera may be an easier alternative to electromagnetic or electro-optical pick-ups for high resolution temporal imaging. Using an optical system to re-image the synchrotron light at the entrance of a streak camera allows the transverse profile of the beam to be captured in one direction (X or Y) with a very fast time resolution (below the picosecond level). Only one transverse axis can be acquired with a given setup, while the other is used for the streaking. Using a sophisticated optical setup it is, however, possible to monitor both axes at the same time, as was performed in LEP [10].

Streak cameras can be used to observe a number of parameters simultaneously: bunch length, transverse profiles along the bunch, longitudinal coherent motion, head–tail motion, etc. The main limitation of the streak camera is the repetition rate of the acquisition, typically <50 Hz, and the limited length of the recorded sample, given by the CCD size. Double scan streak cameras exist that allow an increase in the record length. By using

a CCD with  $1000 \times 1000$  pixels working at 50 Hz and adjusting the optical magnification and scan speed such that the image of each bunch covers an area of about  $100 \times 100$  pixels, it is possible to record a maximum of 100 bunch images per 20 ms, i.e. 5000 bunches/s. This is clearly just an optimistic upper limit with other factors likely to reduce this value.

The longitudinal resolution of around 50 ps required for the HL-LHC is rather easy to achieve using streak cameras, where measurements down to the sub-picosecond range are now possible. In terms of transverse resolution two distinctions have to be made.

- Measurement of the beam width is affected by diffraction due to the large relativistic gamma of the beam, with the diffraction disk of the same order as the beam size. This will significantly reduce the resolution of such measurements.
- The centroid motion (i.e. the centre of gravity) is not directly affected by diffraction, which produces a symmetrical blur, and therefore the resolution for this type of measurement will be much better.

For determining crab cavity non-closure only the average position along the bunch is of importance, and not changes to the beam size. The streak camera should therefore be able to achieve a resolution of a few percent of the beam sigma for this measurement.

Streak cameras are expensive and delicate devices not designed for the harsh environment inside an accelerator. Radiation dose studies are therefore required in order to verify if a streak camera can be installed directly in the tunnel or if, which seems more likely, it has to be housed in a dedicated, shielded, hutch. The latter would imply an optical line to transport the synchrotron light from the machine to the camera, something for which an integration study will be initiated.

Another point to consider is the synchrotron light source. Currently, two synchrotron light telescopes are installed in the LHC, one per beam. These telescopes already share their light amongst three different instruments, the synchrotron light monitor, the abort gap monitor, and the longitudinal density monitor, and in the future will also have to accommodate halo diagnostics (see below). It will therefore be difficult to integrate yet another optical beam line for the streak camera. The installation of additional light extraction mirrors will therefore be necessary to provide the light for the streak cameras. Since the crab cavities are only needed at high energy, dipole magnets can be used as the source of the visible synchrotron radiation for the streak cameras, with no need for the installation of additional undulators that are only required at injection energy, where the dipole radiation is in the infra-red. The best location and corresponding light extraction system for such an additional synchrotron radiation source is currently under study.

### 13.6 Halo diagnostics

Population of the beam ‘halo’, i.e. particles in between the beam core and the limits set by the primary collimators, can lead to important loss spikes through orbit jitter at the collimator locations. Measurement of the beam halo distribution is therefore important for understanding and controlling this mechanism. Such measurements are also important to determine the effectiveness of equipment that influences the beam halo, such as hollow electron lenses or long-range beam–beam compensators. Moreover, in the HL-LHC, any failure of a crab cavity module could result in the loss of the halo in a single turn. If the halo population is too high this could cause serious damage to the collimation system or to other components of the machine. In order to fulfil all of these diagnostic requirements for halo observation in the HL-LHC, the final system should be capable of measuring halo populations at the level of  $10^{-5}$  relative to that of the core.

Three techniques are currently being considered for halo monitoring in the HL-LHC:

- the use of high dynamic range cameras combined with apodization;
- core masking followed by acquisition using standard cameras;
- use of the beam gas vertex detector.

The first two techniques make use of synchrotron light and, as for the streak cameras, may require an additional light source for the final HL-LHC configuration.

### 13.7 Luminosity measurement

The measurement of the collision rate at the luminous interaction points is very important for the optimization of the machine. The LHC experiments can certainly provide accurate information about the instantaneous luminosity, but this information is often not available until stable collisions have been established, and is often missing altogether during machine development periods. For this reason simple and reliable collision rate monitors, similar to those now used in the LHC, are also needed for the HL-LHC. This measurement is currently obtained by measuring the flux of forward neutral particles generated in the collisions using fast ionization chambers installed at the point where the two beams are separated into individual vacuum chambers. The detectors (BRAN) are installed inside the neutral shower absorber (TAN) whose role is to avoid neutral collision debris and the secondary showers these induce, which reach and damage downstream machine components. The luminosity monitors therefore already operate in a very high radiation area, which for the HL-LHC is anticipated to be a further ten times the nominal LHC value. For this reason the technology chosen for the HL-LHC is likely to be based on the radiation-hard LHC design [11], with the geometry adapted to the new TAN (TAXN) design. In order to further increase the radiation resistance some current features, such as their bunch-to-bunch capability, may need to be sacrificed and redundancy added.

### 13.8 Long-range beam-beam compensation

The simulated strong effect of the LHC long-range interactions inspired a proposed long-range beam-beam compensation for the LHC based on current-carrying wires [12]. In order to correct all non-linear effects the correction must be made individually in each high luminosity interaction point, with the wire generating the same integrated transverse force as the opposing beam at the parasitic long-range encounters.

The ideal location for compensation of the long-range beam-beam tune-spread is found where the beta functions are equal; there is little phase advance difference with respect to that between the long-range encounters and the IP, and where the beams are sufficiently well separated. Hence for the HL-LHC the proposed layout features compensators placed after the D1 separation dipole in IP1 and IP5 (Figure 13-6). In order to get the compensation correct for all multipoles the transverse location of a wire compensator must be on the inside of the compensated beam, i.e. between the two circulating beams, at a distance equivalent to the average long-range beam-beam separation. This poses significant technical constraints since, at the ideal longitudinal position, the transverse separation of the beams is only a few centimetres in a region with a high flux of secondary neutrons, and the transverse wire position is only a few mm from the beam. Placing and aligning a ‘wire’ at these locations, in particular between the two counter-rotating proton beams, will be very difficult. An alternative is to replace the ‘wire’ with an electron beam produced in a manner similar to that of well-established electron coolers (Figure 13-7).

Although such systems have been used for head-on beam-beam compensation at both the Tevatron (FNAL) [13] and RHIC (BNL) [14], the implementation required for the HL-LHC is beyond what has been achieved so far. Assuming an effective length of 6 m on both sides of the IP, an electron beam current of about 15–20 A would be needed, significantly higher than for previous implementations. Compensation with one system per beam in both IR1 and IR5 is also possible, and would reduce the necessary infrastructure by a factor of two, but implies electron currents of up to 40 A, almost an order of magnitude larger than what has been achieved so far.

Preliminary simulations and integration studies started to look into the feasibility of such an implementation in the LHC. However, it is clear that such infrastructure could only be installed at the same time as the upgrade of the interaction regions for the HL-LHC, ruling out the possibility of testing such a long-range beam-beam compensator beforehand. Since long-range beam-beam compensation has, so far, never been demonstrated at a long-range beam-beam limited machine, it was deemed essential to install a prototype in the LHC as soon as possible. With a test of the electron beam solution ruled out in the short term, a fall-

back solution relying on wires will be pursued, with a view to installing a demonstrator in the 2015/2016 end-of-year technical stop.

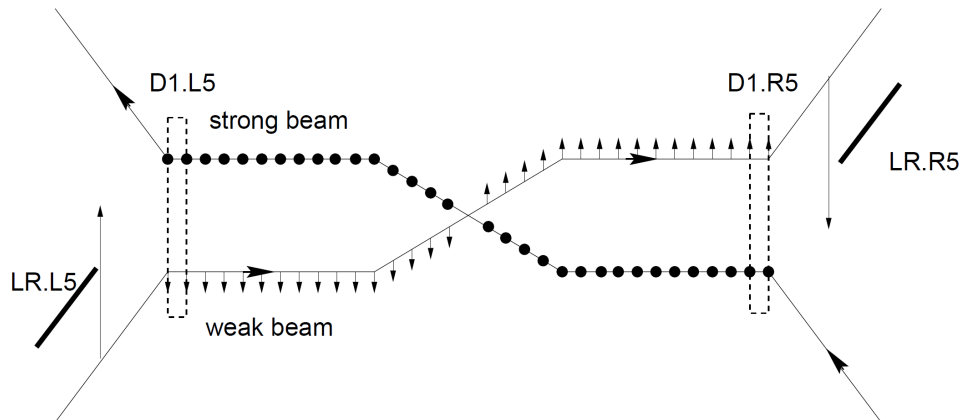


Figure 13-6: Illustration of the compensation principle [12]

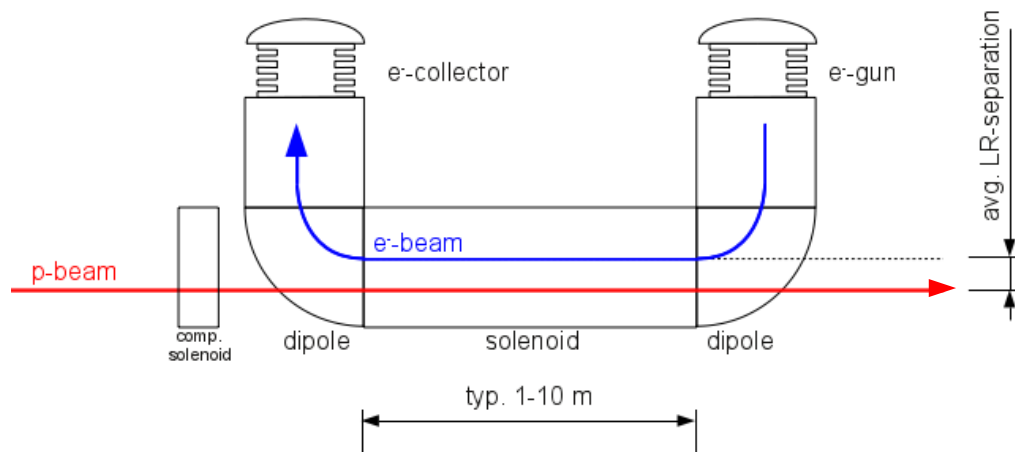


Figure 13-7: Sketch of an electron cooler type layout for long-range beam-beam compensation

### 13.8.1 Long-range beam-beam demonstrator

The only solid objects that can approach the beam accurately to within  $10\sigma$  or less are the LHC collimators. By embedding a wire in such a collimator it would be possible to use the collimator as a host for a demonstrator version of a long-range beam-beam compensator. The best compensation effect in this scenario is obtained by a wire in the tertiary collimators (TCT) located just in front of the D2 magnet. A 1 m long wire at this location would require a DC current of some 180 A at a distance of  $9.5\sigma$  to the beam or over 200 A at a distance of  $11\sigma$ . These values correspond to a symmetric layout with one compensator left of the IP and another on the righthand side, a set-up which will probably be necessary since the ratio of the horizontal and vertical beta functions are not equal at the TCT locations.

Integration of DC-powered wires into collimator jaws seems the only possibility to make realistic beam tests before embarking on a final implementation of the wires for LHC high luminosity operation. This integration itself requires the solution of many important technical issues:

- no interference of the wires with the nominal operation of the collimators;
- transfer of 1 kW resistive heat loss in the wire by heat conduction to the water-cooled collimator jaw;
- shielding of the wire from the beam through a thin metallic layer for impedance reasons.



The design of such a wire-in-jaw tertiary collimator is well advanced (Figure 13-8) and the production of four such collimators is foreseen to start before the end of 2014. The necessary DC cables and power converted infrastructure has been installed during LHC LS1.

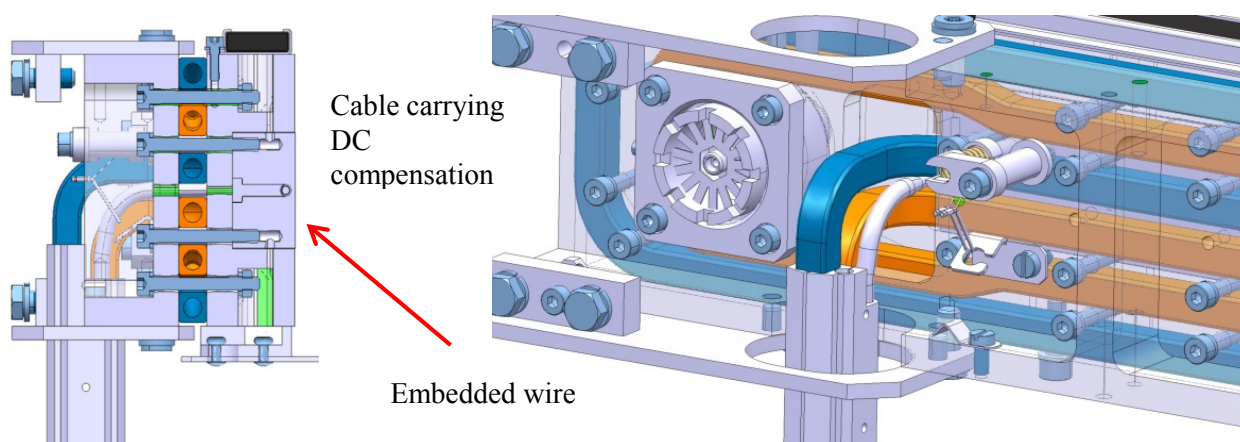


Figure 13-8: Technical drawing of the wire-in-jaw collimator design

The earliest date at which such collimators equipped with a long-range beam-beam compensation wire can be installed in the LHC is the end of year technical stop 2015/2016. Machine experiments are then planned to validate the coherence of predictions by simulation.

### 13.9 References

- [1] C. Kurfuerst *et al.*, Radiation tolerance of cryogenic beam loss monitor detectors, 4th International Particle Accelerator Conf., Shanghai, 12–17 May 2013. J.M. Raby, Biophysical aspects of radiation quality, IAEA, Technical Reports Series No. 58 (1966).
- [2] G. Venturini, F. Anghinolfi, B. Dehning and M. Kayal, Characterization of a wide dynamic-range, radiation-tolerant charge-digitizer ASIC for monitoring of beam losses, Proc. IBIC12, Tsukuba, Japan, 2012.
- [3] E. Calvo *et al.*, The LHC orbit and trajectory system, Proc. DIPAC03, Mainz, Germany, 2003, p. 187.
- [4] A. Nosych *et al.*, Electromagnetic simulations of an embedded BPM in collimator jaws, Proc. DIPAC11, Hamburg, Germany, 2011, p. 71.
- [5] M. Gasior, J. Olexa and R.J. Steinhagen, BPM electronics based on compensated diode detectors – results from development systems, Proc. BIW12, Newport News, Virginia, 2012. CERN-ATS-2012-247.
- [6] B. Dehning *et al.*, Vacuum actuator and controller design for a fast wire scanner, 2012 Beam Instrumentation Workshop, Newport News, VA, USA, 15 - 19 Apr 2012, pp.195-197, pp. TUPG029.
- [7] LHCb Collaboration, Absolute luminosity measurements with the LHCb detector at the LHC, *J. Instrum.* 7 (2012) P01010, IOP and SISSA.
- [8] M.A. Brubaker *et al.*, Electro-optic beam position and pulsed power monitors for the second axis of DARHT, 19th IEEE Particle Accelerator Conference, Chicago, IL, USA, 18 - 22 Jun 2001, pp. e-proc. 534.
- [9] Y. Okayasu *et al.*, The first electron bunch measurement by means of organic EO crystals, Proc. IBIC12, Tsukuba, Japan, 2012, MOCC03, pp 29-33.
- [10] E. Rossa, Real time single shot three-dimensional measurement of picosecond photon bunches, 6th Workshop on Beam Instrumentation, Vancouver, Canada, 3 - 6 Oct 1994, pp. 148-159.
- [11] J.F. Beche, A. Ratti, *et al.*, Rad hard luminosity monitoring for the LHC, 10th European Particle Accelerator Conference, Edinburgh, UK, 26 - 30 Jun 2006, pp. 580.

- [12] J.-P. Koutchouk, Principle of a correction of the long-range beam-beam effect in LHC using electromagnetic lenses, LHC Project Note 223 (2000).
- [13] F. Zimmermann, P. Lebrun, T. Sen, V. Shiltsev and X.L. Zhang, Using the Tevatron electron lens as a wire and other TEL studies at FNAL, CERN AB-Note-2004-041 (2004).
- [14] W. Fischer, R. Calaga, U. Dorda, J.-P. Koutchouk, F. Zimmermann, V. Ranjbar, T. Sen, J. Shi, J. Qiang and A. Kabel, Observation of long-range beam-beam effect in RHIC and plans for compensation, 10th European Particle Accelerator Conference, Edinburgh, UK, 26 - 30 Jun 2006, pp. 2158.

# Chapter 14

## Injection and Dumping Systems

*B. Goddard, A. Lechner and J. Uythoven\**

CERN, Accelerator & Technology Sector, Geneva, Switzerland

### 14 Injection and dumping systems

#### 14.1 Injection and dumping systems overview

The beam transfer into the LHC is achieved by the two long transfer lines TI2 and TI8, together with the septum and injection kicker systems, plus associated machine protection systems to ensure protection of the LHC elements in case of a mis-steered beam. The LHC is filled by approximately 10 injections per beam. The MKI kicker pulse length consists of an 8  $\mu\text{s}$  flat-top, with a rise time of 0.9  $\mu\text{s}$  and a fall time of 2.5  $\mu\text{s}$ . Filling each ring takes 8 minutes with the SPS supplying interleaved beams to other facilities. The foreseen increase in injected intensity and brightness for the HL-LHC means that the protection functionality of the beam-intercepting devices needs upgrading, see Ref. [1]. In addition, the higher beam current significantly increases the beam-induced power deposited in many elements, including the injection kicker magnets in the LHC ring.

The beam dumping system is also based on DC septa and fast kickers, with various beam intercepting protection devices including the beam dump block. Again, the significant change in the beam parameters for the HL-LHC implies redesign of several of the dump system devices, because of the increased energy deposition in the case of direct impact, but also because of increased radiation background that could affect the reliability of this key machine protection system [1].

In the following sections the changes planned in the light of the HL-LHC for the different LHC beam transfer systems are described.

#### 14.2 Injection systems

The high injected beam intensity and energy mean that precautions must be taken against damage and quenches, by means of collimators placed close to the beam in the injection regions. The layout of the injection region and associated protection devices is shown schematically in Figure 14-1. The beam to be injected passes through five horizontally deflecting steel septum magnets (MSI) with a total deflection of 12 mrad, and four vertically deflecting kickers (MKI) with a nominal total kick strength of 0.85 mrad. Uncontrolled beam loss resulting from errors (missing, partial, badly synchronized, or wrong kick strength) in the MKI could result in serious damage to downstream equipment in the LHC injection regions, in particular the superconducting separation dipole D1, the triplet quadrupole magnets near ALICE or LHCb experiments, or in the arcs of the LHC machine itself. Damaging detector components, in particular those close to the beam pipe, with excessive showers generated by lost protons, is also possible.

---

\* Corresponding author: [Jan.Uythoven@cern.ch](mailto:Jan.Uythoven@cern.ch)

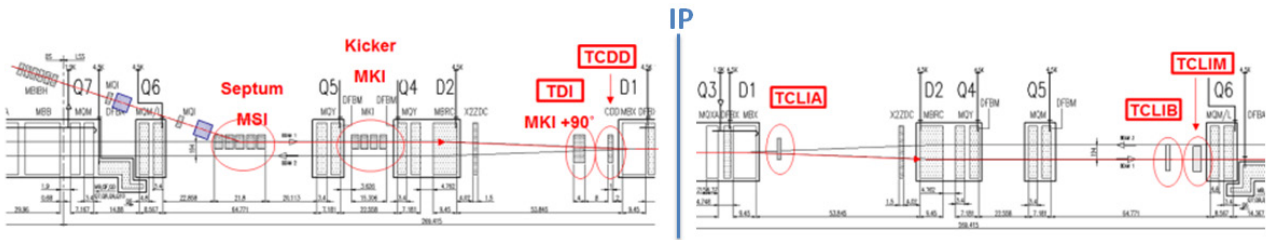


Figure 14-1: Overview of the present injection system into the LHC and the associated protection devices (Beam 1, IR2). The beam is injected from the left hand side.

14.2.1 Injection absorber (TDIS)

The TDI is a movable two-sided absorber. Its purpose is to protect machine elements in case of MKI malfunctions and to intercept low-intensity bunches during set-up or commissioning of the injection system. The present TDI, see Ref. [2], needs to be adapted to HL-LHC and LIU beam parameters. This implies a change of absorber materials but no significant change to the total absorber length. In addition, problems with the present design have become apparent during the first years of LHC operation. Instead of having one long jaw (4.185 m) as in the present TDI, the new TDIS (where the S stands for Segmented) is foreseen to comprise shorter absorbers accommodated in separate tanks, which would imply an increase in the total length.

The protection objective stated above concerns both mis-deflections of the injected beam due to MKI faults as well as accidental kicks of the stored beam due to MKI timing errors. In the first of these cases, too little or zero kick strength causes the incoming beam to impact the upper TDIS jaws. In the second case, the miskicked stored beam impacts the lower TDIS jaws. The protection objectives should be met for any impact condition, including cases where beams are swept over the aperture (misfires during MKI rise time) or where a full batch is grazing the TDIS jaws due to a non-nominal MKI kick strength. The maximum possible impact parameter (vertical distance between equilibrium orbit and impact position) on the absorber front face is estimated to be 3 cm. The largest energy deposition in downstream magnets and the highest stresses in the jaw itself are expected for small impact parameters (around 1–2  $\sigma$ , which is about 1 mm from the absorber edge), which could occur in the case of a magnet breakdown. New low-Z absorber materials, replacing boron nitride (BN5000, 1.93 g/cm<sup>3</sup>) used for the present TDI, are being studied.

If the protection objectives stated above cannot be met for a full injected beam of 288 bunches, the total number of injected bunches will need to be decreased accordingly. This has to be done in conjunction with a reduction of the MKI pulse length in order to limit the number of circulating bunches that could be miskicked onto the TDIS in the case of a timing error.

Apart from the aperture requirements for circulating and injected beams that are identical to the present TDI, see Ref. [2], there are additional aperture requirements coming from the ALICE ZDC, see Ref [3].

The jaw positioning requirements are listed in Table 14-1. Jaws at fully closed positions will be required during optimization of the injection systems. A fully open position is important to reduce beam impedance, and thus reduce heating when not injecting beam. The positions given are relative to the closed orbit, which nominally includes the separation and crossing bumps.

Table 14-1: TDIS position relative to the orbit

Characteristic	Unit	Value
Position fully closed	mm	1.0
Typical position during injection	mm	$\pm 3.8$
Position when no injection	mm	$\pm 55.0$

The beam impedance should be minimized during the injection process (absorber blocks close to the beam) and when injection is finished and the jaws are retracted (absorber blocks in parking position). The

resulting beam impedance should be acceptable from the beam stability perspective and in terms of the deposited power in the TDIS. If necessary water cooling of the absorbers will need to be installed.

The correct positioning of the TDIS is a vital element of the machine protection system during injection. Redundant position measurement of the blocks is required with redundant interlock channels going to the beam interlock system (BIS). Both LVDT and laser interferometric position measurements are foreseen. A beam energy tracking system (BETS) to guarantee the correct position at injection energy is foreseen and will use the laser interferometric position readings. For a multi-module TDIS system the correct alignment with beam between the different modules will be very important, as is illustrated by Figure 14-2.

The new TDISs will be approximately at the same position as the present TDIs, as they need to be at  $90^\circ$  betatron phase advance relative to the MKIs. The extension of the TDIs is to take place in the upstream direction, keeping the distance between the downstream end of the TDI and D1 unchanged. For IP2 this means that the large 800 mm chamber upstream of the TDI needs to be shortened. This has been discussed with the ALICE experiment and is acceptable as long as a minimum opening position is guaranteed when the jaws are retracted.

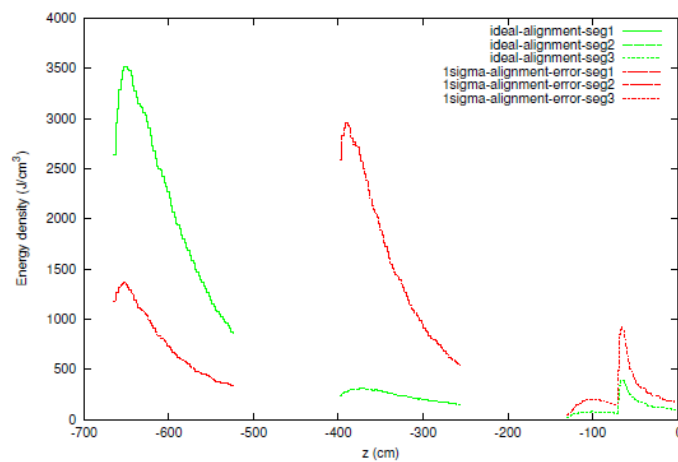


Figure 14-2: Energy deposition in a TDIS consisting of three modules (graphite, graphite and aluminium, and copper) for grazing beam impact and showing the effect of a  $1\sigma$  alignment difference between the first and second module (courtesy of N. Shetty).

#### 14.2.2 Auxiliary injection protection collimator (TCLIA)

The TDIS will be complemented by two auxiliary collimators, TCLIA and TCLIB, which are located on the other side of the IP, at phase advances that are designed to be  $\pm 20^\circ$  (modulo  $180^\circ$ ) relative to the TDI. The position of these auxiliary absorbers is shown in Figure 14-1. The TCLIA is a two-sided auxiliary injection protection collimator located between the separation dipoles in IR2 (righthand side) and IR8 (lefthand side). Owing to its position close to the D1, the TCLIA also hosts the other circulating beam. Together with another auxiliary collimator (TCLIB) it complements the primary injection protection absorber TDIS in case of injection kicker (MKI) failures. The present TCLIA consists of low-Z absorber blocks (graphite R4550,  $1.83 \text{ g/cm}^3$ ) with a total active length of 1 m. It is being evaluated whether the present TCLIA design, in particular the absorber material, can be retained for the HL-LHC era or if a new design is required due to the increased beam brightness. In addition, it is to be determined if the present TCLIA design is compatible with aperture requirements imposed by the ALICE ZDC [3] operation during heavy-ion physics runs. If the present aperture is found to be incompatible, a new design with a larger stroke for the open position will be required.

In the event of beam impact on the TCLIA, no damage must occur to downstream machine elements, in particular to the superconducting separation dipole D2. However, a magnet quench cannot be excluded from all MKI failure scenarios. In all cases, the TCLIA itself must not sustain damage during injection failures.

The TDI and TCLI elements need to protect the LHC arc aperture from mis-steered beams. Tracking studies showed that settings of  $6.8 \sigma$  for the TDI and TCLI systems adequately protect the LHC arc aperture against MKI flashovers, see Ref. [4]. This result depends on the injected intensity, and it may be necessary to reduce the  $6.8 \sigma$  settings slightly for injection of higher intensity beams – this needs to be analyzed in the context of the beam cleaning collimation system settings for injection.

#### 14.2.3 Auxiliary injection protection collimator [TCLIB]

The TCLIB is a two-sided auxiliary injection protection collimator located between the matching section quadrupoles Q5 and Q6 in IR2 (righthand side) and IR8 (lefthand side). Together with the auxiliary collimator TCLIA that has already been described, it complements the primary injection protection absorber TDIS in case of injection kicker failures. The present TCLIB accommodates low-Z absorber blocks (CfC AC150,  $1.67 \text{ g/cm}^3$ ) with a total active length of 1 m. It is complemented by a mask in front of Q6 (TCLIM), which is required to absorb secondary showers from the TCLIB such that damage to the Q6 and other downstream equipment is prevented. It is to be evaluated whether the present TCLIB design, in particular the absorber material, can be retained for the HL-LHC era or if a new design is required due to the increased beam brightness.

Depending on the injection kicker strength, badly injected beam will be absorbed by TDIS, TCLIA, or TCLIB. It is shown in Figure 14-3 that TCLIB intercepts up to 28% of the  $5 \sigma$  area of single particle emittance for injection kicker failures with  $\pm 10\%$  kick nominal strength, which corresponds to a grazing incidence of the beam on the TDIS.

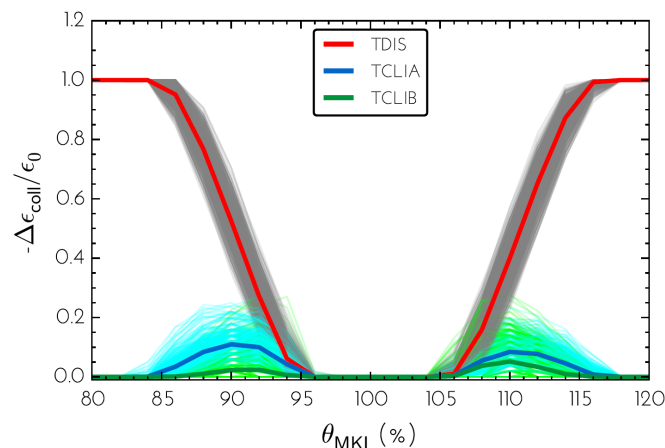


Figure 14-3: Fraction of  $5 \sigma$  single particle emittance absorbed by the different injection protection absorbers TDIS, TCLIA, or TCLIB for different injection kicker amplitudes (courtesy of F.M. Velotti).

#### 14.2.4 Injection protection masks TCDD and TCDDM

TCDD and TCDDM are masks upstream of the superconducting D1 in IR2 (left) and IR8 (right), which complement the primary injection protection absorber TDIS in case of injection kicker malfunctions, see Figure 14-1. The masks are 1 m long Cu blocks, which in IR2 are required to open for ALICE ZDC data-taking during ion runs. The TCDD/TCDDM is required to sufficiently absorb secondary showers or scattered protons from the TDIS such that it prevents damage to D1 and other equipment for any possible TDIS impact conditions and for all HL-LHC and LIU beam parameters. In IR2, any new design or new mask position must account for ALICE ZDC aperture requirements. The aperture of the present TCDD/TCDDM might need to be further minimized to protect D1 against particle showers from the high intensity beams grazing the TDIS absorber. The aperture requirements for the circulating beam and damage limits of the D1 separation dipole are important parameters to be taken into account.

#### 14.2.5 Injection protection mask (TCLIM)

The injection protection mask (TCLIM) is a fixed mask upstream of the superconducting matching section quadrupole Q6 in IR2 (righthand side) and IR8 (lefthand side). It is presently of 1 m active length and made of stainless steel. In the event of injection kicker malfunctions leading to beam impact on the auxiliary injection protection collimator TCLIB, the mask is required to absorb secondary showers from the TCLIB such that it prevents damage to Q6 and other downstream equipment. Protection has to be ensured for all HL-LHC and LIU beam parameters. It is to be evaluated whether the present TCLIM design can be retained or if a new design is required, possibly with a different length and material.

#### 14.2.6 Injection kicker magnet (MKI)

The injection kicker magnets MKI installed in IR2 and IR8, see Figure 14-1, deflect the injected beam onto the LHC closed orbits. During Run 1 of the LHC a number of issues have been encountered with the MKI magnets installed prior to LS1. These include beam-induced heating of the ferrite yoke, inefficient cooling of the ferrite yoke, electrical flashovers, beam losses due to macro particles falling into the beam, and electron cloud [5, 6].

If the ferrites of the injection kicker magnets reach a temperature above their Curie temperature their magnetic properties are compromised and the beam cannot be injected. Reducing beam-induced heating, additional cooling, and/or ferrites with a higher Curie temperature avoid waiting periods without beam before the beam can be injected into the LHC. A reduced magnetic field from the injection kickers is also a machine protection issue, possibly leading to quenches of downstream magnets. The beam impedance of the MKI magnets has been reduced in LS1 by completing the number of beam screen conductors to 24, see Figure 14-4. However it cannot be guaranteed that this will sufficiently reduce beam-induced heating for HL-LHC operation. Operational experience during Run 1 has shown that a beam power deposition of about 160 W/m occasionally limited the ability to inject beam. The present power deposition estimate for HL-LHC beams is 190 W/m, assuming use of the improved beam screen as installed in LS1. For this reason a prototype MKI magnet with additional cooling and different ferrite types will be developed for testing in the LHC. A ferrite such as CMD10, which has a higher Curie temperature than the CMD5005 or 8C11 presently used for the MKI yoke, would permit high intensity beam operation with better availability. However, operating at higher yoke temperatures will result in higher pressure in the vacuum tank, which may result in an increased electrical breakdown and surface flashover rate. Further optimization of the capacitively coupled end of the beam screen is being made to further reduce the electric field strength and so the likelihood of surface flashovers.

The exchange of an MKI during the third technical stop (TS3) of 2012, and its subsequent operation in the LHC, demonstrated that electron cloud in the ceramic tube can limit the beam intensity until conditioning had occurred (~250 hours of beam). Electron cloud in the ceramic tube results in a pressure increase and can therefore prevent operation of the injection kickers. A low SEY coating would eliminate multipactoring, and thus the related pressure rise, permitting more reliable operation of the injection kickers. Thus, research and development of special coatings for the inner surface of the ceramic tube is being carried out, and it is planned to include a coating on the tube of the prototype MKI.

After a comprehensive study programme in 2011, the macro particles causing beam losses around the MKIs were identified as fragments originating from the ceramic tube inside the MKI magnets [7]. Thus, the ceramic tube of MKI8D installed during TS3 was subjected to improved cleaning, which included iterations of flushing of the inside of the tube with N<sub>2</sub> at 10 bar and dust sampling, until no significant further reduction of macro particles was noted. Before TS3, MKI8D exhibited the highest rate of beam–dust particle interactions of all MKIs in P8; the replacement MKI8D, in operation after TS3, exhibited the lowest rate. Extensive additional cleaning was carried out on the ceramic tubes installed during LS1.

Modification of the series of MKI magnets is not part of the HL-LHC baseline. The necessity of the described changes for the series of magnets depends on the performance of the magnets installed in LS1 and

the final beam parameters to be used for the HL-LHC beams (especially the bunch length). The installation of a prototype magnet to test the developed technologies is foreseen.

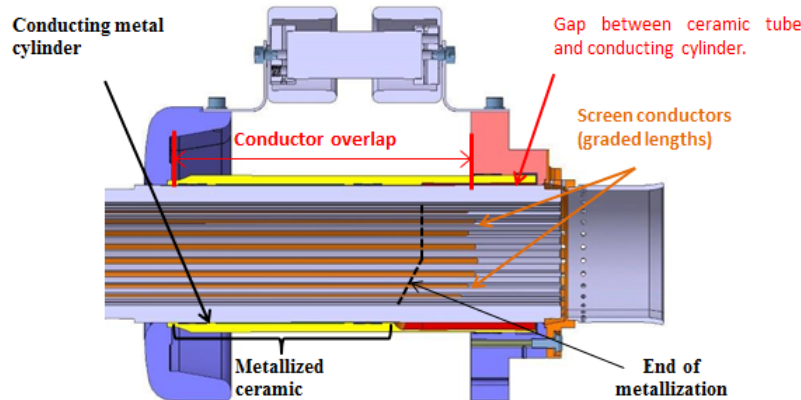


Figure 14-4: View of the capacitively coupled extremity of the MKI beam screen supporting the 24 screen conductors and the conductor overlap (courtesy of M.J. Barnes).

### 14.3 Beam dumping system

The beam in the LHC is aborted or dumped by a dedicated system based on pulsed extraction kickers and DC septum magnets located in the dedicated insertion in P6, followed by a dilution kicker system MKB, a long drift chamber, and a graphite beam dump absorber block (TDE) kept under  $N_2$  gas at atmospheric pressure. The  $3 \mu s$  rise time of the extraction kicker field is synchronized by a highly reliable timing system to a beam-free abort gap in the circulating bunch pattern. The horizontal and vertical dilution kickers are powered with anti-phase sinusoidal currents in order to paint the bunches onto the TDE with an elliptical shape, see Figure 14-5.

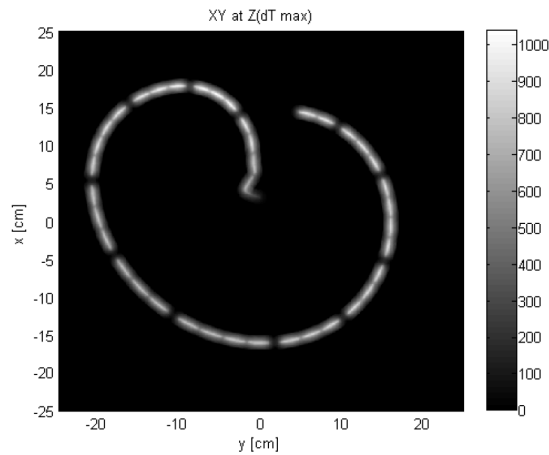


Figure 14-5: Sweep form of 25 ns spacing LHC beam on TDE dump block with a bunch intensity of  $1.7 \times 10^{11}$  protons per bunch and the resulting temperature rise.

#### 14.3.1 Beam dumping system limitations

The LHC beam dump block TDE and its entrance window [8, 9] will need to withstand the high intensity HL-LHC beams. Simulations are foreseen to verify if the present system can withstand the repeated beam impact of these beams. Concerns are the temperature rise of the TDE block, which could lead to a venting of nitrogen overpressure within the TDE. Another concern is the entrance window of the TDE. As a possible solution the installation of additional dilution kicker magnets on the beam dump lines TD62 and TD68 could be required.



As the performance mentioned above can possibly be met by the existing system, any modifications are not part of the present baseline.

14.3.2 Beam dumping system absorber (TCDS)

Several failure modes exist in the synchronization system and in the kicker switches that could lead to an asynchronous dump, in which the full beam intensity would be swept across the LHC aperture by the rising kicker field. Without dedicated protection devices this would lead to massive damage of the LHC magnets in LSS6 and the downstream arcs 5–6 and 6–7 and, depending on the operational configuration, a number of collimators and possibly experimental triplet magnets. The protection devices against asynchronous beam dumps are shown in Figure 14-6: the TCDS is a fixed absorber that protects the downstream extraction septum MSD, and the TCDQ is a movable absorber that, together with the secondary collimator TCS, protects the superconducting quadrupole Q4 and further downstream elements, including the arc. The increased beam intensity and brightness for the HL-LHC requires a redesign of the TCDS and TCDQ absorbers.

An upgraded TCDQ will already be installed before LHC Run 2. The new design, which is described in detail in Ref. [10], includes an extension of the absorber length from 6 m to 9 m, and the replacement of the higher density graphite absorber material by different grades (1.4 g/cm<sup>3</sup> and 1.8 g/cm<sup>3</sup>) of carbon fibre composites (CfC). The energy deposition and induced thermal stresses then remain acceptable during an asynchronous abort and the protection of Q4 and downstream elements remain sufficient, with a maximum energy density in the magnet coils of around 20 J/cm<sup>3</sup>. The TCS collimators will be upgraded with integrated button BPMs in the jaws, which should allow faster and more accurate setup.

A similar level of redesign will be needed for the TCDS absorber. There is one TCDS system, currently consisting of two units per beam. The robustness of the present TCDS and the protection of the MSD magnets in the case of an asynchronous beam dump with full intensity HL-LHC beams need to be verified, and the absorber material and/or length need to be adapted if necessary. Any additional length will slightly reduce the aperture for the circulating or extracted beams by a small fraction of a sigma, which should be acceptable.

A further upgrade of the TCDQ is not part of the HL-LHC baseline; an upgrade of the TCDS is.

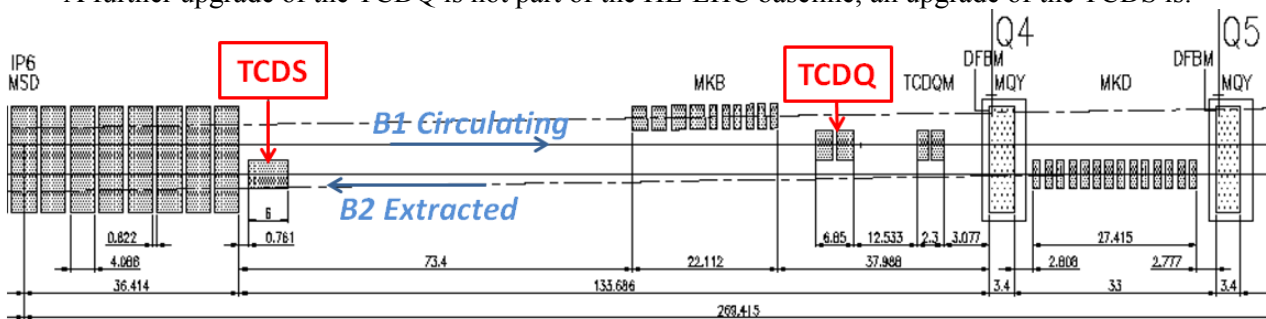


Figure 14-6: Schematic layout of the beam dump area right of P6 as used during LHC Run 1, showing the extraction absorber element TCDS on Beam 2 and the TCDQ on Beam 1.

14.4 References

- [1] J. Uythoven *et al.*, Upgrades to the injection and beam dumping systems for the HL-LHC project, Proc. 5th International Particle Accelerator Conference, Dresden, Germany, 15 - 20 Jun 2014, pp. MOPRO032. <http://www.JACoW.org>.
- [2] B. Goddard, V. Kain and M. Lamont, Function and operating conditions of the TDI beam absorber, functional specification, EDMS 508735 (2004).
- [3] ALICE collaboration, The zero degree calorimeters for the ALICE experiment, CERN-ALICE-PUB-99-17 (1999).
- [4] V. Kain *et al.*, The expected performance of the LHC injection protection system, 9th European Particle Accelerator Conference, Lucerne, Switzerland, 5 - 9 Jul 2004, pp. 584.

- [5] M.J. Barnes *et al.*, Upgrade of the LHC injection kicker magnets, 4th International Particle Accelerator Conference, Shanghai, China, 12 - 17 May 2013, pp.729, MOPWA030. <http://www.JACoW.org>
- [6] T. Baer *et al.*, UFOs: Observations, statistics and extrapolations, Proc. LHC Beam Operation workshop, Evian, 17–20 December 2012.
- [7] B. Goddard *et al.*, Transient beam losses in the LHC injection kickers from micron scale dust particles, IPAC'12, 2012, TUPPR092. <http://www.JACoW.org>
- [8] J. Zazula and S. Péraire, LHC beam dump design study: 1, simulation of energy deposition by particle cascades; implications for the dump core and beam sweeping system, CERN-LHC-Project\_Report-80 (1996).
- [9] B. Goddard *et al.*, A large diameter entrance window for the LHC beam dump line, LHC Project Report 823 (2005).
- [10] R. Versaci, B. Goddard and V. Vlachoudis, LHC asynchronous beam dump: Study of new TCDQ model and effects on downstream magnets, CERN-ATS-Note-2012-084-MD (2012).

# Chapter 15

## Integration and (De-)installation

*P. Fessia\* and S. Weisz*

CERN, Accelerator & Technology Sector, Geneva, Switzerland

### 15 Integration and (de-)installation

#### 15.1 Geographical distribution of HL-LHC upgrade interventions

The HL-LHC will require modifying the machine and infrastructure installations of the LHC in several points along the ring, in particular P1, P2, P4, P5, P6 and P7.

While the equipment in P1, P5, and P6 are meant to be installed during Long Shutdown 3 (LS3), the modifications and improvement in P4, P7 (as far as the superconducting links are concerned), and P2 shall be completed during LS2 and be operational for LHC Run 3. Below we list the activities required point by point according to the presently foreseen chronological order. P8 will have minor modifications during LS2, which are not considered here.

#### 15.2 Point 4

P4 will be equipped with a new cryogenic plant dedicated to the RF systems (and other cryogenic equipment that might be installed in IR4) (Chapter 9 Section 9.5). The installation will require:

- surface: installation of the warm compressors systems in SU4;
- junction surface to the underground cavern via PX46;
- underground: installation of the cold box in TX46 (see Figure 15-1);
- connection between the cold box and QRL via UX45;
- QRL modification between -25 m and +25 m around IP4.

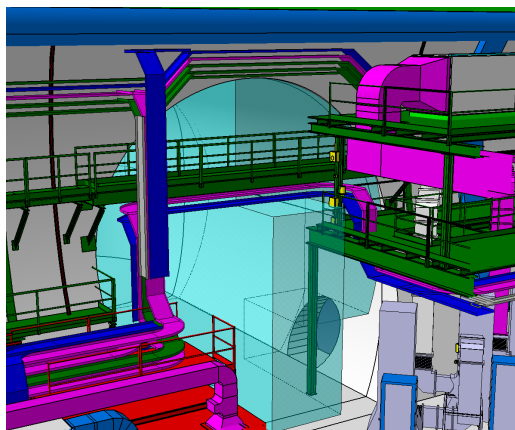


Figure 15-1: Volume reserved for the installation of the new cold box unit dedicated to RF system cooling (light blue).

---

\* Corresponding author: [Paolo.Fessia@cern.ch](mailto:Paolo.Fessia@cern.ch)

The solutions presently adopted make the maximum use of existing volumes, requiring very limited civil engineering work, mainly devoted to the routing of the piping from SU4 to SX4 and to the vertical wall of PX46. The whole system installation shall be completed for the end of LS2. Figure 15-2 provides a schematic of the P4 buildings.

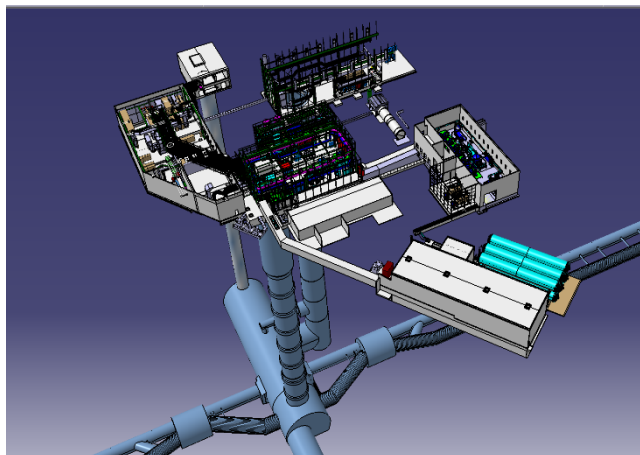


Figure 15-2: View of the LHC civil works at P4

### 15.3 Point 7

#### 15.3.1 The horizontal superconducting links

In P7 two horizontal SC links will be installed in order to electrically feed the 600 A circuits connected to the two DFBAs (DFBAM and DFBAN). The related power converters will be installed in TZ76 and via short warm cables will be connected to the superconducting link. The two superconducting links will then run for about 220 m in TZ76 and then enter the LHC machine tunnel via UJ76. They will then be routed for about 250 m in the LHC tunnel in order to be connected to DFBAM and DFBAN (Figure 15-3). The whole installation shall take place during LS2; no long access period is available before that time. Possibilities to advance part of the interventions in the year end technical stop (YETS) shall be evaluated, and the time for radiological cooling will be used for the preparation of the interventions in the LHC tunnel. Some preparatory work has been performed already during LS, in particular the removal of the chill water pipes. This system was not of use in P7 and its dismantling has made space available for the SC link installation.

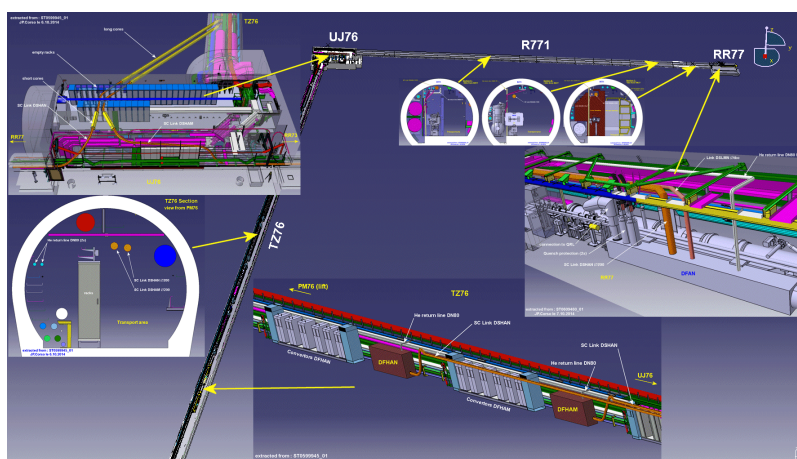


Figure 15-3: View of the foreseen installation of the superconducting link system at P7. Power converters in TZ76, routing of the link from TZ76, via UJ76 to RR77.

In order to perform the installation of the SC links in the LHC tunnel the need for de-installing part of the present equipment (as a precaution for avoiding possible damage) still needs to be fully assessed.

### 15.3.2 New collimators in the dispersion suppressor

In order to protect the superconducting magnets (excess heat deposition) from off-momentum proton leakage from the main collimator system itself, some special collimators must be installed in the dispersion suppression region, i.e. in the continuous cryostat. The evaluation of the real need for this modification will be completed based upon the first results of LHC Run 2. Unless Run 2 shows dramatic and unexpected results, the installation will eventually take place during LS3.

In order to cope with the proton losses in the dispersion suppressor area it has been decided to install two collimators on each side of the IP. In order to do so it will be necessary to:

- de-install MB.B8L7 plus MB.B10L7 and the symmetric MB.B8L7 plus MB. B10L7;
- substitute each removed dipole with a unit composed of two 11 T dipoles (Chapter 11) separated by a cryogenic bypass;
- install the collimator on the top of the cryogenic bypass (Chapter 5).

The magnet installation will also probably require a new dedicated quench protection system and a trim circuit with its own power converter. The location and the installation approach for this equipment are still under evaluation, but very probably it will be located in the nearby RR.

### 15.4 Point 2

In order to limit the heat deposition from collision debris in the superconducting magnets during the ion run, collimators in the dispersion suppressor will also be installed in P2 (Chapter 5). In this case the installation will take place only in one slot on each side of the IP replacing MB.A10L2 and MB.A10R2. This equipment is necessary for LHC Run 3 with ions, to allow Alice to fully profit from the upgrade carried out during LS2. Therefore, the installation of the unit comprising the 11 T dipoles and the cryo-bypass needs to be completed during LS2. The collimator itself can be assembled at the same time or later in a short technical stop or in a YETS. All the other issues listed in Section 15.3.2 are applicable, but the proximity services will probably be installed in the UAs.

### 15.5 Point 6

In P6 the two Q5 quadrupole magnets will be modified in order to fulfil the needs of the new HL-LHC ATS optics. Two options are presently under evaluation leading either to the exchange of the present Q5 with a new Q5 or the installation of Q5-bis near the currently operated Q5. Both options will require the local reshuffling of the vacuum layout and possible modifications to QRL.

The intervention in P6 is required to be completed in LS3, but options to anticipate it in LS2, both to limit the amount of work during LS3 and to reduce personnel exposure to radiation due to the proximity to the beam dump line, are under study.

### 15.6 Point 1 and Point 5

The largest part of the new equipment required by the HL-LHC performance objectives will be installed in P1 and P5. The items to be installed and actions to be carried out are listed below, and are applicable to both points if not otherwise specified. The list is organized by geographical areas.

#### 15.6.1 LHC machine tunnel

De-installation.

- All the machine equipment from the interface with the experimental cavern (TAS included) until the DFBA (included) requires removal.
- The present QRL will be removed from the same area. A new return module will be installed in the ex-DFBA area in order to allow separation of the coolant flows coming from the LHC QRL and one of the new HL-LHC QRLs that will feed part of the machine from Q1 to Q6. This return module should also provide the possibility, if required, to connect the LHC QRL with the newly installed one, ensuring an increased level of redundancy in the system.
- Services linked to the above de-installed equipment will be removed and new ones shall be installed:

Preparation for re-installation.

- Minor works could be necessary in order to prepare the tunnel floor and wall to receive the installation of the new equipment (for larger and dedicated civil engineering works as described below).

Installation of the new equipment, probably in the following sequence:

- TAXS;
- services;
- QRL with related valve and service modules;
- horizontal superconducting links from the DFM to the magnets to be fed;
- Magnets and crab cavity support system;
- magnets and crab cavity;
- distribution feedboxes (DFX) for the Q1 to D1 magnet system and distribution feedboxes (DFM) for the D2 to Q6 magnet system.

The sequence of installation of the vertical superconducting links to be connected to the DFX and DFM still need to be assessed according to the options retained for their routing.

In addition to the interventions described above, it may be necessary to strengthen the collimation system with new collimators in the dispersion suppressor as described for P7 in Section 15.3.2.

#### 15.6.2 Existing LHC tunnel service areas

The RRs on both sides of P1 and P5 will need to be re-organized, and in particular the following will be necessary.

- To de-install the power converter and other related systems (e.g. the quench detection system) linked to the powering of the removed LHC matching section.
- To re-organize the remaining equipment in order to have the most efficient space occupation, increase if necessary the radiation shielding, and place the most radiation-sensitive equipment in the most protected areas. Possible equipment replacement with new radiation-hard elements can be envisaged.

At present no civil work interventions are foreseen in the RRs areas.

#### 15.6.3 New HL-LHC tunnel service areas

The installation of the new cryogenic plant in P1 and P5 will have two objectives:

- to provide independent and redundant cooling capacity to feed the final focus and matching sections left and right of each of the two high luminosity insertions for the LHC;
- to provide redundancy to the cryogenic plant installed to cool the experimental systems.

The cold boxes shall be installed in underground areas. At present the required volume does not exist. Therefore conceptual studies have started in order to identify the best options for building new underground caverns to install this equipment and the related service and control system. Figure 15-4, Figure 15-5, and Figure 15-6 correspond to solutions with power converters in the underground areas while Figure 15-7 corresponds to a solution with magnet power converters on the surface (baseline).

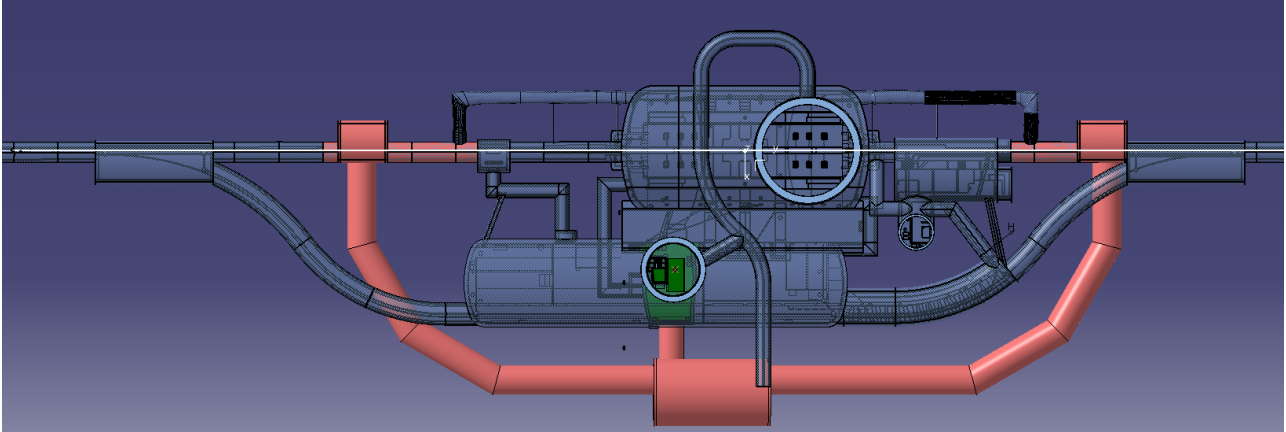


Figure 15-4: Possible option for underground work at P5 including links to the LHC tunnel. This solution is without an independent shaft to access to the surface. New structures are in light red, and zones of the LHC tunnel to be impacted by construction the new structures are in green.

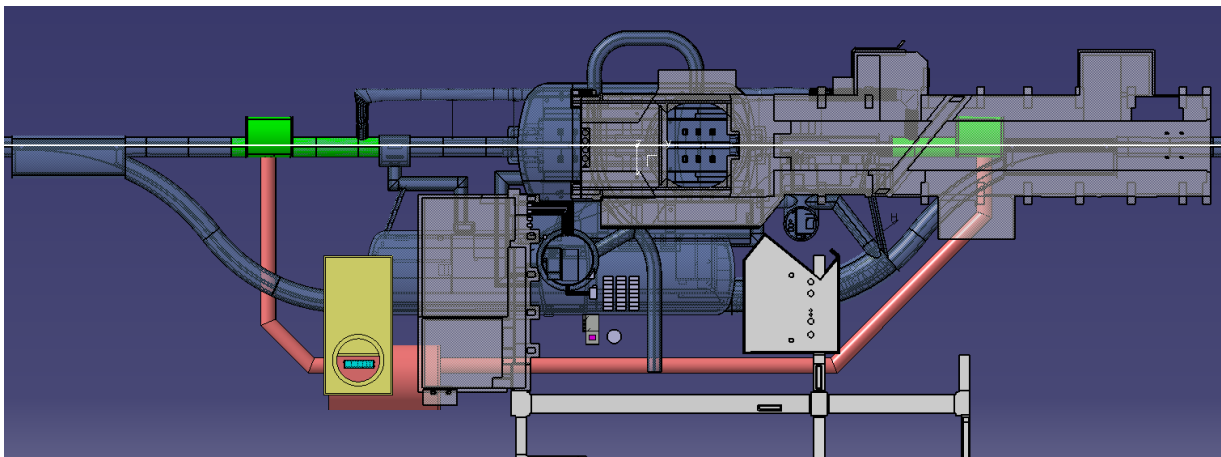


Figure 15-5: Possible option for underground work at P5 including links to the LHC tunnel. This solution has an independent shaft for access to the surface. New structures are in light red and yellow, and zones of the LHC tunnel to be impacted by construction of the new structures are in green.

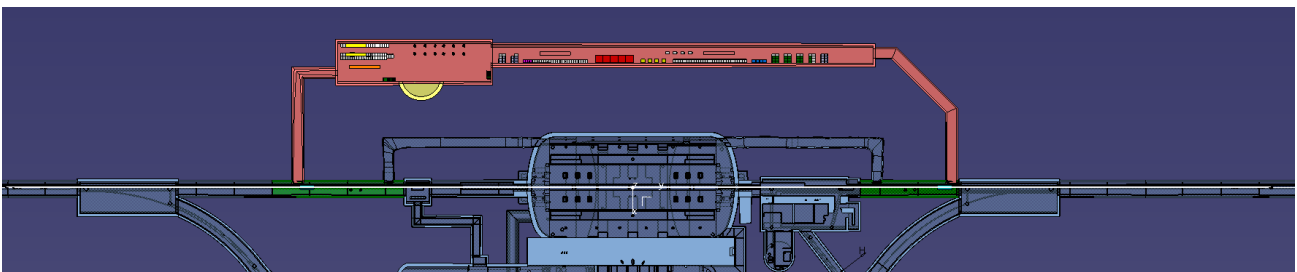


Figure 15-6: Possible option for underground work at P5 including links to the LHC tunnel. This solution has an independent shaft for access to the surface, and a larger connection tunnel for possible power converter underground installation. New structures are in light red and yellow, and zones of the LHC tunnel to be impacted by construction of the new structures are in green.

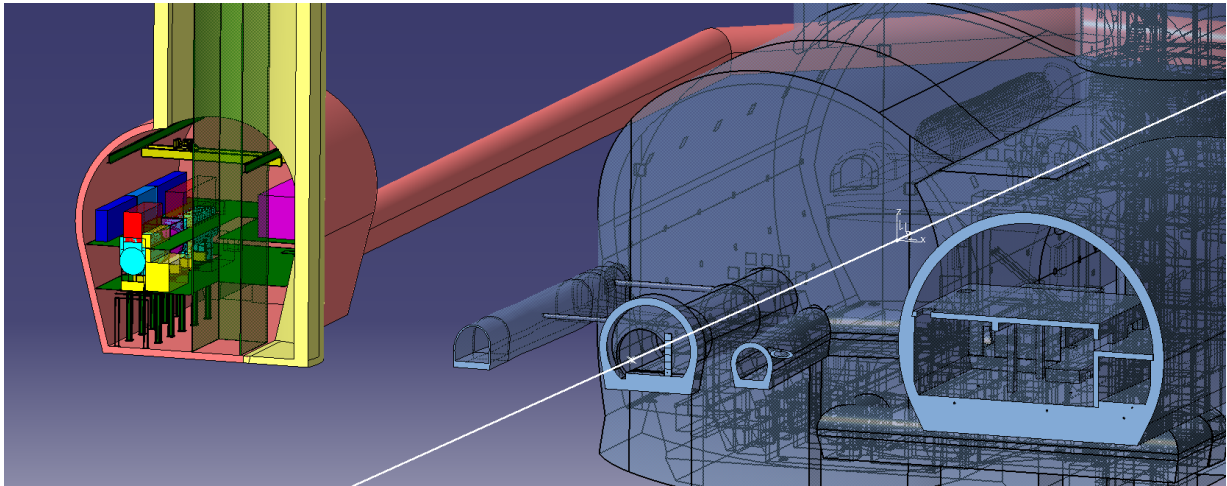


Figure 15-7: Possible option for underground work at P5 including links to the LHC tunnel. This solution has an independent shaft for access to the surface. A cross-section through the cryogenic equipment is shown. New structures are in light red and yellow.

#### 15.6.4 New connection from the LHC tunnel and HL-LHC service areas to the surface

The following connections between the surface and the underground installation shall be made available.

- LHC tunnel and crab cavity area to the surface. The crab cavities need to be connected to the dedicated RF power system and their control system. The present preferred choice is to install these services in dedicated surface buildings (see below). The underground to surface connection will need to house eight RF coaxial cables (each about 300 mm in diameter), plus the required control cables. Two options are being studied.
  - The construction of eight ducts over each crab module, linking directly the tunnel vault with the surface crab service building.
  - The construction of a shaft where all the previously listed cables can be hosted together. In this case a local enlargement of the LHC tunnel will be necessary. Alternatively there will be a need for the construction of a separate small cavern where the shaft will end. The extra underground work is necessary to take into account that the minimum shaft dimension is larger than the LHC tunnel diameter.
- New HL-LHC service area to the surface. These connections are necessary to link the surface part of the cryogenic plant with the cold box installed in the new underground HL-LHC service areas.
- Vertical routing of the superconducting links. In each point at least four superconducting links will need to be routed from the surface to the underground areas. Three options are possible and they are listed from most to least convenient:
  - installation of the superconducting links in the same vertical duct linking the cryogenic plant to the surface;
  - installation of the superconducting links in the same vertical duct linking the crab cavity to the surface;
  - installation of the superconducting links in new dedicated vertical ducts.

#### 15.6.5 New surface installation

The following installations shall find space on the surface for P1 and P5 installations.



## INTEGRATION AND (DE-)INSTALLATION

- Crab cavity RF power and services hosted in two ad hoc surface buildings (yellow boxes in Figure 15-8). They shall be positioned on the surface, directly above the tunnel position where the crab cavities will be installed. There will be two surface buildings for each point, one on the lefthand part of the machine and one on the righthand part. The surface extremities of the ducts/shaft for the crab cavity coaxial leads or shaft shall be housed inside this building. The part of the building with the controls system shall be electromagnetic shielded.
- Cryogenic installation. The warm compressors and the other parts of the cryogenic plant shall be installed on the surface.
- Power converters, upper extremities of the superconducting links, protection systems, and energy extraction system related to the circuits fed via the superconducting link. This area may possibly be located near the surface part of the cryogenic plant and in any event on top of the surface routing of the vertical superconducting link.

Currently it looks very difficult to find the required space in existing buildings; therefore the construction of new structures to host the systems listed above is probably necessary (Figure 15-9).



Figure 15-8: Surface position of the two new crab cavity service buildings (in yellow) at P5

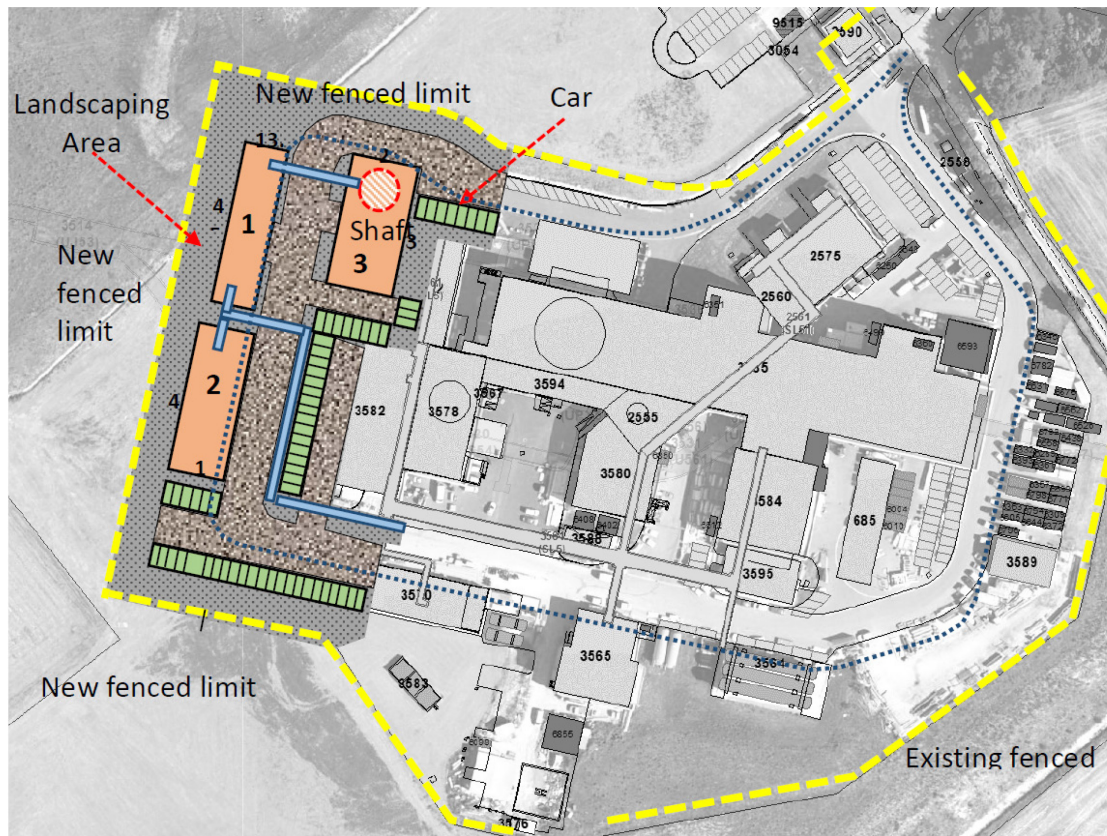


Figure 15-9: Preliminary study of the LHC P5 building footprint. Building 1: power converters and SC link terminals; Building 2: cryogenic surface equipment; Building 3: access to shaft. Possible technical galleries are in light blue.

In addition to the above mentioned options, a solution, where the power converters and the crab cavity ancillaries would also be installed underground, is under study. Such an option would lead to an underground structure of much larger volume, but the increase in cost could be partially balanced by a reduction in the number of cores from the surface to the tunnel, a reduction in the numbers of surface structures to be built, and the simplification of the surface worksite.

#### 15.6.6 Activity sequence considerations

While the sequence of intervention on the underground LHC installed equipment (machine and RR) is quite clear and linked to the end of the LHC Run 3, the sequence for the other installation and civil work activities is still under evaluation. The worksite organization will depend upon the options chosen. This is why, in the evaluation of the selection of the final solutions for the underground caverns, the connection tunnel to the surface, and the surface building, three main parameters shall be taken into account. These are cost, the possibility of performing the work in advance with respect to the LS3 start date, and the ease of installation and connection, since some options could lead to very complex and cross-connected installation worksites, making LS3 unacceptably long.

# Chapter 16

## Commissioning and Operation

*M. Lamont\*, M. Pojer and J.M. Jowett*

CERN, Geneva, Switzerland

### 16 Commissioning and operation

#### 16.1 Commissioning and operation

At the point of commissioning and subsequent operation of the HL-LHC, the LHC itself will have been operational for over 10 years and a wealth of knowledge and experience will have been built up. The key operational procedures and tools will have been well established. The understanding of beam dynamics will be profound and refined by relevant measurement and correction techniques. Key beam-related systems will have been thoroughly optimized and functionality sufficiently enhanced to deal with most challenges up to that point. Availability will have been optimized significantly across all systems. This collected experience will form the initial operational basis following the upgrade.

However, the HL-LHC will pose significant additional challenges. The target integrated luminosity will make considerable demands on machine availability and operational efficiency. The planned beam characteristics will push beam dynamics to new limits. In the following discussion the operational cycle is revisited in light of the key HL-LHC challenges. The expectations and issues relating to availability in the HL-LHC are then outlined.

The planned bunch intensity,  $\beta^*$ , and compensation of the geometrical reduction factor lead to a potential bunch luminosity well above the acceptable maximum in terms of pile-up for the experiments. Thus, as discussed in Chapter 2, an obligatory operational principle of the HL-LHC will be luminosity levelling. The aim is to reduce a potential peak or virtual luminosity to a more manageable levelled value by some luminosity reduction technique. As the number of particles in the beam falls with time, appropriate adjustments keep the luminosity at the levelled value. The options include the use of transverse offsets, crab cavities, variation of the crossing angle, and dynamic change of  $\beta^*$ . A combination (e.g. dynamic change of  $\beta^*$  and crab cavities) will be deployed. The longitudinal pile-up density is another critical parameter for the experiments, which must be taken into account during the levelling process.

##### 16.1.1 The nominal cycle

The nominal operation cycle provides the framework underpinning luminosity production. Given the higher than ever stored beam energy of the HL-LHC era, the nominal cycle must be fully mastered for effective, safe operation. As of 2012, the nominal operational cycle is well established for 50 ns and bunch population exceeding nominal. A brief outline of the phases of the nominal cycle follows.

- Pre-cycle. Following extensive experience during Run 1, it is known that the magnetic state of the machine can be re-established before every fill by rigorous application of either a combined ramp-down/pre-cycle of the main circuits and a de-gaussing of the corrector circuits, or, following an access, by a full cycle of all circuits.
- Set-up. The machine settings are verified with the injection of a limited number of bunches that have a reduced population (pilot, one bunch) or nominal population (intermediate, 12 bunches).

---

\* Corresponding author: [Mike.Lamont@cern.ch](mailto:Mike.Lamont@cern.ch)

- Injection. The two LHC rings are progressively filled with trains of bunches transferred from the SPS to the LHC. The injection process should be well optimized by the time of the upgrade. However, high bunch intensities will have to be anticipated and all necessary mechanisms to minimize particle loss and emittance blow-up, and maximize reproducibility, should be deployed.
- Ramp. Once the machine is filled with the required number of bunches, the beams are accelerated to top momentum (up to 7 TeV/c). The ramp should hold no surprises. The characteristics of snap-back and correction of associated parameter swings can be taken as given. The 10 A/s ramp rate for main dipole power converters will still hold. Transverse feedback and tune feedback, and their healthy cohabitation, should be anticipated. Orbit feedback will be mandatory. Controlled longitudinal blow-up will be required.
- Squeeze. The mechanics of the squeeze including feedback will have to have been fully mastered. Issues of beam instabilities should have been resolved and might include squeezing with colliding beams. Again, this should have been made operational before the HL-LHC era. The possibility of combining the part of the squeeze process in the ramp is being considered to reduce the time required for the squeeze process.
- Adjust. At the end of the squeeze the beams are brought into collision at the interaction points. There is some flexibility in sequencing the order in which the beams are collided in the different interaction points. The process is relatively fast and will be well established.
- Stable beams. Once all the above procedures are completed and no abnormal conditions are detected, the conditions are met for safely switching on the detectors and the start of data taking. In general, this phase is expected to be stable with sufficient Landau damping from beam-beam, and small movements in beam overlap, thanks to good orbit stability. Emittance growth and losses to the collimation regions must be anticipated.

The principal challenges during the cycle involve injection, and transmission through the cycle of high bunch and high beam current, while preserving emittance. Given the experience of LHC operations thus far, the following potential issues may be identified:

- electron cloud;
- UFOs;
- localized beam-induced heating of specific hardware or vacuum assembly non-conformities – this can result in outgassing and bad vacuum as a result;
- cryogenic heat load;
- excessive beam loss in the cleaning sections.

High bunch population implies the need for very good parameter control and the need to properly control beam loss through the cycle. Beam instabilities will have to be fully under control using a variety of measures. Low  $\beta^*$  implies strong non-linearities from the inner triplets and the need for associated correction. On the positive side, the HL-LHC should be able to count on excellent magnetic reproducibility and good stability. Hardware systems such as power converters, RF, and transverse dampers have already demonstrated impressive performance.

### 16.1.2 Availability and operational efficiency

The terms relevant to the year-long operational view are defined below.

- Scheduled proton physics time (SPT) is the time scheduled in a given year for high luminosity proton physics. It does not include initial re-commissioning, special physics runs, ions, machine development (MD), and technical stops. It does include the intensity ramp-up following re-commissioning at the start

of the year. Note that high luminosity running involves a number of challenges not present in other modes of operation, and different machine availability can be expected.

- Availability is the scheduled proton physics time minus the time assigned to faults and fault recovery. It is normally expressed as a percentage of the SPT. Edge effects (e.g. recovery from access, the pre-cycle) should be fully included in the assigned fault time.
- The turnaround time is defined as the time taken to go from stable beam mode back to stable beam mode in the absence of significant interruptions due to fault diagnosis and resolution.
- Physics efficiency is the fraction of the scheduled physics time spent in stable beams.

**16.1.2.1 Standard year of operation**

The longer-term operational planning consists of a series of long years of operation (see Table 16-1) interspersed with long shutdowns of the order of a year or more. The long shutdowns are foreseen for essential plant maintenance, experiment upgrades, and so forth. It is estimated that the required length of a standard long shutdown in the HL-LHC era will alternate between 16 and 20 months. The approximate breakdown of a generic long year is:

- 13 weeks for the Christmas technical stop, including two weeks for hardware commissioning (this would account for three weeks at the end of a year and for 10 weeks at the start of the following year);
- around 160 days proton–proton operation;
- three technical stops of five days duration during the year;
- a four-week ion run (the working assumption is that the ion programme continues into the HL-LHC era; this is not to say that the HL-LHC will operate with ions for its total period of operation);
- time dedicated for special physics and machine development.

A more detailed breakdown is shown in Table 16-1.

Table 16-1: Potential breakdown of a standard HL-LHC year

Activity	Time assigned [days]
Christmas technical stop including hardware commissioning	91
Commissioning with beam	21
Machine development	22
Scrubbing	7 (to 14)
Technical stops	15
Technical stop recovery	6
Proton physics including intensity ramp-up	160
Special physics runs	8
Ion run setup	4
Ion physics	24
Contingency	7

**16.1.2.2 Availability and operation efficiency**

The HL-LHC will place challenging demands on availability and operational efficiency if the ambitious integrated luminosity goals are to be met. Given that the requisite high intensity beam can be injected, ramped, squeezed, collided, and the luminosity levelled, the principle operational challenges will be assuring high availability and maximizing physics efficiency.

### 16.1.2.3 Faults

Faults cover an enormous range from a simple front-end computer reboot, to the loss of a cold compressor with corresponding loss of time, to operations ranging from 10 minutes to potentially days. The impact of a typical fault requiring tunnel access shows the following sequence of steps from the occurrence of the original fault through to full recovery.

- Premature beam dump in stable beams.
- Original diagnosis of fault by control room operator – contact expert.
- Remote diagnosis by expert.
- Access required and prepared.
- Travel of expert to site. Travel of radiation protection piquet to site.
- Intervention, on-site diagnosis, and repair by expert.
- Recovery from access.
- Recovery from the impact of the fault (for example, cool-down following quench).
- Re-establish machine state: pre-cycle, injection, etc.

It can be seen that, besides the cost of fixing a fault, there are also significant additional overheads. Faults often dump the beam with the cost of at least a full turnaround to re-establish the state of the machine. The cost in turnaround time and the fault recovery component are examined in more detail below.

### 16.1.2.4 Turnaround time

A breakdown of the foreseen HL-LHC turnaround time is shown below.

Table 16-2: Breakdown of turnaround and estimated minimum time for each phase

Phase	Time [minutes]
Ramp-down/pre-cycle	60
Pre-injection set-up	15
Set-up with beam	15
Nominal injection	20
Prepare ramp	5
Ramp	25
Flat-top	5
Squeeze	25
Adjust/collide	10
Total	180

From Table 16-2, one can see that realistically a three-hour minimum turnaround time may be assumed in the HL-LHC era. The main components are the ramp-down from top energy, the injection of beam from the SPS, the ramp to high energy, and the squeeze. The ramp-down, ramp, and squeeze duration are given by the current rate limitations of the power converters. Of note is the 10 A/s limit up and down for the main dipoles, the need to respect the natural decay constants of the main quadrupoles, the individually powered quadrupoles, and the triplets during the ramp-down and the squeeze. These quadrupoles are powered by single quadrant power converters, and it takes a considerable time for the current to fall to the required level. A faster pre-cycle via upgrades to the power converters might be anticipated. Two quadrant power converters for the inner triplets, for example, would remove them as a ramp-down bottleneck.

In practice, the turnaround has to contend with a number of issues that could involve lengthy beam-based set-up and optimization. Typical beam-based optimization might include the need to re-steer the transfer lines, occasional energy matching between the SPS and LHC, and the need for the SPS to adjust scraping

during the injection process. Injector and LHC tuning and optimization are accounted for in the average turnaround time.

#### 16.1.2.5 Lost fills and fill length

Another important consideration directly impacting operational efficiency are the overheads of losing a fill (in the ramp, in the squeeze, in physics). In 2012, for example, 70% of all fills were terminated by a fault with costs ranging from a full turnaround plus fault recovery time to curtailed stable beam time. In 2012, having made it into stable beams, operations experienced a lot of short unproductive fills because of premature dumps. The cost of the short fills is a corresponding number of extra turnarounds that directly lead to lost time for physics. All means must be used during Run 2 and Run 3 to target all causes of premature dumps. In the HL-LHC era a choice of robust operating parameters must be made to avoid losing fills to high beam loss and instabilities during the cycle.

#### 16.1.3 Discussion

A number of studies have been made that model the potential integrated luminosity that can be delivered by the HL-LHC at a levelled luminosity of  $5 \times 10^{34} \text{ cm}^{-2} \text{ s}^{-1}$ . All conclude that it will be challenging to deliver  $250 \text{ fb}^{-1}$  per year. Every attempt must therefore be made to target high availability, shorter turnaround times, and a low number of premature dumps. Some of the main areas that might be targeted in the interest of improved availability and operational efficiency have been identified.

- Reduce the number of faults (hardware and software) – this is the natural target for improved availability. It requires targeted improvements and consolidation across all systems.
- Reduce time to fix faults, reduce intervention times, and reduce the number of tunnel interventions (for example by universal remote reset functionality, improved remote diagnostics, or increased redundancy).
- Reduce number of beam-induced faults (R2E, beam-induced heating, vacuum issues).
- Reduce the mean turnaround time. Here it is possible to imagine targeting routine optimization, test runs, and the nominal cycle.
- Choose a robust set of beam parameters to avoid unnecessary dumps from beam-related issues.

## 16.2 Hardware commissioning

### 16.2.1 Commissioning of the superconducting circuits

#### 16.2.1.1 Testing of the superconducting links in short-circuit configuration

All superconducting links [1] will be individually (cryogenically and electrically) tested in the SM18 magnet test facility prior to installation in the tunnel [2]. As is the case for all superconducting elements installed in the machine, these links will have to be further tested in situ to assess that no degradation occurred during transport and installation.

A test similar to those currently performed on the warm part of all superconducting circuits is suggested, with one extremity in short-circuit configuration: the electrical connections to the power converters are the nominal ones; the conductor at the other extremity of the link is not connected to the magnets, but short-circuited, in a configuration that allows powering up to the nominal current of all busbar pairs. The link will have to be cooled down to its nominal temperature; thus the configuration and the precise place of short-circuit installation will be decided in accordance with the final design of the connection boxes (DFMs and DFXs), also taking into account the planning constraints.

Once the short-circuit is installed and the nominal cryogenic conditions established, a high voltage qualification (EIQA) of all lines will be performed in order to validate the galvanic insulation versus ground

and the capacity of all lines to withstand the mutual high voltages developed during a fast change of current in the different circuits (typically during a fast abort or quench). The values of voltages to be applied and the maximum acceptable leakage current values will be defined at a later stage; Ref. [3] will have to be updated correspondingly.

After the EIQA validation, all lines can be powered. The powering will consist of several phases, each of them to be analyzed and approved by the experts, before progressing to the next phase. At each phase the cryogenics team will have to verify the correct behaviour of the cryogenic system and cooling loop. Each circuit should be powered to increasing current levels (e.g. minimum operational current, 25% of nominal, 50% of nominal, and nominal current). At each current level, the powering, protection, and cryogenic systems will be qualified. The detailed steps and qualification criteria will be identical to those prepared for SM18 and will have to include the simultaneous powering of different circuits, and stress tests such as the fast discharge of a line with all of the others powered at nominal current in order to study the cross-talk between them.

### 16.2.2 Electrical Quality Assurance tests

As stated in Ref. [3], the objective of the EIQA tests is to release each individual superconducting circuit for powering, to gather all the necessary electrical parameters for operation, and to track all the data acquired and to manage the related non-conformities.

#### 16.2.2.1 EIQA at warm

At the end of the installation and connection of all magnets, resistance measurements and a high voltage qualification of all circuits will be performed: to check whether the circuit is closed, determine a reference resistance value at warm, and to validate the galvanic insulation versus ground. The values of voltages to be applied and the maximum acceptable leakage current values will be defined at a later stage.

#### 16.2.2.2 EIQA at cold

Similar tests will be performed at cold, with larger test voltages applied. The circuits and the corresponding link will be cooled down to their nominal temperature. For the high voltage qualification of all lines, this will be performed to validate the galvanic insulation versus ground and the capacity of all lines to withstand the mutual high voltages developed during a fast change of current in the different circuits (typically during a fast abort or quench).

The high voltage qualification also includes testing of all the elements that are electrically connected to the tested circuit. Such elements are:

- the instrumentation and feedthrough systems;
- the magnet protection units;
- the temperature sensors with the related tunnel cabling and electronics;
- the tunnel cabling for routing the voltage taps used for the protection of the superconducting circuits.

In addition, transfer function measurements will be performed, with the aim of determining the impedance as a function of the frequency. The results of these measurements are used to spot possible inter-turn shorts, and by the power converter group to adjust the power converter regulation.

The values of voltages to be applied and the maximum acceptable leakage current values will be defined in a later stage and Ref. [3] will be updated accordingly.

### 16.2.3 Powering tests

The HL-LHC magnets present several peculiarities [4] that have to be kept in mind for their commissioning. The most relevant are: the fact that all magnets will be cooled down to 1.9 K (instead of 4.5 K as are all present matching section magnets); that Nb<sub>3</sub>Sn will be used for the first time; that the current of the inner triplet and



the Q4 magnet will be the highest in the machine (close to 20 kA); and, importantly, that some of the high current magnets will be protected only via energy extraction in a dump resistor without quench heaters. In addition, the powering scheme of the inner triplet will be different from the present one, with Q1 in series with Q3; and Q2a and Q2b in series in a separate circuit: this is important in case of a quench of one of the magnets.

The powering of all circuits up to nominal current will be done in steps. At the end of each step, online and offline analyses are performed by equipment owners and protection experts to assess the performance of all hardware in the circuit. In particular, for the powering of individual circuits, several cycles at different current levels will be performed to study the performance of the magnets, the efficiency of the protection mechanisms (by provoking fast aborts and even quenches), and to check all functionalities of the powering interlocks and of the power converters (via provoked powering failures).

A typical series of tests includes:

- at minimum operational current, testing of the full interlock chain, with the verification of cryogenic signals, power permit, powering failure, circuit quench transmission, and fast power abort requests;
- at low current, a check of the power converter performance and verification of all protection functionalities, by means of provoked slow and fast power aborts, with energy extraction;
- repetition of a series of power aborts and, possibly, simulation of quenches from progressively higher current levels, with more and more energy stored (e.g. 25%, 50%, and 100% of the nominal current).

Before starting a new powering test, all previous tests must have been validated. The validation includes approval by power converter and powering interlock experts, magnet owners, and protection experts. Cryogenics experts should also confirm the correct operation of their installations and instrumentation. The criteria for approval, the parameters, and the relevant information to be stored will be discussed in due time. The first time that these will be applied is in 2019–2020, when the test of a full string of magnets (reproducing from Q1 to D1) is foreseen, powered by a superconducting link. All valuable data extracted from the test on the string will be translated in powering procedure steps and criteria.

After the individual test of all circuits up to the design current, the common powering of a set of circuits will be done for magnets that are in the same cryogenic envelope and are powered from the same link (usually referred to as the powering of a group of circuits). The objective of this simultaneous powering is to validate operation of all magnets in nominal conditions; current cycles similar to those applied in normal operation should be used for the powering of a group of circuits. Important at this stage is the behaviour with combined powering in critical conditions, such as the fast power abort of a circuit when the others are at full current. For the inner triplets, in particular, quenching in a triplet quadrupole might induce a quench in a nearby quadrupole or corrector if the current in this related circuit is not extracted fast enough. These tests should be performed on all the magnets and could well trigger the change of detection thresholds and protection configurations. Once more, all tests should be approved by a group of experts and recorded for future reference.

Particular attention also has to be paid to those circuits that are not equipped with heaters and are protected by energy extraction on a dump resistor. For such circuits, a precise estimate of the energy deposited during a quench has to be made, not only in the case of bench tests, but also in the more severe conditions of combined powering in the tunnel. Eventually, the protection threshold should be adapted to reduce energy deposition and improve magnet safety during powering.

It is important to observe that the first commissioning campaign will already take place in Long Shutdown 2 (LS2 in 2018–2019), when the 11 T Nb<sub>3</sub>Sn magnets in the dispersion suppression region around P2 will be installed. The superconducting link at P7 will be installed in the same period to power the circuits presently powered from power converters installed in RR73 and RR77. All powering procedures and commissioning steps will need to be ready by that time.

### 16.3 Hardware commissioning of the HL collimation system

The collimator settings, controls, and operational sequences should be intensively tested during the hardware commissioning phase [5]. A dedicated test to address the reproducibility of collimator movements during critical operational sequences (such as the ramp) will be performed. At this stage the collimators should have been fully installed and the local collimator controls in the tunnel fully validated.

Before beam is injected into the machine, the machine protection (MP) functionality of the collimation system must be guaranteed. Each collimator is connected to the beam interlock system (BIS) and has more than 20 interlocks that will need to be verified. The jaw positions and collimator gaps are monitored via six linear variable differential transformer (LVDT) sensors. These signals are interlocked with inner and outer limit values, making a total of 12 interlocks per collimator. In addition, there are a total of six energy-dependent and  $\beta^*$ -dependent limit functions and an interlock to protect from ‘local’ mode collimation control. The temperature of the collimators is also monitored and interlocked with minimum and maximum adjustable thresholds independently for five sensors per collimator. After successful results from these tests, the system will be ready to allow beam into the machine.

The main upgrade of the collimation system for HL-LHC [6] will ensure cleaning of beam halo and will keep losses in high luminosity experimental regions at an appropriate level. For this, the project foresees the installation of local collimation in the dispersion suppressors (DS). The design of a collimator to be installed between two short 11 T dipoles (TCLD) is ongoing. These collimators will feature the latest design improvements, including embedded BPMs for fast alignment. Altogether, between 10 to 14 TCLDs are foreseen for the HL-LHC in addition to eight new tertiary collimators and some additional secondary collimators. Depending on the final update programme, it should be possible to expect about 30 more collimators with respect to the present LHC system. Unlike other hardware commissioning tests (such as the magnets), most of the collimation commissioning can be done parasitically, the main exception being the testing of the interlock system where the BIS needs to be available.

### 16.4 Commissioning of the cryogenic systems

The HL-LHC foresees numerous modifications of the cryogenic system [7]. Among them are:

- the new cooling system for the superconducting links;
- the modifications to cool the elements that previously were at 4.5 K to 1.9 K;
- the independent RF cooling system;
- the cooling loop for the crab cavities, and much more.

The operation of all of them, together with the time needed to qualify and tune the systems, will be detailed once the design is definitive. Provisionally, an approximate time of three weeks is considered to be mandatory to commission the scheme for the superconducting magnets.

### 16.5 Commissioning of the crab cavities

As for all elements in the LHC, the crab cavities will be first tested on the surface to nominal specification prior to installation in the tunnel. In addition, some modules will be installed in the SPS for a complete qualification of the standard two-cavity module with LHC-type beams. This is presently planned for the 2017 run after the extended year-end technical stop.

The test of the cavities can be differentiated into the commissioning of the RF cavities and associated ancillary systems (cryogenics, vacuum), and RF commissioning with beam. The requirements in terms of time and manpower will be assessed later.

Concerning the commissioning of the cryogenics, the correct operation of the cooling loop and the capacity will be verified, together with the expected behaviour of the instrumentation; proper verification criteria and sequence will be defined at later time with input from the qualification of the cryogenic-module

on the surface tests. The vacuum integrity and the vacuum interlocks will be tested as well, which should cut the RF power in case of issues and during cavity conditioning.

The conditioning of the cavities will first be performed on the surface in the nominal configuration, but the commissioning of the low-level RF system (the tuning control, the regulation loop around the amplifier, plus the RF feedback) will have to be validated in the SPS for the first time in its nominal configuration. A detailed procedure for the verification of all functionalities will be prepared well in advance. The information and issues arising from these tests will directly help in the efficient commissioning of the system in the LHC.

All possible RF manipulations foreseen for the LHC operation cycle will first be performed without beam. An important verification concerns the efficiency of the fast feedback of the cavity field. The delay loops in the SPS between the two cavities will be arranged to mimic the cavity setup in the LHC to both ensure the fast and independent control of the cavity set point voltage and phase, and the slower loop to regulate the cavities on either side of the IP. This is essential to ensure machine protection in the event of an abrupt failure of one of the cavities.

**16.6 Commissioning with beam**

One is fully able to draw on past experience in outlining a commissioning plan for initial operation following LS3. A skeleton plan is shown in Table 16-3.

Table 16-3: Outline of initial commissioning following LS3

Phase	Key objectives
Injection and first turn	Injection region aperture, injection kicker timing
Circulating beam	RF capture, beam instrumentation, initial parameter checks
450 GeV initial commissioning	Transfer line and injection set-up, orbit,
450 GeV measurements and setup	Beam instrumentation, optics, aperture, collimation, LBDS
450 GeV two-beam operation	Separation bump checks, beam instrumentation
Ramp	Snapback, chromaticity control, orbit and tune feedbacks
Flat-top checks	Collimation, optics, orbit, decay
Squeeze	Optics, collimation set-up
Validation	Loss maps, asynchronous dumps
Collide	First stable beam with a low number of bunches

The initial commissioning phase should evolve through initial set-up, system commissioning through the nominal cycle, standard measurement and correction, set-up of protection devices, and validation. It is a relatively complex phase with necessary interplay between the various teams to allow beam-based commissioning of systems such as tune and orbit feedbacks, transverse dampers, RF, etc. under appropriate conditions at the various phases of the operational cycle.

The aims of the initial commissioning phase are as follows.

- Establish nominal cycle with a robust set of operating parameters. This will include commissioning of the squeeze to an appropriate  $\beta^*$  with measurement and correction of the optics and key beam parameters at each stage. One should not expect to probe the limits of the HL-LHC parameter space at this stage.
- Measure and correct the optics. Measure the aperture.
- Set-up injection, beam dump, and collimation, and validate set-up with beam.
- Commission beam-based systems: transverse feedback, RF, injection, beam dump systems, beam instrumentation, and orbit and tune feedbacks.
- Commission and test machine protection backbone with beam.
- Check the understanding of: magnet model; higher order optics.

The initial commissioning phase is performed at low intensity, with a low number of bunches, and a generally safe beam. The output of this phase is taken to be first collisions in stable beams with a small number of bunches. Following this, pilot physics can be delivered with up to 100 widely spaced bunches. Scrubbing will then be required before entering the intensity ramp-up phase. Scrubbing could well follow the two-stage approach deployed following LS1. This approach is outlined below.

- Initial scrubbing with 50 ns and 25 ns beam following initial commissioning opening the way for a period of 50 ns operation.
- Intensity ramp-up with 50 ns is then foreseen. During this stage system commissioning with higher intensity continues (instrumentation, RF, TFB, injection, beam dumps, machine protection, vacuum, etc.). Variables at this stage include: bunch intensity, batch structure, number of bunches, and emittance. Physics fills can be kept reasonably short. The intensity ramp-up is performed in a number of clearly defined steps with associated machine protection and other checks.
- Following the 50 ns intensity ramp-up a reasonably short period of 50 ns operation is envisaged. This will be used to characterize vacuum, heat load, electron cloud, losses, instabilities, UFOs, and impedance.
- Thereafter a further scrubbing period with 25 ns and the doublet beam will be required for 25 ns operation.
- This is followed by an intensity ramp-up with 25 ns dictated by electron cloud conditions, with further scrubbing as required.

Important beam-related characteristics such as lifetime, beam loss through the cycle, stability, quench levels, and UFO rates will only become accessible with an increase in bunch intensity and number of bunches during the intensity ramp-up phase.

#### 16.6.1 Operation with heavy ions

In a typical LHC operating year, one month is reserved for the nuclear collision programme.

##### 16.6.1.1 Pb–Pb operation

Collisions of fully stripped  $^{208}\text{Pb}^{82+}$  nuclei are requested by the ATLAS, ALICE, and CMS experiments. These heavy-ion runs will generally be scheduled following an extended period of p–p operation. The reduced activation of the LHC and injectors will allow interventions to start promptly in the subsequent shutdown periods. The runs will be short, typically of a total of one month, and there is a high premium on rapid commissioning of collision conditions with full luminosity within a few days.

To minimize commissioning time, the heavy-ion magnetic cycle will generally exploit the magnetic reproducibility of the LHC and equal magnetic rigidity of the beams to use as much as possible of the cycle previously established for proton beams. Due care must nevertheless be taken to reproduce the same orbits in the higher-sensitivity mode of the beam position monitors and to adjust the RF frequencies to capture the ion beams [7]. However the collision optics will always be different and a new squeeze process will have to be established to provide a low  $\beta^* = 0.5\text{--}0.6$  m at the ALICE experiment with similar values (generally not as low as for protons) at ATLAS and CMS. Crossing angles will also be changed, with that of ALICE carefully minimized for the benefit of its zero-degree calorimeter. With the 50 ns bunch spacing, the minimum acceptable separations at parasitic encounters will be established empirically [9, 10]. In all cases, the validation of the collimation configuration and machine protection will be an essential step in the set-up of heavy-ion physics conditions. During each run, a reversal of the ALICE spectrometer magnet polarity and flipping of the crossing angle should be foreseen [9].

Controlled blow-up of the longitudinal emittance, using RF noise with a spectrum focussed on the core of the bunch, will play an important role in minimising transverse emittance blow-up due to intra-beam scattering at injection [10] and, very likely, also during stable beams.

Because of the very rapid luminosity burn-off (halving in about two hours with three experiments active), the fills will be short and frequent refilling and recycling of the machine will be required, typically four times per day. Although the experiments will be able to handle the highest peak luminosity foreseen, it may nevertheless be useful to briefly level the luminosity with separation at the start of fills to reduce the intensity burn-off during the initial set-up of collision conditions. This will have negligible impact on average daily luminosity.

Secondary beams created in the collisions [10, 11] will impinge on the beam pipe in the dispersion suppressors on either side of each collision point. The power in these beams is expected to be sufficient to quench a superconducting magnet, and counter-measures will have to be applied immediately when the beams are put into collision. The most effective are expected to be the dispersion suppressor collimators [10] which will be positioned during the squeeze process. Initially these will be installed in IR2 for the ALICE experiment. The attainable peak luminosity for ATLAS and CMS will be maximized using an orbit bump technique that will spread the losses over a larger area. If necessary, similar collimators may be installed in IR1 and IR5 later. In any case, the dump thresholds for the beam-loss monitors in the dispersion suppressors will have to be carefully adjusted.

Because of the more complicated nuclear and electromagnetic processes that can occur when lead ions interact with the material of the collimators, collimation efficiency will be lower than for protons and quite different loss patterns are expected [12]. Here, again, the energy deposition from the losses may approach or exceed quench levels and may necessitate the installation of dispersion suppressor collimators in IR7.

### 16.6.1.2 p–Pb operation

Asymmetric collisions of protons with  $^{208}\text{Pb}^{82+}$  nuclei are requested by the ATLAS, ALICE, CMS, and LHCb experiments. The smaller forward detectors installed around the ATLAS and CMS interaction points also study these collisions. These runs are scheduled in place of the Pb–Pb runs, to a similar timetable, during a fraction of the operating years.

The feasibility of this complex mode of operation, unforeseen in the original LHC baseline design, was demonstrated by the first runs in 2012 and 2013 [13]. Proton beams will be injected first since the Pb beams suffer more from intra-beam scattering at injection energy. The RF frequencies corresponding to capture of the two beams on their central orbits are significantly different at injection energy, requiring the RF systems of the two rings to operate independently. At collision energy the frequencies will be locked together, displacing the proton orbit outwards and the Pb orbit inwards, by a small fraction of a millimetre, onto off-momentum orbits. A ‘cogging’ procedure, again using RF frequencies, will be used to move the collision points to their proper locations in the experiments [14].

Proton–lead runs place a number of requirements on the filling schemes. The basic bunch spacing must be created by both the heavy-ion and proton pre-injector chains to ensure that the bunch patterns largely match each other. The trains must be distributed to provide an appropriate share of collisions in each experiment. As seen in 2013, this can result in a complicated set of beam–beam encounter classes, bunch parameters, and lifetimes. In general, the proton beam size at the collision points will be smaller than the Pb beam, a circumstance that further reduces the lifetime of the Pb beam. Mitigation of this problem would be a second, less obvious, benefit of a stochastic cooling system.

As in Pb–Pb operation a new squeeze process will have to be commissioned, including all four experiments, with different end-points. This will generally be prepared and corrected first, using on-momentum proton beams. Pre-computed chromatic corrections [14] will be incorporated for the final off-momentum squeeze.

Rapid luminosity burn-off of the Pb beam on the proton beam will determine the length of fills. The luminosity will be essentially proportional to the Pb beam intensity, and the integrated luminosity delivered per fill summed over all experiments will be a fraction of  $N_{\text{Pb}}/\sigma_b$  where  $N_{\text{Pb}}$  is the total number of Pb ions in the beam at the start of collisions and  $\sigma_b$  is the cross-section for luminosity burn-off in p–Pb collisions. The

role of the proton bunch intensity is only to determine the lifetime of the Pb beam and the length of the fill. Values a few times less than in proton operation produce fills of reasonable length and satisfy operational constraints related to the functioning of the beam position monitors with unequal beams.

### 16.6.1.3 Other species

Collisions of lighter nuclei may eventually be requested by the experiments. At the time of writing, the injector chain is being commissioned with argon ions (for fixed target operation) for the first time. When this process is well-advanced, the beam quality and intensity data will allow performance projections for Ar–Ar and p–Ar collisions in the LHC.

Since most of the performance limitations for ion beams depend on high powers of the nuclear charge as well as beam intensity, their relative importance may shift considerably. First indications are that collimation losses from lighter ions will be more of a concern than for lead, while losses from collision processes will be less serious.

## 16.7 References

- [1] A. Ballarino *et al.*, Cold Powering, HL-LHC PDR, CERN-ACC-2014-106 (2015).
- [2] A. Ballarino *et al.*, Test of the superconducting links in SM18.
- [3] M. Bednarek *et al.*, ElQA qualification of the superconducting circuits during hardware commissioning, LHC-DE-TP-0007 rev 2.0, EDMS 788197.
- [4] E. Todesco *et al.*, Insertion magnets, HL-LHC PDR, CERN-ACC-2014-103 (2015).
- [5] Th. Weiler *et al.*, LHC Collimation system hardware commissioning, 22nd Particle Accelerator Conference, Albuquerque, NM, USA, 25 - 29 Jun 2007, pp.1625.
- [6] R. Assmann *et al.*, Accelerator physics concept for upgraded LHC collimation performance, EuCARD-CON-2009-047, (2009). <https://cds.cern.ch/record/1307562/files/EuCARD-CON-2009-047.pdf>
- [7] S. Claudet *et al.*, Cryogenics for the HL-LHC, HL-LHC PDR, CERN-ACC-2014-109 (2015).
- [8] J.M. Jowett, G. Arduini, R.W. Assmann, P. Baudrengnien, C. Carli, *et al.*, First Run of the LHC as a Heavy-ion Collider, IPAC 2011, San Sebastian (2011), pp. 1837–1839.
- [9] R. Alemany-Fernandez, G.H. Hemelsoet, J.M. Jowett, M. Lamont, D. Manglunki, S. Redaelli, M. Schaumann, R. Versteegen and J. Wenninger, ALICE spectrometer polarity reversal, CERN-ATS-Note-2012-039 MD (2012).
- [10] J.M. Jowett *et al.*, Future heavy-ion performance of the LHC, Review of LHC and Injector Upgrade Plans Workshop (RLIUP), Archamps, France, 29–31 October 2013.
- [11] R. Bruce, D. Bocian, S. Gilardoni and J.M. Jowett, Beam losses from ultraperipheral nuclear collisions between  $^{208}\text{Pb}^{82+}$  ions in the large hadron collider and their alleviation, *Phys. Rev.ST Accel. Beams* **12** (2009) 071002.
- [12] H.-H. Braun, R.W. Assmann, A. Ferrari, J.-B. Jeanneret, J.M. Jowett and I.A. Pshenichnov, Collimation of heavy ion beams in LHC, IPAC2004, Lucerne (2004) pp. 551–3.
- [13] J.M. Jowett, R. Alemany-Fernandez, P. Baudrengnien, D. Jacquet, M. Lamont, D. Manglunki, S. Redaelli, M. Sapinski, M. Schaumann, M. Solfaroli Camillocci, R. Tomás, J. Uythoven, D. Valuch, R. Versteegen and J. Wenninger, Proton nucleus collisions in the LHC, 4th International Particle Accelerator Conference, Shanghai, China, 12 - 17 May 2013, pp.49.
- [14] R. Alemany, P. Baudrengnien, D. Jacquet, J. M. Jowett, M. Lamont, D. Manglunki, S. Redaelli, M. Sapinski, M. Schaumann, D. Valuch, R. Versteegen and J. Wenninger, p–Pb feasibility test and modifications of LHC sequence and interlocking, CERN-ATS-Note-2012-052 MD (2012).

# Chapter 17

## Safety

*C. Adorisio, I. Bejar Alonso\*, J.C. Gascon, T. Otto and S. Roesler*

CERN, Geneva, Switzerland

### 17 Safety

#### 17.1 Radiation to personnel

##### 17.1.1 Design constraints

Design constraints for new or upgraded facilities should ensure that the exposure of persons working on CERN sites, the public, and the environment will remain below the specified dose limits [1] under normal as well as abnormal conditions of operation, and that the optimization principle is implemented [2, 3]. In particular, the following design constraints apply.

The design of components and equipment must be optimized such that installation, maintenance, repair, and dismantling work does not lead to an effective dose, e.g. as calculated with Monte Carlo simulations, exceeding 2 mSv per person and per intervention. The design is to be revised if the dose estimate exceeds this value for cooling times compatible with operational scenarios.

The annual effective dose to any member of a reference group outside of the CERN boundaries must not exceed 10  $\mu$ Sv. The estimate must include all exposure pathways and all contributing facilities.

The selection of construction material must consider activation properties to optimize dose to personnel and to minimize the production of radioactive waste. In order to guide the user a web-based code (ActiWiz) is available for CERN accelerators [4].

##### 17.1.2 The As Low As Reasonably Achievable (ALARA) principle in the design of the Long Straight Sections

Proton–proton collisions in the LHC experiments produce a secondary radiation field that penetrates into the adjacent accelerator tunnels and can cause severe activation of beam-line elements. Consequently, in such areas the design of components and infrastructure has to be optimized to follow the as low as reasonably achievable (ALARA) principle. The optimization of the design and later intervention is an iterative process: dose equivalent maps per unit time of exposure (called dose rate maps below) of the concerned area(s) are compiled from measurements and/or simulations with Monte Carlo particle transport codes such as FLUKA [5, 6]. Based on these maps, the personal and collective doses of the intervention teams are calculated by using an intervention plan that then allows identification of and optimizing of critical work steps in order to reduce doses. If the latter involves a change in design or work scenario, then doses are re-evaluated by repeating the above steps.

---

\* Corresponding author: [Isabel.BejarAlonso@cern.ch](mailto:Isabel.BejarAlonso@cern.ch)

### 17.1.3 The FLUKA Monte Carlo code for radiation protection studies

The use of general-purpose particle interaction and transport Monte Carlo codes is often the most accurate and efficient choice for assessing radiation protection quantities at accelerators. Due to the vast spread of such codes to all areas of particle physics and the associated extensive benchmarking with experimental data, modelling has reached an unprecedented level of accuracy. Furthermore, most codes allow the user to simulate all aspects of a high energy particle cascade in one and the same run: from the first interaction of a TeV particle to the transport and re-interactions (hadronic and electromagnetic) of the produced secondaries, to detailed nuclear fragmentation, the calculation of radioactive decays, and even the electromagnetic shower caused by the radiation from such decays.

FLUKA is a general-purpose particle interaction and transport code with roots in radiation protection studies at high energy accelerators [5, 6]. It therefore comprises all features needed in this area of application.

Detailed hadronic and nuclear interaction models cover the entire energy range of particle interactions at the LHC, from energies of thermal neutrons to interactions of 7 TeV protons. Moreover, the interface with DPMJET3 [7] also allows the simulation of minimum-bias proton–proton and heavy ion collisions at the experimental interaction points, which enormously facilitates calculations of stray radiation fields around LHC experiments.

FLUKA includes unique capabilities for studies of induced radioactivity, especially with regard to nuclide production, their decay and the transport of residual radiation. Particle cascades by prompt and residual radiation are simulated in parallel based on microscopic models for nuclide production and a solution of the Bateman equations [8] for activity build-up and radioactive decay. The decay radiation and its associated electromagnetic cascade are internally flagged as such in order to distinguish them from the prompt cascade. This allows the user to apply different transport thresholds and biasing options to residual and prompt radiation and to score both independently.

Particle fluence can be multiplied with energy-dependent conversion coefficients to effective dose or ambient dose equivalents [9] at scoring time. Prompt and residual dose equivalent can thus be computed in three-dimensional meshes, the latter for arbitrary user-defined irradiation and cooling profiles.

An integral part of the FLUKA code development is benchmarking of new features against experimental data. It includes both the comparison of predictions of individual models to measurement results (e.g. nuclide production cross-sections) as well as benchmarks for actual complex situations as, for example, arising during accelerator operation.

### 17.1.4 FLUKA simulations

Comprehensive dose rate maps were calculated with FLUKA for the part of Long Straight Section 1 (LSS1) that extends from the Target Absorber Secondary (TAS) to the separation dipole D1 (so-called ‘inner triplet area’), including the inner triplet quadrupole magnets and the corrector package (CP) according to the latest HiLumi LHC layout [10]. The results may also serve as guideline values for dose planning at inner triplet regions of LSS5, due to the similar design of the two LSSs.

The simulations were limited to the high energy secondary radiation field arising from the p–p collisions as they dominate the activation in these areas. The influences due to losses of the beam directed towards the interaction point (IP) and beam–gas interactions are not considered. The FLUKA geometry shown below represents the tunnel on the righthand side of LSS1.

The studies were done for 7 + 7 TeV p–p collisions at two different average luminosity values of  $5 \times 10^{34} \text{ cm}^{-2} \text{ s}^{-1}$  (for the so-called ‘nominal scenario’) and  $7.5 \times 10^{34} \text{ cm}^{-2} \text{ s}^{-1}$  (for the so-called ‘ultimate scenario’) with a 295  $\mu\text{rad}$  half-angle vertical crossing in IP1 using DPMJET-III as the event generator.

The irradiation profiles used are based on the operational scenarios reported in Table 17-1.



Table 17-1: LHC operational parameters. The second and third columns refer to the so-called ‘nominal scenario’, which will lead to a total integrated luminosity of 3060 fb<sup>-1</sup>. The fourth and fifth columns refer to the so-called ‘ultimate scenario’. This scenario will lead to a total integrated luminosity of 3910 fb<sup>-1</sup>. For the total integrated luminosity 310 fb<sup>-1</sup> are taken into account as integrated in the operational period before LS3.

Shutdown	Year of LHC operation	Levelled luminosity [cm <sup>-2</sup> s <sup>-1</sup> ]	Integrated luminosity [fb <sup>-1</sup> ]	Levelled luminosity [cm <sup>-2</sup> s <sup>-1</sup> ]	Integrated luminosity [fb <sup>-1</sup> ]
<b>LS3</b>					
	2026	$5.00 \times 10^{34}$	250	$7.50 \times 10^{34}$	300
	2027	$5.00 \times 10^{34}$	250	$7.50 \times 10^{34}$	300
	2028	$5.00 \times 10^{34}$	250	$7.50 \times 10^{34}$	300
<b>LS4</b>					
	2030	$5.00 \times 10^{34}$	250	$7.50 \times 10^{34}$	300
	2031	$5.00 \times 10^{34}$	250	$7.50 \times 10^{34}$	300
	2032	$5.00 \times 10^{34}$	250	$7.50 \times 10^{34}$	300
<b>LS5</b>					
	2034	$5.00 \times 10^{34}$	250	$7.50 \times 10^{34}$	300
	2035	$5.00 \times 10^{34}$	250	$7.50 \times 10^{34}$	300
	2036	$5.00 \times 10^{34}$	250	$7.50 \times 10^{34}$	300
<b>LS6</b>					
	2038	$5.00 \times 10^{34}$	250	$7.50 \times 10^{34}$	300
	2039	$5.00 \times 10^{34}$	250	$7.50 \times 10^{34}$	300
	2040			$7.50 \times 10^{34}$	300

For the inelastic pp cross-section the value of 85 mb is used, on the basis of the extrapolation [11]. Cycles of three years of continuous operation followed by a long shutdown (LS) of a duration of one year were repeated until integrated luminosities of about 3000 fb<sup>-1</sup> and 4000 fb<sup>-1</sup> are reached for the nominal and ultimate parameters, respectively.

The studies use a FLUKA implementation of the High Luminosity LHC inner triplet region developed by the FLUKA team [12] according to the latest design, mechanical layout, and specifications, including a detailed model of the inner triplet region with new large-aperture Nb<sub>3</sub>Sn magnets (150 mm coil aperture), field maps, corrector packages, and segmented tungsten inner absorbers. As mentioned above, the inner triplet regions at LSS1 and LSS5 are radiologically equivalent and symmetrical around the interaction point. Thus, the simulations were performed for the righthand side of LSS1 only.

### 17.1.5 Results

Three-dimensional residual dose rate maps have been calculated from around 18 m distance from the interaction point up to around 82 m distance (i.e. from TAS to D1), and for six different cooling times: 1 hour, 1 day, 1 week, 1 month, 4 months, and 1 year after the beam stop for both the nominal and the ultimate scenarios, i.e. when 3000 fb<sup>-1</sup> and 4000 fb<sup>-1</sup>, respectively, have been reached.

In order to give examples for the available results, residual dose equivalent rates are reported in the following as two-dimensional maps for the one month cooling time as well as profile plots at four different cooling times (1 week, 1 month, 4 months, and 1 year). The values correspond to the average over 30 cm around the beam pipe height and between 40–50 cm distance from the outer surface of the cryostat (closest possible working distance).

Figure 17-1 shows the ambient dose equivalent rate maps in the inner triplet area after one month of cooling time and Figure 17-2 shows the residual dose rate profiles in the aisle at 40 cm distance from the cryostat at four different cooling times, when a total integrated luminosity of  $3060 \text{ fb}^{-1}$  is reached.

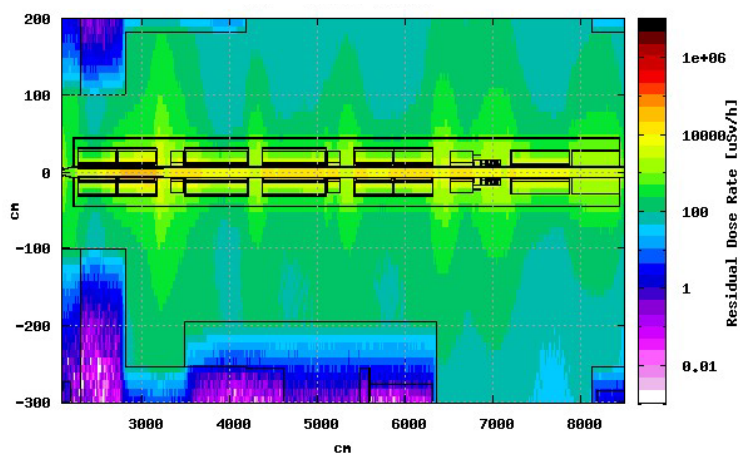


Figure 17-1: Residual dose equivalent rates in units of  $\mu\text{Sv/h}$  around the inner triplet and D1 magnets when  $3060 \text{ fb}^{-1}$  has been reached after one month of cooling time. Doses are shown for a horizontal section at the level of the beam lines. The origin of the coordinate frame is at the interaction point.

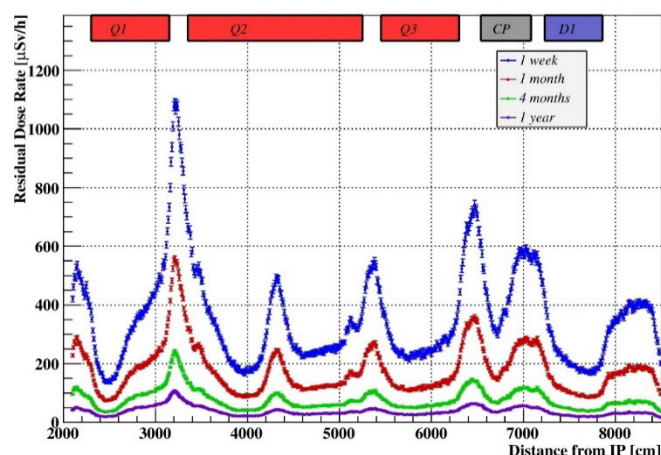


Figure 17-2: Ambient dose equivalent rate profiles for the nominal scenario in the aisle at 40 cm from the cryostat at four different cooling times: 1 week in blue, 1 month in red, 4 months in green and 1 year in violet.

Figure 17-3 shows the ambient dose equivalent rate maps in the inner triplet area after 1 month of cooling time and Figure 17-4 shows the residual dose rate profiles in the aisle at 40 cm distance from the cryostat at four different cooling times, for a total integrated luminosity of  $3910 \text{ fb}^{-1}$ .

The highest radiation levels will be found next to the magnet interconnections and in front of the TAS due to the ‘self-shielding’ provided elsewhere by the magnets themselves.

The plot in Figure 17-5 shows the residual dose rate profiles at 1 month cooling time along the inner triplets, for the ultimate scenario in pink and for the nominal scenario in light blue. The average ratio between the two profiles is 1.35. This average ratio varies with cooling time and it depends solely on the instantaneous luminosity in the case of short cooling times, while for longer cooling times the ratio also depends on the total integrated luminosity.

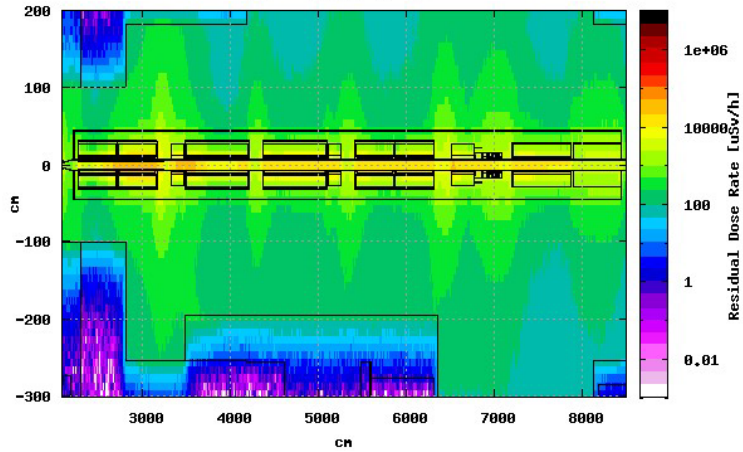


Figure 17-3: Residual dose equivalent rates in units of  $\mu\text{Sv/h}$  around the inner triplet and D1 magnets when  $3910 \text{ fb}^{-1}$  has been reached after one month of cooling time. Doses are shown for a horizontal section at the level of the beam lines. The origin of the coordinate frame is at the interaction point.

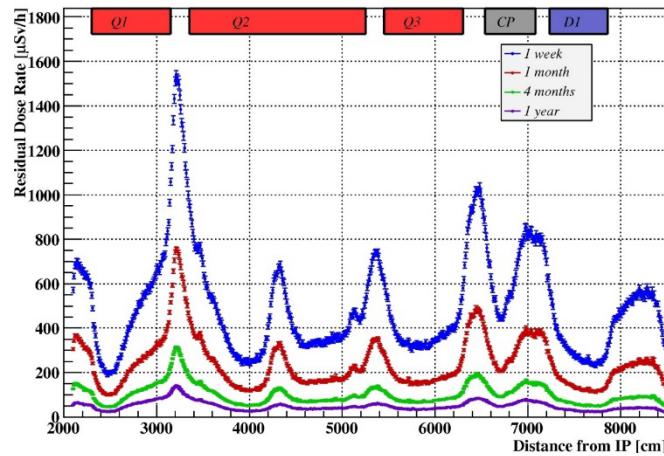


Figure 17-4: Ambient dose equivalent rate profiles for the ultimate scenario in the aisle at 40 cm from the cryostat at four different cooling times: 1 week in blue, 1 month in red, 4 months in green and 1 year in violet.

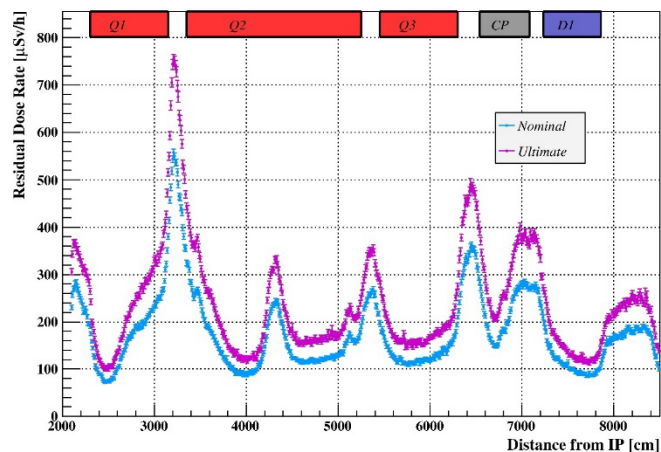


Figure 17-5: Ambient dose equivalent rate profiles along the aisle at 40 cm distance to the cryostat at one month cooling time. The profile in light blue is for the nominal scenario (about  $3000 \text{ fb}^{-1}$  total integrated luminosity), the profile in pink is for the ultimate scenario (about  $4000 \text{ fb}^{-1}$  total integrated luminosity).

### 17.1.6 Conclusions

Three-dimensional ambient dose equivalent rate maps were calculated with the FLUKA Monte Carlo code for the inner triplet region (from the TAS up to the D1 dipole magnet) for nominal and ultimate HiLumi LHC operational parameters and the latest upgrade layout. These predictions are now available and can be considered for the design of components. For example, the results will be used to assess the radiological impact, in terms of individual and collective dose, for typical interventions in the area and, thus, help in optimizing the design and the material choice as required by the ALARA principle. Further studies are also required to address airborne activation and the related environmental impact of the upgrade.

## 17.2 General safety

### 17.2.1 Implementation of safety in the HL-LHC

The HL-LHC presents a number of potential hazards that could pose serious safety risks. - The consequences could include the loss of life, damage to HL-LHC systems and facilities, or damage to the environment. Consequently, all of the HL-LHC work packages (WPs) are classified as projects with major safety implications.

In practice the systems/processes of the HL-LHC WPs shall be submitted for a compulsory safety verification by the HSE Unit and shall only operate once the HSE Unit has granted safety clearance.

In the framework of the HL-LHC project, clearance will be given for the project phase, i.e. any development tests that will be performed on given systems or processes. After the HL-LHC project phase, a second clearance stage may become necessary once the system/process is ready for operation in the LHC.

### 17.2.2 Launch Safety Agreement (LSA)

For each HL-LHC work package a launch safety discussion shall take place with the participation of the WP members, the Project Safety Officer (PSO), and the correspondent from the safety unit (HSE-CO). After the launch safety discussion, the HSE-CO shall release the Launch Safety Agreement that provides the following information:

- description of the WP systems/processes;
- preliminary identification of the hazards and safety risks;
- Identification of the CERN safety rules and host state regulations applicable to the systems/processes;
- tailored safety advice on hazard control measures;
- list of safety checks (including safety checks required to grant safety clearance) on the relevant systems/processes that shall be carried out by the HSE Unit during the WP lifecycle;
- minimal contents of the WP safety file needed to meet the safety requirements.

The Launch Safety Agreement may be reviewed and updated during the different phases of the systems/sub-system's life-cycle. Any changes to the safety requirements will be subjected to change control for integration, as required, in the baseline requirements.

### 17.2.3 Safety folder, safety files and safety documentation

The HL-LHC project will be documented as indicated in the quality management procedure 'Safety Documentation Management' [13]. In this framework a safety folder for the HL-LHC project shall be established and maintained during the project life cycle.

- The Work Package Engineers (WPEs), based on the applicable safety requirements, shall provide the safety documents necessary to demonstrate compliance of the systems/processes (or sub-systems/sub-processes) for which they are responsible.

- The WPE provides a description for systems and processes under their responsibility, with focus on the safety aspects. This forms the basis for the descriptive part of the WP safety file
- The WPL shall establish and maintain the WP safety file. The WP safety file shall serve as an umbrella document where the relevant safety documents, provided by the WPE, are referred to;
- The PSO shall establish and maintain the HL-LHC safety folder. The HL-LHC safety folder shall refer to the safety files of the HL-LHC work packages.

The HL-LHC safety folder will consist of the collection of approved safety files of the HL-LHC WPs. The PSO shall ensure that the HL-LHC safety folder is kept up-to-date and available to the HSE Unit and host CERN safety officers.

The safety folder for the HL-LHC shall be provided to the HSE Unit for purposes of granting safety clearance. The safety folder for HL-LHC will cover the project phase, which will extend until the end of LS3. Many of the material or organizational contributions realized in the WPs will be installed in the LHC accelerator. At this stage their safety files will become part of the LHC accelerator safety folder.

Figure 17-6 shows the organization of the HL-LHC safety documentation.

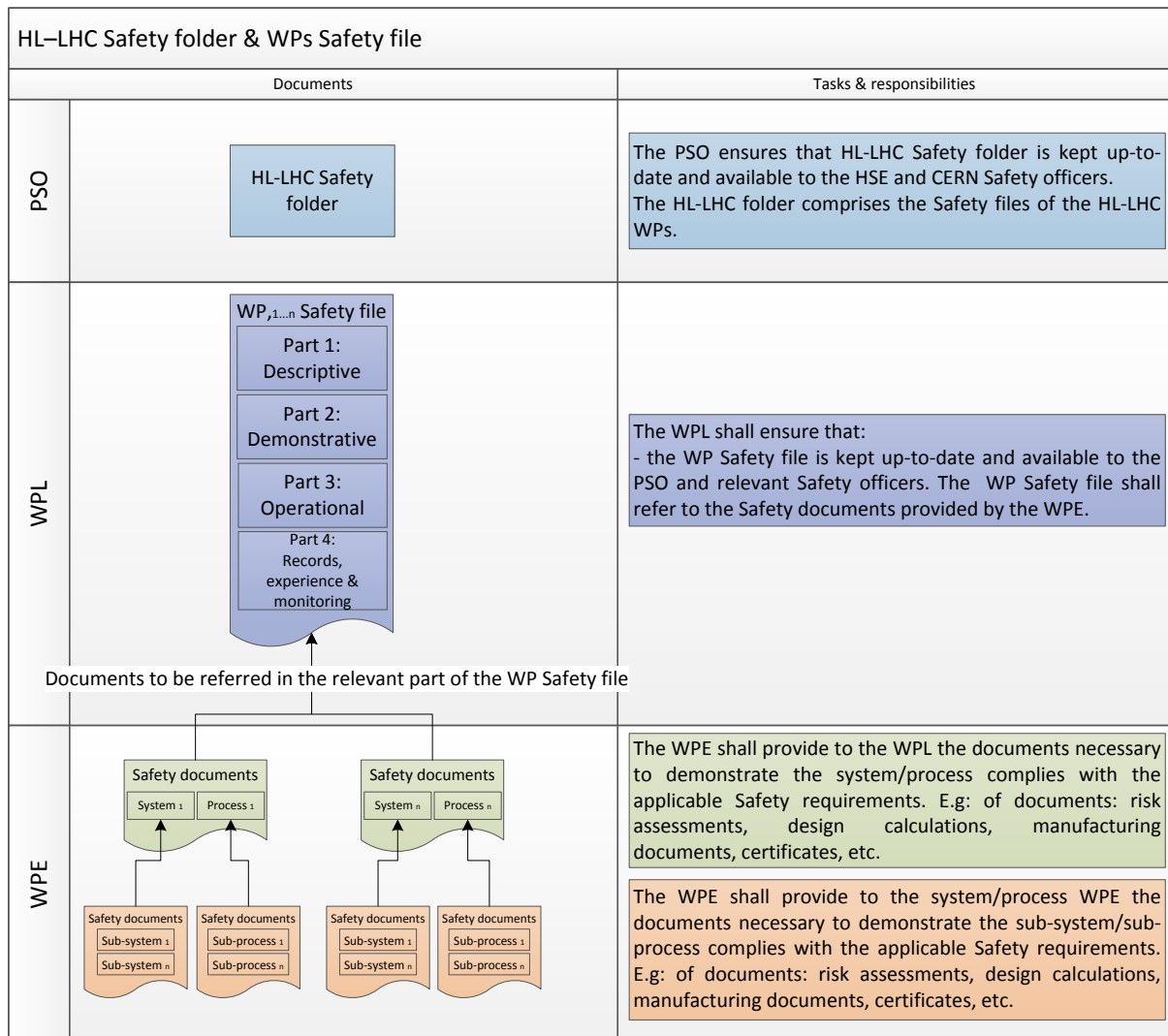


Figure 17-6: Organization of the safety documentation

### 17.3 References

- [1] Safety Code F Radiation Protection, CERN (2006).
- [2] Critères et exigences ALARA applicables aux interventions, CERN (2006).
- [3] ALARA Review Working Group, Final report, CERN (2012).
- [4] H. Vincke and C. Theis, ActiWiz – Optimizing your nuclide inventory at proton accelerators with a computer code. Proc. ICRS-12 & RPSD 2012 Conf., Nara, Japan, 2–7 September 2012, [*Prog. Nucl. Sci. Technol.* (2013)].
- [5] G. Battistoni, S. Muraro, P.R. Sala, F. Cerutti, A. Ferrari, S. Roesler, A. Fasso and J. Ranft, The FLUKA code: description and benchmarking. Hadronic Shower Simulations Workshop, Fermilab, Batavia, IL, USA, 6 - 8 Sep 2006, pp.31-49
- [6] A. Fassó, A. Ferrari, J. Ranft and P.R. Sala, Fluka: A multi particle transport code. CERN-2005-10, INFN/TC\_5/11, SLAC-R-773 (2005).
- [7] S. Roesler, R. Engel and J. Ranft, The Monte Carlo event generator DPMJET-III, Proc. Monte Carlo 2000 Conf., Lisbon, 23–26 October 2000, Eds. A. Kling, F. Barao, M. Nakagawa, L. Tavora and P. Vaz. (Springer-Verlag, Berlin, 2001) pp. 1033–1038.
- [8] H. Bateman, Solution of a system of differential equations occurring in the theory of radioactive transformations, *Proc. Cambridge Philos. Soc.* **15** (1910) 423–427.
- [9] M. Pelliccioni, Overview of fluence-to-effective dose and fluence-to-ambient dose equivalent conversion coefficients for high energy radiation calculated using the FLUKA code, *Radiat. Prot. Dosim.* **88** (2000) 279–297.
- [10] Mechanical layout, LHCLSXH\_0010. <https://edms.cern.ch/document/1395366/AB>
- [11] T. Csörgő *et al.*, Elastic scattering and total cross-section in p+p reactions measured by the LHC Experiment TOTEM at  $\sqrt{s} = 7$  TeV, 41st International Symposium of Multiparticle Dynamics, Hiroshima, Japan, 26 - 30 Sep 2011, pp.180-183.]
- [12] M. Brugger, F. Cerutti and L.S. Esposito, The 'environmental' challenges: Impact of radiation on machine components. (World Scientific, Singapore, 2015). pp177-190
- [13] P. Bonnal et al, Quality Management Procedure - Safety Files Management. EDMS 1177755 v1.1.

## **List of Machine and Beam Parameters**





## A. List of machine and beam parameters

### A.1. Nominal beam parameters

Table A-1: HL-LHC nominal parameters for 25 ns operation [1] for two production modes of the LHC beam in the injectors described in Ref. [2].

Parameter	Nominal LHC (design report)	HL-LHC (standard)	HL-LHC (BCMS)
Beam energy in collision [TeV]	7	7	7
Particles per bunch, $N$ [ $10^{11}$ ]	1.15	2.2	2.2
Number of bunches per beam	2808	2748	2604
Number of collisions in IP1 and IP5*	2808	2736	2592
$N_{\text{tot}}$ [ $10^{14}$ ]	3.2	6.0	5.7
Beam current [A]	0.58	1.09	1.03
Crossing angle in IP1 and IP5 [ $\mu\text{rad}$ ]	285	590	590
Normalized long-range beam-beam separation [ $\sigma$ ]	9.4	12.5	12.5
Minimum $\beta^*$ [m]	0.55	0.15	0.15
$\epsilon_n$ [ $\mu\text{m}$ ]	3.75	2.50	2.50
$\epsilon_L$ [eVs]	2.50	2.50	2.50
r.m.s. energy spread [0.0001]	1.13	1.13	1.13
r.m.s. bunch length [cm]	7.55	7.55	7.55
IBS horizontal [h]	105	18.5	18.5
IBS longitudinal [h]	63	20.4	20.4
Piwinski parameter	0.65	3.14	3.14
Total loss factor $R_0$ without crab cavity	0.836	0.305	0.305
Total loss factor $R_1$ with crab cavity	(0.981)	0.829	0.829
Beam-beam/IP without crab cavity	0.0031	0.0033	0.0033
Beam-beam/IP with crab cavity	0.0038	0.011	0.011
Peak luminosity without crab cavity [ $10^{34} \text{ cm}^{-2} \text{ s}^{-1}$ ]	1.00	7.18	6.80
Virtual luminosity with crab cavity $L_{\text{peak}} \times R_1/R_0$ [ $10^{34} \text{ cm}^{-2} \text{ s}^{-1}$ ]	(1.18)	19.54	18.52
Events/crossing without levelling and without crab cavity	27	198	198
Levelled luminosity [ $10^{34} \text{ cm}^{-2} \text{ s}^{-1}$ ]	-	5.00 <sup>†</sup>	5.00 <sup>†</sup>
Events/crossing (with levelling and crab cavities for HL-LHC) <sup>‡</sup>	27	138	146
Maximum line density of pile-up events during fill [event/mm]	0.21	1.25	1.31
Levelling time [h] (assuming no emittance growth) <sup>‡</sup>	-	8.3	7.6
Number of collisions in IP2/IP8	2808	2452/2524 <sup>**</sup>	2288/2396 <sup>4</sup>
$N$ at LHC injection [ $10^{11}$ ] <sup>††</sup>	1.20	2.30	2.30
Maximum number of bunches per injection	288	288	288
$N_{\text{tot}}/\text{injection}$ [ $10^{13}$ ]	3.46	6.62	6.62
$\epsilon_n$ at SPS extraction [ $\mu\text{m}$ ] <sup>‡‡</sup>	3.40	2.00	<2.00 <sup>***</sup>

\*Assuming one less batch from the PS for machine protection (pilot injection, Transfer line steering with 12 nominal bunches) and non-colliding bunches for experiments (background studies, etc.). Note that due to RF beam loading the abort gap length must not exceed the 3  $\mu\text{s}$  design value.

<sup>†</sup>For the design of the HL-LHC systems (collimators, triplet magnets, etc.), a margin of 50% on the stated peak luminosity (corresponding to the ultimate levelled luminosity) has been agreed.

<sup>‡</sup>The total number of events/crossing is calculated with an inelastic cross-section of 85 mb (also for nominal), while 100 mb is still assumed for calculating the proton burn off and the resulting levelling time.

<sup>\*\*</sup>The lower number of collisions in IR2/8 compared to the general-purpose detectors is a result of the agreed filling scheme, aiming as much as possible at a democratic sharing of collisions between the experiments.

<sup>††</sup>An intensity loss of 5% distributed along the cycle is assumed from SPS extraction to collisions in the LHC.

\*\*A transverse emittance blow-up of 10–15% on the average H/V emittance in addition to that expected from intra-beam scattering (IBS) is assumed (to reach 2.5  $\mu\text{m}$  of emittance in collision for 25 ns operation).

\*\*\*For the BCMS scheme emittances down to 1.7  $\mu\text{m}$  have already been achieved at LHC injection, which might be used to mitigate excessive emittance blow-up in the LHC during injection and ramp.

## A.2. Main machine parameters

Table A-2: HL-LHC nominal machine parameters for proton operation

		<b>Injection</b>	<b>Collision</b>
<b>Geometry</b>			
Ring circumference	[m]	26658.883	26658.883
Ring separation in arcs	[mm]	194	194
Bare inner vacuum screen height in arcs	[mm]	46.5	46.5
Effective vacuum screen height (incl. tol.)	[mm]	44.04	44.04
Bare inner vacuum screen width in arcs	[mm]	36.9	36.9
Effective vacuum screen width (incl. tol.)	[mm]	34.28	34.28
<b>Main magnet</b>			
Number of main bends		1232	1232
Length of main bends	[m]	14.3	14.3
Field of main bends	[T]	0.535	8.33
Bending radius	[m]	2803.95	2803.95
<b>Lattice</b>			
Maximum dispersion in arc	[m]	2.387 (H)/0.281 (V)	2.789 (H)/0.632 (V)
Minimum dispersion in arc	[m]	0.959(H)/−0.281 (V)	0.832 (H)/−0.581 (V)
Maximum $\beta$ in arc	[m]	178 (H)/178 (V)	524 (H)/523 (V)
Minimum $\beta$ in arc	[m]	31.4 (H)/32.1 (V)	25.2(H)/26.4 (V)
Horizontal tune		62.28	62.31
Vertical tune		60.31	60.32
Momentum compaction	[ $10^{-4}$ ]	3.447	3.467
Slip factor $\eta$	[ $10^{-4}$ ]	3.404	3.467
Gamma transition $\gamma_{tr}$		53.86	53.70
<b>RF System</b>			
Revolution frequency	[kHz]	11.2455	11.2455
RF frequency	[MHz]	400.79	400.79
Harmonic number		35640	35640
Number of bunches		2748 (Standard)/2604	2748 (Standard)/2604
Total RF voltage	[MV]	8	16
Synchrotron frequency	[Hz]	66.0	23.8
Bucket area	[eVs]	1.38	7.63
Bucket half height ( $\Delta E/E$ )	[ $10^{-3}$ ]	0.965	0.343

Table A-3: HL-LHC nominal machine parameters at the collision points for proton operation. The crossing angle and separation refer to Beam 1.

		Injection	Collision
Interaction data			
Number of collision points		-	4
Half crossing angle at the IP for ATLAS (IP1)	[ $\mu$ rad]	$\pm 295$ (V)	$\pm 295$ (V)
Half parallel separation at the IP for ATLAS (IP1)	[mm]	-2.0 (H)	0.0 (H)
Half external crossing angle at IP for ALICE (IP2) <sup>2</sup>	[ $\mu$ rad]	$\pm 170$ (V)	$\pm 170$ (V)
Half crossing angle at the IP for ALICE (IP2) <sup>1</sup>	[ $\mu$ rad]	$\pm 1259$ (V)	$\pm 240$ (V)
Half parallel separation at the IP for ALICE (IP2)	[mm]	+2.0 (H)	+0.144 <sup>2</sup> (H)
Half crossing angle at the IP for CMS (IP5)	[ $\mu$ rad]	+295 (H)	+295 (H)
Half parallel separation at the IP for CMS (IP5)	[mm]	$\pm 2.0$ (V)	0.0 (V)
Half external crossing angle at the IP for LHCb (IP8) <sup>2</sup>	[ $\mu$ rad]	-170 (H)	-250 (H)
Half crossing angle at the IP for LHCb (IP8) <sup>2</sup>	[ $\mu$ rad]	1930 (H)	-115 (H)
Half parallel angle at the IP for LHCb (IP8) [3]	[ $\mu$ rad]	$\pm 30$ (V)	0
Half parallel separation at IP for LHCb (IP8) [3]	[mm]	$\pm 3.5$ (V)	0.0 (V)
Minimum $\beta$ at IP1 and IP5	[m]	6	0.15
Minimum $\beta$ at IP2	[m]	10	10
Minimum $\beta$ at IP8	[m]	10	3

<sup>1</sup>The crossing angle in IP2 and IP8 is the sum of an external crossing angle bump and an ‘internal’ spectrometer compensation bump and it depends on the spectrometer polarity. The values quoted above correspond to the configuration with the spectrometer ON providing to the minimum long-range beam-beam normalized separation. The external bump extends over the triplet and D1 and D2 magnets. The internal spectrometer compensation bump extends only over the long drift space between the two triplet assemblies left and right from the IP. For IP2 the vertical external crossing angle sign can be changed and therefore the same sign of the internal and external angle can be chosen to be the same. This is not possible for IP8 as the sign of the crossing angle must be compatible with the recombination scheme.

<sup>2</sup>This corresponds to a full separation of  $5\sigma$  required to reduce the luminosity down to  $10^{31} \text{ cm}^{-2} \text{ s}^{-1}$ .

### A.3. Main insertion region magnet parameters

Table A-4: New or refurbished quadrupoles for HL-LHC, all operating at 1.9 K. The orientation of the rectellipse aperture [4] can be changed to optimize the mechanical aperture.

Magnet	Inner triplet (single aperture)			Matching section (two-in-one)		
	Q1	Q2	Q3	Q4	Q5	Q6
Number per side and per insertion	2	2	2	1	1	1
Type	MQXFA	MQXFB	MQXFA	MQYY	MQY	MQML
Magnetic length [m]	4.0	6.8	4.0	3.8	3.4	4.8
Gradient [T/m]	140	140	140	115	200	200
Coil aperture [mm]	150	150	150	90	70	56
Aperture separation [mm]	n/a	n/a	n/a	194	194	194
Beam screen (BS) shape	Octagon	Octagon	Octagon	Rectellipse	Rectellipse	Rectellipse
BS aperture (horizontal/vertical) [mm]	98/98	118/118	118/118	64/74	44/57.8	35.3/45.1
Mechanical tolerances (R/H/V) <sup>1</sup> [mm]	0.6/1/1	0.6/1/1	0.6/1/1	0.84/1.26/0.6	0.84/1.26/0.6	As built

<sup>1</sup>The definition of the parameters of the mechanical tolerances is given in Ref. [5].

Table A-5: New dipole magnets for HL-LHC, all operating at 1.9 K. The orientation of the rectellipse aperture can be changed to optimize the mechanical aperture. The orbit correctors can be nested or consecutive as indicated.

Assembly	Separation/ recombination dipoles		Orbit correctors			
	D1	D2	Corrector Package	Q2	D2	Q4
Number per side and per insertion	1	1	1 [HV nested]	2 [HV nested]	2 [HV cons.]	2 [HV cons.]
Type	MBXF	MBRD	MCBXFA	MCBXFB	MCBRD	MCBYY
Magnetic length [m]	6.27	7.78	2.2	1.2	1.5	1.5
Integrated field [T m]	35	35	4.5	4.5	4.5	4.5
Coil aperture [mm]	150	105	150	150	100	100
Aperture separation [mm]	n/a	188	-	-	194	194
BS shape	Octagon	Octagon	Octagon	Octagon	Octagon	Rectellipse
BS aperture (H/V) [mm]	118/118	84/84	118/118	118/118	79/79	64/74
Mech. tolerances (R/H/V) [mm]	0.6/1/1	0.84/1.36/1	0.6/1/1	0.6/1/1	0.84/1.36/1	0.84/1.26/0.6

Table A-6: New multipolar superferric correctors for HL-LHC, all operating at 1.9 K

Number	1	1	1	1	1	1	1	1	1
# poles	4	12	12	10	10	8	8	6	6
Normal/Skew	skew	normal	skew	normal	skew	normal	skew	normal	skew
Type	MQSXF	MCTX F	MCTSX F	MCDXF	MCDSX F	MCOX F	MCOSX F	MCSXF	MCSSX F
Magnetic length [m]	0.807	0.43	0.089	0.095	0.095	0.087	0.087	0.111	0.111
Integrated field [mT·m] at 50 mm	1000	86	17	25	25	46	46	63	63
Coil aperture [mm]	150	150	150	150	150	150	150	150	150
BS shape	Octagon	Octagon	Octagon	Octagon	Octagon	Octagon	Octagon	Octagon	Octagon
BS aperture (H/V) [mm]	118/118	118/118	118/118	118/118	118/118	118/118	118/118	118/118	118/118
Mechanical tolerances (R/H/V) [mm]	0.6/1/1	0.6/1/1	0.6/1/1	0.6/1/1	0.6/1/1	0.6/1/1	0.6/1/1	0.6/1/1	0.6/1/1

The implementation of the ATS scheme in HLLHC V1.0 requires hardware changes in other parts of the LHC ring. In particular, an additional sextupole (MS) magnet should be installed in Q10 in IR1 and IR5. Moreover, Q5 in IR6 should be upgraded. The current baseline layout envisages the installation of a second MQY-type quadrupole close to each existing Q5.

#### A.4. Field error specification for the new insertion region magnets

In this section the error tables used in the tracking simulations (as described in Chapter 2, Section 2.3.2) for the various classes of new magnets are collected. Whenever the expected values of the multipoles turned out to cause an unacceptable reduction of the DA, the tables also give the requested values (in red) based on the

beam dynamics studies. Note that the expected error tables at injection turned out to be already compatible with the criterion based on DA computation.

Table A-7: Expected field quality errors at injection energy for the new IT ( $r_0 = 50$  mm). These values represent IT\_errortable\_v66 in Ref. [5].

skew	mean	uncertainty	random	normal	mean	uncertainty	random
a3	0	0.800	0.800	b3	0	0.820	0.820
a4	0	0.650	0.650	b4	0	0.570	0.570
a5	0	0.430	0.430	b5	0	0.420	0.420
a6	0	0.310	0.310	b6	-16.0	1.100	1.100
a7	0	0.190	0.190	b7	0	0.190	0.190
a8	0	0.110	0.110	b8	0	0.130	0.130
a9	0	0.080	0.080	b9	0	0.070	0.070
a10	0	0.040	0.040	b10	4.15	0.200	0.200
a11	0	0.026	0.026	b11	0	0.026	0.026
a12	0	0.014	0.014	b12	0	0.018	0.018
a13	0	0.010	0.010	b13	0	0.009	0.009
a14	0	0.005	0.005	b14	-0.040	0.023	0.023

Table A-8: Expected (blue) and target (red) field quality errors at top energy for the new IT ( $r_0 = 50$  mm). These values represent IT\_errortable\_v66 in Ref. [5].

skew	mean	uncertainty	random	normal	mean	uncertainty	random
a3	0	0.800	0.800	b3	0	0.820	0.820
a4	0	0.650	0.650	b4	0	0.570	0.570
a5	0	0.430	0.430	b5	0	0.420	0.420
a6	0	0.310	0.310	b6	0.800	0.550	0.550
a7	0	0.152	0.095	b7	0	0.095	0.095
a8	0	0.088	0.055	b8	0	0.065	0.065
a9	0	0.064	0.040	b9	0	0.035	0.035
a10	0	0.040	0.032	b10	0.075	0.100	0.100
a11	0	0.026	0.0208	b11	0	0.0208	0.0208
a12	0	0.014	0.014	b12	0	0.0144	0.0144
a13	0	0.010	0.010	b13	0	0.0072	0.0072
a14	0	0.005	0.005	b14	-0.020	0.0115	0.0115

Table A-9: Expected field quality at injection energy for the new D1 ( $r_0 = 50$  mm). These values represent D1\_errortable\_v1 in Ref. [5].

skew	mean	uncertainty	random	normal	mean	uncertainty	random
a2	0	0.679	0.679	b2	0	0.200	0.200
a3	0	0.282	0.282	b3	-16.0	0.727	0.727
a4	0	0.444	0.444	b4	0	0.126	0.126
a5	0	0.152	0.152	b5	-0.500	0.365	0.365
a6	0	0.176	0.176	b6	0	0.060	0.060
a7	0	0.057	0.057	b7	0.900	0.165	0.165
a8	0	0.061	0.061	b8	0	0.027	0.027
a9	0	0.020	0.020	b9	-0.660	0.065	0.065
a10	0	0.025	0.025	b10	0	0.008	0.008
a11	0	0.007	0.007	b11	0.440	0.019	0.019
a12	0	0.008	0.008	b12	0	0.003	0.003
a13	0	0.002	0.002	b13	0	0.006	0.006
a14	0	0.003	0.003	b14	0	0.001	0.001
a15	0	0.001	0.001	b15	-0.040	0.002	0.002

Table A-10: Expected (blue) and target (red) field quality at top energy for the new D1 ( $r_0 = 50$  mm). These values represent D1\_errortable\_v1 in Ref. [5].

skew	mean	uncertainty	random	normal	mean	uncertainty	random
a2	0	0.679	0.679	b2	0	0.200	0.200
a3	0	0.282	0.282	b3	-0.900	0.727	0.727
a4	0	0.444	0.444	b4	0	0.126	0.126
a5	0	0.152	0.152	b5	0	0.365	0.365
a6	0	0.176	0.176	b6	0	0.060	0.060
a7	0	0.057	0.057	b7	0.4→0.2	0.165	0.165
a8	0	0.061	0.061	b8	0	0.027	0.027
a9	0	0.020	0.020	b9	-0.59→-0.295	0.065	0.065
a10	0	0.025	0.025	b10	0	0.008	0.008
a11	0	0.007	0.007	b11	0.470	0.019	0.019
a12	0	0.008	0.008	b12	0	0.003	0.003
a13	0	0.002	0.002	b13	0	0.006	0.006
a14	0	0.003	0.003	b14	0	0.001	0.001
a15	0	0.001	0.001	b15	-0.040	0.002	0.002

Table A-11: Expected field quality at injection energy for the new D2 ( $r_0 = 35$  mm). These values represent D2\_errortable\_v4 in Ref. [5].

skew	mean	uncertainty	random	normal	mean	uncertainty	random
a2	0	0.679	0.679	b2	0	0.200	0.200
a3	0	0.282	0.282	b3	3.8	0.727	0.727
a4	0	0.444	0.444	b4	$\pm 8.0$	0.126	0.126
a5	0	0.152	0.152	b5	3.0	0.365	0.365
a6	0	0.176	0.176	b6	0	0.060	0.060
a7	0	0.057	0.057	b7	0.100	0.165	0.165
a8	0	0.061	0.061	b8	0	0.027	0.027
a9	0	0.020	0.020	b9	0.020	0.065	0.065
a10	0	0.025	0.025	b10	0	0.008	0.008
a11	0	0.007	0.007	b11	0	0.019	0.019
a12	0	0.008	0.008	b12	0	0.003	0.003
a13	0	0.002	0.002	b13	0	0.006	0.006
a14	0	0.003	0.003	b14	0	0.001	0.001
a15	0	0.001	0.001	b15	0	0.002	0.002

Table A-12: Expected (blue) and target (red) field quality at top energy for the new D2 ( $r_0 = 35$  mm). These values represent D2\_errortable\_v4 in Ref. [5]. The value of  $b_2$  requires correction to prevent impact on machine performance due to the large beta-beating induced.

skew	mean	uncertainty	random	normal	mean	uncertainty	random
a2	0	0.679	0.679	b2	$\pm 25 \rightarrow \sim 1$	$2.5 \rightarrow \sim 1$	$2.5 \rightarrow \sim 1$
a3	0	0.282	0.282	b3	$3.0 \rightarrow 1.5$	1.5	1.5
a4	0	0.444	0.444	b4	$\pm 2.0$	0.2	0.2
a5	0	0.152	0.152	b5	-1.0	0.5	0.5
a6	0	0.176	0.176	b6	0	0.060	0.060
a7	0	0.057	0.057	b7	-0.200	0.165	0.165
a8	0	0.061	0.061	b8	0	0.027	0.027
a9	0	0.020	0.020	b9	0.090	0.065	0.065
a10	0	0.025	0.025	b10	0	0.008	0.008
a11	0	0.007	0.007	b11	0.030	0.019	0.019
a12	0	0.008	0.008	b12	0	0.003	0.003
a13	0	0.002	0.002	b13	0	0.006	0.006
a14	0	0.003	0.003	b14	0	0.001	0.001
a15	0	0.001	0.001	b15	0	0.002	0.002

Table A-13: Expected field quality at injection energy for the new Q4 ( $r_0 = 30$  mm). These values represent Q4\_errortable\_v1 in Ref. [5]

skew	mean	uncertainty	random	normal	mean	uncertainty	random
a3	0	0.682	1.227	b3	0	1.282	1.500
a4	0	0.428	0.893	b4	0	0.483	0.465
a5	0	0.177	0.406	b5	0	0.203	0.431
a6	0	0.484	0.277	b6	-10.373	10.373	2.974
a7	0	0.094	0.189	b7	0	0.094	0.189
a8	0	0.193	0.257	b8	0	0.193	0.257
a9	0	0.088	0.088	b9	0	0.088	0.088
a10	0	0.120	0.120	b10	0	3.587	0.956
a11	0	0.326	0.489	b11	0	0.326	0.489
a12	0	0.445	0.222	b12	0	0.445	0.222
a13	0	0.606	0.303	b13	0	0.606	0.303
a14	0	0.827	0.413	b14	0	2.067	0.413
a15	0	1.127	0.564	b15	0	1.127	0.564

Table A-14: Expected field quality at top energy for the new Q4 ( $r_0 = 30$  mm). These values represent Q4\_errortable\_v1 in Ref. [5].

skew	mean	uncertainty	random	normal	mean	uncertainty	random
a3	0	0.682	1.227	b3	0	1.282	1.500
a4	0	0.428	0.893	b4	0	0.483	0.465
a5	0	0.177	0.406	b5	0	0.203	0.431
a6	0	0.484	0.277	b6	0	5.187	1.487
a7	0	0.094	0.189	b7	0	0.094	0.189
a8	0	0.193	0.257	b8	0	0.193	0.257
a9	0	0.088	0.088	b9	0	0.088	0.088
a10	0	0.120	0.120	b10	0	3.587	0.956
a11	0	0.326	0.489	b11	0	0.326	0.489
a12	0	0.445	0.222	b12	0	0.445	0.222
a13	0	0.606	0.303	b13	0	0.606	0.303
a14	0	0.827	0.413	b14	0	2.067	0.413
a15	0	1.127	0.564	b15	0	1.127	0.564



Table A-15: Expected field quality at injection energy for the new Q5 ( $r_0 = 17$  mm). These values represent Q5\_errortable\_v0 in Ref. [5].

skew	mean	uncertainty	random	normal	mean	uncertainty	random
a3	0	0.500	0.900	b3	0	0.940	1.100
a4	0	0.230	0.480	b4	0	0.260	0.250
a5	0	0.070	0.160	b5	0	0.080	0.170
a6	0	0.140	0.080	b6	-3.000	3.000	0.860
a7	0	0.020	0.040	b7	0	0.020	0.040
a8	0	0.030	0.040	b8	0	0.030	0.040
a9	0	0.010	0.010	b9	0	0.010	0.010
a10	0	0.010	0.010	b10	0	0.300	0.080
a11	0	0.020	0.030	b11	0	0.020	0.030
a12	0	0.020	0.010	b12	0	0.020	0.010
a13	0	0.020	0.010	b13	0	0.020	0.010
a14	0	0.020	0.010	b14	0	0.050	0.010
a15	0	0.020	0.010	b15	0	0.020	0.010

Table A-16: Expected field quality at top energy for the new Q5 ( $r_0 = 17$  mm). These values represent Q5\_errortable\_v0 in Ref. [5].

skew	mean	uncertainty	random	normal	mean	uncertainty	random
a3	0	0.500	0.900	b3	0	0.940	1.100
a4	0	0.230	0.480	b4	0	0.260	0.250
a5	0	0.070	0.160	b5	0	0.080	0.170
a6	0	0.140	0.080	b6	0	1.500	0.430
a7	0	0.020	0.040	b7	0	0.020	0.040
a8	0	0.030	0.040	b8	0	0.030	0.040
a9	0	0.010	0.010	b9	0	0.010	0.010
a10	0	0.010	0.010	b10	0	0.300	0.080
a11	0	0.020	0.030	b11	0	0.020	0.030
a12	0	0.020	0.010	b12	0	0.020	0.010
a13	0	0.020	0.010	b13	0	0.020	0.010
a14	0	0.020	0.010	b14	0	0.050	0.010
a15	0	0.020	0.010	b15	0	0.020	0.010

### A.5. References

- [1] HL-LHC Parameter and Layout Committee Parameter table v 4.1.0 (27/8/2014). [https://espace.cern.ch/HiLumi/PLC/\\_layouts/xlviewer.aspx?id=/HiLumi/PLC/SiteAssets/Parameter%20Table.xlsx](https://espace.cern.ch/HiLumi/PLC/_layouts/xlviewer.aspx?id=/HiLumi/PLC/SiteAssets/Parameter%20Table.xlsx)
- [1] G. Arduini, O. Brüning, R. De Maria, R. Garoby, S. Gilardoni, B. Goddard, B. Gorini, M. Meddahi, G. Rumolo and R. Tomás, Beam parameters at LHC injection, CERN-ACC-2014-0006 (2014).
- [2] S. Fartoukh, LHCb crossing scheme for Run II & III, LHC Machine Committee Meeting n. 167, 19/6/2013. [https://espace.cern.ch/lhc-machine-committee/Presentations/1/lmc\\_167/LHCb%20crossing%20scheme%20for%20Run%20II%20and%20III\\_S.Fartoukh.pdf](https://espace.cern.ch/lhc-machine-committee/Presentations/1/lmc_167/LHCb%20crossing%20scheme%20for%20Run%20II%20and%20III_S.Fartoukh.pdf)

- [3] O.S. Brüning, P. Collier, P. Lebrun, S. Myers, R. Ostojic, J. Poole and P. Proudlock (Eds.), LHC Design Report , v.1: the LHC Main Ring, CERN-2004-003-V-1 (2012).
- [4] J.-B. Jeanneret, Geometrical tolerances for the qualification of LHC magnets, LHC Project Report 1007 (2007).
- [5] </afs/cern.ch/eng/lhc/optics/HLLHCV1.0/errors/>

# **Acronyms**



## B. HL-LHC Acronyms

Acronym	Term
a-C	Amorphous carbon
ADT	Transverse damper
ALARA	As low as reasonable achievable
ASIC	Application specific integrated circuit
ATS	Achromatic telescopic squeezing
AUG	Emergency stop buttons
BCMS	Bach compression and beam merging scheme
BETS	Beam energy tracking system
BFPP	Bound-free pair production
BGV	Beam gas vertex profile monitor
BIS	Beam interlock system
BLM	LHC beam loss monitoring system
BPM	Beam position monitor
BRAN	TAN luminosity monitor
BS	Beam screen
BSRT	Synchrotron radiation telescope monitor
CC	Crab cavities
CCB	Cold compressor box
CDD	CERN design directory
CDP	Conductor development programme
CFC	Carbon fibre carbon composites
CMOS	Complementary metal-oxide-semiconductor
COTS	Commercial-off-the-shelf
CVD	Chemical vapour deposition
DA	Dynamic Aperture
DAC	Digital-to-analog converter
DAQ	Data acquisition
DF	Distribution feedbox
DFBAM	Distribution feedbox for arc – IR 7/L
DFBAN	Distribution feedbox for arc – IR 7/R
DPA	Displacements-per-atom
DQW	Double quarter wave cavity
DSs	Dispersion suppressors
DVB	Cryogenic distribution valve box
DWR	Extraction resistors
EC	Electron cloud
EE	Energy extraction systems
EIQA	High voltage qualification
EMD	Electromagnetic dissociation
ERA	European Research Area

ESFRI	European Strategy Forum on Research Infrastructure
EUCARD	Enhanced European Coordination for Accelerator Research and Development
EYETS	Extended yearly technical stop
FMCM	Fast magnet current change monitors
FNAL	Fermi National Accelerator Laboratory
HEB	Hollow electron beam
HL-LHC	High Luminosity Large Hadron Collider
HFM	High-field magnet
HOM	High-order modes
HTS	High temperature superconductor
IBS	Intra-beam scattering
IP	Interaction point
IR	Interaction region
IT	Inner triplet magnets
LARP	LHC Accelerator Research Program
LBDS	LHC beam dumping system
LCB	Lower cold box
LIU	LHC injector complex upgrade
LLRF	Low level RF
LRBB	Long-range beam-beam
LS[X]	Long shutdown [Id Number]
LSS	Long straight section
LVDT	Linear variable differential transformer
MB	Main LHC dipoles
MBH	11 T dipole
MBU	Multiple bit upsets
MCDO	Magnet corrector decapole/octupole
MCS	Magnet corrector sextupole
MD	Machine development
MIM	Multi-band instability monitor
MKB	Diluter dump kicker
MKI	Magnet injection kicker
MP3	Magnet circuits, powering and performance panel
MPP	Machine protection panel
MPS	Machine protection system
MQY	Insertion region wide aperture quadrupole
MS	Matching section
NEG	Non-evaporable getter
NIEL	Non-ionizing energy losses
NIMS	National Institute of Materials Science
P5	Particle Physics Project Prioritization Panel
PIC	Powering interlock system

PIT	Powder-in-tube process
PLC	Programmable logic controller
PU	Pile-up
QPS	Quench protection system
QRL	cryogenic distribution line
QV	Quench buffer
r.m.s.	Root mean square
R2E	Radiation To Electronics
RF	Radio frequency
RFD	RF dipole cavity
RHQT	Rapid-heating, quenching transformation
RRP	Restacked rod process
SC	Superconductor
SCL	Superconducting link
SCRF	Superconducting radio frequency
SEE	Single event effects
SEU	Single bit upsets
SEY	Secondary electron yield
SIL	Safety integrity level
SM	Service module
SPS	Super Proton Synchrotron
SPT	Scheduled proton physics time
SR	Synchrotron radiation
SRF	Superconducting radio frequency
TAXN	Target absorber for insertion region neutrals
TAXS	Target absorber for insertion region secondary
TCAP	Target collimator absorber passive
TCDQ	Collimator for Q4 protection
TCL	Long collimator
TCLA	Target collimator long absorber
TCLD	Auxiliary collimators in DS area
TCPP	Primary collimator with BPM
TCSG	Target collimator secondary graphite
TCSMP	Secondary collimator metallic prototype
TCSP	Secondary collimator with pick-up
TCSPM	Secondary collimator with pick-up metallic
TCT	Target collimators tertiary
TCTP	Target collimator tertiary with pick-up
TCTPM	Target collimator tertiary with pick-up metallic
TDE	Target dump for ejected beam
TDI	Beam absorber for injection
TID	Total ionizing dose

TMCI	Transverse mode coupling instability
TS[X]	Technical stop [Id number]
UA[X]	Service and access tunnel [point number]
UCB	Upper cold box
UFO	Falling particles
UJ[X]	Service cavern [point number]
UPS	Uninterruptable power supplies
VCT	Vacuum chamber transition
VDWB	Vacuum – dump lines – window
VELO	Vertex locator
WBTN	Wide band time normalizer
WCS	Warm compressor station
WIC	Warm magnet interlock system



# **Glossary and Definitions**



### C. Glossary and definitions

<b>Term</b>	<b>Definition</b>
$\beta^*$	Optical $\beta$ -function at the IP.
$\eta$	Machine slip factor.
$\eta_D$	Normalized dispersion, $\eta D = D/\sqrt{\beta}$ , where $D$ is the machine dispersion.
$\gamma$	Optic gamma function, $\gamma(s) = (1 + \alpha^2(s))/\beta(s)$ where $\beta(s)$ is the optical betatron function along the machine and $\alpha(s) = -\frac{d\beta}{2 ds}$ .
$\gamma_r$	The relativistic gamma factor.
<b>Abort gap</b>	Area without any bunches in the bunch train that fits the time required for building up the nominal field of the LHC dump kicker.
<b>Arc</b>	The part of the ring occupied by regular half-cells. Each arc contains 46 half cells. The arc does not contain the dispersion suppressor.
<b>Arc cell</b>	Consists of two arc half-cells and presents the basic period of the optic functions.
<b>Arc half-cell</b>	Periodic part of the LHC arc lattice. Each half-cell consists of a string of three twin aperture main dipole magnets and one short straight section. The cryo magnets of all arc half-cells follow the same orientation with the dipole lead end pointing upstream of Beam 1 (downstream of Beam 2).
<b>Batch</b>	PS batch: train of 72 bunches that is injected into the SPS in one PS to SPS transfer. SPS batch: Train of $4 \times 72$ or $3 \times 72$ bunches that is injected into the LHC in one SPS to LHC transfer.
<b>Beam 1 and Beam 2</b>	Beam 1 and Beam 2 refer to the two LHC beams. Beam 1 circulates clockwise in Ring 1 and Beam 2 circulates counter clockwise in Ring 2. If colours are used for beams, Beam 1 is marked blue and Beam 2 is marked red.
<b>Beam cleaning</b>	Removal of the large amplitude (larger than $6 \sigma$ ) particles from the beam halo. The LHC has two beam cleaning insertions: one is dedicated to the removal of particles with large transverse oscillation amplitudes (IR7) and one dedicated to the removal of particles with large longitudinal oscillation amplitudes (IR3). These insertions are also referred to as the betatron and momentum cleaning or collimation insertions.
<b>Beam crossing angle</b>	Dedicated orbit bumps separate the two LHC beams at the parasitic beam crossing points of the common beam pipe of Ring 1 and Ring 2. The crossing angle bumps do not separate the beams at the IP, but only at the parasitic crossing points. These orbit bumps generate an angle between the orbit of Beam 1 and Beam 2 at the IP. The full angle between the orbit of Beam 1 and Beam 2 is called the crossing angle. In IR2 and IR8 the crossing angle orbit bumps consist of two separate contributions. One external bump generated for the beam separation at the parasitic beam crossing points and one internal bump generated by the experimental spectrometer and its compensator magnets. The LHC baseline foresees vertical crossing angles in IR1 and IR2 and horizontal crossing angles in IR5 and IR8.
<b>Beam half-life</b>	Time during beam collision after which half the beam intensity is lost.
<b>Beam screen</b>	Perforated tube inserted into the cold bore of the superconducting magnets in order to protect the cold bore from synchrotron radiation and ion bombardment.
<b>Beam types</b>	<b>Pilot beam:</b> consists of a single bunch of $0.5 \times 10^{10}$ protons. It corresponds to the maximum beam current that can be lost without inducing a magnet quench.

	<p><b>Commissioning beam:</b> beam tailored for a maximum luminosity with reduced total beam power (i.e. increased operational margins related to beam losses and magnet quenches) and possibly smaller beam sizes (i.e. increased mechanical acceptance in terms of the transverse beam size and larger tolerances for orbit and <math>\beta</math>-beat).</p> <p><b>Intermediate beam:</b> beam tailored for a high accuracy of the beam measurements with reduced total beam power (i.e. increased operational margins related to beam losses and magnet quenches).</p> <p><b>Nominal beam:</b> beam required to reach the design luminosity of <math>L = 10^{34} \text{ cm}^{-2} \text{ s}^{-1}</math> with <math>\beta^* = 0.55 \text{ m}</math> (<math>\rightarrow</math> normalized emittance <math>\epsilon_n = 3.75 \text{ } \mu\text{m}</math>; <math>N_b = 1.15 \times 10^{11}</math>; <math>n_b = 2808</math>).</p> <p><b>Ultimate beam:</b> beam consisting of the nominal number of bunches with nominal emittances (normalized emittance of <math>3.75 \text{ } \mu\text{m}</math>) and ultimate bunch intensities (<math>I = 0.86 \text{ A} \rightarrow N_b = 1.7 \times 10^{11}</math>). Assuming the nominal value of <math>\beta^* = 0.55 \text{ m}</math> and 2808 bunches, the ultimate beam can generate a peak luminosity of <math>L = 2.3 \times 10^{34} \text{ cm}^{-2} \text{ s}^{-1}</math> in the two high luminosity experiments.</p>
<b>BPM</b>	Beam position monitor.
<b>Bunch</b>	Collection of particles captured within one RF bucket.
<b>Bunch duration</b>	<p>The bunch duration is defined as</p> $\sigma_t = \frac{\sigma_s}{v},$ <p>where <math>\sigma_s</math> is the bunch length and <math>v</math> is the speed of the particles in the storage rings.</p>
<b>Bunch length</b>	The bunch length is defined as the r.m.s. value of the longitudinal particle distribution in one RF bucket. The bunch length is denoted as $\sigma_s$ .
<b>Busbar</b>	Main cable that carries the current for powering the magnets outside the magnet coil.
<b>Channel</b>	The two apertures of the double bore magnets form two channels through the LHC. Each arc has one outer and one inner channel.
<b>Cold mass</b>	The cold mass refers to the part of a magnet that needs to be cooled by the cryogenic system, i.e. the assembly of magnet coils, collars, iron yoke, and helium vessel.
<b>Crossings</b>	The two machine channels cross at the experimental insertions, i.e. at IP1, IP2, IP5, and IP8.
<b>Cryo magnet</b>	Complete magnet system integrated into one cryostat, i.e. main magnet coils, collars and cryostat, correction magnets, and powering circuits.
<b>DA</b>	See dynamic aperture
<b>Damper</b>	Transverse or longitudinal feedback system used to damp injection oscillations and/or multi-bunch instabilities of a beam.
<b>Damping time</b>	<p>Time after which an oscillation amplitude has been reduced by a factor <math>1/e</math>.</p> <p><b>Longitudinal emittance damping time:</b> Half of the longitudinal amplitude damping time for a Gaussian approximation of the bunch distribution.</p> <p><b>Transverse emittance damping time:</b> half of the transverse amplitude damping time for a Gaussian approximation of the transverse bunch distribution.</p> <p>If no explicit mentioning of the types of damping times is given the damping times refer to the amplitude damping times.</p>
<b>Decay and snap back</b>	Persistent current decay is a change in the persistent current contribution to the total magnetic field in superconducting magnets powered at constant current (e.g. at injection). This effect varies among magnets and is a function of the powering history (i.e. previous current cycles). When the magnet current is changed (e.g. during the acceleration ramp) the magnetic field comes back to the original value before the

	decay. This effect is called snap back and occurs for the LHC main dipole magnets within the first 50 A change of the LHC ramp.
<b>Dispersion suppressor</b>	The dispersion suppressor refers to the transition between the LHC arcs and insertions. The dispersion suppressor aims at a reduction of the machine dispersion inside the insertions. Each LHC arc has one dispersion suppressor on each end. The length of the dispersion suppressors is determined by the tunnel geometry. Each LHC dispersion suppressor consists of four individually powered quadrupole magnets that are separated by two dipole magnets. This arrangement of four quadrupole and eight dipole magnets is referred to as two missing dipole cells. For the machine lattice these two missing dipole cells are referred to as one dispersion suppressor. However, reducing the dispersion at the IPs to zero requires a special powering of two more quadrupole magnets on each side of the arc. In terms of the machine optics the dispersion suppressor refers therefore to the two missing dipole cells plus one additional arc cell.
<b>Dogleg magnets</b>	Special dipole magnet used for increasing the separation of the two machine channels from standard arc separation. The dogleg magnets are installed in the cleaning insertions IR3 and IR7 and the RF insertion IR4.
<b>Dynamic aperture</b>	Maximum initial oscillation amplitude that guarantees stable particle motion over a given number of turns. The dynamic aperture is normally expressed in multiples of the RMS beam size ( $\sigma$ ) and together with the associated number of turns.
<b>Eddy currents</b>	Eddy currents are screening currents that tend to shield the interior of a conductor or a superconducting cable from external magnetic field changes. In the case of a strand the eddy currents flow along the superconducting filaments in the strand (without loss) and close across the resistive matrix of the strand (copper for the LHC). In the case of a cable the eddy currents flow along the strands (without loss) and close resistively at the contact points among strands in the cable. Eddy currents are also referred to as coupling currents.
<b>Energy spread</b>	The energy spread is defined as the 'RMS' value of the relative energy deviations from the nominal beam energy in a particle distribution. The energy spread is denoted as $\sigma_{\delta E}/E_0.$
<b>Experimental insertion region</b>	Insertion region that hosts one of the four LHC experiments.
<b>Filament</b>	Superconducting filaments are fine wires of bulk superconducting material with typical dimension in the range of a few microns. The superconducting filaments are embedded in the resistive matrix in a strand.
<b>Hourglass effect <math>H</math></b>	Luminosity loss due to longitudinal modulation of beta function over the length of the bunch for small $\beta^*$ .
<b>Insertion region (IR)</b>	Machine region between the dispersion suppressors of two neighboring arcs. The insertion region consists of two matching sections and, in the case of the experimental insertions, of two triplet assemblies and the separation/recombination dipoles.
<b>Interaction point (IP)</b>	Middle of the insertion region (except for IP8). In the insertions where the two LHC beams cross over, the IP indicates the point where the two LHC beams can intersect. In IR8 the experimental detector is shifted by 3/2 RF wavelength and the IP refers to the point where the two LHC beams can intersect and does not coincide with the geometric centre of the insertion.

<b>Ions</b>	The LHC foresees collisions between heavy ions, $^{208}\text{Pb}^{82+}$ (fully stripped) during the first years (208 is the number of nucleons, 82 the number of protons of this particular nucleus).
<b>Ions, nominal scheme</b>	Approximately 600 bunches per beam, with $7 \times 10^7$ Pb ions each, are colliding at 2.76 TeV/u to yield an initial luminosity of $L = 1.0 \times 10^{27} \text{ cm}^{-2} \text{ s}^{-1}$ where $\beta^* = 0.5 \text{ m}$ .
<b>Ions, early scheme</b>	Approximately 60 bunches per beam, with $7 \times 10^7$ Pb ions each, are colliding to yield an initial luminosity of $L = 5.0 \times 10^{25} \text{ cm}^{-2} \text{ s}^{-1}$ with ( $\beta^* = 0.5 \text{ m}$ ).
<b>Lattice correction magnets</b>	Correction magnets that are installed inside the short straight section assembly.
<b>Lattice version</b>	Lattice version refers to a particular hardware installation in the tunnel. It is clearly separated from the optics version and one lattice version can have more than one optics version.
<b>Left, right</b>	See the definition under ‘right and left’.
<b>Long-range interactions</b>	Interaction between the two LHC beams in the common part of Ring 1 and Ring 2 where the two beams are separated by the crossing angle orbit bumps.
<b>Long straight section (LSS)</b>	The quasi-straight sections between the upstream and downstream dispersion suppressor of an insertion, including the separation/recombination dipole magnets.
<b>Longitudinal emittance</b>	The longitudinal emittance is defined as: $\epsilon_s = 4\pi\sigma_t\sigma_{\delta E/E_0}E_0,$ where $\sigma_t$ is the bunch duration in seconds, and $\sigma_{\delta E/E_0}$ the relative energy spread.
<b>Luminosity half-life</b>	Time during beam collision after which the luminosity is halved. The luminosity half-life is generally smaller than the beam half-life.
<b>Luminous region</b>	The 3D distribution of the collision event vertices.
<b>Luminosity reduction</b>	<b>Geometric luminosity reduction factor due to beam offset <math>R</math>:</b> Reduced beam overlap due to transversal offset of collisions, frequently used for reduction of luminosity (levelling) and Van der Meer scans. <b>Luminosity reduction factor due to crossing angle <math>S</math>:</b> reduced beam overlap due to tilted bunch shape due to crossing angle. <b>Total luminosity reduction factor <math>F = R^*H^*S</math></b> (Strictly speaking here there is no direct multiplication, but provides a reasonable indication of the different contributions, while dominated by the crossing angle contribution).
<b>Machine cycle</b>	The machine cycle refers to one complete operation cycle of a machine, i.e. injection, ramp-up, possible collision flat-top, ejection, and ramp-down. The minimum cycle time refers to the minimum time required for a complete machine cycle.
<b>Machine statistics</b>	Run time: annual time allocated to running with beam [days]. Scheduled physics time: annual time allocated to physics (excluding initial beam commissioning, scrubbing, TS, recovery from TS, MDs, special physics) [days]. Physics efficiency: time with both beams present and stable beams, versus scheduled physics time [%]. Machine availability: time during which the machine is in a state allowing operations to take beam and run through a nominal physics cycle, versus run time [%]. Turnaround time: time between the end of one and the start of the next physics run/data taking by the experiments (delimited by the loss of beam presence/beam dump back to declaration of stable beams) [hours].

	Recovery time: time between the end of one cycle and the readiness for injection of new particles for the next cycle (delimited by the loss of beam presence/beam dump and resumption of the normal operational cycle) [hours].
<b>Magnet quench</b>	Loss of the superconducting state in the coils of a superconducting magnet.
<b>Main lattice magnets</b>	Main magnets of the LHC arcs, i.e. the arc dipole and quadrupole magnets.
<b>Matching section</b>	Arrangement of quadrupole magnets located between the dispersion suppressor and the triplet magnets (or the IP for those insertions without triplet magnets). Each insertion has two matching sections: one upstream and one downstream from the IP.
$n_1$	The effective mechanical aperture $n_1$ defines the maximum primary collimator opening in terms of the r.m.s. beam size that still guarantees a protection of the machine aperture against losses from the secondary beam halo. It depends on the magnet aperture and geometry and the local optics perturbations.
$N_b$	Number of particles per bunch.
$n_b$	Number of bunches per beam.
<b>Nominal bunch</b>	Bunch parameters required to reach the design luminosity of $L = 1034 \text{ cm}^{-2} \text{ s}^{-1}$ where $\beta^* = 0.55 \text{ m}$ . The nominal bunch intensity is $N_b = 1.15 \times 10^{11}$ protons.
<b>Nominal powering</b>	Hardware powering required to reach the design beam energy of 7 TeV.
<b>Normalized transverse emittance</b>	<p>The beam emittance decreases with increasing beam energy during acceleration and a convenient quantity for the operation of a hadron storage rings (and linear accelerators) is the ‘normalized emittance’ defined as</p> $\epsilon_n = \epsilon \gamma_r \beta_r,$ <p>where <math>\gamma_r</math> and <math>\beta_r</math> are the relativistic gamma and beta factors</p> $\beta_r = \frac{v}{c}$ $\gamma_r = \frac{1}{\sqrt{1 - \beta_r^2}}$ <p>where <math>v</math> is the particle velocity and <math>c</math> the speed of light in vacuum. The nominal normalized transverse emittance for the LHC is <math>\epsilon_n = 3.75 \text{ } \mu\text{m}</math>.</p>
<b>Octant</b>	An octant starts in the center of an arc and goes to the centre of the next downstream arc. An octant consists of an upstream and a downstream half-octant. A half-octant and a half-sector cover the same part of the machine even though they may not have the same number.
<b>Optical configuration</b>	An optical configuration refers to a particular powering of the LHC magnets. Each optics version has several optical configurations corresponding to the different operational modes of the LHC. For example, each optics version has a different optical configuration for injection and luminosity operation, and for luminosity operation the optics features different optical configurations corresponding to different $\beta^*$ values in the four experimental insertions of the LHC.
<b>Optics version</b>	The optics version refers to a consistent set of optical configurations. There can be several different optics versions for one lattice version.
<b>Pacman bunches</b>	Bunches that do not experience the same number of long-range beam–beam interactions left and right from the IP.
<b>Parallel separation</b>	Dedicated orbit bumps separate the two LHC beams at the IP during injection, ramp, and the optics squeeze. The total beam separation at the IP is called the parallel

	separation. The LHC baseline foresees horizontal parallel separations in IR1 and IR2 and vertical separations in IR5 and IR8.
<b>Parasitic crossing points</b>	Positions in the common part of the Ring 1 and Ring 2 where the two beams can experience long-range interactions.
<b>Persistent currents</b>	Persistent currents are eddy currents with (ideally) infinitely long time constants that flow in the bulk of the superconducting filaments of a strand and tend to shield the interior of the filament from the external magnetic field changes. These screening currents close inside the superconducting filament, with zero resistance (in steady state). Hence, for practical purposes, they do not decay in time and for this reason they are referred to as ‘persistent’.
<b>Physics run</b>	Machine operation at top energy with luminosity optics configuration and beam collisions.
<b>Pile-up</b>	<p><b>Event pile-up <math>\mu</math>:</b> number of visible inelastic proton–proton interactions in a given bunch crossing.</p> <p>Average pile-up: mean value of the pile-up over a fill (averaged over all bunchcrossings).</p> <p>Peak pile-up: maximum pile-up in any bunch crossing at any time (usually at the start of the fill).</p> <p>Peak average pile-up: mean pile-up at the beginning of the fill. It corresponds to the peak luminosity of the fill. In practice, it is determined as the maximum of the pile-up values obtained by averaging over all bunch crossings within time intervals of typically one minute.</p> <p>Average pile-up density: number of inelastic proton–proton interactions in a given bunch-crossing divided by the size of the luminous region in <math>Z</math>.</p>
<b>Pilot bunch</b>	Bunch intensity that assures no magnet quench at injection energy for an abrupt loss of a single bunch but is still large enough provide BPM readings. The pilot bunch intensity of the LHC corresponds to $0.5 \times 10^{10}$ protons in one bunch.
<b>Piwinski parameter</b>	Parameterization of reduced beam overlap due to finite crossing angle.
<b>Ramp</b>	Change of the magnet current. During the beam acceleration the magnets are ‘ramped up’ and after the end of a physics store the magnets are ‘ramped down’.
<b>Resistive matrix</b>	One of the two main constituents of the strand. The resistive matrix embeds the filaments in the strand and provides a low resistance current shunt in case of quench (transition of superconducting material to the normal state).
<b>RF bucket</b>	The RF system provide a longitudinal focusing that constrains particle motion in the longitudinal phase space to a confined region called the RF bucket.
<b>Right, left</b>	Describes the position in the tunnel relative to an observer inside the ring looking out (same definition as for LEP).
<b>Ring 1 and Ring 2</b>	There are two rings in the LHC, one ring per beam. Ring 1 corresponds to Beam 1, which circulates clockwise, and Ring 2 corresponds to Beam 2, which circulates counter-clockwise in the LHC.
<b>Satellite bunch</b>	Collection of particles inside RF buckets that do not correspond to nominal bunch positions. The nominal bunch spacing for the LHC is 25 ns, while the separation of RF buckets is 2.5 ns. In other words, there are nine RF buckets between two nominal LHC bunch positions that should be empty.
<b>Sector</b>	The part of a ring between two successive insertion points (IP) is called a sector. Sector 1-2 is situated between IP1 and IP2.



<b>Separation/recombination magnets</b>	Special dipole magnets left and right from the triplet magnets that generate the beam crossings in the experimental insertions.
<b>Short straight section (SSS)</b>	Assembly of the arc quadrupole and the lattice corrector magnets. Each SSS consists of one quadrupole magnet, one beam position monitor (BPM), one orbit corrector dipole (horizontal deflection for focusing and vertical deflection for defocusing quadrupoles), one lattice correction element (i.e. trim or skew quadrupole elements or octupole magnets). and one lattice sextupole or skew sextupole magnet.
<b>Special straight section (SPSS)</b>	Quadrupole assemblies of the insertion regions. The SPSS features no lattice corrector and sextupole magnets and has only orbit correction dipole magnets and BPMs.
<b>Spool piece correction magnets</b>	Correction magnets directly attached to the main dipole magnets. The spool piece correction magnets are included in the dipole cryostat assembly
<b>Strand</b>	A superconducting strand is a composite wire containing several thousands of superconducting filaments dispersed in a matrix with suitably small electrical resistivity properties. The LHC strands have Nb-Ti as their superconducting material and copper as the resistive matrix.
<b>Superconducting cable</b>	Superconducting cables are formed from several superconducting strands in parallel, geometrically arranged in the cabling process to achieve well-controlled cable geometry and dimensions, while limiting strand deformation in the process. Cabling several strands in parallel results in an increase of the current carrying capability and a decrease of the inductance of the magnet, easing protection. The LHC cables are flat, keystone cables of the so-called Rutherford type.
<b>Super pacman bunches</b>	Bunches that do not collide head-on with a bunch of the other beam in one of experimental IPs.
<b>Synchrotron radiation damping times</b>	<p><b>Longitudinal amplitude damping time:</b> the ratio of the average rate of energy loss (energy lost over one turn divided by the revolution time) and the nominal particle energy.</p> <p><b>Transverse amplitude damping time:</b> time after which the transverse oscillation amplitude has been reduced by a factor <math>1/e</math> due to the emission of synchrotron radiation. For a proton beam it is just twice the longitudinal amplitude damping time due to the emission of synchrotron radiation.</p> <p>If no explicit mentioning of the types of damping times is given the damping times refer to the amplitude damping times.</p>
<b>TAN</b>	Target absorber neutral: absorber for the neutral particles leaving the IP. It is located just in front of the D1 separation/recombination dipole magnet on the side facing the IP.
<b>TAS</b>	Target absorber secondaries: absorber for particles leaving the IP at large angles. It is located just in front of the Q1 triplet quadrupole magnet on the side facing the IP.
<b>Transverse beam size</b>	The transverse beam size is defined as the r.m.s. value of the transverse particle distribution.
<b>Transverse emittance</b>	<p>The transverse emittance is defined through the invariance of the area enclosed by the single particle phase space ellipse. The single particle invariant under the transformation through the storage ring is given by</p> $A = \gamma x^2 + 2\alpha x x' + \beta x'^2,$ <p>where <math>\alpha</math>, <math>\beta</math>, and <math>\gamma</math> are the optical functions. The area enclosed by the single particle phase space ellipse is given by</p>

	<p style="text-align: center;">area of ellipse = <math>\pi A</math></p> <p>For an ensemble of particles the emittance is defined as the average of all single particle invariants (areas enclosed by the single particle phase space ellipsoids divided by <math>\pi</math>).</p> <p>The transverse betatron beam size in the storage ring can be written in terms of the beam emittance as</p> $\sigma_{x,y}(s) = \sqrt{\beta_{x,y}(s)\epsilon_{x,y}},$ <p>where <math>\beta_{x,y}(s)</math> is the optical <math>\beta</math>-function along the storage ring.</p> <p>The transverse emittance is given by the following expression:</p> $\epsilon_z = \sqrt{\langle z^2 \rangle \langle z'^2 \rangle - \langle z z' \rangle^2}; z = x, y,$ <p>where it is assumed that the particle coordinates are taken at a place with vanishing dispersion and where <math>\langle \rangle</math> defines the average value of the coordinates over the distribution. <math>z</math> and <math>z'</math> are the canonical transverse coordinates (<math>z = x, y</math>).</p>
<b>Triplet</b>	Assembly of three quadrupole magnets used for a reduction of the optical $\beta$ -functions at the IPs. The LHC triplet assembly consists in fact of four quadrupole magnets but the central two quadrupole magnets form one functional entity. The LHC has triplet assemblies in IR1, IR2, IR5, and IR8.
<b>Tune</b>	Number of particle trajectory oscillations during one revolution in the storage ring (transverse and longitudinal).
<b>Ultimate bunch intensity</b>	Bunch intensity corresponding to the expected maximum acceptable beam–beam tune shift with two operating experimental insertions. Assuming the nominal emittance (normalized emittance of $3.75 \mu\text{m}$ ) the ultimate bunch intensity corresponds to $1.7 \times 10^{11}$ protons per bunch.
<b>Ultimate powering</b>	Hardware powering required to reach the ultimate beam energy of 7.54 TeV, corresponding to a dipole field of 9 T.
<b>Upstream and downstream</b>	Always related to the direction of one of the two beams. If no beam is specified then Beam 1 is taken as the default. This implies that stating a position as being ‘upstream’ without indicating any beam is equivalent to stating that the position is to the left.

